

2015  
NNIN  
REU  
RA

National Nanotechnology Infrastructure Network

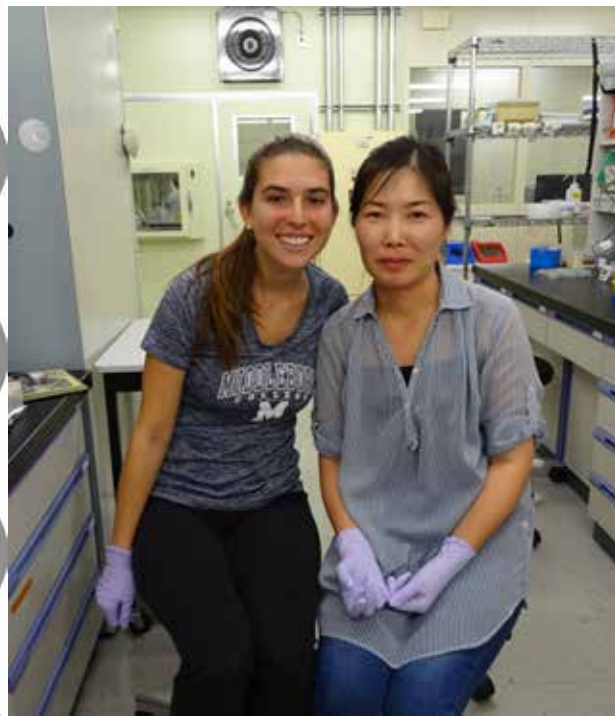
# 2015 NNIN REU

## Research Accomplishments

<b>NNIN REU Reports by Section</b> . . . . .	<b>ii-x</b>
<b>Corporate Sponsors</b> . . . . .	<b>iii</b>
<b>Photography Credits</b> . . . . .	<b>x</b>
<b>Welcome from NNIN Director</b> . . . . .	<b>xi</b>
<b>Thank you! From the Coordinators</b> . . . . .	<b>xii-xiii</b>
<b>Epilogue by NNIN Deputy Director</b> . . . . .	<b>xiv-xvi</b>
<b>NNIN Interns by Site</b> . . . . .	<b>xvii-xxv</b>
ASU NanoFab, Arizona State University .....	xvii
Cornell NanoScale Science & Technology Facility, Cornell University .....	xvii
Institute for Electronics and Nanotechnology, Georgia Institute of Technology .....	xviii
Center for Nanoscale Systems, Harvard University .....	xviii
Howard Nanoscale Science & Engineering Facility, Howard University .....	xix
Penn State Nanofabrication Facility, The Pennsylvania State University .....	xix
Stanford Nanofabrication Facility, Stanford University .....	xx
UCSB Nanofabrication Facility, University of California, Santa Barbara .....	xx
Colorado Nanofabrication Laboratory, University of Colorado, Boulder .....	xxi
Lurie Nanofabrication Facility, University of Michigan, Ann Arbor .....	xxi
Minnesota Nano Center, University of Minnesota-Twin Cities .....	xxii
Microelectronics Research Center, The University of Texas at Austin .....	xxii
Washington Nanofabrication Facility & Molecular Analysis Facility, University of Washington .....	xxiii
Nano Research Facility, Washington University at St. Louis .....	xxiii
NNIN International Research Experience for Graduates (iREG) Program ....	xxiv
NNIN International Research Experience for Undergraduates (iREU) Program .....	xxv
<b>Common Abbreviations</b> . . . . .	<b>xxvi-xxviii</b>
<b>2015 Research Accomplishments</b> . . . . .	<b>2-185</b>
<b>Indexes</b> . . . . .	<b>187-192</b>



## Biological Applications, pages 2-45



Enhancement of High-Performance Graphene Biosensors for Cancer Detection.....	2
<i>Victor Pablo Acero</i>	
<i>NNIN REU Site: University of Minnesota-Twin Cities</i>	
A PEDOT:PSS Process on Textiles for Health Monitoring .....	4
<i>Mariella Arias</i>	
<i>NNIN iREU Site: MINES Saint-Étienne, France</i>	
Tablet Analysis and Display of Semiconductor Biosensors .....	6
<i>Raymond Barakat</i>	
<i>NNIN REU Site: The University of Texas at Austin</i>	
Synergistic Effect of Adhesive Ligand Density and Soluble Factor TGF- $\beta$ on Epithelial Mesenchymal Transition Progression .....	8
<i>Allison Bosworth</i>	
<i>NNIN iREU Site: NIMS, Tsukuba, Ibaraki, Japan</i>	
Fully Printed Organic Electrochemical Transistor on Paper for Glucose Sensing .....	10
<i>Christopher Davidson</i>	
<i>NNIN iREU Site: MINES Saint-Étienne, France</i>	
Imaging Live DU145 Cancer Cells Using Scanning Probe Microscope.....	12
<i>Catherine Demos</i>	
<i>NNIN REU Site: Howard University</i>	
Exploration of Protein Capture Methods for Applications in Microfluidic Devices .....	14
<i>Matthew Devlin</i>	
<i>NNIN REU Site: Cornell University</i>	
Research in a Diagnostic Method for Light Chain Amyloidosis .....	16
<i>Shaun Engelmann</i>	
<i>NNIN REU Site: Washington University in St. Louis</i>	
Optimization of Nanoparticle Delivery to Plants: Do Nanoparticle Properties Affect Cellular Internalization? .....	18
<i>Christina Franke</i>	
<i>NNIN REU Site: Washington University in St. Louis</i>	
Development of a Microfluidic Mimic of the Human Microvasculature to Study Sickle Cell Disease .....	20
<i>Michelle Galarneau</i>	
<i>NNIN REU Site: University of Minnesota-Twin Cities</i>	
Small Interfering RNA Delivery for the Treatment of Hereditary Bone Disease.....	22
<i>Staci Hill</i>	
<i>NNIN iREU Site: NIMS, Tsukuba, Ibaraki, Japan</i>	
Optimization and Characterization of Au Nanoparticle-DNA Conjugate Devices.....	24
<i>Joseph P. Hittinger</i>	
<i>NNIN REU Site: University of Washington</i>	

**Optimization of a Capacitive Sensing Organic  
Electrochemical Transistor Immunoassay.....26**

*Lucy Hu*

*NNIN iREU Site: MINES Saint-Étienne, France*

**The Wrinkling of Thin Elastic  
Membranes as a Cancer Diagnostic .....28**

*Adam Kunesh*

*NNIN REU Site: Arizona State University*

**Fabrication and Design of EGFET Devices for Biosensing.....30**

*Abigail Magee*

*NNIN REU Site: Arizona State University*

**Influence of Cell Spreading Area  
on Uptake of Gold Nanoparticles.....32**

*Adriana Mulero*

*NNIN iREU Site: NIMS, Tsukuba, Ibaraki, Japan*

**Nanoplasmonic Biosensing Microfluidics  
for Immune Status Monitoring of Critically-Ill Children.....34**

*Taylor Pauls*

*NNIN REU Site: University of Michigan, Ann Arbor*

**Currently Unavailable per Principal Investigator .....36**

*Erin Rousseau*

*NNIN REU Site: Georgia Institute of Technology*

**A High-Throughput Image-Processing Based Analysis of  
Dynamic Cell Surface Interactions in a Microfluidic Chip....38**

*Brian Ryu*

*NNIN REU Site: Georgia Institute of Technology*

**High-Throughput Drug Screening *in vivo*  
Using Droplet Microfluidics.....40**

*Alejandro Sanchez*

*NNIN REU Site: Harvard University*

**Micropatterns and PDMS Microdevices  
for the Investigation of Cardiac Muscle  
Cell Structure and Function .....42**

*Anisa Swei*

*NNIN REU Site: Cornell University*

**Development of Dual-Modality Nanoparticles for PET/MR.....44**

*Cyrus Thompson*

*NNIN REU Site: Washington University in St. Louis*



• Corporate Sponsors •

• Agilent Technologies • Analog Devices • Applied Materials •

• Canon • Daihen • Ericsson • IBM • Infineon • Intel •

• MERI JSC • NEC • Qualcomm • Renesas Electronics •

• Robert Bosch • SIX Semiconductores • STMicroelectronics •

• Texas Instruments • Toshiba • Ultratech •

## Chemistry, pages 46-57



Optimization of Thin Film Composite Polyimide Reverse Osmosis Membrane by Polyethylene Glycol for Enhanced Fouling Resistance.....46

*Jyoti Campbell*

*NNIN REU Site: Washington University in St. Louis*

Twisting a C=C Double Bond in Crowded Alkenes: The Synthesis and Characterization of Small-Molecule Electron Acceptors .....48

*Dylan J. Freas*

*NNIN iREU Site: NIMS, Tsukuba, Ibaraki, Japan*

Crumpled Graphene Oxide-Polysulfone Composite Membranes for Water Purification.....50

*Isaac Fuhrman*

*NNIN REU Site: Washington University in St. Louis*

Advanced Dielectrics for Microelectronics: Chemically Amplified, Low- $\kappa$  Materials .....52

*Masashi Fukuzawa*

*NNIN iREG Site: Georgia Institute of Technology*

Surface Adsorption and Enzymatic Hydrolysis of Polyphosphates: Implications for Understanding Phosphorus Cycling .....54

*Margot Hultz*

*NNIN REU Site: Georgia Institute of Technology*

Designing a Conjugated Polymer Consisting of Phenyl-Oxazole Derivatives Using C-H/C-O Coupling .....56

*Alin Miksi Kalayjian*

*NNIN REU Site: University of Washington*



## Electronics, pages 58-73

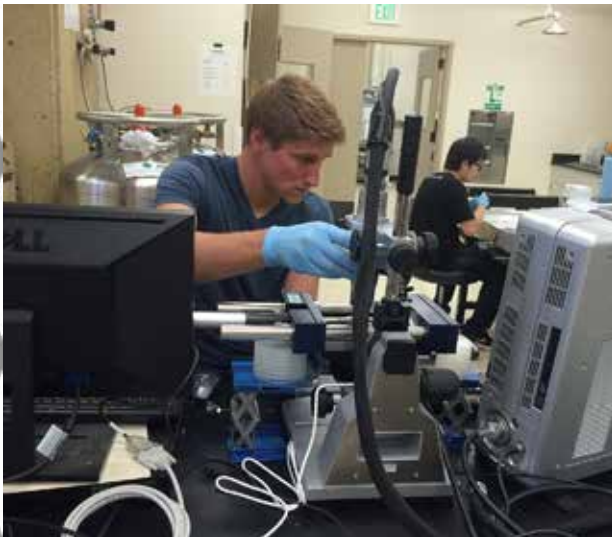
Vanishing Programmable Resources: Design, Materials, and Characterization .....	58
<i>Mary E. Alsobrooks</i> NNIN REU Site: Georgia Institute of Technology	
Electrostatic Gating of MBE-Grown NdTiO <sub>3</sub> Thin Films .....	60
<i>Emilie Benson</i> NNIN REU Site: University of Minnesota-Twin Cities	
Optimizing Contact Resistance for Improved MoS <sub>2</sub> Device Performance .....	62
<i>Justin Goodwill</i> NNIN REU Site: The Pennsylvania State University	
Enhanced Mobility in an Insulator Capped 2D Electron Gas at SrTiO <sub>3</sub> <100> Surface.....	64
<i>Nathan Huber</i> NNIN REU Site: The Pennsylvania State University	
Fiber Flow Rate Sensors Using Thermally Drawn Multi-Material Fluidic Channel Fibers.....	66
<i>Corey Kwok</i> NNIN REU Site: The University of Texas at Austin	
Optimizing Insulator Layer Deposition for Diamond MOSFETs .....	68
<i>Tara Nietzold</i> NNIN iREU Site: NIMS, Tsukuba, Ibaraki, Japan	
Graphene Junction Field-Effect Transistors on a Silicon Carbide Substrate .....	70
<i>Andrea Randolph</i> NNIN REU Site: University of Colorado, Boulder	
Evaluation of TiO <sub>2</sub> as Carrier Selective Contact for High Efficiency Photovoltaic Applications.....	72
<i>Alexander Rosner</i> NNIN REU Site: Arizona State University	



## Materials, pages 74-113

Growth of Graphene by Silicon Carbide Sublimation .....	74
<i>Tanaka Benton</i> NNIN REU Site: Howard University	
Electric Field-Directed Assembly of Nanowires on Patterned Electrodes .....	76
<i>Nermina Brljak</i> NNIN REU Site: The Pennsylvania State University	
ZnO Deposition Methods for Opto-Electronic Applications ....	78
<i>Benjamin Carberry</i> NNIN REU Site: University of California, Santa Barbara	
Mechanical Testing of OPVs using Flextrode: An ITO-Free, Transparent, Polymer-Based Electrode .....	80
<i>Isaac DiGennaro</i> NNIN REU Site: Stanford University	





## Materials, continued

**Infiltration, Imidization, and Cross-Linking  
of Polyimides in Molecular-Scale Confinement .....**82

**Jade Fostvedt**  
NNIN REU Site: *Stanford University*

**Ultrathin, Smooth, and Stable Doped Silver Films.....**84

**Tom George**  
NNIN REU Site: *University of Michigan, Ann Arbor*

**Diblock Copolymers for Diamond  
Patterning and Applications.....**86

**Lorelis González López**  
NNIN REU Site: *Howard University*

**Characterization of Graphene Growth on Pt<111> .....**88

**Taliya Gunawansa**  
NNIN iREU Site: *NIMS, Tsukuba, Ibaraki, Japan*

**Al-Induced Crystallization of Si Thin Films  
on Flexible Glass Substrates .....**90

**Sophia Hu**  
NNIN REU Site: *The Pennsylvania State University*

**Investigation of the Thermoelectric Properties  
of Boron Carbide-Hafnium Diboride Composite Materials ..**92

**Jon-L Innocent-Dolor**  
NNIN iREU Site: *NIMS, Tsukuba, Ibaraki, Japan*

**Carbon Materials Assisted ZnO Nanowire Array Composites  
for Enhanced Photoelectrochemical Water Oxidation.....**94

**Samantha Kang**  
NNIN iREU Site: *NIMS, Tsukuba, Ibaraki, Japan*

**Fundamental Studies of the Synthesis of Graphene  
Using Plasma Enhanced CVD Processes.....**96

**Yasunori Kutsuma**  
NNIN iREG Site: *Georgia Institute of Technology*

**Nanofabrication and Characterization of Quasicrystal  
Metasurfaces using Shadow-Sphere Lithography .....**98

**Emily MacDonald**  
NNIN REU Site: *Harvard University*

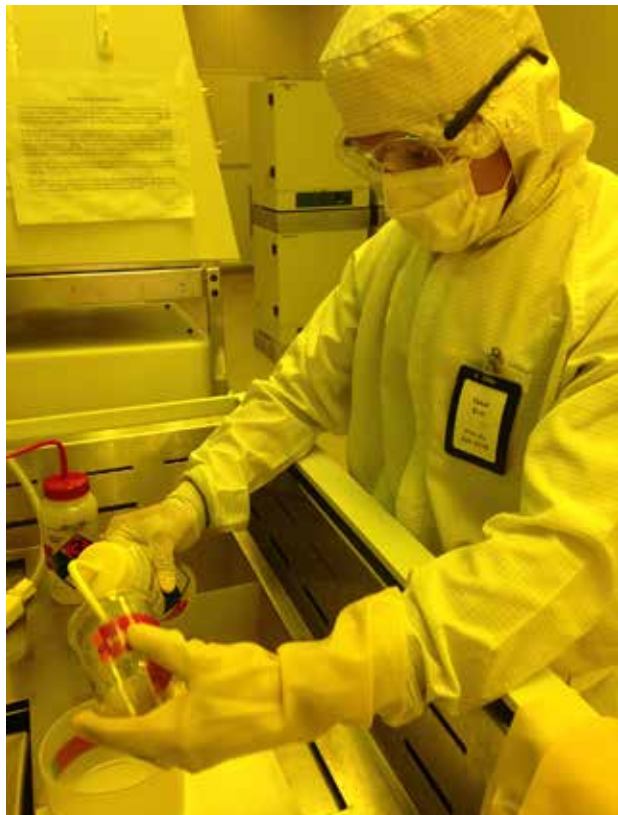


Improved Sputtering Conditions for <i>in situ</i> Crystallization of PZT Thin Films .....	100
<i>Travis O'Neil</i> NNIN REU Site: <i>The Pennsylvania State University</i>	
Delta-Doping of Diamond .....	102
<i>Stephanie Pastor</i> NNIN REU Site: <i>Howard University</i>	
Diverse Patterns and Geometries in Self-Assembled Block Copolymer Thin Films Through Multilayer Mixing.....	104
<i>Christopher Phenicie</i> NNIN REU Site: <i>University of Colorado, Boulder</i>	
Synthesis and Characterization of Size- and Shape-Specific Gold Nanocrystals for Superlattice Assembly.....	106
<i>Elyse Pizzella</i> NNIN REU Site: <i>University of Washington</i>	
The Optimization of Thin Film MoS <sub>2</sub> Synthesis .....	108
<i>Michael Statt</i> NNIN REU Site: <i>Georgia Institute of Technology</i>	
High Storage Capacity Sodium-Ion Battery Electrodes of Solution-Grown Germanium Nanowires .....	110
<i>Yuichi Tsujiura</i> NNIN iREG Site: <i>The University of Texas at Austin</i>	
Characterization of Quantum Confined Two-Dimensional Electron Gasses .....	112
<i>Veronika Werner</i> NNIN REU Site: <i>University of California, Santa Barbara</i>	



## Mechanical Devices, pages 114-123

Microfluidic Pipette Array for Single Cell Mechanics Studies .....	114
<i>Danielle Chase</i> NNIN REU Site: <i>University of Michigan, Ann Arbor</i>	
A Suspended Heater Wire for Low Power Gas Sensing Using the 3-Omega Technique.....	116
<i>Abbas Furniturewalla</i> NNIN REU Site: <i>Georgia Institute of Technology</i>	
Microfabrication & Testing of Directional Piezoelectric Microphones Using AlN .....	118
<i>Marilyn Mathew</i> NNIN REU Site: <i>The University of Texas at Austin</i>	
Design and Fabrication of Piezoresistive Graphene on Nitride Accelerometer .....	120
<i>Zachary Schaffer</i> NNIN REU Site: <i>Cornell University</i>	
Graphene Fabrication with a Motorized Linear Stage Based on the "Scotch Tape" Method.....	122
<i>Bilan Yang</i> NNIN REU Site: <i>Harvard University</i>	





## Optics & Opto-Electronics, pages 124-153

Design and Analysis of Nano-Scale Resonators to be Integrated with Monolayer Heterostructures ..... 124

*Brian Bemis*

*NNIN REU Site: University of Washington*

Fabrication of Bio-Inspired Photonic Structures for Antireflectivity in CdTe for Infrared Detectors ..... 126

*Scott Blankenbaker*

*NNIN REU Site: University of California, Santa Barbara*

Simulation and Nanofabrication for Tip-Enhanced Raman Spectroscopy ..... 128

*Bryan W. Brasile*

*NNIN REU Site: The University of Texas at Austin*

Image Reconstruction through Scattering Media Using a Single-Pixel Camera ..... 130

*Nathan Brooks*

*NNIN REU Site: University of Colorado, Boulder*

Fabrication of Test Samples for Calibration and Testing in 3D Super Resolution Microscopy ..... 132

*Molly Enenbach*

*NNIN REU Site: University of Colorado, Boulder*

Nanoscale LEDs with Tunable Emission Colors ..... 134

*Yaset Evo*

*NNIN REU Site: University of Michigan, Ann Arbor*

Fabrication of Diamond Ultraviolet Light Emitting Diodes ... 136

*Janay Frazier*

*NNIN REU Site: Howard University*

Optical Characterization of AlInAsSb Digital Alloy Films ..... 138

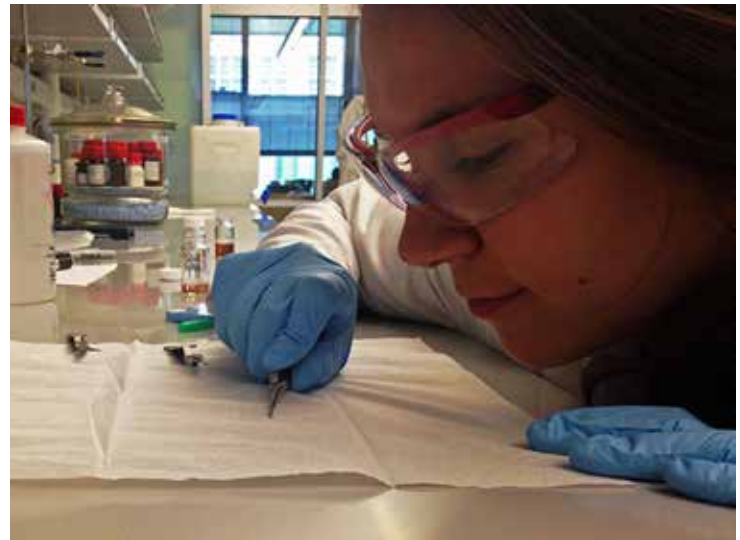
*Harold Fu*

*NNIN REU Site: The University of Texas at Austin*

Optical Resonant Frequency Detection System for Mass-Sensing MEMS Resonators ..... 140

*Kasia Gibson*

*NNIN REU Site: University of Washington*



**Parylene/GaAs Nanowire Composites for Optoelectronics.....142**

*Cristina Guillen*

*NNIN REU Site: University of Michigan, Ann Arbor*

**Graphene/III-V Electro-Optic Hybrid Devices.....144**

*Yusuke Hayashi*

*NNIN iREG Site: University of Colorado, Boulder*

**Optimizing Hard Mask Etching for Quartz NanoDevices .....146**

*Rachel Miller*

*NNIN REU Site: Harvard University*

**Minimizing Losses in  $\text{TiO}_2$  Thin-Film Waveguides  
for Nanophotonic Applications.....148**

*Anoosha Murella*

*NNIN REU Site: Cornell University*

**Bandwidth Expansion for Lippmann-Bragg  
Holographic Photopolymers .....150**

*Michael Valerino*

*NNIN REU Site: University of Colorado, Boulder*

**High-Efficiency Broadband Lippmann-Bragg  
Reflection Holograms.....152**

*Philip Zurek*

*NNIN REU Site: University of Colorado, Boulder*

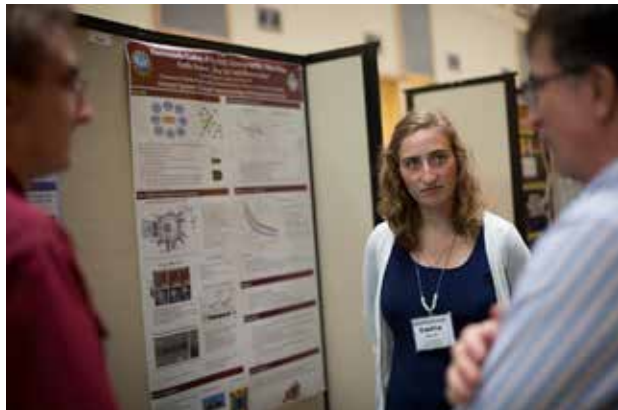


## **Physics & Nanostructure Physics, pages 154-165**

**Temperature Dependence of Carbon Nanotube Growths.....154**

*Joshua Alden*

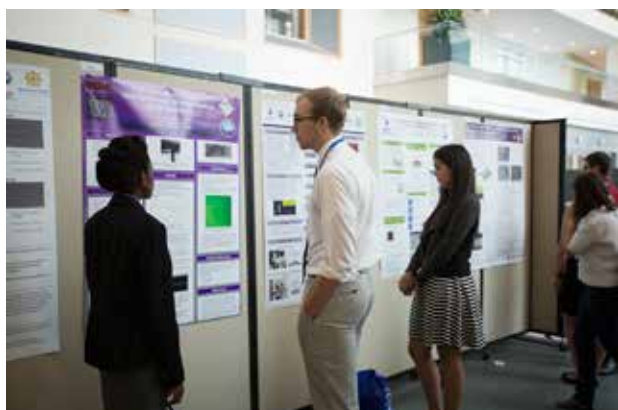
*NNIN REU Site: Cornell University*



**Determining the Spin Hall Angle of Gadolinium .....156**

*Robyn Collette*

*NNIN REU Site: Cornell University*



**Design and Fabrication of Plasmonic Device  
for MIR Absorption Spectroscopy .....158**

*Jacob Heppner*

*NNIN REU Site: University of Minnesota-Twin Cities*



**Quantum Dot Superlattice Hybrid Structures  
for Solar Cell Applications .....160**

*Rachel Lucas*

*NNIN iREU Site: NIMS, Tsukuba, Ibaraki, Japan*

**Multidimensional Metal-Dielectric Plasmonic Array.....162**

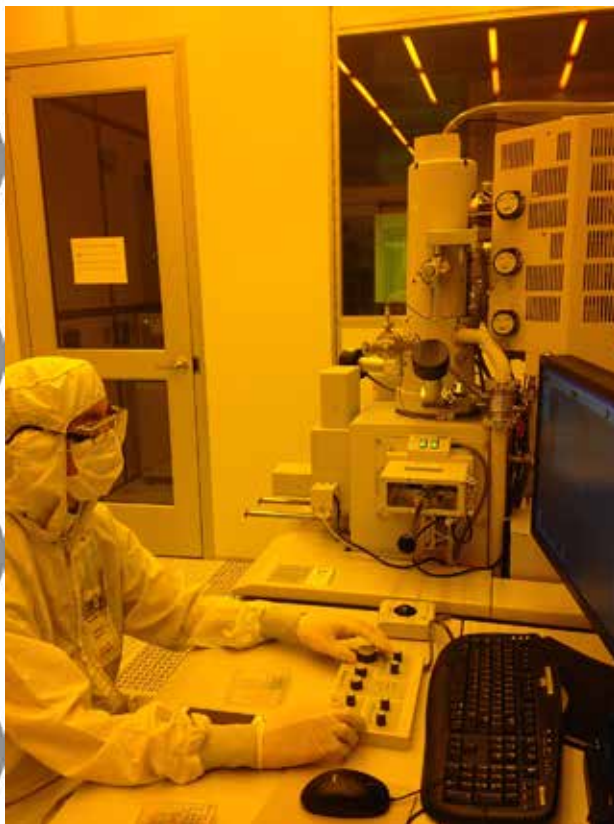
*Quang Nguyen*

*NNIN REU Site: University of Michigan, Ann Arbor*

**Magnetic Fano Interferences in Plasmonic Metal Oligomers..164**

*Claire West*

*NNIN REU Site: University of Washington*



## Process & Characterization, pages 166-185

## High Aspect Ratio Dry Etching of Gallium Nitride ..... 166

*Joshua Bostwick*  
*NNIN REU Site: University of California, Santa Barbara*

## Engineering the Fixed Charge of Aluminum Oxide for Field-Assisted Passivation in Heterojunction Solar Cells .... 168

*Scott Chow*  
*NNIN REU Site: Stanford University*

## SERS Study of BNNS on Au as a Catalyst for Oxygen Reduction Reaction ..... 170

*Emiliana Cofell  
NNIN iREU Site: NIMS, Tsukuba, Ibaraki, Japan*

## Smart-Cut Processing for Transfer of High-Temperature Ceramic Materials to Silicon ..... 172

*Mikayla Essigmann*  
NNIN REU Site: Stanford University

Fabrication of All-Aluminum p-Type Silicon Solar Cells.....174

***Raul Flores***  
*NNIN REU Site: Arizona State University*

## Construction of a Substrate for Characterizing the Real-Time Electrical Conductivity of Thin Films as Deposited.....

*Andrew S. King  
NNIN REU Site: Cornell University*

# Magneto-Optic Characterization of Ferromagnetic Thin Films for Use in Nano-Scale Computer Applications

*Elizabeth Lee*  
NNIN REU Site: *University of California, Santa Barbara*

## Conformation of Organic Electronics to the Hemispherical Shape Using Elastomeric Transfer Elements..... 180

*Anna Smith*  
*NNIN REU Site: Stanford University*

## Measurement and Management of Thin Film Stresses.....182

*Taylor Soucy*  
NNIN REU Site: University of California, Santa Barbara



## • Photography Credits •

*The cover image is from Robyn Collette's Cornell research on "Determining the Spin Hall Angle of Gadolinium" and is used with the research team's permission. Find her full report on page 156. Photographs on pages ii-xiv and xxxii-xxxvi were submitted by the program's interns and staff, except for the August convocation poster session and site photographs on pages xv-xxxii; all taken by Jason Koski, Cornell University Photography, Ithaca NY.*



## Welcome to the 2015 Edition of the NNIN REU Research Accomplishments!

This publication reflects the hard work of the undergraduate researchers, as well as the dedication and commitment of their mentors, the NNIN site staff, REU coordinators, and principal investigators.

Our summer program brings undergraduates from colleges and universities across the U.S. into some of the nation's leading academic nanofabrication laboratories for an intensive ten-week research experience. The participants are trained in safe laboratory practices, learn the essential scientific background for their project, and then perform independent research in nanotechnology, under the guidance of their mentor. For many of the students, the NNIN REU is their first experience when the answer, or even the existence of an answer, is not yet known. The summer experience provides the students with a sample of what life for them could be like as a graduate student in applied science or engineering, both in and outside the clean room. For many, the NNIN REU Program helps them to decide to pursue a career in research and development.

During the summer of 2015, 75 students participated in the final Research Experience for Undergraduates (REU) Program under the NSF's NNIN cooperative research grant. From the previous summer's NNIN REU Program, 13 students were selected to participate in NNIN's International Research Experience for Undergraduates (iREU) Program in France and Japan. In addition, four graduate students from Japan participated in our research exchange (iREG) program at three of our sites.

NNIN is committed to making all three of these programs a significant experience for the participants, by focusing on advanced research and knowledge, seeking strong mentors and staff support, exposing the students to a professional research environment, and having high expectations for the summer research projects, as well as for the presentations at the final convocation. The students' exposure to a wider variety of research conducted by their peers and the other nanofab users across diverse disciplines of science and engineering provides a significant complementary experience.

I would like to thank all of the NNIN REU staff, graduate student mentors, and faculty for their contributions to the success of this year's program, as well as the previous ten years of programs. Particular thanks are due to Ms. Melanie-Claire Mallison and Dr. Lynn Rathbun for their contributions to organizing the logistics of these programs. In addition, I am grateful to Ms. Mallison and Ms. Jan Haldeman for organizing the network-wide convocation in August at Cornell University in Ithaca, NY.

I wish all our program participants the best for their future careers, whether in science, engineering, or in other disciplines. I hope you will build on this summer's experience, as have many of the hundreds of previous participants in our previous REU programs, and I look forward to hearing from you on your future successes!

**Roger T. Howe, Director, NNIN**  
**[rthowe@stanford.edu](mailto:rthowe@stanford.edu)**



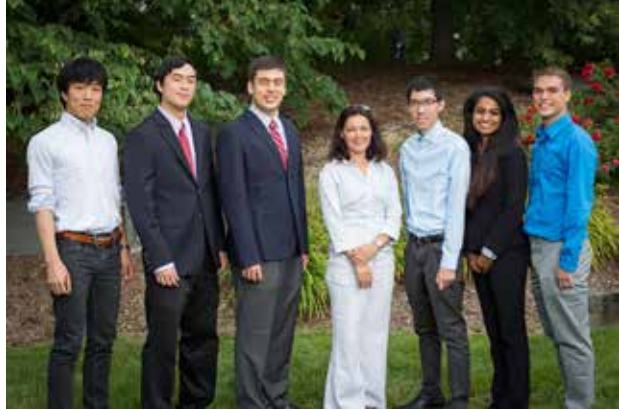
**Thank you for a  
great summer!**

**From all of us, to all of you.....**

**The NNIN REU Coordinators**



# Keep in touch!



# The NNUN/NNIN REU Program Epilogue



After almost twelve years of funding, NNIN came to a close in September 2015. This is according to NSF policy where major research centers have a fixed lifespan of ten years (We got an extra 1.5 years, but that is a long story). NNIN has been replaced by a new network, the National Nanotechnology Coordinated Infrastructure — NNCI. Some former NNIN sites are also members of NNCI, but it is not a re-creation of NNIN. It is a new network with many new players and new plans.

With the end of NNIN necessarily comes the end of the NNIN-networked REU program, which has been remarkably successful for the last 19 years (extending back to the previous network NNUN). Over that time period, we have had 1,219 outstanding participants. Our program contributed greatly to each of their careers, and likewise, their contributions greatly enhanced the research programs and environment of the NNUN/NNIN REU sites.

REU programs are ubiquitous now, but that was not the case in 1997 when we started this. In particular, large REU programs spanning multiple sites were unheard of. At that time, the NNUN included only five sites, but still the concept of a uniform multisite program with a single common application was novel. And I remember the day back in 1996 when I came up with the crazy idea of flying everyone to a common site for an end-of-program “research convocation” — that had never been done before! And yet it is these features, along with the quality of the research experience, which have set NNUN/NNIN REU apart from the pack. And as many of you can attest, it is those features that attracted you to the NNIN REU program.

As a 19 year program with 1,219 participants, with a consistent format over the entire period, the NNUN/NNIN REU program presents an unique opportunity to study the impact of an REU program in more than an anecdotal way. REU is an expensive undertaking, most recently costing NSF about \$9,000 per student. If you add that up, that is about 10M\$ over 19 years for the NNUN/NNIN REU Program. But while anecdotal data on REU “impact” is widely available, actual statistically significant data on education and career outcomes has been lacking. Such information, however, is necessary to assure continued funding of the program and is highly valued by agencies such as NSF. The NNUN/NNIN REU program thus presented us with a valuable opportunity to study a large group of REU students over an extended period of time.

Starting in 2007, Nancy Healy and I began a concerted effort to track the career outcomes of past NNUN/NNIN REU participants. For this, career plans at the end of the program are pretty irrelevant — plans change; even a few years after participation is too early to get real data. So we set a mark of contacting each participant five years after completion of the program. This was long enough that participants would have completed undergraduate education and

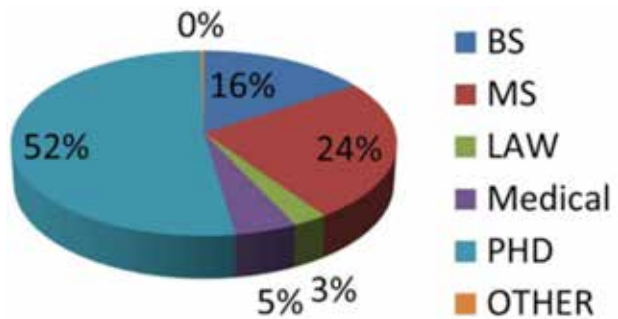
either committed and entered graduate school or entered regular employment. So we embarked on an exercise to find past participants — using email, Google, LinkedIn, Facebook, and all other sorts of modern sleuthing. And it was a bit of a challenge, with foreign names, nicknames, overly common names, married names, etc. But it has become easier in recent years with the advent of more “permanent” email addresses and cell phone numbers. Each year since, we added another year to the pool at the five year horizon. In the end, we have been able to affirmatively contact 617 of the 819 students who participated between 1998 and 2010 (~75%). (It is amazing how many people, even in 2015, have no identifiable internet fingerprint!) Identified participants were emailed a request to complete a brief online survey asking about current employment, career and education path, and the retrospective impact of the NNUN/NNIN REU program.

The results are quite enlightening. The chart at the right shows education paths for the surveyed participants. Over 50% have gone on to a Ph.D., with almost 80% going on to some form of graduate or professional school. This is aggregate data for all participants, but the data set is large enough that we can separately extract data for major demographic groups. Over 45% of women and minority participants, for example, also go on for a Ph.D., so our program has been equally as effective for this group. In addition, 50% of all participants self-identify as being in a “nanotechnology career,” and over 95% of all participants remain in a “scientific career.”

Nancy and I have presented these results at several conferences. We believe it shows the significant impact that REU programs can have on career paths. And I do wish to thank the 617 participants who completed the survey instrument. And I want to take this opportunity to stress to you, the recent participants, how important keeping in touch is. We really do like to hear from you, and reading the personal comments in the surveys is a particularly enjoyable part of the job. I do highly recommend that you establish a free LinkedIn profile and start to establish your professional network, starting with your REU peers. I have found that LinkedIn is the most effective vehicle for finding colleagues and past REU participants. And PLEASE, if you are contacted in the future to participate in an REU program evaluation, please respond. Thank you!

Building upon the success of our REU program, in 2008 NNIN developed another program that has been extraordinarily successful. Our REU activities have always had excellent participants, and many of them wanted to continue with an additional nanotechnology research experience, in NNIN or elsewhere. And we realized that some students were more exceptional than others, and that after observing them over the course of the summer and the convocation, reliable identification of the most exceptional interns was easy. At the same time, we observed that one place where US student preparation was poor was in the international aspects of science. So given these observations, we decided to try to establish a new international program which we called iREU, a second summer program exclusively for the most outstanding NNIN REU students from the prior year, designed to give the most exceptional students a career building experience in the global culture of research.

We applied to two different NSF programs for funding, one to the Engineering Division to send students to Germany and one to the International Division to send students to Japan. Surprisingly, both were funded, so we were faced with the challenging, but rewarding,





***On behalf of myself, Melanie-Claire,  
Dr. Nancy Healy, and all the NNUN/  
NNIN REU coordinators, we thank you  
for your participation.***

***It has been our pleasure.***

***Lynn Rathbun, Ph.D.***

task of setting up two new programs on two different continents. Ultimately, however, this turned out to be easy, thanks to the help of our international partners, the National Institute of Materials Science in Japan and the Forschungszentrum Jülich in Germany. The program was so successful that we supplemented the grant funding with additional funds from the NSF cooperative agreement. Later we expanded to include IMEC in Belgium, TU Delft in the Netherlands, and the Microelectronics Centre of Provence in France. This program has been extremely rewarding and successful for us, for the participants, and for our international partners. I must thank our partners here for the excellent support they have given me and our students over the past eight years. One hundred and nine select students have participated in this program since 2008. As one indication of the success of the program and its impact on participants, 30 of the 74 who have gone on to graduate school have received NSF Graduate Fellowships. We have just begun to collect quantitative data on impacts of the program on “cultural intelligence” and we have applied for separate funding to keep this program alive even after NNIN.

As we close, I want to give special recognition to Melanie-Claire Mallison, the REU Program Assistant for the entire length of the program. She processed every single one of the 8,447 applications, made about 2,000 offers, processed more than 1,400 acceptances (a few people always drop out), sent 10s of thousands of individual emails to applicants and participants, formatted each of the 1,358 technical reports (REU, iREU, and iREG), formatted and published each of the REU Research Accomplishments, and organized the five REU Convocations that were held at Cornell, including both the first and the last ones! And she remembers almost every single one of the participants! The program would not have been successful without her.

And for the last twelve summers, I have worked closely with Dr. Nancy Healy, NNIN Education Coordinator at Georgia Tech, on REU, iREU, and other NNIN education programs. It has been a successful joint effort. And I must also acknowledge the support of the NNUN/NNIN network directors, the NNUN/NNIN site directors, the individual faculty PIs and mentors, and most of all the NNUN/NNIN site REU coordinators, all of whom are too numerous to mention. Their collective efforts have made our programs uniquely successful. These programs clearly demonstrate the success of the “network” concept, that programs can be successfully coordinated and administered uniformly across many sites, and that the result can indeed be larger than the sum of the parts.

Funding for the NNUN/NNIN program has come almost exclusively from the National Science Foundation, most recently from the NNIN Cooperative Agreement, but earlier from REU program funds. We thank Dr. Larry Goldberg, in particular, for his support of our program.

***So, this brings to a close the NNUN/NNIN REU Programs.***

It is not yet clear what direction NNCI will take with REU. Since NNCI is still forming its organizational structure, it is clear that for the summer of 2016 there will not be a network-wide coordinated REU program. That is unfortunate, but unavoidable. Some of the sites will, however, have individual programs.

***We will be sure keep you updated! Please keep us updated too!***



*The original NNUN REU staff — who are still in the network!*



**ASU NanoFab,  
Arizona State University,  
Tempe, AZ**

*Left to Right:*

Alexander Rosner	72
Abigail Magee	30
Adam Kunesh	28
Raul Flores	174



**Cornell NanoScale Science  
& Technology Facility,  
Cornell University, Ithaca, NY**

*Left to Right:*

Zachary Schaffer	120
Anisa Swei	42
Andrew King	176
Anoosha Murella	148
Matthew Devlin	14
Robyn Collette	156
Joshua Alden	154





**Institute for Electronics  
and Nanotechnology,  
Georgia Institute of Technology,  
Atlanta, GA**

*Left to Right:*

<b>Yasunori Kutsuwa</b> .. . . . .	96
<b>Michael Statt</b> .. . . . .	108
<b>Masashi Fukuzawa</b> .. . . . .	52
<b>Margot Hultz</b> .. . . . .	54
<b>Brian Ryu</b> .. . . . .	38
<b>Erin Rousseau</b> .. . . . .	na
<b>Abbas Furniturewalla</b> .. . . . .	116
<b>Mary Alsobrooks</b> .. . . . .	58



**Center for Nanoscale Systems,  
Harvard University,  
Cambridge, MA**

*Left to Right:*

<b>Bilan Yang</b> .. . . . .	122
<b>Rachel Miller</b> .. . . . .	146
<b>Emily MacDonald</b> .. . . . .	98
<b>Alejandro Sanchez</b> .. . . . .	40
<b>Caroline Zellhofer</b> .. . . . .	184





## Howard Nanoscale Science & Engineering Facility, Howard University, Washington, DC

*Left to Right:*

<b>Stephanie Pastor</b> .....	<b>102</b>
<b>Catherine Demos</b> .....	<b>12</b>
<b>Janay Frazier</b> .....	<b>136</b>
<b>Lorelis González López.</b> .....	<b>86</b>
<b>Tanaka Benton</b> .....	<b>74</b>



## Penn State Nanofabrication Lab, The Pennsylvania State University, University Park, PA

*Left to Right:*

<b>Travis O'Neil</b> .....	<b>100</b>
<b>Nermina Brljak</b> .....	<b>76</b>
<b>Nathan Huber</b> .....	<b>64</b>
<b>Sophia Hu..</b> .....	<b>90</b>
<b>Justin Goodwill..</b> .....	<b>62</b>





## Stanford Nanofabrication Facility, Stanford University, Stanford, CA

*Left to Right:*

Mikayla Essigmann	172
Jade Fostvedt	82
Isaac DiGennaro	80
Anna Smith	180
Scott Chow	168

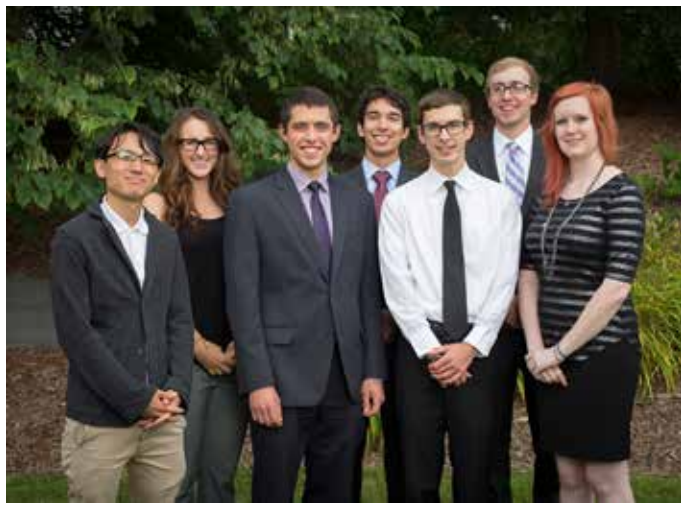


## UCSB Nanofab Facility, University of California, Santa Barbara, CA

*Left to Right:*

Joshua Bostwick	166
Veronika Werner	112
Taylor Soucy	182
Elizabeth Lee	178
Scott Blankenbaker	126
Benjamin Carberry	78





## Colorado Nanofabrication Lab, University of Colorado, Boulder, CO

*Left to Right:*

<b>Yusuke Hayashi</b> .....	<b>144</b>
<b>Molly Enenbach</b> .....	<b>132</b>
<b>Philip Zurek</b> .....	<b>152</b>
<b>Nathan Brooks</b> .....	<b>130</b>
<b>Christopher Phenicie</b> .....	<b>104</b>
<b>Michael Valerino</b> .....	<b>150</b>
<b>Andrea Randolph</b> .....	<b>70</b>



## Lurie Nanofabrication Facility, University of Michigan, Ann Arbor, MI

*Left to Right:*

<b>Quang Nguyen</b> .....	<b>162</b>
<b>Danielle Chase</b> .....	<b>114</b>
<b>Tom George</b> .....	<b>84</b>
<b>Tayler Pauls</b> .....	<b>34</b>
<b>Yaset Evo</b> .....	<b>134</b>
<b>Cristina Guillen</b> .....	<b>142</b>

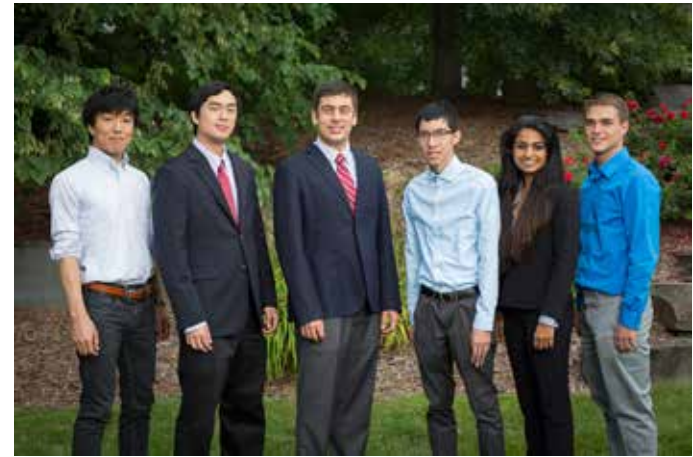




Minnesota Nano Center,  
University of  
Minnesota-Twin Cities,  
Minneapolis, MN

*Left to Right:*

<b>Emilie Benson</b> . . . . .	60
<b>Jacob Heppner</b> . . . . .	158
<b>Victor Pablo Acero</b> . . . . .	2
<b>Michelle Galarneau</b> . . . . .	20



Microelectronics Research Center,  
The University of Texas,  
Austin, TX

*Left to Right:*

<b>Yuichi Tsujiura</b> . . . . .	110
<b>Harold Fu</b> . . . . .	138
<b>Raymond Barakat</b> . . . . .	6
<b>Corey Kwok</b> . . . . .	66
<b>Marilyn Mathew</b> . . . . .	118
<b>Bryan W. Brasile</b> . . . . .	128





**WNF & MAF,  
University of Washington,  
Seattle, WA**

*Left to Right:*

<b>Kasia Gibson</b> .. . . . .	<b>140</b>
<b>Brian Bemis</b> .. . . . .	<b>124</b>
<b>Elyse Pizzella</b> .. . . . .	<b>106</b>
<b>Joseph P. Hittinger</b> .. . . . .	<b>24</b>
<b>Claire West</b> .. . . . .	<b>164</b>
<b>Alin Miksi Kalayjian</b> .. . . . .	<b>56</b>

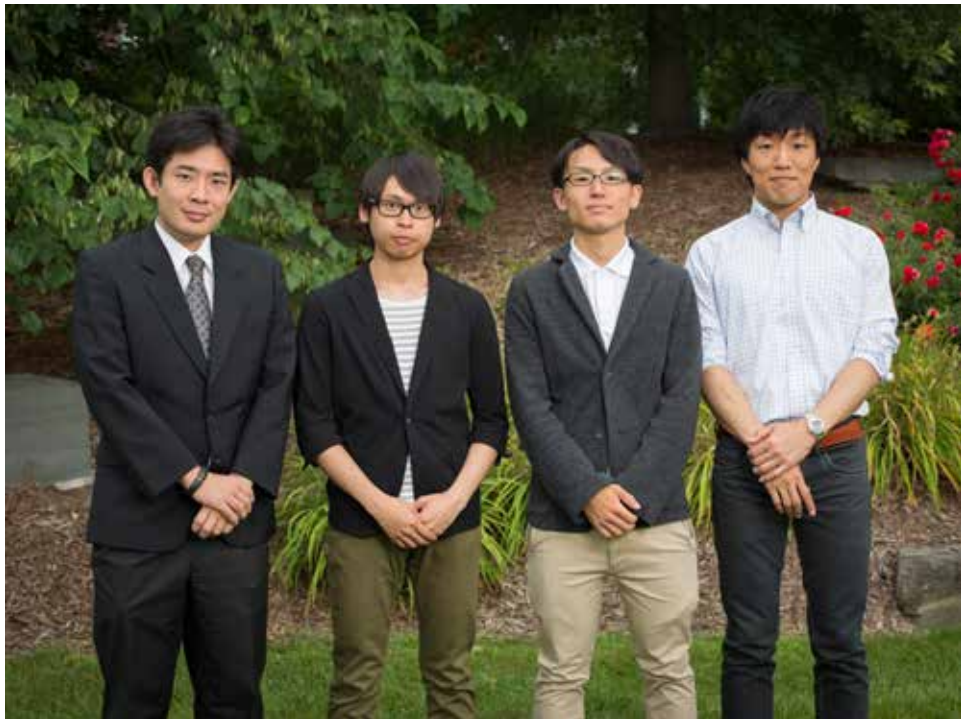


**Nano Research Facility,  
Washington University in  
St. Louis, St. Louis, MO**

*Left to Right:*

<b>Jyoti Campbell</b> .. . . . .	<b>46</b>
<b>Shaun Engelmann</b> .. . . . .	<b>16</b>
<b>Isaac Fuhrman</b> .. . . . .	<b>50</b>
<b>Cyrus Thompson</b> .. . . . .	<b>44</b>
<b>Christina Franke</b> .. . . . .	<b>18</b>

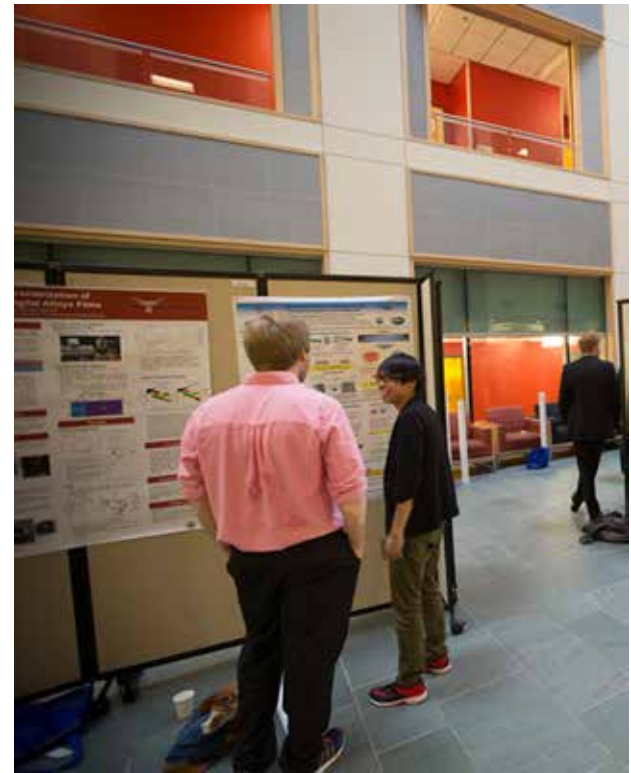




## International Research Experience for Graduates Program

*Left to Right:*

Yasunori Kutsuma .. . . . .	96
Masashi Fukuzawa .. . . . .	52
Yusuke Hayashi .. . . . .	144
Yuichi Tsujiura .. . . . .	11





## International Research Experience for Undergraduates Program

*Left to Right:*



<b>Lucy Hu</b> .. . . . .	26
<b>Mariella Arias</b> .. . . . .	4
<b>Tara Nietzold</b> .. . . . .	68
<b>Christopher Davidson</b> .. . . . .	10
<b>Emiliana Cofell</b> .. . . . .	170
<b>Jon-L Innocent-Dolor</b> .. . . . .	92
<b>Rachel Lucas</b> .. . . . .	160
<b>Allison Bosworth</b> .. . . . .	8
<b>Taliya Gunawansa</b> .. . . . .	88
<b>Samantha Kang</b> .. . . . .	94
<b>Adriana Mulero</b> .. . . . .	32
<b>Dylan J. Freas</b> .. . . . .	48
<b>Staci Hill (not pictured)</b> .. . . . .	22

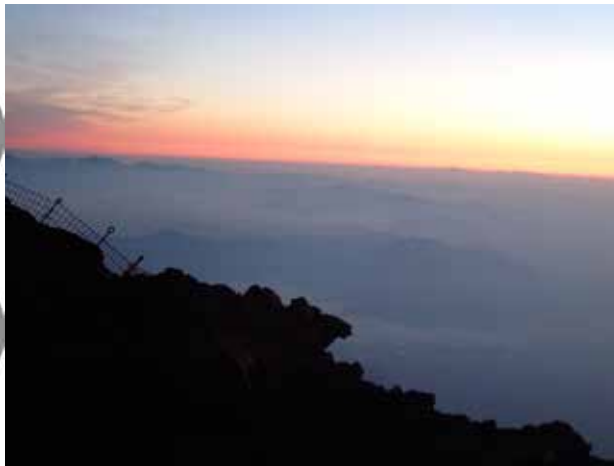
# Commonly Used Abbreviations & Their Meaning



µl	microliter
µm	micron, micrometer
µN	micro-Newton
µs	microsecond
Ω	Ohm
<	is less than
>	is greater than
~	approximately
1D	one-dimensional
2D	two-dimensional
2DEG	two-dimensional electron gas
3D	three-dimensional
α-Si	amorphous silicon
AFM	atomic force microscopy/microscope
Ag	silver
AIC	aluminum-induced crystallization
Al	aluminum
Al <sub>2</sub> O <sub>3</sub>	aluminum oxide
ALD	atomic layer deposition
Ar	argon
Au	gold
AuNPs	gold nanoparticles
B	boron
Bi	bismuth
BN	boron nitride
BOE	buffered oxide etch
BSA	bovine serum albumin
C	carbon
C	centigrade
C-V	capacitance-voltage
CAD	computer-aided design
Cd	cadmium
CDW	charge-density-wave
CF <sub>4</sub>	carbon tetrafluoride or tetrafluoromethane
CH <sub>4</sub>	methane
CHF <sub>3</sub>	trifluoromethane
Cl	chlorine
cm	centimeter
CMOS	complementary metal oxide semiconductor
CMP	chemical mechanical polishing
Co	cobalt
CO <sub>2</sub>	carbon dioxide
Cr	chromium
Cu	copper
CVD	chemical vapor deposition
DC	direct current
DI	de-ionized
DNA	deoxyribonucleic acid
DRIE	deep reactive ion etch
DUV	deep ultraviolet
e-beam	electron beam lithography
EBL	electron beam lithography
EDS	energy dispersive spectroscopy
EG	ethylene glycol
ELISA	enzyme-linked immunosorbent assays
Er	erbium

EUV	.....extreme ultraviolet
<i>ex situ</i>	.....Latin phrase translated literally as 'off-site' -- to examine the phenomenon in another setting than where it naturally occurs
<i>ex vivo</i>	.....Latin for "out of the living" -- that which takes place outside an organism
F	.....fluorine
Fe	.....iron
FET	.....field-effect transistor
FIB	.....focused ion beam
Ga	.....gallium
Gd	.....gadolinium
Ge	.....germanium
GHz	.....gigahertz
GPa	.....gigapascal
h	.....hours
H	.....hydrogen
$H_2O_2$	.....hydrogen peroxide
He	.....helium
Hf	.....hafnium
HF	.....hydrofluoric acid
Hg	.....mercury
high- $\kappa$	.....high dielectric constant
HSQ	.....hydrogen silsesquioxane
HSQ/FOx	.....negative electron beam resist hydrogen silsesquioxane
Hz	.....Hertz
I-V	.....current-voltage
In	.....indium
<i>in situ</i>	.....Latin phrase translated literally as 'in position' -- to examine the phenomenon exactly in place where it occurs
<i>in vitro</i>	.....Latin for "within glass" -- refers to studies in experimental biology that are conducted using components of an organism that have been isolated from their usual biological context in order to permit a more detailed or more convenient analysis than can be done with whole organisms.
<i>in vivo</i>	.....Latin for "within the living" -- experimentation using a whole, living organism
Ir	.....iridium
ITO	.....indium tin oxide
J/m	.....Joules/meter
$\kappa$	.....dielectric constant
K	.....Kelvin (a unit of measurement for temperature)
K	.....potassium
kg	.....kilogram
kHz	.....kilohertz
KOH	.....potassium hydroxide
La	.....lanthanum
LED	.....light-emitting diode
Li	.....lithium
low- $\kappa$	.....low dielectric constant
LPCVD	.....low pressure chemical vapor deposition
MEMs	.....microelectromechanical systems
MgO	.....magnesium oxide
MGs	.....molecular glasses
MHz	.....megahertz
micron	.....micrometer, aka $\mu m$
min	.....minutes
ml	.....milliliter
mm	.....millimeter





**This book was printed on 10% post-consumer paper, using soy-based inks and regular inks.**

**We encourage you to reduce, reuse, and recycle!**



mM	millimolar
Mo	molybdenum
MOCVD	metal oxide chemical vapor deposition
MOSFET	metal oxide semiconductor field effect transistor
ms	millisecond
mTorr	millitorr
mV	millivolt
MVD	molecular vapor deposition
N	nitrogen
NaCl	sodium chloride
Nb	niobium
Nd	neodymium
NEMs	nanoelectromechanical systems
Ni	nickel
nL	nanoliter
nm	nanometer
NPs	nanoparticles
NPs	nanopores
ns	nanosecond
NSF	National Science Foundation
O	oxygen
Pb	lead
Pd	palladium
PDMS	polydimethylsiloxane
PECVD	plasma enhanced chemical vapor deposition
PEDOT:PSS	poly(3,4-ethylenedioxythiophene):poly(styrenesulfonate)
PEG	polyethylene glycol
pH	a measure of the activity of hydrogen ions (H <sup>+</sup> ) in a solution and, therefore, its acidity.
PMMA	poly(methyl methacrylate)
PS- <i>b</i> -PMMA	polystyrene-block-poly(methyl methacrylate)
Pt	platinum
Q	quality factor
RF	radio frequency
RIE	reactive ion etch
s	seconds
S	sulfur
sccm	standard cubic centimeters per minute
Se	selenium
sec	seconds
SEM	scanning electron microscopy/microscope
SERS	surface enhanced Raman spectroscopy
SF <sub>6</sub>	sulfur hexafluoride
Si	silicon
Sn	tin
<i>t</i> -BOC	tert-butoxycarbonyl
Ta	tantalum
Te	tellurium
TEM	transmission electron microscopy/microscope
Tg	glass transition temperature
THz	terahertz
Ti	titanium
UV-Vis	ultraviolet-visible
V	vanadium
V	voltage
XPS	x-ray photoelectron spectroscopy
XRD	x-ray diffraction
Zn	zinc
Zr	zirconium
ZTO	zinc tin oxide

National Nanotechnology Infrastructure Network  
Research Experience for Undergraduates  
(NNIN REU) Program

National Nanotechnology Infrastructure Network  
International Research Experience for  
Graduates (NNIN iREG) Program

National Nanotechnology Infrastructure Network  
International Research Experience for  
Undergraduates (NNIN iREU) Program

2015

*Research*  
*Accomplishments*

# Enhancement of High-Performance Graphene Biosensors for Cancer Detection

**Victor Pablo Acero**

**Engineering Science, The Pennsylvania State University**

**NNIN REU Site: Minnesota Nano Center, University of Minnesota-Twin Cities, Minneapolis, MN**

NNIN REU Principal Investigator: Tianhong Cui, Mechanical Engineering, Tian Group, University of Minnesota-Twin Cities

NNIN REU Mentor: Shota Sando, Mechanical Engineering, Tian Group, University of Minnesota-Twin Cities

Contact: acero002@gmail.com, cuixx006@me.umn.edu, ssando@umn.edu

## Abstract:

Current alpha-fetoprotein (AFP) sensing technologies such as enzyme-linked immunosorbent assays (ELISA) require a lot of equipment, time, and skill. Still, they would be less sensitive than our proposed graphene biosensors, which in theory could detect a single AFP. Graphene's unique material properties and sensitivity to the surrounding environment are exploited in our sensor for the detection of AFP. A U-shaped gold electrode containing a small gap for the sensing area would then be patterned using photolithography. The gap would be closed by covering the bare substrate with our few-layer-graphene (FLG) structure. We tune the thickness, and thus the properties, of graphene through a unique layer-by-layer self-assembly process that uses graphene solution and polyelectrolytes. The graphene sensing area is further prepared with poly-L-lysine and then functionalized with anti-AFP. Also, due to the fact that the ability to detect AFP is heavily limited by the signal-noise ratio, we redesigned the basic interface between gold and graphene in multiple ways to achieve a better signal-noise ratio in our sensors. The sensors that were fabricated were successful in detecting alpha-fetoprotein even in concentrations as low as 1 pg/ml. Lastly, the redesigned gold/graphene interface showed promising results and seems to have only been limited by our fabrication procedure.

## Introduction:

Graphene, the two-dimensional counterpart of graphite, has been extensively studied in terms of its properties and manufacturing since its discovery in 2004. Since its discovery a plethora of techniques have been developed for creating this new material [1]. Though popular methods produce quality graphene, they are not scalable to meet industry demand. However, this work uses layer-by-layer self-assembly to produce few-layer-graphene (FLG), which is indeed scalable.

This bio-sensor would be a candidate for phasing out and replacing the current bio-chemical assay known as ELISA, which is the industry standard for antigen screening. ELISA is a great tool, however it is complicated to screen antigens, it requires great technician skill, and takes hours to run. Conversely our sensor is simple to prepare for testing, the screening is simple, and data is visible in a matter of seconds/minutes.

We wanted to enhance our sensor sensitivity as well by reducing 1/f noise in our sensors. In order to do this we decided to try reducing the overall contact resistance present, thus we reduced the contact area between the graphene and gold [2,3].

## Methods and Techniques:

**Fabrication.** We fabricated our sensors using a photolithography process, as demonstrated in Figure 1, which involves the patterning of the gold electrode, patterning of graphene onto the sensing area, and the patterning of a protective KMPR coating.

**Modified Gold-Graphene Interface.** In order to reduce contact area between gold and graphene, the junction at which they meet was redesigned. This work used three different designs, as seen in Figure 2 — a 31 strip design, 95 strip designs, and 950 strip designs that reduced the

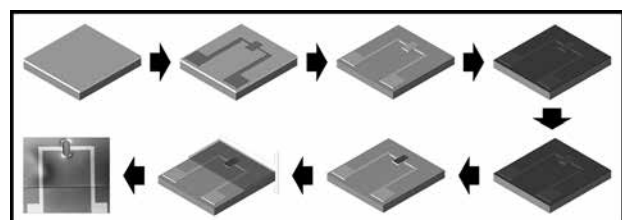


Figure 1: Process scheme.

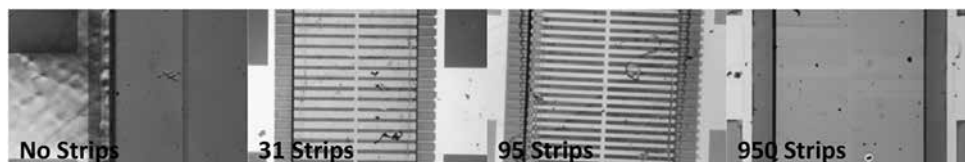


Figure 2: The 31 strip design, 95 strip design, and 950 strip design.

surface area to 33%, 50%, and 50% respectively. The small feature size lead to occasional complications with fabrication, especially in the 950 strip design due to the 2  $\mu\text{m}$  strip width.

**Graphene Self Assembly.** Next we facilitated the layer-by-layer self-assembly of few-layer-graphene onto the entire wafer. This was done by alternating immersion of the graphene wafer between a solution of poly(diallyldimine chloride) (PDDA), which is positively charged, and poly(styrene sulfonate) (PSS), which is negatively charged; it enabled us to create a thin layer of polymer that distanced the graphene, once formed, away from the silicon oxide. Next we alternated immersion into PDDA and a solution of suspended negatively charged graphene platelets for five cycles to form FLG.

**Graphene Charge Sensitivity and Debye Length.** If there is a charge within the Debye length of the sensing area, the graphene's carrier mobility and resistance will be affected, however the affects vary depending on the charge present. Since graphene in our sensing area was P-doped, a negative charge within its Debye length would decrease resistance throughout the material, whilst contrariwise, a positive charge would increase the resistance in the graphene.

**Functionalization.** The sensing area was prepared in the following progression: immersion in poly-L-lysine, cleaned with distilled water, immersed in a solution of anti-alpha fetoprotein (anti-AFP), cleaned with Dulbecco's phosphate-buffered saline (DPBS), and finally immersed in diluted 1% bovine serum albumin (BSA).

## Results:

**Alpha-Fetoprotein Sensing.** We allowed the sensor to calibrate when exposed to DPBS with no AFP and then began to slowly increase the concentration of AFP, as can be seen in Figure 3.

**Noise Reduction.** This approach of 1/f noise reduction by reduction of contact area between gold/graphene was successful. Though poor performance is seen in the 950 strip design, which can be attributed to poor fabrication of electrodes, the 95 strip and 31 strip designs had less 1/f noise than the original sensor design, as is seen in Figure 4. If applied to our sensors we would surely surpass sensitivity of tests such as ELISA.

## Future Work:

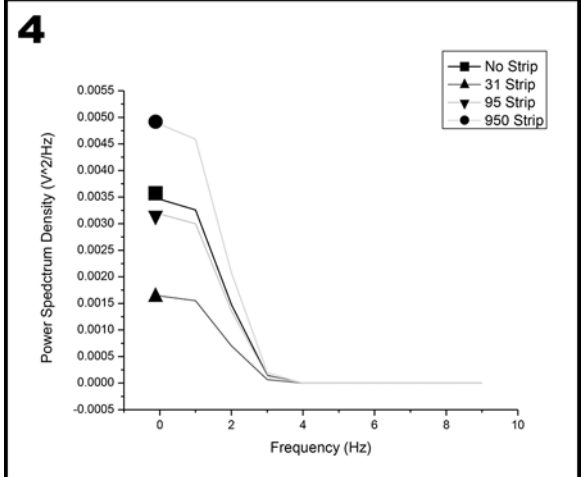
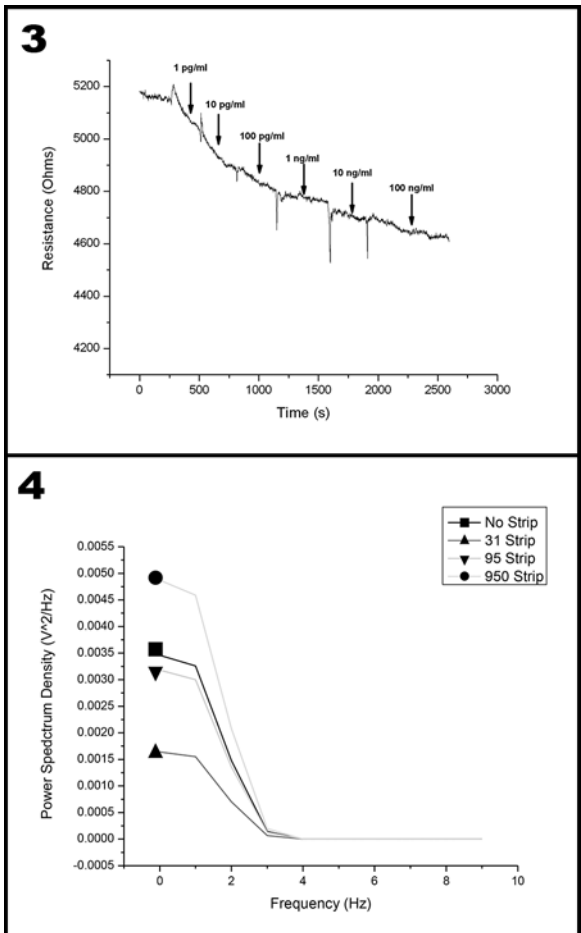
We would like to focus on two areas for future work. We would want to apply our work to flexible substrates to prove the potential application of our sensor as an *in vivo* bio-sensor, which is the consummation of our work. Lastly, we want to better understand the graphene-gold interface by finding the optimal value for contact area reduction and number of gold strips, in order to further improve the signal-to-noise ratio.

## Acknowledgments:

I would like to acknowledge the TIAN lab at the University of Minnesota for their guidance and support, specifically Tianhong Cui and Shota Sando. I also want to thank the NSF and National Nanotechnology Infrastructure Network Research Experience for Undergraduates (NNIN REU) Program (Grant No. ECCS-0335765) for funding this research.

## References:

- [1] Zhu, Y., Murali, S., Cai, W., (2010), Graphene and Graphene Oxide: Synthesis, Properties, and Applications. *Adv. Mater.*, 22: 3906-3924. doi:10.1002/adma.201001068.
- [2] Smith JT, Franklin AD. Reducing contact resistance in graphene devices through contact area patterning. *ACS Nano*, 7, 3661 (2013). <http://dx.doi.org/10.1021/nn400671z>.
- [3] Hyungwoo L. Wide Contact Structures for Low-Noise Nanochannel Devices Based on a Carbon Nanotube Network *ACS Nano* 2010 4 (12), 7612-7618 DOI: 10.1021/nn102296e.



# A PEDOT:PSS Process on Textiles for Health Monitoring

**Mariella Arias**

**Biomedical Engineering, El Camino College**

**NNIN iREU Site: Centre Microélectronique de Provence, École Nationale Supérieure des Mines de Saint-Étienne, France**

**NNIN iREU Principal Investigator: George Malliaras, Centre Microélectronique de Provence,**

**École Nationale Supérieure des Mines de Saint-Étienne, France**

**NNIN iREU Mentors: Thomas Lonjaret and Esma Ismailova, Centre Microélectronique de Provence,**

**École Nationale Supérieure des Mines de Saint-Étienne, France**

**Contact: ariasmariella.br@gmail.com, malliaras@emse.fr, thomas.lonjaret@emse.fr, ismailova@emse.fr**

## **Abstract:**

Wearable electronic textiles are good candidates for achieving low cost, flexible, and light-weight health monitoring devices. The integration of biocompatible organic polymers, such as poly(3,4-ethylenedioxythiophene):polystyrene sulfonate (PEDOT:PSS), and ionic gels with textiles allows for the development of conformable and high performance electronics for cutaneous applications. For these reasons, we developed a fabrication process for PEDOT:PSS based electrodes. Such electrodes were used for recording electrocardiography (ECG) activity and for developing an electrochromatographic display of such activity. An ionic liquid gel was used to aid in the electrochemical doping and de-doping of the PEDOT:PSS electrodes. Color changes on the electrochromatographic display were analyzed via optical spectroscopy. The PEDOT:PSS electrodes were also used as capacitive pressure sensors, with polydimethylsiloxane (PDMS) as dielectric, for physiotherapeutic applications. Results obtained using this process pave the way for technology that can be further integrated on an electronic textile glove that can perform several health monitoring tasks at once.

## **Introduction:**

There is an increasing interest for combining the capabilities of electronics with textiles. This emerging field of research provides new tools for a variety of applications such as in the medical field. Detection of electrical activity of the heart by external electrodes, also referred to as electrocardiography (ECG), is a method used by physicians to investigate heart rhythm. This test can help physicians detect anomalies in the functions of the heart. To perform ECG testing, two or more metal electrodes are placed directly on top of skin. However, such metal electrodes can be expensive and, as they lack flexibility, do not conform well with skin. Having textile-based electrodes could allow for improved ECG testing as the flexibility of the textile enables to follow the movement of most human body parts. Furthermore, in this work we seek to expand the applications of textile-based electrodes to be used as capacitive sensors to detect changes in pressure. This technology can provide crucial information in the field of physiotherapy regarding pressure applied on patients.

## **Device Fabrication:**

All materials used in this process are biocompatible, which allows for applications

in direct contact with skin. The textile electrodes were constructed by patterning the conductive polymer on polyester-based fabric. A negative polyimide master was used to define the desired pattern. On such master, a layer of PDMS was deposited by spin coating. The polyimide master was then placed on top of textile, with the PDMS in direct contact with the fabric (see Figure 1).

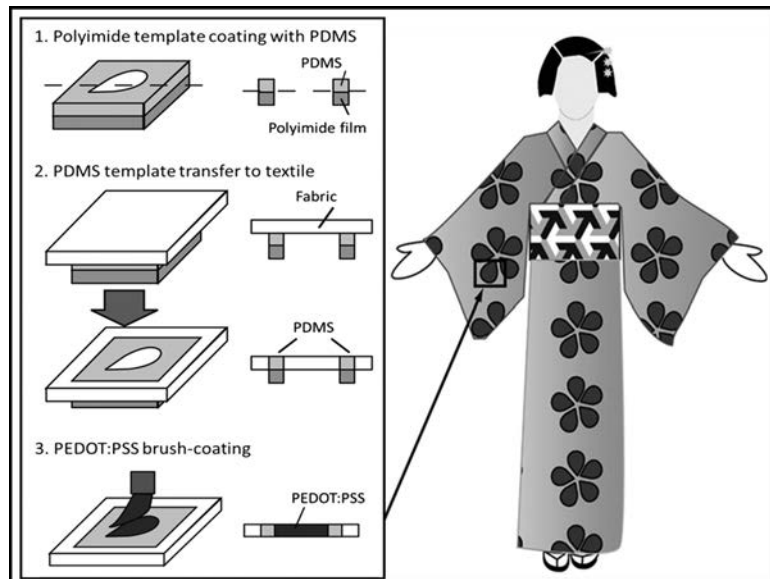
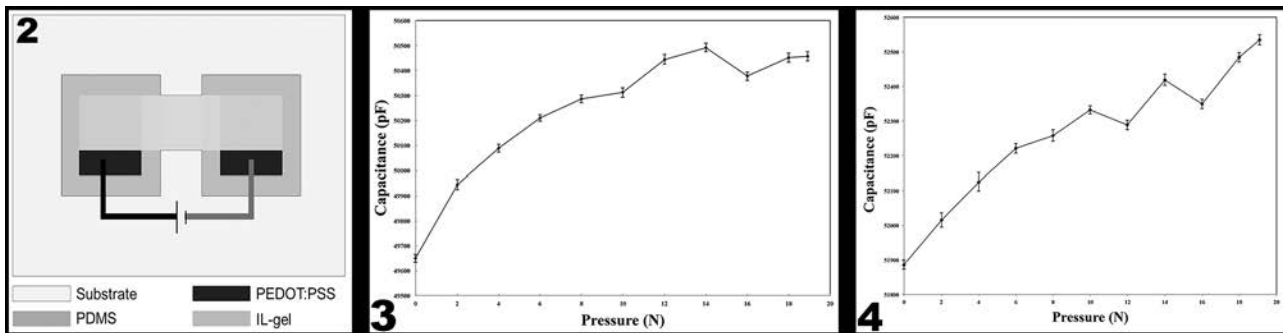


Figure 1: Patterning process.



**Figure 2, left:** Schematic of ECG display experimental setup. **Figure 3, middle:** Pressure sensing characterization. 920  $\mu\text{m}$  thick PDMS layer as dielectric. **Figure 4, right:** Pressure sensing characterization. 560  $\mu\text{m}$  thick PDMS layer as dielectric.

The PDMS was cured onto textile via thermal annealing for ten minutes at 100°C. The polyimide master was then removed from the PDMS surface. The hydrophobic properties of PDMS allowed for confinement of the PEDOT:PSS aqueous solution on textile substrate. Then, PEDOT:PSS solution was paint brushed on textile, and subsequently annealed for five hours at 100°C. The PEDOT:PSS solution was prepared in a 0.80/0.20/0.40/0.01 ratio of PEDOT:PSS aqueous dispersion, ethylene glycol, 4-dodecylbenzenesulfonic acid, and (3-glycidyloxypropyl) trimethoxysilane, respectively. Solution was then mixed, and sonicated for thirty minutes. The films were subsequently baked at 100°C for five hours.

### Experimental Procedure:

An ionic liquid gel was used aid in the electrochemical doping and de-doping of the PEDOT:PSS electrodes. The ionic gel consisted of the mixture of ionic liquid 1-ethyl-3-methylimidazolium-ethyl sulfate, 0.1M phosphate buffer solution, poly(ethylene glycol)diacrylate and the photoinitiator 2-hydroxy-2-8-methylpropiophenone at a ratio of 0.12/0.48/0.35/0.05, respectively. Two sets of experiments were arranged for testing the textile electrodes for two applications: electrodes as ECG-signal display, and electrodes as capacitive sensors. On this device, a sine wave of 100 mHz was applied, using potentials ranging from 0.2V to 2V (see Figure 2). This signal promoted ion migration between the electrodes. Because of the elecrochromatographic properties of PEDOT:PSS, we observed changes in color with the naked eye alternating from light blue to dark blue. A glass slide was used as a substrate for the PEDOT:PSS electrodes.

The PEDOT:PSS electrodes were also used as capacitive pressure sensors, with polydimethylsiloxane (PDMS) as dielectric, for physiotherapeutic applications. The capacitor was formed by one layer PEDOT:PSS-textile electrode plates, and one of PDMS on top. The terminal of such textile electrode is connected to the circuit. The second conducting plate was a grounded metal electrode, to allow applied pressure variation. A range of pressures was applied to two capacitors with different dielectric thickness

(see Figures 3 and 4). Information regarding capacitance changes on device was obtained from the configuration of the setup of textile-PEDOT:PSS electrodes, capacitance measurement circuit in MCUs, and PC.

### Conclusion and Future Work:

We have successfully patterned textile electrodes for health monitoring practices using materials that are all biocompatible and inexpensive. Capacitance changes as a function of pressure were detected, varying with dielectric thickness, agreeing with theory. Textiles as capacitance sensors are promising for physiotherapy applications as we detected pressure changes in the range of 0.1N to 200N, which is the ideal range for such applications. ECG display process needs to be further investigated as the working frequency is not yet reaching 1 Hz, which is a normal ECG frequency. For this reason, we would like to investigate alternative ionic gels that will enable faster doping/de-doping response to match ECG signal frequency, and allow for transferring of process to textiles. Furthermore, future work will focus on optimizing patterning techniques to allow for further integration onto different shapes of substrates such as textile gloves.

### Acknowledgements:

This work was funded and supported by the National Nanotechnology Infrastructure Network International Research Experience for Undergraduates (NNIN iREU) Program and the National Science Foundation Grant No. ECCS-0335765, and was performed using the facilities at the Center of Microelectronics in Provence. I would like to thank the Department of Bioelectronics for their help and support.

### References:

- [1] G. D. Clifford, et al., "Advanced Methods and Tools for ECG Data Analysis", 1st Edition (2006). E-book.
- [2] S. Takamatsu, et al., "Meter-scale large-area capacitive pressure sensors with fabric with stripe electrodes of conductive polymer-coated fibers", Microsystem Technologies, March 2015.

# Tablet Analysis and Display of Semiconductor Biosensors

**Raymond Barakat**  
Electrical Engineering, Arizona State University

**NNIN REU Site: Microelectronics Research Center, The University of Texas, Austin, TX**

NNIN REU Principal Investigator: Prof. Ray Chen, Electrical and Computer Engineering, University of Texas at Austin

NNIN REU Mentor: Dr. Swapnajit Chakravarty, Omega Optics-Austin, Texas

Contact: [rjbaraka@asu.edu](mailto:rjbaraka@asu.edu), [chen@ece.utexas.edu](mailto:chen@ece.utexas.edu), [swapnajit.chakravarty@omegaoptics.com](mailto:swapnajit.chakravarty@omegaoptics.com)

## Abstract and Introduction:

Photonic crystals using silicon-on-insulator (SOI) processes have applications as extremely sensitive biosensors. By taking advantage of the photonic bandgap (PBG), light can be guided through the photonic crystal (PC) using PC micro-cavities to block light and PC waveguides to allow light through. When light shines through the PC biosensor, depending on the design, the output spectrum will display distinct resonances. When a sample is pipetted on the PC biosensor and a wavelength shift is observed. This shift can be used to determine what is in the sample and what its concentration is. Previous work has shown that PC biosensors have the capability to reliably detect biomarkers related to various cancers and dangerous elements in extremely low concentrations.

The goal of this project is to develop software in MATLAB that quickly collects and analyzes spectrum data received from the biosensor. The software is also able to control a near-infrared SLED light source in order to perform repeated scans and analyses on data collected from an optical spectrum analyzer (OSA). This software will run on a tablet in order to explore the feasibility of a portable biosensing platform. Tests were performed on a biosensor using the 2A81G5 antibody as a probe in order to detect cadmium ions in solution. Current work is being done to refine the software suite developed, such as improving the accuracy of resonance detection and tracking. This will make data collection easier so the biosensor will be more practical to use.

## Experimental Procedure:

To collect data from the PC biosensor the following tools were used: an OSA with USB connectivity, a near-infrared SLED source, and MATLAB software loaded onto a Surface Pro 2 tablet. MATLAB code was written to interface with the OSA and the SLED source. Further code was written to analyze the collected data and plot the results in a graphical user interface (Figure 1). The *findpeaks()* MATLAB function was used to find and initially plot all the local minima to approximate the location of multiple resonances (Figure 2). Next the *smooth()* function was used to smooth noisy spectrum data from the OSA using a moving average (Figure 3). Finally, *lorentzfit()* was used to fit a Lorentzian curve to the smoothed data using a least squares approximation, and *mins()* was used to find the final location of the resonance wavelength (Figure 2) [1]. All of this functionality was controlled using the MATLAB GUI. For the repeated scans of the biosensor the Surface Pro 2 was connected to the OSA and optical fibers were connected between the OSA, positioning stage, and the SLED. The biosensor was then placed and aligned on the positioning stage and a sample solution was pipetted onto the sensor. Next the user configured the SLED, OSA, and scan time using the GUI. A timer appeared while the scans were in progress, while the spectrum data and the detected minima were plotted and saved in real time. The user could stop the scans or reset the GUI using the onscreen buttons. The CSV files of the spectrum and minima data were saved in a folder for future analysis.

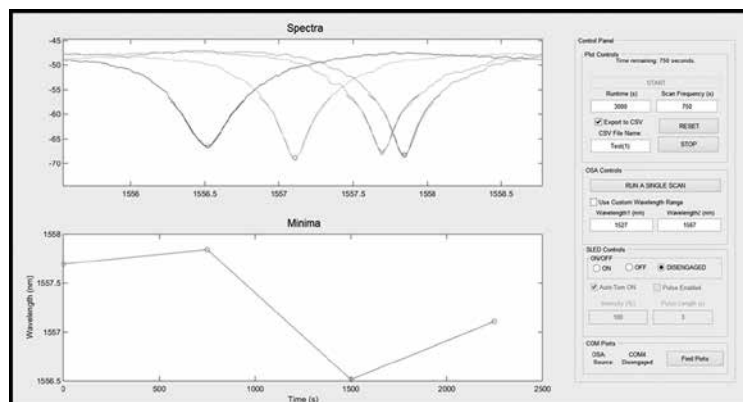


Figure 1: MATLAB GUI performing real time scans and tracking the chosen resonance's wavelength shift.

## Results:

Tests were performed using samples such as DI-water, glycerol, glutaraldehyde, BSA with and without probe proteins, and cadmium-ion solution. The sensor preparation is described in Reference 2, Part C. Preliminary tests were done using an L13 comparing the wavelength shift between water and glycerol to calibrate the OSA and test the minimum detection software. Subsequent tests were also done using an L13 biosensor conditioned using established methods from the lab group's previous work [2]. The wavelength shift observed in the most successful (Figure

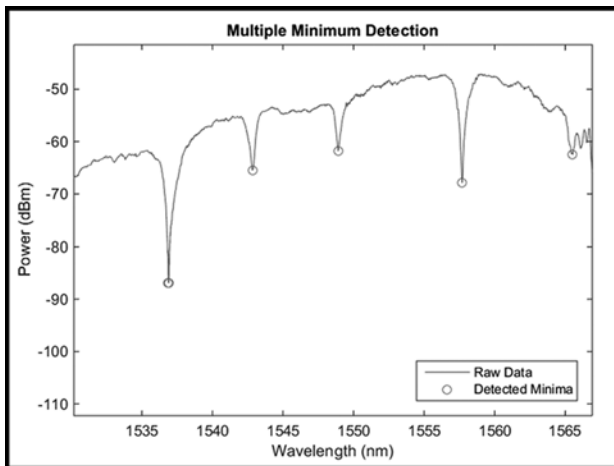


Figure 2: Example of multiple minima being detected by MATLAB.

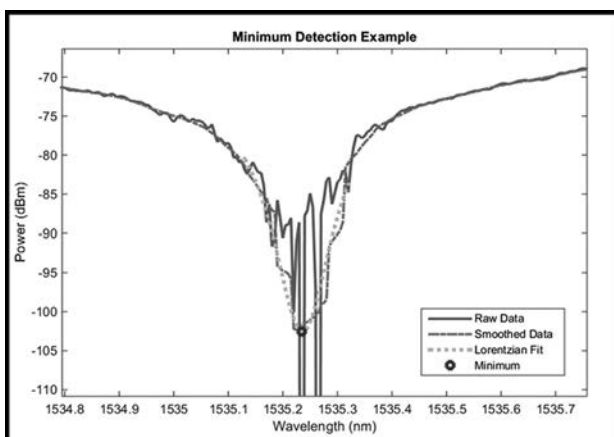


Figure 3: MATLAB smoothing raw data and fitting a Lorentzian curve to find a more accurate minimum.

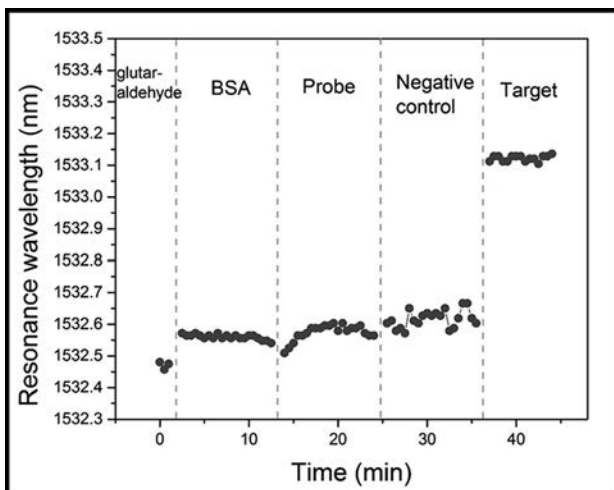


Figure 4: Data from an L13 biosensor during a repeated scan test where a resonance wavelength shift can be observed.

4) matches expected values of about a 0.5 nm wavelength shift for about 50 ppm cadmium-ions in solution.

### Conclusions:

The software developed performs at a level equal to or better than manual analysis. Biosensor behavior is more easily characterized in response to different samples in solution. More work on this software will make PC biosensors more practical sensor for use in real-world applications. Future work includes automating sample placement over the sensor using microfluidics and specialized pumps [3]. The biosensors could potentially be used to detect many different materials with more complete characterization data. These advances will allow more widespread use of PC biosensors and more accurate detection of materials in solution.

### Acknowledgements:

I would like to thank Dr. Swapnajit Chakravarti and Professor Ray Chen for their expertise. Thanks to Melvin Gutierrez for his work on the GUI and the SLED software and to Peter Grubb for his guidance on the project. Also, thanks to Hai Yan and Yi Zou for their help setting up the PC biosensor for testing. Finally, thanks to both the National Nanotechnology Infrastructure Network Research Experience for Undergraduates (NNIN REU) Program and the National Science Foundation (NSF) for providing this research opportunity under Grant No. ECCS-0335765.

### References:

- [1] *lorentzfit(x,y,varargin)* by Jered Wells, MATLAB File Exchange, August 3, 2015.
- [2] Zou, Y.; Chakravarty, S.; Chen, R.; et al.; "Waveguide Coupling Engineered High Sensitivity Silicon Photonic Crystal Microcavity Biosensors With High Yield"; *IEEE Journal of Selected Topics in Quantum Electronics*, 20, 4 (2014).
- [3] Wang, Z.; Yan, H.; Chakravarty, S.; Chen, R.; et al.; "Microfluidic channels with ultralow-loss waveguide crossings for various chip-integrated photonic sensors"; *OPTICS LETTERS*, 40, Page 1563-1566 (2015).

# Synergistic Effect of Adhesive Ligand Density and Soluble Factor TGF- $\beta$ on Epithelial Mesenchymal Transition Progression

## **Allison Bosworth** **Biological Engineering, Louisiana State University**

**NNIN iREU Site: National Institute for Materials Science (NIMS), Tsukuba, Ibaraki, Japan**

NNIN iREU Principal Investigator: Prof. Jun Nakanishi, International Center for Materials Nanoarchitectonics (MANA),

National Institute of Materials Science (NIMS), Tsukuba, Japan

NNIN iREU Mentor: Dr. Saw Marlar, International Center for Materials Nanoarchitectonics (MANA), NIMS, Tsukuba, Japan

Contact: [allison.bosworth1@gmail.com](mailto:allison.bosworth1@gmail.com), [nakanishi.jun@nims.go.jp](mailto:nakanishi.jun@nims.go.jp)

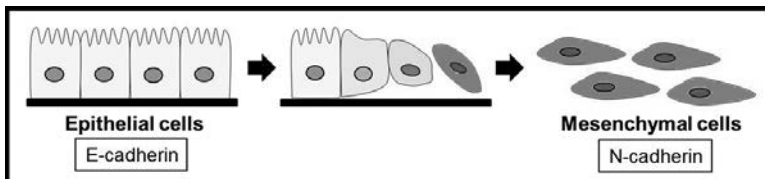


Figure 1: Visual schematic of EMT progression.

## Introduction:

Characterized by a change in cellular phenotype and an adjustment in protein expression, the epithelial-mesenchymal transition (EMT) describes the transformation of epithelial cells into a mesenchymal cell type. This transition is involved in the initial stages of cancer metastasis and enhances the migratory capacities and evasiveness of cancer cells [1]. In this study, we investigated the impact of two factors—surface density of an extracellular matrix protein-derived ligand and soluble transforming growth factor- $\beta$ 1 (TGF- $\beta$ 1)—on the progression of EMT. Gold surfaces functionalized in various ratios of adhesive ligand cRGD to bio-inert ethylene glycol (EG) were seeded with epithelial cells. This technique allows for simultaneous comparison of different stages of EMT in which morphological differences and changes in protein expression can be recorded. By investigating EMT in smaller, discrete steps, we can more accurately analyze the underlying mechanisms that drive this transformation and that ultimately drive cancer metastasis. For these experiments, Madine-Darby canine kidney (MDCK) cells were used.

## Materials and Methods:

To study EMT progression, a five-day procedure was employed. On day one, gold (Au)  $5 \times 5 \text{ mm}^2$  surfaces were cleaned via sonication in acetone and UV-ozone treatment. The bare Au surfaces were then coated with various concentrations of cyclic [Arg-Gly-Asp-D-Phe-Lys], or cRGD, in EG overnight.

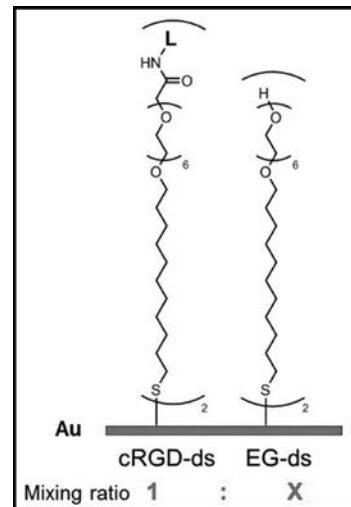


Figure 2: Surface self-assembled monolayers on a gold surface with “L” representing cRGD.

Figure 2 illustrates the structure of cRGD, represented by L, alongside EG bound to a Au surface. Because cRGD binds to  $\alpha_v\beta_3$ -integrin receptors on the MDCK cell membrane,

it renders the Au surface adhesive to MDCK cells. Since EG repels protein absorption, MDCK cells attach to the surface exclusively by integrin binding to surface cRGD peptides. Adjusting the mixing ratio of adhesive ligand cRGD to protein-repellent ligand EG on the surface allows for effective tuning of surface adhesiveness to cells. Two mixing ratios of cRGD:EG were used in these experiments—1:100 (100x) and 1:10,000 (10k); 100x represents a high-density cRGD surface, while 10k represents a low-density cRGD surface.

On day two, approximately  $5 \times 10^4$  MDCK cells per  $10\text{cm}^2$  were seeded onto each of the cRGD-coated surfaces in serum-free medium to preempt any unwanted interaction of serum proteins with cell attachment at the beginning. Three hours after initial cell seeding, serum-free medium was aspirated and replaced with complete medium. On the following day, complete medium was supplemented with TGF- $\beta$  at 10 ng/mL to induce EMT in two of the four samples. After two days of incubation with adhesive ligand cRGD and soluble growth factor TGF- $\beta$ , MDCK

cells were fixed to the gold surfaces with a 1:1 methanol:acetone solution. From there, primary antibodies bound to membrane proteins E-cadherin and N-cadherin. Fluorescently-tagged secondary antibodies then bound to the primary antibodies. These secondary antibodies fluoresce upon exposure to UV light to aid in visualization of membrane proteins. This process of immunofluorescent staining was utilized to study the presence of cadherin proteins in MDCK cells on day five. Localization of E-cadherin or N-cadherin to the MDCK membrane indicates an epithelial or mesenchymal phenotype, respectively.

### Results and Discussion:

Both the adhesive ligand cRGD, and the soluble factor, TGF- $\beta$ , played a role in controlling EMT progression in MDCK cells. Figures 3 and 4 show EMT progression from left to right with a decrease in cRGD concentration from 100x to 10k and with the addition of TGF- $\beta$ . At high cRGD densities and no TGF- $\beta$ , cells form tight clusters with a localization of F-actin in the cortical region of the cells. As cRGD density is decreased and TGF- $\beta$  is added, cells begin to elongate, move away from the tightly-bound clusters, and organize F-actin into intracellular fibers. Finally at low cRGD and the presence of TGF- $\beta$ , cells are completely elongated and F-actin is almost completely intracellular. This elongation and migration of cells coupled with the reorganization of actin within the cells allowed us to evaluate the EMT progression into four discrete steps.

To confirm this interpretation, protein localization of E-cadherin, an epithelial marker, and N-cadherin, a mesenchymal marker, was compared. At high cRGD densities and no TGF- $\beta$ , cells localized E-cadherin proteins to the membrane while at low cRGD densities and the presence of TGF- $\beta$ , cells localized N-cadherin to the cell membrane. Membrane localization of E-cadherin was less apparent than localization of N-cadherin perhaps because cells on 100x surfaces formed tight aggregates. Moreover, these trends in protein localization to the membrane support the conclusion that EMT progression was separated into four discrete steps.

### Conclusions:

Lowering cRGD surface density and adding TGF- $\beta$  gives a controlled progression of EMT in MDCK cells. Adjusting

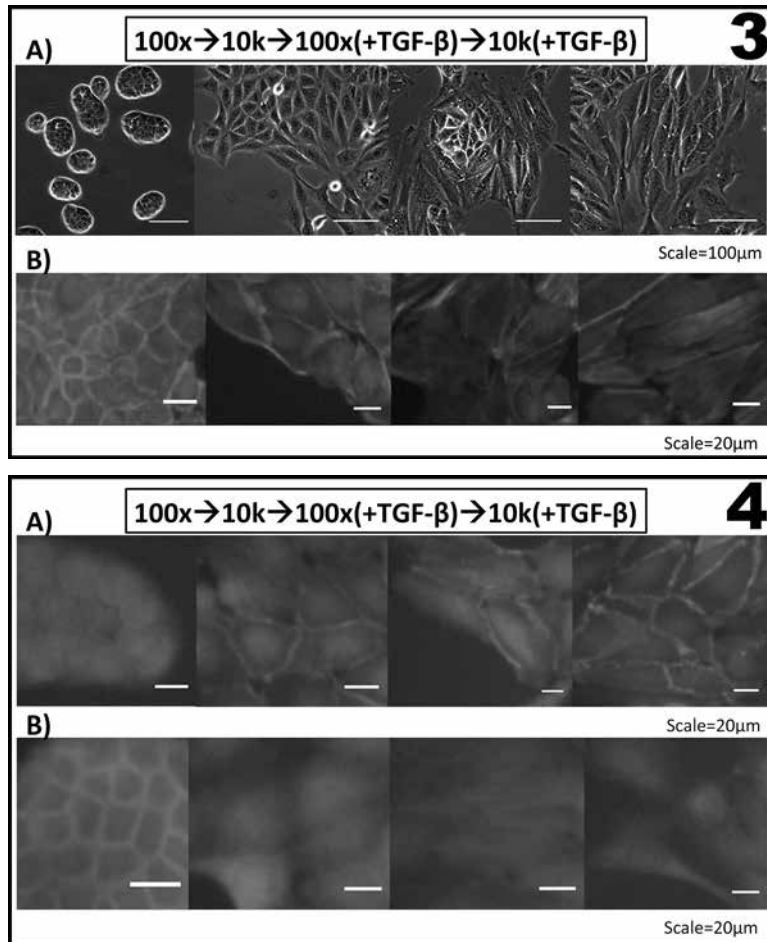


**Figure 3, top:** (A) Phase contrast images at day five. (B) Actin stained MDCK cells at day five. **Figure 4, bottom:** (A) N-cadherin and (B) E-cadherin stained MDCK cells at day five.

the concentration of TGF- $\beta$  and surface density of cRGD allows for analysis of underlying mechanisms at various degrees of EMT progression, which may give rise to novel metastatic therapeutic techniques. Future work for this project includes the quantification of gene expression via PCR or western blot to determine specifically the degree of EMT progression of each sample.

### Acknowledgments:

Funding for this project was provided by the National Science Foundation under Grant No. ECCS-0335765. Special thanks to National Nanotechnology Infrastructure Network International Research Experience for Undergraduates (NNIN iREU) Program coordinators and members of the Nakanishi lab group at the National Institute for Materials Science in Tsukuba, Japan.

### References:

[1] Kalluri, Raghu, et al. *J. Clinical Invest.*, 119, 6, 1420-1428 (2009).

# Fully Printed Organic Electrochemical Transistor on Paper for Glucose Sensing

Christopher Davidson

Biological Systems Engineering, University of Nebraska-Lincoln

NNIN iREU Site: Centre Microélectronique de Provence, École Nationale Supérieure des Mines de Saint-Étienne, France

NNIN iREU Principal Investigator: Dr. George Malliaras, Department of Bioelectronics, École Nationale Supérieure des Mines de Saint-Étienne

NNIN iREU Mentor: Eloïse Bihar, Department of Bioelectronics, École Nationale Supérieure des Mines de Saint-Étienne

Contact: cdavidson222@gmail.com, malliaras@emse.fr, bihar@emse.fr

## Abstract:

Inkjet printing of conductive polymers is a versatile, low-cost, and non-contact fabrication method for bioelectronic devices. In this study, an all-plastic glucose biosensor based on an organic electrochemical transistor (OECT) was printed on a paper substrate. An aqueous bioelectronic ink consisting of the conductive polymer poly(3,4-ethylenedioxythiophene)-poly(styrene sulfonic acid) (PEDOT:PSS) was used to print the source, drain, channel, and gate of the transistor. An ink containing chitosan/ferrocene solution was also printed to functionalize the PEDOT:PSS gate. Bioenzymatic sensing of glucose was then completed with these devices by using glucose oxidase (GOx) and phosphate buffered saline (PBS) as the enzyme and electrolyte, respectively. Initial results show glucose detection between 2.70 and 10.00 millimolar, consistent with the concentration in human blood. These results pave the way to establishing a simple, low-cost, and paper based biosensing platform suitable for point of care diagnostics.

## Introduction:

OECTs have recently gained great attention due to their high biocompatibility, ease of fabrication, and operation in low voltages, making them ideal candidates for bioelectronic applications. PEDOT:PSS is a conductive polymer ideal for fabricating OECTs due to its high conductivity, commercial availability, and its exceptional film forming properties [1]. In this study, we focused on inkjet printing a glucose sensing device. Inkjet printing is an ideal fabrication process as it presents advantages such as speed, flexibility, and low cost [2]. It can also successfully print on a multitude of substrates, including paper. Paper is an ideal substrate, as it is eco-friendly, disposable, and very inexpensive.

In this work, glucose is detected by inducing the enzyme specific reaction of glucose and GOx coupled with ferrocene, as shown in Figure 1. Ferrocene acts as an electron shuttle from the GOx to the PEDOT:PSS gate, causing de-doping of the channel and thus decreasing the drain current. This decrease is proportional to the concentration of glucose in the working solution [3].

## Experimental Procedure:

A Dimatix Materials Printer (DMP) was used to print the device, and its dimensions are shown in Figure 2. The channel and gate dimensions (length and width) were 5 mm × 1 mm and 5 mm × 2 mm, respectively. We printed

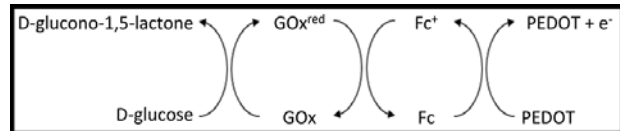


Figure 1: Reaction cycle for glucose detection using a ferrocene mediator.

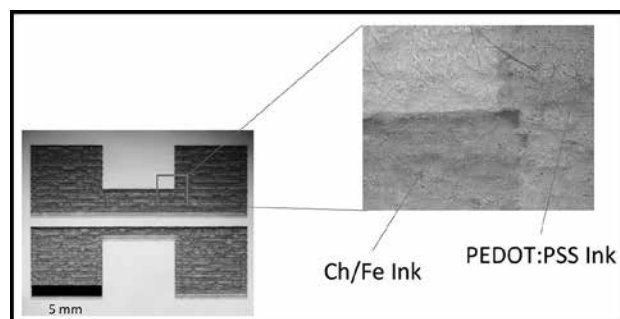


Figure 2: Fully printed OECT with zoom on gate.

two layers of pre-developed PEDOT:PSS ink recipe to fabricate the channel, drain, source, and gate of the transistor.

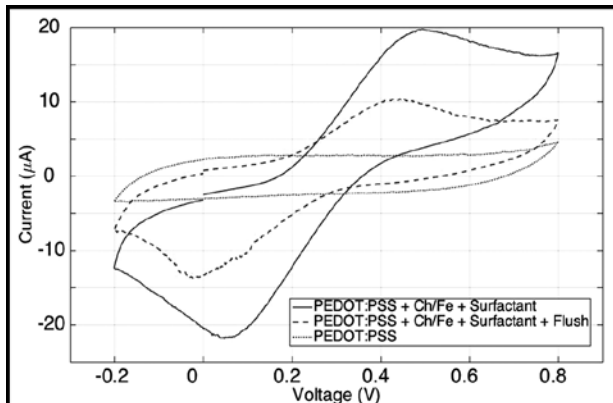


Figure 3: Cyclic voltammograms for different chitosan/ferrocene inks compared to PEDOT:PSS.

To make the electron mediator ink, a chitosan/ferrocene solution in acetic acid (0.3%wt) was first made by dissolving 15 mg of chitosan/ferrocene copolymer in 5 mL of 0.2 M acetic acid. To match this solution with the requirements of inkjet (rheological properties of the ink), we added a surfactant (Dynol 810) and a flush solution (water and ethylene glycol).

To assess the electrochemical performance of the ink in each step of its development, cyclic voltammetry was employed using a platinum wire as counter electrode, an Ag/AgCl reference electrode, and our ink as the working electrode, and can be seen in Figure 3.

Electrical characterization of the printed devices was carried out at a constant gate voltage of 0.5 V and a drain voltage of -0.7 V. In order to confine the electrolyte, a polydimethylsiloxane (PDMS) well was placed on top of the gate and channel, and the electrolyte (16  $\mu$ L) and the enzyme (2  $\mu$ L) were added. After stabilization of the drain current, different concentrations of glucose solutions were added. Figure 4 shows the device response to incremental steps in glucose concentration.

## Results and Conclusion:

Figure 3 shows the cyclic voltammograms of the chitosan/ferrocene ink after addition of surfactant, after further addition of flush solution, and a control of PEDOT:PSS. Peaks can be observed at around 0.4 V and 0.1 V for both inks containing chitosan/ferrocene solution, confirming the electrochemical activity of ferrocene.

Figure 2 shows a fully printed device. There is a clear color change between the gate and the rest of the device, indicating that the chitosan/ferrocene ink was selectively printed onto the gate of the device.

Figure 4 shows the device response upon successive additions of different glucose concentrations onto the device. There are clear changes in the current values for

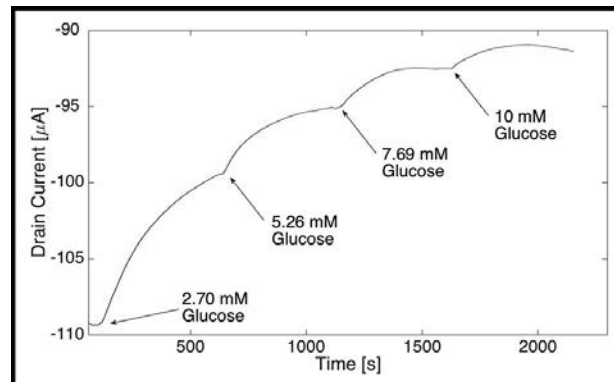


Figure 4: Device response to 2.70, 5.26, 7.69, and 10.00 mM glucose concentrations.

a range of concentrations between 2.70 mM and 10 mM, which are consistent with those in human blood [4].

## Conclusions and Future Work:

In this study, PEDOT:PSS and chitosan/ferrocene based inks were successfully printed on paper towards the development of an all printed paper OECT based glucose sensor. The detection of glucose was successful in a range of concentrations between 2.70 and 10.00 mM, similar to that in human blood. There is room for optimization, like immobilizing the enzyme on the gate and improving the sensor's sensitivity to the  $\mu$ M range, which is consistent with levels in human saliva. This work shows great potential as a disposable noninvasive sensing platform for point of care diagnostics.

## Acknowledgments:

I would like to thank the NNIN iREU Program and NSF for funding this project (under Grant No. ECCS-0335765). I would also like to thank Eloïse Bihar, Anna-Maria Pappa, Xenofon Strakosas, Mary Donahue, Vincenzo Curto, and Dr. George Malliaras for their individual help and guidance.

## References:

- [1] Shim, N, et al. All-Plastic Electrochemical Transistor for Glucose Sensing Using a Ferrocene Mediator. *Sensors* 2009;9:9896-9902.
- [2] Yun, YH, et al. A Glucose Sensor Fabricated by Piezoelectric Inkjet Printing of Conducting Polymers and Bienzymes. *Anal. Sci.* 2011;27:375-379.
- [3] Strakosas X, Bongo M, Owens RM. The organic electrochemical transistor for biological applications. *J. Appl. Polym. Sci.* 2015;132:41735.
- [4] Panchbhai, AS, et al. Correlation of Salivary Glucose Level with Blood Glucose Level in Diabetes Mellitus. *J. Oral. Maxillofac. Res.* 2012;3(3):e3.

# Imaging Live DU145 Cancer Cells Using Scanning Probe Microscope

**Catherine Demos**

**Bioengineering, Clemson University**

**NNIN REU Site: Howard Nanoscale Science and Engineering Facility, Howard University, Washington, DC**

NNIN REU Principal Investigator: Dr. Tina Brower-Thomas, College of Engineering Architecture and Computer Science, Howard University

NNIN REU Mentor: Dr. Paulette Furbert-Harris, Cancer Center, Howard University Hospital

Contact: cdemos@clemson.edu, tina.browerthomas@howard.edu, pfurbert-harris@howard.edu

## Abstract:

Different body cells have unique surface proteins that conduct electricity. Cell electrophysiology is the key to differentiating cancerous cells from healthy cells *in vivo*. Silicon carbide (SiC) is a biocompatible, chemically inert, thermally stable material on which we have tested the viability of DU145 cells. Using highly doped SiC, the relative conductivity of cells can be detected via current-sensing atomic force microscopy (CSAFM) with a flow cell to examine the living DU145 cells in media. A parallel part of this experiment is to functionalize the SiC surface to achieve specificity when attaching cells to confirm that the CSAFM method of identification is successful. After cleaning, an oxide layer is formed on the surface, then 3-aminopropyltriethoxysilane (APTES) is attached to result in a surface amenable to protein attachment followed by antibody attachment, which is the key to binding specific cells in specific areas of the substrate.

## Introduction:

SiC possesses properties that make it an ideal substrate for a new method of detection and treatment. This experimental method relies on the ability to identify different types of cells based on the electrical signatures of the membranes from a unique combination of surface proteins, ion channels, and membrane potentials [1].

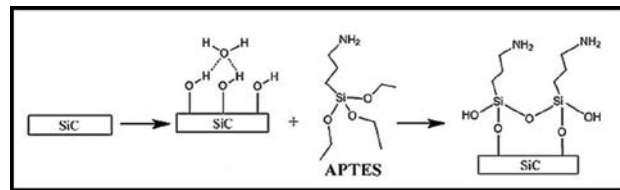


Figure 1: The APTES reaction with SiC.

## Experimental Procedure:

All experiments were performed with commercially purchased 6H highly doped SiC. All samples were ultra-sonicated for three minutes each in methylene chloride, acetone, and isopropanol, sequentially. Next they were submerged in a 5:1:1 mixture of deionized (DI) water,  $H_2O_2$ , and  $NH_4OH$  at 80°C for 10 minutes, which is the standard RCA cleaning procedure.

Two methods of oxidation and further cleaning were used to increase the reactivity of the SiC surface. One was oxygen plasma etching using a Plasma-Therm model 790 plasma enhanced system using a 20% oxygen/80% argon gas mixture for one and five minutes. The other was a tube furnace at 1000°C for 10, 30, and 60 minutes, with oxygen flowing for the duration of the heating period and argon as the samples cooled. After a thin oxide layer developed on the SiC, the samples were left exposed to air for three hours to ensure surface chemisorption of water molecules and increase the ability of the SiC to hydrolyze APTES in the next stage.

APTES silanization was performed in a class 100 clean room in an anhydrous  $N_2$  environment. The samples

were placed in a 1:49 solution of APTES in toluene for a duration of 30 minutes. They were then ultra-sonicated in toluene for 10 minutes and isopropanol for one minute, then dried under a stream of  $N_2$  gas to remove any loose APTES molecules [2]. The steps are illustrated in Figure 1.

Additionally, DU145 prostate cancer cells were tested for viability on SiC. Cells were combined with RMPI media and the concentration was adjusted to  $5 \times 10^4$  cells/ml—the optimal seeding count determined in previous experiments. SiC was placed in a sterile 6-well culture plate, some carbon-face up, others silicon-face up; 2 ml of the cells were added to each well and incubated overnight at 37°C at 5%  $CO_2$ . Inverted light microscopy was used to confirm binding of cells to the substrate. Two plates were used for sizing, with the cells on the substrates measured after 24 hours, and another two examined viability of the cells for an extended growing period of eight days, one checked every 24 hours and one left undisturbed.

CSAFM is the method used to evaluate the electrophysiological properties of the DU145 cells once they were bound to a substrate. The goal was to examine

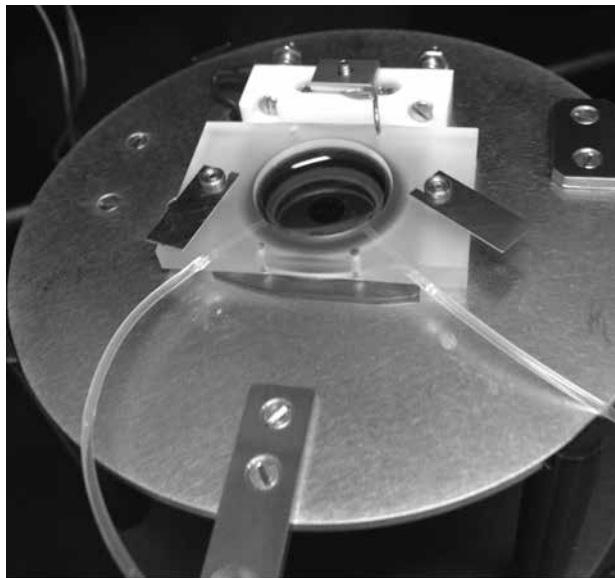


Figure 2: Flow cell and sample in media.

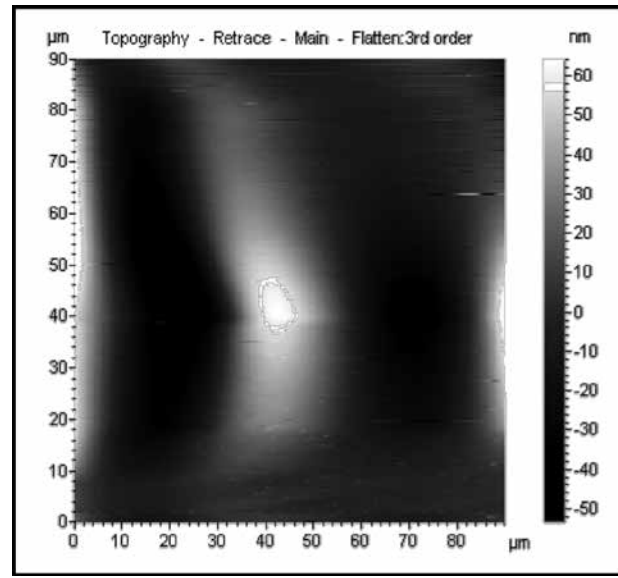


Figure 4: A topographical AFM image of a fibroblast.

living cells, so a method of keeping them in fresh media while being scanned was necessary. We constructed a pump system with a flow cell for Agilent Technologies 5500 AFM shown in Figure 2 to allow media to flow in and overflow to be drawn out of the sealed area containing the sample. This allowed the cells to be scanned while living for about six hours out of the incubator and sterile environment.

### Results and Conclusions:

The carbon-face samples grew the most and the largest cells, though both carbon- and silicon-face samples did as well as or better than the control well in cell attachment after 24 hours. Images of this experiment are found in Figure 3. These findings confirm previous experiments done by this lab.

For CSAFM, it was found that when the cells were left for at least six days in undisturbed incubation, they were attached enough to probe with the tip of the AFM and examine topographically. Before that time, the cells were either not confluent enough or not attached strongly enough to remain in place when probed with the tip of the sensor. In Figure 4 are some of the first topographical images

obtained. The current-voltage part of the examination was not completed, as the media was too ionic to obtain accurate electrical profiles of the cells themselves. This is being addressed by our lab's collaborators.

### Future Work:

In the future, the method of functionalization needs to be confirmed and taken further with the attachment of Protein A and IgG antibodies. This will allow for specific attachment of cells in predetermined locations, so the AFM can be confirmed as a valid method of identification. Also, the cells need to be more strongly adhered to the surface of the SiC so the AFM tip does not remove them during scanning. A different media or additive may help with creating more junctions for cell attachment.

### Acknowledgements:

Thank you to Dr. Tina Brower-Thomas, Dr. Paulette Furburt-Harris and the staff of the Howard Nanoscale Facility for their guidance, the NNIN REU Program for the opportunity and the NFS for funding the project under Grant No. ECCS-0335765.

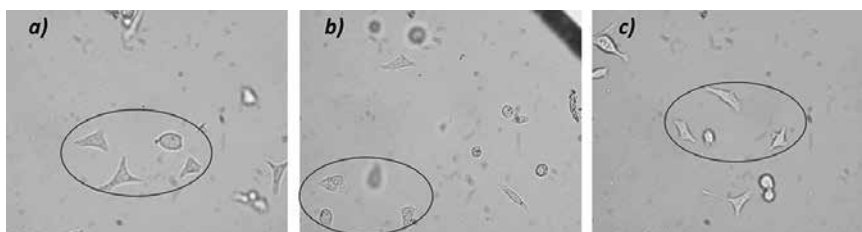


Figure 3: a) Carbon-face. b) Silicon-face. c) Control (empty well). Images taken at 24 hours (20x 1.6x).

### References:

- [1] Rzany A, Schaldach M. Progress in Biomedical Research. 2001; 6: 182-194.
- [2] Williams, E., et al. Applied Surface Science. 258, (16), 6056-6063 (2012).

# Exploration of Protein Capture Methods for Applications in Microfluidic Devices

**Matthew Devlin**

**Biomedical Engineering, Georgia Institute of Technology**

**NNIN REU Site: Cornell NanoScale Science and Technology Facility, Cornell University, Ithaca, NY**

NNIN REU Principal Investigator: Haiyuan Yu, Weill Institute for Cell and Molecular Biology,

Department of Biological Statistics and Computational Biology, Cornell University

NNIN REU Mentor: Robert Fragoza, Weill Institute for Cell and Molecular Biology,

Department of Molecular Biology and Genetics, Cornell University

Contact: [mrdevlin@gatech.edu](mailto:mrdevlin@gatech.edu), [haiyuan.yu@cornell.edu](mailto:haiyuan.yu@cornell.edu), [rf362@cornell.edu](mailto:rf362@cornell.edu)

## Abstract:

On-chip protein immunoprecipitation is often a substantial limitation in the continued development of microfluidic tools for detecting protein-protein interactions in high throughput. Though adaptable surface chemistry on glass and polydimethylsiloxane (PDMS) lend themselves to robust, on-chip protein immobilization, problems such as non-specific protein adsorption, rigorous washing conditions, and low protein synthesis yields readily diminish assay sensitivity in protein interaction screens. In an effort to improve on-chip protein expression levels, we explored various chip-protein conjugation methods, including antibody crosslinking via (3-aminopropyl)triethoxysilane-derivatized (APTES) surfaces, Protein A-conjugated surfaces, as well as streptavidin-biotin coated surfaces. Increasing sensitivity to expressed protein was also explored through varying concentrations of both capture and probe antibodies as well as through the adjustment of enzyme-conjugated or fluorescently-labeled probe antibodies. Through our protein-surface conjugation experiments, we are able to successfully synthesize and capture protein on-chip. Continued development towards quantifying the binding strengths of protein-protein interactions would mark a substantial advancement in cellular proteomics and may also help unveil new drug targets in human disease.

## Introduction:

A longstanding goal in biological research has been to fully uncover the function of proteins encoded by human genomes as well as how their expression is regulated. Consequently, researchers have been working adamantly towards the development of high-throughput systems for expressing proteins and detecting their interactions under the paradigm that the function of a protein can be better understood by knowing who its interaction partners are. Though many well characterized high-throughput methodologies for detecting protein-protein interactions exist, including yeast two-hybrid and nucleic acid programmable protein array, these methods often suffer from limited specificity and high expense [1].

Microfluidic approaches such as Protein Interaction Network Generator demonstrate promise towards improving specificity and throughput but, due to difficulties in expressing and isolating human proteins through cell-free expression systems, have not been used to screen for human protein interactions on a large scale — a gap we aim to address [2]. The ability to quantify and generate protein-protein interactions networks could, in consequence, improve our understanding of how human disease alters cell signaling networks and potentially unveil new pharmaceutical drug targets.

## Experimental Procedure:

Glass microscope slides underwent an oxygen plasma treatment before a 5 min bath in a 5% APTES/acetone solution. The slides were then rinsed with acetone then deionized water and dried with nitrogen gas. For Protein A-treated PDMS microwells, a 10:1 ratio of polymer to crosslinker (Silgard 184 Elastomer) was poured onto 500  $\mu$ m tall SU-8 columns and cured for at least 2 hrs at 60°C. Slides are then crosslinked to protein using 2 mM bissulfosuccinimidyl suberate (BS3) and then quenched in 2M Tris and 0.3M glycine for 20 min. Next, 20  $\mu$ L TnT® Reticulocyte Lysate is spotted on-chip containing 0.5  $\mu$ g of protein pairs expressed in pANT7\_nHA and pANT7\_cGST vectors. This solution is incubated for 1.5 hrs in a humid environment at 30°C.

Following incubation, TnT® solution-coated slides were moved into a 4°C environment under high humidity for 2 hrs. After incubation, slides were washed in 1x PBS with 0.1% Tween-20 (PBST) three times for 5 min per wash. Anti-GST mouse antibody (Cell Signaling Technology, #2624) was applied at 1:500 concentration, followed by 1 hr incubation at room temperature in a humid environment. Slides were then washed in PBST three times for 5 min each. HRP-conjugated anti-mouse (Cell Signaling Technology, #7076) secondary antibody was

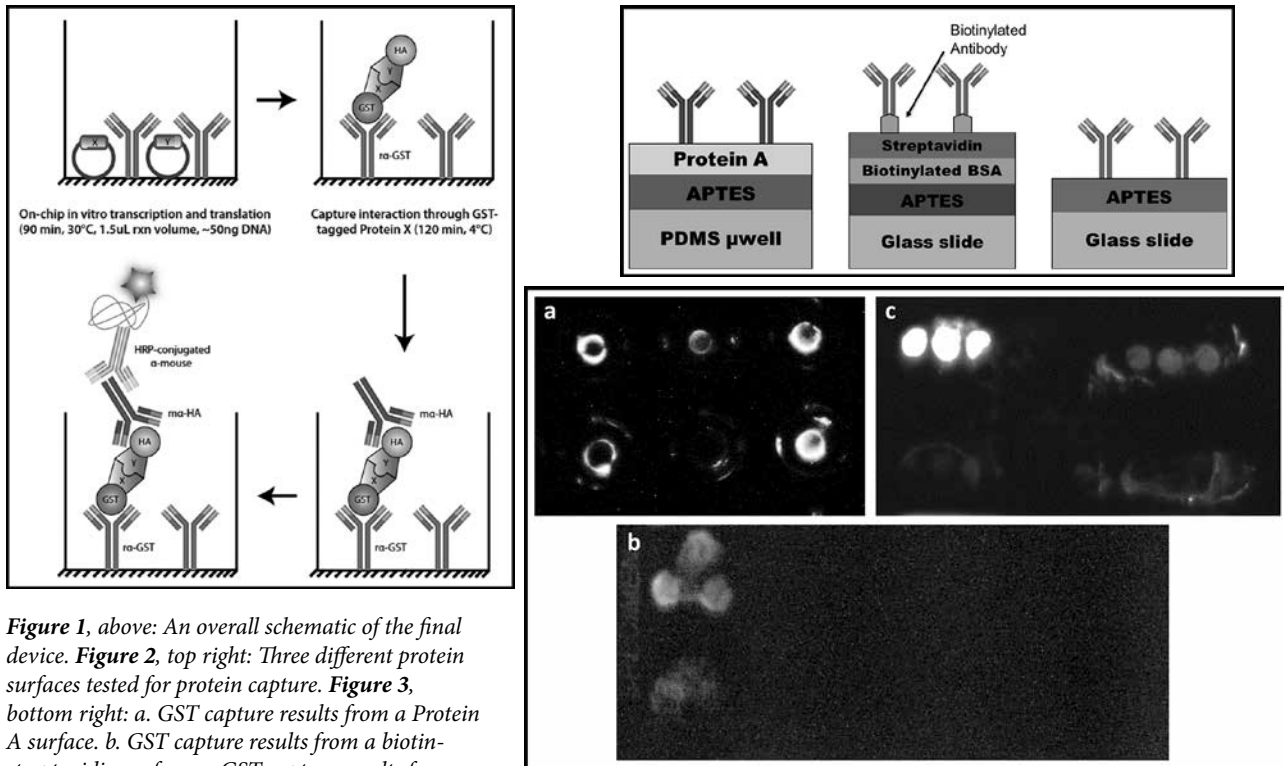


**Figure 1, above:** An overall schematic of the final device. **Figure 2, top right:** Three different protein surfaces tested for protein capture. **Figure 3, bottom right:** a. GST capture results from a Protein A surface. b. GST capture results from a biotin-streptavidin surface. c. GST capture results from an APTES only surface.

then incubated for 1 hr at room temperature in a humid environment. Next, slides were washed with PBS three times for 5 min each. ECL substrate (GE, RPN2232) was then applied and slides were imaged for up to 10 min using a Bio-Rad ChemiDoc system.

### Results and Discussion:

The APTES coated surface with direct application of antibody was the most effective, validated with high specificity when probing for the capture antibody alone. On the Protein A surface, false positives were observed as seen in Figure 3a. In Figure 3a, the rightmost column of luminescing points is composed of a positive control for GST capture on top and a negative control for GST capture on bottom. However, these points are indistinguishable from each other, and probing for GST capture on this protein surface did not yield conclusive results.

The biotin-streptavidin surface had less luminescence than APTES alone when probed solely for capture antibody, as observed in Figure 3b. The leftmost column is a positive control for GST capture; this luminescence was distinguishable from the negative control for GST capture in the rightmost column. The APTES-alone surface was able to repeatedly detect purified protein amounts as low as femtograms of protein as seen in Figure 3c. In Figure 3c, the upper left set of points is the positive control for GST while the negative control is in the middle of the figure. The positive and negative controls are clearly distinguishable

from one another. Also, the lower left portion of Figure 3c illustrates femtogram-levels of GST capture.

### Future Work:

Moving forward, protein tagged for both capture and probe antibodies must be expressed on-chip. Testing a dual-tagged protein will ensure that the antibodies in this procedure are valid to thoroughly measure interaction strength between two proteins. Once the final device is constructed and capable of quantifying tens of thousands of protein-protein interactions at a time, changes in protein-protein networks as a result of environment changes (introduction of drugs, pH, etc.) could be rapidly modeled and evaluated.

### Acknowledgements:

I would like to extend thanks to my mentor Robert Fragoza, Dr. Haiyuan Yu, the Cornell NanoScale Facility Staff, Dr. Lynn Rathbun, and Melanie-Claire Mallison for all of their support. This research was made possible by the support of the National Science Foundation under Grant No. ECCS-0335765, and the National Nanotechnology Infrastructure Network REU Program.

### References:

- [1] Ramachandran, N., et al. *Nat Meth* 5, 535-538 (2008).
- [2] Glick, Y., et al. *Journal of Visualized Experiments*, e3849 (2012).

# Research in a Diagnostic Method for Light Chain Amyloidosis

**Shaun Engelmann**

**Mechanical Engineering, Bradley University**

**NNIN REU Site: Nano Research Facility, Washington University in St. Louis, St. Louis, MO**

NNIN REU Principal Investigator: Dr. Jan Bieschke, Department of Biomedical Engineering, Washington University in St. Louis

NNIN REU Mentor: Kathrin Andrich, Department of Biomedical Engineering, Washington University in St. Louis

Contact: [sengelmann@mail.bradley.edu](mailto:sengelmann@mail.bradley.edu), [bieschke@wustl.edu](mailto:bieschke@wustl.edu), [kandrich@wustl.edu](mailto:kandrich@wustl.edu)

## Abstract:

Multiple myeloma (MM) is a disease where a plasma B cell clone is excessively replicated in the bone marrow. Systemic light chain amyloidosis (AL) is a complication in some MM patients in which excess light chain (LC) proteins from the plasma B cell clones deposit as amyloid aggregates in various organs, mainly the heart and kidney. The diagnosis of AL and its differentiation from MM is challenging and traditionally is done through invasive tissue biopsies [1]. Early handling of AL is important for effectively treating the condition, so simple and effective diagnostic methods are desired. Our goal was to develop a technique for AL diagnosis based on LC proteins from MM patients excreted in urine using an *in vitro* aggregation assay. First, *in vitro* amyloid fibril formation was optimized in order to create fibrils. Buffer pH, NaCl concentration, and temperature were varied in aggregation assays, and the aggregation kinetics were monitored using the amyloid-specific dye Thioflavin T (ThT) [2]. Samples were also shaken during aggregation, and the time intervals between shaking were also varied. This was done to alter the formation of amyloid seeds, which act as bases for LC proteins add to [3]. Amyloid aggregate morphologies then needed to be confirmed, which was done through atomic force microscopy (AFM) and transmission electron microscopy (TEM). This was performed and conditions that generated LC aggregates with fibrillar structures within a week were found.

## Methods:

**Aggregation Assays.** Aggregation assays were performed in a 96-well plate and monitored by ThT fluorescence with a Tecan Infinite F200 multimode reader. The aggregation buffers consisted of either 50 mM Glycine (pH 2.8) or sodium phosphate buffer (NaP, pH 7.2). The buffers contained either 0, 50, 150, or 300 mM NaCl. They also contained 10 mM dithiothreitol, 20  $\mu$ M ThT, and 20  $\mu$ M LC protein extracted from AL patient urine. LC proteins were aggregated in three separate sessions – one in 25°C that was shaken every 15 minutes, another in 37°C that was shaken every 15 minutes, and the last one in 37°C that was shaken every 30 minutes. Fluorescence was read at an excitation of 436 nm and an emission of 485 nm.

**Imaging.** AFM images were gathered from protein adsorbed to mica using tapping mode on a Bruker Dimension Atomic Force Microscope (AFM) and Etalon HA\_NC/15 tips. The solutions adsorbed to mica were diluted 1:4 with either glycine or NaP. Images with

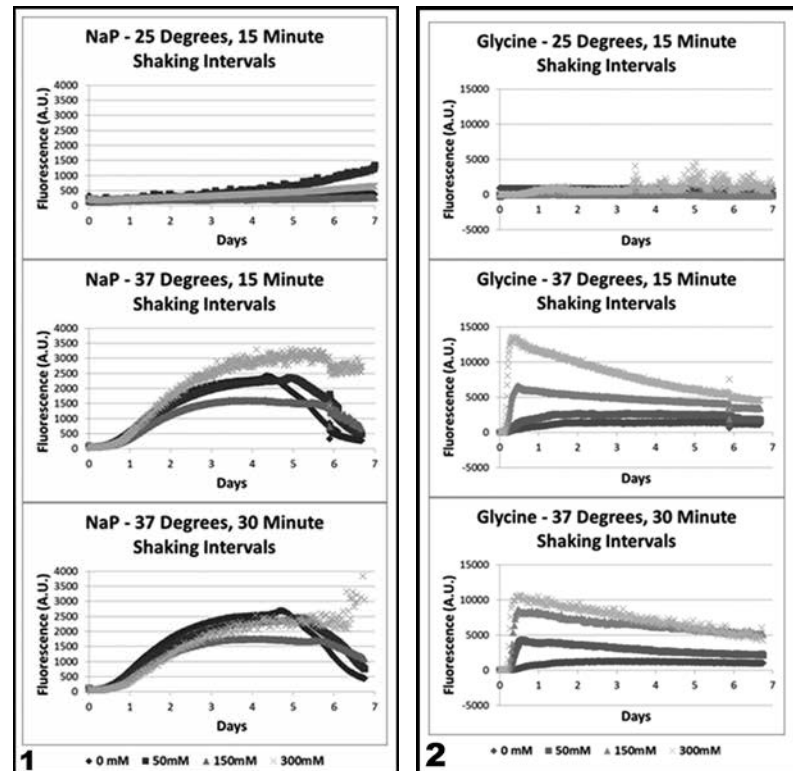
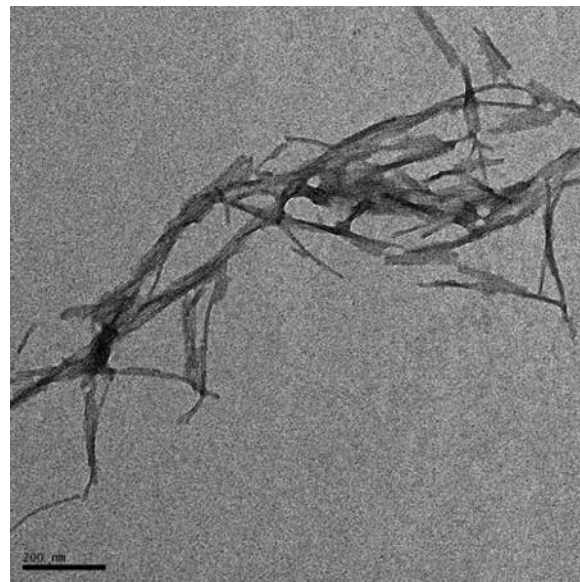


Figure 1: Plots showing LC seven day aggregations in NaP with different conditions.

Figure 2: Plots showing LC seven day aggregations in glycine with different conditions.



**Figure 3, above:** AFM image confirming amyloid formation. The image is of an area 3.3  $\mu\text{m}$  wide. **Figure 4, right:** TEM image of LC amyloids. Scale bar is 200  $\mu\text{m}$  wide.



transmission electron microscopy (TEM) were taken from protein solution adsorbed to Ted Pella 200 mesh carbon coated copper grids. Negative staining was originally performed with uranyl acetate replacement (UAR) stain. A switch to 4% uranyl acetate (UA) was made later on.

### Results and Discussion:

**Aggregation Assays.** The plots shown in Figures 1 and 2 represent the aggregation assays performed with the LC proteins. It can be seen that ThT fluorescence did increase in the aggregations performed at 37°C, which indicates the formation of amyloid structures. The aggregations performed in NaP at 37 degrees slowly reached a maximum over the aggregations. The aggregation occurred much faster in glycine, followed by a slow decrease in fluorescence after peaking. The aggregation performed in NaP in 25°C did not peak, but did increase by the end of seven days. This slowed fluorescence increase when compared to the 37°C aggregations suggests that temperature alterations could be used to control aggregation. The difference in aggregation kinetics between shaking every 15 minutes when compared to 30 minutes was negligible. NaCl concentration had a positive correlation with fluorescence amplitudes and accelerated aggregation kinetics in glycine, but such a correlation was not seen in NaP.

**Imaging.** AFM and TEM were used to determine if aggregates with fibrillar morphologies were formed during the aggregations. Previously, LC amyloid formation was only observed after 24 day aggregation with our proteins. An image of our LC amyloid fibrils is shown in Figure 3. It is from the seven day aggregation sample performed in glycine that contained no NaCl, and was shaken for 5 s every 15 minutes at 37°C. TEM imaging of the proteins proved to be difficult at first, as UAR stain resulted in precipitate that appeared like fibrillar protein structures even on grids with no protein adsorbed. This discovery

encouraged the switch to 4% UA that was used to identify fibrillar structures. A TEM image of our amyloid fibrils is shown in Figure 4.

### Conclusions:

AL is currently difficult to diagnose without invasive medical procedures. Multiple conditions for *in vitro* aggregation of LC isolated from AL patient urine were investigated to determine if it could be used in AL diagnosis. Temperature and NaCl concentration were shown to affect aggregation, suggesting that control over LC amyloid aggregation is possible. AFM and TEM were used to show amyloids were formed during aggregation assays. The optimized aggregation protocol accelerated LC amyloid fibril formation to a few days instead of three weeks, encouraging its future utility as a diagnostic tool.

### Acknowledgements:

I would like to thank Dr. Jan Bieschke, Kathrin Andrich, Nathan Reed, and Remya Nair of Washington University in St. Louis for all their help and the opportunity to work on this project. I would also like to thank Melanie-Claire Mallison of Cornell University, and the NNIN and the NSF for the invitation to participate in the NNIN REU program, and for funding under Grant No. ECCS-0335765.

### References:

- [1] Merlini, G; "Molecular Mechanisms of Amyloidosis"; The New England Journal of Medicine, 349, 583-596 (2003).
- [2] Levine, H; "Quantification of Beta-Sheet Amyloid Fibril Structures with Thioflavin T"; Methods in Enzymology, 309, 274-284 (1999).
- [3] Dobson, C; "Protein Folding and Misfolding"; Nature, 426, 884-890 (2003).

# Optimization of Nanoparticle Delivery to Plants: Do Nanoparticle Properties Affect Cellular Internalization?

**Christina Franke**

**Biomedical Engineering, Case Western Reserve University**

**NNIN REU Site: Nano Research Facility, Washington University in St. Louis, St. Louis, MO**

NNIN REU Principal Investigator: Dr. Pratim Biswas, Energy, Environmental and Chemical Engineering, Washington University in St. Louis

NNIN REU Mentor: Dr. Ramesh Raliya, Department of Energy, Environmental and Chemical Engineering, Washington University in St. Louis

Contact: christina.franke@case.edu, pbiswas@wustl.edu, rameshraliya@wustl.edu

## Abstract:

To minimize damage to the ecosystem and enhance sustainability in farming practices, intervention of nanotechnology in agriculture has increased in recent years. The purpose of this work was to study the effects of various gold nanostructures of 30 to 80 nm delivered by foliar application on uptake, translocation, and accumulation in a watermelon plant. Cellular uptake and translocation of gold nanoparticles from leaf to root was confirmed by ICP-MS. Accumulation and transport of nanoparticles depends on nanoparticle shape and application method.

## Introduction:

Gold nanoparticles (AuNPs) have been extensively studied in recent years due to the abundance of their potential applications to biological systems; being biologically inert, AuNPs are less toxic to cells than nanoparticles of other materials [1]. Because they also adsorb DNA easily, AuNPs can be used in agricultural biotechnology for delivery of genetic material to plant cells [2] and detection of plant viruses [3]. Researchers have asked the questions: How do we measure the ecotoxicity of these emerging technologies, and how do we make these technologies safe and sustainable? To answer these questions, it is essential to understand the fundamental mechanisms of morphology-dependent cellular uptake of gold nanoparticles and their subsequent fate in a plant system.

## Experimental Procedure:

**Gold Nanoparticle Synthesis and Characterization.** AuNPs of spherical, cubic, rhombic dodecahedral (RD), and rod morphologies were chemically synthesized using seed-mediated methods [4,5] and characterized for physical diameter, hydrodynamic size and zeta potential using transmission electron microscopy (TEM) and dynamic light scattering respectively, and surface plasmon resonance determined with UV-visible spectrophotometry. Finally, concentrations of nanoparticles in suspension were analyzed using inductively coupled plasma-mass spectroscopy (ICP-MS).

**Application of Nanoparticles to Plant.** Foliar aerosol delivery of nanoparticles (NPs) may help to reduce environmental harm by increasing uptake by plants

and limiting contamination of the soil environment [6]. Consequently, we employed a foliar application of AuNPs that delivered them through the stomatal openings, avoiding direct contact with the soil ecosystem. The phloem subsequently transports NPs from shoot to root [7]. Watermelon plants (*Citrullus lanatus*) were chosen for this experiment due to their large stomata and vessel size, which may facilitate NP translocation [6]. In this study, drop-cast and aerosol based foliar applications were compared to determine the effect of applied droplet size on AuNPs-plant interactions. The drop-cast method uses an auto pipette to render  $800 \pm 175 \mu\text{m}$  droplets that may contain soft agglomerations of nanoparticles. An aerosol method, the atomizer, breaks up agglomerations, producing tiny droplets in the mean size range of  $250 \pm 50 \text{ nm}$ . Real-time applied particle size was monitored using scanning mobility particle size (SMPS) measurement.

**Nanoparticle Uptake Analysis.** Plants were harvested 48 hours after applying the nanoparticles and washed to remove soil. Roots, stems, and leaves of each plant were separated, dried, and digested. The resulting concentration of elemental gold in each plant section was analyzed with the aid of ICP-MS.

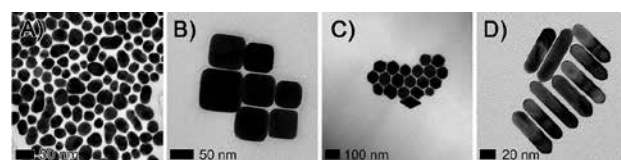


Figure 1: TEM images of gold (A) spheres, (B) truncated cubes, (C) rhombic dodecahedra, and (D) rods.

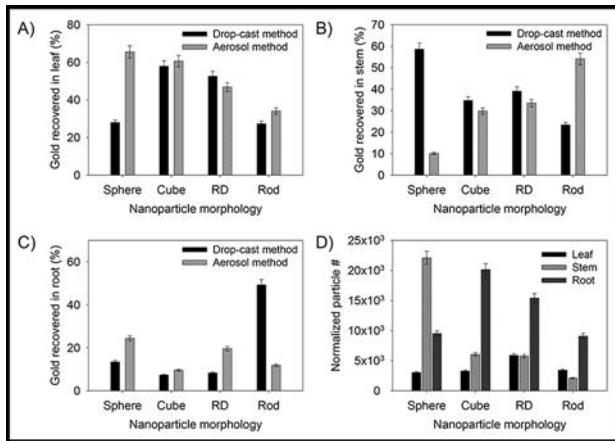


Figure 2: Percent of total gold in plant that was recovered by ICP-MS in (A) root, (B) shoot, and (C) root sections of treated plants, comparing results of drop-cast and aerosol methods. (D) Number of particles recovered in sections of aerosol-treated plants, normalized to number concentration of particles.

Particle Size <sup>a</sup> (nm)	Hydrodynamic Size <sup>b</sup> (nm)	PDI <sup>c</sup> 0.5	$\lambda_{\text{max}}^{\text{d}}$ (nm)	Zeta Potential <sup>e</sup> (mV)	Concentration, Au (ppm)
Sphere	35	61.0 $\pm$ 31.6	0.457	527	-40.5
Cube	70	99.2 $\pm$ 25.1	0.034	563	56.7
Rhombic	65	99.8 $\pm$ 30.4	0.066	550	64.3
Dodecahedra					1.18 $\times$ 10 <sup>4</sup>
Rod	20, 60 <sup>f</sup>	114.1 $\pm$ 52.1	0.296	816	43.9
					1.44 $\times$ 10 <sup>3</sup>

<sup>a</sup> Mean geometric diameter, obtained from TEM images (Fig. 1)  
<sup>b</sup> Diameter, length  
<sup>c</sup> From DLS, intensity particle size distribution  
<sup>d</sup> Polydispersity index  
<sup>e</sup> Surface Plasmon Resonance, obtained from maximum UV-vis peak

Table 1: Characterization data for nanoparticles in aqueous suspension.

	Method	Amount in leaf (%)	Amount in stem (%)	Amount in root (%)	Percent difference, drop-cast vs aerosols
Sphere	Drop-cast	28.0	58.6	13.4	10.9
	Aerosol	65.5	10.1	24.4	
Cube	Drop-cast	57.9	34.8	7.3	2.3
	Aerosol	60.6	29.8	9.6	
Rhombic	Drop-cast	52.6	39.1	8.3	11.3
	Aerosol	46.8	33.6	19.6	
Rod	Drop-cast	27.4	23.4	49.3	37.4
	Aerosol	34.0	54.1	11.8	

Table 2: Results of elemental analysis of gold in plant sections by ICP-MS.

## Results and Conclusions:

All characterization data is depicted in Table 1. Images confirming nanoparticle geometric diameters and morphologies were obtained with TEM (Figure 1). Uptake and distribution of AuNPs throughout the plant system was confirmed by ICP-MS. The measured concentrations of elemental gold in each sample were normalized by the dried mass of the plant section, and this data was processed to determine the percent of recovered gold in each plant section (Figure 2).

Comparing the two application methods, the aerosol method enhanced the transport of low aspect ratio NPs (Sphere, Cube, RD) while the larger droplet size applied by the drop-cast method improved the transport of high aspect ratio, rod-shaped NPs. For sphere, cube, and RD morphologies respectively, the increase in translocation rate of the aerosolized versus drop-cast nanoparticles was 10.9, 2.3, and 11.3%, whereas a 37.4% decrease in translocation rate was observed for the nanorods (Table 2).

Among drop-cast NPs, a trend in the efficacy of translocation (percent of recovered gold accumulated in roots) was observed as: rod (49.3%) > sphere (13.4%) > RD (8.3%) > cube (7.3%) (Table 2). In order to account for any discrepancies in the number of particles applied by the aerosol method, the aerosol results were normalized by the acquired concentration of gold obtained by our SMPS number concentration measurements.

From these normalized results (Figure 2D), a trend in the efficacy of translocation (number of particles recovered in root) was observed as: cube (2.0  $\times$  10<sup>4</sup>) > RD (1.5  $\times$  10<sup>4</sup>) > sphere (9.5  $\times$  10<sup>3</sup>) > rod (9.0  $\times$  10<sup>3</sup>), a trend that again suggests the aerosol application method results in improved translocation of low aspect ratio particles. Further experiments are needed to confirm these results, as well as to study the effects of other nanoparticle properties on their uptake and fate.

## Importance of the Study:

From the morphology-dependent trends in nanoparticle translocation, it can be concluded that accumulation and transport of nanoparticles depends on nanoparticle shape. Our evidence also suggests that different application methods may be optimal for delivery of different morphologies of nanoparticles to plants.

## Acknowledgements:

I would like to thank Dr. Pratim Biswas, my mentor Dr. Ramesh Raliya, and the NRF staff for their guidance and expertise. This project was made possible by the NNIN REU Program under NSF Grant No. ECCS-0335765.

## References:

- Shukla, R., et al. Langmuir, 2005. 21(23): p. 10644-10654.
- Nair, R., et al. Plant Science, 2010. 179(3): p. 154-163.
- Zhao, W., et al. Biosensors and Bioelectronics, 2011. 26(10): p. 4241-4244.
- Becker, R., et al. J Colloid Interface Sci, 2010. 343(1): p. 25-30.
- Wu, H.-L., et al. Langmuir, 2010. 26(14): p. 12307-12313.
- Wang, W.-N., et al. J Nanopart Res, 2013. 15(1): p. 1417-1430.
- Wang, Z., et al. Environ Sci Technol, 2012. 46(8): p. 4434-4441.

# Development of a Microfluidic Mimic of the Human Microvasculature to Study Sickle Cell Disease

Michelle Galarneau

Chemical and Biomolecular Engineering, University of Notre Dame

NNIN REU Site: Minnesota Nano Center, University of Minnesota-Twin Cities, Minneapolis, MN

NNIN REU Principal Investigator: Dr. David Wood, Department of Biomedical Engineering, University of Minnesota-Twin Cities

NNIN REU Mentor: Xinran (Daniel) Lu, Department of Biomedical Engineering, University of Minnesota-Twin Cities

Contact: mgalarne@nd.edu, dkwood@umn.edu, luxxx794@umn.edu

## Introduction:

Often characterized by severe pain crises and organ damage due to hypoxia, sickle cell disease (SCD) is a genetic disorder caused by a mutation in the hemoglobin molecule of red blood cells (RBCs) [1]. This mutation leads RBCs to stiffen under hypoxic conditions, in turn making the cells more susceptible to obstructing blood flow. Known as a vaso-occlusive crisis (VOC), this obstruction stands as the major cause of morbidity and mortality in SCD [2]. Currently, hydroxyurea (HU) is the sole FDA-approved drug treatment option available to patients, and yet HU is ineffective in one-third of those treated [3]. Consequently, there is a clear need for more effective drug treatments, as well as a screening platform to evaluate drug efficacy. Thus, we created an *in vitro* microfluidic disease model to screen new drug treatments. A remarkable alternative to *in vivo* techniques, microfluidics provides a convenient and reproducible platform with which to simulate the rheological occurrences of SCD.

## Methods:

The optimal design for the device was to produce a linear oxygen tension gradient across the microvasculature, mimicking physiological conditions. AutoCAD was used to design the device layers.

Design considerations for the microvasculature layer included channel width (vessel diameter), bifurcations, segmental length, total length, and channel height. The most important consideration was channel width, as the range of diameters across vessels composing the microvasculature (small arteries, arterioles, capillaries, venules, small veins) differs according to the anatomical region of interest. To account for these differences, we designed twelve microvasculature layers featuring varied channel width ranges. The design we fabricated for experimental purposes has a range of 10  $\mu\text{m}$  to 60  $\mu\text{m}$ , which is both physiologically accurate and amenable to the dimensional constraints imposed by polydimethylsiloxane (PDMS). In addition, the design we fabricated and tested was 3 mm in total length.

We then designed a layer containing a series of gas channels that, when overlaid onto the microvasculature layer, produced an oxygen tension gradient. The oxygen layer we fabricated consisted of five gas channels, whose dimensions were determined via finite element modeling of oxygen diffusion in COMSOL.

We used soft photolithography with SU-8 2000 series photoresist to fabricate the master for each layer. We then cast these masters with PDMS, and the layers were subsequently cured and bonded to each other and to a glass slide via oxygen plasma treatment.

Specific oxygen tensions were created by cycling an air stream and a  $\text{N}_2$  stream via solenoid valves. The duty cycles necessary to produce the desired tensions were specified in a MATLAB/Ardiuno system. To ensure proper calibration, oxygen tensions were also measured at each gas outlet.

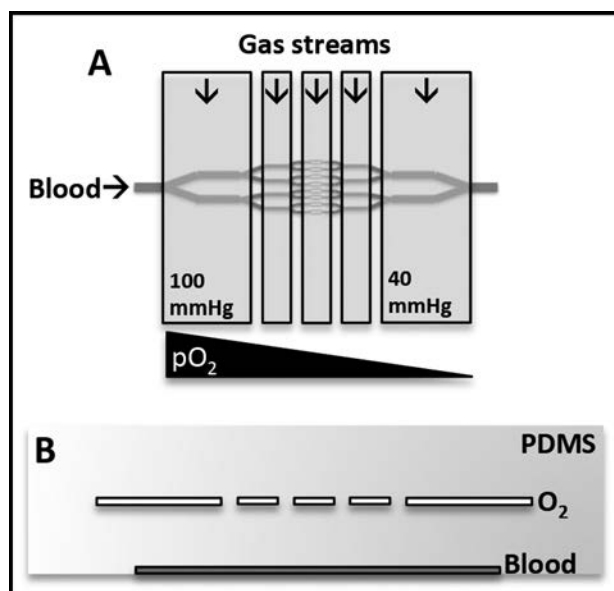


Figure 1: A. Top-down view of device. B. Cross-sectional view of device.

## Results and Discussion:

During the modeling phase of this project, we found the most important parameters in obtaining the optimal design to be width of the gas channels, distance between the gas channels, and gap width between the microvasculature and oxygen layers. Furthermore, while a large gap width between layers corresponded to a more linear oxygen gradient, we sought to minimize this gap width for construction purposes. Thus, series of stationary studies were run in COMSOL, each for a specific gap width, and tension data across the microvasculature layer were plotted. After fitting a line to the data and determining variance for each data point, a threshold for the average variance was set (this threshold was applied to all five-channel oxygen layer designs) and an optimal gap width was obtained. Figure 2 displays the modeled tension curve for this final design.

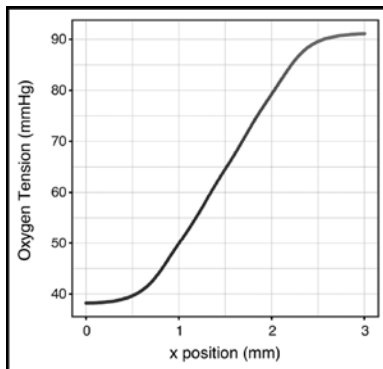


Figure 2: Finite element model of oxygen gradient.

To validate the oxygen gradient experimentally, we used 4 mM tris(2,2'-bipyridyl)dichlororuthenium(II) hexahydrate (RuBPy), an  $O_2$ -sensitive dye whose luminescence is quenched in the presence of  $O_2$ . We perfused this solution through channels directly beneath the oxygen layer (i.e., channels analogous to the microvasculature layer), and measured luminescence intensity values using an inverted epifluorescence microscope. Intensity readings were then converted into tensions based on a calibration curve. These tensions are plotted in Figure 3.

Characterization with RuBPy showed that the experimental oxygen tension gradient has a decreasing trend; however, it is not perfectly linear, as the model predicts. Using a luminophore with a higher sensitivity, as well as minimizing the presence of unwanted features/

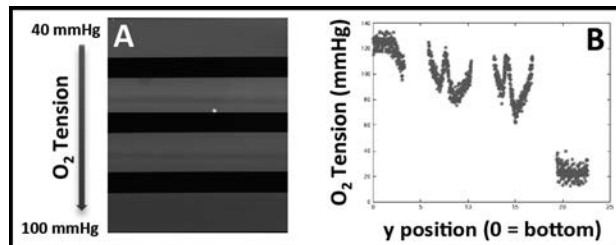


Figure 3: A. Image of RuBPy luminescence intensity gradient across four channels. Light regions correspond to low  $O_2$  tensions. B. Experimental  $pO_2$  vs. position data.

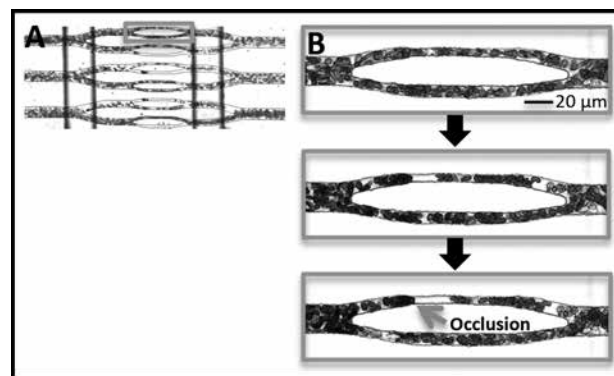


Figure 4: A. Brightfield image of a region of the device, through which sickle cell blood flows. B. Time progression of blood flowing through the 10  $\mu$ m-wide channels of device as the oxygen gradient develops. In the bottom image, gradient is fully developed.

debris in the device, would likely lead to validation of a more linear gradient.

We experimented with running a sickle cell blood sample through the device under a pressure of 1 psi. Upon gradient development, we observed significant slowdowns in blood flow, as well as occlusions within the capillary-sized channels (Figure 4). Knowing that sickle RBCs respond to these conditions, such experiments lend insight into the mechanical effects on the rheology of SCD.

## Conclusions:

We developed a microfluidic device to serve as a SCD model, and determined that the device is capable of reproducing hallmark rheological occurrences of the disease. By capturing even more physiologically relevant parameters in future designs, we hope this device ultimately becomes an accurate, accessible means of screening new drug treatments for SCD.

## Acknowledgements:

I would like to thank Dr. David Wood, Daniel Lu, and all other members of the Living Devices Lab and the Minnesota Nano Center for their incredible guidance. I would also like to acknowledge the NNIN REU Program and the NSF for funding this research under Grant No. ECCS-0335765.

## References:

- [1] Belcher, J.D., et al. "Activated monocytes in sickle cell disease: potential role in the activation of vascular endothelium and vaso-occlusion." *Blood* 96.7 (2000): 2451-2459.
- [2] Wood, D.K., et al. "A biophysical indicator of vaso-occlusive risk in sickle cell disease." *Science trans. medicine*, 4.123 (2012): 1-7.
- [3] Fathallah, H., and G.F. Atweh. "Induction of fetal hemoglobin in the treatment of sickle cell disease." *American Society of Hematology Education Program Book* 2006.1 (2006): 58-62.

# Small Interfering RNA Delivery for the Treatment of Hereditary Bone Disease

**Staci Hill**

**Chemistry, Middlebury College**

**NNIN iREU Site: National Institute for Materials Science (NIMS), Tsukuba, Ibaraki, Japan**

**NNIN iREU Principal Investigator: Dr. Nobutaka Hanagata, Nanotechnology Innovation Station, NIMS, Tsukuba, Japan**

**NNIN iREU Mentor: Xianglan Li, Nanotechnology Innovation Station, National Institute for Material Science, Tsukuba, Japan**

**Contact: staciannhill@gmail.com, hanagata.nobutaka@nims.go.jp, li.xianglan@nims.go.jp**

## Introduction:

Osteogenesis imperfecta (OI) is a heterogeneous bone disease classified into eight different types based on phenotype and genotype [1]. OI type V is caused by a mutation of interferon-induced transmembrane protein 5 (IFITM5) [2]. The mutant protein has an additional five amino acids (Met-Ala-Leu-Glu-Pro) at the N-terminus in individuals with OI type V [2].

IFITM5 is an osteoblast-specific membrane protein previously seen to be a positive regulator for bone formation in *in vitro* studies [3]. Despite this evidence, recent studies show that bone formation of *Ifitm5* knockout mice are comparable to bone formation of the wild type [3,4]. The discrepancy between the *in vitro* and *in vivo* experiments suggests that there exists an *in vivo* mechanism in place to ensure healthy bone formation in the absence of the protein. Given that OI type V is caused by a mutation in IFITM5, suppressing IFITM5 protein translation should restore healthy bone growth for individuals with the disease.

In this report, small interfering RNA (siRNA) was used to suppress the translation of the mutant protein IFITM5 *in vitro*. Four transfection reagents were tested using mouse osteoblast cells: DOTAP, Lipofectamine2000, Lipofectamine RNAiMAX (RNAiMAX), and calcium phosphate (CaP) nanoparticles. Following transfection, cells were lysed to extract and purify RNA. RNA was subsequently converted to DNA using PCR, and q-PCR was used to determine relative gene expression. Among the transfection reagents used, RNAiMAX was the most effective, suppressing gene translation by an average of 60%.

## Materials:

Mouse osteoblasts (MC3T3) and MEM-alpha medium (10% FBS) were used throughout the study. Lipofectamine2000 and RNAiMAX were purchased from Invitrogen Corporation by Life Technologies (Carlsbad, CA, USA). DOTAP was purchased from Roche Diagnostics GmbH (Mannheim, Germany). CaP nanoparticles were made using reagents from the CalPhos Mammalian Transfection Kit obtained from Clontech Laboratores, Inc.

(Mountain View, CA, USA). Isogen used for RNA extraction was obtained from Nippon Gene Co. (Tokyo, Japan). Real-time PCR (q-PCR) was carried out on a LightCycler System. Glycerol 3-phosphate dehydrogenase (GAPDH) was used as a housekeeping gene.

## Methods:

All incubations not specified were carried out at 37°C in a 5% CO<sub>2</sub> controlled environment. All siRNA complexes were made following manufacturer protocol.

For liposomal transfection, cells were seeded at 1.5 × 10<sup>4</sup> cells/cm<sup>2</sup> on six well plates. Cells were immediately exposed to the transfection reagent complexed with either IFITM5 siRNA (50 pmol/well) or control siRNA (SCN01) (50 pmol/well).

	Condition A	Condition B	Condition C
Total siRNA (ug)	0.34	0.68	1.60
[siRNA] (ug/mL)	20	20	40
[CaP] : [siRNA]	5 : 1	2.7 : 1	2.7 : 1

For CaP nanoparticle transfection, cells were seeded overnight at 7.0 × 10<sup>3</sup> cells/cm<sup>2</sup>. The next day, medium was replaced with a mix of serum free medium and CaP nanoparticles complexed with either IFITM5 siRNA or SCN01 siRNA. Table 1 details the three conditions. Three hours after transfection, serum-free medium incubated in a 10% CO<sub>2</sub> environment was added so that the medium volume was doubled. The addition of slightly acidic medium aided the dissolution of the nanoparticles.

After a 24 hr incubation period, all wells were replaced with fresh medium and a mix of mutant IFITM5 plasmid (2 ug/well) and Lipofectamine2000 transfection reagent. A subsequent incubation period of 24 hours ensured complete transfection and replication of the genetic material.

Cells were washed with PBS, and then total RNA was extracted with Isogen according to manufacturer protocol.

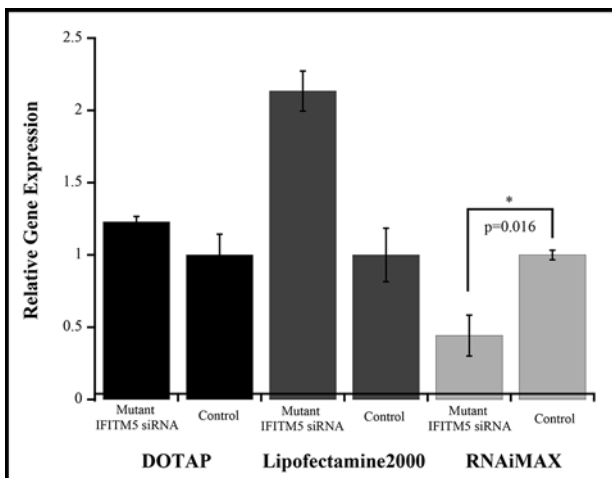


Figure 1: Relative expression of mutant IFITM5 genetic material. Three different commercially available liposomal transfection reagents are compared.

Concentration of extracted RNA was determined using UV/Vis spectroscopy. RNA was diluted to 500 ng/uL and then converted to DNA using reverse transcriptase. Resulting DNA was diluted to 5 ng/uL. Expression was quantitatively measured using the cross-point of amplification as determined by real-time polymerase chain reaction (q-PCR).

## Results and Discussion:

Figure 1 and 2 show the relative expression of mutant IFITM5 genetic material, comparing osteoblasts transfected with IFITM5 siRNA and control siRNA. Figure 1 highlights the liposomal transfection reagents studied, among which RNAiMAX suppressed IFITM5 gene expression 60% relative to the control. DOTAP and Lipofectamine2000 both failed to suppress gene expression. The success of RNAiMAX is difficult to ascertain because its chemical and structural properties are not distributed by the manufacturer. Additionally, the release mechanism of siRNA into the cell after endocytosis is still unclear. These conceptual barriers prevent a detailed explanation for siRNA suppression using RNAiMAX. Factors that may influence the transfection efficiency include the size of the liposome complex and its chemical composition.

Figure 2 shows the results from individual studies using CaP nanoparticles as the siRNA transfection reagent. The condition with a greater CaP:siRNA ratio and lower concentration of siRNA was seen to suppress gene expression 30% relative to the control.

Because siRNA is foreign genetic material, excess siRNA can induce apoptosis while too little siRNA would decrease the knockdown effect. Therefore, concentration of siRNA is critical to the survival of the cells and transfection

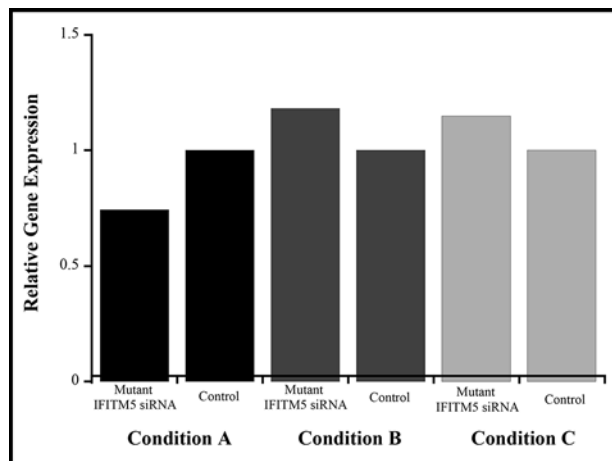


Figure 2: Relative expression of mutant IFITM5 genetic material. Three different compositions of CaP nanoparticles are compared.

efficiency. This experiment suggests that 20 ug/mL of siRNA is sufficient to suppress gene expression, but the CaP study included a single experiment per variation. The reproducibility of these results is yet to be determined.

## Conclusions:

The transfection reagent RNAiMAX demonstrates that gene suppression is feasible on the cellular level. Due to the limited information of the compound, RNAiMAX is not a desirable method for *in vivo* studies at this time. CaP nanoparticles as a known biologically degradable compound should be investigated further to determine if it is a viable method to suppress gene expression both on the cellular and physiological level. Furthermore, the method of siRNA delivery subsequent to endocytosis should be investigated for optimization of transfection efficiency.

## Acknowledgements:

The NSF (Grant No. ECCS-0335765) and National Nanotechnology Infrastructure Network International Research Experience for Undergraduates (NNIN iREU) Program are acknowledged for funding and supporting this research. In addition, the unwavering support of Dr. Hanagata-san and inspiring mentorship under Li-san is greatly appreciated.

## References:

- [1] Semler, O., et al. Am. J. Hum. Genet. 2012, 91 (2), 349-357.
- [2] Cho, T.-J., et al. Am. J. Hum. Genet. 2012, 91 (2), 343-348.
- [3] Hanagata, N., et al. J. Bone Miner. Metab. 2011, 29 (3), 279-290.
- [4] Hanagata, N. J. Bone Miner. Metab. 2015, 1-9.

# Optimization and Characterization of Au Nanoparticle-DNA Conjugate Devices

**Joseph P. Hittinger**

**Chemical and Biomolecular Engineering, Vanderbilt University**

**NNIN REU Site: Washington Nanofabrication Facility and Molecular Analysis Facility, University of Washington, Seattle, WA**

NNIN REU Principal Investigators: Dr. James M. Carothers, Chemical Engineering, University of Washington;

Dr. David G. Castner, Chemical Engineering and Bioengineering, University of Washington

NNIN REU Mentor: Michael A. Newton, Chemical Engineering, University of Washington

Contact: [joseph.p.hittinger@vanderbilt.edu](mailto:joseph.p.hittinger@vanderbilt.edu), [jcaroth@uw.edu](mailto:jcaroth@uw.edu), [castner@uw.edu](mailto:castner@uw.edu), [manewton@uw.edu](mailto:manewton@uw.edu)

## Abstract:

In this project, spherical gold nanoparticles (AuNP) were loaded with deoxyribonucleic acid (DNA) oligonucleotides to make a series of single- and double-stranded conjugates, which were characterized via various established methods to optimize loading efficiency and functionality. Characterization methods used include ultraviolet-visible spectrophotometry (UV-Vis) to measure absorbance and estimate loading efficiency; dynamic light scattering (DLS) and zeta potential (ZP) measurements to estimate conjugate size and extent of aggregation; and gel electrophoresis to separate and analyze conjugates based on size and charge. Toehold-mediated strand displacement DNA fluorescent gates were tested in order to relate characterization to device performance. Salt aging to 100 mM NaCl provided high loading ( $131 \pm 7$  strands per particle) with low particle aggregation and relatively high hybridization efficiency ( $58 \pm 6\%$ ), while maintaining strand displacement logic gate device capability.

## Introduction:

AuNPs have been broadly studied as platforms for small molecule, antibody, and aptamer delivery to cells because of the variety of functional groups that can be bound to the AuNP surface [1]. However, many reports of AuNP applications in biomedical diagnostics and therapeutics lack sufficient characterization to fully understand and optimize their loading [2,3].

This project aimed to utilize the multitude of characterization techniques at our disposal in order to provide a more holistic understanding of AuNP loading. Optimizing our AuNP-DNA conjugates while balancing device performance can provide greater functionality for applications such as high payload drug delivery agents.

## Experimental Procedure:

We began with approximately 14 nm diameter, citrate-capped AuNPs synthesized via the citrate reduction method [4]. We made a series of conjugates at varying NaCl concentrations (50, 100, 200 mM) to establish a trend between DNA loading and salt concentration. The single-strand DNA covered AuNPs (ssAuNPs) were synthesized by adding the initial DNA oligo capture strand to the AuNP solution in a molar ratio of 195 DNA/AuNP, then left to shake for approximately 16 hours [5]. The conjugates were then salt-aged to the desired NaCl concentrations over a period of six hours to minimize aggregation, then centrifuged for 30 minutes at 10,500 RCF.

Supernatant was collected in separate tubes and the conjugates were resuspended in the same volume and concentration NaCl. This was done three times total. Residual DNA in the supernatant was quantified via ultraviolet visible spectrophotometry (UV-Vis) absorbance measurements to estimate DNA loading on the AuNP surface.

The double-stranded DNA covered AuNPs (dsAuNPs) were synthesized by adding the complementary oligonucleotide to the ssAuNP solution in a 1:1 molar ratio based on the single-stranded loading estimate. They were then left to shake for approximately two hours before quantifying DNA hybridization with UV-Vis as before. Dynamic light scattering (DLS) and zeta potential (ZP) measurements of the conjugates were taken before conducting a second trial at the same concentration (100 mM) to test repeatability. Gel electrophoresis (1.5% agarose gel) was also performed on all samples from each trial.

Single- and double-stranded conjugates were synthesized with a new set of oligos capable of efficient strand displacement [6]. For this trial, the hybridizing strand had a ROX fluorophore modification that upon hybridization would be close to the AuNP surface. Toehold mediated strand displacement reactions were performed on this batch of conjugates in order to test device performance. A fluorometer (2x Gain) was used to monitor fluorescence during hybridization and strand displacement (two hours each).

## Results:

By varying the salt concentration of the conjugate solution, we found hybridization efficiency increased with increasing NaCl concentration (Figure 1). DLS measurements gave us an indication of the relative extent of aggregation for each salt concentration. While conjugates synthesized in 200 mM NaCl showed the highest hybridization efficiency, they also showed the most aggregation (Figure 2).

ZP measurements of the conjugates were distinctly different than that of the bare AuNP control, varying by an average of about 20 mV. The conjugates had ZP values around -40 mV, indicating particle stability.

We used 100 mM NaCl for our second trial testing repeatability. The conjugates synthesized at this concentration showed slightly reduced hybridization efficiency than the higher salt concentration, but also showed less aggregation (about 3% by volume).

Slight mobility differences between the ssAuNPs and dsAuNPs in gel electrophoresis (Figure 3) indicated hybridization had occurred in both trials. The gel for the 100 mM NaCl conjugates also showed our process to be repeatable.

Our final round of conjugates employing new oligos tested device performance via strand displacement (Figure 4). The hybridizing strand had a fluorescent dye modification (ROX) that quenched in proximity to the AuNP, as seen in the fluorescence decrease during hybridization in Figure 4. As the invading strand displaced the fluorescent oligo, fluorescence increased again as expected. This successful strand displacement proved the capability of our device and assay.

## Conclusions:

Our results show promising possibilities for attaining optimal DNA loading efficiency on spherical gold nanoparticles. Our data suggests salt-aging to 100 mM NaCl could be a good starting point from which to continue studying characterization and performance of nucleic acid devices and their relation to DNA loading. In the future we would like to pursue different DNA tethers, vary the length of the carbon linker chain, and incorporate aptamers onto the device to study the full extent of its performance. Further quantification of device performance is possible based on the tested strand displacement assay.

## Acknowledgments:

This project was made possible by the National Science Foundation [ECCS-0335765], National Nanotechnology Infrastructure Network Research Experience for Undergraduates (NNIN REU) Program, University of Washington, Molecular Engineering & Sciences Institute, and NESAC/BIO [NIH NIBIB EB-002027].

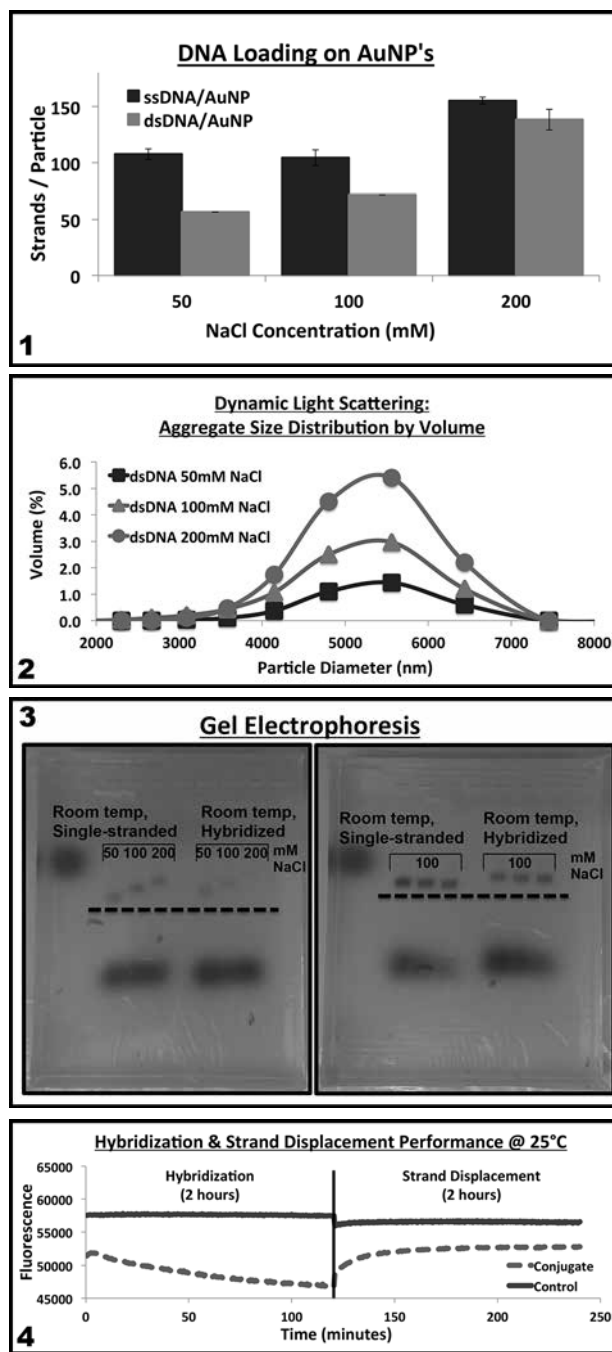


Figure 1: Single- and double-stranded DNA loading on AuNP surface, estimated from UV-Vis absorbance measurements.

Figure 2: DLS measurements in aggregate size range; dsDNA refers to hybridized DNA on conjugate surface. Figure 3: Gel electrophoresis for varying salt concentration trial (left) and same salt concentration trial (right). Figure 4: Fluorometer measurements during hybridization and strand displacement.

## References:

- [1] DeLong, R. K., et al. (2010). NS&A, 3(1), 53-63.
- [2] Baer, D. R., et al. (2010). An.&Bio.Chem. 396(3), 983-1002.
- [3] Lee, C.-Y., et al. (2007). J. of the ACS, 129(30), 9429-9438.
- [4] Turkevich, J., et al. (1951). Discussions of the Faraday Soc. (11), 55.
- [5] Demers, L. M., et al. (2000). Analytical Chemistry, 72(22), 5535-41.
- [6] Zhang, D. Y., et al. (2009). J. of the ACS, 131(47), 17303-14.

# Optimization of a Capacitive Sensing Organic Electrochemical Transistor Immunoassay

Lucy Hu

Bioengineering, University of California, Berkeley

NNIN iREU Site: Centre Microélectronique de Provence, École Nationale Supérieure des Mines de Saint-Étienne, France

NNIN iREU Principal Investigator: Dr. Roisin Owens, Bioelectronics, École Nationale Supérieure des Mines de Saint-Étienne, France

NNIN iREU Mentor: Anna-Maria Pappa, Department of Bioelectronics, École Nationale Supérieure des Mines de Saint-Étienne, France

Contact: lucyhu@berkeley.edu, owens@emse.fr, anna-maria.pappa@emse.fr

## Introduction:

The development of fast, accurate and sensitive immunoassays is of major importance for the early detection of several diseases. Traditional methods, such as the ELISA and Western Blot, operate on the time scale of hours to days; we thus aim to integrate organic electrochemical transistor (OECT) arrays with traditional immunoassays to provide both the molecular specificity of an immunoassay and the speed of a microelectronic system. Previous work in this field has been based on the integration of external enzymes [1] or on complex fabrication methods[2]. We herein present initial results of a simple capacitive OECT sensing platform for direct immunodetection.

The sensing principle was based on the capacitive change caused by the antigen-antibody affinity binding to the biofunctionalized poly(3,4-ethylenedioxythiophene) polystyrene sulfonate (PEDOT:PSS) transistor channel. When molecules are immobilized onto the channel, they add a resistive and capacitive element to the equivalent circuit of the OECT. Accordingly, the impedance changes due to the added mass to the channel, and a complex combination of the induced electrostatic charges of the added molecules is reflected in a shift in

the transconductance. A schematic representation of the OECT along with a the simplified equivalent circuit, and the transistor characteristic curves depicted in Figure 1.

## Experimental Methods:

Gold electrodes were patterned onto glass slides via photolithography and chemical vapor deposition. A layer of Parylene-C was also deposited through vapor deposition, followed by a layer of 2% MicroClean soap solution followed by a sacrificial layer of Parylene-C. The last part of the fabrication process involved the development of photolithographically patterned channels, the dimensions of which were  $10 \times 10 \mu\text{m}^2$ . Finally, the (semi)conducting solution was spin-coated to the channel, and the gate that were exposed via reactive ion etching.

In order to introduce hydroxyl groups onto the transistor channel, a PEDOT:PSS:polyvinyl alcohol (PVA) blended solution was used as the active solution [3]. Following, the channel was further functionalized and treated with a (3-glycidyloxypropyl) trimethoxysilane (GOPS) solution in order to introduce epoxy groups on top of the channel and thus allow protein immobilization.

Initially, in order to standardize our OECT based immunoassay, a model system was employed, consisting of a primary and a secondary (fluorescent) antibody. The primary antibody was primarily immobilized onto the epoxy-modified transistor channel, and a bovine serum albumin (BSA) solution was deposited prior to the immobilization of the secondary antibody, in order to avoid unspecific binding. All the aforementioned steps, including the biofunctionalization of the channel are schematically represented in Figure 2.

## Results and Discussion:

We herein fabricated PEDOT:PSS-based OECT towards the development of an immunosensing platform. Initially our work involved the study of, different biofunctionalization methodologies. It was found that the thicker the GOPS layer onto the transistor channel, the higher the standard

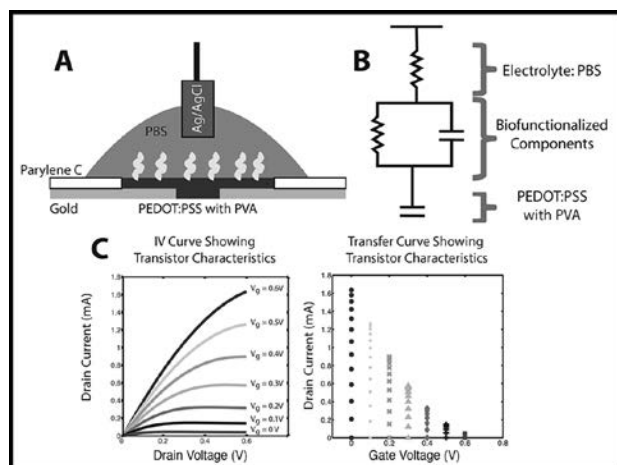


Figure 1: A) Schematic representation of the OECT. B) design of a simplified equivalent circuit. C) Steady state characteristics: output and transfer curves of the fabricated OECTs

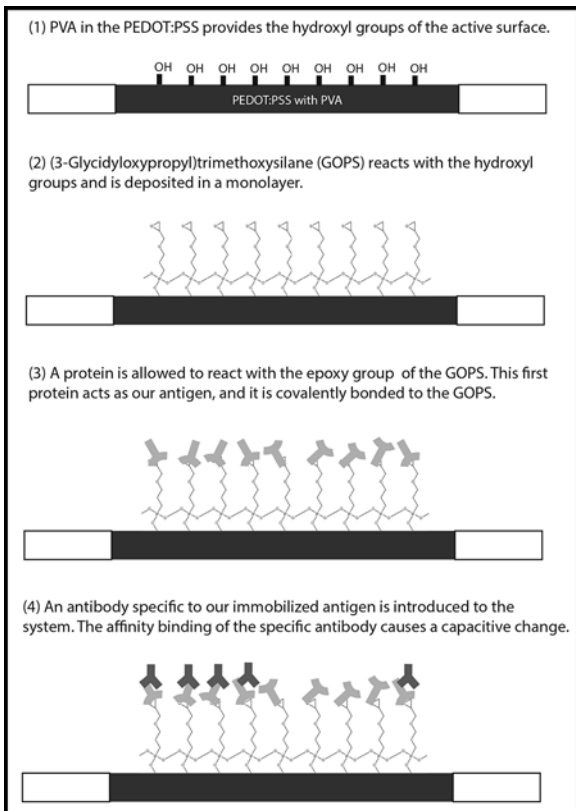


Figure 2: Biofunctionalization concept diagram.

deviations were observed leading to less consistent data, thus indicating the necessity of developing a GOPS mono-layer deposition method. The biofunctionalization methodology was validated by checking the fluorescence of the device after the immobilization of the secondary antibody.

Additionally, we studied the effect of the electrolyte (PBS) concentration on the transconductance cut-off frequency. It was found that the transconductance cutoff frequency decreases as the PBS concentration decreases, due to the electrolyte's equivalent resistance in the equivalent circuit. Given that the theoretical transconductance cutoff is dependent on the combined impedance of all the elements in the circuit and in order to be able to sense small changes in impedance, the OECTs were tested after each critical immobilization step with varying PBS concentrations (i.e., 1X, 0.1X, 0.01X, and 0.001X). Those results are graphed and shown Figure 3. Ultimately, none of the higher electrolyte concentrations (1X, 0.01X, and 0.01X) show clear shifts between steps in the biofunctionalization procedure; the trendlines have large error bars that all overlap giving null results. The OECT tested under PBS 0.001X, however, shows promising results, as there are clear, distinguishable transconductance shifts for

the covalent bonding of GOPS to the channel and for the covalent bonding of the first antibody to the GOPS. The lack of shift in subsequent steps for the PBS 0.001X sample makes sense if the secondary antibody is not binding or is currently too small to detect. To validate that the normalized shifted curves are an accurate representation of the transconductance cutoff relationship, the derivative functions were graphed and yielded the same results as the visual shifts.

These results indicate that the capacitive method can successfully detect covalent bonding onto the transistor channel.

### Future Work:

The next step of this work is to successfully detect the antigen-antibody affinity binding via a transconductance shift. We plan to improve the biofunctionalization process by focusing on the GOPS monolayer formation onto the transistor channel, since variations in a thick GOPS layer interfere creates noise in the transconductance that obscures the desired shift. Moreover specific disease detection models will be also studied.

### Acknowledgements:

The authors acknowledge support from the Department of Bioelectronics at the École Nationale Supérieure des Mines de Saint-Étienne, the National Nanotechnology Infrastructure Network International Research Experience for Undergraduates (NNIN iREU) Program, and the National Science Foundation, Grant No. ECCS-0335765.

### References:

- [1] B. Kavosi, et al., Biosens. Bioelectron. 74, 915-923 (2015).
- [2] W. T. Li, et al., J. Biomed. Nanotechnol. 11, 2050-2056 (2015).
- [3] X. Strakosas, et al., J. Mater. Chem. B, 2, 2537-2545 (2014).

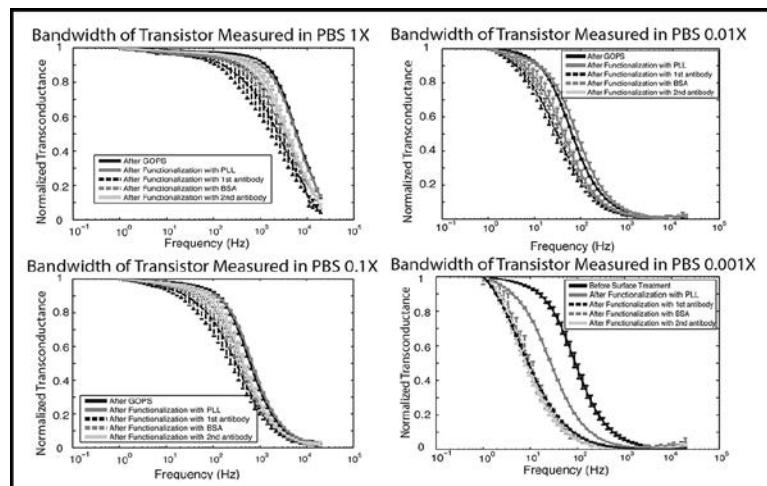


Figure 3: Frequency dependence of the transconductance in varying PBS concentrations between all the critical immobilization steps.

# The Wrinkling of Thin Elastic Membranes as a Cancer Diagnostic

**Adam Kunesh**

**Physics and Mathematics, University of North Carolina at Chapel Hill**

**NNIN REU Site: ASU NanoFab, Arizona State University, Tempe, AZ**

NNIN REU Principal Investigator: Junseok Chae, School of Electrical, Computer, and Energy Engineering (ECEE), Arizona State University

NNIN REU Mentor: Jennie Appel (2010 NNIN REU at Arizona State University), ECEE, Arizona State University

Contact: apkunesh@live.unc.edu, junseok.chae@asu.edu, appeljh@tigermail.auburn.edu

## Abstract:

Cancerous cells generate wrinkles on sufficiently thin elastic membranes. Exploiting this phenomenon could enable the fabrication of a point-of-care bladder cancer diagnostic device. Historically, there has been difficulty producing thin, large membranes; while this remains a difficulty, a limited number of membranes were fabricated. Membranes as thin as 150 nanometers were produced. The wrinkles generated by bladder cancer cells, large enough to be observed under optical microscope, were characterized for each of these membranes.

## Introduction:

Cell locomotion is dependent on the forces a cell exerts on its exterior environment, called cell traction forces. When this exterior environment is composed of an ultra-thin elastic membrane, these traction forces result in significant wrinkling of the surrounding membrane. As a cell attempts to move, it inadvertently draws the ultra-thin membrane towards localized focal points at the outer edge of the cell membrane, and the angular component of the stress in the surrounding membrane becomes negative. This angular compression results in a localized buckling of the membrane.

Because cancer cells produce distinctly different forces from healthy cells [1], this wrinkling phenomenon could be applied as a point-of-care cancer diagnostic device. One of the great strengths of such a device is that a heterogeneous sample of cells might be used for reliable diagnosis of cancer; for example, the cells found in urine samples could be used to diagnose bladder cancer.

Attempts to find a quantifiably testable predictor for the formation of wrinkles yielded a numerical study [2]. Fitting curves to the simulated data yielded equations predicting length and number of wrinkles based on the physical qualities of the membrane (radius, thickness,

Poisson's Ratio, residual stress) and those of the cell (radius, force exerted by a half-cell). These equations are found in Figure 1, with  $R^*$  as the wrinkle length,  $N$  the number of wrinkles,  $\delta_c$  the critical membrane displacement for wrinkle formation (linearly related to idealized cell traction force),  $R$  the membrane radius,  $r_0$  the cell radius,  $\beta$  the distance pulled at the boundary of the membrane (linearly related to residual stress),  $h$  membrane thickness, and  $\sigma$  Poisson's Ratio.

## Experimental Procedure:

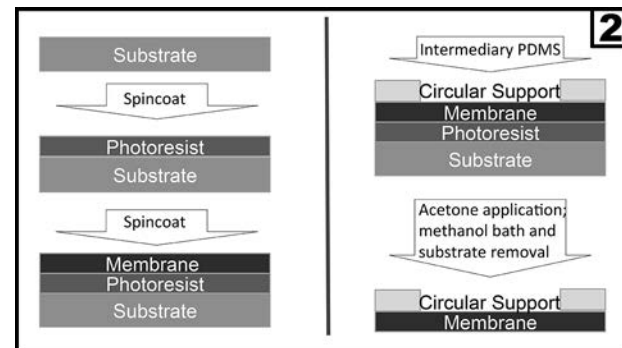
The membrane fabrication process is summarized in Figure 2. First, several microns of AZ 4330 photoresist were spun onto a 4-inch silicon wafer. After baking for one minute at 100°C, we placed hexane-diluted polydimethylsiloxane (PDMS) on top of the photoresist and again spun the sample, this time at 6000 rpm for three minutes. At this point, our sample was placed on a hot plate at 80°C for 16-18 hours.

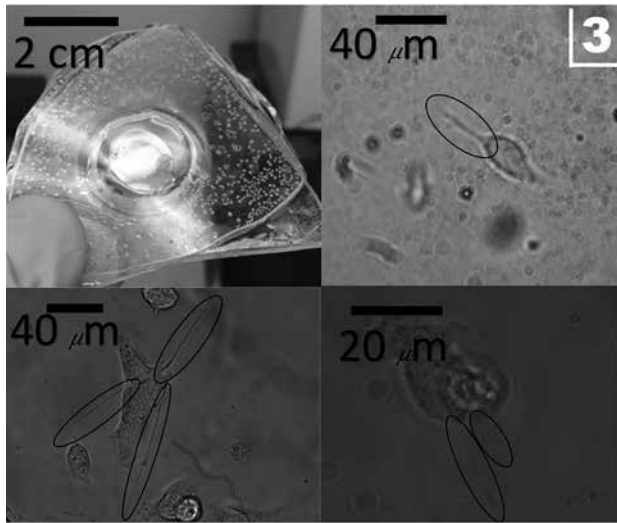
After the PDMS membrane cured, a thick PDMS support structure was adhered to the sample via intermediary

$$R^* = \sqrt{\frac{1 - \sigma \delta R + \beta r_0}{1 + \sigma \delta r_0 + \beta R}} R r_0 \quad 1$$

$$N = 3/2500 \beta r_0 / h^2 + 69/400 r_0 / h + 1/50 \beta / h + 2$$

$$\delta_c = \frac{23}{20} \beta - \frac{1}{250} \frac{r_0 \beta}{h} + \frac{131}{5} \frac{h^{5/3}}{r^{2/3}} + \frac{56}{10} h - \frac{19}{20} \ln\left(\frac{r_0}{h}\right)$$





PDMS layer and cured at 100°C for two hours. After cooling, the sample was treated with an acetone mist via spray bottle and subsequently immersed in a methanol bath. Careful peeling of the support structure resulted in the production of a bounded membrane, which could be seen to oscillate in the methanol. The membrane was then carefully removed from the methanol bath [3].

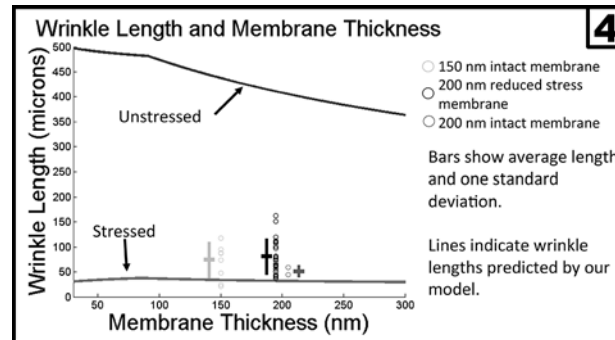
T24 bladder cancer cells were cultured. The cells were incubated on the membrane at 37°C in 5% CO<sub>2</sub> for 24 hours. Over this time period, cells adhered to the surface and contracted, creating the wrinkles observed via inverted microscope (Figure 3).

## Results and Conclusions:

Five membranes were fabricated: 1 × 150 nm, 3 × 200 nm, and 1 × 300 nm. Membranes of each thickness were tested and T24 cells were unable to generate wrinkles in the 300 nm membrane. The length and number of wrinkles formed on the 150 nm, 200 nm, and 200 nm reduced-stress membrane after 24 hours were 70±35 microns and eight; 52±10 microns and two; and 82±33 microns and twenty-nine, respectively. After 48 hours, these quantities were: 40±27 microns and thirteen; 40±7 microns and two; and 85±54 microns and 26. The 24 hour data is summarized in Figure 4.

The reduced-stress membrane was a 200 nm membrane with hole in the center (roughly a quarter of the area of the membrane). This hole allowed the membrane to relax and relieve some of its residual stress, which likely accounts for the substantial increase in both length and number of observed wrinkles.

We were unable to reduce the membrane thickness below 150 nm. Although membranes as thin as 125 nm were observed in the methanol environment, removal of the membrane from the bath caused breakage.



While we did find an upward trend in length and number of wrinkles as membrane thickness was reduced, our results indicated that our membrane was stressed as a side effect of our fabrication process. This residual stress substantially increased the minimum force required for cells to generate wrinkles, and likely reduces the device's power to differentiate between cells producing different ranges of force.

## Future Work:

In the future, we hope to refine our fabrication process to increase control over the residual membrane stress and thickness while improving membrane stability. This will allow for the statistical analysis of wrinkle formation by a variety of cells and an optimization of membrane characteristics for the fabrication of a point-of-care bladder cancer diagnostic device.

## Acknowledgments:

Many thanks to my PI, Dr. Junseok Chae, and my mentor Jennie Appel for all of their guidance and assistance. Thanks also to the National Nanotechnology Infrastructure Network Research Experience for Undergraduates (NNIN REU) Program and to the National Science Foundation for enabling my research under Grant No. ECCS-0335765. Dr. Trevor Thornton and the CSSER staff at ASU were instrumental to my learning and my experience. Finally, thanks to my fellow interns (Raul Flores, Alex Rosner, and Abby Magee) for providing a sounding board and a source of entertainment.

## References:

- [1] Li, et al., Quantifying the Traction Force of a Single Cell by Aligned Silicon Nanowire Array, *Nano Letters*. 2009: 9, No. 10, 3575-3580. DOI: [10.1021/nl901774m].
- [2] Geminard, et al., Wrinkle formations in axi-symmetrically stretched membranes, *Eur. Phys. J. E*. 2004: 15, 117-126 [DOI: 10.1140/epje/i2004-1004101].
- [3] Kang, et al., Large-Scale, Ultrapiable, and Free-Standing Nanomembranes, *Adv. Mater.* 2013: 25, 2167-2173 [DOI: 10.1002/adma.201204619].

# Fabrication and Design of EGFET Devices for Biosensing

**Abigail Magee**

**Biomedical Engineering, University of Central Oklahoma**

**NNIN REU Site: ASU NanoFab, CSER Facility, Arizona State University, Tempe, AZ**

**NNIN REU Principal Investigator: Jennifer Blain Christen, Electrical Engineering, Arizona State University, Tempe, AZ**

**NNIN REU Mentor: Uwa Obahiagbon, Electrical Engineering, Arizona State University, Tempe, AZ**

**Contact: amagee@uco.edu, jennifer.blainchristen@asu.edu, uwa@asu.edu**

## Abstract:

Ion-sensitive field effect transistors (ISFET) measure the presence of ions in a solution via their effect on current flow within the device. The ions induce charge in the device via capacitive coupling from the ion-sensitive membrane. The extended gate field effect transistor (EGFET) is a modified version of the ISFET that uses low cost FET transistors combined with a sensing membrane and reference electrode structure fabricated separately. This structure requires fewer fabrication steps and enables flexibility and adaptability in application. The EGFET is more suitable for continuous monitoring in harsh environments, since the sensing area is external to the transistor. While the EGFET's sensing area is physically remote, the principles of operation remain the same. This project focused on design and fabrication of EGFETs with different sensing membranes and geometries. The systematic investigation of the device parameters enables informed designs for increased sensitivity to pH. The devices were fabricated with chrome/gold reference electrodes and either a silicon nitride or silicon dioxide sensing membrane. The devices were tested with pH buffer solutions to provide consistent pH samples. Initial testing determined the silicon nitride layer had poor quality, with pinholes and cracks evident when surface features were analyzed with an optical profilometer, resulting in poor characterization and etching of the electrode.

## Introduction:

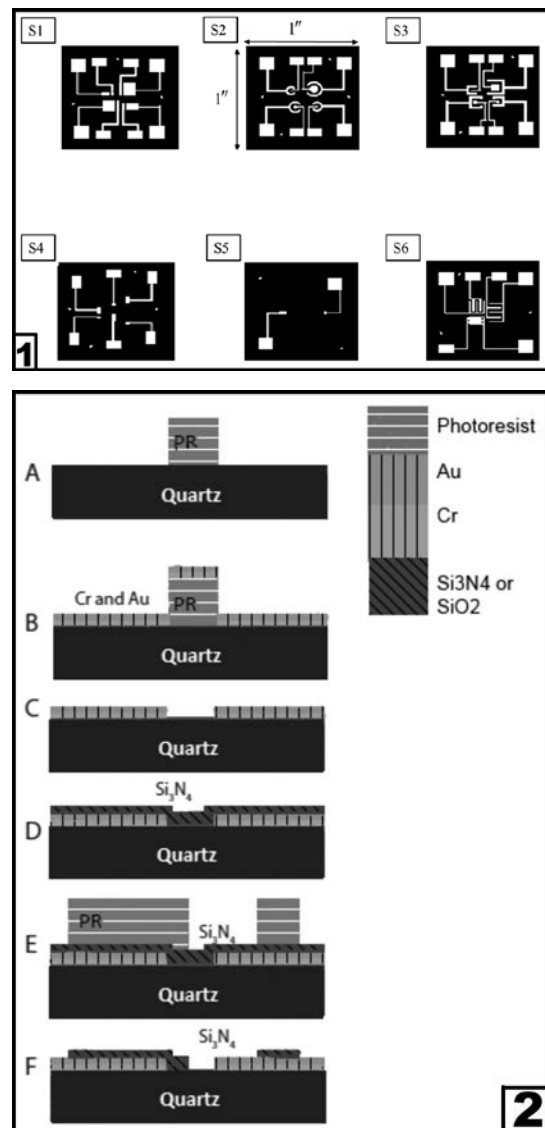
Many sensors rely on pH in order to detect a change in a system and adjust pH or trigger another response. As an environmental sensor, EGFETs could be used to track pH changes in water to determine if there is contamination. In biological or biomolecule applications, EGFETs can be used to detect pathogens, antibodies, or proteins; they can also track pH levels for cultured cells.

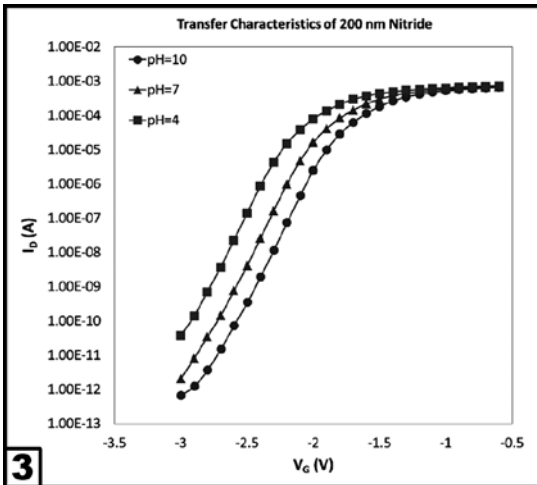
Increasing sensitivity of the device would increase the ability of the device to distinguish between minute pH changes in an electrolyte or pH changes due to biomolecules bound to its surface. This research project investigates several geometric and spacing variations to optimize for pH sensitivity.

## Experimental Procedure:

**Fabrication of the Biosensor.** The masks for the fabrication steps were designed using L-Edit, as shown in Figure 1. The designs were printed on a Mylar film using a 25,400 dpi printer, attached to a soda-lime glass substrate, and used in the photolithography steps. Positive photoresist was used for photolithography.

The fabrication of the devices followed the process shown in Figure 2. An adhesion layer of 10 nm chromium was deposited





followed by 170 nm of gold; both were deposited using evaporation. The thickness of nitride or oxide deposition was intentionally varied between the sets. Sets 2, 3, and 4 had 200 nm of silicon nitride, 400 nm of silicon nitride, and 200 nm of silicon dioxide, respectively. For the set that contained oxide rather than nitride, the process followed the same format as in the previous sets; the nitride was simply replaced with silicon dioxide.

**Setup for Experimentation.** Wires were attached to the contact pads of the sensors using a silver-based conductive epoxy. A centrifuge tube, with a section cut off from the tip, was used in packaging the device by creating a confinement for the electrolyte. The centrifuge tube was bonded to the quartz substrate using a marine-grade epoxy, exposing the sensing areas so that the solutions used would be in contact with the correct locations on the device. The devices were exposed to an electrolyte for 24 hours without taking any measurements, allowing the interfaces and surfaces to reach a steady state.

**Data Acquisition.** In order to measure the pH values versus the voltage, we used a program in MATLAB in order to automate the measurements to determine this relationship. A Keithley source meter was also used for data acquisition purposes with TSP Express.

The devices were measured using buffer and titrated solutions. Once the solution was added to the device, we waited five minutes to start the program. A computer program was run for five sweeps and the device was reset within the first sweep. The sweeps were set up with a  $V_{GS}$  of -3.5V to -0.5V, a  $V_D$  of 0.2V and 0.5V, and a step size of 0.05V. Transfer and output characteristics were plotted in Excel and analyzed once data acquisition was complete.

## Results:

During initial testing, it was observed that the nitride and the gold electrodes were being etched due to poor quality of the nitride layer. This affected the characterization,

Sensor	Area/Spacing	pH Sensitivity
	$12\text{mm}^2$	49.97 mV/pH
	$3.14\text{mm}^2$	50.39 mV/pH
	$4\text{mm}^2$	49.98 mV/pH
	1mm	49.98 mV/pH
	$11\text{mm}^2$	49.99 mV/pH
	1mm	49.98 mV/pH

because the transistor and program picked up the etching mechanism rather than just the pH reaction.

The devices with the improved sensing membranes had no visible etching with the new buffer solutions. Transfer characteristics of these corrected devices had the expected pH sensitivities, as in Figure 3. Details concerning the pH sensitivity of the devices are shown in Figure 4.

## Conclusions:

The results from testing in Figure 4 indicate the devices have the sensitivities expected. These results are not final, as more testing is needed to confirm these results. However, the current results demonstrate the devices are working as expected and could be used in further testing to determine a difference in pH sensitivity in relation to geometry, spacing, and surface area.

In the future, a better PECVD process will need to be used so the sensing membrane is deposited more evenly and with fewer defects. This would improve the characterization of the devices due to the elimination of etching processes. It would also prove beneficial to fabricate devices with different geometric structures, but with the same area, in order to compare the effect of geometry and spacing on pH sensitivity more effectively and with fewer compounding factors.

## Acknowledgements:

Many thanks to Dr. Jennifer Blain Christen and my mentor, Uwa Obahigbon for helping me with this research and giving me the opportunity to work in their lab. Thanks to the CSSER staff at Arizona State University for being available to help with the fabrication process and to my fellow interns. Thanks to the NNIN REU Program and to the National Science Foundation, Grant No. ECCS-0335765, for giving me this opportunity.

# Influence of Cell Spreading Area on Uptake of Gold Nanoparticles

**Adriana Mulero**

**Chemical Engineering, University of Puerto Rico-Mayaguez**

**NNIN iREU Site: National Institute for Materials Science (NIMS), Tsukuba, Ibaraki, Japan**

**NNIN iREU Principal Investigator: Dr. Guoping Chen, Tissue Regeneration Materials Unit, National Institute for Material Science**

**NNIN iREU Mentor: Xinlong Wang, Tissue Regeneration Materials Unit, National Institute for Material Science**

**Contact: adriana.mulero1@upr.edu, guoping.chen@nims.go.jp, wang.xinlong@nims.go.jp**

## **Abstract:**

Nanoparticles (NPs) have been proved to be a promising material for drug delivery, cancer therapy, and bioimaging. However, there is growing concern about their cytotoxicity, which may cause an inverse effect on human health. In order to develop safer and efficient NPs, people need to fully understand how cells react with the NPs. Previous studies investigated the influence of NPs properties on cellular uptake. However, little attention was paid to understand the influence of cell membrane tension on the uptake. Micropatterns were used to control the membrane's tension on single cell scale; the greater the spreading area, the greater the tension on the cell membrane [1]. Thus in this study, a series of microdots with various diameters (20, 40, 60, and 80  $\mu\text{m}$ ) were developed using photolithography techniques. Gold nanoparticles (AuNPs) with sizes of 50 nm were synthesized following the Turkevich method and coated with FITC labeled PEG. Mesenchymal stem cells (MSCs) were cultured on the micropatterns and treated with FITC-PEG-AuNP to investigate the influence of cell spreading area on uptake of NPs. The results indicate that PEG-coated AuNP are non-toxic to the MSCs. Patterned cells with different spreading areas and cellular tension can uptake the FITC-PEG AuNPs.

## **Introduction:**

Nanoparticles (NPs) have been found to be a promising way for visualizing specific cell types, delivering drugs directly into the cell, and cancer therapies. For all these applications to be successful, it is important to study the NPs and cell interaction, including cellular uptake and cellular toxicity. Endocytosis is the mechanism that cells use to bring the nutrients and NPs into the cell. The cellular membrane bends forming a vesicle, providing them transportation into the cell. Previous studies [1] have analyzed NPs properties and their effects on the uptake. However, little attention was paid to understand how the cellular membrane properties influence the cellular uptake. These include the cellular membrane tension affecting the membrane's capacity to bend to form the vesicles.

Micropatterns have been proved to efficiently control the cellular membrane tension on a single cell scale; the greater the spreading area, the greater the tension on the membrane [2]. In this project, we evaluated how the cellular membrane tension, of mesenchymal stem cells (MSCs), controlled by micropatterns of different size dots affects the uptake of gold nanoparticles (AuNP).

## **Experimental Procedure:**

**Micropatterning Process.** By using photolithography techniques, the micropatterns were developed on a transparent polystyrene square surface ( $6.25 \text{ cm}^2$ )

cut from a tissue culture dish, which supported cell adhesion. Poly(vinyl alcohol) (0.3 mg/mL) was used as the photoreactive solution. The design consisted of dots with diameters of 20, 40, 60, and 80  $\mu\text{m}$ . The micropatterned surfaces were characterized using atomic force microscopy.

**AuNP Synthesis.** Following the Turkevich method, we synthesized the 50 nm sphere AuNP [3] using 0.01% chloauric acid ( $\text{HAuCl}_4$ ) and 1% tri-sodium citrate solution as the reduction solution. The synthesis was kept at constant stirring and a temperature of 110°C. It was later ultrasonicated to disperse the molecules before the surface modification. The mPEG-SH and the FITC-PEG-SH were added to AuNP solution at a 3:2 ratio. The mix was stirred overnight to obtain the FITC-PEG modified AuNP.

**Cell Experiments.** The cell experiments were divided into two groups: flat and patterned surface. For the flat surface, we seeded the cells on a 96-well-plate with a cell density of 1,000 cells/well. For the patterned surface, the micropatterns were sterilized with ethanol and water, then placed one square per well on a six-well-plate; cell density 5,000 cells/well. After the cells attached, the previous medium was aspirated and the growth medium containing the AuNPs was added to the cells. They were treated with 0.1, 0.5, 1 and 3 nMFITC-PEG AuNP concentrations. The cells were then tested for cell viability with WST-1, and cellular uptake studied with fluorescence microscope.

## Results and Conclusions:

Micropatterns were characterized to measure the diameter and depth of each pattern. Patterns were proved to go according to the design, with a depth around 60 nm (Figure 1). Nanoparticles were characterized with scanning and transmission electron microscope to analyze their shape and size distribution (Figure 2). Size was proved to be spherical, and from the increase in size, we said that FITC-PEG layer was successfully added. Cell viability test (WST-1), was performed 6, 12, and 24 hours post-seeding. The WST-1 results showed no statistical difference between the NPs treated group and the control group (Figure 3). For the NPs uptake (Figure 4), cells were examined under the fluorescence microscope to view the NPs fluorescence due to the FITC modification.

On the bright field, the NPs were observed with a red color, pointed with arrows. Whenever the NPs were aggregated, the green fluorescence intensity increases. The nucleus, stained blue, showed there was one cell per dot. There is green fluorescence inside the contour of the cell every size dot, suggesting there are NPs inside the cells.

We concluded the following. First, the FITC-PEG AuNP was non-toxic to MSCs, and they presented a promising way to visualize cellular uptake. Second, the patterned cells with different spreading areas, and cellular tension could uptake FITC-PEG AuNPs. Future work includes quantifying the fluorescence intensity to obtain quantitative NPs uptake results and visualizing the NPs distribution inside cells using laser confocal microscope.

## Acknowledgements:

I want to thank my mentor Wang for all his support, Professor Chen for his guidance, the National Nanotechnology Infrastructure Network International Research Experience for Undergraduates (NNIN iREU) Program, National Institute for Materials Science, Japan, and National Science Foundation (under Grant No. ECCS-0335765). Also a very special thank you to Dr. Lynn Rathbun and Dr. Nancy Healy for coordinating the iREU Program.

## References:

- [1] ACS Nano, 7, 1961, 2013. J. Colloid Interface Sci., 438, 68, 2015. Biomaterials, 54, 226, 2015.
- [2] Biophysical Journal, 94, 4984, 2008.
- [3] Environmental Toxicology and Chemistry, 33, 481, 2014.

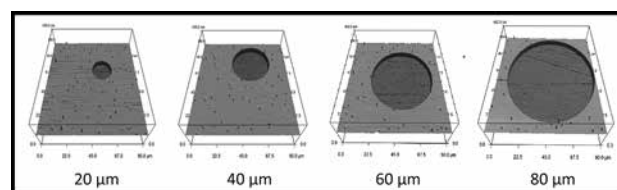


Figure 1: Micropatterns, 3D view of the different size dots.

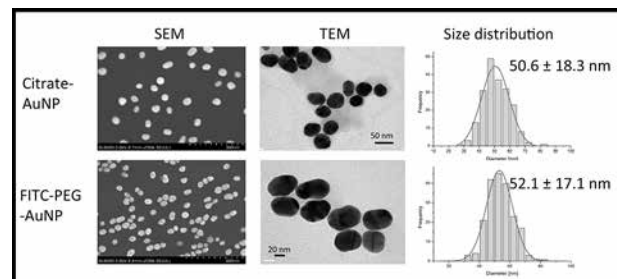


Figure 2: Gold nanoparticles shape and size characterization.

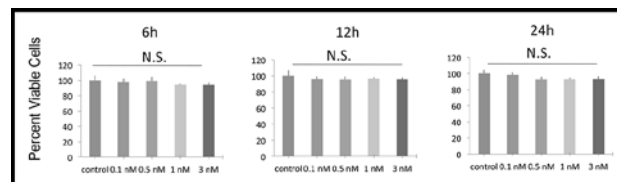


Figure 3: Cell viability test or measurement of the NP toxicity to cells.

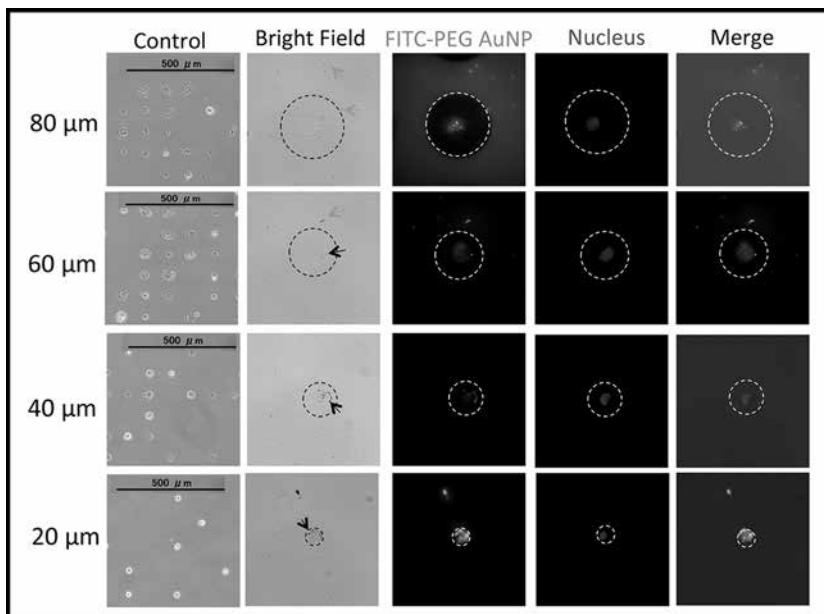


Figure 4: NP uptake test on patterned surface examined under fluorescence microscope.

# Nanoplasmonic Biosensing Microfluidics for Immune Status Monitoring of Critically-Ill Children

**Taylor Pauls**

**Biomedical Engineering and Physics, University of Arkansas**

**NNIN REU Site: Lurie Nanofabrication Facility, University of Michigan, Ann Arbor, MI**

NNIN REU Principal Investigator: Dr. Katsuo Kurabayashi, Mechanical Engineering, EE and CS, University of Michigan

NNIN REU Mentor: Dr. Robert Nidetz, Mechanical Engineering, University of Michigan

Contact: [tpauls@uark.edu](mailto:tpauls@uark.edu), [katsuo@umich.edu](mailto:katsuo@umich.edu), [nidetz@umich.edu](mailto:nidetz@umich.edu)

## Introduction:

The availability of a real time immune system monitoring system can be extremely useful in the laboratory and has potential clinical uses. The current standard for monitoring is an enzyme-linked immunosorbent assay (ELISA), which takes 1-2 days and requires large amounts of sample in comparison to a microfluidic system. Using a microfluidic system that can detect and monitor the activity of immune system in real time has many promising applications. Monitoring specific cytokines, which are proteins expressed from white blood cells that are triggered, and trigger the immune system, provides information as to the current state of the immune system. Information gathered from the microfluidic assay based on the cytokines can aid physicians to determine the best possible treatment and can have near immediate updates of the patient's state. This can prove extremely useful in immune-status updates pre-and post-operation, as well as a system of monitoring during an infection or disease. Single cell capture enables studying the most basic unit of our bodies and can potentially transform treatment and understanding of diseases.

Recently, the Fu group incorporated micropipette aspiration as a mechanism to study the mechanical differences of cancerous versus non-cancerous cells and the consequences for future cancer treatments [1].

The device proposed here aims to capture single cells to monitor their isolated behavior for relevant time periods for critical immune status updates. The microfluidic device consists of distinct chambers for single cell capture (see Figure 1). A cross-linked, biocompatible, synthetic polymer, polyethylene glycol (PEG-gel), will be patterned on top of the chambers to enable cell capture. In conjunction with the PEG-gel pattern, the previously developed technology of localized surface plasmonic resonance (LSPR) of gold nanorods can be implemented for biosensing secreted proteins [2].

## Experimental Procedures:

**CAD and Device Fabrication.** K-layout was used for the design of the microfluidic device. Two designs were ultimately used in our process. The first design consisted of an inlet, outlet, and three arrays of cell capture chambers throughout the channel, varying with different sizes of the chambers per device, see Figure 1. A silicon wafer was fabricated following the device design (Figure 2) using standard DRIE procedures. The second design consisted of holes displaced relative to the center of the cell capture chambers in the first design, which was used to pattern PEG-gel.

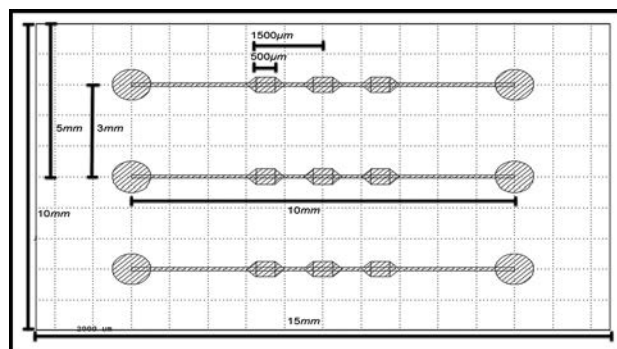


Figure 1: A CAD drawing of the device design that is used for PDMS molding. Dimensions not listed are; channel width of 100 mm, and channel depth of 50 mm. Each channel has three cell capturing wells.

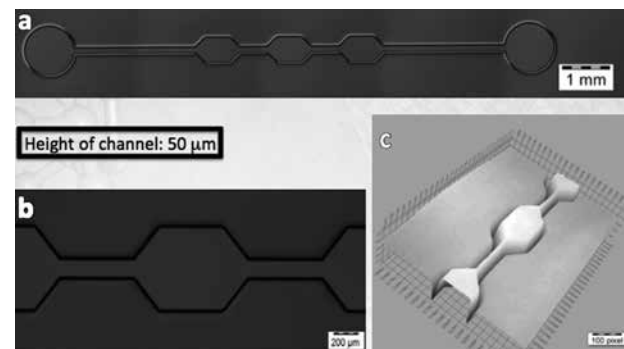


Figure 2: Images of the fabricated silicon wafer. (a) Entire channel. (b) Cell capture chamber. (c) 3-D image of (b) to show topography.

**Soft Lithography.** PDMS and glass substrates were activated via oxygen plasma treatments prior to silanization. Polyethylene glycol diacrylate, MW 575 g/mol, was spun on the samples and exposed over the mask via UV-light for 2-3 seconds. After development by deionized water, the samples were dried by nitrogen gun.

**Cell Capture.** Human T-Helper cells (THP-1) were used in conjugate with CD14 primary antibody. First, the antibody was deposited and dried onto the features. After a sufficient drying time, at least 30 minutes, a PDMS microchannel was placed over the features and THP-1 cells concentrated to  $10^5$  cells/mL are flown through the channel. Approximately every ten minutes, for 30 minutes, 10 ml of cells were manually pumped via micropipetting, see Figure 3.

**Data Acquisition.** All cell capture experiments were performed with a Nikon Eclipse Ti-S microscope under brightfield view. Fabrication images were taken by an Olympus BX-51 microscope under bright view.

### Results and Conclusions:

Soft lithography and cell capture proved successful on both PDMS and glass samples, but poor surface adhesion of PEG-gel onto PDMS substrates limited PDMS patterned PEG-gel experiments. Varying the exposure time, oxygen plasma treatments, silanization baths, and development times with PDMS patterning did not substantially improve the lithography. Swelling of the PDMS during the silanization step proved to be quite difficult to overcome for consistent or accurate patterning. Therefore, most cell capture experiments were carried out with PEG-gel features on glass slides.

However, cell capture was successful on a large area of PEG-gel on a PDMS sample. After many trial and error experiments, favorable antibody dry time coupled with sufficient cell flow exposure to the features was established. Single cell capture has not yet proved successful on the tested 50 mm diameter PEG-gel features, but double cell capture has (see Figure 4). Lithography of the 25 mm PEG-gel features have not yet been detected on the glass slide substrate.

### Future Work:

With double cell capture being possible onto the PEG features, more efforts will be employed for successful lithography onto PDMS including the use of a dessicator chamber for vapor silanization to avoid the swelling due to the solvent used. An addition, altering the cell capture design may be a possibility to improve the efficiency of cell capture on the PEG-gel features, as well as using a syringe pump to control the cell flow over the features. Employing fluorescent antibodies will prove helpful for both quantifying antibody presence on the PEG-gel features and detecting of the smaller 25 mm features.

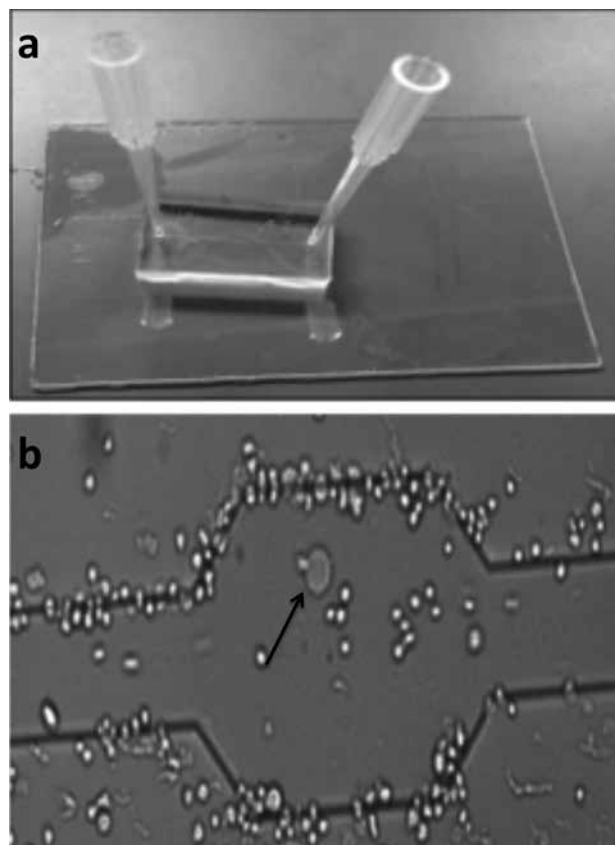


Figure 3: (a) Cell capture experimental set up. (b) Cell capture experiment, arrow pointing at PEG-feature patterned on glass.

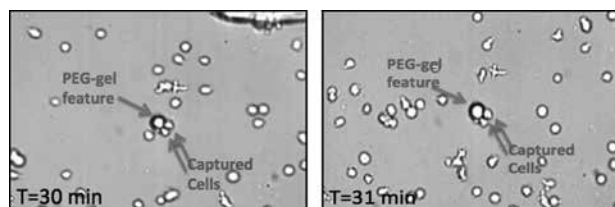


Figure 4: Time lapse demonstrates two cells captured on the PEG-gel feature after 30 and 31 minutes.

Once successful PEG-gel lithography onto PDMS and single cell capture is a reality, the sensing with LSPR AuNRs can be implemented for completion of this device.

### Acknowledgments:

I thank my PI, Dr. Katsuo Kurabayashi, my mentor, Dr. Robert Nidetz, the entire Kurabayashi lab for help and support, as well as the LNF staff, and the NNIN REU Program and the NSF (Grant #ECCS-0335765) for funding.

### References:

- [1] Lee, L. M., and Liu, A. P., *J. Nanotechnol. Eng. Med.* 5, 0408011-0408016 (2014).
- [2] Chen, P., et al. *ACS Nano* 9, 4173-4181 (2015).

**blank page**

**blank page**

# A High-Throughput Image-Processing Based Analysis of Dynamic Cell Surface Interactions in a Microfluidic Chip

**Brian Ryu**

**Chemical and Biomolecular Engineering, Johns Hopkins University**

**NNIN REU Site: Institute for Electronics and Nanotechnology, Georgia Institute of Technology, Atlanta, GA**

NNIN REU Principal Investigator: A. Fatih Sarioglu, Electrical Engineering, Georgia Institute of Technology

NNIN REU Mentor: Ruxiu Liu, Bioengineering, Georgia Institute of Technology

Contact: bryu2@jhu.edu, sarioglu@ece.gatech.edu, rliu76@gatech.edu

## Abstract:

Immunoaffinity-based lab-on-a-chip technologies offer high-throughput, label-free methods of cell characterization and are attractive for developing low cost point-of-care devices for cellular diagnostics. A biologically functionalized microfluidic channel would allow for detection of cells of particular interest, such as cancer cells as different cells have varying levels of affinity for different antibodies. This project focused on the development of an image-based analysis method combined with a microfluidic platform to identify cells using surface affinities of plasma membranes. A microfluidic channel was designed and constructed with polydimethylsiloxane (PDMS) using soft lithography. The channel was partially functionalized with different coatings including poly-L-lysine (PLL), a positively charged amino acid polymer that electrostatically attracts the negatively charged plasma membrane of cells. It was predicted that the cells would slow down as they traverse the coated region due to the electrostatic attraction. The motion of cell population traversing the channel was captured before and after they reach the PLL-coated region using a high-speed camera. A custom image processing software was developed to analyze and compare average velocity profiles of cells and neutral particles that are similar in size. The developed platform can be used to study the dynamics of immunoaffinity-based cell capture in microfluidic devices.

## Experimental Procedure:

**Microfluidic Device Design and Fabrication.** The microfluidic device was designed in the form of a serpentine channel with an inlet and an outlet at respective ends to maximize the channel length. The serpentine microfluidic channel was 34  $\mu\text{m}$  high, 1.4 mm wide, and 1.9 m long. The length of the channel ensures that cells sediment and reach a steady state on the floor of the channel before they interact with the coated region. The sedimentation process was modeled using Stokes flow [1], assuming a cell density ( $\rho_c$ ) of 1.05 g/cm<sup>3</sup> and a fluid density ( $\rho_f$ ) of 0.996 g/cm<sup>3</sup>. The calculated sedimentation velocity was 7.6  $\mu\text{m/s}$ . Therefore, the time required for all cells to sediment was approximated to be 5 s, which is much shorter than the time cells spend in the microfluidic channel during our experiments.

The device was fabricated using soft lithography (Figure 1). SU-8 negative photoresist was spun on a 4-inch silicon wafer and was patterned using standard photolithography to create a mold. The fabricated mold was inspected using a Dektak 150 profilometer to ensure consistent channel height across the device.

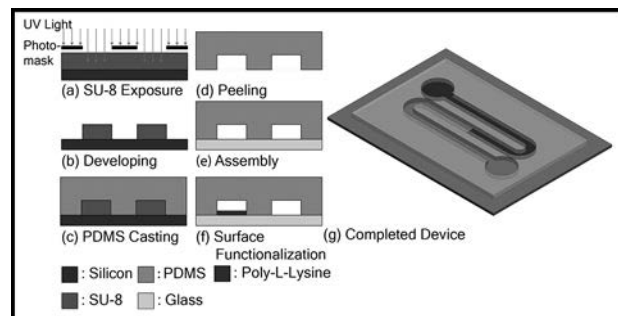


Figure 1: Overview of device fabrication process using soft lithography.

PDMS prepolymer and cross-linker (Sylgard 184) mixed at 10:1 ratio was poured on the SU-8 mold and cured for at least four hours at 65°C. The cured PDMS was peeled off from the master mold and was bonded to a 1-inch by 3-inch glass slide following surface activation using oxygen plasma. The bonded microfluidic channel

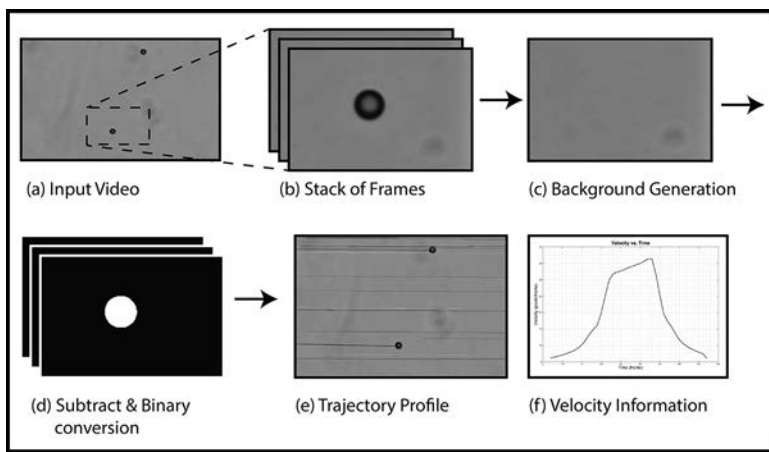


Figure 2: Schematic of developed image processing software.

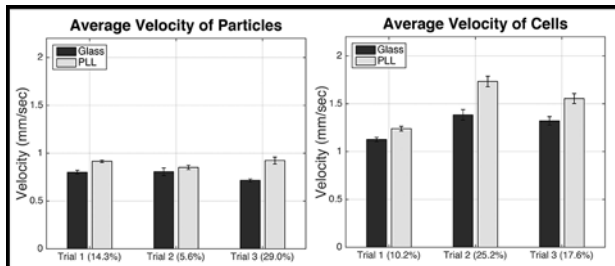


Figure 3: Velocities of particles and cells in the device. Error bars represent 95% confidence intervals of mean velocities. Values next to trial numbers represent percent change in mean velocities.

was then partially coated by flowing a 0.01% PLL solution from the outlet to cover approximately half of the channel. Following a 30 min incubation, the device was flushed thoroughly with de-ionized (DI) water from the inlet.

**Data Acquisition and Image Processing.** Using a syringe pump, cells and polymer beads (Polybead® Microspheres with 15  $\mu$ m diameter) suspended in phosphate-buffered saline (PBS) were driven through the microfluidic device from the inlet at a rate of 5  $\mu$ L/min. The cells used in the experiment were human ovarian cancer (HEY) cells. Confluent cultures of cells were trypsinized and dissociated by gentle pipetting to create single cell suspension in PBS.

A high-speed camera (Vision Research, Phantom v7.3) connected to an inverted optical microscope (Nikon Ti) was used to record the movement of the cells and particles as they flow in the uncoated and the PLL-coated region. The field of view in each video was aligned such that the measurements were taken at identical points along the width of microfluidic channel to account for the parabolic flow profile. The recorded video was analyzed using a cell-tracking program developed using MATLAB for this experiment. The program was designed to; 1) analyze the video frame by frame, 2) create a static background, and 3) perform background subtraction to find the location of

cells and particles in each frame. Using the known frame capture rate and calibrated pixel dimension, actual particle velocities were calculated (Figure 2).

## Results:

We measured the average velocities of particles and cells in repeated experiments. Overall, the polymer beads showed a 16.2% increase in mean velocity, whereas the cells showed a 17.7% increase in mean velocity when they entered the PLL-coated region (Figure 3). These results are in conflict with our initial predictions. We hypothesized that the cells should move slower on the

PLL-coated region due to the electrostatic attraction between plasma membranes and the PLL layer. Our measurements indicate higher velocities for both cells and particles over PLL-coated surface. Moreover, there is negligible difference between the cells and particles' velocities suggesting an effect independent of electrostatic interactions.

## Future Work:

Future experiments will focus on the investigation of various factors that can affect the changes in velocity of moving particles and cells. We will use surface characterization tools to analyze device surface coatings and then optimize our surface functionalization protocols. The image analysis program will be improved to increase the signal-to-noise ratios in cell and particle velocity measurements. Following the analysis of the parameters that mainly affect the motion of cells, functionalization of the channel using antibodies will be studied to study specific cell detection.

## Acknowledgements:

I would like to thank Professor Fatih Sarioglu, Ruxiu Liu, and the Georgia Tech coordinators for their assistance. This research was supported by the National Nanotechnology Infrastructure Network Research Experience for Undergraduates (NNIN REU) Program and National Science Foundation under Grant No. ECCS-0335765.

## References:

- [1] R. J. Garde. 2000. Mechanics of Sediment Transportation and Alluvial Stream Problems. 3<sup>rd</sup> ed. Delhi, India: New Age International.

# High-Throughput Drug Screening *in vivo* Using Droplet Microfluidics

**Alejandro Sanchez**  
**Chemistry, University of Houston**

**NNIN REU Site: Center for Nanoscale Systems, Harvard University, Cambridge, MA**

NNIN REU Principal Investigator: Dr. David Weitz, Applied Physics, Harvard University

NNIN REU Mentor: Dr. Anindita Basu, Applied Physics, Harvard University; Broad Institute of MIT and Harvard

Contact: alejandro.sanchez1794@gmail.com, weitz@physics.harvard.edu, abasu@broadinstitute.org

## Introduction:

Early stages of drug screening involve a broad library of drug compounds. Oftentimes the limiting factor in initial screening is the low volumes of candidate drugs. Microliter well assays are the current conventional method for initial screening. However, a well can only efficiently pipette 10  $\mu\text{L}$  while in a droplet of 50  $\mu\text{m}$  diameter the volume is 65 pL, 10<sup>5</sup> times less than a well. The aim of this project was to develop a platform to screen chemotherapeutic drugs at different doses on cancer cell lines at high-throughput using; a) live/dead cell assay, b) fluorescent dye as indicator of drug concentration, and c) photomultiplier tubes (PMT) for readout for both drug concentrations and cell state within each droplet.

The novelty of high-throughput drug screening using droplet microfluidics has the capability of decreasing time for analysis, volumes of reagents, and cost using polydimethylsiloxane (PDMS) microfluidic technology, while increasing the number of quantified interactions in comparison to conventional drug screening. High throughput is describing the fact that in 20 minutes  $\sim 10^5$  cell and drug interaction chambers can be screened with PMT sensor technology. Droplet chambers and PMT allow us to rapidly screen for candidate drugs by quantifying their efficacy at distinct concentrations in killing cancer cells as function of time with high statistical resolution.

## Experimental Procedure:

PDMS is favored as a material for microfluidic device fabrication because it is optically transparent, biocompatible, and gas permeable, among other benefits. Device fabrication consisted of standard soft lithography methods. First, SU-8 photoresist was spun onto a silicon wafer and placed under UV. After developing with a photo-mask, it became a master mold to make PDMS devices. Photoresist was poured onto the mold and then bonded to a glass slide by plasma oxidation. Lastly the channels were coated with aquapel to make the micro-channels hydrophobic [1].

The feature size of the co-encapsulation flow device was 50  $\mu\text{m}$ , which determined the size of the droplets. It is these narrow micro-channels diameters that give laminar fluid dynamics, which are governed by low Reynolds numbers.

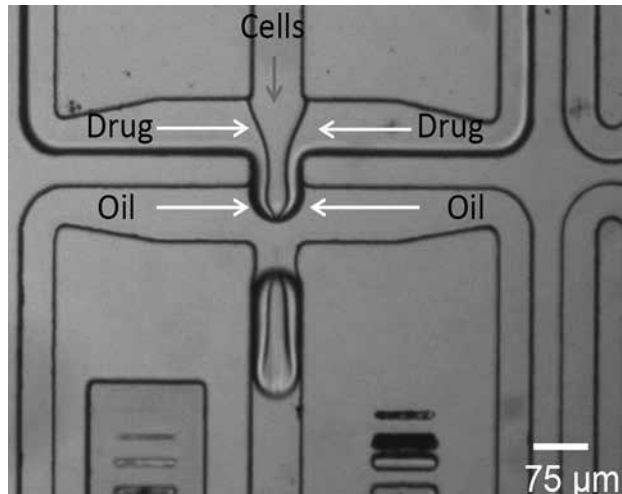


Figure 1: The junction of the co-encapsulation flow device showing formation of water-in-oil emulsions.

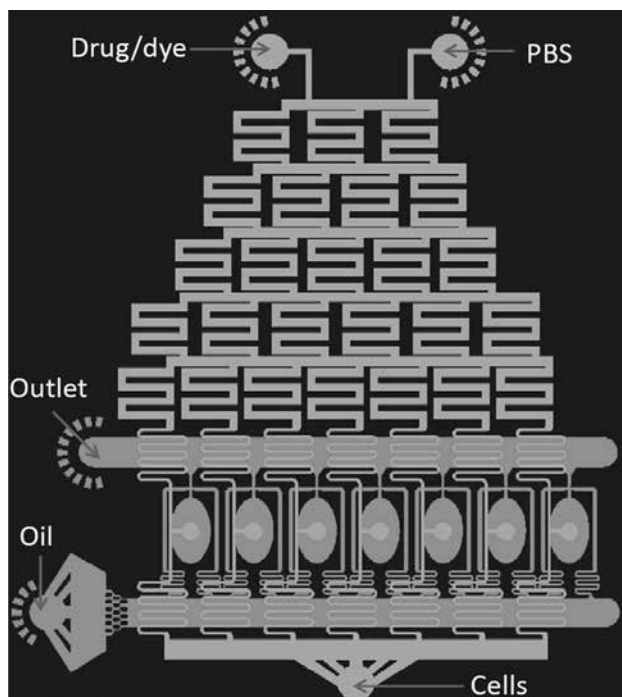


Figure 2: CAD of the bilayer PDMS microfluidic device generating droplets with varying drug concentrations.

Droplets were water-in-oil emulsions that were stabilized by a fluorinated surfactant. The aqueous media contained phosphate-buffered saline (PBS) and a hydrophilic fluorescent dye. The emulsions were formed by a continuous flow of the oil; droplet fission occurred when the continuous oil phase exerted sufficient viscous stress that caused an imbalance in the surface tension [2].

The water-in-oil emulsion occurred in a flow-focused geometry as seen in Figure 1. The manipulation of the flow rates of the PBS and dye with respect to each other determined the concentration of the dye within the droplet.

If 800  $\mu\text{L/s}$  of oil was pumped with 300  $\mu\text{L/s}$  of PBS and 100  $\mu\text{L/s}$  of dye, then you would expect the droplets to have a relative dye concentration of 25%. We strived to generate drug concentrations that would be of interest. After emulsification, there was a serpentine region in the device that promoted mixing of the droplet contents before the mixture exited the device through the outlet and was subsequently incubated.

Figure 2 shows a computer aided design (CAD) for a bilayer PDMS microfluidic device that generates a drug gradient by serial mixing in micro-channels within one layer, and another layer for creating picoliter-sized water-in-oil emulsion where the drug at different concentrations and lymphoblast cancer cells are co-encapsulated in a droplet in parallel. In the drug concentration gradient generating device, mixing is induced by the changes in velocity created by the changes in channel widths (Bernoulli's principle) and tree branching pattern. The advantage of this device is to reliably produce same size droplets with varying concentrations all at once rather than generating varying concentration droplets independently using a co-flow device.

For developmental and experimental purposes chemotherapeutic drugs and cancer lymphoma cells were not used, because the concept has already been proven. More so the focus was to improve the reproducibility of dye concentration within droplets, size of droplets, and design of the serpentine drug concentration gradient generating device.

## Results and Conclusions:

The data acquisition was driven by the PMT to identify cell state (live/dead), drug concentration in droplets, relative sizes of droplets, and presence of cell in droplet at high-throughput. A PMT heat map showed the distribution of different concentration clusters and relative sizes.

In Figure 3, there is a vertical smear indicating diffusion between the droplets. After changing surfactant and

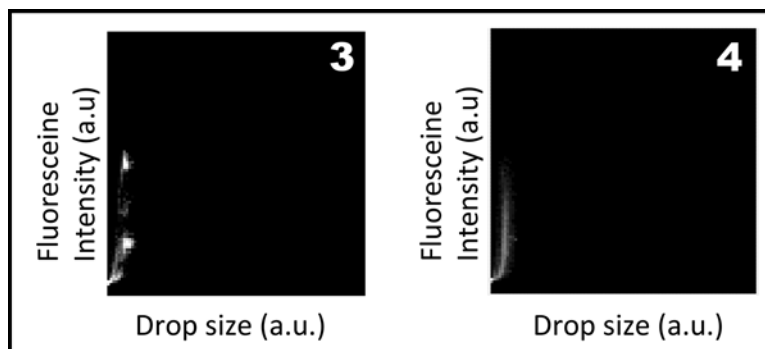


**Figure 3, left:** PMT heat map representative of same size droplets that have diffused during droplet incubation. **Figure 4, right:** PMT heat map demonstrating suppressed diffusion during droplet incubation.

adding a greater concentration of “empty” drops, diffusion was suppressed.

A horizontal smear would be indicative of droplets lacking size uniformity. As seen in Figure 4, the diffusion was suppressed successfully by having independent clusters of varying dye concentrations. Fluorescence imaging was also used to observe and quantify dye concentration in the drops, however it is labor intensive and impractical for high throughput and the reason for using PMT.

## Future Work:

Moving forward we would like to optimize flows and tree design for best mixing and reproducible concentration gradients. Using the PMT, we would like to perform time plots to observe diffusion during droplet incubation periods. Summation effects of drugs would also be interesting to observe drug synergy attacking different cell mechanisms leading to apoptosis. In addition, we would like to evaluate toxicity in healthy cells, not only drug efficacy.

## Acknowledgements:

I would like to thank God, my research mentor Dr. Anindita Basu, my principal investigator Dr. David Weitz, the National Nanotechnology Infrastructure Network Research Experience for Undergraduates (NNIN REU) Program, Dr. Randall Lee, and NSF for funding under Grant ECCS-0335765.

## References:

- [1] YC Tan, et al. Design of microfluidic channel geometries for the control of droplet volume, chemical concentration, and sorting. *Lab on a chip*, 4, 292-298, 2004.
- [2] Whitesides, G., et al. *Basic Microfluidic and Soft Lithographic Techniques. Optofluidics: Fundamentals, Devices, and Applications*, McGraw-Hill Biophotonics, 2009.

# Micropatterns and PDMS Microdevices for the Investigation of Cardiac Muscle Cell Structure and Function

**Anisa Swei**

**Biomedical Engineering, Worcester Polytechnic Institute**

**NNIN REU Site: Cornell NanoScale Science and Technology Facility, Cornell University, Ithaca, NY**

NNIN REU Principal Investigator: Prof. Jan Lammerding, Biomedical Engineering/Weill Institute for Cell and Molecular Biology, Cornell University

NNIN REU Mentors: Dr. Patricia Davidson and Gregory Fedorchak, Biomedical Engineering/Weill Institute for CMB, Cornell University

Contact: [aswei@wpi.edu](mailto:aswei@wpi.edu), [jan.lammerding@cornell.edu](mailto:jan.lammerding@cornell.edu), [patricia.davidson@cornell.edu](mailto:patricia.davidson@cornell.edu), [grf44@cornell.edu](mailto:grf44@cornell.edu)

## Abstract and Introduction:

Heart disease is the leading cause of death in the United States, responsible for an estimated 787,000 deaths in 2011 [1]. Genetic mutations are the cause of up to one-third of cases of dilated cardiomyopathy; mutations in the gene encoding lamin A/C alone accounts for 10% of inherited cases. Lamin A/C is an important component of the nuclear envelope: these proteins are essential for many cellular functions, such as preservation of the nucleus' shape, DNA replication, regulation of transcription, and chromatin organization [2]. One hypothesis is that these mutations interfere with heart muscle cell organization and/or the exertion of contractile forces, which are essential for these cells to properly function. In this project we designed and built polydimethylsiloxane (PDMS) devices to (a) examine the organization of the cytoskeleton and (b) assess the contractile forces of healthy and lamin A/C mutant human cardiac cells. By developing these two devices for the examination of cardiac cell functions, we hope to understand the role lamin A/C has on dilated cardiomyopathy.

## Experiment Procedure:

The first device consisted of PDMS stamps that were used to pattern rectangular shapes of extracellular matrix proteins with various aspect ratios. The stamp design consisted of

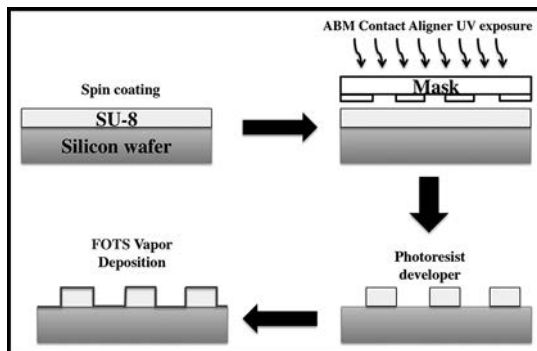


Figure 1: Overview of SU-8 photolithography used for the development of the micropattern device.

10 mm × 10 mm squares containing rectangles with an area of 50  $\mu\text{m}^2$ , but different aspect ratios, with rectangles spaced 200  $\mu\text{m}$  apart. From the design, we fabricated a mask and prepared the molds for the stamps using SU-8 photolithography techniques. The resulting features on the wafer were rectangular pillars 20  $\mu\text{m}$  tall. Figure 1 shows a schematic of the procedures used to produce the micropattern device.

After microfabrication, molds were fabricated using PDMS. A 50  $\mu\text{g/mL}$  solution of fibronectin, an extracellular matrix protein, was incubated on the PDMS stamps for an hour. The fibronectin-coated PDMS was placed into contact with a plasma cleaned glass coverslip to print rectangular fibronectin areas. The glass coverslips were then immersed in poly(L-lysine)-graft-poly(ethylene glycol) (PLL-g-PEG), which deposited on the glass that was not covered in fibronectin and prevents cell adhesion, so that cells could only adhere to the rectangular fibronectin patterns.

The glass coverslips were prepared for tissue culture by incubating in antibiotic solution, and human fibroblasts were cultured and then observed on the microscope.

The second device consisted of flexible PDMS micropillars, ranging in sizes and center-to-center distances. As the cells exerted forces onto the pillars, the quantification of cardiac cell contractile forces could be determined from their deflections. A mask, consisting of circles with a 1  $\mu\text{m}$  diameter and 2  $\mu\text{m}$  pitch, was used to microfabricate the pillars using standard lithography techniques.

Hexamethyldisilizane (HMDS) and nLOF-2020 (negative photoresist) was spin-coated on a silicon wafer, which was then exposed on the Autostep, post-exposure baked and developed. The wafer was placed in the Oxford 80 and processed for oxygen descum (straightening the pillar edges) and then oxide-etched to remove the silicon wafer's native oxide. The wafer was placed in the deep reaction ion etcher to perform a Bosch process, followed by oxide stripping to remove the photoresist.

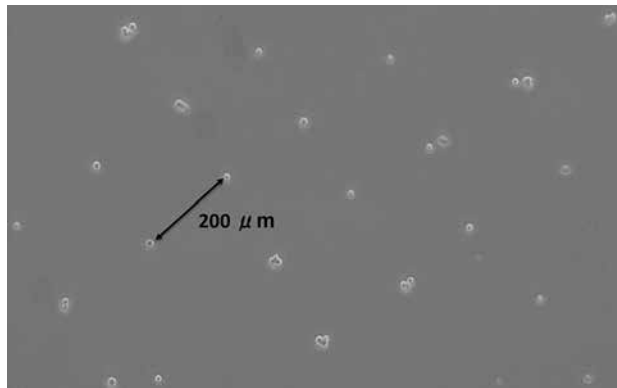


Figure 2: Bright-field contrast of the  $70 \times 35 \mu\text{m}^2$  stamp, spaced at 200  $\mu\text{m}$ , imaged at 5 $\times$  objective.

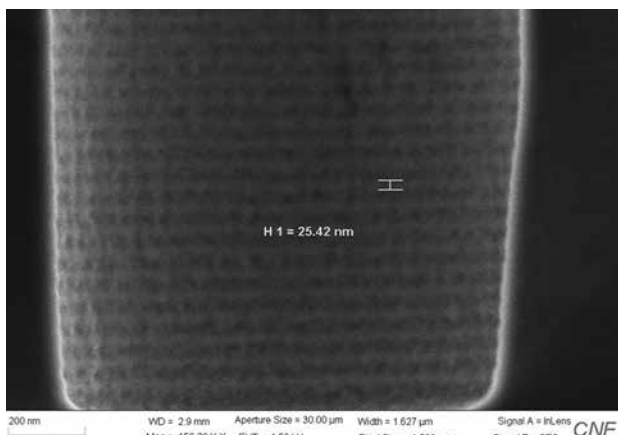


Figure 3: SEM image of the Bosch process with each scallop having a height of 25.42 nm.

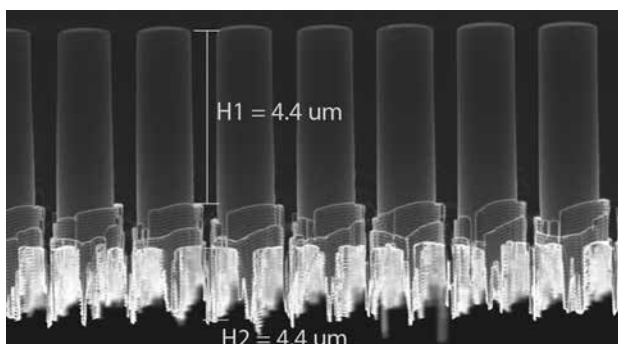


Figure 4: SEM image of the 1  $\mu\text{m}$ , with a center-to-center pitch of 2  $\mu\text{m}$ , device having a height of 4.44  $\mu\text{m}$ . (See cover!)

## Results and Conclusions:

The fabrication process for the micropattern device successfully created the desired height of 20  $\mu\text{m}$  as well as obtaining PDMS stamps from the molds. This was verified by optical microscopy, where the molds had proper shape and size. Following the microfabrication process, the preliminary studies with human fibroblasts showed

that the cells had adhered to the stamped patterns. The initial studies have shown that the application of a PDMS stamps with various patterns has the ability to control cell adhesion and placement. Figure 2 shows the bright-field contrast of cells adhering to a substrate patterned with the  $70 \times 35 \mu\text{m}^2$  stamp, where (mostly) individual cells are being spaced 200  $\mu\text{m}$  apart.

Initially, the micropillar device fabrication process had used similar SU-8 photolithography techniques as the micropattern device. However, this method resulted in cracked SU-8, as well as pillars floating off the device in the SU-8 developer. Thus, the method described in the experimental procedure was used. From the results, the device had successfully performed the Bosch process, where the pillars had scallops that were fairly linear, with an approximate scallop height of 25 nm as seen in Figure 3. However, issues arose in the deep reaction ion etcher process, causing the photoresist to burn, resulting in pillars not fully developing. Figure 4 shows that the pillar height was approximately 4.44  $\mu\text{m}$ . Unfortunately, due to the burns, the pillar height did not meet the goal of 10  $\mu\text{m}$ .

## Future Work:

The micropattern device will be used to assess variations in cytoskeletal alignment between mutated and wild-type cardiac cells. The micropillar device is being finalized for the quantification of cellular force generation, where optimizing techniques being considered include a positive photoresist, changing feature sizes and the addition of an oxide layer prior to spin-coating HMDS and photoresist.

From the initial studies conducted, the fibroblasts adhered to micropattern stamps, while cardiomyocytes contracted on PDMS pillars. Using these devices, we will be able to better understand the role of lamin mutations in dilated cardiomyopathy.

## Acknowledgements:

I acknowledge the National Nanotechnology Infrastructure Network Research Experience for Undergraduates (NNIN REU) Program, the Cornell NanoScale Science and Technology Facility, the National Science Foundation (ECCS-0335765). Thank you to the CNF staff, Christopher Martin (CNF user), Ryan Badman (CNF fellow), Jan Lammerding, and the members of the Lammerding lab.

## References:

- [1] Roger, V., et al. AHA Statistical Update. 2011.
- [2] Fox, S.I. Human Physiology 13<sup>th</sup> Edition 2011. McGraw-Hill Publishing. New York, New York.

# Development of Dual-Modality Nanoparticles for PET/MR

**Cyrus Thompson**

**Materials Science and Engineering, University of Wisconsin Madison**

**NNIN REU Site: Nano Research Facility, Washington University in St. Louis, St. Louis, MO**

NNIN REU Principal Investigator: Yongjian Liu, Radiology, Washington University School of Medicine

NNIN REU Mentor: Yongfeng Zhao, Radiology, Washington University School of Medicine

Contact: crthompson3@wisc.edu, liuyo@mir.wustl.edu, zhaoyo@mir.wustl.edu

## Abstract:

Behind strong medical treatments lie accurate diagnostics that commonly involve imaging—such as magnetic resonance imaging (MRI) and positron emission tomography (PET). Recently, to overcome limitations of each individual modality, PET and MRI are combined into a more efficient and accurate procedure for functional evaluation of imaging agent uptake with high resolution anatomy. However, this new technique requires new contrast agents enabling the dual-modality assessment. To date, numerous nanoparticles have been researched, but many require chelators for conjugation of radioisotopes to the nanoparticle surface. This raises concerns of radiolabeling stability and diagnostic accuracy. To address these issues, our project aimed at developing new PET/MR dual-modality nanoparticles by doping MRI contrast agents such as iron oxide (IO) and gadolinium oxide (GdO) with positron-emitter  $^{64}\text{Cu}$ . We first focused on the synthesis of nanoparticles through one-step reduction, copper doping efficiency, size and shape uniformity, contrast magnitude, structural stability, and surface modification. We then successfully incorporated  $^{64}\text{Cu}$  into IO with  $\sim 30\%$  incorporation of total radioactivity and achieved high specific activity for sensitive PET detection. Further, phantom studies and *in vivo* pharmacokinetic evaluations suggested potential applications of this particle for PET/MR. We will continue the optimization for further *in vivo* animal PET/MRI studies.

## Introduction:

With MRI we are able to achieve excellent soft tissue and soft organ contrast providing images with high anatomical accuracy. This can be helpful in locating a patient's specific medical condition such as a tumor. However, it cannot provide functional information such as tissue growth rate and metabolism. In order to collect this information a patient might have to undergo additional imaging techniques. A common approach is PET imaging, which offers the needed sensitivity through detection of extremely minute amounts of radioactive labeled agents.

When these imaging techniques are combined we then need dual-modality agents. In our research, nanoparticle systems were exploited because of their multifunctionality capability. Specifically, we combined two detection elements, radionuclides and MRI agents, but future work could involve additional components used for targeting and therapeutic payloads. Operating on the nanoscale also offers enhanced *in vivo* stability, efficacy, and reduced toxicity. With such potential it is no surprise that six nanoparticle delivery systems for cancer are already on the market and numerous others in clinical development [1].

## Experimental Procedure:

**Cu-IO Synthesis.** Iron oxide particles were synthesized following a modified one-step copper incorporation

thermal decomposition procedure [2]. To study effects of copper incorporation on particle characteristics we varied the percentage of copper in the reaction medium (0%, 2% and 10%) through addition of copper chloride dihydrate.

**Cu-GdO Synthesis.** Gadolinium oxide particles were synthesized following a modified one-step copper incorporation polyol process [3]. Similarly to IO we studied the effects of copper incorporation by varying the presence of copper in the reaction medium (0% and 5%).

**Surface Modification.** Before conducting any *in vivo* study, particle surfaces first needed to be modified for stable aqueous dispersion. This was achieved through the exchange of initial hydrophobic coatings, a product of synthesis reagents, with polyethylene glycol (PEG) through a modified PEGylation process [2]. Particles were first synthesized with non-radioactive copper and studied via transmission electron microscope (TEM) in order to characterize size and shape. Copper incorporation was then confirmed with inductively coupled plasma mass spectrometry (ICP-MS). Finally, after successful surface modification for stable aqueous dispersion the synthesis was repeated except with the use of  $^{64}\text{Cu}$ . Further studies were then conducted on structural stability via thin layer chromatography (TLC), contrast magnitude via PET and MR phantom, and pharmacokinetic properties via mouse biodistributions.

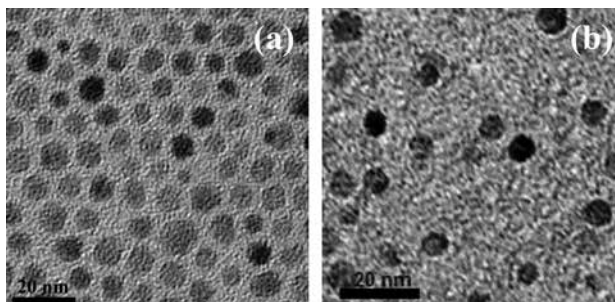


Figure 1: TEM images of (a) IO-0% Cu and (b) GdO-0% Cu with 20 nm scale bars.

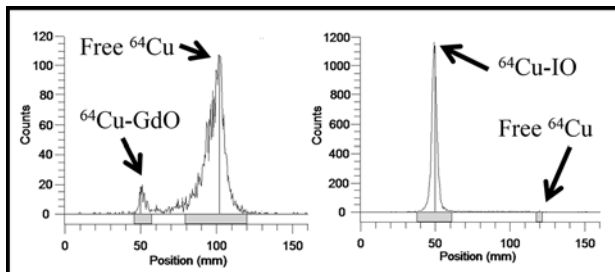


Figure 3: Radio-TLC plots showing  $^{64}\text{Cu}$  incorporation into (left) GdO and (right) IO.

Target	Measured Cu	TEM size
IO	--	$7.0 \pm 1.2$ nm
IO-2% Cu	1.4%	$8.2 \pm 1.0$ nm
IO-10% Cu	1.8%	$9.6 \pm 1.4$ nm
GdO	--	$6.3 \pm 1.6$ nm
GdO-5% Cu	0.23%	$4.6 \pm 0.9$ nm

Figure 2: Particle diameters via TEM and measured copper percentage via ICP-MS.

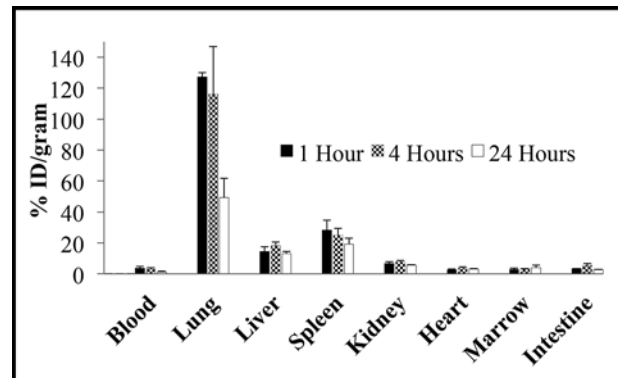


Figure 4: Mouse biodistribution study of  $^{64}\text{Cu}$ -IO.

## Results and Conclusions:

Synthetic procedures produced particles monodisperse in size and shape for both IO and GdO as seen in Figure 1 and 2. It can also be seen that there were only slight changes in particle diameters as the percentage of copper increased. This consistency and stability is beneficial as it allows for the variable tuning of copper incorporation without significant changes to other features such as PET and MR contrast magnitude; confirmed via phantom studies. Further, we were able to confirm the presence of copper by ICP-MS. While the actual values are lower than amounts present during synthesis we were successful nonetheless as the high sensitivity of PET is capable of detecting such minute amounts of  $^{64}\text{Cu}$ .

When particles were synthesized with  $^{64}\text{Cu}$  we measured radiolabeling stability by observing how much  $^{64}\text{Cu}$  remained intact versus how much broke free from the main particle system; seen in Figure 3. For both IO and GdO we saw that  $^{64}\text{Cu}$  remained intact, but in the case of GdO there was also detachment; signified by the "Free  $^{64}\text{Cu}$ " peak.

Since current progress with IO showed greater radiolabeling success we then studied pharmacokinetic properties of  $^{64}\text{Cu}$ -IO via mouse biodistributions. As seen in Figure 4, particle concentration in the lungs was greater than any other organ. While this suggests a potential application for drug delivery to the lungs further studies are needed to explore the underlying mechanism behind the accumulation.

## Future Work:

While this preliminary work was successful in using IO, GdO, and  $^{64}\text{Cu}$  for the development of dual-modality particles, we hope to increase radiolabeling incorporation and stability through synthetic procedure modifications. After optimization of both IO and GdO systems we can then continue with PET/MR imaging and exploration of *in vivo* particle accumulation.

## Acknowledgements:

I would like to thank Hannah Luehmann, Debbie Sultan, the small animal imaging facility, and  $^{64}\text{Cu}$  production team at MIR. I would also like to thank the National Nanotechnology Infrastructure Network Research Experience for Undergraduates (NNIN REU) Program and National Science Foundation for their financial support under Grant No. ECCS-0335765.

## References:

- [1] Egusquaguirre SP, et al; Clinical and Translational Oncology, 14:2, 83-93 (2012).
- [2] Bridot, Jean-Luc, et al; Journal of the American Chemical Society, 129:16, 5076-5084 (2007).
- [3] Xie, Jin, et al; Advanced Materials, 19:20, 3163-3166 (2007).

# Optimization of Thin Film Composite Polyimide Reverse Osmosis Membrane by Polyethylene Glycol for Enhanced Fouling Resistance

**Jyoti Campbell**

**Chemistry, Wellesley College**

**NNIN REU Site: Nano Research Facility, Washington University in St. Louis, St. Louis, MO**

NNIN REU Principal Investigator: Dr. Young-Shin Jun, Energy, Environmental, and Chemical Engineering, Washington University in St. Louis

NNIN REU Graduate Mentor: Zongsen Zou, Energy, Environmental, and Chemical Engineering, Washington University in St. Louis

Contact: jcampbe5@wellesley.edu, ysjun@wustl.edu, zou.zongsen@wustl.edu

## Introduction:

Water scarcity is a serious concern for the world and it is projected to get worse. Water desalination is an important source of fresh water to alleviate water scarcity, especially in water stressed regions, and it will continue to grow in importance. Many desalination plants use reverse osmosis (RO) to generate fresh water [1]. RO is a high pressure process that uses thin film composite polyamide (TFC-PA) membranes to remove contaminants from the water. Unfortunately, these membranes commonly experience fouling, which can decrease water flux and salt rejection [1]. Polyethylene glycol (PEG) is a hydrophilic material that, when attached to the membrane surface, can enhance fouling resistance and increase membrane flux by making the surface both more neutrally charged and hydrophilic [2]. However, multi-component foulant resistance of modified membrane has not been tested. Thus, in this study, we investigated the efficacy of the PEG-modified TFC-PA RO membranes in fouling resistance to calcium carbonate ( $\text{CaCO}_3$ ), calcium sulfate ( $\text{CaSO}_4$ ), and humic acid.

## Experimental Procedure:

One commercially available TFC-PA membrane (BW30) was used to investigate the effect of PEG modification on mineral fouling ( $\text{CaSO}_4$  and  $\text{CaCO}_3$ ) and organic fouling (humic acid). The membrane was soaked in deionized (DI) water for 24 hours before testing or modifying. The membrane was modified in a solution of PEG monomer, PEG crosslinker (ethyleneglycol dimethacrylate), and initiators (potassium persulfate and potassium disulfite). The membrane was then pretreated for membrane compaction and conditioning with DI water for seven hours at 260 psi. Then the membrane was tested with fouling influent for four hours.

There were three fouling influents of interest, all dissolved into DI water. First,  $\text{CaCO}_3$ -forming solution was made by mixing 10 mM  $\text{NaCl}$  with 3.3 mM  $\text{CaCl}_2$  and 3.3 mM  $\text{Na}_2\text{CO}_3$ . Second,  $\text{CaSO}_4$ -forming solution was made by

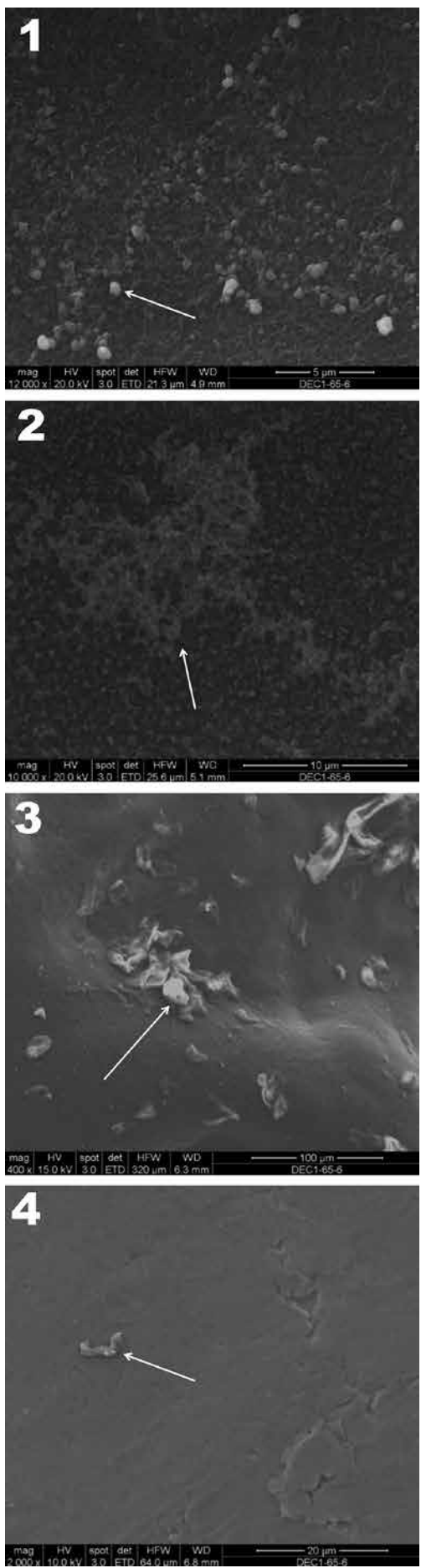
mixing 19.5 mM  $\text{CaCl}_2$ , and 19.5 mM  $\text{Na}_2\text{SO}_4$ . Third, humic acid solution was prepared to contain 10 ppm humic acid. Continuous samples of effluent were taken every five minutes. Water flux and salt rejection were tested every five minutes for the first hour, then every 30 minutes. The extent of membrane fouling was examined by contact angle measurement and scanning electron microscopy (SEM).

## Results and Discussion:

Before fouling experiments, SEM images showed PEG attached to the modified membrane. Also, contact angle analysis done before fouling showed that PA-PEG had a much lower contact angle at  $13.2^\circ$  than PA at  $42.2^\circ$ .

For fouling experiments, overall, there was less fouling for PA-PEG membranes than for PA membranes. For the  $\text{CaCO}_3$  fouling experiment, we found the PA and PA-PEG membranes had comparable flux and salt rejection. However, the SEM images show that the PA-PEG membrane has fewer foulants than the PA membrane (Figures 2 and 4). For the  $\text{CaSO}_4$  fouling experiment, we found that PA-PEG had higher initial flux and  $\text{Ca}^{2+}$  rejection. However the PA membrane had higher  $\text{SO}_4^{2-}$  rejection, most likely due to the negative membrane surface having more repulsion with the negatively charged ion than the neutral modified membrane surface. Figure 2 showed no  $\text{CaSO}_4$  fouling on the PA-PEG membrane, but  $\text{CaSO}_4$  fouling was present on the PA membrane shown in Figure 1. For the humic acid fouling experiment, PA had higher flux, but based on contact angle showing that the PA surface was more hydrophobic and this should result in a lower flux, this can be an error and should be retested.

The PA-PEG membrane had a higher humic acid and  $\text{Cl}^-$  rejection. It also had a lower contact angle after fouling at  $38.3^\circ$  than the PA membrane after fouling at  $55.8^\circ$  and the SEM image in Figure 4 showed less fouling on the PA-PEG membrane than the PA membrane in Figure 3.



PEG modification makes the PA membrane more hydrophilic resulting in higher initial flux than PA in these experiments. PEG modification of the PA membrane increases fouling resistance to humic acid in particular. Based on contact angle analysis, after humic acid fouling, PA-PEG is still more hydrophilic than PA. At very high mineral foulant concentrations, PEG does not obviously enhance salt rejection, but it enhances resistance to inorganic foulants based on smaller foulant sizes in Figure 2 and SEM images of  $\text{CaCO}_3$  fouled membranes. More tests should be conducted under different concentrations of foulants.

### Conclusions and Future Work:

PEG modification of commercially available TFC-PA membrane makes the surface more hydrophilic which increases initial flux and enhances fouling resistance to humic acid in these fouling experiments. However, at very high mineral foulant concentrations, PEG modification does not obviously enhance salt rejection but does decrease mineral precipitation on the surface. To confirm the trend, replicate experiments are needed. Studies of different influent concentrations, pressures, and combinations should be conducted to determine the impact of PEG modification with realistic and complex influents. In addition, the PEG modification should be further studied and optimized to enhance the fouling resistance of PA RO membranes.

### Acknowledgments:

Thank you to Dr. Young-Shin Jun, Mr. Zongsen Zou, Dr. Jessica R. Ray, and everyone at the Environmental Nanochemistry Lab for their guidance and support. I would also like to thank the Nano Research Facility and the National Nanotechnology Infrastructure Network Research Experience for Undergraduates (NNIN REU) Program for giving me this opportunity and unforgettable experience. Support from the National Science Foundation under Grant No. ECCS-0335765, Washington University's International Center for Advanced Renewable Energy & Sustainability (I-CARES).

### References:

- [1] Menachem Elimelech, William A Phillip. The Future of Seawater Desalination: Energy, Technology, and the Environment [J]. *Science* 333: 712-717 (2011).
- [2] Jessica Ray, et al. Hydrophilic, Bactericidal Nanoheater-Enabled Reverse Osmosis Membranes to Improve Fouling Resistance[J]. *ACS Appl. Mater. Interfaces* 7(21), 11117-11126 (2015).

**Figure 1:** SEM of PA membrane after  $\text{CaSO}_4$  fouling test. The white structures are foulant deposits. **Figure 2:** SEM of PA-PEG membrane after  $\text{CaSO}_4$  fouling test. The white cloud like structures are PEG, not fouling, attached to the membrane surface. **Figure 3:** SEM of PA membrane after humic acid fouling test. The debris on the membrane surface is believed to be humic acid fouling. **Figure 4:** SEM of PA-PEG membrane after humic acid fouling test. The membrane is mostly clear, with one possible smaller foulant.

# Twisting a C=C Double Bond in Crowded Alkenes: The Synthesis and Characterization of Small-Molecule Electron Acceptors

**Dylan J. Freas**  
Chemistry, Williams College

**NNIN iREU Site: National Institute for Materials Science (NIMS), Tsukuba, Ibaraki, Japan**

NNIN iREU Principal Investigator: Dr. Masayuki Takeuchi, Polymer Materials Unit, National Institute for Materials Science

NNIN iREU Mentor: Dr. Atsuro Takai, International Center for Young Scientists, National Institute for Materials Science

Contact: [dylan.j.freas@williams.edu](mailto:dylan.j.freas@williams.edu), [takeuchi.masayuki@nims.go.jp](mailto:takeuchi.masayuki@nims.go.jp), [takai.atsuro@nims.go.jp](mailto:takai.atsuro@nims.go.jp)

## Abstract:

There is currently a need for novel, non-fullerene-based electron acceptors in organic photovoltaic devices (OPVs). The synthesis and characterization of various 9,9'-bifluorenylidene (9,9'-BF) derivatives are described. The dihedral angles of the derivatives were determined using DFT calculations and were determined to increase upon introduction of methyl substituents on the inner C1 and C8 atoms. The red shifted UV-vis absorption spectra and negative shift in oxidation potential, determined by cyclic voltammetry, were observed with increasing the C=C dihedral angles of the derivatives. This is, to our knowledge, the first experimental evidence that the degree of C=C bond twisting has profound effects on the bandgap and redox properties of small molecules.

## Introduction:

One of the major objectives for materials science is the optimization of the performance of organic photovoltaic devices (OPVs). In such devices, an appropriate combination of donor and acceptor materials is necessary for efficient charge separation and migration. While several research groups have recently reported a wide range of new polymeric donor molecules, there have been fewer reports on new structures of acceptor molecules [1]. Most current acceptor molecules contain fullerene derivatives — however, due to their difficulty in synthesis and purification, along with their weak absorption in the visible region, the synthesis of new and versatile acceptor molecules is urgently required [2].

There is an inherent potential in acceptor molecules based on 9,9'-bifluorenylidene (9,9'-BF), because the one-electron reduction of 9,9'-BF affords a stable radical anion due to steric strain relief and gain in aromaticity to a 14 $\pi$  electron system [3]. The purpose of this study was to synthesize and characterize a series of novel 9,9'-BF derivatives that differ in the twisting angle of the central C=C double bond, but are similar in other electronic properties. The twisting angle of each 9,9'-BF derivative was correlated to its bandgap and redox properties, which were determined by UV-vis spectroscopy and cyclic voltammetry, respectively.

## Experimental Section:

Chemicals were purchased from Sigma-Aldrich and used as received without further purification. All dry solvents

were freshly distilled under argon prior to use.  $^1\text{H}$  and  $^{13}\text{C}$  NMR measurements were performed in  $\text{CDCl}_3$  using a JEOL ECS-400 spectrometer. Chemical shifts are expressed in ppm relative to  $\text{CHCl}_3$  (7.26 ppm for  $^1\text{H}$  NMR and 77.36 ppm for  $^{13}\text{C}$  NMR). Mass spectrometry was performed by a Shimadzu AXIMA-CFR Plus. Computational analysis and graphical representation were carried out with Spartan '14 software. Optimized equilibrium geometries were obtained with DFT (B3LYP/6-31G\*\* level basis set) calculation. UV-vis spectra were recorded on a JASCO V-670 using  $\text{CH}_2\text{Cl}_2$  solutions of the 9,9'-BF derivatives in 1 cm quartz cuvettes at 298K. The spectrum of each derivative was then normalized to its maximum absorption (typically 450-500 nm). The electrochemical measurements were carried out with an Eco Chemie AUTOLAB PGSTAT12 potentiostat in a deaerated solvent containing TBAPF6 (0.10 M) as a supporting electrolyte at 298K. A conventional three-electrode cell was used with a glassy carbon working electrode and a platinum wire as a counter electrode. The redox potentials were measured with respect to a reference electrode:  $\text{Ag}/\text{AgNO}_3$  ( $1.0 \times 10^{-2}$  M) with TBAPF6 (0.10 M) in acetonitrile. Ferrocene was employed as an external standard.

## Results and Discussion:

Compounds **1**, **2**, and **3**, shown in Figure 1, were synthesized via a coupling reaction according to a previous work [1]. The formation of these compounds was confirmed using  $^1\text{H}$  and  $^{13}\text{C}$  NMR, along with mass spectrometry.

Although the introduction of methyl groups was shown to increase the twisting angle, they should not significantly alter the electronics of the 9,9'-BF derivatives because they are very weak electron donors. This is proven by the comparison of the reduction potentials between non-substituted fluorenone (-1.80 V vs.  $\text{Fc}/\text{Fc}^+$ ) and 1,4-dimethylfluorenone (-1.89 V vs.  $\text{Fc}/\text{Fc}^+$ ). Methyl groups are therefore an ideal substituent to investigate the effect of C=C twisting on bandgap and redox properties.

The UV-vis absorption spectra for compounds **1**, **2**, and **3** are shown in Figure 2. It was observed that as the twisting angle increased, there was a red-shift in the absorption spectra, indicating a decrease in the bandgap energy. Additionally, the degree of red shift was observed to be directly related to the increase in twisting angle. These results suggest that the bandgap of 9,9'-BF derivatives can be selectively tuned by modifying the twisting angle.

To investigate the redox properties of the derivatives, cyclic voltammetry was performed, shown in Figure 3. Each HOMO-LUMO bandgap of the derivatives was determined from the oxidation and the reduction potentials,  $E_{\text{ox}} - E_{\text{red}}$ . There was a significant decrease in the HOMO-LUMO bandgaps of the derivatives upon an increase in twist angle (from 2.50 eV for compound **1** to 2.27 eV for compound **3**). This result clearly indicates that the C=C twisting angle of the 9,9'-BF derivatives affects the redox potentials, which is fairly consistent with the UV-vis absorption change.

### Conclusions and Future Directions:

We showed the synthesis and characterization of a series of new 9,9'-bifluorenylidene derivatives. The central C=C twist angle was correlated to the bandgap and redox properties of the 9,9'-BF derivatives. Future work will involve performing x-ray crystallography on the 9,9'-BF derivatives to accurately determine C=C twisting angles. Additionally, the versatile synthetic scheme established in this work will be applied to the synthesis of other 9,9'-BF derivatives that have even greater C=C twisting angles, such as derivatives with  $-\text{Si}(\text{CH}_3)_3$  substituents.

### Acknowledgements:

It's very sad to conclude my time with NNIN! Many thanks to my PI, Dr. Masayuki Takeuchi, my mentor, Dr. Atsuro Takai, and the National Nanotechnology Infrastructure Network International Research Experience for Undergraduates (NNIN iREU) Program (Grant No. ECCS-0335765).

### References:

- [1] Brunetti, et al. *Angew. Chem. Int. Ed.*, 2010, 49, 532-536.
- [2] Eakins, et al. *Can. J. Chem.*, 2013, 91, 1059-1071.
- [3] Kim, et al. *Chem. Comm.*, 2013, 49, 10950-10952.

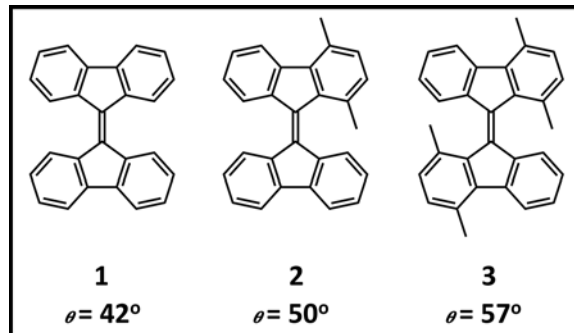


Figure 1: Structures and C=C double bond twisting angles of compounds **1**, **2**, and **3**.

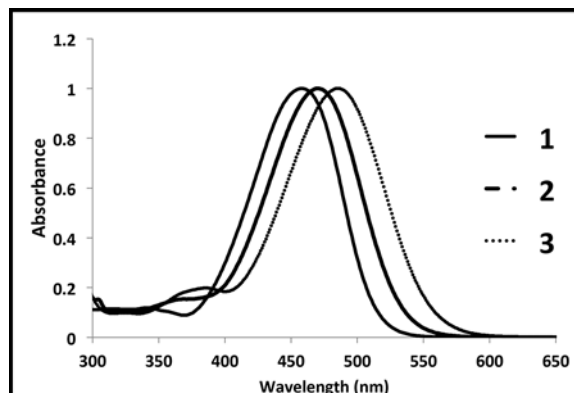


Figure 2: UV-vis absorption spectra of compounds **1**, **2**, and **3**.

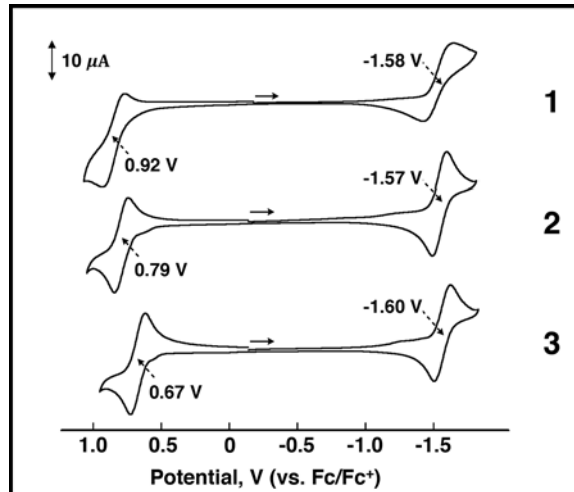


Figure 3: Cyclic voltammograms of compounds **1**, **2**, and **3**.

# Crumpled Graphene Oxide-Polysulfone Composite Membranes for Water Purification

**Isaac Fuhrman**

**Mechanical Engineering, University of Nebraska-Lincoln**

**NNIN REU Site: Nano Research Facility, Washington University in St. Louis, St. Louis, MO**

NNIN REU Principal Investigator: Dr. John Fortner, Energy, Environmental and Chemical Engineering, Washington University in St. Louis

NNIN REU Mentor: Yi Jiang, Energy, Environmental and Chemical Engineering, Washington University in St. Louis

Contact: isaacokoboji@gmail.com, jfortner@wustl.edu, jiang.y@wustl.edu

## Abstract:

Previously, crumpled graphene oxide (CGO) has been layered on surfaces of commercial water treatment membranes to increase water flux as well as antimicrobial (anti-biofouling) properties. This study explored CGO's effects on flux, rejection, fouling, and antifouling properties when structurally incorporated into polysulfone (PSF) membranes. Different ratios of CGO were added into the casting solution for a phase-inversion process. The synthesized membranes were then tested in an effort to optimize CGO mass loadings. Proper methods and variables were found and accounted for throughout the series of experiments. Flux and rejection were found as high as 100 L/m<sup>2</sup> h bar and 90% of BSA respectively. It was hypothesized that surface openings from CGO could serve as water channels through the selective surface toward the more porous region of the membrane, creating higher flux.

## Introduction:

Current water treatment methods employ hollow-fiber ultrafiltration (UF) membranes in vast quantities to filter macromolecular impurities and bacteria from feed water for various industrial and residential applications. These modules of membranes require expensive and time-consuming cleaning processes, such as backwashing, in order to remove residue buildup on membrane surfaces. Given the hydrophilic properties of graphene oxide (GO), some research for advancements in water treatment membranes has been geared towards GO nanoparticles.

Previous research has shown that crumpled graphene oxide (CGO) structures can increase flux due to its hydrophilic properties and porous nature [1]. In this study, the effects on polysulfone membrane properties were investigated extensively to determine the performance of CGO as a nanofiller to membrane casting solutions prior to solidification.

## Experimental:

Membranes were created using the phase-inversion method [2]. CGO (5-10 mg) was sonicated in n-methyl-2-pyrrolidone (NMP), then stirred with polysulfone (PSF) and polyvinylpyrrolidone (PVP) at 60°C until becoming homogenous. The solution was cast using a casting knife and then submerged in MilliQ water overnight. Subsequently, 63 mm diameter membranes were cut with razor blades.

Transmission electron microscopy (TEM, Tecnai TM Spirit) was utilized to obtain information on CGO and

CGO nanocomposites' size and morphologies. Scanning electron microscopy (SEM) images of the membranes (sputtered with Au for 60 s) were taken to examine surface structure.

Membranes were then tested for flux by filtering pure water with a stirred cell under 1.5 bar (Amicon 8200) and measuring permeate weight over 60 s time intervals. Membranes were compacted under 1.5 bar for one hour before any measurement. Water was filtered through the membrane until flux plateaued. Bovine serum albumin (BSA) (1 g/L) was filtered separately as a model foulant. Rejection was determined by the difference between inflow and permeate BSA concentrations that were analyzed at 278 nm using UV-visible spectrophotometry (UV-Vis). All samples were washed with water for several minutes before storing in pure water. Filtration processes were repeated to obtain consistent data as well as fouling and antifouling properties.

## Results and Conclusions:

SEM and TEM images in Figure 1 and Figure 2 of CGO membranes show embedded CGO particles directly underneath and protruding from the surface of the membrane. Pristine (control) membranes showed smooth surfaces without notable inconsistencies, forming a smooth solid barrier. CGO nanoparticles channel water from the surface directly into the porous region of the membrane. These particles could be acting as hydrophilic pathways with lower resistance and higher localized flux

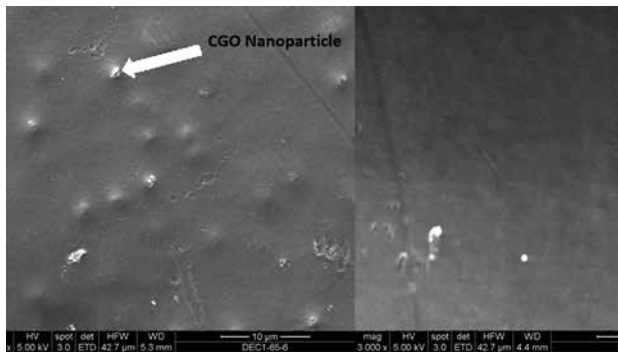


Figure 1: SEM images of CGO nanoparticles protruding through surface of CGO membrane (left) and surface of pristine membrane (right).

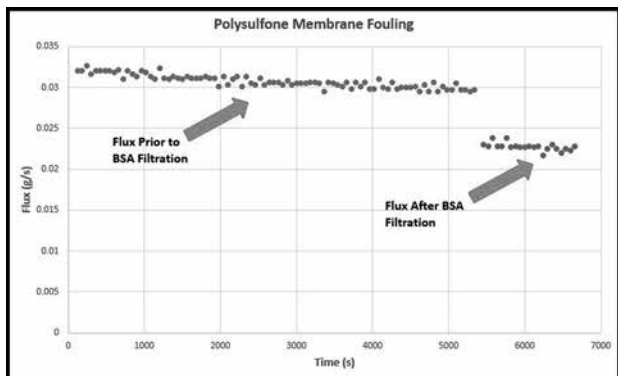


Figure 3: Control membrane fouling before and after BSA filtration.

than the surrounding surface, resulting in larger overall flux than membranes without such channels.

Figure 3 shows the fouling process for a pristine membrane. Water flux was found to plateau until a constant value of 0.0295 g/s was reached. After BSA was filtered through the membrane, water flux decreased to 0.0226 g/s — 76.6% of the initial value. Foulant built up on the membrane surface, obstructing pores and decreasing flux. Despite a washing process, not all foulant was removed, damaging the membrane and resulting in a permanently lower flux. This pattern was consistent for both control and CGO membranes alike.

During UV-Vis tests for BSA, absorbance peaked at a wavelength of 278 nm. The linear relationship between concentration and absorbance was compared with the BSA permeate absorbance of each membrane to obtain the remaining BSA in the permeate. An example of a control membrane is given in Figure 4, which has the inflow solution peaking at 0.616 and the permeate at 0.0238, indicating a 96.1% rejection for the given filtration trial.

Rejection for control and CGO membranes ranged from 73.9-96.1% and 70.9-99.2%, respectively, while flux ranged from 0.0176-0.0307 g/s and 0.0155-0.0317 g/s, respectively. Methods to measure both fouling and rejection were refined and will be used for future experiments. Though no statistical differences between CGO and control membranes were found, our preliminary results give

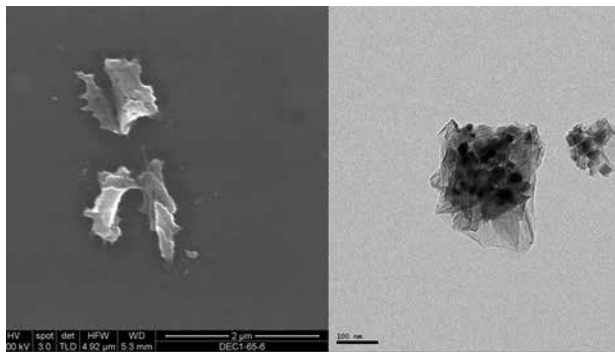


Figure 2: SEM of embedded CGO particle (left) and TEM of CGO with titanium and  $\text{CuCl}_2$  from aerosolized process [3] (right).

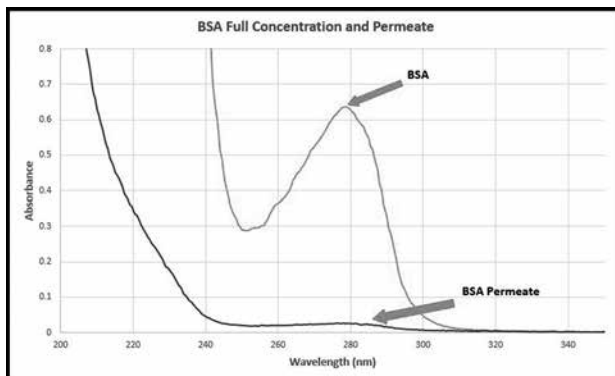


Figure 4: UV-Vis spectrum for inflow BSA and permeate used to determine rejection.

base data and processes that will be built further upon by continued research.

### Future Work:

The largest issue with results was variability within casting solutions. In future studies the focus should be on consistency and repeatability at each step of experimental processes. Strong evidence was found to support that without the drying process, membranes had up to 10 times higher water flux than dried samples of the same composition, but with a drop of rejection as low as much as 50%. This relationship should be investigated to obtain optimum performance.

### Acknowledgements:

I would like to thank my mentor Yi Jiang and PI Dr. John Fortner for the guidance and opportunity to work with them on this project. I would also like to thank NNIN REU and NSF under Grant No. ECCS-0335765.

### References:

- [1] Jiang, Y, et al., Environ.Sci.& Tech., 49(11), 6846-6854 (2015).
- [2] Kim, J, Lee, Y, J. of Membrane Science, 128(2) 153-163 (1998).
- [3] Wang, W, Jiang, Y, Biswas, P, The Journal of Physical Chemistry Letters, 3(21), 3228-3233 (2012).

# Advanced Dielectrics for Microelectronics: Chemically Amplified, Low- $\kappa$ Materials

Masashi Fukuzawa

Applied Chemistry, Kyushu University, Fukuoka, Japan

NNIN iREG Site: Institute for Electronics and Nanotechnology, Georgia Institute of Technology, Atlanta, GA

NNIN iREG Principal Investigator: Prof. Paul A. Kohl, Chemical and Biomolecular Engineering, Georgia Institute of Technology

NNIN iREG Mentor: Jared M. Schwartz, Chemical and Biomolecular Engineering, Georgia Institute of Technology

Contact: m.fukuzawa@mail.cstm.kyushu-u.ac.jp, paul.kohl@chbe.gatech.edu, jschwartz38@gatech.edu

## Abstract and Introduction:

Shrinking of the microelectronics package requires advanced low dielectric constant (low- $\kappa$ ) materials. Organic polymers offer more environmentally friendly and moldable options than inorganic materials.

In organic polymers, photo-definable dielectrics can be directly patterned by photolithographic means [1]. Lithographically printed dielectrics do not require the use of photoresist or additional pattern transfer steps, which can be costly and expose the device to aggressive wet or dry etch process steps. Some organic, photo-definable polymers can be catalytically depolymerized by a small light stimulus.

The catalytic phenomenon is called chemical amplification, and the polymers that depolymerize completely are called self-immolative polymers (SIPs) [2]. Photo-definable SIPs are depolymerized and become monomers through the light stimulus. Here, if vapor pressure of the monomer is high, the exposed material can evaporate and disappear completely, which can skip the developing steps in traditional processing because only light exposure and dry developing are needed. However, a conventional photo-definable SIP such as polyphthalaldehyde [3] has inherent problems, for example, low mechanical strength and low vapor pressure of monomers.

Low mechanical strength makes them difficult to use as an interlayer insulating film, and low vapor pressure increases dry develop time.

In this report, the preparation method of copolymers that have high mechanical strength and higher vapor pressure is discussed. In order to obtain the ideal copolymer, butyraldehyde (BA) or pivalaldehyde (PVA) are used as a monomer with PHA. BA and PVA has high vapor pressure and their polymers are expected to have high mechanical strength because of their high crystallinity.

## Experimental:

Figure 1 shows the monomers used in this research. Copolymers were synthesized by following a paper that describes the anionic polymerization of polyphthalaldehyde [4]. Scheme 1 shows the synthesis procedure of copolymers. PHA (1.0 equiv), BA or PVA (0.25 equiv), and *N*-hydroxysuccinimide in THF (0.01 M, 0.00024 equiv) were added to a vial in a glovebox under an argon atmosphere. THF was added to create a 1.0 M aldehyde solution. The reaction mixture was cooled to -70°C.

After 30 min, a solution of 1-*tert*-butyl-2,2,4,4,4-pentakis(dimethylamino)-2 $\lambda^5$ ,4 $\lambda^5$ -catenadi-phosphazene (P2-*t*-Bu base) in THF (2.0 M, 0.0048 equiv) was added to the solution, and the reaction mixture was stirred at -70°C. After two hours, the polymer was end-capped via sequential addition of pyridine (0.6 equiv) and methylchloroformate (0.04 equiv) to the -70°C solution. The solution was allowed to warm to room

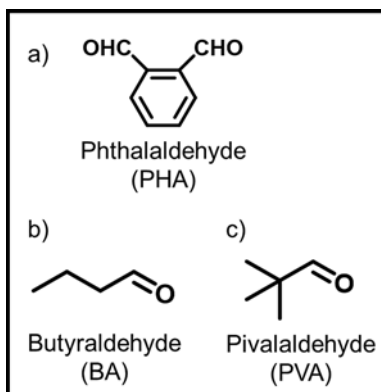
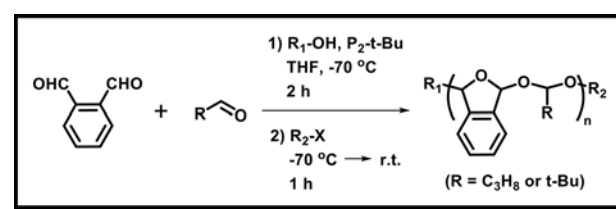


Figure 1: Chemical structures of a) phthalaldehyde (PHA), b) butyraldehyde (BA), and c) pivalaldehyde (PVA).



Scheme 1: Synthesis procedure of copolymer.

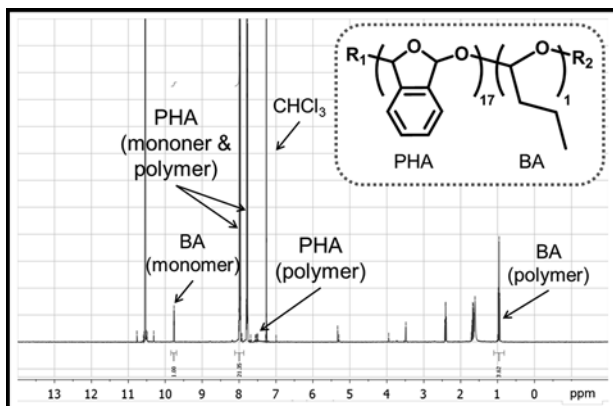


Figure 2:  $^1\text{H}$  NMR spectrum of PHA-BA copolymer.

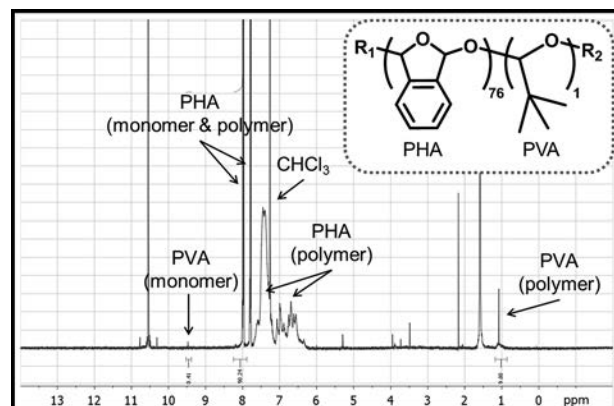


Figure 3:  $^1\text{H}$  NMR spectrum of PHA-PVA copolymer.

temperature an hour later. The polymer was precipitated by adding the reaction mixture to a solution of 200 mL cold methanol. The resulting suspension was filtered, and the precipitate was washed using methanol. The resulting polymer was dried overnight.

The yields of the PHA-BA and PHA-PVA copolymers were 42 wt% and 20 wt%, respectively.

## Results and Discussion:

Figure 2 shows  $^1\text{H}$  NMR spectrum of the copolymer, which suggests the mole ratio of PHA to BA is 17 to 1. It suggests the synthesis did not go as expected because the mole ratio was initially 4 to 1. One possible explanation is the acidic  $\alpha$ -hydrogens of BA caused a side reaction with the anionic propagation that impeded the polymerization. A copolymer of PHA and PVA was then tried, which has no  $\alpha$ -hydrogens to interrupt the polymerization. Figure 3 shows  $^1\text{H}$  NMR spectrum of the PHA-PVA copolymer, which suggests the ratio of PHA to PVA is 76 to 1. This means almost all of the monomers in the polymer chain are PHA, which is not desired. The low PVA content is probably due to the methyl groups of PVA having high steric hindrance. A new monomer whose methyl groups are substituted for less bulky groups such as fluorine should be used in the future.

## Conclusions and Future Work:

A PHA-BA copolymer was synthesized with the goal of obtaining a copolymer with high mechanical strength and high vapor pressure of the monomers.  $^1\text{H}$  NMR of the

copolymer shows the mole ratio of PHA to BA is 17 to 1, which does not substantially improve the monomer vapor pressure after depolymerization as desired. The differences between expected and actual copolymer content is likely due to the  $\alpha$ -hydrogens of BA. A PHA-PVA copolymer, which has no  $\alpha$ -hydrogens, was attempted, but  $^1\text{H}$  NMR showed only small amounts of PVA were polymerized. The bulky methyl groups of PVA likely prevented incorporation into the polymer chain. A less bulky monomer that has no  $\alpha$ -hydrogens, like 2,2,2-trifluoroacetaldehyde, will be investigated in the future.

## Acknowledgements:

This research was supported by the National Nanotechnology Infrastructure Network International Research Experience for Graduates (NNIN iREG) Program and the National Science Foundation (NSF) under Grant No. ECCS-0335765, and the National Institute for Material Science (NIMS). I would like to thank the Dr. Kohl Lab for their valuable guidance and assistance, and Institute for Electronics & Nanotechnology at the Georgia Institute of Technology for providing the equipment and training necessary for this project.

## References:

- [1] K. Fujikawa, et al., *Polym. J.* 2008, 40, 281.
- [2] A. J. Boydston, et al., *Macromolecules* 2012, 45, 7317.
- [3] S. T. Phillips, et al., *J. Am. Chem. Soc.* 2010, 132, 9234.
- [4] S. T. Phillips, et al., *Macromolecules* 2013, 46, 2963.

# Surface Adsorption and Enzymatic Hydrolysis of Polyphosphates: Implications for Understanding Phosphorus Cycling

**Margot Hultz**

**Materials Science and Engineering, The Johns Hopkins University**

**NNIN REU Site: Institute for Electronics and Nanotechnology, Georgia Institute of Technology, Atlanta, GA**

NNIN REU Principal Investigator: Yuanzhi Tang, Earth and Atmospheric Sciences, Georgia Institute of Technology

NNIN REU Mentor: Rixiang Huang, Earth and Atmospheric Sciences, Georgia Institute of Technology

Contact: mhultz1@jhu.edu, yuanzhi.tang@eas.gatech.edu, rixiang.huang@eas.gatech.edu

## Abstract:

Phosphorus (P) is a key, yet often limited, nutrient in aquatic environments. Among various species of P, polyphosphate (polyP) constitutes a significant portion of total P in aquatic environments [1]. PolyP is a polymer of phosphate ions joined by phosphoanhydride (P-O-P) bonds of variable chain length ranging from a few to thousands of phosphate units. It is mainly synthesized by bacteria and plankton. Synthesis of polyP by bacteria is exploited in enhanced biological phosphorus removal (EBPR), a process used to remove excess phosphorus during sewage water treatment. Despite its environmental significance, little is known of the transport, transformation, and fate of polyP.

The goal of this project was to characterize the chemical reactions that may control the transport and stability of polyP in order to understand the larger scale P cycling. Adsorption of polyP onto iron and aluminum oxides was studied using quartz crystal microbalance with dissipation (QCM-D). PolyP hydrolysis catalyzed by alkaline phosphatase was studied by monitoring orthophosphate (orthoP) formation using UV-Vis spectroscopy. It was observed that polyphosphate can be degraded through enzyme-catalyzed hydrolysis with the rate and extent dependent on chain length. In the presence of calcium, precipitation of calcium-phosphate (Ca-P) solid phase(s) was monitored by dynamic light scattering, and the precipitates were characterized using scanning electron microscopy with energy dispersive spectroscopy (SEM-EDX), and Fourier transform infrared spectroscopy (FT-IR). FT-IR spectra and elemental analysis from EDX suggested the precipitate to be a non-apatite phase, likely a type of amorphous Ca-P.

## Experimental Procedures:

**Total Dissolved Phosphate Assay.** Determination of total phosphate in solution was done according to the colorimetric protocol developed by Murphy and Riley [2]. This method was used to measure the free orthoP in the adsorption and hydrolysis studies.

**QCM-D.** Samples of polyP (50 mg/L, 15 and 60 phosphate units) were combined with sodium chloride solution (0.1 M, pH 6). Solutions were flowed into the modules of the Q-Sense E4 QCM-D containing sensors coated with iron oxide,  $\text{Fe}_2\text{O}_3$ , or aluminum oxide,  $\text{Al}_2\text{O}_3$ .

**Enzymatic Hydrolysis.** Alkaline phosphatase (0.5 units/mL) was prepared in Tris buffer (0.1M, pH 9) containing  $\text{MgCl}_2$  (0.005 M). Enzyme solution (9 mL) was combined with polyP (15, 60, and 130P) stock solution to reach a final orthoP concentration of 980  $\mu\text{M}$ . In parallel,  $\text{CaCl}_2$  (0.5 M, 0.2 mL) was added to separate polyP-enzyme solutions (15 and 130P) to reach a concentration of 10 mM  $\text{Ca}^{2+}$ . All samples were incubated at 37°C.

**Characterization Studies.** Nucleation of precipitates during hydrolysis of polyP with calcium was monitored via

dynamic light scattering (DLS) using the Malvern nano-ZS zetasizer. Precipitates were characterized alongside amorphous and crystalline hydroxylapatite (HAP), a model Ca-P species, using the LEO1530 SEM-EDX and ThermoScientific Nicolet iS50 FT-IR ATR with diamond crystal (2 cm step, 64 scans per read).

## Results:

**Transport.** QCM-D results showed the real-time adsorption of 15 and 60P polyP onto  $\text{Fe}_2\text{O}_3$  and  $\text{Al}_2\text{O}_3$  (Figure 1). It was observed that polyP is capable of adsorbing onto these naturally abundant mineral species, and due to the fairly uniform adsorbed masses despite the different chain lengths, we hypothesized that the polyP adsorbs on its side instead of terminally. The low loss of mass after the reintroduction of a background solution around 2250 seconds also suggests that the adsorption was irreversible.

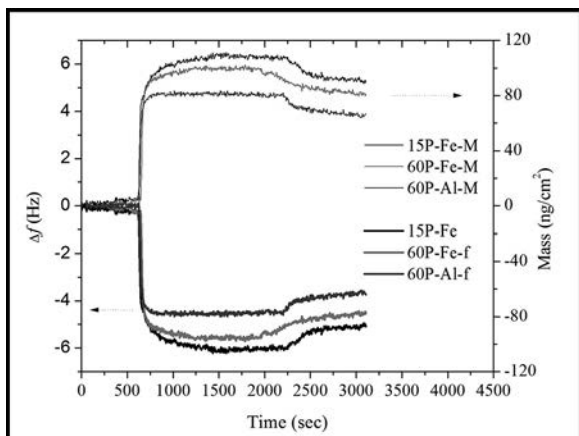


Figure 1: QCM-D monitoring of the adsorption of polyP onto amorphous  $\text{Al}_2\text{O}_3$  and  $\text{Fe}_2\text{O}_3$ .

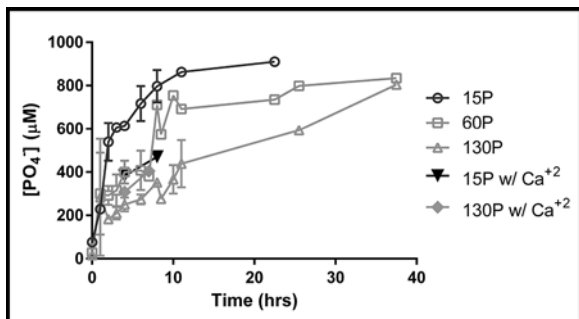


Figure 2:  $\text{PO}_4$  produced from APase catalyzed hydrolysis of polyP for varying chain lengths with or without calcium.

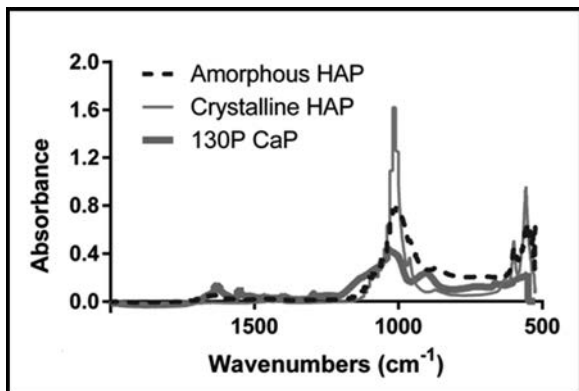


Figure 3: FT-IR spectra of Ca-P and HAP species.

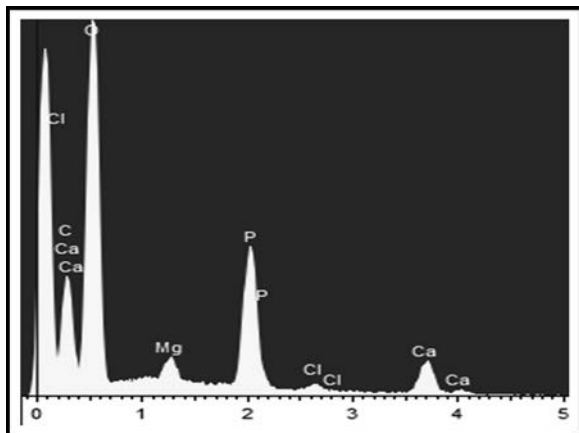


Figure 4: EDX spectrum of Ca-P precipitate.

**Transformation.** Figure 2 shows orthoP formed over time from different polyP with and without the presence of calcium. Incubation with APase resulted in a faster rate and greater extent of degradation for the shorter polyP compared to that of longer polyP. We believe the hydrolysis was via the terminals of the polyP and followed a consecutive first-order kinetic model. This can be modeled using the equation  $[\text{orthoP}] = [\text{orthoP}]_0 (1 - \exp(-k_1 t))$  [3]. The experimental parameters for hydrolysis of 15, 60, and 130P were 0.2204, 0.1049, and 0.05, respectively.

**Mineralization.** Precipitation of a possible Ca-P mineral was observed during the hydrolysis of all polyP lengths in the presence of calcium. FT-IR spectra of the observed Ca-P and both amorphous and crystalline HAP is shown in Figure 3. Based on the vibrational mode peaks, we can confirm that the precipitate was some type of Ca-P species. EDX elemental analysis is shown in Figure 4. The observed Ca/P ratio is around 1.0, nearly fitting into the amorphous Ca-P ratio of 1.2 - 2.2. The ratio observed in crystalline HAP is 1.67 [4]. Based on these results, the observed Ca-P was most likely some type of amorphous intermediate phase.

## Conclusions and Future Work:

PolyP was found to irreversibly adsorb onto  $\text{Fe}_2\text{O}_3$  and  $\text{Al}_2\text{O}_3$ , and was hydrolyzed with a rate and extent dependent on chain length. In the presence of calcium and APase, Ca-P precipitates formed. Future work is needed to characterize the effects of more environmentally relevant conditions and different solution chemistries on the behavior of polyP as well as other potential mineralization pathways.

## Acknowledgements:

I would like to express my gratitude for the guidance I received from my PI, Yuanzhi Tang, and mentor, Rixiang Huang, as well as the entire Tang group. I would also like to thank the Institute of Electronics and Nanotechnology at the Georgia Institute of Technology, the NNIN REU Program staff, and NSF, Grant No. ECCS-0335765, for making this research possible.

## References:

- [1] Diaz, J.; Ingall, et al. *Science* 2008.
- [2] Murphy, J., et al. *Anal. Chim. Acta*. 1962.
- [3] Robertson, K. "The Study of Polyphosphate Hydrolysis using  $^{31}\text{P}$  NMR." 2015.
- [4] Berzina-Cimdina, L., et al. "Infrared Spectroscopy - Materials Science, Engineering and Technology." 2012.

# Designing a Conjugated Polymer Consisting of Phenyl-Oxazole Derivatives Using C-H/C-O Coupling

**Alin Miksi Kalayjian**

**Chemistry, University of California, Berkeley**

**NNIN REU Site: Washington Nanofabrication Facility and Molecular Analysis Facility, University of Washington, Seattle, WA**

NNIN REU Principal Investigator: Dr. Christine K. Luscombe, Materials Science and Engineering, University of Washington

NNIN REU Mentor: Jason Lee, Chemistry, University of Washington

Contact: [akalayjian@berkeley.edu](mailto:akalayjian@berkeley.edu), [luscombe@uw.edu](mailto:luscombe@uw.edu), [leejason@uw.edu](mailto:leejason@uw.edu)

## Abstract:

Organic  $\pi$ -conjugated semiconducting polymers that have good electronic properties are very important in the development of organic solar cells. Traditionally, organometallic reagents are used in order to perform carbon-carbon coupling reactions of monomers to synthesize conjugated polymers. This requires stoichiometric amounts of organometallic compounds and additional synthetic steps compared to C-H activation chemistry in polymer synthesis. C-H activation eliminates the need to pre-functionalize the normally inert C-H bond found in many organic compounds with metals or other harsher reagents. The C-H activation will reduce byproducts, waste, and inorganic materials, which will aid in the development of “green” reactions. Itami, et al., found that easily synthesized phenol derivatives (containing a C-O-R electrophile) could activate the C-H bond in the 5-position of oxazoles to form a C-C bond [1]. Our work was inspired by this, and the goal of this research was to draw from this methodology to design and synthesize a monomer that had both an electrophilic C-O-R group containing a phenyl ring and an oxazole such that it could undergo polymerization via C-H activation to make a donor-acceptor polymer. Future work includes the study of polymerization growth kinetics and its semiconducting properties.

## Introduction:

In recent years, semiconductors have changed the course of human technological advancement. Semiconductors are used in solar cells and in all electronic devices. Silicon (Si) is the most widely used semiconductor. However, making Si based devices is expensive where Si must be extremely pure, which requires energy and time. It also utilizes toxic materials during production that adds more inorganic waste to our environment.

Organic semiconductors, specifically  $\pi$ -conjugated polymers, have been attracting interest as an alternative to Si. Devices made out of organic polymers have advantages over Si based devices because they can be made to be semi-transparent, colorful, and flexible, which give them further range of usage such as in photovoltaics and solar cells. In addition, they require a lower cost of production.

Organic polymer synthesis techniques have developed through the years. However, it has a problem, which is the usage of organometallic reagents (Sn, Li). In order to overcome this issue, C-H activation has been presented as an alternative method to use less organometallic reagents during synthesis. C-H activation utilizes C-H/C-X (X is a halogen) that replaces C-M/C-X (M is metal) in traditional C-C coupling. This eliminates excess transition metal usage creating “green” reactions and less waste product.

The target of this work was to synthesize a  $\pi$ -conjugated polymer by first creating the monomer that is made of phenyl-oxazole derivatives, and by utilizing the C-H/C-O coupling method (inspired by Itami, et al. [1]) polymerize the monomer in order to achieve the conjugated organic semiconducting polymers for its usage in solar cells.

## Methodology:

The synthetic steps are shown in Figure 1.

Phenyl-oxazole derivatives are synthesized from the starting material, 2,4-dimethoxy benzaldehyde **1**, which is transformed into first phenyl-oxazole derivative by ring closure **2**. Then, the product is dealkylated to yield the next product **3**, and finally by protection using *p*-toluenesulfonyl group followed by an alkylation, product **5** is obtained.

## Results and Discussion:

Analysis of hydrogen nuclear magnetic resonance ( $^1\text{H}$  NMR) data shows that the monomer precursors (phenyl-oxazole derivatives) **2** and **3** were formed (Figure 2). The labeled peaks clearly show that the desired monomer was formed.

In Figure 3, the final monomer synthesis step (protection via *p*-toluenesulfonyl group and alkylation by bromohexane) gave mixed results. <sup>1</sup>H NMR data showed extra peaks that were not identified. There are extra peaks, d, of tosylate in Figure 3. This may be due to mixed protection where the tosylate reacted at the *ortho* position rather than the *para* position. However, the promising signs are the identification of oxazole peaks a, b, and some aromatic peaks labeled c, g, and f of benzene.

### Conclusions:

The synthesis of monomer 5, consisting of a phenyl-oxazole derivatives, was attempted. The synthesis of the first two precursors proved successful, but the final monomer was not completely synthesized. Oxazole formation by ring closure using toluensulfonylmethyl isocyanide was accomplished. Although the synthesis of the monomer initially was promising, further work needs to be done in order to fully obtain the monomer to perform the synthesis of the desired polymer by utilizing C-H/C-O cross coupling reaction.

### Future Work:

So far, the only step that failed was the final step required to fully obtain the desired monomer consisting of phenyl-oxazole derivatives. Therefore, changing the tosylate group with triflate group would be an option. In addition, triflate group would be a better reactive C-O functional group for the polymerization step. If proven to be successful, polymerization will be attempted and further investigation will be done to characterize the polymer such as its growth kinetics and its capacity as a semiconductor for solar cell usage.

### Acknowledgments:

I would like to thank Jason Lee for his great help and patience. Thanks to Vicky Pakhnyuk for her help in the lab during my mentor's absence. Most importantly, I would like to thank Dr. Christine K. Luscombe for giving me the opportunity of working in her lab and being part of her interesting research work and group as well as her help with my presentations and papers. Lastly, thank you to the National Nanotechnology Infrastructure Network Research Experience for Undergraduates (NNIN REU) Program and National Science Foundation (NSF) for funding under Grant No. ECCS-0335765.

### References:

[1] Muto, K.; Yamaguchi, J.; Itami, K.; Nickel Catalyzed C-H/C-O Coupling of Azoles with Phenol Derivatives. *Journal of the American Chemical Society*. 2012, 134, 169-172.

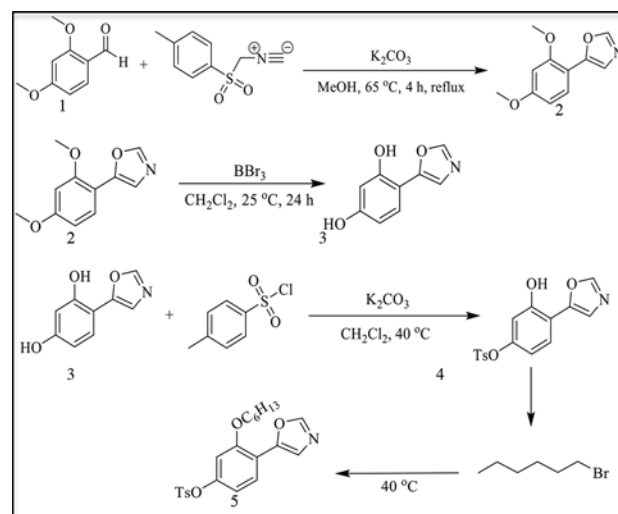


Figure 1: Monomer synthesis scheme in order from top to bottom.

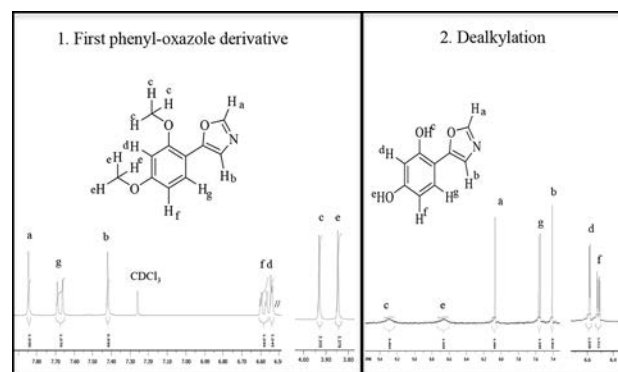


Figure 2: <sup>1</sup>H NMR of molecules 2 and 3.

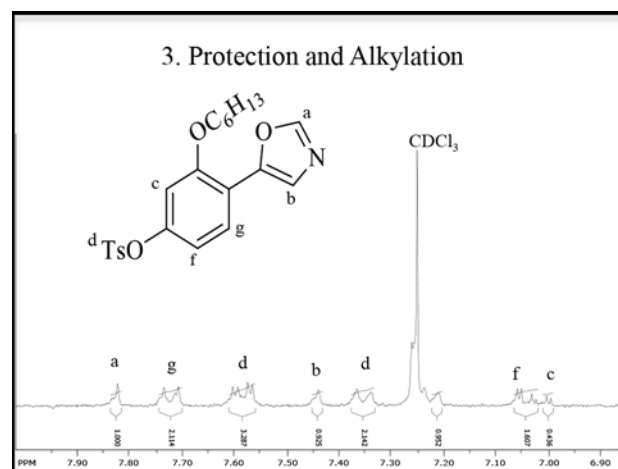


Figure 3: <sup>1</sup>H NMR of product 5 mixture.

# Vanishing Programmable Resources: Design, Materials, and Characterization

**Mary E. Alsobrooks**

**Chemical Engineering, the University of Alabama**

**NNIN REU Site: Institute for Electronics and Nanotechnology, Georgia Institute of Technology, Atlanta, GA**

NNIN Principal Investigator: Dr. Paul A. Kohl, Chemical and Biomolecular Engineering, Georgia Institute of Technology

NNIN Mentor: Jared M. Schwartz, Chemical and Biomolecular Engineering, Georgia Institute of Technology

Contact: [mealosbrooks@crimson.ua.edu](mailto:mealosbrooks@crimson.ua.edu), [paul.kohl@chbe.gatech.edu](mailto:paul.kohl@chbe.gatech.edu), [jschwartz38@gatech.edu](mailto:jschwartz38@gatech.edu)

## Abstract and Introduction:

Printed wiring boards (PWBs) act as the mechanical structure supporting the electronic connections between the different functional components in microelectronic devices. Stable materials are generally desired so that long mission life can be achieved, however, there is growing interest in self-decomposing materials because of environmental concerns. Sustainability requires an effective way to dispose of the multitude of PWBs currently in use. This has prompted the development of PWBs that can be triggered to disappear after a time-independent, fully-functional life span.

For this project, an optically-triggered disappearance mechanism was explored. UV-sensitive polymers, poly(phthalaldehyde-co-butyraldehyde) and poly (dihydroxy-tetrahydro naphthalene), Figure 1, were characterized using nanoindentation. Four-point probe analysis was used to analyze composite films that contained 3  $\mu\text{m}$  dendritic copper nanoparticles; the addition of copper provided the conductive portion of the PWB. Composite films were also made using photo-acid generator (PAG), an iodonium salt, to improve the optical-trigger. Layered-films, comprised of stacked composite films, were analyzed using exposure techniques. This method of construction was used to test the permeability of the stacked films.

## Experimental Procedure:

In order to test the different films, formulations were made following the same basic procedure: the polymer solids, solvent, and additional materials were combined in a vial and vortexed/sonicated. See Table A for the list of formulations made,

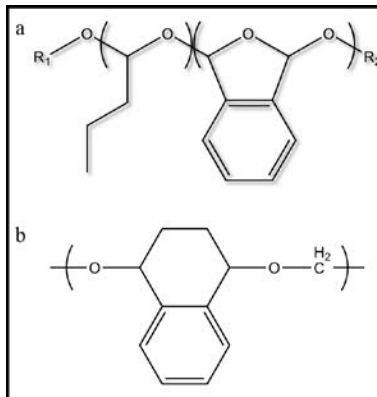


Figure 1: Polymer structures –  
a) p(PHA-co-BA), b) p(DHTN).

including the use, basis, solvent, and soft-bake/cure procedure for each. The optimum loading for metal nanoparticles is 70-80 vol% [1], so 75 vol% was chosen as our loading. The copper used was cleaned in an acid bath and stored under PGMEA. All formulations containing PAG were made and worked with in the dark. Films were made using a doctor-blading technique.

Nanoindentation was done to find the reduced Young's modulus and hardness of the polymers. A 10-second load, 10-second hold, 4-second unload function was used, and a 9-point matrix of decreasing force from 650  $\mu\text{N}$  to 50  $\mu\text{N}$  was used to collect data points. An area function was created using polycarbonate as a standard. Four-point probe analysis was done on the copper and polymer films to measure sheet resistance to be used to calculate conductivity.

The layered-films were exposed to a dose of UV-light that we knew would activate all of the PAG to determine if the copper/polymer film was permeable to the acid generated from the top film. The layered-films were exposed to a dosage of 10000  $\text{mJ/cm}^2$ , and before, immediately after, and every hour after the exposure, the resistance of the copper/polymer film was tested using a multimeter.

Solids	Solvent	Basis	Soft-Bake/Cure	Use
p(PHA-co-BA)	GBL	30-40 wt% polymer	100°C for 5 min	nanoindentation
p(DHTN)	GBL	30-40 wt% polymer	100°C for 5 min	nanoindentation
Cu/polymer	PGMEA	75 vol% Cu	100°C for 5 min	four-point probe
Cu/polymer	THF	75 vol% Cu	air cure for 10 min	layered-films
PAG/polymer	THF	30 wt% polymer/ 10 pphr PAG	air cure for 10 min	layered-films

Table A: Formulations.

## Results and Conclusions:

Nanoindentation testing of p(PHA-*co*-BA) and p(DHTN) gave reduced Young's moduli of 4.56 GPA and 0.055 GPA, and hardness readings of 270 MPa and 3.1 MPa, respectively. We compared the polymers to ideal values represented by FR4: a reduced modulus of 24 GPA and a hardness of 200 MPa. FR4 is a fully cross-linked, epoxy board with fiberglass matrix and is meant to be rigid and long-lasting. The p(PHA-*co*-BA) values are promising, especially the hardness because it is above the ideal. The modulus and hardness of p(DHTN) are far enough below the ideal values. This polymer did display tacky qualities, both qualitatively through observation and quantitatively by the unloading function displayed in its indentation profile. The low values dismissed p(DHTN) as a possible bulk material for the PWB, but the adhesive quality it has made it potentially useful for areas like conductive contacts connecting devices to the board.

Four-point probe analysis resulted in a conductivity of  $4.5 \times 10^3 \Omega^{-1} \cdot \text{m}^{-1}$  for a 75 vol% Cu film. This is several magnitudes below the bulk copper value of  $4.9 \times 10^7 \Omega^{-1} \cdot \text{m}^{-1}$  due to the nature of nanoparticles and the resulting oxidation issues. These were combatted using cleaning methods on the copper and by using the layered-films as a construction technique. Copper nanoparticles are still effective for the conductive portions of the PWB even with a lower conductivity in the polymer matrix.

Initially, we attempted to create formulations that included the polymer, copper, and PAG in solvent. These formulations were not successful because the copper and PAG interacted in a way that depolymerized the matrix and oxidized the copper before being triggered. A new construction technique, layered-films, Figure 2, was considered to combat the oxidation/depolymerization issue. Layered-films showed an increase in the resistance of the copper/polymer film after exposure. The resistance increased several magnitudes over the course of three hours, from  $2 \text{ M}\Omega$  to  $200 \text{ M}\Omega$ . This showed that the acid was diffusing through the

copper paste and depolymerizing the polymer matrix after triggering, and that layered-films would be an applicable construction technique.

## Future Work:

In order to improve upon the material used in the transient PWBs, several areas may be investigated or expanded upon. An investigation of newly synthesized polymers with faster rates of depolymerization and vapor evolution will be helpful for improving the bulk and conductive matrices. Expanded testing of the adhesion strength of p(DHTN) should be done to determine the full extent of use for the material. The ultimate end goal of the future work is to fabricate a fully functional PWB using the explored methods and materials. This PWB will need conductivity testing to ensure electrical connections are functional before triggering and non-functional after. Devices can then be added to the PWB to create a multi-functioning sensor.

## Acknowledgments:

Special thanks to Dr. Paul Kohl, Jared Schwartz, and the entire Kohl Group, as well as to the helpful people at Georgia Tech: Nancy Healy, Joyce Palmer, Leslie O'Neill, and Walter Henderson. The summer would not have gone so well without their assistance. Thanks to the National Nanotechnology Infrastructure Network Research Experience for Undergraduates (NNIN REU) Program, the National Science Foundation (Grant No. ECCS-0335765), and Defense Advanced Research Projects Agency for this great opportunity.

## References:

- [1] H. Lee, K. Chou and Z. Shih, 'Effect of nano-sized silver particles on the resistivity of polymeric conductive adhesives', *International J. of Adhesion and Adhesives*, vol. 25, no. 5, pp. 437-441, 2005.

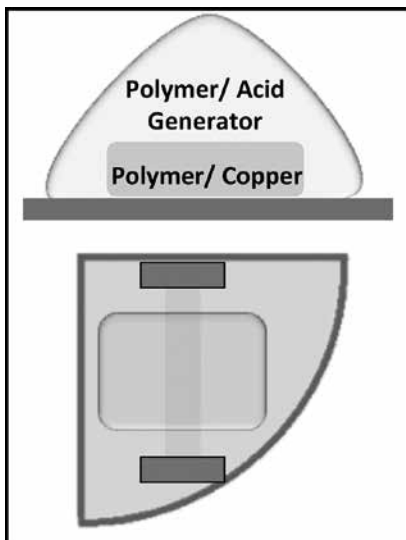


Figure 2: Layered-films construction model.

# Electrostatic Gating of MBE-Grown NdTiO<sub>3</sub> Thin Films

**Emilie Benson**

**Physics and Chemistry, Gustavus Adolphus College**

**NNIN REU Site: Minnesota Nano Center, University of Minnesota-Twin Cities, Minneapolis, MN**

NNIN REU Principal Investigator: Professor Bharat Jalan, Department of Chemical Engineering and Materials Science, University of Minnesota

NNIN REU Mentor: Andrew Xu, Department of Chemical Engineering and Materials Science, University of Minnesota

Contact: ebenson@gustavus.edu, bjalan@umn.edu, andrewxu@umn.edu

## Abstract:

With the emergence of ionic gel gating in an electric double-layer transistor, materials that could not be easily chemically doped, or had significant structural changes upon being doped, can now be examined. Neodymium titanium oxide (NdTiO<sub>3</sub> or NTO) is a Mott-Hubbard antiferromagnetic insulator, with the insulating state being sensitive to doping and chemical distortions. This experiment explores the use of ionic gel gating to investigate the insulator-to-metal transition in NTO thin films using electrostatic doping. Single crystalline, epitaxial NTO films were grown onto an insulating substrate using a hybrid molecular beam epitaxy technique. The device was patterned using two shadow masks, one for etching with ion milling and the other to deposit metal contacts with sputtering. The ion gel, 1-ethyl-3-methylimidazolium-bis (trifluoromethylsulfonyl) imide (EMI-TFSI), was placed on top of the patterned NTO films and electronic measurements were taken in an electromagnet. Voltage-dependent leakage current through the ionic gel was established, allowing for calculation of injected charge. Temperature-dependent resistivity measurements were performed for each gate bias.

## Introduction:

Perovskites, having the general chemical formula of ABO<sub>3</sub>, are characterized by a wide range of fascinating functionalities including superconductivity, thermoelectricity and a metal-to-insulator transition. NdTiO<sub>3</sub> (NTO), a pseudo cubic perovskite, is a Mott-Hubbard antiferromagnetic insulator with the insulating state being sensitive to doping and chemical distortions. Past research has found a Mott transition induced by chemical doping using holes [1], although it was accompanied by distortions in the structure. These structural distortions may influence the electronic transport properties of NTO; therefore, this experiment used ionic gel to minimize any distortions in the lattice parameters. This experiment was designed to inject electrons and holes using an external bias to control the insulator to metal transition of NTO.

## Experimental Procedure:

A hybrid molecular beam epitaxy technique was used to grow single crystalline, epitaxial neodymium deficient NTO film onto lanthanum aluminate-strontium aluminium tantalite (LSAT), an insulating substrate [2]. A shadow mask was placed over the NTO film and ion milling was used to etch the desired pattern so that Van der Paw geometry could be used to determine resistance. A second shadow mask was positioned to deposit the metal contacts, 40 nm of titanium followed by 100 nm of gold, with sputtering. The ion gel, 1-ethyl-3-

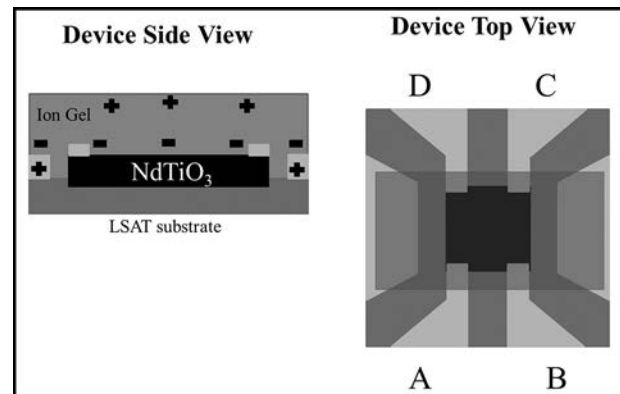


Figure 1: A schematic of the NTO device designed for electrostatic gating using Van der Pauw measurements and side gating.

methylimidazolium-bis (trifluoromethylsulfonyl) imide (EMI-TFSI), was placed by hand on top of the patterned NTO film, a schematic of the device is shown in Figure 1. The electronic measurements were controlled with a LabView program using a Keithley source-meter K-2400 and electrometer K-6514. Advanced Research Systems cryostat and GMW 5403 electromagnet were used for the temperature dependent measurements. Resistance measurements were taken before device development, once the ion gel was applied and throughout the gating process. The gate voltage was changed at 290 K, when the ion gel was not frozen, and the gate current was measured

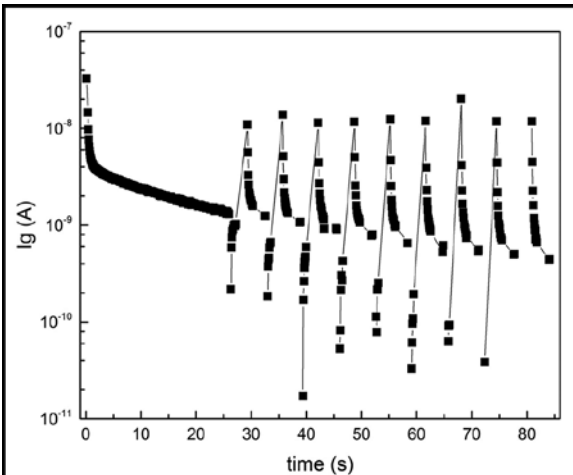


Figure 2: The gate current was measured with respect to time when the gate voltage was changed from -1 to 0 V at 290 K and is representative of the other gate current measurements. The periodic noise was a result of measuring the resistance with van der Pauw geometry, thus applying an alternating current.

as a function of time. The device was then cooled to 50 K and resistance versus temperature was measured up to 290 K, at which point the gate voltage was altered and the process repeated.

### Results and Conclusions:

The gate current was integrated with respect to time to determine the charge injected, verifying that positive gate voltages resulted in electron injection while negative gate voltages resulted in hole injection. The data was not clean due to measuring resistance, thus applying a current, too early. This created periodic noise in the data, as seen in Figure 2, which affected the calculation of charge injection.

The resistance data from the experiment was compared to determine the effects of electrostatic gating on NTO. It was determined that positive gate voltages, electron injection, did not change the resistance of the sample, evidenced in Figure 3, while the resistance increased with negative gate voltages, hole injection. At this point it is unclear if these trends are due to electrostatic or electrochemical properties.

NTO thin film was successfully patterned with ion milling and an ion gel was applied. Electrostatic gating resulted in an increase in resistance with hole injection, while electron injection had no observable change in resistance.

### Future Work:

In continuing this research, different gate voltages should be examined to develop a better understanding of the

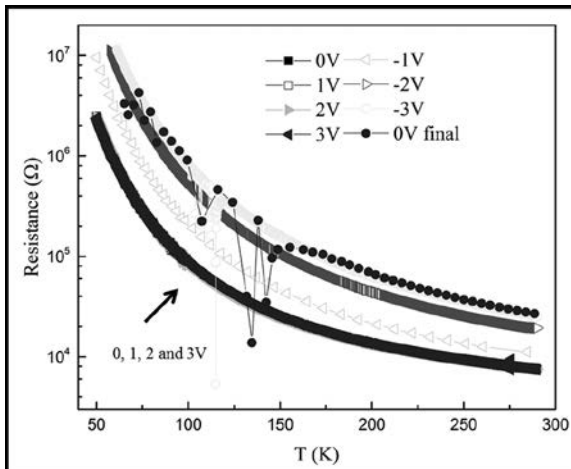


Figure 3: Resistance of NTO was measured with respect to temperature in an electromagnet. The positive gate voltages corresponded with electron injection and no noticeable change in resistance was observed. The negative gate voltages, hole injection, corresponded with an increase in resistance that remained high when the gate voltage was returned to zero.

entire system. Larger positive gate voltages should be used to determine if NTO can be affected by electron injected using electrostatic gating. Negative gate voltages should be examined in further detail to determine if there is a maximum and at which point it is no longer reversible. The increase in resistance, which accompanied the negative gate voltages, should be examined for evidence of degradation. Other samples of NTO with different neodymium vacancies should be used to determine the effect of stoichiometry. Future research should also examine the effect of ion gel on NTO.

### Acknowledgements:

I would like to thank Professor Bharat Jalan, Andrew Xu, and the rest of the Jalan research group for this opportunity and their guidance throughout this research. I would like to thank the National Nanotechnology Infrastructure Network Research Experience for Undergraduates (NNIN REU) Program (NSF Grant No. ECCS-0335765) and UMN MRSEC (DMR-1420013) for funding this project as well as the Minnesota Nanofabrication Center and the University of Minnesota CharFac for providing the necessary equipment and training, which has received capital equipment funding from the NSF through the UMN MRSEC program under Award Number DMR-1420013.

### References:

- [1] Sefat, et al., Phys. Rev. B 74, 104419 (2006).
- [2] Xu, et al., Appl. Phys. Lett. 104 082109 (2014).

# Optimizing Contact Resistance for Improved MoS<sub>2</sub> Device Performance

**Justin Goodwill**

**Physics, Duquesne University**

**NNIN REU Site: Penn State Nanofabrication Laboratory, The Pennsylvania State University, University Park, PA**

NNIN REU Principal Investigator: Dr. Joshua Robinson, Materials Science and Engineering, The Pennsylvania State University

NNIN REU Mentor: Brian Bersch, Materials Science and Engineering, The Pennsylvania State University

Contact: goodwil2@duq.edu, jrobinson@psu.edu, bmb5382@gmail.com

## Abstract:

In recent years, much attention has been directed toward two-dimensional materials given their possible applications in next-generation nanoelectronic devices. Graphene, the most widely studied two-dimensional material, has enjoyed major success due to its attractive electronic, thermal, and optical properties. However, graphene lacks a band gap, which renders it unviable for use as a semiconductor in transistor devices. Like graphene, molybdenum disulfide (MoS<sub>2</sub>) is a two-dimensional material with the exception that it has a tunable 1.2-1.9 eV bandgap. As such, transistor devices have been fabricated using MoS<sub>2</sub>, but major issues have arisen, including high contact resistance, that have stifled device performance. In this paper, we examine the contact resistances between 7 nm MoS<sub>2</sub> films and various metals — including Au, Ti, Ni, Nb, and Mo — using the two-terminal transmission line method. We also investigate the effect of annealing processes on decreasing contact and sheet resistances.

## Introduction:

Semiconducting MoS<sub>2</sub>, one of many transition metal dichalcogenides, exhibits strong intralayer covalent bonding combined with weak interlayer van der Waals bonding. MoS<sub>2</sub> has a band gap ranging from approximately 1.9 eV at monolayer thickness to 1.2 eV in bulk, making it ideal for use as a semiconductor in field-effect transistor devices [1]. MoS<sub>2</sub> transistors have displayed large current on/off ratios of  $\sim 10^8$ , a subthreshold slope of  $\sim 60$  mV/dec, and a field effect mobility of 10-100 cm<sup>2</sup>·V<sup>-1</sup>·s<sup>-1</sup> [2].

However, forming true ohmic contacts to MoS<sub>2</sub> has proven difficult due to a phenomenon known as Fermi-level pinning. Conventionally for semiconductor-metal interfaces, metals are chosen based on their work function alignment with the semiconductor's conduction band or valence band. In contrast, for the MoS<sub>2</sub>-metal interface, the Fermi level is partially pinned, resulting in large Schottky barriers for a wide range of metal work functions [2].

Thus, if a metal can be found to not form a large Schottky barrier at the interface, we could significantly enhance device performance.

## Experimental Procedure:

Electron-beam evaporation was used to deposit 1-2 nm of Mo on five sapphire substrates. These films were sulfurized in a horizontal tube furnace at 1050°C for 45 minutes. We characterized the films using atomic force microscopy (AFM), Raman spectroscopy, and photoluminescence

spectroscopy (PL). AFM indicated a film height of 5-7 nm with 100-200 nm sized grains. A weak PL signal and a Raman peak spacing of  $\sim 25$  wavenumbers also indicated few-layer thick films.

Combined with photolithography, we isolated MoS<sub>2</sub> channels by sulfur hexafluoride (SF<sub>6</sub>) plasma etching of the surrounding film. For our contact study, we deposited five metals with a range of work functions: Au, Ti, Ni, Mo, and Nb. These were chosen based on previous reports of low contact resistance using these metals and based on the fact that some of these metals form similar or identical TMD structures with sulfur (i.e., NbS<sub>2</sub> and MoS<sub>2</sub>) [3-4].

A finished device is pictured in Figure 1. With the photolithography mask, an array of these devices was fabricated such that the channels varied in length from 0.75  $\mu$ m to 6.5  $\mu$ m.

The array of devices allowed for two-terminal transmission line measurements (TLM) to be carried out. Using electrical probes, two-terminal current vs. voltage curves were used to calculate the total resistance of all devices. A linear relationship exists between channel length and total resistance such that the y-intercept, corresponding to zero-length channel resistance, allows for the calculation of the contact resistance while the slope allows for the calculation of sheet resistance through the channel. We computed the contact resistance and sheet resistance values using multiple TLM sets for each metal post-deposition, after a 250°C anneal, and after a subsequent

300°C anneal. All electrical measurements were carried out at room temperature in ambient.

## Results and Conclusions:

The results for the effect of the annealing processes on Ni are shown in Figure 2. We concluded that the 250°C anneal was an effective heat treatment as for all the metal contacts there were decreases in contact resistance and/or total resistance. While Ti and Mo contacts saw a slight increase in sheet resistance, other metals showed a decrease in sheet resistance to varying degrees. We also observed that the subsequent 300°C anneal was not an effective heat treatment as it either resulted in little change or an increase in all resistance values.

Figure 3 is a table comparing the sheet resistance and contact resistance for each metal. Ti contacts are inconclusive and unreliable due to a significant scatter in the data (low  $R^2$ ) and much smaller sheet resistance than all other samples. The data for Au, Ni, Mo, and Nb contacts display true linear trends. However, negative y-intercept values suggest very low contact resistances.

## Future Work:

Due to the variation in the data and negative y-intercept values, we plan to repeat TLM measurements in vacuum, after a vacuum anneal, to remove water and other adsorbed species from the  $\text{MoS}_2$  surface. We will finish gated devices and perform TLM measurements at different gate biases. Gated TLM measurements are crucial for a fair comparison of devices as there is likely to be variation in the doping levels of the films. That is, we will compare the contact and sheet resistances of all devices at the same bias conditions (i.e., at threshold). We will also use smaller channel lengths as they are more accurate for measuring small contact resistances via TLM method.

## Acknowledgements:

I would like to thank Dr. Josh Robinson and my mentor, Brian Bersch, as well as the NNI REU program for all of their support (under NSF Grant No. ECCS-0335765).

## References:

- [1] Xu, Mingsheng, et al. "Graphene-Like Two-Dimensional Materials." *ACS Chem. Rev.* 113, 3766-3798 (2013).
- [2] Fiori, Gianluca, et al. "Electronics Based on Two-Dimensional Materials." *Nature Nanotechnology* 9, 768-779 (2014).
- [3] Cheng, Rui, et al. "Few-layer Molybdenum Disulfide Transistors and Circuits for High-speed Flexible Electronics." *Nature Communications* 5:5143, 1-9 (2014).
- [4] Krasnozhon, Daria, et al. "MoS<sub>2</sub> Transistors Operating at Gigahertz Frequencies." *Nano Lett.* 14, 5905-5911 (2014).

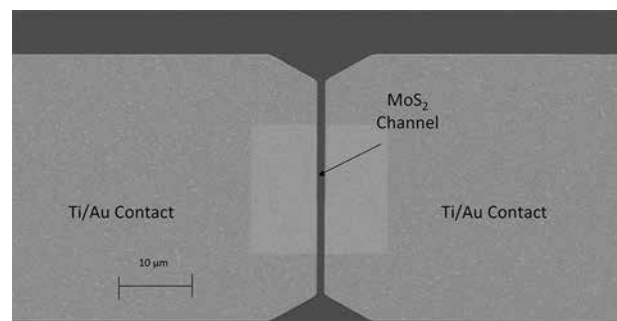


Figure 1: A finished device.

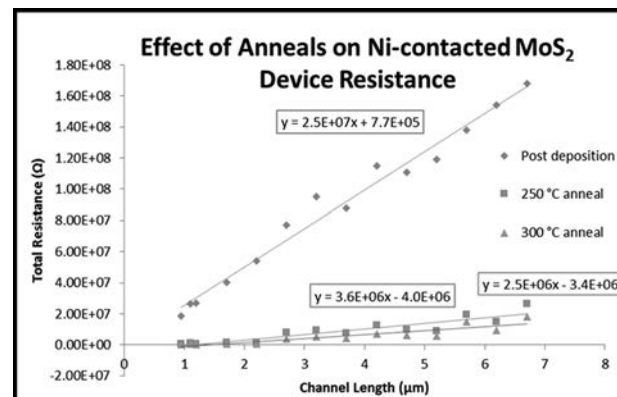


Figure 2: Total Resistance vs. Channel Length for Ni.

Metal	Property	Post-Deposition ( $\times 10^3$ )	10 min anneal at 250 °C ( $\times 10^3$ )	10 min anneal at 300 °C ( $\times 10^3$ )	Coeff. Of determin. ( $R^2$ )
Ti	$R_C$ (k $\Omega$ ·μm)	2.8	2.3	0.11	0.462
	$R_S$ (k $\Omega$ /□)	3.3	3.8	2.4	
	$R_T$ (Ω)	550	650	530	
Au	$R_C$ (k $\Omega$ ·μm)	200	42	78	0.893
	$R_S$ (k $\Omega$ /□)	260	60	58	
	$R_T$ (Ω)	5.4E+4	1.4E+4	1.8E+4	
Ni	$R_C$ (k $\Omega$ ·μm)	9.6	*	*	0.891
	$R_S$ (k $\Omega$ /□)	620	37	59	
	$R_T$ (Ω)	7.6E+4	6700	5500	
Mo	$R_C$ (k $\Omega$ ·μm)	650	190	240	0.898
	$R_S$ (k $\Omega$ /□)	2300	2700	1100	
	$R_T$ (Ω)	3.4E+5	3.2E+5	7E+5	
Nb	$R_C$ (k $\Omega$ ·μm)	*	*	*	0.968
	$R_S$ (k $\Omega$ /□)	590	250	580	
	$R_T$ (Ω)	7.3E+4	2.8E+4	6.7E+4	

\* - Indicates negative y-intercepts for linear regression fit  
All values are averages of multiple TLM arrays

$R_C$  - Contact Resistance  
 $R_S$  - Sheet Resistance  
 $R_T$  - Total Resistance for 3.0  $\mu\text{m}$   $L_{ch}$  device

Figure 3: Comparison of sheet and contact resistances for all metals.

# Enhanced Mobility in an Insulator Capped 2D Electron Gas at $\text{SrTiO}_3 <100>$ Surface

**Nathan Huber**

**Physics, Gustavus Adolphus College**

**NNIN REU Site: Penn State Nanofabrication Laboratory, The Pennsylvania State University, University Park, PA**

NNIN REU Principal Investigator: Prof. Qi Li, Physics, The Pennsylvania State University

NNIN REU Mentors: Dr. Ludi Miao and Renzhong Du, Physics, The Pennsylvania State University

Contact: [nhuber2@gustavus.edu](mailto:nhuber2@gustavus.edu), [qil1@psu.edu](mailto:qil1@psu.edu), [lxm66@psu.edu](mailto:lxm66@psu.edu), [rud145@psu.edu](mailto:rud145@psu.edu)

## Abstract and Introduction:

Two-dimensional electron gases (2DEGs) at oxide surfaces and interfaces have attracted much attention due to their fascinating exotic properties such as superconductivity, large magneto-resistance, and ferromagnetism.  $\text{SrTiO}_3$  (STO) based 2DEGs are a typical example. These include 2DEGs at the interface of  $\text{LaAlO}_3$ /STO heterostructures and on STO surfaces [1]. With their high mobility and high dielectric constant at the ground state, these 2DEGs are promising in developing next generation all-oxide devices including field effect transistors and spintronic devices [2].

In this study we have created 2DEGs at STO  $<100>$  surfaces by  $\text{Ar}^+$  ion irradiation. We found that a  $\text{SiO}_2$  capping layer on the 2DEG surfaces significantly decreased surface resistance, while no effect was observed for other oxide capping layer tests ( $\text{MgO}$ ,  $\text{Al}_2\text{O}_3$ , and STO). Specifically the electron mobility of the  $\text{SiO}_2$  capped channel had an eight-fold increase relative to uncapped 2DEG at 1.8 K. The bare channel had a resistance ratio ( $R_{300\text{ K}}/R_{1.8\text{ K}}$ ) of 85 compared with the  $\text{SiO}_2$  capped channel ratio of 625; this indicates significantly better metallic behavior for capped channels. Our results open a path to create 2DEGs with high mobility in an effective and economic way.

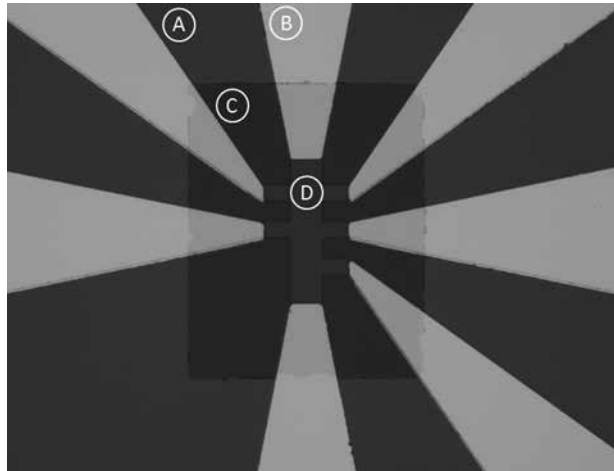


Figure 1: Standard Hall bar layout used for STO 2DEG fabrication and measurements. A. STO substrate B. Titanium and gold contacts C. Capping layer D. Ion milled STO 2DEG channel.

## Experimental Procedure:

2DEG measurement units were fabricated at STO surfaces (Figure 1). First, photolithography was used to pattern a Hall bar. The exposed substrate was then subject to  $\text{Ar}^+$  ion irradiation (Figure 2). The  $\text{Ar}^+$  ion irradiation generates oxygen deficiencies at the surface. Carriers were thus increased in order to neutralize charge at the STO surface. Electrical contacts were fabricated by sputtering titanium and gold. The contact patterns were defined by photolithography. Finally the irradiated surface was capped by sputtered  $\text{SiO}_2$ .

Experimental variations were made to the 2DEG. The STO substrate was tested at a  $\text{SiO}_2$  capped and uncapped state. The dose of ion milling and thickness of capping was also varied. The capping layer effect was tested for several other materials including:  $\text{MgO}$ ,  $\text{Al}_2\text{O}_3$ , and STO.

The Hall bars allowed for five probe and Hall effect measurements. These measurements were made in a physical property measurement system (PPMS). The sample resistance, carrier density, and mobility were measured as function of temperature from 300 K to 1.8 K.

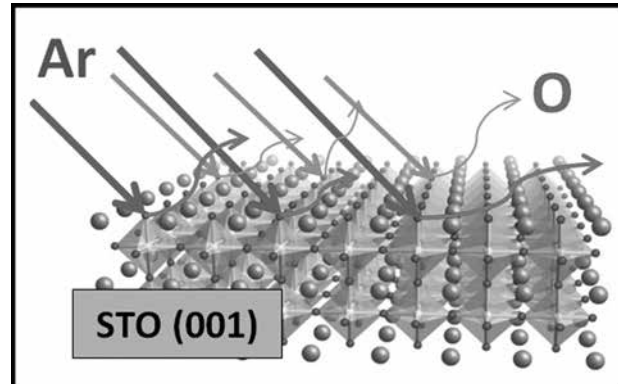


Figure 2:  $\text{Ar}$  irradiation (ion milling) reduces STO  $<001>$  surface to form 2DEG.

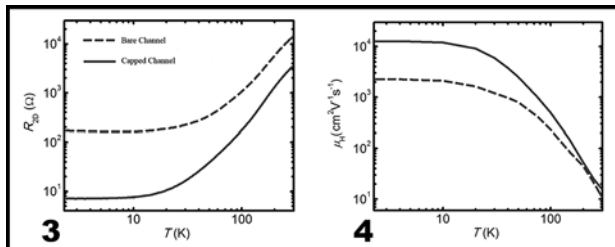


Figure 3, left: 2DEG resistance measure of a bare channel (dashed) compared to a capped channel (solid). The four probe measurement was used to measure channel resistance.

Figure 4, right: Electron mobility in bare 2DEG channel (dashed) compared to a capped channel (solid). The Hall effect was used in coalition with the four probe measurement to solve for mobility. The mobility at 1.8 K was enhanced from its uncapped mobility of  $2,100 \text{ cm}^2/\text{Vs}$  to the capped channel mobility of  $13,000 \text{ cm}^2/\text{Vs}$ .

## Results and Conclusions:

From the resistance measurement, it was found that the capped and uncapped STO 2DEG were fully metallic; this is evident from the decrease in resistance as temperature decreases (Figure 3). It was also observed that the  $\text{SiO}_2$  capped channel had lower resistance compared to the uncapped channel at all temperatures. The bare channel had a resistance ratio ( $R_{300 \text{ K}}/R_{1.8 \text{ K}}$ ) of 85 compared with the significantly higher  $\text{SiO}_2$  capped channel's ratio of 625. This indicates improved mobility in the capped channel.

Several other oxides were tested as capping layers for the possibility of 2DEG enhancement. Among those capping layers tested ( $\text{MgO}$ ,  $\text{Al}_2\text{O}_3$ , STO, and  $\text{SiO}_2$ ),  $\text{SiO}_2$  was the only material to exhibit enhancement. This observation may be explained with a possible mechanism of band bending at the ion milled STO and  $\text{SiO}_2$  interface. The shallow work function of  $\text{SiO}_2$  could potentially bend the conduction band of the STO below the Fermi level. Further theoretical work must be completed to verify this explanation.

It was also observed that terminated STO substrate increased the conductivity in the 2DEG channel. This increase was expected because the terminated substrate has fewer imperfections to hinder electron flow. Observing this increase motivates future research in depositing more

uniform coats of  $\text{SiO}_2$ . This could lead to increases in channel conductivity.

Finally it was observed that decreasing the ion milling duration and capping layer thickness led to decreases in carrier density of the 2DEG. This is important information because control of conductive channels with low carrier density would be applicable for future field effect transistors.

These results introduce  $\text{SiO}_2$  capping of STO 2DEG as a promising method for fabrication of oxide conductors. The enhancement of mobility obtained by this capping has significant implications for oxide electronics.

## Future Work:

In the future, the Li research group will continue the characterization of  $\text{SiO}_2$  capped STO 2DEG. To attain increased mobility, the group plans to explore  $\text{SiO}_2$  capping thickness and uniformity. Basic control of carrier density has been observed by way of gating techniques. Further increasing the mobility and control of the carrier density in this 2DEG would be important for future applications.

## Acknowledgments:

I would like to especially thank principal investigator Dr. Qi Li, mentor Dr. Ludi Miao, mentor Renzhong Du, and all of the Li research group. I would also like to thank The Pennsylvania State University and Materials Research Institute staff. Finally, the funding from the National Science Foundation (NSF; Grant No. ECCS-0335765) and the National Nanotechnology Infrastructure Network Research Experience for Undergraduates (NNIN REU) Program support staff are greatly appreciated.

## References:

- [1] A. Ohtomo, H.Y. Hwang. A high-mobility electron gas at the  $\text{LaAlO}_3/\text{SrTiO}_3$  heterointerface. *Nature* 427, 423-426. (2003).
- [2] A. F. Santander-Syro, et al. Giant spin splitting of the two-dimensional electron gas at the surface of  $\text{SrTiO}_3$ . *Nature Materials*. 13, 1085-1090. (2014).

# Fiber Flow Rate Sensors Using Thermally Drawn Multi-Material Fluidic Channel Fibers

**Corey Kwok**

**Materials Science Engineering, Purdue University**

**NNIN REU Site: Microelectronics Research Center, The University of Texas, Austin, TX**

NNIN REU Principal Investigator: Dr. Zheng Wang, Electrical and Computer Engineering, University of Texas at Austin, TX

NNIN REU Mentor: Boxue Chen, Electrical and Computer Engineering, University of Texas at Austin, TX

Contact: corey.g.kwok@gmail.com, zheng.wang@utexas.edu, boxuechen@gmail.com

## Abstract:

Thermally drawn multi-material fibers with conductive polyethylene (CPE) film incorporated fluidic channels were developed. The initial resistivity of CPE was recorded as  $0.35 \Omega \cdot \text{m}$  and  $0.18 \Omega \cdot \text{m}$  after fiber draw. The effect of flow rate on their resistance was observed. The “in fiber” flow sensor can determine the flow rate with a sensitivity of  $5.237 \times 10^5 \mu\text{V}/\mu\text{L} \cdot \text{min}^{-1}$  in the  $0\text{-}40 \mu\text{L}/\text{min}$  range at bias current  $1 \text{ mA}$ .

## Introduction:

Preforms made up of polycarbonate (PC) slabs and conductive polymer films are drawn into fibers by heating the mold while pulling the preform through the furnace. This method maintains the preform's cross sectional geometry proportionally based on a set reduction ratio (16 to 17 times smaller) [1]. Conductive polyethylene (CPE) film contains carbon black mixed with the polyethylene chain structure. Carbon black is made up of highly conductive fine carbon particles. These particles form conductive pathways in between polymer chains [2].

As water flow cools a resistor, the measured resistance will be less than initially. This change is characterized for a range of flow rates and the flow sensor uses the relation to determine the flow [3]. By containing the process within the fiber, the sensor can be integrated into various applications such as lab equipment, catheters, and fuel injectors [4].

## Experimental Procedure:

CPE film was cut to five different lengths, 1-6 cm long and 1.27 cm wide. Resistance was recorded using a four point probe method with four silver paint contact points on each sample [5]. A power supply generated a  $0.01 \text{ mA}$  current and the voltage across the inner contact points was recorded. The relation between resistance and length denotes the resistivity of CPE film.

Two PC slabs 38.1 mm wide, 381 mm long, and 5.35 mm thick were place on top of another and then wrapped twice with CPE film. The preform is thermally drawn down to a 2 mm wide fiber. CPE is removed so that only one surface is covered to ensure the dimensions of the film.

The resistivity of CPE, as a fiber, is determined using the four point probe method with five different lengths at the same current of  $0.01 \text{ mA}$ .

Two PC slabs individually wrapped three times with CPE film with smaller slabs are placed in between leaving a gap between them. The preform is thermally drawn and reduced to a 1 mm fluidic channel in a 2 mm wide fiber. CPE is removed such that only the resistance of the inner channel layers are measured. Plastic tubing added to both ends to prevent shorting equipment.

A syringe pump induced  $0\text{-}1000 \mu\text{L}/\text{min}$  of water flow into the channel fiber samples. Flow rate is generated based on the total volume and length of the syringe. Along with the four point probe power supply setup, the resistance was measured at incrementing flow rates.

## Results and Conclusions:

The resistivity of CPE decreased from  $0.35$  to  $0.18 \Omega \cdot \text{m}$  after thermal drawing. Similar sample sets have a consistent resistivity. The thickness and width of the CPE layers in the fiber samples varied greatly. In Figure 2, at lengths beyond 1.5 cm, the conductive pathways become more complex and less linear resulting in a wider range of resistance. In Figure 3, an exponential relation between flow rate and resistance results from the convective cooling process that cools exponentially with flow rate.

This CPE channel design should be only applied in the  $0\text{-}40 \mu\text{L}/\text{min}$  range because this range produces the most linear data. Within this range we can more precisely determine the flow rate with a sensitivity of  $5.237 \times 10^5 \mu\text{V}/\mu\text{L}/\text{min}$ , higher than other micro sensors.

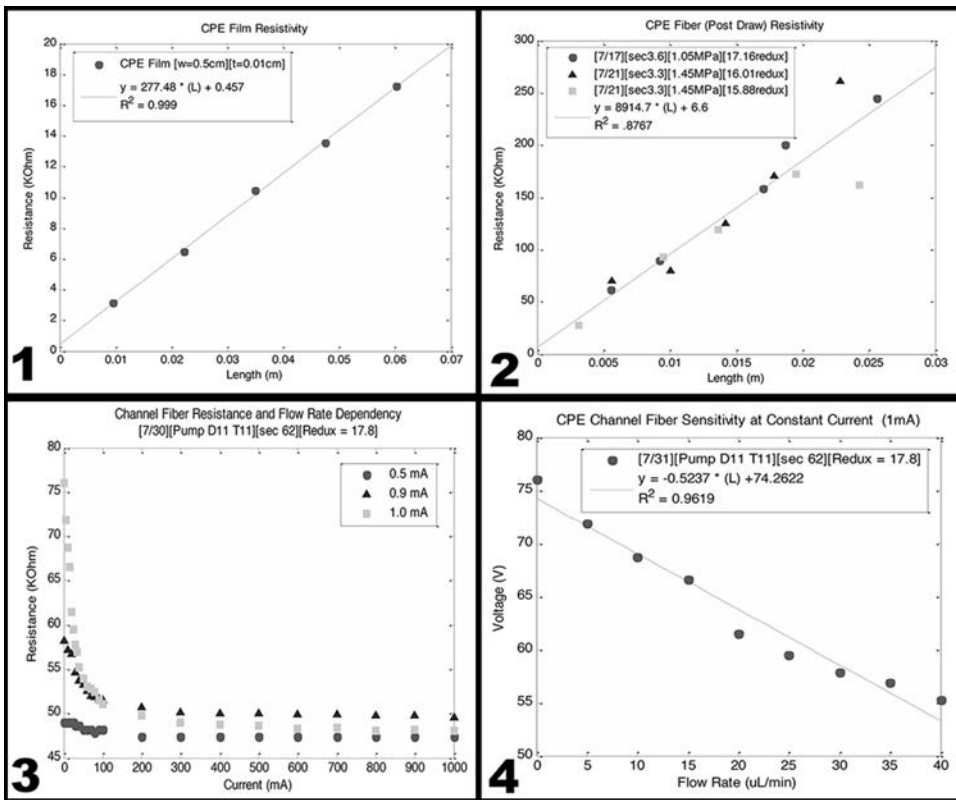


**Figure 1, top left:** Resistance values from five different lengths of CPE film. The data closely follows a linear trend implicating a resistivity value  $0.35 \Omega\text{m}$ . **Figure 2, top right:** CPE fibers were tested to observe the effects thermal drawing. The linear trend indicates the resistivity of CPE fiber to be  $0.18 \Omega\text{m}$ . **Figure 3, bottom left:** CPE channel fibers were tested under a range of flow rates. Different values for current were used to increase the initial resistance. **Figure 4, bottom right:** A linear region was isolated by using 1 mA and smaller range of flow rates. The channel fiber sensor was found to have a sensitivity of  $5.237 \times 10^5 \mu\text{V}/\mu\text{L}/\text{min}$ .

The channel fiber has comparable range but greater power consumption (76 mW) due to high current for increasing the initial resistance [6].

### Future Work:

An automated setup for determining the response time. Verify the consistency of our results by testing fiber draws using the same preform design to explore the possibility customizing the resistivity of fibers. Vary the amount of layering of CPE or PC film insulation in the channel fiber to lessen the cooling rate and increase the resistance for a larger flow rate range. A proof of concept to demonstrate the easy integration the in fiber design professes.

### Acknowledgements:

This project was sponsored by the National Nanotechnology Infrastructure Network Research Experience for Undergraduates Program and funded by the National

Science Foundation under Grant No. ECCS-0335765. My thanks to my principal investigator, Dr. Zheng Wang, my mentor, Boxue Chen and my research group for their help and guidance; also to Dr. Marylene Palard and the University of Texas at Austin's Micro Electronic Research Center staff for their assistance.

### References:

- 1] Wang, Z.; "Fabrication and Characterization of thermally drawn fiber capacitors"; App.Physics Letters, Volume 102, 152908 (2013).
- 2] Yu, G., et al. "Conductive polymer blends filled with carbon black: Positive temperature coefficient behavior." Polymer Engineering & Science 39(9): 1678-1688.
- 3] Tan, Zhiyong, et al. Characteristics of on-wall in-tube flexible thermal flow sensor under radially asymmetric flow condition. Sensors and Actuators A: Physical, 138(1), 87-96.
- 4] Beeby, S. MEMS Mechanical Sensors: Artech House.
- 5] Smits, F. M. (1958). Measurement of Sheet Resistivities with the Four-Point Probe. Bell System Technical Journal, 37(3), 711-718.
- 6] Kuo, J. T., et al. Micromachined thermal flow sensors—A review. Micromachines, 3(3), 550-573.

# Optimizing Insulator Layer Deposition for Diamond MOSFETs

**Tara Nietzold**

**Materials Science and Engineering, Rutgers University**

**NNIN iREU Site: National Institute for Materials Science (NIMS), Tsukuba, Ibaraki, Japan**

NNIN iREU Principal Investigator: Yasuo Koide, Center of Materials Research for Low Carbon Emission, NIMS

NNIN iREU Mentor: Masataka Imura, NIMS, Tsukuba, Ibaraki, Japan

Contact: [ttmn313@aim.com](mailto:ttmn313@aim.com), [koide.yasuo@nims.go.jp](mailto:koide.yasuo@nims.go.jp), [imura.masataka@nims.go.jp](mailto:imura.masataka@nims.go.jp)

## Abstract:

Field effect transistors (FETs) are important components in electronic devices due to their ability to act as electrical switches. They are comprised of a source, drain and gate, and there must be enough energy potential difference in order for the carriers, electrons or holes, to flow from the source to the drain. One of the ways the effectiveness of these devices can be improved is by applying an insulator or oxide layer on top of the channel layer in order to reduce the number of carriers that escape through the gate contact. In the case of this research, aluminum oxide was analyzed for its application as an oxide layer in these devices.

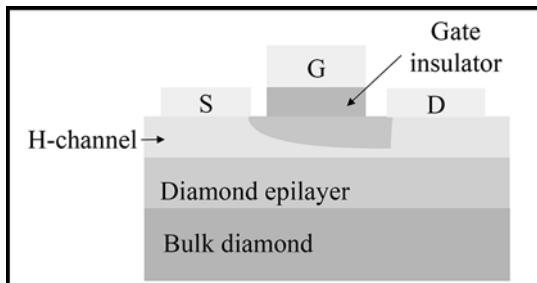


Figure 1: A graphic depicting the cross-sectional structure of the fabricated MOS devices.

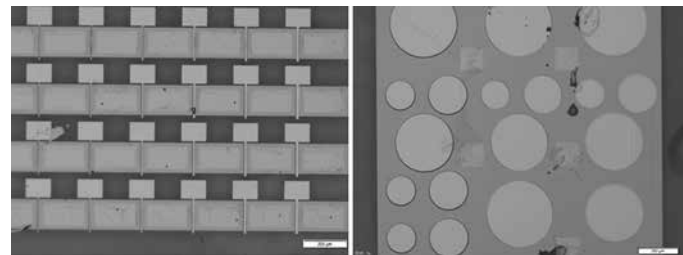


Figure 2: A microscope image of a fabricated FET (left) and diode (right). It should be clear to see the individual source, gate, and drain pairs for the individual FET devices.

## Introduction:

It has been found that diamond can be used as a viable substrate for fabricating both field effect transistor devices and diode devices. This is because it is a wide band gap material with a high degree of hardness, thus making it ideal in high-power applications. Additionally, diamond has the ability to have a hydrogen-terminated surface providing it with a high concentration of holes that then act as the carriers in the device. So in a metal oxide semiconductor field effect transistor, or MOSFET, the diamond behaves as the base semiconductor.

Figure 1 shows the current device set up, including demarcations for the source (S), the drain (D), the gate (G), and the gate oxide, aluminum oxide ( $\text{Al}_2\text{O}_3$ ). In the image, it also shows two diamond layers, the bulk layer and an epilayer. This epilayer is a high-quality layer that improves the quality of the contacts that are made.

## Procedure:

The fabrication process was a multi-step process beginning with the development of the H-terminated surface, which was done through microwave plasma chemical vapour deposition. This also created the diamond epilayer on the bulk diamond to improve the surface quality. Afterwards, photolithography, followed by dry etching and electron gun evaporation, was used to deposit the metals for the key pattern, the mesa structure for the fabricated FETs, and the source and drain. The metals used were titanium, platinum, and then gold.

After the source and drain were completed, the oxide layer of  $\text{Al}_2\text{O}_3$  was deposited by means of atomic layer deposition (ALD). Three different deposition temperatures were used in order to understand the influence of temperature on the deposition quality and furthermore, on the total current output. After the ALD, photolithography and e-gun

evaporation were used again in order to create the metal component of the gate. Finally, the samples were annealed in order to improve the drain current values.

A set of successfully fabricated MOSFETs and MOS diodes can be seen in Figure 2.

## Results and Conclusion:

The electrical properties of the  $\text{Al}_2\text{O}_3/\text{H-diamond}$  based metal-oxide-semiconductor (MOS) diodes and MOSFETs were studied. This was done by using a semiconductor probe measuring system where contacts were made to the source, drain and gate, and then the total current observed in the drain was measured. Based on the results, it was found that there exists an ideal deposition temperature range for the  $\text{Al}_2\text{O}_3$ .

The best results were found when the oxide was deposited at 300°C, because it produced ideal capacitance-voltage behavior without flat-band shift in the MOS-diode devices. Figure 3 shows the shift in the hysteresis curve as the deposition temperature was varied.

Additionally, the MOSFET showed good operation with normally-on, ohmic characteristics. The standard drain current versus voltage (IV) was expected to have a linear piece beginning at the origin, before it plateaued into the saturated region. Figure 4 shows an IV-curve for an FET device fabricated at 300°C and then annealed for an hour at 180°C. The maximum drain current it produced was -7.0 mA/mm, which is relatively low.

## Future Work:

After establishing a reliable deposition technique and discovering the existence of the ALD temperature window, the next steps are to continue to manipulate the ALD parameters and observe the maximum drain current that is produced. Once devices with a reasonable drain current can be produced and reproduced, it will be able to prove diamond to be a practical and beneficial MOSFET semiconductor substrate.

## Acknowledgments:

I would like to express my gratitude to my PI, Yasuo Koide, and my mentors, as well as Nancy Healy and Lynn Rathbun for all their assistance and guidance. I would also like to thank everyone at the National Institute of Materials Science for all their resources and help and the NSF for making the NNIN iREU Program possible under Grant No. ECCS-0335765.

## References:

- [1] Kawarada, H., et al. (2014). C-H surface diamond field effect transistors for high temperature (400°C) and high voltage (500 V) operation. *Applied Physics Letters*, 013510-013510.
- [2] J. Liu, L. Meiyong, M. Imura, E. Watanabe, H. Oosato, Y. Koide: "Electrical properties of atomic layer deposited  $\text{HfO}_2/\text{Al}_2\text{O}_3$  multilayer on diamond" *Diam. Relat. Mat.* 54 (2015) 55-58 DOI:10.1016/j.diamond.2014.10.004.

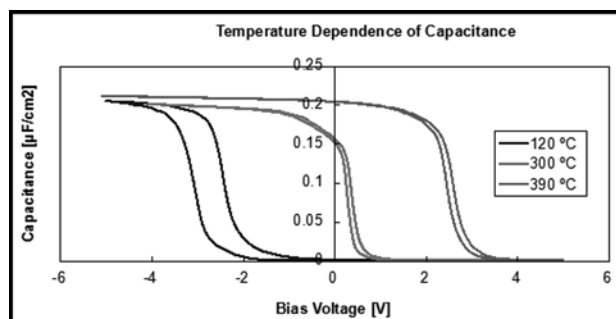


Figure 3: An overlay of the capacitance dependence found for devices fabricated at 120°C, 300°C, and 390°C. The shift in the curve represents an existence of positive charges (shifted left) and negative charges (shifted right), which are not desired.

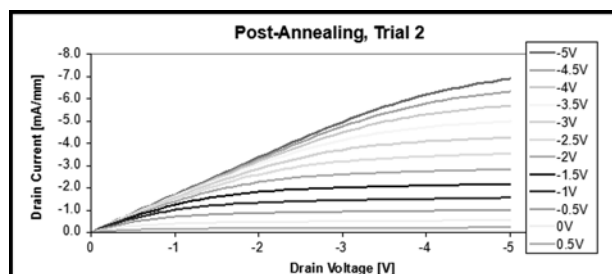


Figure 4: A drain current versus voltage curve for the 300°C trial.

# Graphene Junction Field-Effect Transistors on a Silicon Carbide Substrate

**Andrea Randolph**

**Chemical and Biological Engineering, University of Colorado Boulder**

**NNIN REU Site: Colorado Nanofabrication Laboratory, University of Colorado, Boulder, CO**

NNIN REU Principal Investigator: Dr. Bart Van Zeghbroeck, Electrical and Computer Engineering, University of Colorado Boulder

NNIN REU Mentor: Tzu-Min Ou, Electrical and Computer Engineering, University of Colorado Boulder

Contact: andrea.randolph@colorado.edu, bart@colorado.edu, tzumin.ou@colorado.edu

## Abstract:

Quantum mechanics predicts that the advancement of silicon transistors will soon reach its physical limit and thus a replacement transistor material is needed. We investigated silicon carbide (SiC) for this use due to its compatibility with existing semiconductor fabrication methods and with graphene growth processes. Graphene was chosen as a channel material due to its superior charge carrier properties. It can be either epitaxially grown directly on the SiC substrate or grown on metal and then transferred. We explored the viability of both types of graphene as laterally-conducting channels for junction field effect transistors (JFETs) on SiC substrates. The direct contact between our channel and semiconductor created a unique and novel heterojunction. The epitaxial graphene JFETs (epi-GJFETs) failed to modulate current due to discontinuity between the electrodes; however, our transferred-graphene JFET (GFET) devices were functional. An additional degree of freedom for current control was created compared to traditional transistors since the channel conductivity can be tuned by altering the applied voltage and the Dirac voltage can be tuned by altering the substrate doping. Our JFET design is compatible with other two-dimensional materials.

## Introduction:

Transistors are extensively used in mainstream electronics and are primarily fabricated on silicon substrates. Until now, we have been able to produce increasingly smaller transistors; however, a quantum effect referred to as “charge tunneling” will soon limit this continual smaller scaling [1]. As a widely-researched hexagonal allotrope of carbon, graphene (G) has potential for use as a semiconductor channel material due to its superior charge carrier properties, including over 100 $\times$  greater mobility and 30 $\times$  faster velocity than silicon [2]. As a two-dimensional material, graphene carries current laterally and avoids vertical charge dissipation [3]. Graphene tends to be chemically p-doped by air, so we chose heavily n-doped SiC for our underlying substrate.

As seen in Figure 1, our GJFETs consisted of a graphene channel lying across the SiC substrate, atop which the source and drain electrodes rested. We chose to design JFETs over the more widely-used metal-oxide-semiconductor field effect transistors (MOSFETs) because our devices were back-gated and lacked oxide insulation layers.

These JFET devices are always on and require an applied voltage at the gate to turn the device off: moving electrons from the n-doped SiC into the holes of the p-doped graphene induces a depletion region where no carriers are present, eventually growing large enough to decrease the conductivity and cut off the charge flow.

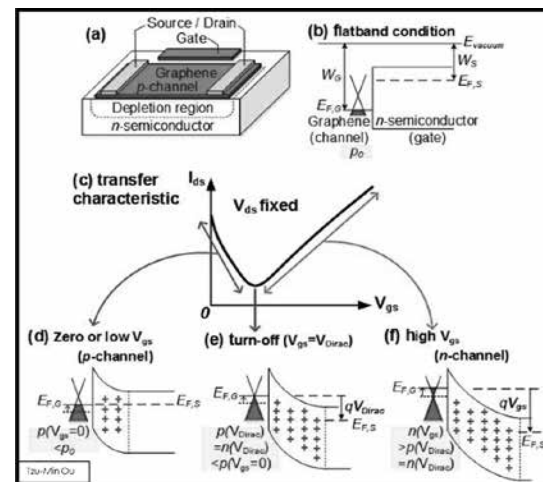


Figure 1: (a) GJFET schematic, (b) energy band diagram for the graphene-semiconductor heterojunction, (c) transfer characteristic curve showing graphene's transition, (d) from an initially on p-doped device, (e) to the neutral turn-off condition, and (f) to an n-doped channel.

## Fabrication Procedure:

The fabrication procedure for our epitaxial GJFETs is shown in Figure 2 (a) and for our transferred GJFETs in (b). Our epi-G on SiC samples were commercially prepared by thermal decomposition.

We patterned and etched channels into the top graphene layer using optical lithography followed by oxygen plasma, respectively. We then blanket evaporated nickel on the backside to create the gate. Photoresist insulating layers

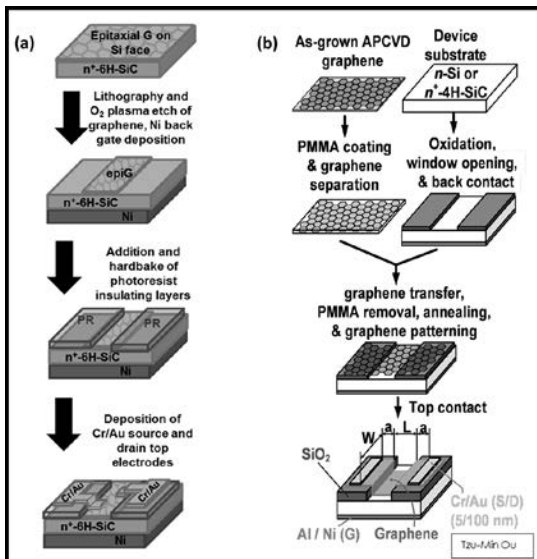


Figure 2: Fabrication steps for (a) an epi-GJFET and (b) a transferred G-JFET.

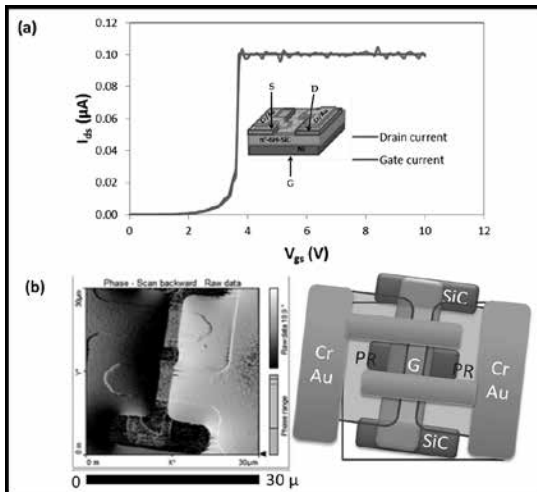


Figure 3: Epi- GJFET (a) transfer curve and (b) AFM phase image of the devices and reference.

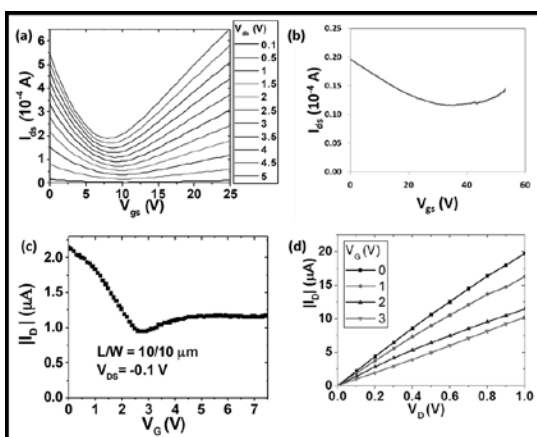


Figure 4: (a) Simulated transfer curve for Si, (b) actual SiC transfer curve ( $N_d = 10^{16}$ ), (c) Tzu-Min Ou's transfer curve ( $N_d = 10^{19}$ ), (d) Tzu-Min Ou's output curve ( $N_d = 10^{19}$ ).

were added, and then finally the chrome/gold (Cr/Au) source and drain electrodes were deposited by thermal evaporation. The transferred GJFET process was similar, but first involved growth of a graphene layer on a copper (Cu) substrate and then a transfer process. This was done using a polymethylmethacrylate (PMMA) layer and electrolysis to separate the graphene sheet. The SiC wafer was oxidized and back-gated with nickel (Ni) by thermal evaporation. The graphene was then applied to our SiC wafer and annealed so it would fold into the oxide template channels. Finally, we removed the excess graphene, added the top Cr/Au electrodes, and began our probe tests.

## Results and Conclusions:

The epi-GJFET failed to modulate current. The IV curve in Figure 3 shows that all the applied gate voltage leaked out the drain, without traveling through the graphene channel to the source as desired. We would need some of this voltage to travel through from source to drain in order to induce the depletion region, decrease conductivity, and shut the device off.

From the AFM phase scan, it appears that the graphene channel was non-continuous and that bare SiC was exposed in between the source and drain electrodes. We suspect that either the fabrication process or contamination may have removed the graphene there, resulting in non-functional devices.

In contrast, the transferred GJFET did demonstrate the expected behavior (Figure 4 (a)). The parabolic shape of this curve is indicative of graphene's progression from p-doped through the turn off Dirac voltage, and then to n-doped. We achieved microamp current in our channel, and an on/off ratio of approximately 2. Our results (Figure 4 (b)) were obtained using SiC with a doping density of about  $10^{16} \text{ cm}^{-3}$ ; previous work done by my mentor using a SiC wafer with a doping density of  $10^{19} \text{ cm}^{-3}$  shows similar behavior (Figure 4 (c) and (d)).

We successfully introduced a second degree of freedom for tuning channel conductivity: not only can we vary the applied voltage, but we can also additionally change the doping density for further modulation. Our best finished device demonstrated a sheet resistance of  $3.33 \text{ k}\Omega/\text{sq}$ , a hole mobility of  $2000 \text{ cm}^2/(\text{V}\cdot\text{s})$ , and an initial hole density of  $1.5 \times 10^{12} \text{ cm}^{-2}$ . We were unable to extrapolate far enough to obtain the electron mobility.

Our devices show the feasibility of modulating current using GJFETs on a SiC substrate.

## Acknowledgments:

Thanks to Bart Van Zegbroeck, Tzu-Min Ou, Tomoko Borsa, the NNIN REU Program and NSF under Grant No. ECCS-0335765, and the Colorado Nanofabrication Laboratory.

## References:

- [1] F. Bonaccorso, et al., Nat. Photonics 4, 611 (2010).
- [2] F. Schwierz, Nat. Nanotechnol. 5, 487 (2010).
- [3] H. Yang, et al., Science 336, 6085 (2012).
- [4] L. Britnell, et al., Science 335, 6071 (2012).

# Evaluation of $\text{TiO}_2$ as Carrier Selective Contact for High Efficiency Photovoltaic Applications

**Alexander Rosner**  
**Electrical Engineering, University of Notre Dame**

**NNIN REU Site: ASU NanoFab, Arizona State University, Tempe, AZ**

NNIN REU Principal Investigator: Dr. Mariana Bertoni, Electrical Engineering, Arizona State University

NNIN REU Mentor: Dr. Laura Ding, Electrical Engineering, Arizona State University

Contact: arosner@nd.edu, mariana.bertoni@asu.edu, laura.ding@asu.edu

## Abstract:

Herein we evaluate titanium dioxide ( $\text{TiO}_2$ ) as a carrier selective contact for silicon solar cells. Additionally, we investigate aluminum oxide ( $\text{Al}_2\text{O}_3$ ) as a dedicated passivation layer that could be combined with  $\text{TiO}_2$  for improved performance. Using a photoconductance lifetime tester, we found that  $\text{TiO}_2$  presents a poor passivation of the silicon surface and that the best minority carrier lifetime was achieved on an 8 nm thick  $\text{Al}_2\text{O}_3$  layer annealed in forming gas. We then created heterojunction with intrinsic thin (HIT) solar cells using  $\text{TiO}_2$  as the electron carrier-selective contact, and found low open-circuit voltages and efficiency consistent with the poor surface passivation.

## Introduction:

The most efficient silicon solar cell today uses amorphous silicon (a-Si) to passivate the surface and selectively collect carriers from the c-Si. However, a-Si absorbs some of the light that the c-Si could turn into carriers. We investigated  $\text{TiO}_2$  as a replacement candidate since, with a band gap of 3.2 eV, it is transparent to visible light and its band-structure theoretically should line up with c-Si's, making it a good electron-selective contact [1]. However,  $\text{TiO}_2$ 's ability to prevent surface recombination of minority carriers is variable and our project's aim was to quantify it.

## Experimental Procedure:

We prepared  $\text{TiO}_2$  and  $\text{Al}_2\text{O}_3$  films using thermal atomic layer deposition (ALD) on n-type Czochralski c-Si wafers after removing the native oxide. We varied the deposition temperature and film thickness to investigate the relationship between films' properties and passivation capability. Next, we annealed the wafers to activate the passivation and varied the annealing temperature, duration and atmosphere (air or forming gas). The films were deposited on both sides of the wafer for lifetime measurement, while only on the back side of the cells.

We evaluated surface passivation of c-Si by quasi-steady-state photoconductance decay measurements to extract the minority carrier lifetime, at a minority carrier density (MCD) of  $1 \times 10^{15} \text{ cm}^{-3}$ .

We report effective lifetimes ( $\tau_{\text{eff}}$ ), which account for bulk and surface lifetimes. Solar cell performances were characterized by current-voltage and by external quantum efficiency (EQE) measurements.

## Results and Conclusions:

The effective lifetimes of the different thicknesses of  $\text{TiO}_2$  prepared at different temperatures are presented in Figure 1, for the as-deposited state and after annealing. The highest lifetimes originate from the thinnest coatings, and annealing has only a minor effect for 3 min, while a drop in lifetime was observed for 30 min. The detrimental impact of thicker layers and longer annealing is possibly related to stress-induced phase transformation leading to more defects in the films and a higher recombination rate [2]. The deposition temperature seems to have no effect on the passivation quality. Using  $\text{TiO}_2$ , we could only achieve a surface recombination velocity of  $70 \text{ cm.s}^{-1}$ , whereas a-Si can produce  $> 1 \text{ cm.s}^{-1}$  (15  $\text{cm.s}^{-1}$  in our case).

We prepared cells with the best  $\text{TiO}_2$  films—8 nm (230°C), 5 nm (180°C), 6 nm (130°C)—as the electron-selective contact. Figure 2 shows the EQE of the best cell compared to two reference cells, a standard HIT and HIT with Al back. At higher wavelengths, the current generated by the cell with  $\text{TiO}_2$  is lower than that of the references mainly because of a difference in back side light reflection.

Figure 3 shows a table of the solar cells' performance. The  $\text{TiO}_2$  thickness-dependence was only observed in the fill factor (FF), due to the high resistivity of  $\text{TiO}_2$  (typically  $\sim 10^5 \Omega.\text{cm}$ ), with the thinnest  $\text{TiO}_2$  layer resulting in a FF as high as the reference cells. All open-circuit voltage ( $V_{\text{oc}}$ ), short circuit current density ( $J_{\text{sc}}$ ) and efficiencies were lower than for the reference cells. The  $V_{\text{oc}}$  of the best  $\text{TiO}_2$  cell was 564 mV, which is comparable to the implied  $V_{\text{oc}}$  value (given by the lifetime tester as the highest  $V_{\text{oc}}$  attainable by the cell if passivation is the only limiting

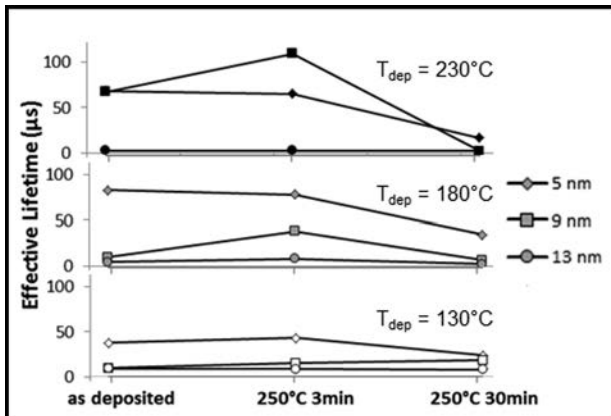


Figure 1: Effective lifetime of samples with different  $\text{TiO}_2$  coatings.

$\text{TiO}_2$ thickness	$T_{\text{dep}}$ (°C)	Efficiency (%)	$V_{\text{oc}}$ (mV)	$J_{\text{sc}}$ (mA/cm <sup>2</sup> )	FF(%)
6 nm	130	12.8	564	30.9	73.2
9 nm	180	12.2	558	31.0	70.7
9 nm FGA	180	11.2	559	31.0	64.6
8 nm	230	12.0	562	30.7	69.6
8 nm FGA	230	4.4	524	30.8	27.1
Standard HIT	NA	20.2	696	39.0	74.6
HIT w/ Al back	NA	15.6	707	36.7	60.3

Figure 3: Summary of the performance of solar cells with different  $\text{TiO}_2$  thicknesses, compared to two HIT cells.

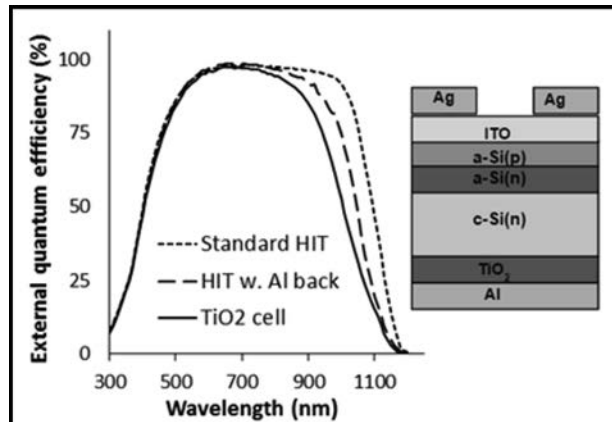


Figure 2: EQE and structure of a solar cell with  $\text{TiO}_2$  compared to two HIT cells.

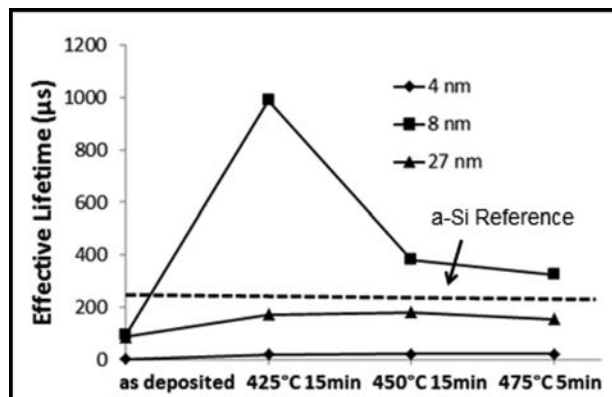


Figure 4: Effective lifetime of samples with different  $\text{Al}_2\text{O}_3$  coatings.

factor) of 580 mV. This demonstrates that the passivation and not the carrier selectivity is the most significant factor in poor cell performance. Therefore,  $\text{Al}_2\text{O}_3$  was investigated as an alternative passivation coating.

In Figure 4, we show the lifetime of Si wafers with different thicknesses of ALD  $\text{Al}_2\text{O}_3$  against different annealing conditions. We found that 8 nm thick films lead to the best lifetime > 1 ms after a 15 min 425°C anneal in forming gas.

Although annealing in air revealed that thicker layers (15 and 3 nm) result in better passivation as they contain more hydrogen to passivate the dangling silicon bonds, this advantage decreases when hydrogen can be provided by annealing in forming gas [3]. Moreover, thicker layers may suffer from increased stress, explaining why the 8 nm thick film gave the best passivation.

In summary, we found that the poor passivation ability of  $\text{TiO}_2$  on silicon for a wide range of depositions and post-deposition treatment conditions resulted in underperforming solar cells, however the passivation ability of  $\text{Al}_2\text{O}_3$  seems to be comparable to  $\alpha\text{-Si}$ , presenting a potential path for high efficiency devices.

## Future Work:

We would like to combine  $\text{Al}_2\text{O}_3$  and  $\text{TiO}_2$  layers, and implement them at the sun-facing side instead of backside to improve passivation and benefit from higher transparency than the  $\alpha\text{-Si}$  layers. Changing the deposition method or trying different post-deposition treatments such as light-soaking could improve the passivation ability of  $\text{TiO}_2$ .

## Acknowledgements:

I would like to thank my PI, Dr. Mariana Bertoni, my mentor, Dr. Laura Ding, and Simone Bernardini for all of their help and guidance. I also want to acknowledge the National Nanotechnology Infrastructure Network Research Experience for Undergraduates Program and the National Science Foundation for making this research possible under Grant No. ECCS-0335765.

## References:

- [1] S. Avasthi, et al. Applied Physics Letters 102, 203901 (2013).
- [2] I. Yu, et al., Proceeding of the 40<sup>th</sup> IEEE PVSC, 1271-1274, (2014).
- [3] N. M. Terlinden, et al. Applied Physics Letters, 96 112101 (2010).

# Growth of Graphene by Silicon Carbide Sublimation

**Tanaka Benton**

**Applied Mathematics and Pre-Engineering, Atlanta Metropolitan State College**

**NNIN REU Site: Howard Nanoscale Science and Engineering Facility, Howard University, Washington, DC**

**NNIN REU Principal Investigator: Dr. Gary Harris, Department of Electrical and Computer Engineering, Howard University**

**NNIN REU Mentor: Mr. Crawford Taylor, Department of Electrical and Computer Engineering, Howard University**

**Contact: benton1tanaka@gmail.com, gharris1124@gmail.com, c\_taylor@howard.edu**

## Abstract:

Graphene has become the material of choice for several investigators because of its desirable properties. This two-dimensional “super” material is hexagonally bonded in an  $sp^2$  carbon arrangement. Successful methods for growing graphene include chemical vapor deposition (CVD) on metal surfaces like copper or nickel and by sublimation of silicon carbide (SiC). Graphene on SiC is of particular interest because it does not require transferal onto another substrate like graphene grown on copper does and the process is not as strenuous and damage-prone. This work investigates the conditions necessary for producing graphene on C-terminated 6H-SiC wafers by sublimation. Hydrogen ( $H_2$ ) surface etching was performed at 1200°C, while sublimation was done between 1500°C-1700°C in the presence of argon (Ar) gas, at a pressure of 200 Torr. The growth times were varied from 15-60 minutes. Scanning electron microscopy (SEM) and Raman spectroscopy were used to characterize the results obtained for single and multilayer graphene.

## Introduction:

Graphene, due to its specific aggregation of carbon atoms, forms a two-dimensional honeycomb crystal lattice. Graphene’s first experimental discovery, via micromechanical cleavage using Scotch tape, catalyzed many researchers’ interest. Since its discovery, unforeseen conclusions regarding the immense strength, thinness and durability of the material have spun into copious research topics within engineering and science. Since graphene’s first experimental discovery, many techniques have been explored to increase its reproducibility. Core problems remain in regards to growing defect-free large area graphene.

Experimentation was designed to determine growth parameters for producing single, bi-layer and/or multi-layer graphene with large grain boundaries. Therefore, we chose to investigate the formation of graphene by sublimation of SiC substrates using a high temperature CVD system.

## Experimental Procedure:

In this work, 4H and 6H SiC substrates were cut into smaller  $1 \times 1$  cm pieces, which were then cleaned by acetone and methanol sonication, followed by a hydrofluoric acid dip. The samples were then loaded into the CVD system, where they were purged with  $H_2$  for two cycles of five minutes at 200 Torr. The temperature was then increased from room temperature to the etch temperature

of 1200°C in  $H_2$ , after which the temperature was again increased to the sublimation temperature of 1500 -1700°C in Ar. C-terminated 6H-SiC substrates were etched for 30 minutes at 1200°C in  $H_2$  and sublimed for 30 minutes at 1700°C in Ar. Conversely, Si-terminated 6H-SiC substrates were etched for 60 minutes in  $H_2$  at 1200°C and sublimed at 1500°C for 60 minutes in Ar. At the end of the growth cycle, the temperature was decreased to room temperature with the system being purged with Ar before removing the samples.

## Results:

We concentrated on graphene by sublimation of 6H-SiC substrates relative to the other polytypes. Originally, it was observed that  $H_2$  etch times contributed greatly to how efficiently silicon would sublime. Etch times ranged from 15-120 minutes and SEM was used to obtain surface imaging. There was expectancy for the surface to be smooth and consistent, but etch times longer than 60 minutes showed pits and scratches; depicting over-etching or high penetration. With this discovery, further etches were done for 30-60 minutes instead.

The sublimation growths under argon were then conducted, firstly at 1500°C and later increased to 1700°C. Increasing the growth temperature to 1700°C was the pinnacle modification for C-terminated samples.

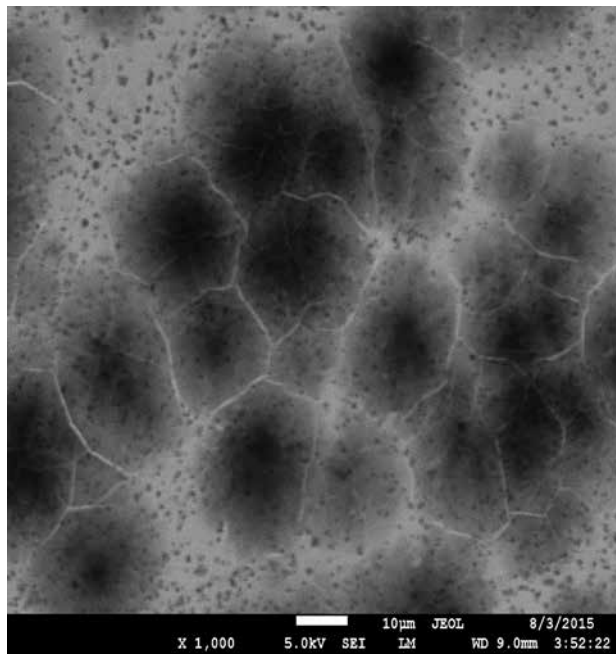
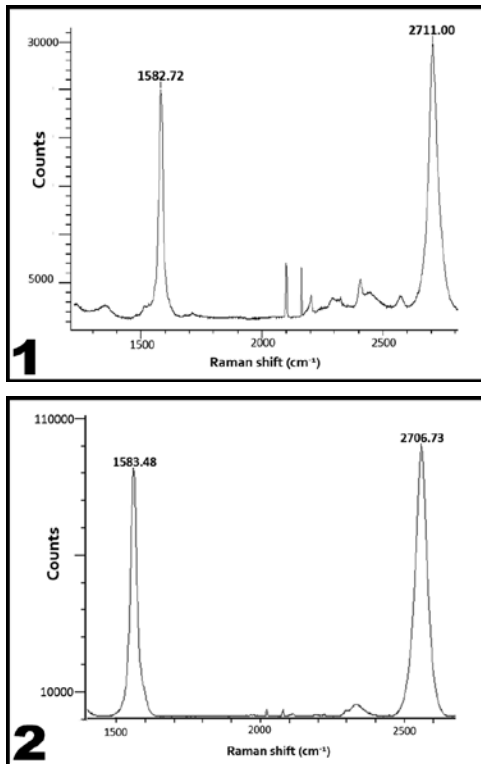


**Figure 1, top left:** Raman spectroscopy results of graphene on C-terminated 6H-SiC. **Figure 2, bottom left:** Raman spectroscopy results of graphene on Si-terminated 6H-SiC. **Figure 3, above:** SEM image of C-terminated 6H-SiC.

Using Raman spectroscopy, we characterized a G-band of  $1587.82\text{ cm}^{-1}$  and 2D-band of  $2711.00\text{ cm}^{-1}$  with a 2:1 ratio between the bands (Figure 1). Additionally, Si-terminated samples showed progress in growth when etch and growth times were increased to 60 minutes. Here the temperature remained at  $1500^\circ\text{C}$  with a G-band of  $1583.48\text{ cm}^{-1}$  and 2D-band of  $2706.73\text{ cm}^{-1}$  with a 3:1 ratio between bands (Figure 2).

### Conclusions:

Small deviations in growth parameters caused significant variations in results. After numerous adjustments to the growth parameters and studying each result, patterns of epitaxial graphene growth arose for very specific conditions; noticeable for both the Si-terminated and C-terminated 6H-SiC substrates. Characterization by Raman spectroscopy, indicated bi-layer and multi-layer graphene growth by SiC sublimation. Si-terminated 6H-SiC grain sizes were  $5.0\text{--}7.5\text{ }\mu\text{m}$ . In comparison, C-terminated 6H-SiC grain sizes were three times larger than those on Si-terminated, measuring  $20\text{--}31\text{ }\mu\text{m}$  (Figure 3).

### Future Work:

We intend to investigate the cause of grain boundary size deviations in C-terminated and Si-terminated 6H-SiC substrates. Also, we hope to further understand the parameter augmentations that affect graphene growth.

Lastly, growth of graphene by sublimation on 3C-SiC grown on silicon may be useful in understanding and achieving high quality graphene growths.

### Acknowledgements:

I would like to acknowledge the National Science Foundation (Grant No. ECCS-0335765) and the National Nanotechnology Infrastructure Network Research Experience for Undergraduates (NNIN REU) Program for this immense opportunity in science. I would like to thank the Howard Nanoscale Science and Engineering Facility and its staff for selecting me to perform research within their laboratories and assisting me throughout this process. Lastly, I would like to acknowledge my advisors, mentors, and home institution, Atlanta Metropolitan State College, for advocacy in my many endeavors.

### References:

- [1] Hodkiewicz, J; "The Importance of Tight Laser Power Control When Working with Carbon Nanomaterials"; Thermo Scientific Application Note ANS1948, 4 (2010).
- [2] de Heer, W; "Large Area and Structures Epitaxial Graphene Produced by Confinement Controlled Sublimation of Silicon Carbide"; PNAS, vol. 108, 6 (2011).
- [3] Murray, S.; "Graphene Growth Studies on Copper (111) and Silicon Carbide Substrates"; SUNY College of Nanoscale Science and Engineering, 2014. Web. 2014.
- [4] Dumé, Belle; "Graphene has record-breaking strength"; IOP Physics World, 17 Jul 2008. Web. 2008.

# Electric Field-Directed Assembly of Nanowires on Patterned Electrodes

**Nermina Brljak**

**Chemistry, Florida State University**

**NNIN REU Site: Penn State Nanofabrication Laboratory, The Pennsylvania State University, University Park, PA**

**NNIN REU Principal Investigator: Dr. Christine Keating, Chemistry, The Pennsylvania State University**

**NNIN REU Mentor: Sarah Boehm, Chemistry, The Pennsylvania State University**

**Contact: nb13e@my.fsu.edu, keating@chem.psu.edu, sjb340@psu.edu**

## Abstract:

Many researchers have shown that the assembly of nanowires could lead to future electronic and optical devices [1]. This project focused on assembly of gold nanowires in an alternating current (AC) electric field between parallel electrodes. Assembling nanowires requires a great deal of control, which is why the electric field system is ideal. The bottom electrode was lithographically fabricated and contained organized micro-patterned pillars made from photoresist on top of a layer of titanium and gold. The top electrode was an indium tin oxide (ITO)-coated glass coverslip. Since this electrode was transparent, the assembly could be monitored in real time. Pillars were 3  $\mu\text{m}$  tall and 3-20  $\mu\text{m}$  in diameter, with spacing varying from 10-55  $\mu\text{m}$ . These pillars acted as nucleation sites for the assemblies. Electric field-induced dipoles aligned the nanowires parallel to the field lines between the two electrodes. By varying different parameters, such as voltage and frequency, specific and controlled placement of the nanowires was possible and could be varied in real time. The assemblies could be reversed and replicated by switching the field on and off. This technique is promising for generating nanowire assemblies for electronic applications.

## Patterned Electrode:

The patterned substrate was photolithography fabricated to create photoresist posts with desired diameters and separation distances. Figure 1 shows the fabrication process. First, a layer of 10 nm of titanium (Ti) was deposited by electron beam evaporation onto a glass coverslip, followed by a 30 nm layer of gold (Au). A 3.2  $\mu\text{m}$  layer of positive photoresist was then spin-coated onto the substrate. Using a stepper exposure tool, the area around the desired posts was exposed to high intensity UV light through a patterned mask. The sample was then developed in MF CD 26 to remove the exposed areas of the photoresist. Two designs were used; a hexagonal configuration and a square pattern.

## Experimental Design:

As shown in Figure 2, voltage was applied through the patterned Au electrode and a transparent ITO-coated glass coverslip. A spacer was placed in between the two electrodes. This spacer was completely filled with 2.75  $\mu\text{L}$  diluted solution of nanowires in deionized water. The nanowires used were silica-coated gold nanowires that measured 2.5  $\mu\text{m}$  in length and 300 nm in diameter. Frequency and voltage were slowly increased over time to monitor the different assemblies at various conditions.

## Results:

Prior to electric field application, the nanowires diffused in solution, lying down above the bottom electrode. Once the field was applied,

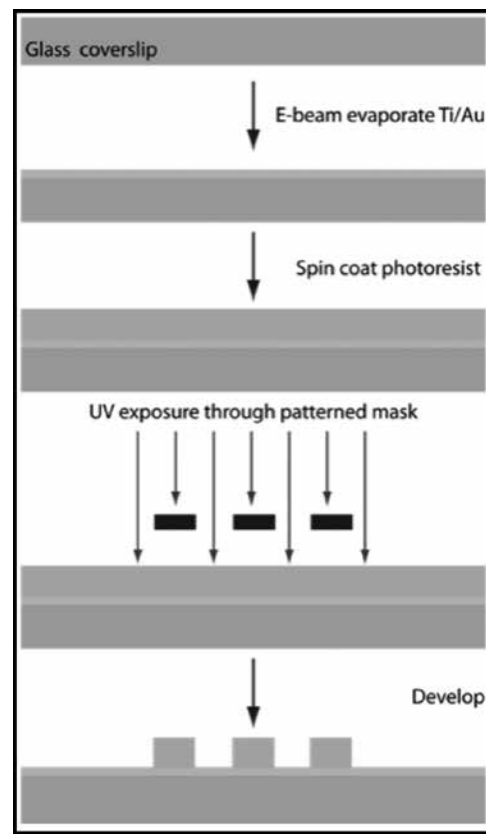


Figure 1: Photolithography fabrication process for patterning photoresist posts atop a gold-coated glass coverslip.

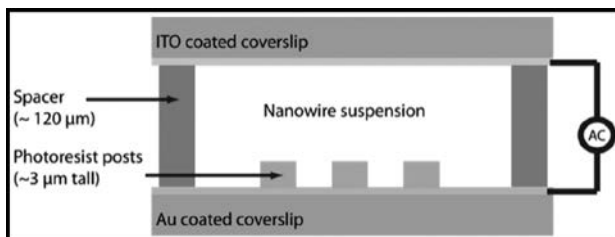


Figure 2: Side view of experimental set-up. Electric field is applied vertically, across the top and bottom electrodes through the nanowire solution.

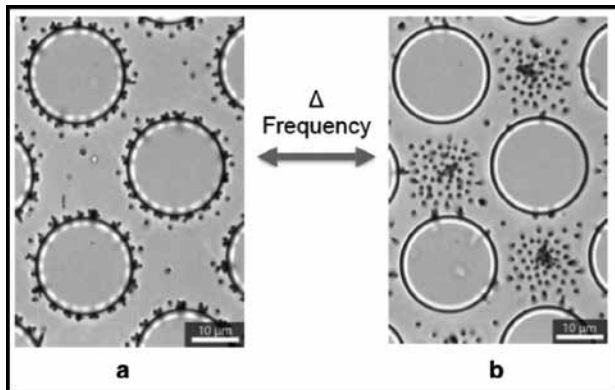


Figure 3: Optical microscope images taken from the bottom of the assembly using transmitted light. The large grey circles are the photoresist posts and the small black dots are the standing nanowires. This shows the different assemblies at two field conditions, (a) 330 V/cm, 400 kHz, and (b) 330 V/cm, 25 kHz.

the nanowires stood between the two electrodes, parallel to the electric field lines (Figure 3a). As the frequency increased, the dielectrophoretic (DEP) force increased. DEP occurred when the electric field caused the nanowires to obtain a field-induced dipole causing them to stand [2]. The local electric field strength around the fabricated posts was intensified, which caused the nanowires to nucleate around them. The posts with a smaller diameter required a higher field strength to nucleate these nanowires than the posts with larger diameters. As the frequency decreased, the electrohydrodynamic flow within the solution increased. This flow caused the nanowires to assemble in the stagnation areas between the posts (Figure 3b).

These assemblies could be reversibly formed and disassembled. When the field conditions were turned off, the nanowires separated from one another and diffused (Figure 4b). When the electric field was turned back on, the nanowires stood parallel to the field lines once again (Figure 4c). The nanowires reassembled not into the same exact positions as before but into similar organizations. However, the time it took for the nanowires to change orientation varied

depending on the field conditions. This allowed for the assemblies to be reversible. When the field conditions were turned off, the number of visible nanowires increased. When the field was on, what appeared to be two nanowires (circled in Figure 4a), ended up being three nanowires when the field was turned off (circled in Figure 4b). Since the assemblies were being viewed from the bottom, the extra nanowires were not visible.

It can be hypothesized that since the nanowires had a field-induced dipole-dipole interaction, chaining in the z-direction occurred [3]. Figure 4d shows the possible chaining in the z-direction of a pair of nanowires. This kind of cluster trend occurred within every pattern organization and was not affected by the field conditions.

### Conclusions and Future Work:

Overall, using a photoresist-patterned electrode successfully served as nucleation sites for nanowires to assemble around. By tuning the electric field conditions, different assemblies could be created. The AC electric field is ideal for assembling these nanowires because it enables control and tunability in real time.

### Acknowledgements:

I would like to thank my mentor, Sarah Boehm, for all of her help and guidance. I would also like to thank the Keating group and especially my principal investigator, Dr. Christine Keating. Another thank you to the Materials Research Institute at Pennsylvania State University, the National Nanotechnology Infrastructure Network Research Experience for Undergraduates Program and NSF funding under Grant No. ECCS-0335765.

### References:

- [1] Grzelczak, M.; Vermant, J.; Furst, E. M.; Liz-Marzán, L. M. ACS Nano, 2010 4(7), 3591-3605.
- [2] Smith, B. D.; Mayer, T.S.; Keating, C. D.; Annu. Rev. Phys. Chem. 2012, 241-263.
- [3] Boehm, S. J.; Lin, L.; Betancourt, K. G.; Emery, R.; Mayer, J. S.; Mayer, T.S.; Keating, C. D.; Langmuir, 2015, 31(21), 5779-5786.

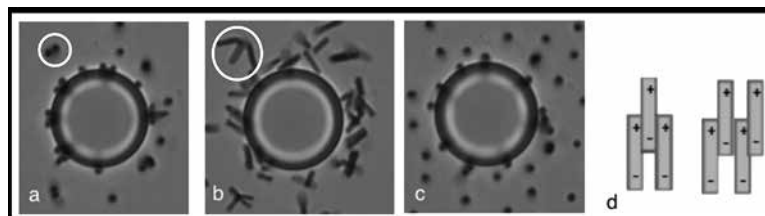


Figure 4: Images of when the field conditions are turned on (a), turned off (b) and turned back on (c). Possible chaining of pairs (d).

# Zinc Oxide Deposition Methods for Opto-Electronic Applications

**Benjamin Carberry**

**Electrical Engineering, University of Florida**

**NNIN REU Site: UCSB Nanofabrication Facility, University of California, Santa Barbara, CA**

NNIN REU Principal Investigator: Dr. Steven DenBaars, Materials Department and Department of Electrical and Computer Engineering, UCSB

NNIN REU Mentor: Asad Mughal, Materials Department, University of California, Santa Barbara

Contact: bcarberry93@aol.com, denbaars@engineering.ucsb.edu, asad\_mughal@umail.ucsb.edu

## Abstract:

The purpose of this study is to investigate the feasibility of combining the atomic layer deposition (ALD) and hydrothermal deposition methods for growing zinc oxide (ZnO) thin films for opto-electronic applications. The main application considered throughout this study is the transparent conductive oxide (TCO) layer in gallium nitride (GaN) LEDs. The focus of this research was to maximize the optical transparency and minimize electrical resistivity of the grown ZnO films. A resistivity value as low as 2.75 milli-ohm centimeters ( $\text{m}\Omega\cdot\text{cm}$ ) was obtained for ZnO, which is comparable to the measured resistivity of ITO, 1.09  $\text{m}\Omega\cdot\text{cm}$ . Optical transmission measurements showed that a ZnO film with a thickness of 1.34 micrometer ( $\mu\text{m}$ ) stays within around 10% of an ITO film with a thickness of 0.33  $\mu\text{m}$ . Despite already yielding values comparable with ITO, the ZnO film performance can probably still improve since further optimizations can be made to the hydrothermal deposition process.

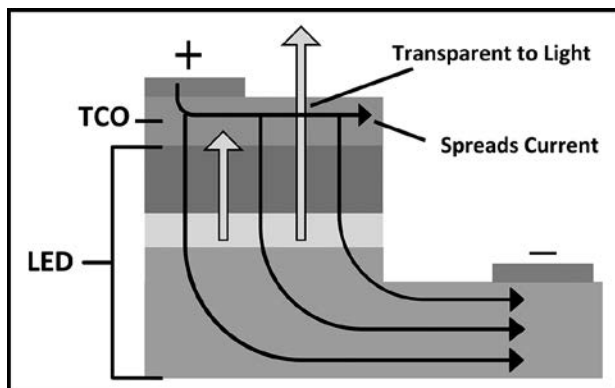
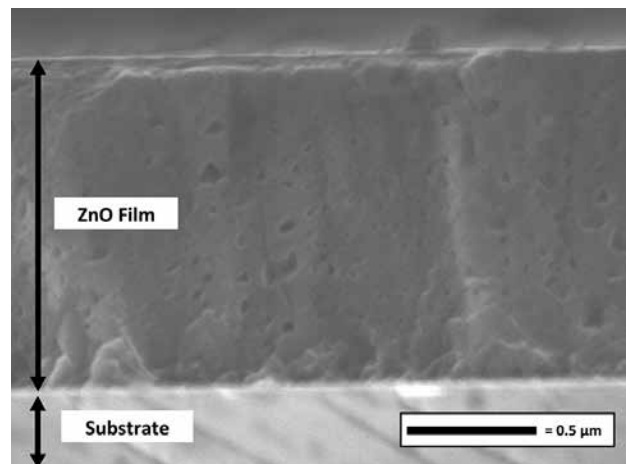


Figure 1, above: Basic diagram of LED with TCO layer.

Figure 2, right: SEM image of ZnO film.



## Introduction:

Due to its relatively low cost, ZnO is receiving attention as a viable alternative to the current industry standard, indium tin oxide (ITO), for use as the TCO material [1]. The TCO layer is an essential component of opto-electronic devices because of its ability to spread current while also being transparent to light. Figure 1 shows a basic diagram of the TCO layer on an LED.

Numerous methods exist for depositing a thin film of ZnO onto a substrate, but several of these methods require expensive machinery and very controlled environments. Hydrothermal deposition, however, is a relatively simple method because it does not have these requirements [2]. The only prerequisite is a thin seed layer on which to grow

the hydrothermal film, which is precisely grown using ALD. The main goal of the research this summer was to observe the electrical and optical performance of the ZnO films grown specifically using ALD and hydrothermal deposition. Figure 2 shows a scanning electron microscope (SEM) image of the ZnO thin film.

## Process:

ZnO thin films were deposited on  $\text{Al}_2\text{O}_3$  (sapphire) substrates in four steps: 1) ALD seed layer, 2) anneal treatment, 3) hydrothermal layer, and 4) final anneal treatment.

In the ALD seed layer step, diethylzinc was used as the zinc precursor, or source, and we found that using  $H_2O$  as the oxygen precursor, while running the process at 300°C, gave the highest quality seed layer structure with the highest conductivity. The standard number of cycles was chosen to be 25, which yielded a thickness of around 4 nanometers (nm). The self-limiting nature of ALD means that each cycle produces only single layers of a certain thickness; this makes ALD an excellent method for growing the seed layer.

The annealing (heat treatment) step had the best results when done at 700°C for 30 minutes in the presence of nitrogen gas. The hydrothermal deposition process was carried out in an aqueous solution heated to and held at 90°C for two hours. The standard solution used consisted of 1.3 milli-liters (mL) of  $NH_4OH$ , 25mL of 5 millimolar (mM)  $ZnNO_3$  and 5 mM of Na-Citrate. To help increase conductivity, the solution was also doped with aluminum (Al), gallium (Ga), and indium (In) before the hydrothermal process began. The amounts of dopants used ranged from 0.1 mM to 4 mM.

The main mechanism behind hydrothermal deposition is that as the temperature and pH level increases, the solubility of the aqueous solution decreases, and  $ZnO$  becomes more likely to form. First, the ionized zinc and

hydroxide particles will form zinc hydroxide, and then the zinc hydroxide will dehydrate into zinc oxide and water.

## Data:

Some of the best results recorded are shown in Figures 3 and 4. Figure 3 shows the different resistivity values of doped and undoped  $ZnO$  films compared to the measured resistivity of ITO. While ITO has the lowest resistivity at 1.089 mΩ·cm, one of the best results obtained for  $ZnO$  was with a 0.4 mM Ga-doped film. Other dopants and amounts seemed to increase the resistivity relative to the undoped  $ZnO$  film, which had a resistivity of 3.86 mΩ·cm.

Figure 4 shows the difference in transmission between a sapphire substrate without a film, ITO, and doped  $ZnO$ . Without any film, the substrate transmits around 85%. With a 0.33 micrometer (μm) thick ITO film, the transmission ranges between 68-86% in the visible spectrum. Despite being thicker, the 1.33 μm film of  $ZnO$  remains within 10% of the ITO film throughout most of the visible spectrum.

## Conclusions:

This research confirmed that using the combination of ALD and hydrothermal deposition is a feasible method for growing  $ZnO$ , yielding optical and electrical performance comparable to the industry standard, ITO. However, there is still room for improvement. The hydrothermal deposition method needs to be investigated further to obtain a film with more transparency and a more controlled thickness. In addition, attenuation coefficients need to be obtained so optical performance can be accurately quantified independently of film thicknesses. Finally, LEDs need to be processed to assess the actual light quality and efficiency.

## Acknowledgements:

I would like to thank the NNIN REU Program for providing me with an opportunity to participate in nanotechnology research, and I thank my mentor, Asad Mughal, for introducing me to graduate and materials science research. I would also like to thank my principal investigator, Dr. Steven DenBaars, and my site coordinator, Wendy Ibsen. The National Science Foundation supported this research under Grant No. ECCS-0335765.

## References:

- [1] Ellmer, K. (2012). Past achievements and future challenges in the development of optically transparent electrodes. *Nature Photonics*, 6(12), 809–817. <http://doi.org/10.1038/nphoton.2012.282>.
- [2] Kim, J. H., Andeen, D., and Lange, F. F. (2006). Hydrothermal growth of periodic, single-crystal  $ZnO$  microrods and microtunnels. *Advanced Materials*, 18(18), 2453–2457. <http://doi.org/10.1002/adma.200600257>.

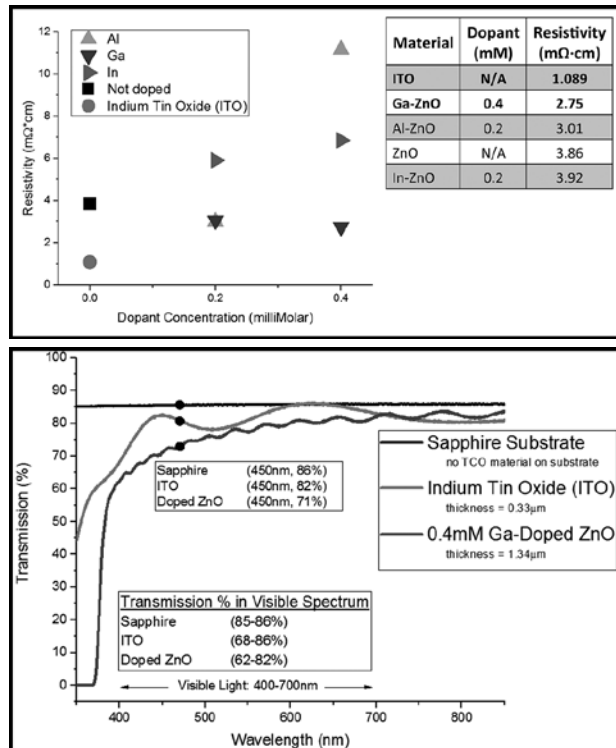


Figure 3, top: Left; Resistivity values vs. Dopant Concentration (lower resistivity means higher conductivity). Right; Table of lowest resistivity values for comparison.

Figure 4, bottom: Optical Transmission vs. Wavelength for the sapphire substrate alone, ITO, and doped  $ZnO$ .

# Mechanical Testing of OPVs using Flextrode: An ITO-Free, Transparent, Polymer-Based Electrode

**Isaac DiGennaro**

**Chemistry, Missouri University of Science and Technology**

**NNIN REU Site: Stanford Nanofabrication Facility, Stanford University, Stanford, CA**

NNIN REU Principal Investigator: Professor Reinhold H. Dauskardt, Materials Science and Engineering, Stanford University

NNIN REU Mentor: Nick Rolston, Applied Physics, Stanford University

Contact: [isdwxc@mst.edu](mailto:isdwxc@mst.edu) [dauskardt@stanford.edu](mailto:dauskardt@stanford.edu) [rolston@stanford.edu](mailto:rolston@stanford.edu)

## Abstract:

Organic photovoltaic (OPV) cells may offer a means to rapidly produce low-cost devices by printing thin films onto plastic substrates in ambient conditions. Indium-tin oxide (ITO) is the standard electrode for OPVs, but is brittle, prohibitively expensive, and not scalable. Flextrode, a transparent, flexible electrode composed of conductive polymers, was recently developed as a move towards cheaper materials with better mechanical properties than ITO. This project investigated effects of mechanical strain on the cohesion and function of the flextrode layer as part of an OPV. Films on a plastic substrate were deformed to varied strains, while monitoring film behavior with an optical microscope. Changes in surface morphology were characterized with optical and atomic force microscopy to determine the strain tolerance of the films. Additionally, *in situ* measurements of conductivity and photovoltage during tensile tests determined the effect of strain on the functionality of the layers. Flextrode proved to be a mechanically robust alternative to ITO that resists cracking up to a 25% strain with minimal loss of conductivity.

## Introduction:

Organic photovoltaics is a recently developed field that uses polymers in electron donor-acceptor pairs to harness the photoelectric effect. OPVs offer solutions to a number of the limitations of silicon cells. For instance, they may be mass-produced at much lower cost due to cheap starting materials and simple fabrication processes. In addition, the light weight and flexibility is compatible with easy transport and deployment, and wearable electronics applications. However, OPV research still faces a number of hurdles in reliability and power conversion efficiency (PCE). OPV efficiency lags behind that of traditional cells, and they degrade due to environmental stressors, further lowering PCE. In addition, the cells must withstand stresses from deformation of the plastic substrate. Heretofore, adhesive and cohesive strength of OPVs has been low, causing mechanical failure. Flextrode, a polymer based, printed electrode, was developed as an alternative to ITO, which is brittle and plagued by many of the limitations of silicon cells. Prior work has characterized its fabrication and electrical properties [1]; this project investigated the tensile strain tolerance of a flextrode based OPV and the films that comprise it.

## Methods:

The films of interest are printed sequentially onto the plastic substrate: beginning with only flextrode and zinc oxide

electron transport layers (ETL), followed by active layer, then the conductive polymer hole transport layer (HTL), and finally the complete device. Samples were prepared with one, two, or three layers and each was incrementally strained by tensile loading. The resulting changes in surface morphology were characterized using optical and atomic force microscopy (AFM). Electrical measurements were also taken to determine the functionality of the cells under strain. The resistance of the flextrode layer and photocurrent generated by the full device were measured during tensile tests using a multimeter.

## Results and Discussion:

Cohesive cracking due to strain was characterized with AFM in order to determine the robustness of the individual films. Table 1 shows the strain at which cracks were first detected (crack onset) and at which they propagated

Cell Layer	Crack onset (% Strain)	Cracks through (% Strain)
HTL (PEDOT:PSS)	No cracking	Delamination at 15 %
Active (P3HT:PCBM)	6	30
ETL (ZnO)	5	10
Flextrode (PEDOT:PSS)	25	30

Table 1: Strain tolerance of films.

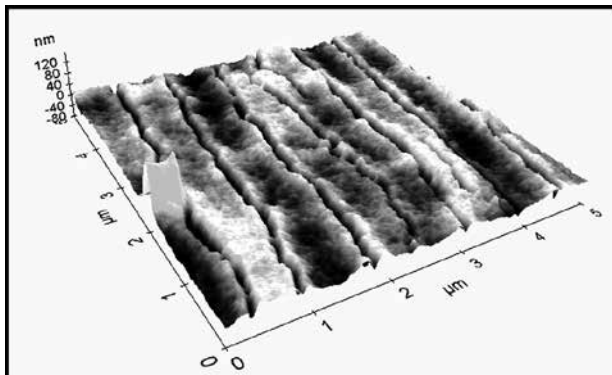


Figure 1: AFM image cracked ETL on flextrode at 20% strain (60-80 nm cracks).

through the film (cracks through). Delamination of the HTL due to poor adhesion to the underlying active layer was found to be the first cause of total device failure. Onset of surface cracking of the active layer occurred at 6% strain, but the devices continued to function despite this. Figure 1 shows surface cracking of the ETL on flextrode in a 5  $\mu\text{m}$  square AFM topography image. Before straining, the surface was very smooth with 3-5 nm surface features; crack depth, width, and density increased with greater strain. Flextrode was shown to be mechanically robust to 25% strain. This is nearly an order of magnitude above the strain tolerance of ITO, which begins to crack at 3% strain [2].

The changes in surface morphology were correlated with the functionality of the films. Strain slightly decreased the conductivity of the flextrode layer, as shown in Figure 2, but it retained 75% of its function at 25% strain. The layer had not failed catastrophically even by 60% strain, a deformation that requires kilonewtons of force.

Next, function of the full devices under strain was tested by photocurrent measurements, the results of which are shown in Figure 3. Background effects interfered with quantitative measurements, but qualitative trends were apparent. At strains less than five percent (comparable to operating conditions), cracks reclose and function is restored upon relaxation. The full device retains functionality to 25% strain. Though crack onset in the active layer at 6% strain causes some decrease in output, the complete cell is able to withstand deformations well beyond those expected in service.

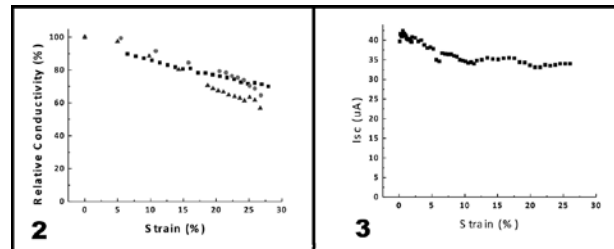


Figure 2, left: Conductivity measurements of flextrode during tensile testing. Figure 3, right: Photocurrent ( $I_{sc}$ ) measured as a function of strain.

## Conclusions:

Though OPVs face a number of challenges before they are market-ready, we have shown flextrode-based devices to be quite robust towards tensile strain. Surface morphology of the films was characterized with AFM to determine onset of cohesive cracking, and this was correlated with film functionality. Flextrode tolerated an order of magnitude higher strain than conventional ITO, retaining 75% of its original conductivity at 25% strain. Though the active layer begins to crack at 6% strain, actual device failure was caused by delamination of the HTL. Straining cells decreased their PCE, but the device continued to function at 25% strain, far beyond normal operating conditions. Flextrode is therefore shown to be a viable replacement for ITO, and more compatible with the fabrication process and applications of OPVs. Improvement of adhesion at the active layer-HTL interface will improve cells' mechanical durability, a critical step in realizing the potential of OPVs.

## Acknowledgements:

Nick Rolston (mentor), Professor Reinhold Dauskardt (PI), Dr. Michael Deal (site coordinator), SNF, CIS, NNIN REU Program, NSF (ECCS-0335765).

## References:

- [1] Frederik C. Krebs, 2009, 93, 4, 394-412.
- [2] Mora, et al. Electronic Materials Letters 2010, 10, 1033.

# Infiltration, Imidization, and Cross-Linking of Polyimides in Molecular-Scale Confinement

Jade Fostvedt

Chemistry, University of South Dakota

**NNIN REU Site: Stanford Nanofabrication Facility, Stanford University, Stanford, CA**

NNIN REU Principal Investigator: Professor Reinhold H. Dauskardt, Materials Science and Engineering, Stanford University

NNIN REU Mentor: Scott G. Isaacson, Materials Science and Engineering, Stanford University

(2009 NNIN REU at Cornell; 2010 NNIN iREU at NIMS in Tsukuba, Japan)

Contact: [jade.fostvedt@coyotes.usd.edu](mailto:jade.fostvedt@coyotes.usd.edu), [rhd@stanford.edu](mailto:rhd@stanford.edu), [sgi@stanford.edu](mailto:sgi@stanford.edu)

## Abstract:

Nanocomposite materials with a polymeric phase have novel properties—including exceptional toughness, strength, and low density—making them desirable for a variety of applications. Previous studies have shown that when the polymer within the nanocomposite material is confined to molecular-scale dimensions, polymer and nanocomposite properties are dramatically altered. In this work, we studied the effect of molecular-scale confinement on the synthesis and toughness of a nanocomposite material composed of polyimide in a nanoporous matrix. We optimized the properties of this composite material by varying the processing time and temperature. The extent of polymer infiltration, the ring-closing imidization reaction, and cross-linking of the polymer were studied. Finally, we measured the toughness of the composite material and found it to be increased by 87% as compared to the empty matrix. This work led to a better understanding of the effect of nanometer-scale confinement on the toughness of nanocomposite materials.

## Introduction:

Composite materials combine dissimilar materials to produce improved properties, including low density and increased toughness and strength. One method of composite material synthesis involves infiltrating a polymer into the interconnected pore structure of a stiff inorganic matrix, which induces confinement of the polymer phase. In this work, we synthesized nanocomposite materials with polymers confined at molecular length-scales in order to test the limits of toughening with polymers in extreme confinement. The materials were created through a unique backfilling approach in which polymers are infiltrated into the pores of a nanoporous glass scaffold. This synthesis technique leads to uniform mixing of the two phases at small length-scales and produces uniform, high-quality films over large areas.

The confining matrix for this work was ethylene oxycarbosilane (Et-OCS), a porous organosilicate with a porosity volume of 47% and interconnected pores roughly 7 nm in diameter. Polyimide was chosen for the polymer phase in this work, as its ability to withstand high temperatures makes it ideal for future applications as a material for high-performance aerospace applications. Our objective for this work was to optimize the processing conditions for the Et-OCS/polyimide nanocomposite material and to test its mechanical properties.

## Experimental:

The porous Et-OCS matrix was synthesized as a ~ 600 nm film on a silicon wafer and then cut into  $1 \times 1 \text{ cm}^2$  samples [1]. Each sample was then spin-coated with a thin film (~ 300 nm) of polyamic ethyl ester, a polyimide precursor manufactured by the U.S. Air Force. The sample was then cured under an inert atmosphere in a Yield Engineering Systems oven (Figure 1).

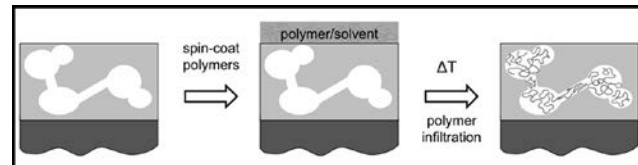


Figure 1: Infiltration strategy for Et-OCS/polyimide nanocomposite material.

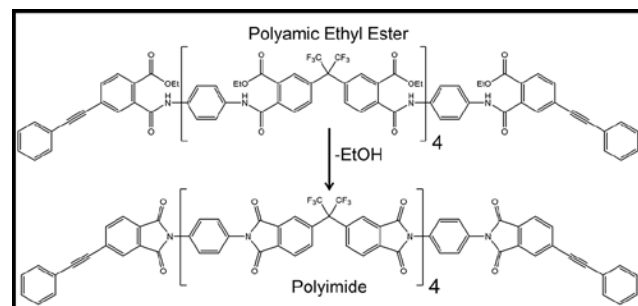


Figure 2: Imidization of polyamic ethyl ester to form polyimide.

During this high-temperature curing process, a number of changes can occur within the sample, all of which can affect the properties of the final product. First, the polymer infiltrates the pores of the matrix. Additionally, the polymer itself undergoes reactions in confinement: a ring can close in the polyamic ethyl ester structure, forming polyimide (Figure 2) and possible side products, and cross-linking can occur at the alkyne end-groups of the polymer chains. Infiltration of the polymer was monitored using depth profiling x-ray photoelectron spectroscopy (XPS). Chemical changes within the polymer structure were monitored using Fourier transform infrared spectroscopy (FTIR).

FTIR peaks for the various polymer species in the sample were then assigned and used to elucidate an imidization reaction mechanism for this process [2]. From the XPS and FTIR data, an ideal curing profile was selected to make nanocomposite samples with the maximum degree of infiltration, the largest amount of desired polyimide product, and the desired density of cross-linking. Finally, toughness of samples was assessed by making double cantilever beam (DCB) specimens containing the nanocomposite material of interest between two silicon beams (Figure 3). These specimens allowed us to measure the energy required to propagate a crack through the nanocomposite film, providing a quantitative measure of toughness.

## Results and Discussion:

We found that imidization was most successful (gave the greatest ratio of desired product to side product) when the samples were cured at higher temperatures ( $>300^{\circ}\text{C}$ ) for one hour. We also observed that infiltration was most complete when the samples were cured at a lower

temperature ( $<200^{\circ}\text{C}$ ) for four hours. Cross-linking did not occur until the cure temperature reached  $360^{\circ}\text{C}$ .

In order to synthesize a sample with optimized degrees of imidization, infiltration, and cross-linking, we chose a cure profile of  $170^{\circ}\text{C}$  for four hours to allow the polymer to infiltrate the pores and begin imidizing, followed by an hour-long period of increased temperature ( $370^{\circ}\text{C}$ ) in order to complete imidization and cross-link the confined polymer chains. Then, we measured the fracture energy of two nanocomposite films: one consisting of an Et-OCS matrix containing no polymer in the pores, and one containing polyimide processed according to the optimized curing conditions described above.

The sample with no polyimide in the pores had a cohesive fracture energy of  $2.3\text{ J/m}^2$ , a low toughness that is common for nanoporous glasses. The sample with cross-linked polyimide in the pores exhibited increased cohesive fracture energy of  $4.3\text{ J/m}^2$ , an 87% increase

in toughness compared to the unfilled film (Figure 4). Therefore, the objective of this project was met: we synthesized a novel nanocomposite material, tested its mechanical properties, and found it to be tougher than the empty matrix.

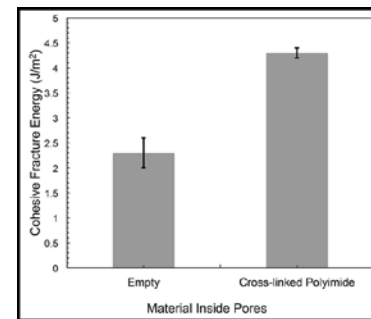


Figure 4: Cohesive fracture energy, a measure of toughness, increases when the pores of a nanoporous glass are filled with cross-linked polyimide.

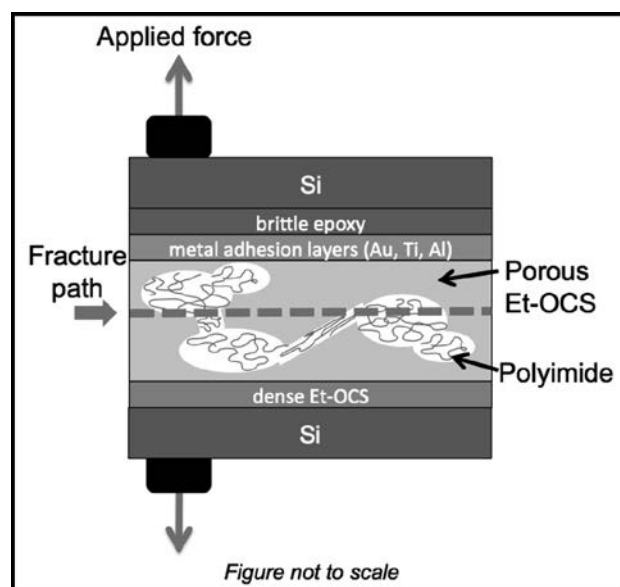


Figure 3: A schematic of a double cantilever beam specimen.

## Future Work:

Future work will focus on further mechanical testing of samples containing polyimide with various degrees of cross-linking, investigating thermal stability of the nanocomposite material, and investigating other polyimides for filling the pores of the Et-OCS matrix.

## Acknowledgements:

Thanks to Professor Reinhold Dauskardt, Scott Isaacson, Dr. Michael Deal, the Stanford Nanofabrication Facility, the NNIN REU Program, and IBM for their contributions. This work was supported by the Air Force Office of Science Research Grant No. FA9550-12-0120 and by the National Science Foundation Grant No. ECCS-0335765.

## References:

- [1] Frot, T., et al. *Adv. Mater.* 23, 2828-2831 (2011).
- [2] Brekner, M.J., et al. *J. Polym. Sci.* 25, 2479-2490 (1987).

# Ultrathin, Smooth, and Stable Doped Silver Films

**Tom George**

**Electrical Engineering, San Jose State University**

**NNIN REU Site: Lurie Nanofabrication Facility, University of Michigan, Ann Arbor, MI**

NNIN REU Principal Investigator: Professor L. Jay Guo, Electrical Engineering and Computer Science, University of Michigan

NNIN REU Mentor: Cheng Zhang, Electrical Engineering and Computer Science, University of Michigan

Contact: tom.george@sjtu.edu, guo@umich.edu, chengzh@umich.edu

## Abstract:

Silver's low resistivity, high conductivity, and low loss in the visible and near-infrared (NIR) regions makes it perfect for many optoelectronic applications. However, pure silver deposited on a dielectric substrate is unstable, rough, and requires a thick layer to form a continuous film. Aluminum (Al)-doped silver has been shown to circumvent these issues and provide an ultrathin and low loss film with sub-nanometer roughness. This makes Al-doped silver (Ag) a viable alternative to indium tin oxide (ITO) as a flexible transparent conductor. With the benefits of Al-doped Ag known, the purpose of this project was to co-sputter other metals with Ag and observe the results. The roughness, resistivity, and optical properties of these different doped Ag films were measured and a comparison study was performed to compare their properties to that of Al-doped Ag.

## Introduction:

Low loss in the visible and NIR regions makes Ag advantageous for use in many optoelectronic and metamaterial applications. However, the Volmer Weber growth of Ag on dielectric substrates and instability at room temperature results in a rough surface [1]. This significantly reduces Ag's use in many devices and makes it difficult to achieve an ultrathin and smooth film.

To circumvent these issues, a 1-2 nm germanium (Ge) seeding layer can be used resulting in Ag films with a smooth surface [1]. However, seeding layers are undesirable for low loss optical applications. This is especially true for Ge, because it is a low band gap semiconductor. Other methods to achieve stable and smooth Ag thin films have been proposed, but are either too optically lossy or too expensive and time consuming.

A way to create ultrathin, smooth, and stable Ag films with minimal time and cost has been shown by using Al in a co-deposition process with Ag. Al is co-sputtered along with Ag and this reduces the percolation threshold to 6 nm with an RMS roughness less than 1 nm for a 15 nm thick Al-doped Ag film [2]. This is a significant reduction from a pure 15 nm thick Ag film, which has a percolation threshold of 10-20 nm and an RMS roughness of about 6 nm [2].

With the knowledge that Al-doped Ag results in an ultrathin, smooth, and stable thin film, we created titanium (Ti)-doped Ag and chromium (Cr)-doped Ag films and investigated their properties. In this work, we compare the properties of the Ti- and Cr-doped Ag films to Al-doped Ag films.

## Theory:

Metals, such as Al, affect the nucleation growth of Ag on dielectric substrates such as silicon dioxide ( $\text{SiO}_2$ ). When Al and Ag are co-sputtered together, the strong bond Al has with oxygen from  $\text{SiO}_2$  forms a high density of

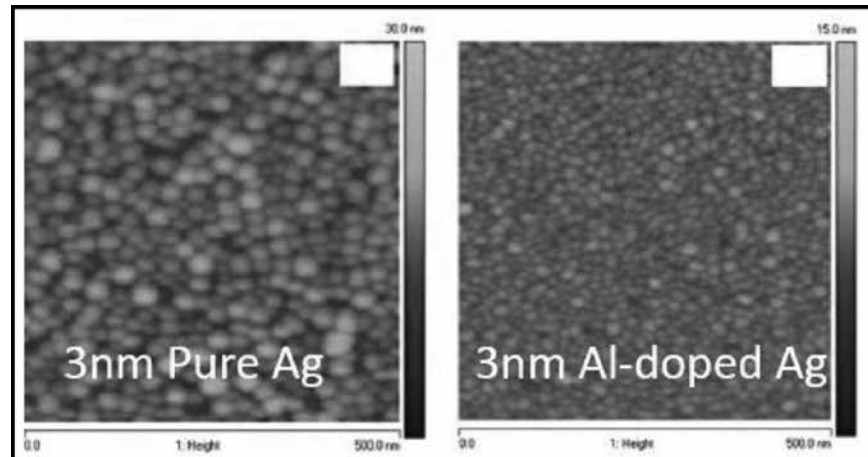


Figure 1: Nucleation sites.

nucleation sites on the surface of the  $\text{SiO}_2$  substrate [1]. This acts as a seeding layer from which Ag can easily grow. This enhanced density of nucleation sites has been viewed from a 3 nm thick layer of Ag and Al-doped Ag deposited on  $\text{SiO}_2$  as seen in Figure 1.

It is clearly seen that Al-doped Ag has a significantly larger number of nucleation sites compared to Ag deposition.

Along with an enhanced nucleation layer another benefit of co-sputtering with a metal is the formation of a capping layer. After deposition, when the sample is brought out into an oxygen ambient, there is a sudden in-diffusion of  $\text{O}_2$  and an out-diffusion of Al, which results in a capping layer [1]. The benefit of a capping layer is that it prevents de-wetting, the agglomeration of Ag, and stabilizes the thin film. It is this combination of an enhanced nucleation layer and a capping layer that results in an ultrathin, smooth, and stable film.

### Experimental Procedure:

Samples were made using diced  $<100>$  Si and fused silica resulting in  $1\text{ cm} \times 1\text{ cm}$  substrates to deposit on. Using a Kurt J Lesker Lab18 sputtering tool, recipes were created to perform Ti-Ag and Cr-Ag co-sputtering, resulting in Ti-doped Ag and Cr-doped Ag films. During deposition, the Ag target power was kept at a fixed value, while the Ti and Cr targets were varied from a low to high power. The purpose of this was to find the optimal power value to run the Ti and Cr targets that resulted in the least amount of optical loss from the thin film sample. After deposition, thickness and optical measurement were performed using the J.A Woollam ellipsometer. An atomic force microscope (AFM) was then used to provide surface roughness measurements while an SEM was used to observe film grain and continuity.

### Results and Discussion:

The results from the Ti-doped Ag and Cr-doped Ag films showed that both metals did promote the growth of thin silver films just like Al. However, both films were inferior to Al-doped Ag films during initial testing.

The 9 nm thick Ti-doped Ag film resulted in an RMS surface roughness of 0.549 nm, with a sheet resistance of  $51\ \Omega/\text{sq}$ , while the 9 nm thick Cr-doped Ag film was 0.709 nm and  $25\ \Omega/\text{sq}$ , respectively. Comparatively, a 9 nm thick Al-doped Ag film has an RMS surface roughness of 0.6 nm with a sheet resistance of  $24\ \Omega/\text{sq}$ .

### Acknowledgments:

I would like to thank my mentor Cheng Zhang and my PI Professor Jay Guo for all they have taught me this summer. Also, to Sandrine Martin, Pilar Herrera-Fierro, Nadine Wang, Dhruv Mevada, and Christian Manlutac for their guidance and support. This work would have been impossible without the LNF staff especially David Sebastian. I am grateful to the NNIN REU Program and the National Science Foundation for providing this opportunity (under Grant No. ECCS-0335765).

### References:

- [1] Zhang, C., Zhao, D., Gu, D., Kim, H., Ling, T., Wu, Y.-K. R. and Guo, L. J. (2014), An Ultrathin, Smooth, and Low-Loss Al-Doped Ag Film and Its Application as a Transparent Electrode in Organic Photovoltaics. *Adv. Mater.*, 26: 5696-5701. doi:10.1002/adma.201306091
- [2] Gu, D., Zhang, C., Wu, Y.-K. R. and Guo, L. J. (2014), Ultrasmooth and Thermally Stable Silver-Based Thin Films with Subnanometer Roughness by Al Doping, *ACS Nano* 2014 8 (10), 10343-10351.

# Diblock Copolymers for Diamond Patterning and Applications

**Lorelis González López**

**Chemical Engineering, University of Puerto Rico-Mayagüez**

**NNIN REU Site: Howard Nanoscale Science and Engineering Facility, Howard University, Washington, DC**

NNIN REU Principal Investigator: Dr. Gary L. Harris, Electrical Engineering, Howard University

NNIN REU Mentor: Dr. Michelle Chavis, Material Science and Engineering, Howard University

Contact: [lorelis.gonzalez@upr.edu](mailto:lorelis.gonzalez@upr.edu), [gharris1124@gmail.com](mailto:gharris1124@gmail.com), [mac238@cornell.edu](mailto:mac238@cornell.edu)

## Abstract:

Nitrogen-vacancy ( $\text{NV}^-$ ) centers have been recently forecasted as possible quantum bits — the fundamental unit of quantum information. Their properties include long spin lifetimes and the ability to store quantum information and transmit it in the form of light [1]. However, interaction with their environment leads to decoherence in the presence of nearby nitrogen spins. The key to enhancing  $\text{NV}^-$  centers is to control their location and reduce their interaction with the environment. Here, we present an innovative method that allows for control over the size and location of diamond nanopillars (DNPs). A hot filament chemical vapor deposition (HFCVD) reactor was used to grow polycrystalline diamond on silicon wafers. The diblock copolymer poly(styrene)-*block*-(2-vinyl pyridine) (PS-*b*-P2VP) was used to create a mask that directs the location and size of the DNPs. Reactive ion etching (RIE) was then used to transfer the patterns from the mask to the underlying substrate. We achieved  $\sim 10$  nm sized diamond nanopillars, which were characterized using atomic force microscopy (AFM) and scanning electron microscopy (SEM).

## Introduction:

Nitrogen-vacancy ( $\text{NV}^-$ ) centers are point defects found in diamond that consist of a nitrogen substitutional atom that is adjacent to a lattice vacancy. These  $\text{NV}^-$  centers have recently emerged as a potential candidate for qubits, the basic information unit for quantum computers. Their unique optical and spin properties makes them attractive for applications in areas such as magnetometry, biomedicine and spintronics [2]. The challenge when working with  $\text{NV}^-$  centers is that they can easily decohere (lose quantum state) when there are other defects close by. In order to enhance the  $\text{NV}^-$  center's properties, interaction with the environment must be reduced by keeping them separate.

A fabrication process employing diblock copolymers (DBCP) was developed to create diamond nanopillars (DNPs) as a way to isolate  $\text{NV}^-$  centers. DBCPs are macromolecules that consist of two polymers covalently linked that self-assemble into various equilibrium ordered nanostructures upon annealing. The DBCP used, poly(styrene)-*block*-(2-vinyl pyridine) (PS-*b*-P2VP) was dissolved in a selective solvent for one block and a precipitant for the other, forming micellar aggregates. These micelles consist of a condensed core of the insoluble block surrounded by a swollen shell of the soluble block in solution phase. The micelles offer advantages for surface modification because they are individual nanoscale entities that can be easily coated over many types of substrates. [3]

The array can be switched between two complementary surface topographies simply by changing the selective solvent used.

## Materials and Methods:

Monolayers of PS-*b*-P2VP (91,500-*b*-105,000 g/mol, PDI 1.1) micelles (PS matrix, P2VP core) were created by spin coating a 0.5 wt% solution in toluene at 2000 rpm for 60 seconds on a clean silicon substrate. The substrate was then dipped in methanol, a selective solvent for P2VP, and an inversion of the polymer film forms, P2VP matrix and a PS core.

Reactive-ion etching (RIE) (Plasma-Therm 790) was used to transfer the pattern created by the polymer film into the underlying silicon substrate. The inverted thin film was exposed to a five second oxygen ( $\text{O}_2$ ) etch that removed the PS block, leaving holes in the P2VP matrix layer that reached the underlying silicon substrate. The sample was then further subjected to a sulfur hexafluoride ( $\text{SF}_6$ ) etch (2½ min, 55W, 187.5 mT), which allowed the exposed silicon to be etched, thus creating holes in the substrate.

Poly-crystalline diamond was grown on the etched substrate via a hot filament chemical vapor deposition (HFCVD) process. The silicon substrates were first cleaned with acetone, methanol and toluene and then

seeded by sonicating in a methanol:nanodiamond seed (1:1) solution. The diamond was grown at a filament temperature of 2300°C and a substrate temperature of 750°C with a ratio of hydrogen to methane of 80:1, for three hours.

The diamond surface was then waxed onto a SiC substrate to remove the silicon substrate and expose the DNP s grown inside the substrates' holes. A wet etch solution was used to etch away the silicon substrate completely. The wet etch solution consisted of a hydrofluoric and nitric acid aqueous solution in a 2:2:3 ratio.

### Results and Conclusions:

PS-*b*-P2VP was successfully used as a mask to create DNP s with tunable size and distribution. Figure 1 shows an AFM image of the micelles formed (P2VP core) after an O<sub>2</sub> etch to remove the PS matrix. Next, a film of similar characteristics was dipped into a methanol bath, which inverted the core and matrix. After O<sub>2</sub> and SF<sub>6</sub> etches, ~ 15 nm deep holes were obtained on the silicon substrate, as seen in Figure 2. A poly-crystalline diamond layer was grown on the silicon substrate by HFCVD and then transferred to a silicon carbide substrate with a wet etch method. We achieved DNP s with a diameter of approximately 10 nm (Figure 3), which are several orders of magnitude smaller than what can be currently found in literature. Smaller sized DNP s increases the possibility of having just one NV<sup>-</sup> center per pillar. This would avoid any center interactions, making them more stable and therefore more ideal as qubits.

Future work includes adjusting the RIE parameters to obtain taller DNP s and growing a nitrogen-doped layer of diamond on the substrate to create NV<sup>-</sup> centers.

### Acknowledgements:

I would like to thank my Principal Investigator, Dr. Gary Harris, my mentor, Dr. Michelle Chavis, site coordinator, Mr. James Griffin, Mr. Crawford Taylor, and the staff of the Howard Nanoscale Science and Engineering Facility. I would also like to thank the NNIN REU Program, and the NSF for funding, Grant No. ECCS-0335765.

### References:

- [1] Hausmann, B. J. M.; et al. Diam. Relat. Mater. 2010, 19 (5-6), 621-9.
- [2] Ananyina, O. Y.; Severina, E. V. Bull. Russ. Acad. Sci. Phys. 2012, 76 (5), 595-599.
- [3] Krishnamoorthy, S.; et al. Langmuir 2006, 22 (8), 3450-3452.

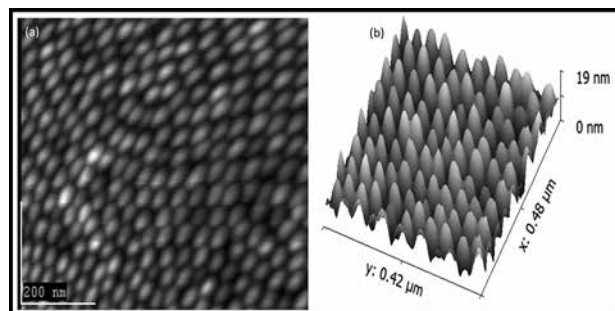


Figure 1: AFM image of (a) PS-*b*-P2VP coated silicon substrate after O<sub>2</sub> etch; (b) corresponding 3D image.

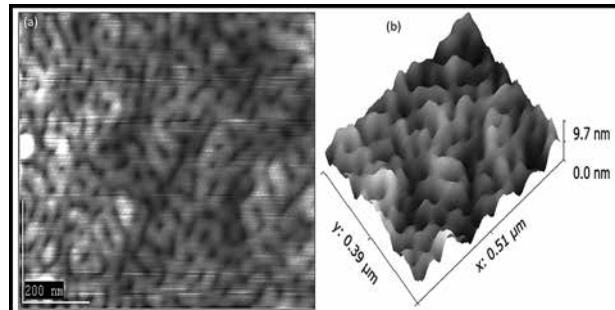


Figure 2: AFM image of (a) PS-*b*-P2VP silicon substrate after O<sub>2</sub> and SF<sub>6</sub> etch; (b) corresponding 3D image.

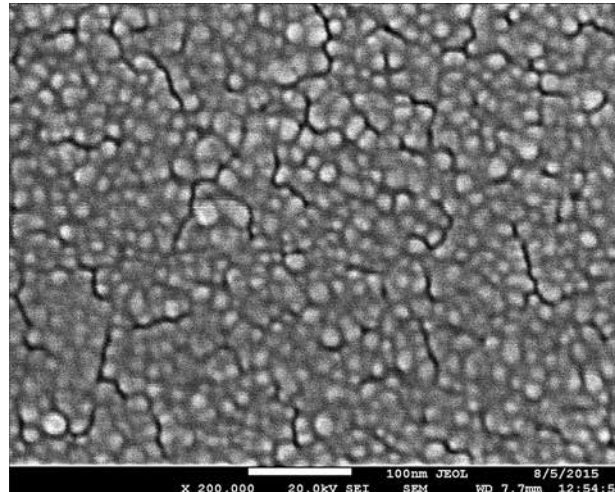


Figure 3: SEM image of diamond nanopillars with an average diameter of 10 nm.

# Characterization of Graphene Growth on Pt<111>

**Taliya Gunawansa**

**Optical Engineering, Norfolk State University**

**NNIN iREU Site: National Institute for Materials Science (NIMS), Tsukuba, Ibaraki, Japan**

**NNIN iREU Principal Investigator: Dr. Daisuke Fujita, Advanced Key Technologies Division, National Institute for Materials Science**

**NNIN iREU Mentor: Dr. Keisuke Sagisaka, Surface Characterization Group, Nano Characterization Unit, Advanced Key Technologies Division, NIMS**

**Contact: t.s.gunawansa@spartans.nsu.edu, fujita.daisuke@nims.go.jp, sagisaka.keisuke@nims.go.jp**

## Abstract:

Characterization of sizable graphene sheets grown on metal surfaces is key to understanding the interaction between graphene and the substrate for future applications. It is confirmed by Auger electron spectroscopy (AES) and helium ion microscopy (HIM) that graphene was successfully grown on Pt<111> surface through segregation. The graphene consisted of single-layer graphene across the majority of the substrate with various sections of bi-and tri-layer graphene islands and Pt patches. X-ray photoelectron spectroscopy (XPS) reveals the C1s peak from graphene on Pt<111> has lower binding energy than those from graphite (HOPG) and graphene on Ni<111>, suggesting that graphene on Pt<111> has a weaker interaction than other substrates. Topographic images and cross-section data from atomic force microscopy (AFM) depicted that graphene islands are 1.10 nm lower than the surrounding Pt region, in spite of the fact that graphene is grown on Pt. This observation speculated that water adsorption on the Pt region may indicate the nanoscale hydrophobicity of graphene and nanoscale hydrophilicity of Pt<111>.

## Introduction:

Graphene, as a single layer of carbon atoms arranged in a honeycomb lattice, has many electronic and physical properties desired for potential applications [1,2]. For graphene to be employed in various prospective applications, large-scale fabrication of graphene on transition metal substrates need to be analyzed [2]. Graphene grown on Pt<111> provided data on the weak bonding interaction with the platinum substrate and aided in the understanding of properties of graphene. Surface segregation of carbon-doped metals has the capability of producing large sheets of graphene on Pt<111>. The produced graphene consisted of a single-layer majority with fractions of bi-and tri-layer graphene islands and platinum sections. Image measurements showed growth of graphene on Pt<111> and suggested a possible relationship between the hydrophobicity of graphene and hydrophilicity of platinum.

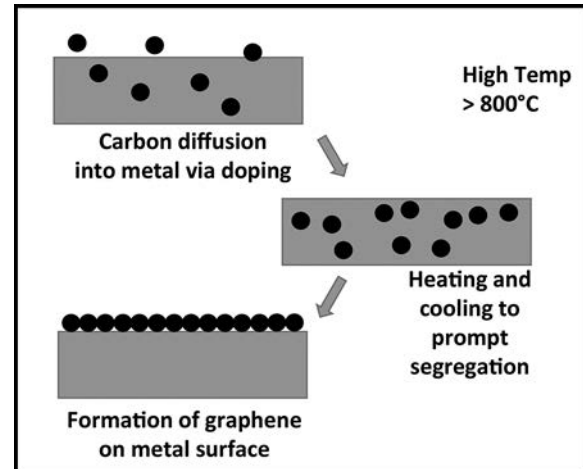


Figure 1: Schematic of segregation method.

## Experimental Procedure:

Carbon was doped into a pristine platinum sample by holding the crystal in high purity carbon powder at 800°C in high vacuum for 40 days, which yielded a 0.017 atomic percent concentration of carbon. Afterwards, it was heated to 1000°C for one minute and cooled to prompt segregation of graphene. Figure 1 illustrates the process of surface segregation and the importance of slowly cooling the sample to prompt larger amounts of graphene growth.

Auger electron spectroscopy (AES) was employed to observe growth as well as helium ion microscopy (HIM) since it provided

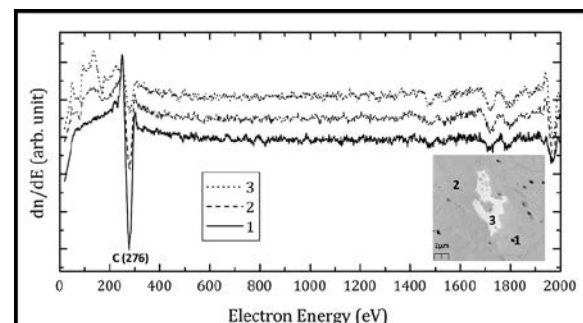


Figure 2: Carbon and Pt peaks (graph) from points 1, 2, and 3 on the SEM image.

better material contrast and depth. The characterization techniques included scanning tunneling microscopy (STM) to measure the surface morphology in the atomic scale, AFM that highlighted the topography, potential and mechanical property distributions, and x-ray photon spectroscopy (XPS) to analyze the interaction between graphene and the substrate.

### Results and Conclusions:

Figure 2 represents the scanning electron microscope (SEM) image of the center of the surface and identifies three different point spectroscopy on the sample. The corresponding graph depicts the peaks of carbon and platinum at points 1, 2, and 3. Measurements of the peak heights indicate that section 1 contains the highest amount of carbon and least amount of platinum while section 3 observes the opposite. The data calculates section 2 as having higher quantities of carbon than platinum, leading to the assumption that section 2 is a single-layer sheet of graphene. Element mapping confirmed the assumption and identified section 1 as multi-layer graphene and section 3 as platinum.

Figure 3 shows the binding energy in the carbon peak for graphene grown on Pt<111> as measured with XPS. The

dash peak represents the higher binding energy of multi-layer graphene, HOPG. Graphene grown on Ni<111> has a range of 284.7 to 285.0 eV, which indicates that nickel has the stronger interaction with graphene [3]. The peak position was sensitive to the environment and changed how graphene settled on the substrate.

Figure 4 portrays the topography and potential of graphene on Pt<111>. The topographic image obtained by AFM proved difficult to distinguish the divisions of graphene and platinum. However, the potential image depicted in the Kelvin probe force microscope mode clearly identifies the dark area to be graphene and the lighter area to be platinum. An interesting observation shows the darker islands of graphene in the topographic image to be lower than the platinum sections, even though graphene was grown on top of the platinum surface. The corresponding graph displays the cross section to determine that the graphene was 1.10 nm lower than platinum on the substrate. The reason for this peculiar observation might be explained by expansion of the platinum sections due to oxidation, since graphene is stable in air while metal surfaces are generally not. However, the possible scenario of an oxide layer being on the surface was excluded due to the lack of oxygen peaks in the Auger data. A more plausible speculation is the formation of water layer on platinum. If a water layer was present on the surface, the conclusion could indicate the hydrophobicity of graphene and hydrophilicity of platinum.

### Future Work:

Water admitted on the sample should be considered to clarify the hydrophobicity of graphene and hydrophilicity of Pt to support the experimental data collected thus far. Furthermore, experimental studies regarding graphene grown on Ni<111> should be conducted to compare the shift in energy bonds with XPS imaging.

### Acknowledgments:

I sincerely thank my PI, Dr. D. Fujita, and my mentor, Dr. K. Sagisaka, for all of their assistance and guidance. I extend my thanks to Dr. Kusawake, Dr. Masuda, K. Matsushita, S. Nagano, and the National Nanotechnology Infrastructure Network International Research Experience for Undergraduates (NNIN iREU) Program, the National Institute of Material Sciences, and the National Science Foundation, Grant No. ECCS-0335765, for providing the opportunity and funding for this research experience.

### References:

- [1] Novoselov, K., et al., *Science* 306, (5696):666-669, (2010).
- [2] Gao, J., et al., *Nanotechnology* 23, 055704 (5pp), (2012).
- [3] Fujita, D., et al., *American Vacuum Society* 12(4), (1994).

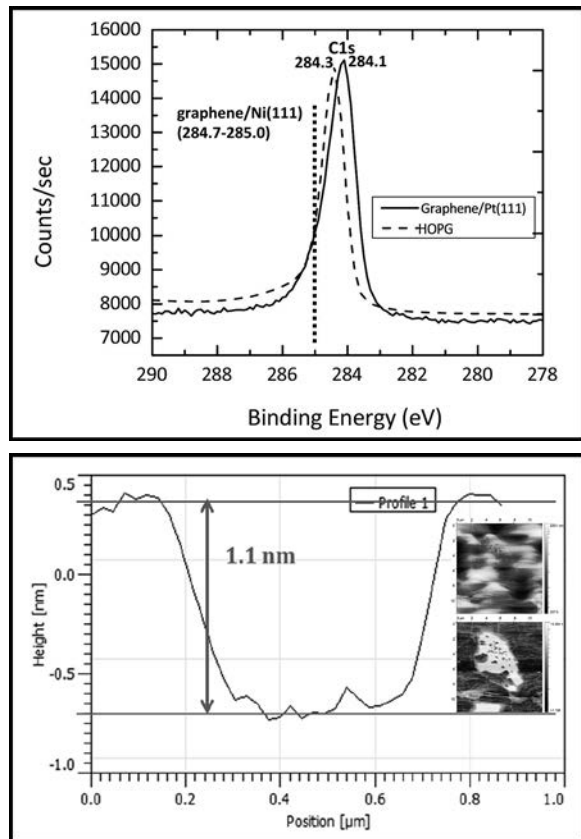


Figure 3, top: Comparison of graphene interaction on Ni<111> and Pt<111>. Figure 4, bottom: Cross section between graphene and Pt (graph), topography (top image), and potential (bottom image).

# Al-Induced Crystallization of Si Thin Films on Flexible Glass Substrates

**Sophia Hu**

**Chemistry, University of Pennsylvania**

**NNIN REU Site: Penn State Nanofabrication Laboratory, The Pennsylvania State University, University Park, PA**

NNIN REU Principal Investigator: Dr. Joan Redwing, Department of Materials Science and Engineering, The Pennsylvania State University

NNIN REU Mentor: Mel Hainey, Jr., Department of Materials Science and Engineering, The Pennsylvania State University

Contact: sophiahu\_426@yahoo.com, jmr31@psu.edu, mfh5099@psu.edu

## Abstract:

Highly-oriented silicon (Si) films on flexible substrates are attractive for thin-film electronic and energy applications. Ultra-thin flexible glasses are of special interest for substrate use because they offer flexibility and higher thermal stability than polymers. Thus, the goal of this project was to investigate the growth of silicon (Si) films on 50  $\mu\text{m}$  thick flexible glasses, using an aluminum-induced crystallization (AIC) process. AIC lowers the Si crystallization temperature to temperatures below the softening temperatures of the glasses; furthermore, it produces Si films with large grains and preferential orientation. Large-grain polycrystalline Si thin films of 30 nm thick and 100 nm thick were successfully grown on 50  $\mu\text{m}$  thick flexible glass substrates. Films 30 nm thick demonstrated larger grain size but higher electrical resistance than 100 nm thick films. Mechanical flexibility was tested by bending the samples around a tube of radius 5.75 cm, close to the maximum curvature radius of the glass substrate ( $\sim 4.5$  cm). Bending caused the samples (glass substrates with Si films on top) to fracture but did not produce any new cracks or delamination in the films themselves; bending also did not change the films' electrical resistance. These results suggested high flexibility of the Si films. In comparison, bare glasses (with no films) did not fracture, further suggesting the Si films added stress to the glass substrates.

## Introduction:

Silicon (Si) thin-film technology has garnered widespread attention for its advantageous properties over bulk silicon materials. Compared with bulk Si substrates, Si thin films grown on inexpensive substrates allow for far more cost-effective manufacture and handling of Si devices. Commonly used substrates for Si films include conventional (rigid) glasses and polymers. However, both substrates have drawbacks. While conventional glasses have high thermal stability, they are heavy and inflexible, making installation of these materials difficult and expensive. Polymers are lighter and flexible but have low thermal stability, so they cannot be used for high-temperature or high-power applications [1]. Therefore, research has recently turned to ultra-thin flexible glasses (thickness:  $\leq 100 \mu\text{m}$ ), which contain both flexibility and high thermal stability. Si thin films grown on these flexible glasses open up new possibilities for small, lightweight, bendable, and durable devices. Potential applications range from high-efficiency thin-film solar cells to flexible biosensors to scrollable displays.

Aluminum-induced crystallization (AIC) offers a convenient way to grow Si films on flexible glasses. Amorphous Si ( $\alpha$ -Si) cannot be deposited directly on glass because the Si crystallization temperature is  $\sim 600^\circ\text{C}$ , which exceeds the softening temperatures of the glass

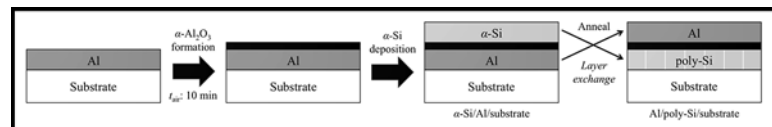


Figure 1: Schematic of the AIC process.

substrate ( $T_g \leq 600^\circ\text{C}$ ) [2]. The addition of aluminum (Al) lowers the Si crystallization temperature to temperatures below  $T_g$  (in this case, 450°C), allowing Si to be crystallized without deforming the glass substrate. Figure 1 illustrates the scheme of the AIC process.

First, Al is deposited on the glass substrate and exposed to air for 10 minutes to form  $\alpha$ -Al<sub>2</sub>O<sub>3</sub>, which is important for controlling crystal orientation of Si. Si is then deposited on top. Annealing causes Si atoms to diffuse through the Al<sub>2</sub>O<sub>3</sub> layer into the Al layer, and Al atoms are pushed to the top. This results in complete layer exchange of Al and Si, giving rise to Si films with large grains and preferential orientation [3].

## Experimental Procedure:

Al films were deposited (thicknesses: 30 and 100 nm, deposition rate: 1.5 Å/s) onto flexible glasses (Nippon Electric Glass, OA-10G 50  $\mu\text{m}$ ) via electron-beam evaporation. The films were exposed to air for 10 minutes

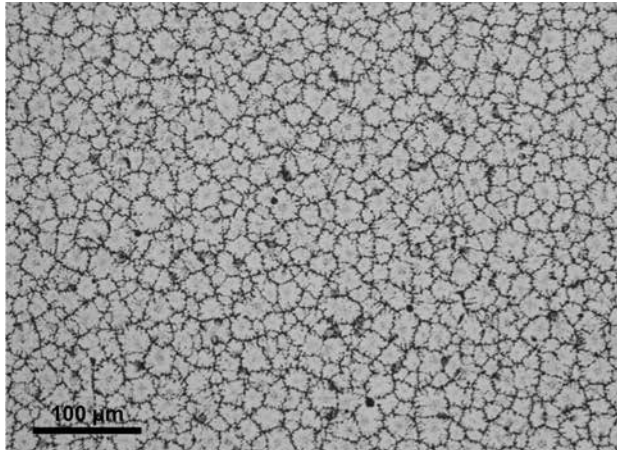


Figure 2: Optical microscopy image of 30 nm thick Si film.

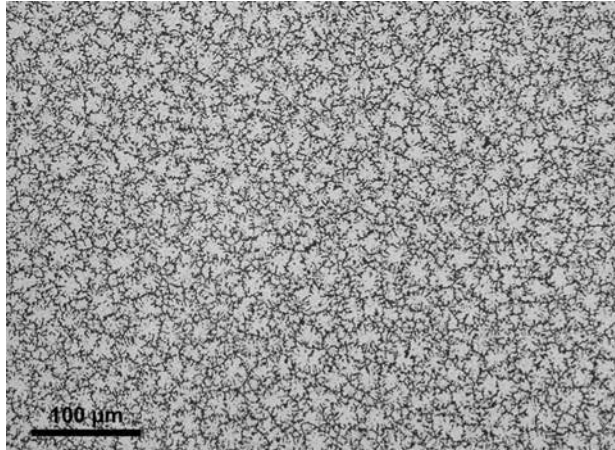


Figure 3: Optical microscopy image of 100 nm thick Si film.

to form  $\alpha$ -Al<sub>2</sub>O<sub>3</sub>. Amorphous Si films, with identical thicknesses as Al, were deposited on top. The samples were annealed at 450°C (4 hours for 30 nm films, and 10 hours for 100 nm films) in N<sub>2</sub> to cause AIC. Al was etched off with Aluminum Etch Type A.

Morphology and electrical resistance of the films were characterized by optical microscopy and ohmmeter measurements. Mechanical flexibility was tested by bending the samples eleven times on each side (alternating between each side) around a tube of radius 5.75 cm. Changes in morphology, such as cracks or delamination, were observed via optical microscopy. Bare glasses (with no films), annealed under identical conditions, were also bent eleven times on each side for comparison.

### Results and Conclusions:

Si films with thicknesses of 30 nm and 100 nm were successfully grown on 50  $\mu$ m thick glasses via AIC. Optical microscopy demonstrated the films to be polycrystalline and large-grained. The 30 nm films (Figure 2) had a grain size of  $\sim$  16  $\mu$ m, while the 100 nm films (Figure 3) had a slightly smaller grain size of  $\sim$  14  $\mu$ m. Using an ohmmeter, the 30 nm films were measured to have a resistance of  $\sim$  3-5 M $\Omega$ , and the 100 nm films had a resistance of  $\sim$  130 k $\Omega$ .

Bending the samples (glass substrates with Si films coated on top) up to a total of eleven times fractured them into a few pieces, but produced no additional cracks or other new changes in the films themselves. Electrical resistance of the films was not changed either. The lack of change in morphology or electrical resistance suggested high flexibility of the Si thin films.

The flexibility of the samples was compared with that of bare glasses (with no films). The bare glasses, annealed under identical temperatures and durations, did not fracture in the bending tests. This suggested that the Si films, while highly flexible, added stress to the glass

substrates, causing them to become more brittle than the bare glasses. Introduction of internal compressive stress by Al during annealing might explain this additional stress on the glasses [4]. However, cracks at the edges of the glass substrates and defects (e.g., black spots) in the films were observed prior to bending and could have made the samples more fragile, thus distorting the bending test results.

### Future Work:

Further investigation into the flexibility of the Si films, especially possible external factors in the bending tests, will be necessary. External factors, such as cracks (from cutting the glasses, cleaning, and handling) and stress from metal tweezers, could have made the samples more fragile and prone to breaking. Plastic tweezers are softer than metal tweezers and will be used instead in the future. In addition, the Si films were not “clean-looking” and contained defects, which were likely caused by contamination from the surrounding environment. Screening out such external factors in the bending tests will help assess the flexibility of the Si films more accurately.

### Acknowledgments:

I would like to thank Mel Hainey, Jr., and Dr. Joan Redwing for their mentorship and support in the lab. I am also thankful to the Penn State Nanofabrication Laboratory staff and the NNIN REU Program. This research was made possible by the National Science Foundation (NSF) under Grant No. ECCS-0335765.

### References:

- [1] Manoharan, M. P.; et al., Energy Technol. 2013, 1, 313-318.
- [2] Gall, S. In “Crystal Growth of Silicon for Solar Cells”; Nakajima, K.; Usami, N., Eds.; Springer Berlin Heidelberg: Berlin, Germany, 2009; pp 193-218.
- [3] Kurokawa, M. et al., Appl. Phys. Lett. 2009, 95, 132103.
- [4] Hekmatshoar, B. et al., J. Vac. Sci. Technol., A. 2004, 22, 856.

# Investigation of the Thermoelectric Properties of Boron Carbide-Hafnium Diboride Composite Materials

**Jon-L Innocent-Dolor**

**Chemical Engineering, Syracuse University**

**NNIN iREU Site: National Institute for Materials Science (NIMS), Tsukuba, Ibaraki, Japan**

NNIN iREU Principal Investigator: Prof. Takao Mori, International Center for Materials Nanoarchitectonics, National Institute for Materials Science

NNIN iREU Mentor: Dr. Satofumi Maruyama, International Center for Materials Nanoarchitectonics, National Institute for Materials Science

Contact: jcinnoc@syr.edu, mori.takao@nims.o.jp, maruyama.satofumi@nims.go.jp

## Abstract and Introduction:

In primary energy conversion, it is estimated that only about one-third of the total energy used becomes useful work. Of the two-thirds wasted, the majority is in the form of heat. Thermoelectric modules can be used to directly convert some of this waste heat back to effective use, thus, improving the overall conversion efficiency. Thermoelectric materials research has experienced a renewed interest in recent years as several new candidate materials are being discovered and optimized. One class of materials that have emerged for use in high temperature thermoelectric applications is borides. Borides such as boron carbide exhibit several favorable mechanical and thermoelectric properties such as high thermal and chemical stability, and a Seebeck coefficient that increases with temperature. The thermoelectric performance of borides can be improved by using composites – usually metal borides [1]. In this work, the effect of hafnium diboride composition on the thermoelectric properties of boron carbide was studied.

Boron carbide-hafnium diboride ( $B_4C/HfB_2$ ) composites were prepared by spark plasma sintering (SPS) of a mixture of hafnium diboride powder and boron carbide powder. The boron carbide powder was prepared with a 13.3 wt% composition of carbon, which a previous study found to be the ideal carbon content for the dimensionless figure of merit [2]. The hafnium diboride content was varied between 0 and 20 percent by weight and the effect on the thermoelectric properties was studied. The samples were characterized using x-ray diffraction (XRD). The electrical resistivity and Seebeck coefficient were measured using the four-probe method and differential method, respectively. The thermal conductivity was measured by the laser flash method. The optimal hafnium diboride content was found to be 10 wt%, leading to an improvement in the figure of merit ZT from 0.188 for the non-composite material to 0.200 for the 10% wt  $HfB_2$  composite at 730°C.

## Experimental:

Firstly,  $B_4C$  powder was prepared with a 13.3 wt% composition of carbon by heating of a boron and carbon powder mixture in an induction tube furnace. This  $B_4C$  powder was then mixed with  $HfB_2$  powder to create 0, 5,

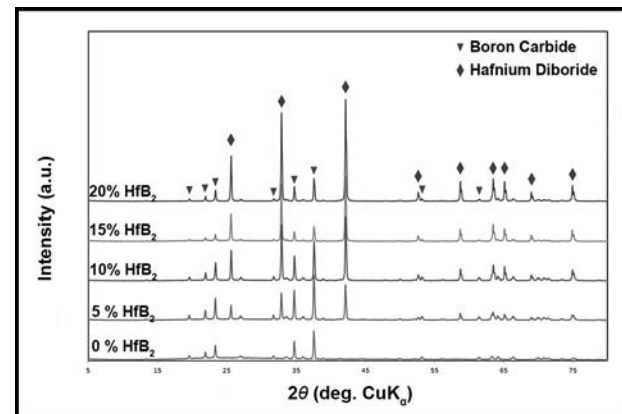


Figure 1: X-ray diffraction data for composite samples showing relative peak heights.

10, 15 and 20%  $HfB_2$  by weight samples. The powder was weighed out into 0.7 g samples for sintering and placed into a graphite dye. A SPS system was then used to sinter the composite powders at 1750°C. The sintered pellets were then polished and cut for thermoelectric measurements.

The electrical resistivity was determined by the four-probe method, while the Seebeck coefficient was measured by the differential method. We then used the laser flash method to determine the thermal conductivity of the samples. The samples were ground into a powder for XRD measurements in order to characterize their compositions.

## Results and Discussion:

The XRD measurements (Figure 1) were used to confirm the composition of the samples based on the peak positions, and height. In addition, the lack of a shift of peak position for each sample indicates that the crystal structure is not affected by the addition of  $HfB_2$ .

For all compositions, the Seebeck coefficient first decreases with temperature, then increases with temperature beyond approximately 480°C (Figure 2). The increasing Seebeck coefficient with temperature beyond this point makes boron carbide a favorable material for high temperature applications. It can be seen from Figure 1 that the Seebeck

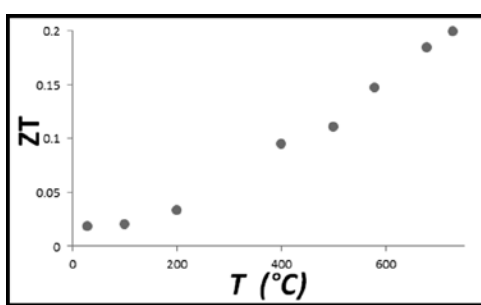
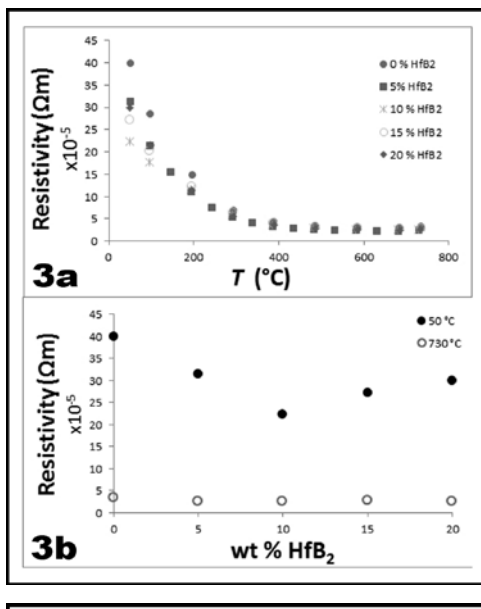
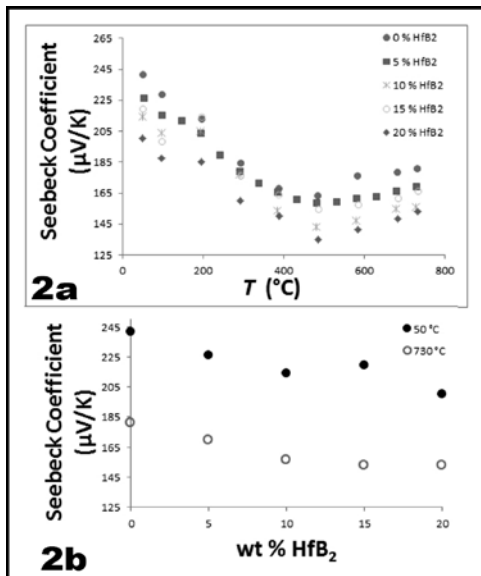


Figure 2, top: Seebeck coefficient as a function of a) temperature, and b) HfB<sub>2</sub> composition.

Figure 3, middle: Electrical resistivity as a function of a) temperature, and b) HfB<sub>2</sub> composition.

Figure 4, bottom: Thermoelectric figure of merit ZT as a function of temperature for 10% HfB<sub>2</sub> sample.

coefficient decreases with increasing HfB<sub>2</sub> composition. This is expected because boron carbide is being replaced by a material with a lower Seebeck coefficient, therefore the overall composite material should have a lower Seebeck coefficient.

Similarly, the electrical resistivity of the samples was compared with changing temperature and composition (Figure 3). The electrical resistivity was found to decrease with temperature for all the compositions examined. The electrical resistivity decreases with increasing HfB<sub>2</sub> content up to 10 wt%, then increases. This result is unusual because the resistivity would be expected to continuously decrease with increasing HfB<sub>2</sub> composition. However, we believe the density of the samples, which was lower than would be expected, is to blame. Further work will be done in order to explain this anomaly.

The thermal conductivity was found to decrease with increasing HfB<sub>2</sub> composition. At 100°C, the thermal conductivity was found to be 4.56 W/mK, 4.52 W/mK and 4.28 W/mK for the 0%, 5% and 10% samples, respectively.

The thermoelectric figure of merit ZT (Figure 4) was found to be the highest for the 10 wt% HfB<sub>2</sub> sample. The ZT value for each sample was found to still be increasing with temperature within the range investigated. The ZT value was increased from 0.188 for the non-composite material to 0.200 for the 10% wt HfB<sub>2</sub> composite at 730°C, an increase of 6%.

### Conclusions and Future Work:

The addition of hafnium diboride to boron carbide to form a composite material is a viable means of improving the thermoelectric performance of boron carbide. The measurements show that with an optimum composition, the decrease in the value of the Seebeck coefficient caused by the addition of HfB<sub>2</sub> is countered by the relatively larger decrease in both thermal conductivity and electrical resistivity. The results also show that boron carbide has excellent potential as a high temperature thermoelectric material as the Seebeck coefficient increases with temperature while the thermal conductivity and electrical resistivity decrease with temperature, which leads to a ZT value that increases with temperature.

In the future we hope to fine-tune the optimum composition of hafnium diboride by creating samples that vary by smaller increments of HfB<sub>2</sub> composition. We would also like to measure the thermoelectric properties at higher temperatures as the ZT value is still increasing within the temperature range investigated.

### Acknowledgements:

I would like to thank the National Science Foundation and the National Nanotechnology Infrastructure Network International Research Experience for Undergraduates (NNIN iREU) Program for funding and support of this research (under Grant No. ECCS-0335765).

### References:

- [1] Feng, B., H.-P. Martin, and A. Michaelis. J of Elec Mats (2013): 2314-319.
- [2] Bouchacourt, M., and F. Thevenot. J of Materials Science: 1237-247.

# Carbon Materials Assisted ZnO Nanowire Array Composites for Enhanced Photoelectrochemical Water Oxidation

**Samantha Kang**  
**Mechanical Engineering, University of Washington**

**NNIN iREU Site: National Institute for Materials Science (NIMS), Tsukuba, Ibaraki, Japan**

NNIN iREU Principal Investigator: Professor Jinhua Ye, International Center for Materials Nanoarchitectonics (MANA), Environmental Remediation Materials Research Unit, NIMS, Tsukuba, Ibaraki, Japan

NNIN iREU Mentor: Li Mu, Catalytic Materials Group, MANA, NIMS, Tsukuba, Ibaraki, Japan

Contact: [kangsam7@uw.edu](mailto:kangsam7@uw.edu), [jinhua.ye@nims.go.jp](mailto:jinhua.ye@nims.go.jp), [li.mu@nims.go.jp](mailto:li.mu@nims.go.jp)

## Abstract:

In an effort to enhance water oxidation kinetics, ternary structured zinc oxide nanowire (ZnO NW) array composites were investigated. ZnO NW arrays were grown via hydrothermal synthesis, electrodeposited with cobalt oxide ( $\text{Co}_3\text{O}_4$ ) as the co-catalyst, and then loaded with carbon materials to achieve hierarchical ZnO- $\text{Co}_3\text{O}_4$ -carbon NW structures to prevent electron-hole recombination and increase oxidation reaction rates. Initial PEC testing indicates that adding a co-catalyst and multi-walled carbon nanotubes (CNTs) enhances PEC water oxidation currents when compared to pristine ZnO NW photocurrents. At a potential of 0.6 V vs. Ag/AgCl (1.23 V vs. RHE), the PEC water oxidation current of ZnO- $\text{Co}_3\text{O}_4$ -CNT NW arrays measured was 1.61 mA/cm<sup>2</sup>, which is nearly double the photocurrent achieved by pristine ZnO NWs (0.8618 mA/cm<sup>2</sup>). These results demonstrate that the  $\text{Co}_3\text{O}_4$  co-catalyst in combination with CNTs promote electron-hole pair charge separation, a feature essential for water oxidation. Lastly, hierarchical graphene oxide-ZnO- $\text{Co}_3\text{O}_4$  NW array composites were fabricated to study how 1D-ZnO-2D-GO- $\text{Co}_3\text{O}_4$  influences the photoelectrochemistry of water oxidation.

## Introduction:

Achieving total photoelectrochemical (PEC) water splitting can help combat the energy crisis by providing clean alternative fuels. However, total water splitting is difficult due to the slow reaction rates of the water oxidation half reaction and rapid recombination of photogenerated electron-hole pairs in semiconductor photocatalytic materials [1]. Using the PEC approach, we can separate the total water splitting reaction into its redox half-reactions. To suppress electron-hole recombination and accelerate water oxidation kinetics, carbon materials such as CNTs and a  $\text{Co}_3\text{O}_4$  co-catalyst were hierarchically added to the ZnO semiconductor photocatalyst to achieve enhanced PEC water oxidation [2].

## Experimental Methods:

**Fabrication of Ternary Structured ZnO Nanowires.** The ZnO NWs were grown via hydrothermal synthesis [2]. As seen in Figure 1A, conductive fluorine-doped tin oxide (FTO) substrates were spin-coated five times with 0.01 M Zn acetate seed solution and then annealed at 350°C for 30 minutes. The substrates were then vertically suspended in a Teflon® autoclave, in 0.06 M  $\text{Zn}(\text{NO}_3)_2$  and HMT solution, for 24 hours at 110°C to synthesize ZnO NWs [3]. The NWs were then rinsed with deionized (DI) water and dried in air. Next, the substrates were electrodeposited with 0.06 M  $\text{CoCl}_2$  (aq) at -1 mA for 10 seconds, rinsed with DI water, and dried in air. The substrates were then soaked

in aqueous CNT solution (0.25 mg/mL, functionalized with 3:1  $\text{H}_2\text{SO}_4/\text{HNO}_3$  mixture) for 20 seconds and then annealed for two hours at 300°C. Figure 1B shows the intended ZnO- $\text{Co}_3\text{O}_4$ -CNT NW structure.

**PEC Water Splitting Set Up.** Linear sweep voltammetry (current-voltage and current-time) tests were conducted to analyze and compare the photoelectrochemical activity of pristine ZnO NWs, binary ZnO- $\text{Co}_3\text{O}_4$  and ZnO-CNT NWs, and ternary structures. All experiments were conducted using AM 1.5G simulated sunlight in aqueous 0.5 M  $\text{Na}_2\text{SO}_4$  (pH of 6.8) solution, using a saturated Ag/AgCl reference electrode and platinum counter electrode. Measurements were conducted at a scan rate of 10 mV/s over a potential range of -0.3 V to 1.2 V vs. Ag/AgCl. Figure 3 shows the PEC cell testing set up in which the ZnO- $\text{Co}_3\text{O}_4$ -CNT hierarchical NWs act as the photoanode where water oxidation occurs.

## Results:

X-ray diffraction tests (Figure 2A) confirmed that the main peak at a  $2\theta$  value of 35.1° can be indexed to the  $\langle 002 \rangle$  crystal phase, which confirms preferential  $\langle 001 \rangle$  ZnO NW growth on the FTO substrate [2]. The effects of hierarchically adding a co-catalyst and CNTs to the ZnO NWs are clearly shown in the PEC current-time ON-OFF illumination cycle plots (see Figure 3A,B). In Figure 3B at 0.6 V

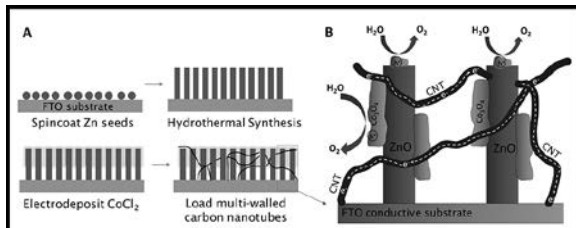


Figure 1: ZnO NW synthesis; ternary structure.

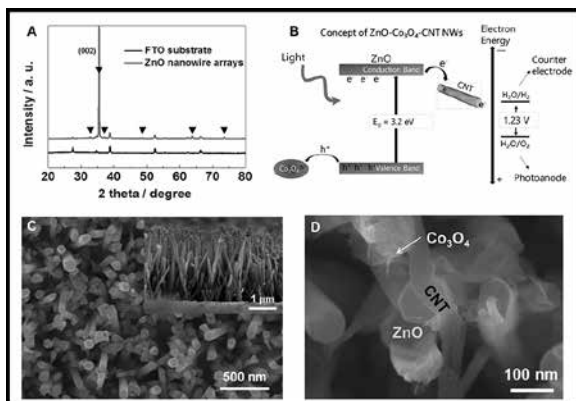


Figure 2: (A) XRD pattern. (B) Bandgap concepts. (C) ZnO NWs. (D) ZnO-Co<sub>3</sub>O<sub>4</sub>-CNT NWs.

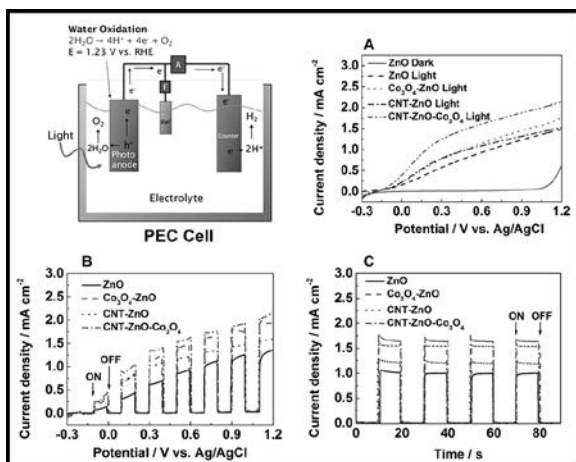


Figure 3: (A-C) PEC results.

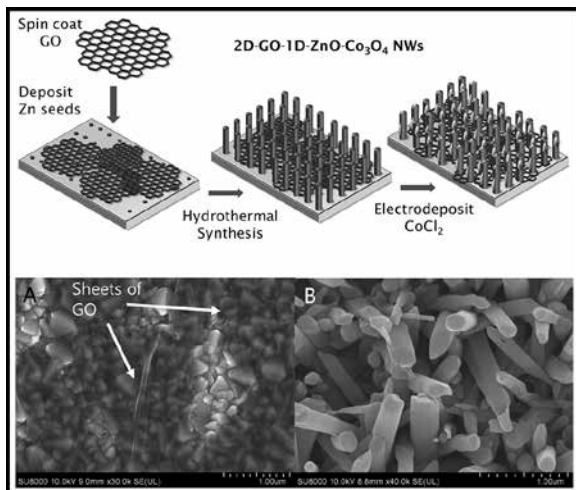


Figure 4: GO-ZnO-Co<sub>3</sub>O<sub>4</sub> NW synthesis. (A) GO on FTO. (B) ZnO on GO-FTO.

potential (~ 1.23 V vs. RHE), the PEC water oxidation current density achieved by the ternary structures is 1.61 mA/cm<sup>2</sup>, which is nearly double the current density achieved by pristine ZnO NWs (0.862 mA/cm<sup>2</sup>).

These results also show that ZnO-Co<sub>3</sub>O<sub>4</sub>-CNT structures exhibit enhanced photoelectrochemical response, which means the Co<sub>3</sub>O<sub>4</sub> co-catalyst acts as an effective oxidation site (where holes oxidize H<sub>2</sub>O) that accelerates water oxidation kinetics, and the CNTs act as bridges for electrons to transport to the conductive substrate, thus preventing rapid electron-hole recombination. This concept (Figure 2B) explains why our photocurrent densities (ZnO-Co<sub>3</sub>O<sub>4</sub>-CNT > ZnO-Co<sub>3</sub>O<sub>4</sub> > ZnO-CNT > ZnO) are enhanced with the ZnO ternary structure.

## Conclusion and Future Work:

Ternary structured ZnO NWs were successfully fabricated in which the PEC water splitting results indicate that ZnO-Co<sub>3</sub>O<sub>4</sub>-CNT NW array composites enhance PEC water oxidation kinetics by improving photogenerated charge separation dynamics and electron transfer efficiency.

Novel ternary graphene oxide-ZnO-Co<sub>3</sub>O<sub>4</sub> NW structures were also fabricated. Similar to how the CNTs act as bridges for enhanced electron transfer to the conductive substrate, we hypothesized that adding 2D graphene oxide (GO) would facilitate improved charge transfer due to its planar geometry in combination with the ZnO NWs' 1D geometry. The 2D GO-1D ZnO-Co<sub>3</sub>O<sub>4</sub> NW array composites were fabricated by first spin coating GO onto FTO substrates (Figure 4). The samples were then spin coated with Zn acetate seed solution and annealed at 350°C in N2 for 30 minutes to grow Zn seeds. The samples were processed via hydrothermal synthesis at the same preparation conditions as the ZnO-Co<sub>3</sub>O<sub>4</sub>-CNT NW structures. Initial SEM images (Figure 4A, B) and PEC testing indicate non-uniform GO deposition and ZnO NW growth on FTO substrates must be further investigated to synthesize stable NWs.

## Acknowledgements:

I would like to thank the National Science Foundation and the National Nanotechnology Infrastructure Network International Research Experience for Undergraduates (NNIN iREU) Program for funding and support of this research (under Grant No. ECCS-0335765). Also, special thanks to my PI Professor Jinhua Ye, my mentor Li Mu, and the Catalytic Materials Group at the National Institute for Materials Science.

## References:

- [1] Y. Tachibana, L. Vayssières, J. Durrant, *Nature Photonics*, Vol. 6, no., pp. 511-518, 31 July 2012.
- [2] M. Li, K. Chang, J. Ye, *Journal of Materials Chemistry*, Vol.3, no., pp. 13731-13737 2015.
- [3] H. M. Chen, C. K. Chen, and K.-H. Chen, *Angew. Chem. Int. Ed.*, 2010, 49, 5966-5969.

# Fundamental Studies of the Synthesis of Graphene Using Plasma Enhanced Chemical Vapor Deposition Processes

**Yasunori Kutsuma**

**The School of Science and Technology, Kwansei Gakuin University, Japan**

**NNIN iREG Site: Institute for Electronics and Nanotechnology, Georgia Institute of Technology, Atlanta, GA**

NNIN iREG Principal Investigator: Prof. Eric M. Vogel, Material Science and Engineering, Georgia Institute of Technology

NNIN iREG Mentors: Christopher Perini and Brian Beatty, Material Science and Technology, Georgia Institute of Technology

Contact: amb81817@kwansei.ac.jp, chrisjperini@gatech.edu, bbeatty7@gatech.edu

## Abstract and Introduction:

Graphene, the two-dimensional form of carbon, has a linear electronic dispersion with high electronic mobility. Much research has utilized graphene in high performance devices to realize practical applications [1]. However, these innovative devices require large, uniform and high crystallinity graphene sheets. In plasma enhanced chemical vapor deposition (PECVD), the decomposition process of hydrocarbon atoms is facilitated by the plasma as opposed to by thermal decomposition, allowing for low temperature synthesis [2]. This is the reason that PECVD growth is well suited for the mass production of graphene wafers.

Low crystallinity of graphene grown using PECVD is a barrier to realize practical applications [1]. D. A. Boyd, et al., improved PECVD graphene synthesis by using a mixed gas of nitrogen and methane in hydrogen plasma [3]. They claimed high quality graphene synthesis was achieved with copper etching by  $\text{CN}^-$  radicals. In addition, the bottom side of copper foils was used to grow graphene to inhibit the direct plasma exposure. High quality graphene synthesis was achieved at low temperature. The nitrogen has an impact pre growth, but the role during growth is not understood. In this study, we investigated the synthesis of graphene using PECVD with nitrogen to realize reproducible synthesis of high quality graphene wafers.

## Experimental Procedure:

Growth occurred on the bottom side of copper foils elevated by small silicon wafer pieces in a Black Magic (Aixtron) PECVD furnace. The copper was cleaned before synthesis for 10 minutes under a 700 sccm hydrogen and 100 sccm nitrogen flow at 300°C in a 40W DC plasma. After cleaning, a mixture gas of nitrogen and methane in hydrogen plasma was used for growth with a total

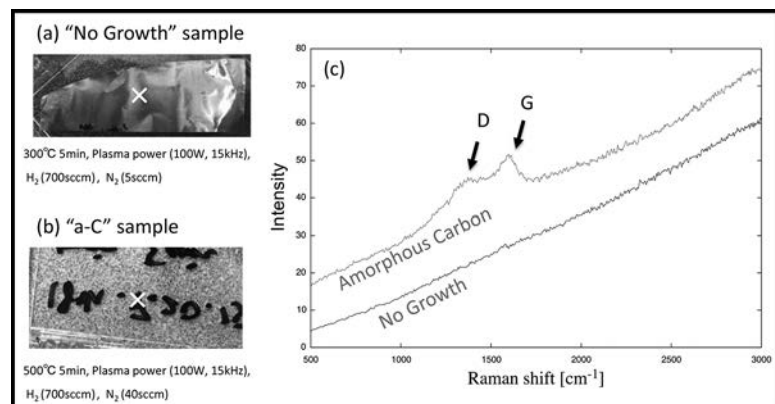


Figure 1: (a) and (b) Optical images after the PECVD growth, and (c) Raman spectra taken from grown samples.

pressure of 23 mbar. Growth temperature ranged from 300°C to 700°C and flow rates of methane and nitrogen were controlled in the range of 5 to 40 sccm. Samples were analyzed with Raman spectroscopy (Thermo Nicolet Alema XR dispersive Raman utilizing 488 nm laser wavelength).

## Results:

The optical images of two samples under different growth conditions are shown in Figure 1(a) and (b). One is an "amorphous carbon ( $\alpha$ -C)" sample and the other is a "no growth" sample. Typical Raman spectra are shown in the right side of Figure 1(c). Using these spectra, we evaluated the crystallinity of the deposited carbon on copper foils. At 300°C, no carbon was deposited on the foil, as evidenced by the lack of D (1350  $\text{cm}^{-1}$ ) and G (1580  $\text{cm}^{-1}$ ) peaks, whereas at 500°C,  $\alpha$ -C was deposited, evidenced by the broad D and G peaks and lack of 2D (2700  $\text{cm}^{-1}$ ) peak. The cause of the "no growth" condition can be due to either the low adsorption coefficient of carbon species or the existence of carbon etchants.

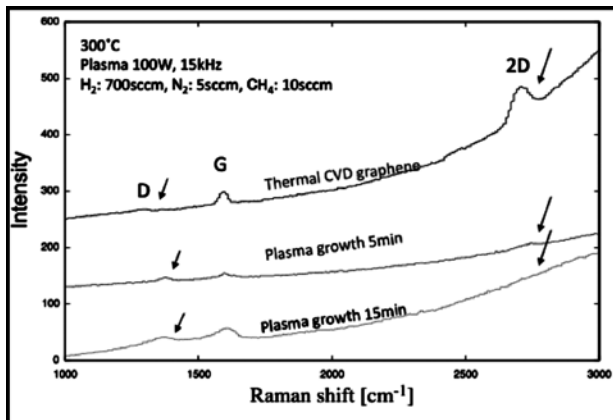


Figure 2: Raman spectra taken from a thermal CVD graphene sample and post plasma growth samples for 5 and 15 minutes.

To verify these possibilities, we put pre-grown thermal CVD graphene samples into the “no growth” condition. The graphene surface was face down and placed on wafer pieces for elevation. Figure 2 shows Raman spectra taken from a thermal CVD graphene sample showing a clear 2D peak and a small D peak. From the Raman spectrum, this graphene is found to have good crystallinity.

This sample was separated into two pieces, and each of them processed in the “no growth” condition for 5 and 15 minutes respectively. As a result, it was found that graphene was etched under these growth conditions, which explain the disappearance of the 2D mode and the appearance of the D peak.

The possible etchants are reactive hydrogen or CN<sup>-</sup> radicals. In these experiments, the copper foils were etched and deposited on the chamber walls of the PECVD furnace. The primarily etchant of copper species in the plasma condition are the CN<sup>-</sup> radicals. The CN<sup>-</sup> radicals are generated by a reaction between reactive C and reactive N, reducing the available carbon species for graphene synthesis. Thus, the balance of methane to nitrogen is an important factor to determine the carbon deposition regime. Additionally, hydrogen is known to etch carbon, which also contributes to the carbon deposition regime [4]. In this research, we did not successfully synthesize graphene, but we hypothesize that a transition regime (shown in Figure 3) exists in which graphene growth is possible at low temperatures.

## Conclusions and Future Works:

In this research, we attempted to grow graphene on copper foils using the PECVD method with a mixture of nitrogen and methane in hydrogen plasma. We found two regimes: the “carbon etching” regime and the “ $\alpha$ -C deposition” regime. These conditions were achieved by varying the ratio of methane flow to nitrogen flow. While no graphene growth was observed, future work will investigate the hypothesized transition region.

## Acknowledgements:

Special thanks to Prof. Eric M. Vogel, Christopher Perini and Brian Beatty for guiding me throughout the project. Also, thanks go out to the Georgia Institute of Technology staff, including Dr. Nancy Healy, Joyce Palmer and Leslie O’Neill for their efforts and assistance. Finally, I would like to acknowledge the NSF (under Grant No. ECCS-0335765), the National Nanotechnology Infrastructure Network International Research Experience for Graduates (NNIN iREG) Program, and NIMS.

## References:

- [1] A. C. Ferrari, et al., *Nanoscale* 7 (2015) 4598.
- [2] T. Yamada, et al., *J. Phys. D: Appl. Phys.* 46 (2013) 063001.
- [3] D. A. Boyd, et al., *Nature Communications*, 6 (2015).6620.
- [4] Zhang, et al., *ACS Nano*, 6 (2012) 126-132.

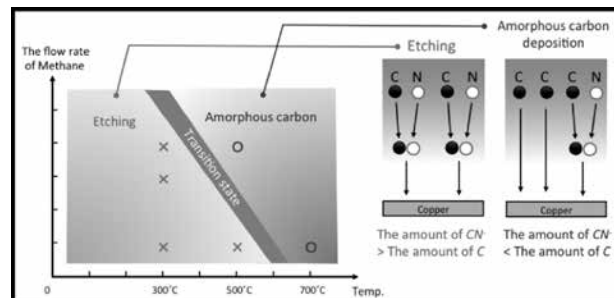


Figure 3: The plot of growth condition and the characteristics of deposited carbon.

# Nanofabrication and Characterization of Quasicrystal Metasurfaces using Shadow-Sphere Lithography

**Emily MacDonald**  
**Physics, Whitworth University**

**NNIN REU Site: Center for Nanoscale Systems, Harvard University, Cambridge, MA**

NNIN REU Principal Investigator: Prof. George M. Whitesides, Chemistry and Chemical Biology, Harvard University

NNIN REU Mentors: Alex Nemiroski and Mathieu Gonidec, Chemistry and Chemical Biology, Harvard University

Contact: emacdonald16@my.whitworth.edu, gwhitesides@gmwgroup.harvard.edu, alex.nemiroski@gmail.com

## Abstract:

The fabrication and screening processes of quasicrystalline metasurfaces have been optimized to reduce the time and the cost using shadow-sphere lithography (SSL) and template-directed self-assembly. Characterization of these quasicrystals has revealed sharp peaks in reflectance, as well as features as small as 20 nm. The parallel configuration of the these quasicrystals allows for hundreds to be fabricated and characterized within hours — much faster than they could be simulated.

## Introduction:

Aperiodic and quasiperiodic metasurfaces have great potential for application to ultrasensitive biosensing, but their development has been slowed by difficulties in; i) fabricating them over large areas, and ii) simulating their optical properties computationally. To address these challenges in nanophotonics, the Whitesides lab has recently developed a method for high-throughput fabrication and screening of quasicrystalline metasurfaces using template-directed self-assembly combined with shadow-sphere lithography (SSL). In this project, we focused on optimization of the self-assembly process and on the quasicrystal fabrication and characterization. The speed, versatility of the patterns, and reproducibility of the fabrication process allow for a remarkably quicker and cheaper method for fabrication.

## Method:

**Templated Self-Assembly.** Templated self-assembly reduces the time of fabrication from weeks for a single to a few hours for hundreds. The silicon template was created by first direct writing a pattern into a mask. The image on the mask was a  $6 \times 13$  array of different quasicrystals, with changing incremental spacing between the holes and different rotational orientations. This image, a single  $3.5 \times 7$  mm rectangle, was then projected five times smaller using an i-line stepper onto a 76.2 cm photoresist-covered silicon wafer 77 times, until the wafer was covered. The spheres were assembled into the holes of the wafer and then transferred to a glass slide using PDMS. This process is more clearly laid out in Figure 1.

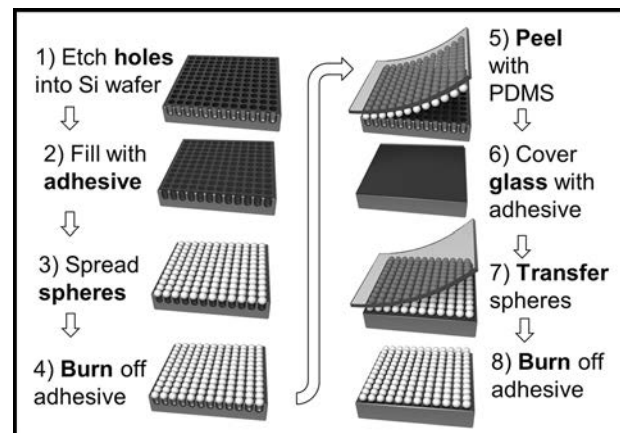


Figure 1: Diagram of the templated self-assembly process [1]. This template shows an arbitrary square pattern.

The spheres retain the pattern initially etched into the silicon. The template is then reusable 10-20 times, allowing for thousands of quasicrystals to be created using a single wafer.

**Shadow-Sphere Lithography.** Shadow-sphere lithography (SSL) combines techniques from shadow lithography and nanosphere lithography, optimizing both to obtain the finest features. To fabricate, the substrate was placed on a custom-made stage at anywhere between a  $45^\circ$ - $70^\circ$  angle to the horizontal inside an electron-beam evaporator. Using electron beam physical vapor deposition (EBPVD), a thin film of titanium and then gold was deposited onto

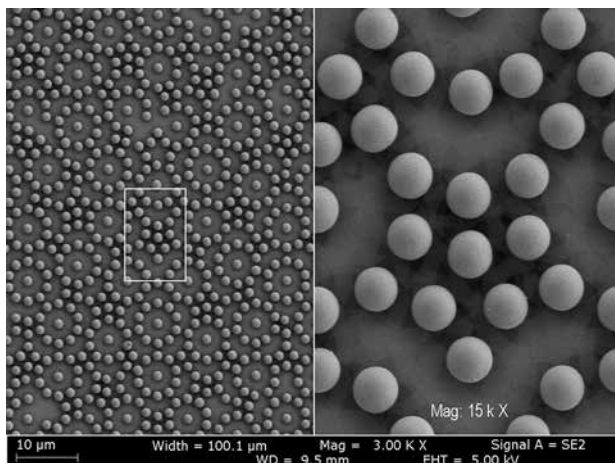


Figure 2: Spheres assembled in a Penrose tiling pattern on the left. On the right is a 5 $\times$  magnified image of one of the central features with the shadow patterns in between.

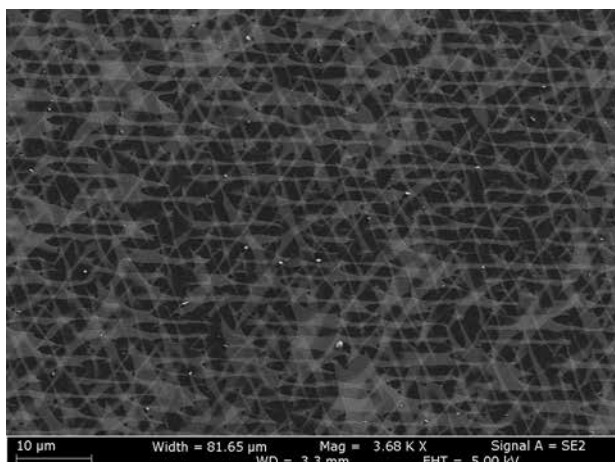


Figure 3: The shadow patterns after the spheres have been removed of a Penrose tiling pattern. The lighter gray is the deposited gold with features smaller than 100 nm.

the stage, which was suspended upside down inside the vacuum chamber. The sample was then rotated while maintaining the original tilt from the horizontal for each deposition of titanium, and then repeated for gold. The spheres were then removed using a simple piece of tape, leaving the shadow patterns — the places where the spheres blocked — behind. Figure 2 shows the spheres and the shadow patterns between them. Figure 3 shows the shadow patterns after the spheres have been removed.

## Results:

Using scanning electron microscopy (SEM), it was possible to measure the width of the features on the metasurfaces. Each sample was also characterized using Fourier transform infrared spectroscopy (FTIR). Ideally, the thinner the lines, the sharper the peak in reflectance at certain mid-IR wavelength values. The desired result for sharp peaks was obtained as can be seen in Figure 4,

although not as sharply defined as expected. The difference in spacing led to a sharper peak for the patterns with more densely packed spheres, where the shadow patterns were finer.

## Conclusions and Future Work:

We provided proof-of-concept for the fabrication of metasurfaces. Templatized self-assembly is possible and allows for a rapid, low-cost method of patterning spheres for the fabrication of quasicrystals, with minimal defects. Mechanizing this process could lead to an almost 100% transfer rate of the spheres. Shadow-sphere lithography creates fine features with replicable accuracy and allows for quasicrystals to be created in parallel. This drastically decreases the time and money required to fabricate and characterize these metasurfaces. Trends can be seen in changing the spacing of the spheres and the rotational orientation in an array of quasicrystals; however, more in-depth analysis needs to be conducted.

## Acknowledgements:

Special thanks to my Principal Investigator, George M. Whitesides, and to my mentors Alex Nemirovski and Mathieu Gonidec, as well as to Baris Unal and the staff of Harvard University's Center for Nanoscale Systems. Funding was provided by the NNIN REU Program and the NSF with grant NSF ECCS-0335765.

## References:

[1] Nemirovski, A., et al., Engineering shadows to fabricate optical metasurfaces, *ACS Nano*, 8(11): 11061-70, 2014.

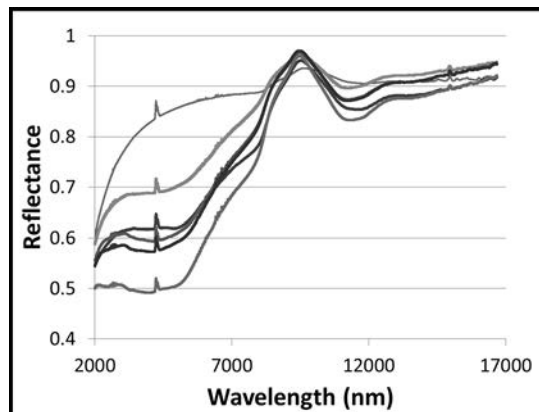


Figure 4: Graph of reflectance from an FTIR scan from 2-17  $\mu$ m of one column, as spacing increases. The highest line is the background reflectance of the substrate. The lowest line belongs to the most densely packed pattern of spheres. A sharp peak is visible around 10  $\mu$ m.

# Improved Sputtering Conditions for *in situ* Crystallization of PZT Thin Films

Travis O'Neil

Chemical Engineering, Clarkson University

NNIN REU Site: Penn State Nanofabrication Laboratory, The Pennsylvania State University, University Park, PA

NNIN REU Principal Investigator: Dr. Susan Trolier-McKinstry, Materials Science and Engineering, The Pennsylvania State University

NNIN REU Mentor: Hong Goo Yeo, Materials Science and Engineering, The Pennsylvania State University

Contact: oneilm@clarkson.edu, set1@psu.edu, hxy162@psu.edu

## Abstract:

The applications of piezoelectric microelectromechanical systems based on  $\text{Pb}(\text{Zr}_x\text{Ti}_{1-x})\text{O}_3$ , or PZT, thin films could be expanded by the use of flexible metal foil substrates. Strongly oriented  $\langle 001 \rangle$  PZT thin films showing high piezoelectric response with a low dielectric constant have been grown on flexible nickel foil substrates by chemical solution deposition (CSD), which improved the figure of merit for piezoelectric energy harvesters [1]. The goal of this research was to develop a process for growing comparable films by high temperature sputtering, thereby simplifying the deposition process for obtaining desired film thickness with high density and allowing for *in situ* crystallization.

## Introduction:

Lead zirconate titanate ( $\text{Pb}(\text{Zr}_x\text{Ti}_{1-x})\text{O}_3$ , or PZT) has been used for various applications including transducers, sensors, actuators [2] and energy harvesters. Typically, research on these thin films involves platinized silicon substrates. Using flexible metal substrates, such as nickel foil, could vastly improve the uses of PZT thin films due to the improved mechanical durability and flexibility of the metal foil, and because the foil does not mechanically constrain the PZT layer as much as a rigid substrate.

Growth of films greater than  $\sim 0.2 \mu\text{m}$  by CSD requires that the spin deposition-pyrolysis-crystallization process be run multiple times. Developing a process for sputtering PZT onto flexible metal substrates would allow for just one deposition step to be done using *in situ* crystallization, thereby eliminating potential drawbacks caused by CSD.

In this experiment, PZT was sputtered onto platinum/titanium/silicon dioxide/silicon substrates with and without a PZT seed layer. This substrate was used because the passivated nickel (Ni) foil requires additional processing steps. Controlling both chamber pressure and oxygen flow during the deposition alters the lead content of the deposited film, which is vital for obtaining pure perovskite PZT without the presence of the non-piezoelectric pyrochlore phase. Temperature was also adjusted to determine the *in situ* crystallization temperature for perovskite PZT.

## Experimental Procedure:

PZT thin films were deposited by radio-frequency (RF) magnetron sputtering. The target used for the process

was  $\text{Pb}(\text{Zr}_{0.52}\text{Ti}_{0.48})\text{O}_3$ , or PZT (52/48), with 10 mole percent excess lead oxide. Additional PbO compensated for loss due to evaporation and/or resputtering, since the sputtering occurred at elevated temperatures and PbO is easily volatilized.

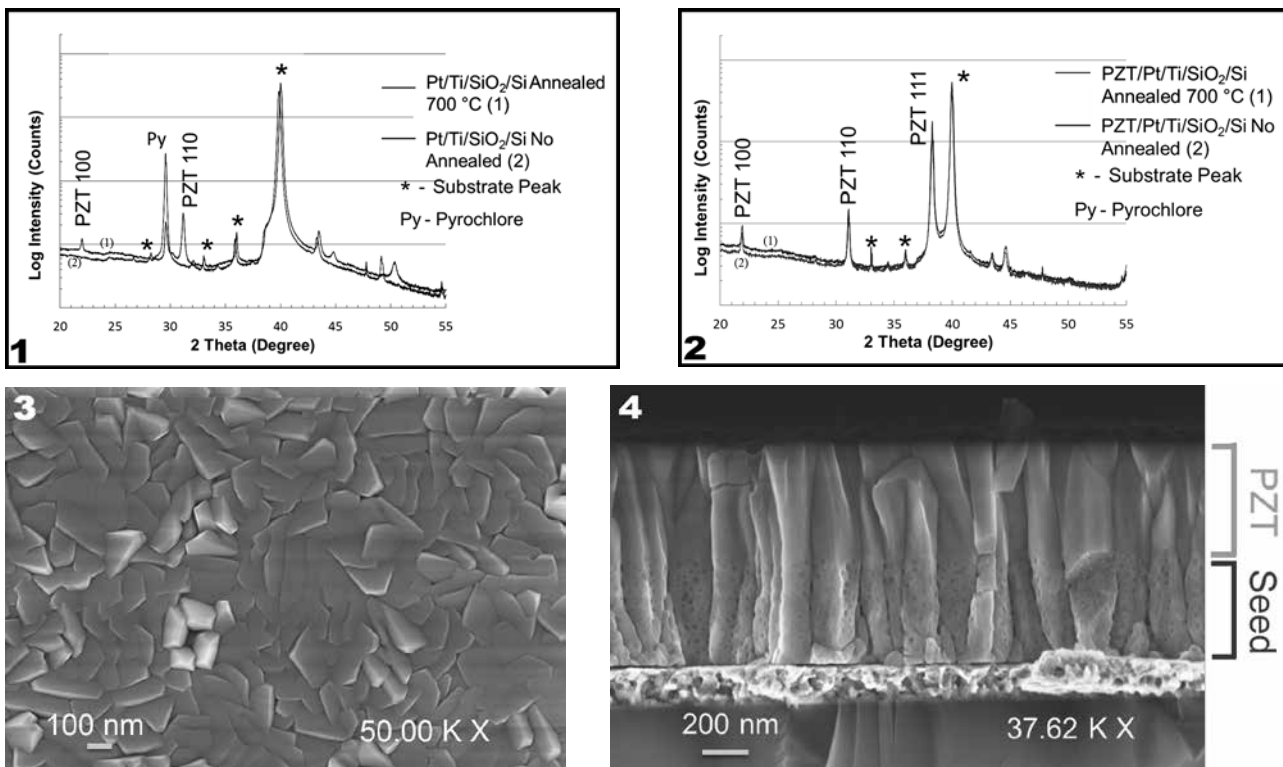
Before the deposition started, the substrates were first gradually heated up and stabilized at a desired temperature. The heating dwell time for the samples in this experiment was set at 90 minutes.

After that, the deposition was run for 15,000 seconds at 90 watts RF power in an argon atmosphere, under varying conditions of temperature, chamber pressure, and oxygen flow. The conditions were optimized sequentially based on the results of previously sputtered samples. Films were sputtered onto the non-seeded and the seeded PZT substrates at the same time. Half of each sample was then rapid thermal annealed (RTA) at  $700^\circ\text{C}$  in  $\text{O}_2$  to check for phase and microstructure changes.

X-ray diffraction (XRD) patterns, microstructure images taken by field-emission scanning electron microscopy, and electrical characterization (low field dielectric constant and polarization hysteresis data) were obtained to analyze each sample.

## Results and Conclusions:

For the first series of experiments, the chamber Ar pressure was increased. At higher chamber pressures, the bombardment of the growing films is reduced. This, in turn, reduces the presence of the pyrochlore phase. The set temperature was also adjusted in the range of  $600\text{--}700^\circ\text{C}$ .



It was found that changing only the Ar pressure did not lead to phase-pure perovskite films. Without oxygen flow during sputtering, the best sample was grown at 12 millitorr and 670°C. However, the non-seeded sample showed pyrochlore and the seeded sample showed low intensity perovskite peaks. The seeded sample did show saturated polarization hysteresis loops. These experiments indicated that 670°C was around the crystallization temperature. Neither the XRD perovskite peak intensity nor the microstructure for samples sputtered at this temperature showed much change after annealing.

It has been shown that introducing oxygen into the sputter gas can help initiate perovskite growth on Pt/Ti/SiO<sub>2</sub>/Si [3]. In addition, increasing the ratio of oxygen to argon in the sputter gas decreases the lead content of the deposited film [4]. For the next series of experiments, samples were sputtered at 670°C with either 3 or 5% oxygen flow rate in the sputter gas, at different set pressures. It was found that having 3% oxygen flow in the sputter gas, as opposed to 5%, better reduced the pyrochlore present on the XRD patterns. The best sputter conditions of 670°C, 9 mTorr with 3% oxygen flow resulted in an intense pyrochlore peak for the non-seeded sample (Figure 1), yet very intense perovskite peaks for the seeded sample (Figure 2). Samples sputtered under these conditions but with lower pressure showed decreased perovskite crystallinity and increased pyrochlore. It was also shown that sputtering at higher temperatures led to dense films, as seen in Figures 3 and 4.

### Moving Forward:

In future work, electrical characterization is needed for films grown at a 9 mTorr chamber pressure at 670°C with 3% oxygen in the sputter gas. It is likely that final optimization will be done by iterative experiments based on structural and electrical characterization. After optimum conditions are found, Ni foil substrates will be used.

### Acknowledgements:

I would like to thank my principal investigator Dr. Susan Trolier-McKinstry, mentor Hong Goo Yeo, Kathy Gehoski, and the entire Penn State Nanofab staff for their help throughout this project. This research was supported by the NNIN REU Program and the National Science Foundation under grant no. ECCS-0335765.

### References:

- [1] Yeo, H., Trolier-McKinstry, S. (2014). *J. Appl. Phys* 116. 014105-014105.
- [2] "Physical Basis." Morgan Technical Ceramics. Web. 25 July 2015. <[http://www.morgantechicalceramics.com/sites/default/files/documents/chapter2\\_1.pdf](http://www.morgantechicalceramics.com/sites/default/files/documents/chapter2_1.pdf)>.
- [3] Velu, G., et al. (n.d.). *Vacuum* 56, 199-204.
- [4] Komaki, K., et al. (1994). *Jpn. J. Appl. Phys* 33, 443-446.

# Delta-Doping of Diamond

Stephanie Pastor

Aerospace and Mechanical Engineering, University of Florida

NNIN REU Site: Howard Nanoscale Science and Engineering Facility, Howard University, Washington, DC

NNIN REU Principal Investigator: Dr. Gary Harris, Electrical and Computer Engineering, Howard University

NNIN REU Mentor: Mr. James Griffin, Electrical Engineering, Howard University

Contact: [snpastor5@hotmail.com](mailto:snpastor5@hotmail.com), [gharris1124@gmail.com](mailto:gharris1124@gmail.com), [jagriffin@howard.edu](mailto:jagriffin@howard.edu)

## Abstract:

The nitrogen-vacancy (NV) center in diamond has emerged as a possible versatile tool for data storage in quantum information processing. The NV center consists of a substitutional nitrogen atom located adjacent to a naturally occurring vacancy within the diamond lattice. The spins of the unbound electrons within the bond can be coherently controlled at room temperature and read out optically. The focus of this project was to determine the optimal conditions for NV center production in synthetic, polycrystalline diamond by growing and doping with  $^{15}\text{N}$  gas in a hot filament chemical vapor deposition (HFCVD) reactor. The nitrogen isotope allowed us to distinguish our deposited nitrogen atoms from other impurities, such as  $^{14}\text{N}$  or silicon atoms, that may also be present within the grown diamond.

## Introduction:

Quantum computers are considered to be the next revolution in data processing because they will have much faster computing power than modern-day computers. Quantum bits (qubits), the basic unit for quantum information, are formed by electron spins that can be controlled and manipulated to store and read out data. The NV center will allow us to implement logic in the form of these qubits.

## Experimental Procedure:

Silicon (Si) and silicon carbide (SiC) samples were cleaned by sonication in acetone and then methanol for one minute each. Nanodiamonds, approximately 5 nm diamond seeds used to increase nucleation density, were deposited by sonicating the samples in an equal volume mixture of

nanodiamond solution and methanol for 10 minutes, then rinsing in methanol.

The diamond films were grown in an HFCVD reactor. As seen in Figure 1, the introduction of hydrogen ( $\text{H}_2$ ) and methane ( $\text{CH}_4$ ) gases into the hot filament zone causes decomposition of the gases into simpler molecules and atoms. Atomic hydrogen helps to further decompose the hydrocarbon species at and above the heated substrate surface, leaving behind only carbon atoms for diamond and/or graphitic growth. The atomic hydrogen was also used to etch any graphitic material formed during the growth process.

During the diamond growth process, the flow rate of hydrogen and methane were maintained at 80 sccm and 1 sccm respectively. The chamber pressure and substrate

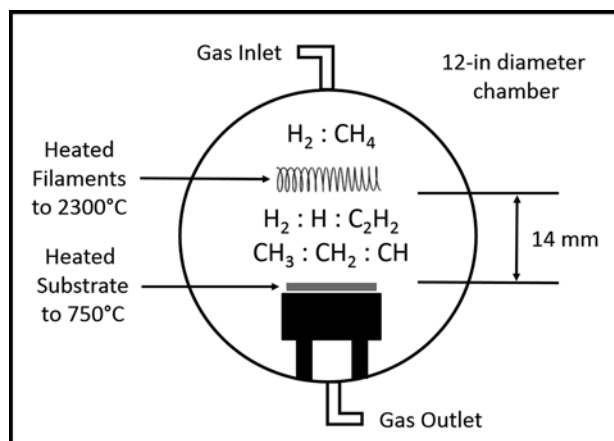


Figure 1: Diagram of HFCVD growing chamber.

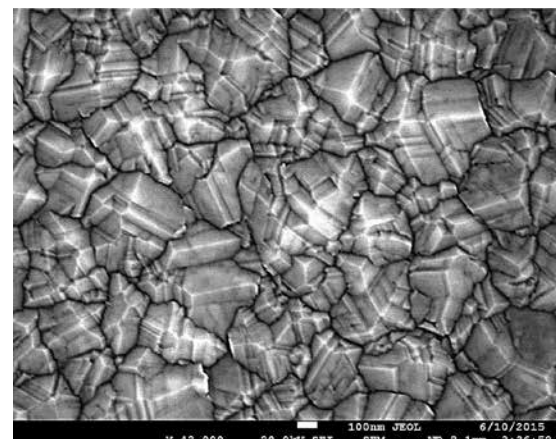


Figure 2: SEM image of diamond grown on Si.

temperature were maintained at 20 torr and 750°C respectively. These conditions yielded a diamond growth rate of 0.167  $\mu\text{m}/\text{hour}$  at a substrate-to-filament gap of 14 mm. Figure 2 shows a scanning electron microscope (SEM) image of diamond grown on Si after this process.

Delta doping of diamond with  $^{15}\text{N}$  gas was performed during diamond growth at the surface or a few nanometers below the surface. In one experiment, the  $^{15}\text{N}$  gas flow rate was varied from 4 to 12 sccm while growing on both Si and SiC substrates with a substrate-to-filament gap of 14 mm. The goal of this experiment was to determine how NV center concentration varied with  $^{15}\text{N}$  gas flow rates.

In a second experiment, the  $^{15}\text{N}$  gas flow rate was varied from 2 to 12 sccm with a substrate-to-filament gap reduced to 7 mm. The goal of this experiment was to see if NV center concentration varied with substrate-to-filament gap. Since the mean-free path of atomic nitrogen is finite, reducing the distance the atomic nitrogen has to travel before incorporation in the diamond lattice may increase NV center production.

## Results:

Figure 3 shows a typical Raman spectrum of HFCVD diamond grown throughout this work. This particular sample was grown on silicon and the diamond was

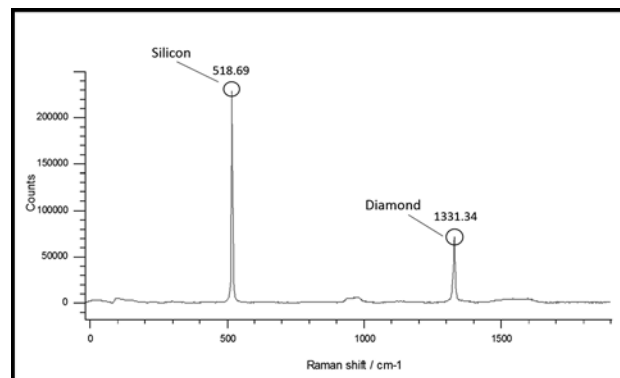


Figure 3: Raman data of undoped diamond on Si.

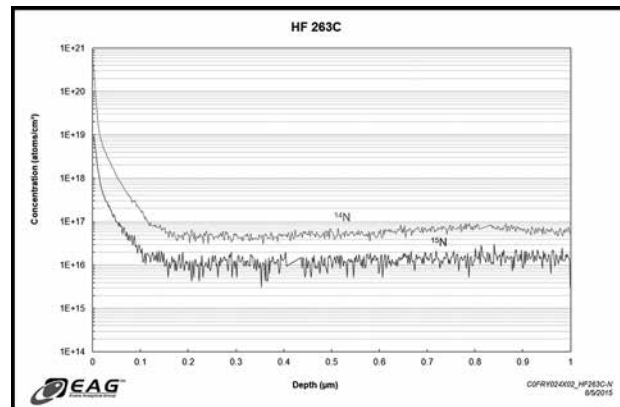


Figure 4: SIMS data indicating nitrogen concentration of a doped diamond on Si sample.

undoped with an average roughness of 40 nm. The sharp diamond peak at 1331.34  $\text{cm}^{-1}$  with a FWHM of 7.6  $\text{cm}^{-1}$  is indicative of high quality diamond. All of the diamond films grown by the seeding process are polycrystalline. Because the equipment necessary for NV center detection was not available locally, the samples were sent out for characterization. Unfortunately the tool that was used did not detect any NV centers in the samples. This was believed to be an equipment malfunction and not an absence of NV centers. Previous experiments using the same tool indicated NV center presence with a 637 nm zero-phonon emission on  $^{14}\text{N}$  doped HFCVD diamond.

Secondary ion mass spectrometry (SIMS) analysis of one surface delta doped diamond sample was obtained, see Figure 4. This plot shows the concentration of  $^{14}\text{N}$  and  $^{15}\text{N}$  atoms as a function of depth from the surface. At the surface it is clear that both  $^{14}\text{N}$  and  $^{15}\text{N}$  were incorporated in the diamond film at very high concentrations, with  $^{14}\text{N}$  reaching over  $10^{20}$  atoms/ $\text{cm}^3$  and  $^{15}\text{N}$  reaching about  $10^{19}$  atoms/ $\text{cm}^3$ .

## Conclusions:

High quality diamond was grown on Si and SiC substrates by HFCVD. The fact that the diamond films were polycrystalline may or may not prove detrimental for NV center purposes. However, growth of diamond on diamond substrates is desirable due primarily to a much smoother surface. SIMS data indicated a delta doped behavior of both  $^{14}\text{N}$  and  $^{15}\text{N}$  in diamond films. Unfortunately, determination of how  $^{15}\text{N}$  gas flow rates and filament-to-sample gaps affect NV center production is still unknown for this reactor. However, in previous experiments involving the doping of diamond with  $^{14}\text{N}$  gas, NV centers were characterized and produced under similar parameters. Therefore, it is reasonable to conclude that NV centers exist in diamond films doped with  $^{15}\text{N}$  gas.

## Acknowledgements:

I would like to thank the following individuals and organizations for their support: Dr. Gary Harris, Mr. James Griffin, the Howard Nanoscale Science and Engineering Facility at Howard University, the Laboratory for Nanoscale Optics at Harvard University, the National Nanotechnology Infrastructure Network International Research Experience for Undergraduates (NNIN iREU) Program and the National Science Foundation, Grant No. ECCS-0335765.

## References:

- [1] May, P.; CVD Diamond - a New Technology for the Future? *Endeavour*, Volume 19, Issue 3, Pages 101-106, 1995.
- [2] Wöhrl, N. (Director) (2014, December 30). Diamonds Are a Quantum Computer's Best Friend. 31<sup>th</sup> Chaos Communication Congress of the Chaos Computer Club. Lecture conducted from, Hamburg.

# Diverse Patterns and Geometries in Self-Assembled Block Copolymer Thin Films Through Multilayer Mixing

**Christopher Phenicie**

**Physics, University of Minnesota-Twin Cities**

**NNIN REU Site: Colorado Nanofabrication Laboratory, University of Colorado, Boulder, CO**

NNIN REU Principal Investigator: Mark P. Stoykovich, Chemical and Biological Engineering, University of Colorado, Boulder

NNIN REU Mentor: Garrett Chado, Chemical and Biological Engineering, University of Colorado, Boulder

Contact: pheni004@umn.edu, mark.stoykovich@colorado.edu, garrett.chado@colorado.edu

## Abstract:

Lithography via the self-assembly of block copolymers is a promising tool for nanostructure fabrication on the order of 10 nm. Once assembled, one block of the copolymer can be selectively removed and metal can be deposited on the remaining pattern. This can be used to create structures such as metal nanodots and highly connected metal nanowire networks with varying periodicities. The morphology of the block copolymer self-assembly is dependent on the volume fraction of each block in the copolymer. A technique called multilayer mixing is presented, whereby we are able to change the morphology of block copolymer after the block copolymer has self-assembled, by increasing the volume fraction of one of the blocks. This is accomplished through spin casting a layer of homopolymer on top of it and solvent annealing the sample to let it reach the equilibrium morphology.

## Introduction:

Block copolymers (BCPs) are a class of macromolecules consisting of two chemically distinct, covalently bonded polymer chains. The BCP phase separates into regular patterns with structures on the order of 10 nm. These features have long range ordering, consistent across chips at least one square centimeter in size. The patterns formed through BCP self-assembly is dependent on the volume fraction of each block in BCP.

## Materials and Methods:

A substrate with neutral preference for each block of the BCP was prepared by coating a silicon wafer with the random copolymer poly(styrene-r-methyl methacrylate-r-glycidyl methacrylate)  $P(S_{0.58}-r-MMA_{0.41}-r-GMA_{0.01})$  brush layer, where the subscripts indicate the mole fraction of each monomer. Silicon wafers were purchased from Montco Silicon and rinsed with DI water, acetone, and toluene via spin casting prior to depositing the brush layer. The neutral substrate was then thermally annealed at 190°C for 60 min under vacuum, followed by sonication in toluene for 5 min and spin coating in toluene for 30 s at 5000 rpm.

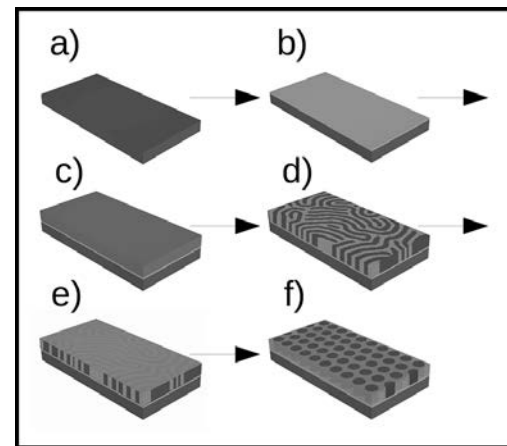


Figure 1: (a) All block copolymer is deposited on a silicon substrate (b), which is functionalized with a brush layer of PS-r-ePMMA. (c) Then, lamellar BCP is deposited on the brush via spin casting. (d) The block copolymer is then solvent annealed to form lamellae. (e) After annealing, PMMA homopolymer is deposited on top of the lamellae via spin casting and (f) the samples is solvent annealed once again, allowing the PMMA to mix with the lamellae (“multilayer mixing”) to form cylinders.

Lamellar forming poly(styrene-*b*-(methyl methacrylate-r-glycidyl methacrylate), PS-*b*-(PMMA-*r*-GMA), was synthesized by sequential atom transfer radical polymerization of styrene (Sigma-Aldrich, 99%), methyl methacrylate (Acros, 99%), and glycidyl methacrylate (MP Biomedicals, 99%) as reported elsewhere [1]. All BCP samples were deposited via spin casting at 5000 rpm for 30 s. The BCPs were self-assembled through solvent vapor annealing in an even mixture of acetone and cyclohexane for 4 hr. The solvents were degassed in a 25 mTorr vacuum to remove any dissolved gases prior to solvent annealing.

Multilayer mixing was achieved by depositing a layer of PMMA homopolymer on the lamellar BCP after annealing. The PMMA homopolymer used for the multilayer mixing was purchased from Polymer Source (M.W. = 21.2 kg mol<sup>-1</sup>, PDI = 1.07). Prior to deposition of this PMMA homopolymer, BCP samples were baked at 90°C for

30 min. The PMMA homopolymer was deposited via spin casting at 5000 rpm for 30 s. Samples were solvent annealed in the same conditions as the first solvent anneal. Samples were etched to improve image clarity (RIE, 160 mTorr oxygen plasma, 55W, 5 s).

### Discussion:

Multilayer mixing was achieved as shown schematically in Figure 1. In essence, the method allowed the equilibrium morphology of the BCP to be changed, from lamellae to cylinders, through the addition of PMMA homopolymer. As shown in Figure 2, the addition of PMMA homopolymer increased the volume fraction of PMMA in the thin film, inducing a phase transition from the lamellar to the cylindrical morphology. A BCP that is 77% PMMA has an equilibrium morphology of hexagonally packed cylinders. This shows that multilayer mixing is capable of transitioning one equilibrium BCP morphology to a distinct equilibrium morphology.

However, for the samples with less than 77% PMMA, notice in Figure 2 that the cylinders tended to follow the lamellae rather than have hexagonal packing. This suggests that the mechanism of multilayer mixing involves lamellae breaking up into cylinders. This was further substantiated by annealing BCP with 77% PMMA for less than 4 hr, as shown in Figure 3. With less annealing time, the samples did not have enough time to reach their equilibrium morphology of hexagonally packed cylinders. These images then show how the process of solvent annealing evolved over time. Figure 3 suggests that, in this process, cylinders first formed following the previously existing lamellae and then reorganized to achieve hexagonal packing. If so, the spacing of cylinders can be controlled by first directing the assembly of lamellae before the multilayer mixing.

### Conclusions:

It has been shown that it is possible to control the self-assembled patterns of block copolymers via the technique of multilayer mixing. This has applications, for instance, to computer memory devices, allowing the creation of smaller nanodots and nanowires for computer chips. Future research could include directing the assembly of lamellae to guide cylinder formation.

### Acknowledgements:

This research was supported by the National Science Foundation under Grant No. ECCS-0335765. The author would like to thank CNL and NCF staff for help with sample preparation and characterization, and NNIN staff for organizing this National Nanotechnology Infrastructure Network Research Experience for Undergraduates (NNIN REU) Program.

### References:

[1] He, C. et al., Small, 2015 DOI: 10.1002/smll.201403364.

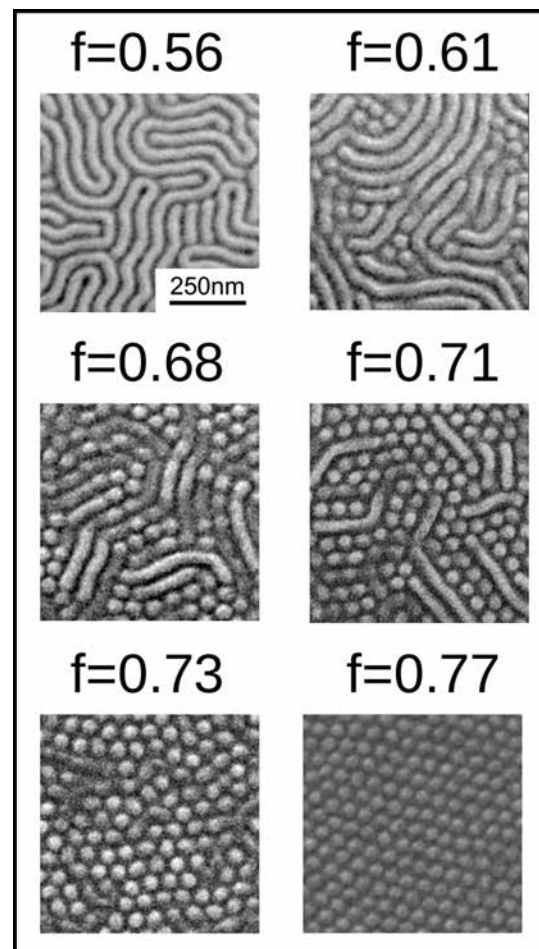


Figure 2: SEM images of BCP morphology after multilayer mixing with varying volume fraction of PMMA. A second layer of varying concentration of PMMA ( $M.W. = 21.2 \text{ kg mol}^{-1}$ ) was spin cast and allowed to mix with the BCP layer under solvent vapor for 4 hours to create samples with varying volume fraction of PMMA ( $f$ ).

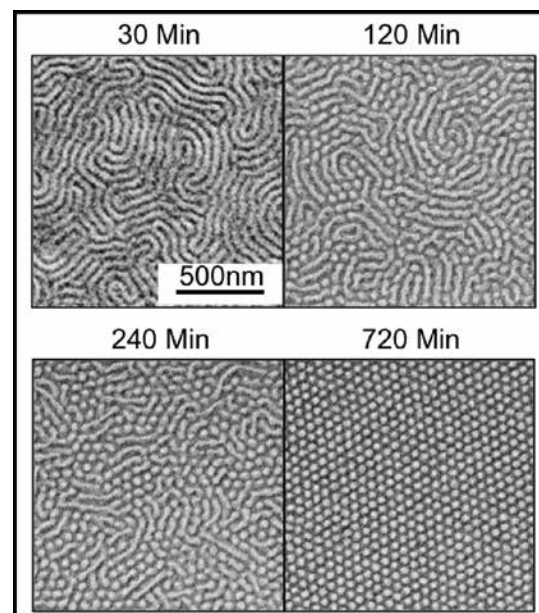


Figure 3: SEMs of cylinders created from multilayer mixing with PMMA annealed at varying times. Each image is a snapshot of the annealing process as a function of time.

# Synthesis and Characterization of Size- and Shape-Specific Gold Nanocrystals for Superlattice Assembly

**Elyse Pizzella**

**Chemical Engineering, North Carolina State University**

**NNIN REU Site: Washington Nanofabrication Facility and Molecular Analysis Facility, University of Washington, Seattle, WA**

NNIN REU Principal Investigator: Vincent Holmberg, Chemical Engineering, University of Washington

NNIN REU Mentors: Soohyung Lee and Elena Pandres, Chemical Engineering, University of Washington

Contact: [ecpizzel@ncsu.edu](mailto:ecpizzel@ncsu.edu), [holmvc@uw.edu](mailto:holmvc@uw.edu), [shlee16@uw.edu](mailto:shlee16@uw.edu), [epandres@uw.edu](mailto:epandres@uw.edu)

## Abstract:

In this work, gold nanoparticles of different shapes and sizes were systematically synthesized, characterized, and assembled. The best control over their size distribution and morphology was achieved using seed-mediated growth. By varying reaction and sample preparation conditions, gold nanocrystal (AuNC) growth was directed into various shapes. These nanocrystals were characterized using UV-vis spectroscopy, scanning electron microscopy (SEM), and transmission electron microscopy (TEM) to determine final shapes and packing structures. The amount of free ligand in solution and the concentration of seeds used in the growth solution resulted in visible differences in both nanocrystal morphology and their packing assemblies. Sample preparation conditions, including drying temperature, drying speed, and droplet orientation, were also investigated. By successfully controlling reaction parameters and sample preparation conditions, it is possible to synthesize uniform, ordered structures with tailored shape- and size-specific properties.

## Introduction:

Colloidal AuNCs have many applications in optical [2] and medical sensing, and when assembled into collective structures, their properties are even further tunable. In this work, AuNCs were synthesized and assembled into close-packed structures.

## Experimental Procedure:

Size- and shape-specific gold nanocrystals were fabricated using seed-mediated growth [4], which involved making aqueous seed solutions and growth solutions separately. By exploring parameters involved in synthesis and preparation, we hoped to achieve ordered, close-packed structures of AuNCs by producing crystals with monodisperse shape and size.

**Seed Solution Preparation.** A 10 mL aqueous solution of  $2.5 \times 10^{-4}$  M hydrogen tetrachloroaurate trihydrate ( $\text{HAuCl}_4$ ) and 0.10 M cetyltrimethylammonium chloride (CTAC) was prepared. Next, a cold, 10 mL aqueous solution of sodium borohydride ( $\text{NaBH}_4$ ) was prepared. When ready, 45  $\mu\text{L}$  of the  $\text{NaBH}_4$  solution was added to the  $\text{HAuCl}_4$  solution and allowed to stir for two minutes to initiate nucleation of AuNC seeds. The solution was then aged for at least one hour at 30°C.

**Growth Solution Preparation.** Multiple aqueous growth solutions were prepared (10 mL total volume). The synthesis of two shapes of gold nanocrystals (cubes and rhombic dodecahedra) were targeted. To direct the nanocrystal shape, different amounts of ascorbic acid (the shape-directing agent) were added. All reagent volumes

in the growth solutions were kept constant (0.32 g CTAC, 250  $\mu\text{L}$  stock  $\text{HAuCl}_4$ , and 10  $\mu\text{L}$  of 0.01 M NaBr solution) except for the water and ascorbic acid. For cubic shapes, 9.625 mL deionized water and 90  $\mu\text{L}$  ascorbic acid were added to the other reagents in the vials; for rhombic dodecahedral shapes, 9.565 mL deionized water and 150  $\mu\text{L}$  ascorbic acid were added.

**Directing the AuNC Size.** To tune the nanocrystal size, the volume of seed solution added to the growth solutions was varied. For each target shape (cubes and rhombic dodecahedra), three different nanocrystal sizes were prepared by adding 25  $\mu\text{L}$ , 45  $\mu\text{L}$ , and 100  $\mu\text{L}$  of seed solution to the growth solutions.

**Purification and Deposition.** The final solutions were purified via centrifugation, and droplets of the different solutions were deposited onto silicon wafers. Cleanliness of solution, drying temperature, and evaporation rate all affected the AuNC assembly process and SEM image quality.

## Results and Conclusions:

The AuNCs displayed a clear size trend, depending on the volume of seed solution that was added to the growth solution, as shown in Figure 1. As the number of seeds added to the growth solution increased, final nanocrystal size decreased, and vice versa. This is because if larger quantities of seed are added to a growth solution, there is less growth reagent available per seed, resulting in smaller crystals.

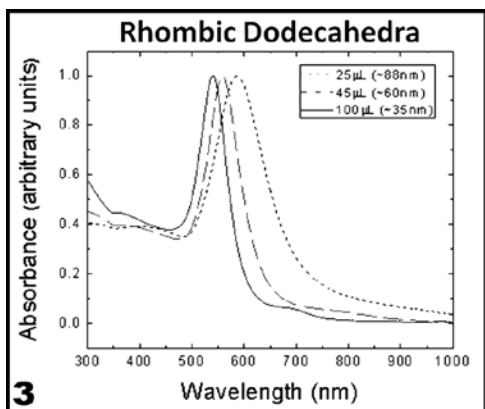
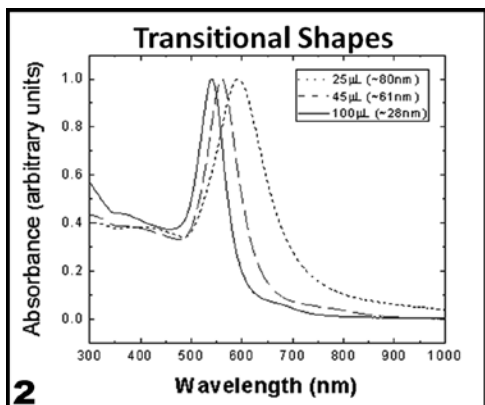
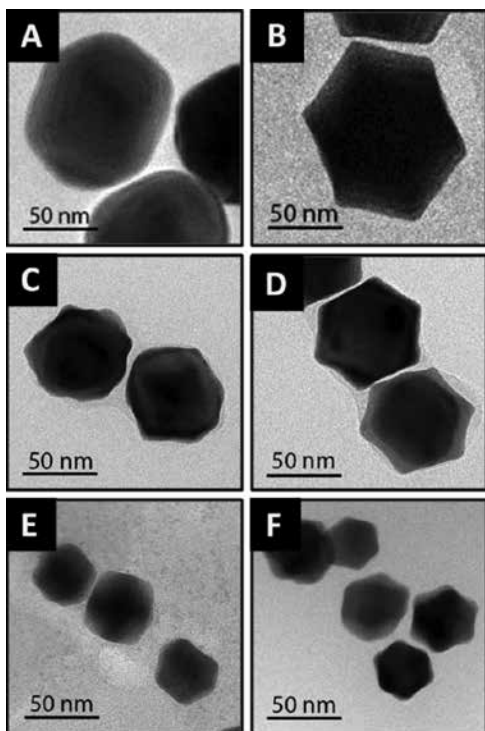


**Figure 1, top:** AuNCs with different volumes of seed solution added. Left column: Transitional shapes; A) 25  $\mu$ L, C) 45  $\mu$ L, E) 100  $\mu$ L. Right column: Rhombic dodecahedra; B) 25  $\mu$ L, D) 45  $\mu$ L, F) 100  $\mu$ L. **Figure 2, middle:** The largest size AuNC (80 nm) has the plasmon band furthest in the infrared because its electrons oscillate at a longer wavelength than smaller size AuNCs. **Figure 3, bottom:** A similar trend in plasmon frequency is seen here with a red-shift in peak position as the AuNC increases in size.

In Figures 2 and 3, there is shown a clear trend between the optical properties of the AuNCs and their size. Since gold is a plasmonic material, different AuNC diameters resulted in different plasmon bands (the peaks in the graphs). This is because the electrons in the particles oscillated collectively at different frequencies for particles with different dimensions [2].

Although rhombic dodecahedral nanocrystals were synthesized successfully, the cubic shapes that were targeted more closely resembled a transitional shape somewhere between a cube and a rhombic dodecahedron. Figure 4 displays several of the close-packed assemblies that were achieved. It is evident that the size and shape monodispersity of the AuNCs was the most important factor in achieving well-ordered structures.

### Future Work:

With greater control over AuNC size and shape, it is possible to assemble them into chains, 2D superlattices, and 3D supercrystals. These structures enable a variety of applications in metamaterials [2], optical sensors, and acoustic wave sensors [1], due to their collective plasmonic properties [3] when assembled into ordered supercrystals.

### Acknowledgements:

I would like to thank the NNIN REU Program, as well as the NSF, Grant No. ECCS-0335765, for funding this research opportunity. I would like to also express my deepest gratitude to my mentors, Soohyung Lee and Elena Pandres, and my principal investigator, Vincent Holmberg, for what they taught me over the course of this project.

### References:

- [1] Chiu, Chi-Shun, et al. *J. Phys. Chem.*, 117, 2442-2448 (2012).
- [2] Gwo, Shangjr, et al. *Langmuir*, 28, 8902-8908 (2012).
- [3] Lin, M.-H, et al. *J. Am. Chem. Soc.*, 132, 11259-11263 (2010).
- [4] Wu, H.-L, et al. *Langmuir*, 26(14), 12307-12313 (2010).

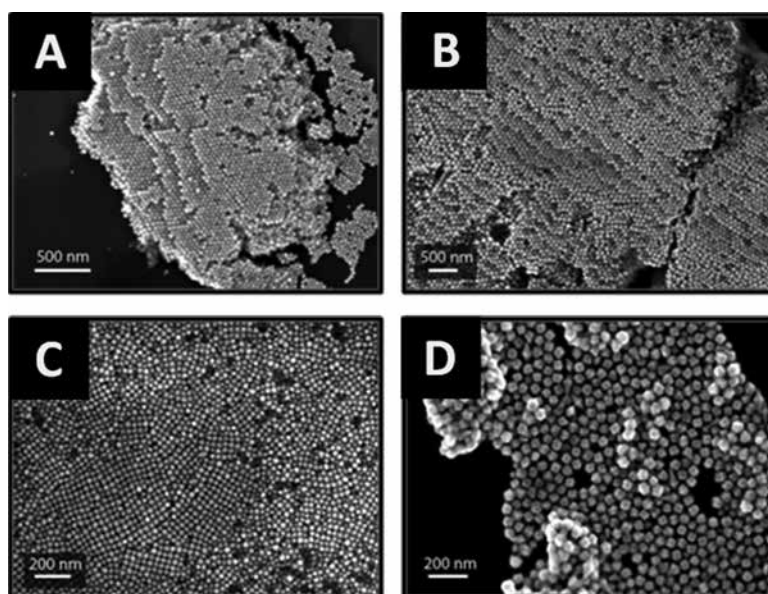


**Figure 4:** Some of the most closely-packed AuNC structures achieved under various conditions. Well-ordered structures occurred largely because of the monodispersity of the crystals within the sample.

# The Optimization of Thin Film Molybdenum Disulfide Synthesis

**Michael Statt**

**Chemical and Biomolecular Engineering, Cornell University**

**NNIN REU Site: Institute for Electronics and Nanotechnology, Georgia Institute of Technology, Atlanta, GA**

**NNIN REU Principal Investigator: Prof. Eric Vogel, School of Materials Science and Engineering, Georgia Institute of Technology**

**NNIN REU Mentors: Philip Campbell and Dr. Alexey Tarasov, School of Materials Science and Engineering, Georgia Institute of Technology**

**Contact: mjs488@cornell.edu, eric.vogel@mse.gatech.edu, philip.campbell@gatech.edu, alexey.tarasov@mse.gatech.edu**

## Abstract and Introduction:

Two-dimensional materials have been a source of great interest and promise due to their interesting thickness-dependent properties. One class of these materials are transition metal dichalcogenides (TMDCs). TMDCs are layered materials with formula  $MX_2$ , where M is a transition metal (Mo, W, etc), and X is a chalcogen (S, Se, Te). TMDCs exhibit high mechanical strength and thickness-tunable band gaps that transition to direct band gaps in the monolayer limit for most TMDCs.

Molybdenum disulfide ( $MoS_2$ ) is one example of a TMDC that has garnered significant interest recently due to its direct band gap at a monolayer thickness, high on/off ratios, and moderate mobilities. These properties make  $MoS_2$  well-suited for applications such as 2D vertical heterostructure devices, thin film optoelectronics, and flexible, transparent electronics [1].

For TMDCs to be compatible with modern electronic fabrication processes, uniform, high quality, wafer-scale growths must be achieved. One straightforward approach to  $MoS_2$  synthesis is the sulfurization of an evaporated thin film of molybdenum by annealing in a sulfur-containing environment at high temperatures. This method has been shown to create highly uniform, wafer-scale, trilayer  $MoS_2$  films [2]. The resulting films, however, suffer from small grain sizes (~ 10 nm), which increase charge-carrier scattering, limit carrier mobility and reduce on/off ratios. This study investigated the effects of high temperature annealing on the crystallinity of  $MoS_2$  films synthesized through sulfurization of thin molybdenum films.

High temperature annealing has been shown to cause lattice recrystallization and coarsening of the resultant grain structure [3]. Experimental results suggest that extended sulfur-rich and sulfur-deficient anneals are currently incompatible with high quality  $MoS_2$  synthesis.

## Experimental Methods:

Silicon wafers were thermally oxidized to form a 300 nm thick layer of  $SiO_2$ . A 1 nm layer of molybdenum was deposited on the  $SiO_2$  using e-beam evaporation. The samples were then placed in a sulfurization furnace and

pumped down to the chamber base pressure (~ 30 mTorr). The samples were annealed at 300°C for 30 minutes in an Ar:H<sub>2</sub> (4:1) atmosphere to remove atmospheric contaminants. In a separate vessel, a powder sulfur source was concurrently heated to 150°C to increase its vapor pressure. The sulfur vapor was injected into the chamber, which was backfilled with argon gas to a total pressure of approximately 5 Torr. The chamber was then heated to 1000°C and allowed to dwell at that temperature for times varying from five minutes to 12 hours to allow for sulfur to diffuse into the molybdenum layer and react to form  $MoS_2$ . This step will be referred to as the sulfur anneal step.

Next, the chamber was purged with argon gas at temperatures varying from 750°C-1000°C to remove any remaining sulfur gas. This process step required a minimum dwell time of 30 minutes to prevent sulfur precipitation on film surface and was extended up to 12 hours to thermally anneal the sample. This step will be referred to as the argon anneal step. The chamber was then cooled to room temperature under an argon flow.

XPS was used to characterize film stoichiometry and elemental composition. Raman spectroscopy was used to identify  $MoS_2$  film uniformity and thickness through the appearance and separation of characteristic  $MoS_2$   $A_{1g}$  and  $E_{2g}^1$  peaks, which have been shown to be correlated with film thickness [4].

## Results and Conclusions:

Sulfur anneal times longer than two hours yielded partially oxidized  $MoS_2$  films, as indicated by the appearance of  $MoO_2$  and  $MoO_3$  peaks in the XPS spectra shown in Figure 1. These films also showed large areas with no characteristic  $MoS_2$  Raman spectroscopy peaks. It was also found that small, ordered, circular regions of anomalous  $MoS_2$  growth occurred in extended sulfur anneal time samples, as shown in Figure 2. These regions grew in size and density when sulfur anneal time was increased. Raman spectroscopy analysis of these regions indicated bulk thickness  $MoS_2$  growth and atomic force microscopy (AFM) analysis showed that these regions were steps

approximately 10-30 nm above the rest of the film. It is currently unknown what caused these bulk thickness regions, but they limited the viability of extended sulfur anneals to increase grain size.

When argon anneal temperatures were kept at 1000°C, argon anneal times longer than two hours yielded samples

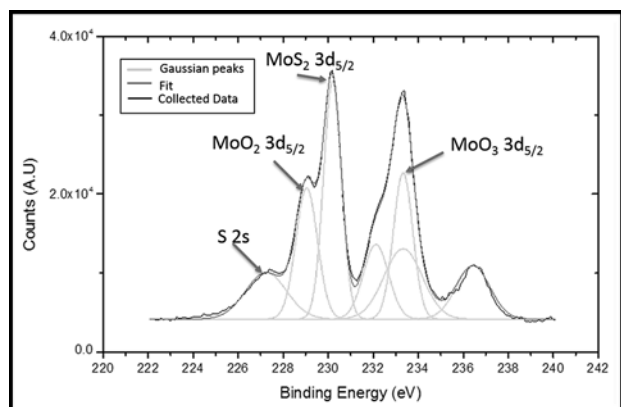


Figure 1: XPS spectra of sample annealed in sulfur-rich environment for 120 minutes.

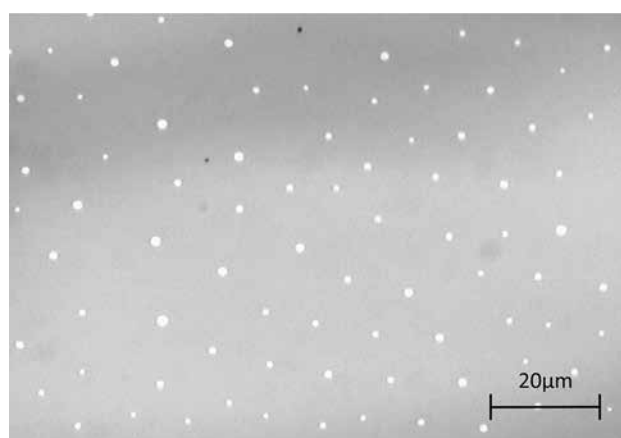


Figure 2: Optical micrograph shows bulk thickness spots on sample grown at 120 minute sulfur anneal time.

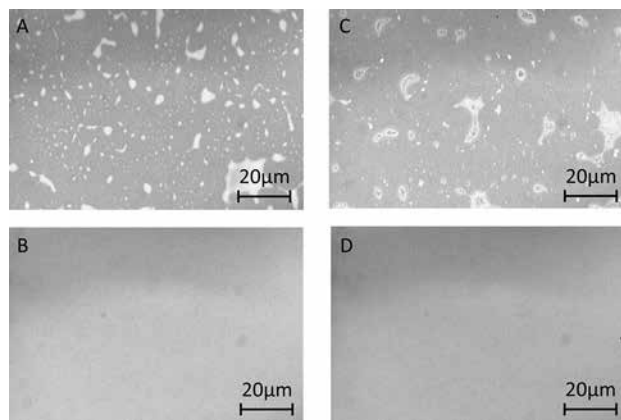


Figure 3: A and B are pre-sulfurization, C and D are post-sulfurization. A and C were cleaned with IPA and acetone, B and D were not.

with little to no sulfur content, as indicated by XPS analysis, and no characteristic MoS<sub>2</sub> peaks in Raman analysis. When temperatures were reduced to 750°C, a two hour argon anneal resulted in MoS<sub>2</sub> peaks in Raman analysis, but peak separation indicated highly varying thickness across the sample ( $\pm$  3 monolayers). This indicated that sulfur may be evaporating from the MoS<sub>2</sub> film due to a concentration gradient between the film and the sulfur-deficient atmosphere. Currently, this limitation makes extended argon anneals an unviable option for increasing crystallinity in MoS<sub>2</sub> films.

During this investigation it was found that using organic solvents, isopropyl alcohol and acetone, to clean samples caused bulk thickness MoS<sub>2</sub> growth similar to that seen in extended sulfur anneal times. Figure 3 shows this through two samples grown concurrently: one cleaned with organic solvents and one cleaned only with a nitrogen gun. Bulk MoS<sub>2</sub> grew in regions where residue from organic solvents was present, while no MoS<sub>2</sub> grew in regions without residue. This indicates that organic surface contamination on the sample is altering the surface chemistry of the reaction.

### Future Work:

These preliminary results indicate that high temperature anneals detrimentally affect MoS<sub>2</sub> film quality. In the future, conditions causing bulk thickness growth during long sulfur anneals must be quantified and mitigated to allow for uniform thickness growths. Transmission electron microscopy (TEM) and low energy electron diffraction (LEED) must be used to image MoS<sub>2</sub> grain structure.

### Acknowledgements:

I would like to thank Professor Eric Vogel for this opportunity, the Vogel group for their mentorship; and Joyce Allen, Leslie O'Neill, and Dr. Nancy Healy for their coordination. This research was supported by the National Nanotechnology Infrastructure Network Research Experience for Undergraduates (NNIN REU) Program and NSF (Grant No. ECCS-0335765).

### References:

- [1] Wang, Q. H; Nature Nanotechnology; 7(11), 699-712, (2012).
- [2] Tarasov, A; Advanced Functional Materials; 6389-6400 (2014).
- [3] Humphreys, F. J.; Recrystallization and related annealing phenomena, Elsevier; (1995).
- [4] Lee, C.; ACS Nano; 4(5), 2695-2700. (2010).

# High Storage Capacity Sodium-Ion Battery Electrodes of Solution-Grown Germanium Nanowires

**Yuichi Tsujiura**

**Mechanical Engineering, Kobe University, Japan**

**NNIN iREG Site: Microelectronics Research Center, The University of Texas, Austin, TX**

NNIN iREG Principal Investigator: Dr. Brian A. Korgel, Chemical Engineering, The University of Texas at Austin

NNIN iREG Mentor: Taizhi Jiang, Chemical Engineering, The University of Texas at Austin

Contact: [tsujiura@stu.kobe-u.ac.jp](mailto:tsujiura@stu.kobe-u.ac.jp), [korgel@che.utexas.edu](mailto:korgel@che.utexas.edu), [tjiang@utexas.edu](mailto:tjiang@utexas.edu)

## Introduction:

Sodium-ion batteries (NIBs) have attracted attention as an alternative to lithium-ion batteries (LIBs) because sodium (Na) is so much more abundant and inexpensive than lithium (Li). NIBs, however, require much higher performance in order to displace the use of LIBs. One problem is that graphite—the negative electrode material used in LIBs—has no considerable reversible capacity for NIBs [1]. Therefore, NIBs require the development of new electrode materials. Germanium (Ge) is one promising candidate for the negative electrode, with reversible sodiation at room temperature with a relatively high theoretical capacity (NaGe, 369 mAh/g) [2], comparable to graphite for LIBs. In nanowire form, Ge can also tolerate the volume changes that occur during cycling without degradation, and a high surface area-to-volume ratio yields suitable charge/discharge kinetics in the battery.

Ge nanowires (GeNWs) were synthesized by a supercritical-fluid-liquid-solid (SFLS) growth process [3] and three procedures were applied to improve NIB performance. First, GeNWs were activated for sodiation by an initial lithiation cycle that amorphized the nanowires. Kohandehghan, et al., showed that crystalline GeNWs do not sodiate until being activated with Li [4]. Second, the surface of Na foil counter electrodes were polished to remove surface oxide, which greatly enhanced the performance of GeNW half-cells. Third, the role of the thickness of GeNW electrode layer was studied to understand kinetic limitations of the battery.

## Experimental Procedure:

GeNWs were produced by the SFLS growth process. A reactant solution containing 25  $\mu$ L of Au nanocrystal stock solution, 190  $\mu$ L of DPG, and 85  $\mu$ L of monophenylsilsane (MPS) in toluene was injected into a reactor heated to 380°C and pressurized to 6.2 MPa at a rate of 0.5 mL/min for 40 minutes.

For testing in coin cells, GeNWs were combined with poly(acrylic acid) (PAA) binder and conductive carbon at a weight ratio of 70:20:10 [5]. To obtain a viscous slurry,

the mixture was dispersed in 1-methyl 2-pyrrolidinone (NMP). Then, the slurry was doctor-bladed (50-200  $\mu$ m gap) onto copper (Cu) foil and vacuum dried at 150°C. Individual 11 mm diameter circular electrodes were hole-punched from the coated Cu foil.

The GeNWs were activated for sodiation by an initial lithiation step. An LIB half-cell was assembled from stainless steel coin cells, GeNW anode, Li foil counter

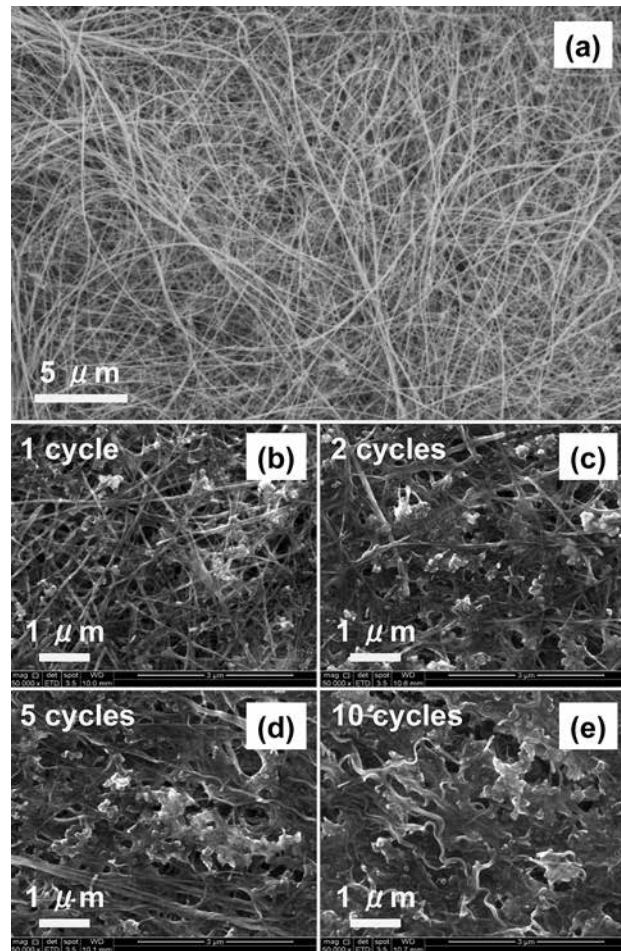
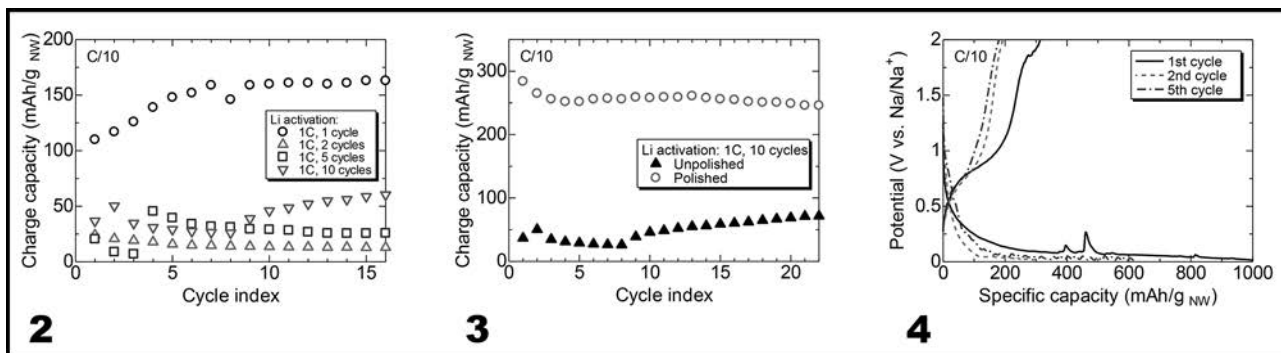


Figure 1: SEM images of (a) as-grown GeNWs and (b)-(e) Li-activated GeNWs with 1, 2, 5, and 10 cycles.



**Figure 2, left:** The charge capacity of NIBs with Li-activated GeNW anode with each cycle. **Figure 3, middle:** The charge capacity of NIBs with polished and unpolished Na foil counter electrode. **Figure 4, right:** The voltage profile of NIB with GeNW electrode film thickness of 1.0  $\mu\text{m}$ .

electrode, a few drops of electrolyte, and separator. After charging and discharging with Li for one cycle at a rate of 1C, the LIB is disassembled. The GeNW anode is then reassembled into a half-cell with a Na foil counter electrode. The NIB was tested at a rate of C/10.

## Results and Conclusions:

Figures 1(a) and (b)-(e) show SEM images of the GeNWs before and after cycling against Li. In Figures 1(b)-(e), the SEM images show that the solid electrolyte interphase (SEI) layer increased in thickness with each lithiation cycle. Figure 2 shows the cycle performance of NIBs made with GeNWs activated with Li with a different number of cycles. The highest charge capacity in the NIB was obtained with a single lithiation/delithiation activation cycle. Based on the SEM data, it appears that thicker SEI layers formed during the Li activation step hampers NIB performance and should be limited as much as possible.

Figure 3 shows NIB data for GeNW coin cells made with polished and unpolished Na foils. The polished Na foil counter electrode led to charge capacities that were three times higher than the NIBs made with unpolished electrodes. To improve reversibility, the effect of GeNW electrode film thickness was studied. Figure 4 shows the voltage profile of the NIB with a GeNW layer thickness of 1.0  $\mu\text{m}$ . A charge capacity of more than 300 mAh/g was obtained. Changes in the layer thickness from 0.7  $\mu\text{m}$  to 1.3  $\mu\text{m}$  did not affect the battery performance. This electrode layer thickness probably represents a rate-limiting thickness.

## Future Work:

Future work will involve the synthesis of tin (Sn)-coated GeNWs to enhance reversibility and rate capability in

the electrode. The influence of thinner electrode layers on the NIB rate capability and charge capacity will also be studied. Further optimization of the electrode layer density to improve the specific capacity and the Coulombic efficiency of NIBs is also desirable.

## Acknowledgments:

The author would like to appreciate his principal investigator Dr. Brian A. Korgel, mentor Taizhi Jiang, and all the other members of Korgel research group at the University of Texas at Austin. Dr. Marylene Palard and Jean L. Toll helped as the site coordinators. The author would also like to acknowledge the financial support from the National Nanotechnology Infrastructure Networks International Research Experience for Graduates (NNIN iREG) Program and the National Science Foundation (NSF) in the U.S. (under Grant No. ECCS-0335765), and the National Institute for Materials Science (NIMS) in Japan.

## References:

- [1] M. D. Slater, et al., *Adv. Funct. Mater.* 23, 947-958 (2013).
- [2] P. R. Abel, et al., *J. Phys. Chem. C* 117, 18885-18890 (2013).
- [3] V. C. Holmberg and B. A. Korgel, *Chem. Mater.* 22, 3698-3703 (2010).
- [4] A. Kohandehghan, et al., *Nano Lett.* 14, 5873-5882 (2014).
- [5] A. M. Chockla, et al., *ACS Appl. Mater. Interfaces* 4, 4658-4664 (2012).

# Characterization of Quantum Confined Two-Dimensional Electron Gasses

**Veronika Werner**

**Electrical Engineering, Purdue University**

**NNIN REU Site: UCSB Nanofabrication Facility, University of California, Santa Barbara, CA**

**NNIN REU Principal Investigator: Prof. Chris Palmstrøm, Electrical and Computer Engineering, and Materials, UCSB**

**NNIN REU Mentor: Mihir Pendharkar, Electrical and Computer Engineering, University of California, Santa Barbara**

**Contact: v Werner@purdue.edu, cpalmstrom@ece.ucsb.edu, mihir@ece.ucsb.edu**

## Introduction:

Spintronics, or spin electronics, which depend on electron spin, could be faster, smaller and more energy efficient than traditional charge-based electronics. Here, two-dimensional sheets of electrons, or two-dimensional electron gasses (2DEGs), were characterized. They showed properties important to spintronics, such as high electron mobilities and long mean free path. Quantum confined 2DEGs formed in gallium arsenide/aluminum gallium arsenide (GaAs/AlGaAs) heterostructures were simulated using a Poisson/Schrödinger equation solver before the heterostructures were grown by molecular beam epitaxy (MBE). Hall bars were fabricated using photolithography, etching and metal contact formation for use in magnetotransport measurements. The Integer Quantum Hall Effect was observed in these devices and temperature dependence of electron mean free path, mobility and density were studied. These results will be used to develop better material systems for next-generation electronics and spintronics.

## Experimental Procedure:

The four basic steps in characterizing two-dimensional electron sheets are design of material structures for quantum confinement, growth of materials, fabrication of Hall bar devices and measurement and analysis.

In the design stage, a Poisson/Schrödinger equation solver [1] was used to simulate the heterostructures. A heterostructure was made up of two or more kinds of dissimilar materials layered on top of one another [2], in this case—materials with different energy band gaps. Gallium arsenide (GaAs) has a relatively low band gap of 1.424 eV at 300 K. Aluminum arsenide (AlAs) has a band gap of 2.12 eV at 300 K [3]. For the heterostructures used here, GaAs was layered with AlGaAs, because the band gap of AlGaAs can be adjusted by changing the Al content.

Two different quantum wells were used, a square well, and an inverted well. The square well had a symmetric layer structure, with gallium arsenide layer in between layers of aluminum gallium arsenide. The inverted quantum well had only one layer of gallium arsenide, with one GaAs/AlGaAs interface, as seen in Figure 1. This differs from a triangular, or conventional quantum well, in that the

low band gap material was at the surface, rather than the higher band gap material.

After a design was chosen, the heterostructure was grown by MBE. Elemental source materials were used and the environment was kept at ultra high vacuum, enabling sharply defined interfaces, sub-monolayer control of thickness, precise control of material composition and minimization of unintentional impurities. This process was essential in achieving the high quality heterostructures necessary for 2DEGs displaying high electron mobility and long mean free path.

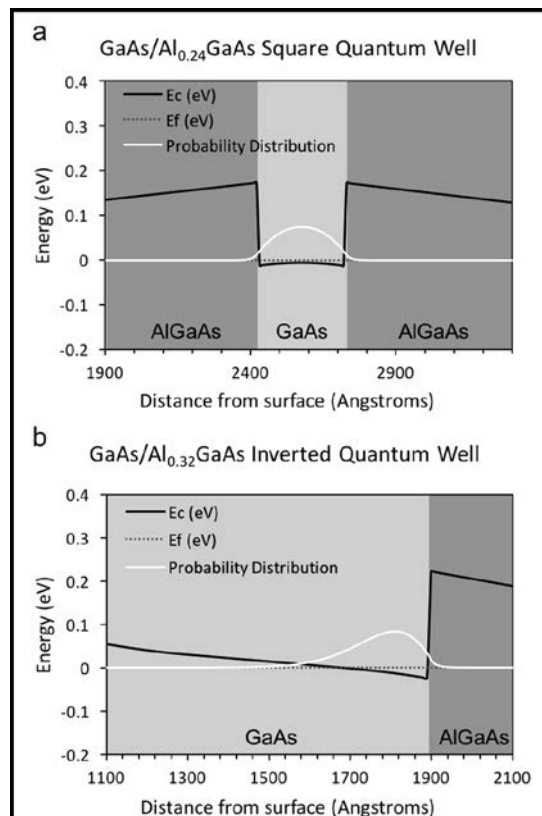


Figure 1: This image shows the conduction bands, Fermi levels and electron waveform probability distribution for; a. a square well, and b. an inverted quantum well.

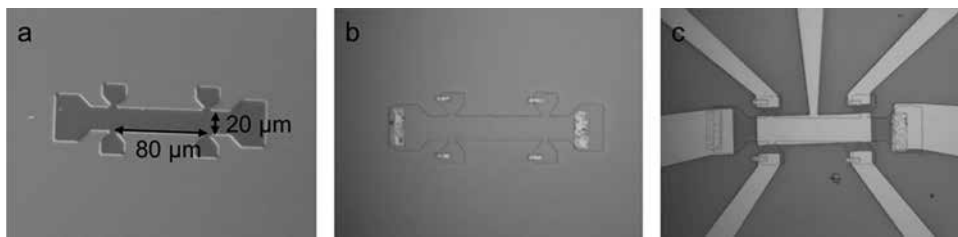


Figure 2: This is a Hall bar; a. after chemical wet etch, b. after metal contact deposition, lift-off and anneal, and c. after metal lead deposition and lift off. Note that the dimensions are  $80 \times 20 \mu\text{m}$ .

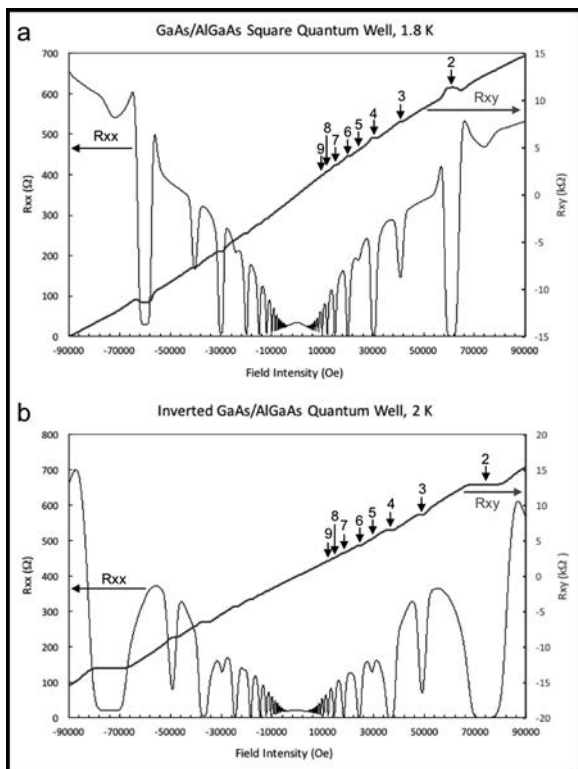


Figure 3: The Integer Quantum Hall Effect observed in; a. a square well, and b. an inverted well. Plateaus in  $R_{xy}$  correspond to dips in  $R_{xx}$  and occur where  $R_{xy}$  is equal to  $1/i$  times  $h/e^2 \approx 25.813 \text{ k}\Omega$ ,  $i$  being an integer.

Hall bars were fabricated using photolithography. They were simple devices, consisting of a basic rectangle, with connection points for voltage probes and current sources.

Figure 2 shows a Hall bar at various points in fabrication. Figure 2a. shows the pattern after the unnecessary material has been etched away using a chemical wet etch, leaving behind a Hall bar shaped mesa. Figure 2b. shows the device after the deposition of metal contact pads by electron beam deposition and subsequent annealing. The annealing step is necessary to form an ohmic contact, or one that is linear in current/voltage relationship, between the semiconductor and the metal. Finally, metal leads are deposited, as seen in Figure 2c. Their purpose is to connect to the pads and provide a larger surface area to which wires can be bonded.

To determine electron mobility and mean free path, measurements were taken for a range from -9 to 9 Tesla magnetic field and from 1.8 to 300 K for temperature. An alternating current was sourced and lock-in amplifiers were used to measure AC voltages

in order to reduce electrical noise. Two resistances were measured: parallel to current,  $R_{xx}$ , and perpendicular to it,  $R_{xy}$ , defined as the perpendicular voltage,  $V_{xy}$ , divided by longitudinal current,  $I_{xx}$ . These values were used to calculate electron mobility, electron sheet density, and mean free path.

## Results:

The Integer Quantum Hall Effect, which is a hallmark of 2D electron transport, was observed for the samples tested [4]. Figure 3 shows some of the measured results.

The fact that this effect was observed shows that the structure produced successfully confined the electrons to a two-dimensional sheet. For the two samples whose results are shown, the mobility and mean free path at 2 K for the square well were  $870,000 \text{ cm}^2/\text{Vs}$  and  $5.48 \mu\text{m}$  and for the inverted quantum well,  $1,200,000 \text{ cm}^2/\text{Vs}$  and  $7.6 \mu\text{m}$ .

## Conclusion and Future Work:

These results were typical for the structures that achieved 2DEG confinement, indicating that these samples show promise for future spintronics research. The next steps in this research would be to investigate spin injection into these quantum wells, using ferromagnetic contacts.

## Acknowledgements:

I would like to thank my mentor, Mihir Pendharkar, for teaching me about these exciting topics and guiding me through my research. I would also like to thank Prof. Chris Palmstrøm and the rest of his lab group for being so welcoming and sharing their knowledge. This experience was made possible through the NNIN REU Program, and the NSF (under Grant No. ECCS-0335765). The facilities used were part of the Nanofabrication Facility and the Materials Research Laboratory at UCSB.

## References:

- [1] Snider, G. 1D Poisson Solver (computer program), UND.
- [2] Kroemer, H. (2000). Quasi-Electric Fields and Band Offsets: Teaching Electrons New Tricks. Nobel Lecture.
- [3] Ioffe Physico-Technical Institute. NSM Archive.
- [4] Störmer, H. L. (1998). The Fractional Quantum Hall Effect. Nobel Lecture.

# Microfluidic Pipette Array for Single Cell Mechanics Studies

Danielle Chase

Mechanical Engineering, University of Minnesota

NNIN REU Site: Lurie Nanofabrication Facility, University of Michigan, Ann Arbor, MI

NNIN REU Principal Investigator: Prof. Allen Liu, Mechanical Engineering, University of Michigan

NNIN REU Mentor: Dr. Lap Man Lee, Mechanical Engineering, University of Michigan

Contact: chase230@umn.edu, allenliu@umich.edu, melmlee@umich.edu

## Introduction:

Pathological processes are mediated by a disruption in biochemical signaling, where cell mechanics can play a critical role [1]. For example, the stiffness of a cancer cell can affect its ability to deform and squeeze through the extracellular matrix to lymphatic or blood vessels during metastasis to distant organs. The study of cell mechanics requires micro-engineered tools to apply a localized force and make precise physical measurements. Micropipette aspiration is a classical tool used for mechanical analysis of single cells, and several cell mechanical properties can be measured by studying cell deformation [2]. This technique, however, is limited by its low throughput and requires highly specialized training in practice. Recently, our lab has developed a microfluidic device based on multilayer polydimethylsiloxane (PDMS) soft-lithography to study single cell mechanics in an automatic and parallel manner [3]. Through the manipulation of volume flow rates, this device is able to trap and apply a precise pressure difference across single cells. In this work, we incorporated a flow control layer intended to improve the trapping efficiency of single cells and conducted simulations and experimental studies to characterize the device. This novel microfluidic device was used to characterize the mechanical properties of human breast cells. The potential to increase the throughput of this microfluidic pipette array device will enable clinical applications in mechanophenotyping.

## Method:

Figure 1 depicts the three main components that constitute the microfluidic pipette array. The PDMS membrane of the control channels was deflected using a pneumatic system to increase the flow resistance in the main channel and force fluid to flow through the micropipettes to load single cells into the aspiration chambers. Upon the release of the control layer, increasing the flow rate in the main channels exerted a pressure across the cell to aspirate it into the micropipette.

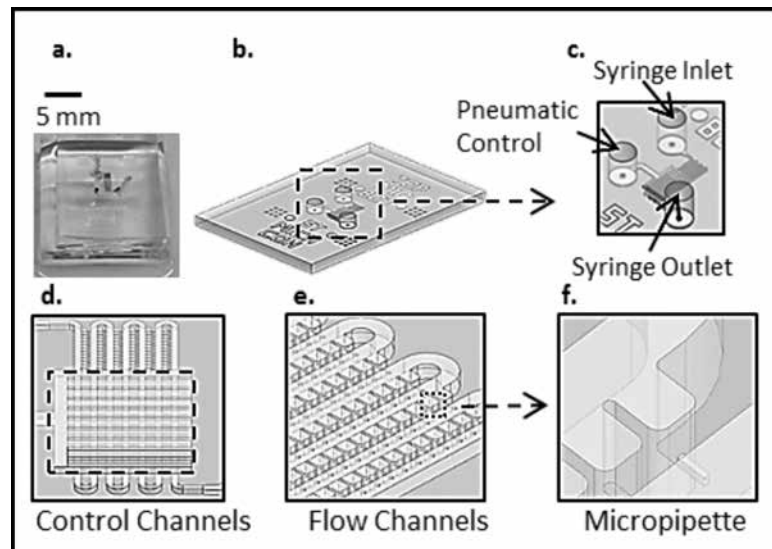


Figure 1: The microfluidic pipette array device. (a) PDMS device, (b) overall schematic, (c) device components and controls (d) control channels, (e) flow channels, (f) aspiration chamber and micropipette.

Three silicon molds were fabricated for PDMS casting of both flow and control layers using SU-8 photoresist patterning. The first mold defines the top half of the flow layer and micropipettes, while a second mold defines the bottom half of the flow layer. The third mold defines the control channels. After demolding the control layer, it was bonded to the top flow layer using a custom PDMS alignment setup. The top and bottom flow layers were then demolded, aligned, and bonded together to form the flow channel.

Numerical simulations of an incompressible, laminar flow model in COMSOL were used to characterize the deflection of the control channels under pneumatic pressure and the effect on single cell trapping efficiency. For experimental operation, a syringe pump was used to control the flow of cells into the microfluidic channels, and a pneumatic control was used to pressurize the control channels. An optical microscope (Nikon TiS) with 20 $\times$  magnification objective was used for time lapse imaging of cell deformation. MatLab image analysis of the radius of the cell and protrusion length during aspiration can

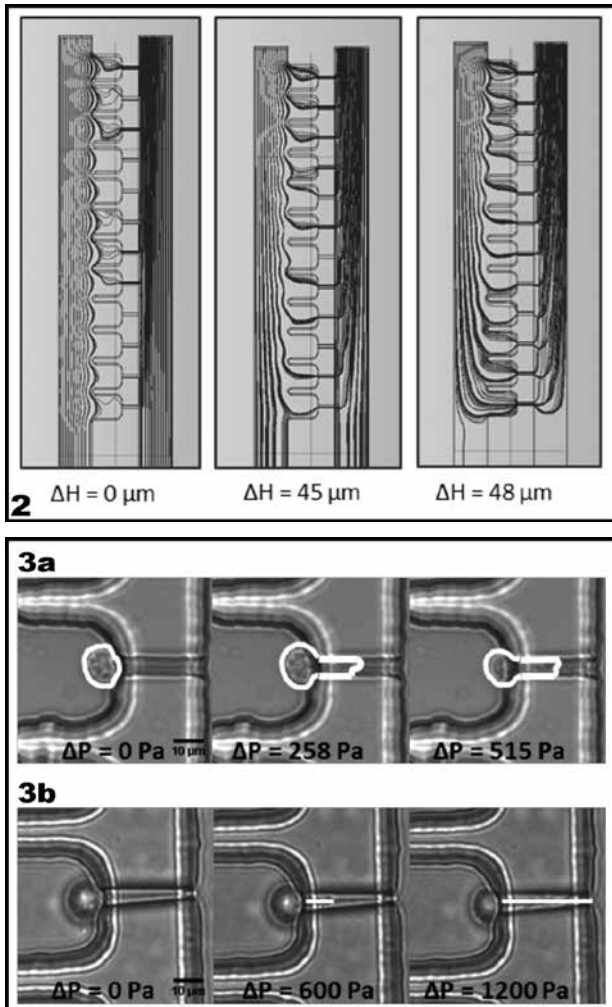


Figure 2, top: Streamlines in the microfluidic pipette array indicating where cells will follow the streamlines and be trapped in the aspiration chambers for varying deflections of the PDMS membrane, where  $\Delta H$  is the deflection. (COMSOL simulations.) Figure 3, bottom: Aspiration of cells into the micropipettes. (a) MDA-MB-231 cell in a straight pipette, where the white line indicates the contour of the cell, (b) MCF-10A cell in a tapered pipette, where the white line indicates the protrusion length.

be used to determine the Young's modulus and cortical tension of human breast cell lines of non-tumorigenic MCF-10A cells and metastatic MDA-MB-231 cells.

### Results and Conclusions:

Figure 2 shows the numerical simulation results of streamlines in the microfluidic channels for varying deflection of the PDMS membrane. An increase in deflection corresponds to an increase in the ratio of fluid flowing through the pipettes compared to the main channel. A deflection of 45  $\mu\text{m}$  in the 50  $\mu\text{m}$  channel resulted in a flow ratio greater than one, which means that more fluid is flowing through each pipette than through the main channel. Experimentally, we observed that the control channels had a minimal effect on the streamlines, and saw no significant improvements in trapping efficiency. This result is possibly due to the challenge

of blocking a rectangular channel by the deflection of a PDMS membrane without rupturing the membrane or causing air bubbles to enter the flow channels through the porous PDMS. Mineral oil could potentially be used to prevent air bubbles, and using a thinner PDMS membrane and a wider flow channel might improve deflection and the flow resistance. Upon trapping, micropipette aspiration was conducted by increasing the flow rate to exert a pressure on the cells as shown in Figure 3. The lengths of the protrusions were measured in order to calculate the stiffness of the cell.

Figure 4 shows the increase in the protrusion in the micropipette of an MDA-MB-231 human breast cancer cell as the pressure difference across the cell increases over time. The Young's modulus of the MDA-MB-231 cell was measured to be 125 Pa, and the cortical tension of the MCF-10A cell is 1.47 mN/m. These preliminary results indicate that successful operation of the control channels will improve trapping efficiency to increase throughput for studying single cell mechanics. The stiffness of cells can easily be measured using the microfluidic pipette array.

### Acknowledgements:

I would like to thank Professor Allen Liu, Dr. Lap Man Lee, the members of the Liu lab, and the staff of the Lurie Nanofabrication Facility for their guidance and support. This work was supported by the NSF under Grant No. ECCS-0335765 and by the National Nanotechnology Infrastructure Network Research Experience for Undergraduates (NNIN REU) Program.

### References:

- [1] J. Guck and E.R. Chilvers. *Sci. Transl. Med.*, 2013, 5, 212fs41.
- [2] R. M. Hochmuth, *J. Biomech.*, 2000, 33, 15-22.
- [3] L.M. Lee and A.P. Liu, *Lab on a Chip*, 2015, 15, 264-73.

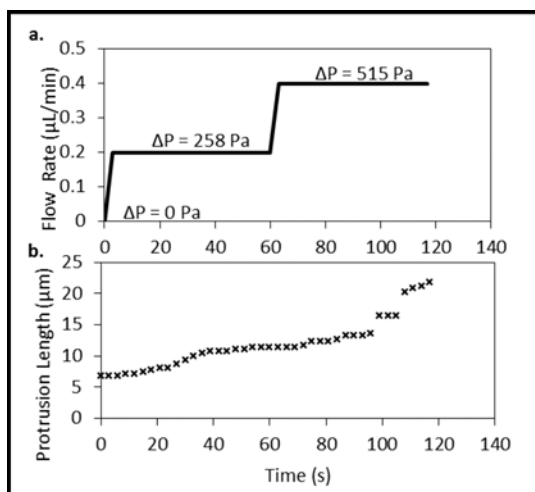


Figure 4: (a) Increasing the flow rate over time corresponds to an increasing pressure difference across the cell. (b) The pressure increases over time with a corresponding increase in protrusion into the micropipette for an MDA-MB-231 cell.

# A Suspended Heater Wire for Low Power Gas Sensing Using the 3-Omega Technique

**Abbas Furniturewalla**  
Electrical and Computer Engineering, Rutgers University

**NNIN REU Site: Institute for Electronics and Nanotechnology, Georgia Institute of Technology, Atlanta, GA**

NNIN REU Principal Investigators: Dr. Shannon Yee and Dr. Peter Hesketh, Mechanical Engineering, Georgia Institute of Technology

NNIN REU Mentors: Sampath Kommandur and Alireza Mahdavifar, Mechanical Engineering, Georgia Institute of Technology

Contact: abbas.furniturewalla@gmail.com, shannon.yee@me.gatech.edu,

peter.hesketh@me.gatech.edu, ksam.1990@gmail.com, mahdavi@gatech.edu

## Introduction:

Gas sensors have been used for nearly four decades in order to measure gas mixture composition or identify certain gases [1]. The majority of conventional gas sensors function via electrochemical detection, but electrochemical sensors face certain disadvantages, including having a low shelf-life, requiring individual sensor calibration, and containing corrosive sensor components.

Recently, a gas sensor based on the 3-Omega technique was developed [2]. In a standard 3-Omega technique, a current of root-mean-square value (RMS)  $I_{\omega, \text{RMS}}$  and angular frequency  $\omega = 2\pi f$  is driven through a metal heater line, causing Joule heating at frequency  $2\omega$ . The resulting thermal wave penetrates the surrounding environment, causing a temperature fluctuation at the source at a frequency  $2\omega$ , but at a phase lag  $\phi$ . The temperature oscillation causes the resistance of the heater to oscillate at  $2\omega$ . The current driven at a frequency  $1\omega$  and the resistance fluctuation at frequency  $2\omega$  causes a voltage fluctuation at a frequency  $3\omega$  across the heater-line that is dependent on the thermal environment of the sensor. The  $3\omega$  voltage amplitude and phase are directly measurable and depend on the composition of the surrounding gas. Since different gases result in different  $3\omega$  signals, the 3-Omega technique can be applied for gas sensing purposes. The purpose of this study was to fabricate heater lines that will improve the sensitivity of the technique while consuming lower power ( $< 1 \text{ mW}$ ) than many commercially available sensors.

## Design and Fabrication:

The 3-Omega technique is best applicable for 1-D geometries and therefore, a cylindrical geometry with Length $\gg$ Diameter is preferred. To improve the sensitivity

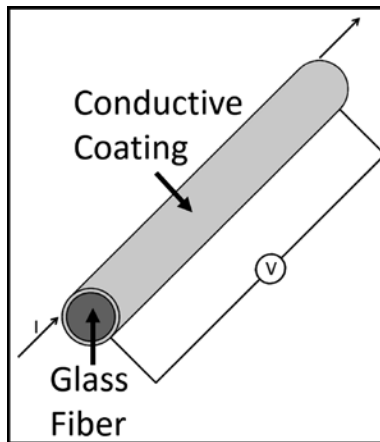


Figure 1: Schematic for cylindrical heater line geometry.

of the technique, most of the heat generated in the heater line should diffuse through the gas medium. To satisfy both the criteria, a heater line geometry as shown in Figure 1 was designed. A thin layer ( $\sim 50 \text{ nm}$ ) of metal (e.g., gold) deposited on the circumference of an insulating core (e.g., glass fiber) of larger dimension ( $\sim 50 \mu\text{m}$ ) served as the heater line.

In this study, borosilicate glass fiber was used as the insulating core and gold, platinum, and copper were deposited circumferentially onto the core. The fibers were cleaned in acetone, deionized water, and isopropyl alcohol prior to deposition. The fibers were then suspended

across a deposition lathe designed to rotate and provide a uniform circumferential coating, as shown in Figure 2. The metal coating of desired thickness was achieved by placing the lathe within a vacuum sputtering system. The rotation of the lathe was controlled by the planetary motors of the sputtering system. An 8 nm thick titanium layer was first deposited as the adhesion layer, and was followed by a 300 nm thick layer of the metal.

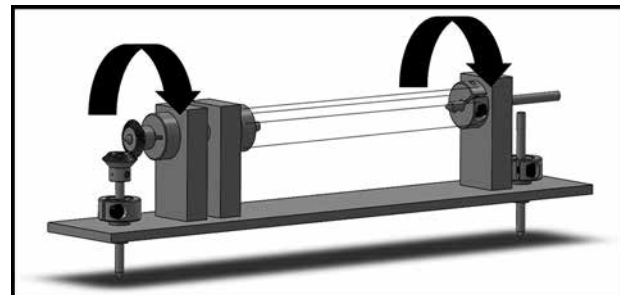


Figure 2: Rotating deposition lathe designed for vacuum sputtering system.

Because the sputtering system deposited metal in a rectangular plane while the lathe was rotating in a cylindrical motion, the actual thickness on each fiber was theoretically calculated to be  $300/\pi = 95.5$  nm. The factor of  $\pi$  results from the ratio of the fiber's actual surface area ( $\pi DL$ ) to the area projected onto a horizontal plane ( $DL$ ).

Since the deposition process was set to a custom calibrated run for the lathe, the thickness and uniformity of the metal layer had to be characterized. The cross section of the fiber was analyzed under a scanning electron microscope (SEM) for two configurations. The first configuration involved embedding the fiber in a solidified epoxy, which was then sliced and polished before imaging. The second configuration involved vertically placing the coated fibers onto the SEM stand via double sided copper tape. The second configuration yielded better images as the presence of epoxy interfered with the imaging process.

Energy dispersive x-ray (EDX) tests were performed to verify the presence of metal coating on the surface of the sensor. It was observed that gold and platinum coatings

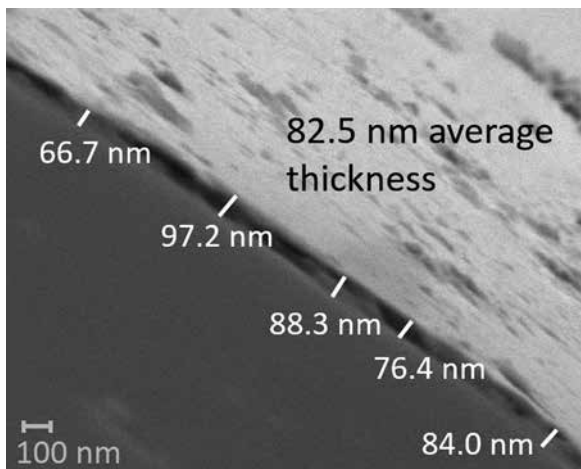


Figure 3: Thickness analysis on an SEM of Au coated fiber.

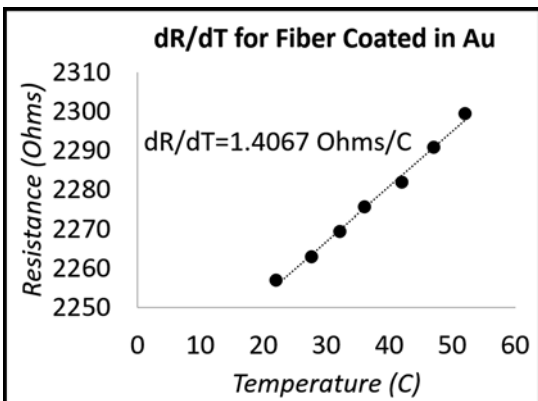


Figure 4: dR/dT measurement of Au coated fiber.

were uniform, whereas copper showed inconsistency. Figure 3 shows the measured thickness of the metal layer in small region of the cross-section. The average thickness in this region was determined to be 82.5 nm with a standard deviation of 11.6 nm, which was lower than the theoretical value of 95.5 nm. Further depositions are required to calibrate sputter deposition rates.

## Experiments:

The first test was to determine the rate of change of resistance with temperature,  $dR/dT$ , as it plays a vital role in analyzing the 3-Omega signal. The fibers were suspended across a dual in-line chip package (DIP) and connections to the pins were established using gold wires. The gold wire was connected to the fiber using conducting silver paste, which was cured at 60°C for a period of 36 hours, and the other end was wire bonded to the pin. The sensor was placed in an oven, and resistance was measured across a range of temperatures. Figure 4 shows the variation of resistance with temperature and the value of  $dR/dT$ . 3-Omega measurements were taken with the sensor placed in ambient air to verify the functionality of the sensor.

## Future Steps:

To fully characterize the sensor, experiments need to be carried out in the presence of different gas mixtures. The resulting 3-Omega data will be used to determine the sensitivity. An iterative study involving the deposition parameters and input current will be performed to optimize the sensitivity and power consumption of the sensor.

## Acknowledgements:

I would like to thank NSF (Grant No. ECCS-0335765), NNIN REU Program, and Georgia Institute of Technology for making this project possible. I also appreciate the guidance of my principal investigators and mentors. Lastly, I appreciate the support from my fellow interns, friends, and family.

## References:

- [1] A. Azad, S. Akbar, S. Mhaisalkar, L. Birkefeld, K. Goto, Solid-state gas sensors: A review, *Journal of the Electrochemical Society*, 139(1992) 3690-704.
- [2] S. Kommandur, A. Mahdavifar, P. Hesketh, S. Yee, A microbridge heater for low power gas sensing based on the 3-Omega technique, *Sensors and Actuators A: Physical*, 233(2015), 231-238.

# Microfabrication & Testing of Directional Piezoelectric Microphones Using AlN

**Marilyn Mathew**

**Cell and Molecular Biology, Texas Tech University**

**NNIN REU Site: Microelectronics Research Center, The University of Texas, Austin, TX**

NNIN REU Principal Investigator: Dr. Neal A. Hall, Electrical and Computer Engineering, University of Texas at Austin

NNIN REU Mentor: David Gawalt, Electrical and Computer Engineering, University of Texas at Austin

Contact: marilyn.mathew@ttu.edu, nahall@mail.utexas.edu, dpgawalt@utexas.edu

## Abstract:

This project focused on the fabrication and characterization of piezoelectric microphones with out-of-plane directivity. These devices use a 1.2  $\mu\text{m}$  thick aluminum nitride (AlN) thin film as the piezoelectric transduction material in place of lead zirconate titanate (PZT), utilized in earlier prototypes. Previous devices exhibited undesirably high resonance quality factors close to 40 at a frequency of 2.6 kHz, distorting recorded sound. One of the main focuses of this project was to provide an even response within the audible frequency range. AlN shows a lower dielectric loss ( $\tan\delta$ ) than PZT (i.e., a smaller leakage resistance and thus achieves a higher signal-to-noise ratio). In addition, AlN opens the possibility for complementary metal-oxide semiconductor (CMOS) integration in system-on-a-chip designs. Lastly, AlN does not require a poling process, as the internal polarization of AlN is defined by crystalline orientation (i.e., c-axis) achieved in this study via direct current (DC) reactive sputtering. Fabricated prototypes had a diaphragm made of 10  $\mu\text{m}$  thick epitaxial Si, supported by a thin Si beam — both the beam and the diaphragm being the same thickness — and on top of which, the piezoelectric thin film and electrodes were deposited. In preliminary testing, application of an AC voltage signal across the device electrodes yielded motion of the diaphragm detected with a laser doppler vibrometer, showing evidence of a functional piezoelectric AlN film.

## Purpose:

Directional microphones are used in products where consumers would like to receive sound from a particular direction or source rather than give all directions equal weighting. These directional microphones could be used in devices to detect movement, to capture higher quality signals for hearing aids, and in products such as video game devices where noise from the back of the console can be ignored and only signal from the front of the device captured.

## Introduction and Background:

A PZT-based microphone with out-of-plane directivity was previously explored. To achieve a higher signal-to-noise ratio (SNR) than the previous prototype, a new piezoelectric material (AlN) is implemented to create a new prototype sensor. The lower dielectric loss of AlN compared to PZT is the key for a high SNR. In addition, new designs are developed and fabricated followed by device characterization.

## Design:

The mask layouts of various microphone designs are shown in Figure 1a. The cross-section and top view of one such structure are shown in Figure 2. The designs included a perforated paddle, which would allow for a reduction in mass of the paddle, classic

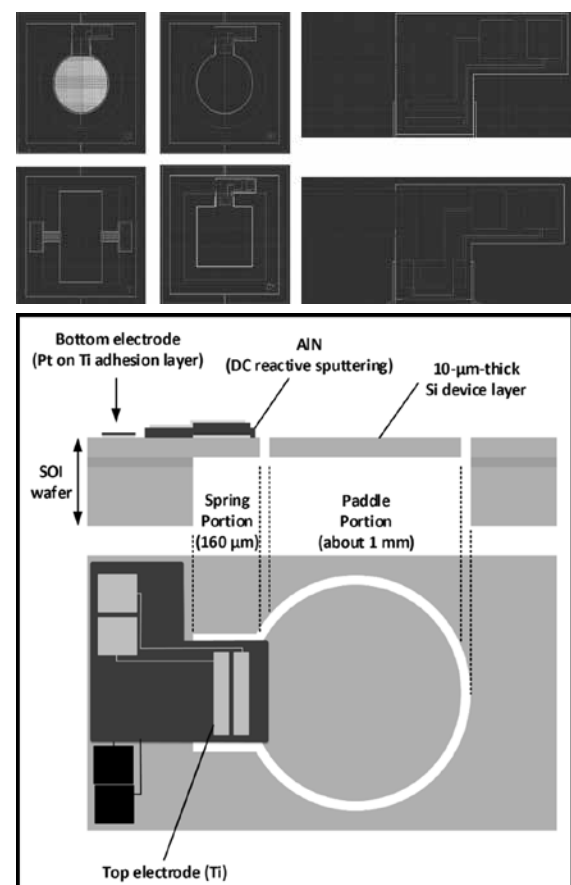


**Figure 1, top:** Computer-aided design layouts of paddle and electrode structures. **Figure 2, bottom:** Cross section and top view of the proposed microphone that was fabricated.

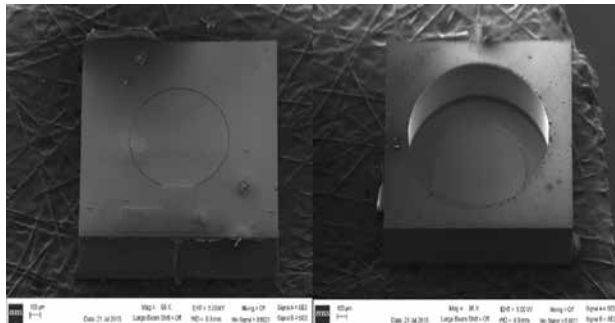


Figure 3(a-b): SEM images showing the front and back of one of the fabricated microphones.

circular and square paddles, and a biologically inspired torsional microphone. In addition, the diaphragm designs had two different electrode configurations, which theoretically would increase the sensitivity of our devices.

### Experimental Procedure and Fabrication:

The fabrication of the microphones used a silicon-on-insulator (SOI) wafer as the starting substrate. Aluminum oxide ( $\text{Al}_2\text{O}_3$ ) masking layers were deposited using an atomic layer deposition tool and then patterned using a reactive ion etch (RIE) process. The device layer was then etched using this mask and a deep RIE (DRIE) tool. The etch was stopped by the insulator layer of the SOI wafer. The masking layers were then removed and the bottom electrodes were fabricated using a layer of platinum/titanium (Pt/Ti). This was followed by deposition and patterning of the aluminum nitride (AlN). Finally, top electrodes were realized using titanium.

The moving element of the design was the suspended silicon region formed by a deep silicon etch of the backside of the SOI wafers. This backside etch was completed with a DRIE process using  $\text{Al}_2\text{O}_3$  as a hard mask. The completed microphones had AlN as the piezoelectric material, thin silicon suspended diaphragms, and Pt/Ti electrodes. These devices were further characterized to determine their electrical and physical proprieties.

### Physical and Electrical Characterization:

The completed devices were singulated and are shown in Figure 3 a-b. Scanning electron microscope (SEM) characterization of these devices showed well-defined diaphragm regions. Dynamic frequency response measurements are shown in Figure 4. In these measurements, the motion of a paddle was measured using an LDV while the paddle was excited by applying a broadband electrical signal into the piezoelectric port. As shown, the devices were functional and the results of these

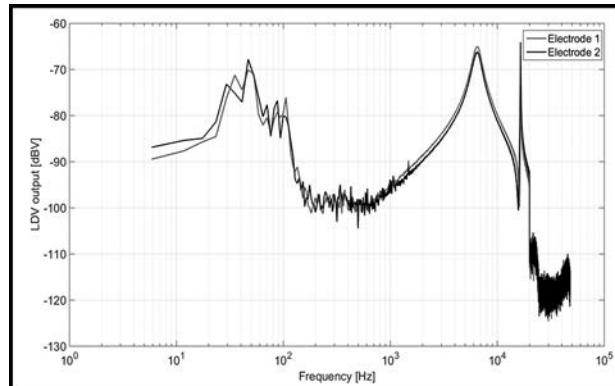


Figure 4: Velocity measurements of a diaphragm taken using a laser doppler vibrometer. The diaphragm is actuated by applying AC voltage across the AlN film on the device.

tests met the goals for this project to realize a resonance with a quality factor close to unity. The previous device's resonance peak was located at 2.3 kHz whereas these devices had a resonance peak at 6.3.

### Results and Future Work:

Rigorous characterization of the microphones will be conducted including acoustic frequency response and directivity measurements in an anechoic chamber, as well as further characterization of each device structure (perforated, square, circle, and torsional). Optimization of process conditions for uniform AlN deposition will be further explored as well as methods for depositing higher quality AlN film with less surface defects and higher c-axis orientation, as measured in the x-ray diffraction (XRD) tool.

### Acknowledgements:

I would like to thank my mentor David Gawalt, Dr. Neal A. Hall, the entire Hall research group, Dr. Marylene Palard, Jeannie Toll at UT-Austin MRC and all of the staff the UT Austin Microelectronics Research Center for their support and guidance, and The Texas Tech University CISER program for introducing me to technical research. I would also like to thank the NNIN REU Program, National Science Foundation Grant No. ECCS-0335765, Melanie-Claire Mallison, and Lynn Rathbun for providing me with this research opportunity and supporting this undergraduate research experience.

### References:

- [1] Kim, Donghwan, et al. "Piezoelectric micromachined microphones with out-of-plane directivity." *AP Letters* 103.1 (2013): 013502.
- [2] Kuntzman, Michael L., et al. "Micromachined Piezoelectric Microphones with Directivity." *Applied Physics Letters* 102.5 (2013): 054109.

# Design and Fabrication of Piezoresistive Graphene on Nitride Accelerometer

**Zachary Schaffer**

**Nanoscale Engineering, University at Albany SUNY**

**NNIN REU Site: Cornell NanoScale Science and Technology Facility, Cornell University, Ithaca, NY**

NNIN REU Principal Investigator: Amit Lal, Electrical and Computer Engineering, Cornell University

NNIN REU Mentors: Ved Gund and Alexander Ruyack, Electrical and Computer Engineering, Cornell University

Contact: [zschaffer@sunypoly.edu](mailto:zschaffer@sunypoly.edu), [amit.lal@cornell.edu](mailto:amit.lal@cornell.edu), [vg3@cornell.edu](mailto:vg3@cornell.edu), [arr86@cornell.edu](mailto:arr86@cornell.edu)

## Abstract:

Piezoresistive materials change resistance in response to strain. In a piezoresistive accelerometer, displacement of a proof mass causes strain on the proof mass support—consisting of a piezoresistive element—translating to measurable changes in resistance. In this project, an accelerometer was designed and fabricated using piezoresistive graphene on silicon nitride. Graphene is atomically thin, allowing for scalability to extremely small accelerometers for potential implementation in large arrays of sensors. In general, an atomically thin mechanical transduction element can provide new pathways to realizing nanoscale arrays of nano-electro-mechanical systems. Fabrication of the devices took place at the Cornell NanoScale Facility (CNF). Low stress silicon nitride was deposited on a wafer, followed by deep reactive ion etching to etch high aspect ratio trenches from the backside and release a silicon proof mass. The nitride layer connecting the proof mass to the substrate served as the spring for out-of-plane acceleration measurements using the device. Nickel was deposited for metallization contacts via a lift-off process, and piezoresistors made of transferred graphene patterned using oxygen plasma. Devices were successfully fabricated and tested for response. Extremely high gauge factor of graphene on nitride was measured: 17451.

## Introduction:

Accelerometers are used for a broad range of applications, from image stabilization, to airbag deployment, to biomedical implants. Typical accelerometers are a multiple  $\text{mm}^2$  in size, limiting their implementation in small scale devices. This project aimed to create a higher sensitivity to size ratio accelerometer, reducing cost of manufacture, and allowing creation of multi-sensor arrays in order to further improve signal to noise ratio and detect specific frequency accelerations.

Piezoresistive materials are characterized by gauge factor (GF), a measure of fractional change in resistance divided by strain on the material. Single crystal silicon has a GF of 200. Previous research reported an extremely high GF (17980) for graphene on nitride [1]. Displacement of a silicon proof mass causes strain on the proof mass support—consisting of a piezoresistive element—translating to measurable changes in resistance. An accelerometer's sensitivity to force increases with GF and lateral dimensions, while decreasing with piezoresistor thickness. The ultra-high GF of graphene on nitride and low thickness of graphene cause increased sensitivity without increased lateral dimensions.

## Device Fabrication:

Device fabrication steps are shown in Figure 1; 350 nm of  $\text{SiO}_2$  was grown in an oxide furnace followed by deposition of 650 nm of low-stress (~150-200 MPa) silicon nitride ( $\text{Si}_x\text{N}_y$ ), then 2  $\mu\text{m}$  of  $\text{SiO}_2$  was deposited using plasma-enhanced chemical vapor deposition (PECVD) on the backside as an etch-mask for deep reactive ion etching (DRIE) of the silicon substrate (I). The backside dielectric stack of PECVD oxide, nitride and thermal oxide was etched with  $\text{CHF}_3/\text{O}_2$  using a 10  $\mu\text{m}$  thick photoresist mask (II). Next, a trench was cut around the central proof mass, through the silicon substrate, using DRIE (III). The  $\text{SiO}_2$

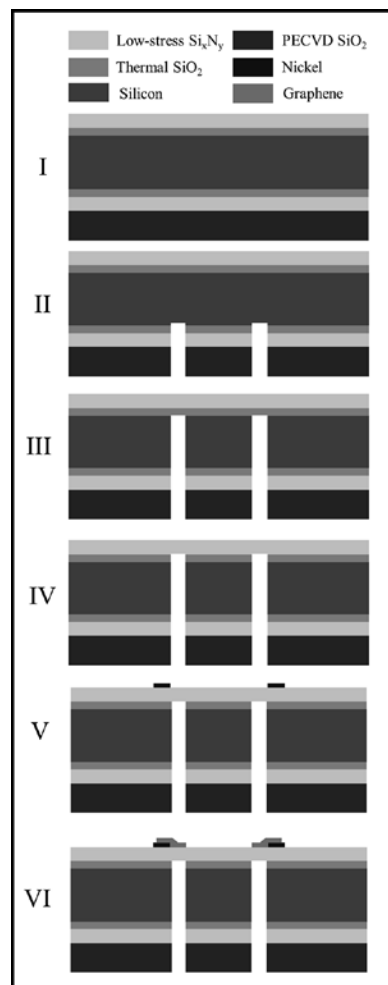


Figure 1: Process flow for accelerometer fabrication.

layer on the front side served as a DRIE etch-stop, and was subsequently removed using vapor HF etching, leaving the central proof mass connected to the bulk silicon wafer only by the  $\text{Si}_x\text{N}_y$  layer (IV). Next, a 40 nm layer of nickel was deposited and patterned using a lift-off process. A sacrificial lift-off resist layer was patterned, followed by e-beam thermal evaporation of nickel. The sacrificial resist layer was removed leaving only the patterned nickel layer (V). The graphene piezoresistors were added next. Graphene was grown via  $\text{CH}_4$  chemical vapor deposition onto a copper foil substrate at 1000°C. A polymer layer, used for transfer handling, was spin-coated on top of the graphene. After chemical etching of the copper foil, the graphene with polymer handle layer was cleaned through serial dilution in DI water before being transferred on the device. The graphene was patterned through oxygen plasma etching with a photoresist mask (VI). Finally, remaining resist and polymer were removed chemically.

The diced device can be seen in Figure 2.

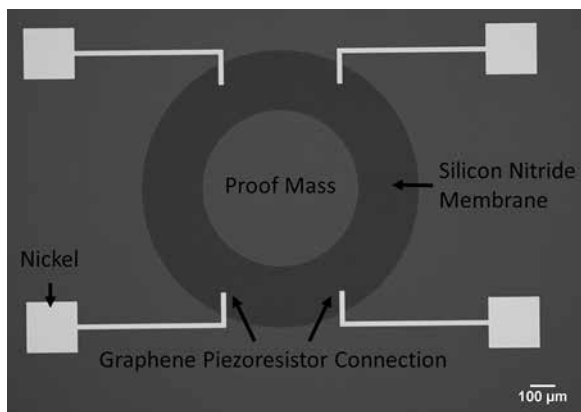


Figure 2: Optical image of topside of accelerometer.

## Experiments:

The piezoresistive accelerometers were tested using a Wheatstone bridge with three off-chip resistors. The differential signal from the bridge was amplified and then filtered for 60 Hz noise. An external shaker-table was used to actuate the device at precise acceleration amplitudes and frequencies. Acceleration was translated to a strain on the graphene piezoresistor using a COMSOL model of the accelerometer. The output voltage signal was converted to a fractional resistance change of the piezoresistor, which was then divided by strain to measure GF. A linear regression of these values over a range of accelerations, as seen in Figure 4, was used to measure GF.

## Conclusions and Future Work:

The accelerometer was successfully fabricated and showed linear response to acceleration. As seen in Figure 4, a GF of 17451 was measured, in accordance with previously

reported values. Further work includes measuring the noise floor of the device piezoresistors and studying the variation of proof mass size in order to quantify its relation to resonant frequency. Response at resonance will also be examined. Extensions of this work will include downscaling of devices, fabrication of multi-sensor arrays, and 3-axis sensitivity using torsional motion of the proof-mass.

## Acknowledgments:

This work was conducted through the SonicMEMS laboratory at the Cornell NanoScale Science and Technology Facility (CNF). I would like to thank Professor Lal, and my mentors Ved Gund and Alexander Ruyack, for the help and support, as well as the CNF staff. I would like to acknowledge the National Nanotechnology Infrastructure Network Research Experience for Undergraduates (NNIN REU) Program, and the National Science Foundation, Grant No. ECCS-0335765, for funding.

## References:

[1] Hosseinzadegan, et al., (n.d.). Graphene has ultra-high piezoresistive gauge factor. 2012 IEEE 25<sup>th</sup> International Conference on Micro Electro Mechanical Systems (MEMS).

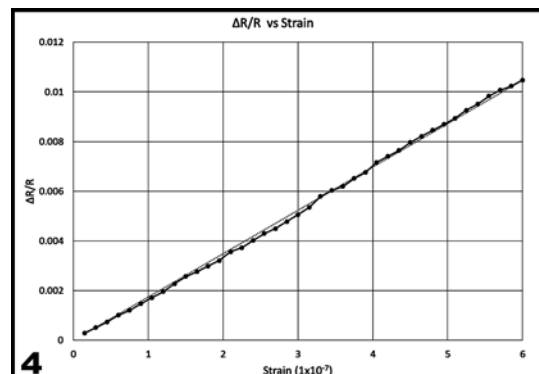
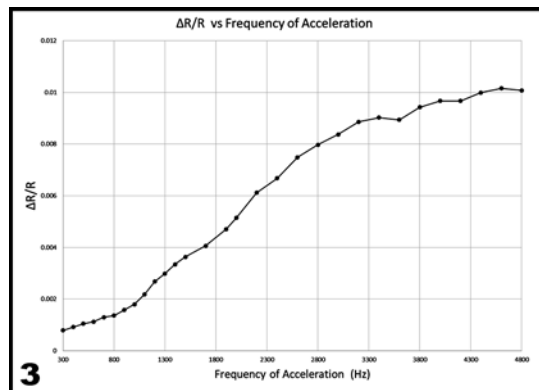


Figure 3, top: Graph of  $\Delta R/R$  vs. Frequency of Acceleration at Force of 3 g. Figure 4, bottom: Graph of  $\Delta R/R$  vs. Strain at 3000 Hz.

# Graphene Fabrication with a Motorized Linear Stage Based on the “Scotch Tape” Method

**Bilan Yang**  
**Mechanical Engineering, Rice University**

**NNIN REU Site: Center for Nanoscale Systems, Harvard University, Cambridge, MA**

NNIN REU Principal Investigator: Robert Westervelt, Applied Physics, Harvard University

NNIN REU Mentor: Sagar Bhandari, Applied Physics, Harvard University

Contact: bilan.yang@rice.edu, westervelt@seas.harvard.edu, sbhandar@fas.harvard.edu

## Introduction:

With its amazing electrical and optical properties that grant potential applications of ultrafast transistors, liquid crystal display (LCD) screens, solar and fuel cells, and so forth, an efficient method to fabricate graphene is very important. Based on the principle of the “Scotch tape” method, a mechanical approach using a motorized linear stage is demonstrated to systematically isolate graphene from graphite. Previously graphene was produced by manually splitting graphite flake with adhesive tapes. Since a manual approach is unfavorable for consistent and

stable results, a mechanical setup is considered to simulate the process of “folding” and “peeling” in the “Scotch tape” method.

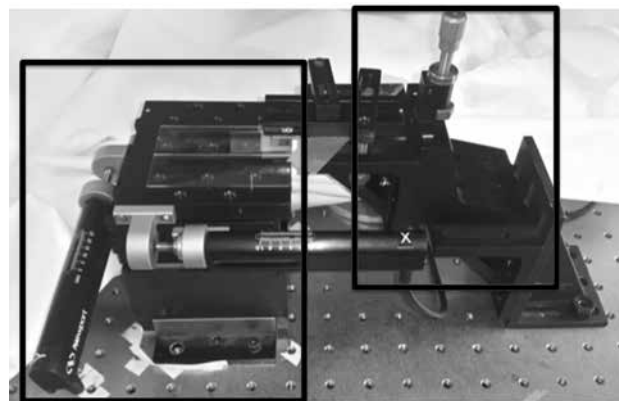


Figure 1: The motorized XYZ linear stage and manual Z-axis translational stage.

## The LabVIEW Program:

A LabVIEW program was designed specifically for the motorized linear stage, running in a Virtual Instrument Software Architecture (VISA) supported operation environment. After VISA was initialized and a new session was opened, the motor would be turned on and the desired channel (any of the x, y, z positioners) was selected to receive further commands. Then the stage entered the phase of creating the designated patterns of thin layers of graphite from a single thick flake by moving in x, y, z directions in a chosen sequence. Finally, the motor was turned off and the session was closed.

## The Mechanical Setup:

A systematic alternative to the “Scotch tape” method involves the mechanical setup of a motorized XYZ linear stage and a manual Z-axis translational stage, both of which are products of Newport Corporation, Irvine, California.

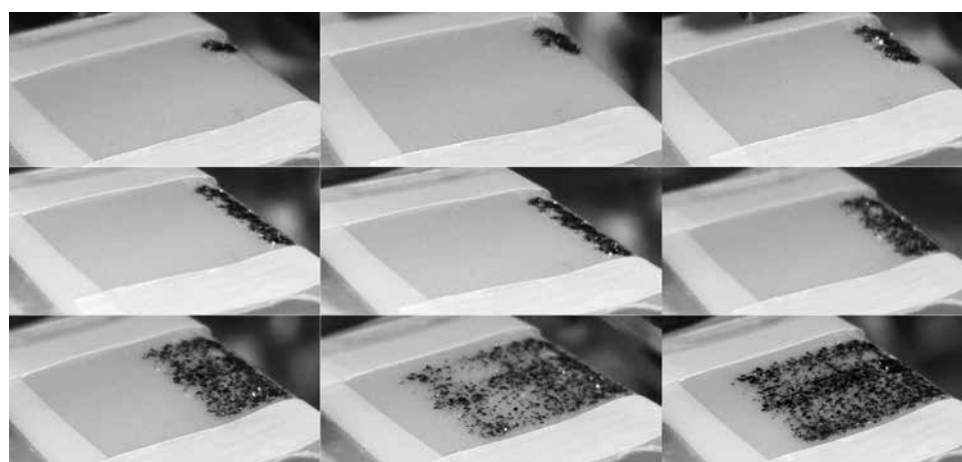


Figure 2: The process of forming a line of flakes from dots and that of forming a block of flakes from lines.

One piece of Scotch tape was attached to a piece of glass slide fixed on the motorized stage; another piece of tape was attached to an aluminum slide, which was mounted on the manual stage. When the basic setup was completed, the system was ready to create the pattern of thin layers of graphite.

As the program was running, the motorized stage would move up and down so that the first flake was halved. Then the controller would command the y-positioner to move a unit distance and repeat the z-axis movement to make the second flake “dot.” On either of the two pieces of tapes, there would appear 1 dot, 2 dots, 4 dots, and 8 dots in sequence (Figure 2). Similarly, as the first line had been made, the controller would direct the x-positioner to move a unit distance and then had the z-positioner perform the z-axis movement, which would ultimately lead to the formation of a whole block of thin layers of graphite. When the setup was set to make the whole block of thin layers of graphite automatically, after the two pieces of tape were fixed in the desired positions, the entire process took approximately 20 to 30 minutes.

### Peeling Angle:

In the further investigation of the capacity of the mechanical method to fabricate graphene, the angle between the two pieces of tapes was taken into consideration. In the application of the basic method of producing a block of thin layers of graphite described in the last section, the angle between tapes was 0 degree. It was found that samples made in this way contained much more thick flakes of graphite than those produced with the manual “Scotch tape” method, which has 180 degrees of angle between two pieces of tapes. A sample environment that has more thick flakes usually has a lower possibility of containing graphene. Also, the “Scotch tape” had already been tested to be successfully in producing graphene. Therefore, it was presumed that a larger peeling angle would be more capable to create thinner layers of graphite.

Two types of mechanical setup, which involved the usage of springs, were proposed (Figure 3).

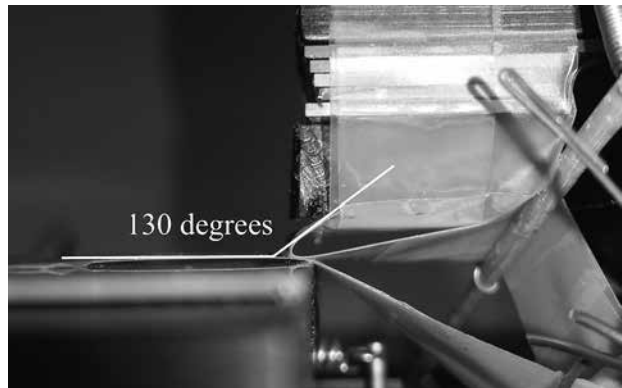


Figure 3: A proposed setup that includes four springs and has a 130° peeling angle.

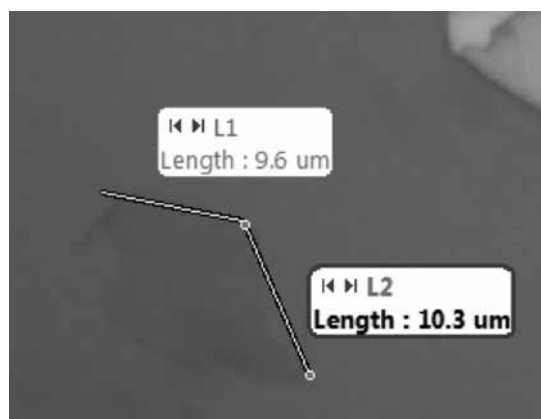


Figure 4: The graphene flake produced with 0 degree peeling angle and manual z direction movement.

### Results and Future Work:

From the resulting block of thin layers of graphite as well as the sample under optical microscope, it was found that the zero peeling angle method was more capable of producing consistent samples even though it might not necessarily have higher possibility in fabricating graphene. Also, with a larger peeling angle, the sample appeared to have a lot of long glue on it, which was from the tape and could unfavorably cover graphene if there was any.

Currently, with no less amount of thick flakes, even more glue on the sample, and higher possibility of contamination due to more steps in the procedures, the methods with larger peeling angles do not seem to help produce samples of higher quality. However, if these problems can be resolved, the setup that can achieve 130 degrees peeling angles can still be promising since it is closest to the “Scotch tape” method, which has 180 degrees peeling angle and has been proved to be capable of providing productive results.

So far one flake of graphene with acceptable size (8  $\mu\text{m}$   $\times$  8  $\mu\text{m}$ ) has been produced with 0 degree peeling angle and manual z direction movement (Figure 4). We will still need to enhance both methods to see which one has higher potential to produce as many and large area of graphene as possible.

### Acknowledgements:

I wish to thank Harvard University, CNS, and the NNIN REU Program, my mentor, Dr. Sagar Bhandari, and my PI, Dr. Robert Westervelt, my site coordinator, Dr. Kathryn Hollar, and the National Science Foundation for funding via Grant No. ECCS-0335765.

### References:

- [1] A. H. Castro Neto, F. Guinea, N. M. R. Peres, K. S. Novoselov and A. K. Geim, The electronic properties of graphene, *Reviews of Modern Physics*, Volume 81, January-March 2009.

# Design and Analysis of Nano-Scale Resonators to be Integrated with Monolayer Heterostructures

**Brian Bemis**

**Electrical and Computer Engineering, Oregon State University**

**NNIN REU Site: Washington Nanofabrication Facility and Molecular Analysis Facility, University of Washington, Seattle, WA**

NNIN REU Principal Investigator: Dr. Arka Majumdar, Electrical Engineering and Physics, University of Washington

NNIN REU Mentors: Taylor Fryett, Electrical Engineering, University of Washington, and Alan Zhan, Physics, University of Washington

Contact: [bemisb@onid.oregonstate.edu](mailto:bemisb@onid.oregonstate.edu), [arka@uw.edu](mailto:arka@uw.edu), [tfryett@uw.edu](mailto:tfryett@uw.edu), [azhan137@gmail.com](mailto:azhan137@gmail.com)

## Abstract:

Unprecedented material compatibility and unusual optoelectronic properties of single-atom thick monolayer materials have generated strong interest in building devices with them in the recent years. The full potential of such materials can, however, be realized if one stacks such materials, and integrates them with nano-scale resonators to increase the light-matter interaction. However, for this process to be effective with such monolayer heterostructures, specifically the interlayer excitons observed in previous results, the resonator must be able to support a transverse magnetic (TM) mode in order to possess a strong electric field in the direction perpendicular to the monolayer material stack, or the surface of the cavity. This requirement is fundamentally different from resonators designed for single monolayers, where light only with polarization parallel to the surface is effective. In this report, we present a design methodology to build photonic crystal resonators to support TM modes. Previous results used a much thicker geometry for the resonator, which poses a problem for fabrication due to long etching time. Using those as starting designs, using finite-difference-time-domain simulation, we design a cavity with only 250 nm thickness exhibiting TM resonances at 900-950 nm range, the typical wavelength range for the tungsten diselenide ( $WSe_2$ )-molybdenum diselenide ( $MoSe_2$ ) interlayer excitons. Additionally, we present a doubly resonant ring resonator that will be used to enhance the nonlinear properties of monolayer heterostructures.

## Introduction:

Current research involves optical resonators integrated with single two-dimensional (2D) material monolayers [1]. These resonators are stimulated using a transverse electric (TE) mode with light polarization parallel to the cavity surface and in-plane with the single-atom thick monolayer. However, when these monolayers are stacked together into 2D material heterostructures, interesting properties arise [2]. Of these properties, the presence of interlayer excitons [3] and applications to nonlinear optics are particularly noteworthy. In order to interact

with interlayer excitons, it is necessary to use light with a polarization perpendicular to the cavity surface and therefore in the direction of the interlayer excitons, or a TM mode. For our purposes, we are interested in  $WSe_2$ - $MoSe_2$  heterostructures that require a TM resonance at 900-950 nm wavelength range. We report on two designs for optical resonators, scaled to have a TM resonance in this wavelength range. To explore the use of heterostructures in nonlinear optics a doubly resonant ring resonator was designed for future experiments.

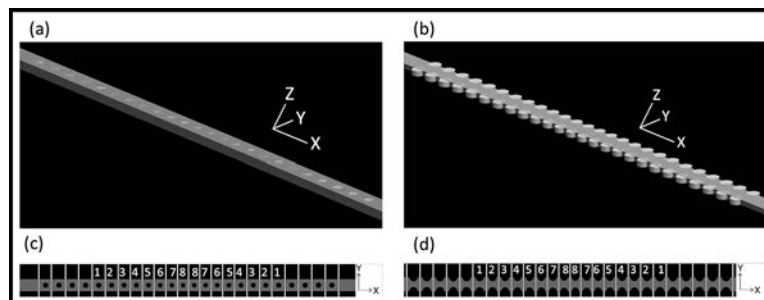


Figure 1: (a) Nanobeam schematic. (b) Fishbone schematic. (c) Nanobeam taper. (d) Fishbone taper.

## Simulation Procedure:

The first design was based on the photonic crystal nanobeam by Zhang, et al. [4]. However, when this design was scaled to have a resonance within 900-950 nm, it was 595.5 nm thick. Such a thick structure is difficult to etch, and in our design, the thickness was reduced to 250 nm and the periodicity was increased by 101.5 nm to be 300 nm, while the width was increased

by 75 nm to become 273.5 nm. The cavity periodicity and radii tapers, respectively, are described by the formulas:  $P(k) = 42(a+101.5 \text{ nm})/(42+k)$  and  $R(k) = 0.34(42a/(42+k))$  where “a” is the original periodicity and  $\{k: 1 \leq k \leq 8\}$  (see Figure 1). Note that the original periodicity was not increased for the radii formula as the radius parameter remained unchanged.

The second design was based on the “Fishbone” version of the photonic crystal nanobeam by Lu, et al. [5].

However, this design also faced similar challenges and was adjusted from a thickness of 370 nm to 250 nm; while the periodicity was increased by 30 nm to become 400 nm and width was increased by 50 nm to become 420 nm. The cavity periodicity and radii tapers, respectively, are described by the formulas:  $P(k) = (1-0.02k)(a+30 \text{ nm})$  and  $R(k) = 0.34((1-0.02k)a)$  where, again, “a” is the original periodicity and  $\{k: 1 \leq k \leq 8\}$ .

The doubly resonant ring resonator was designed for two modes, one at twice the frequency of the other to enhance both the fundamental and the second harmonic frequency. This resonator will be used to explore the application of heterostructures to nonlinear optics. The 330 nm thick silicon nitride (SiN) ring resonator on a silicon dioxide ( $\text{SiO}_2$ ) base consists of a waveguide with a width set to 1193 nm such that the 1550 nm and 775 nm

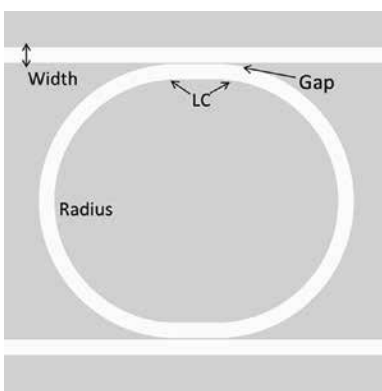


Figure 2: Ring resonator schematic.

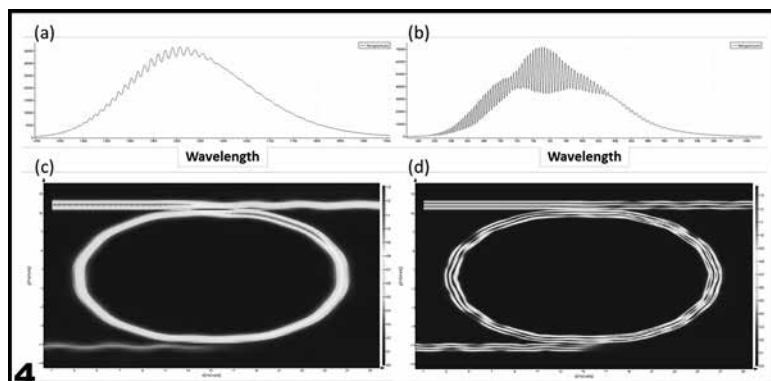
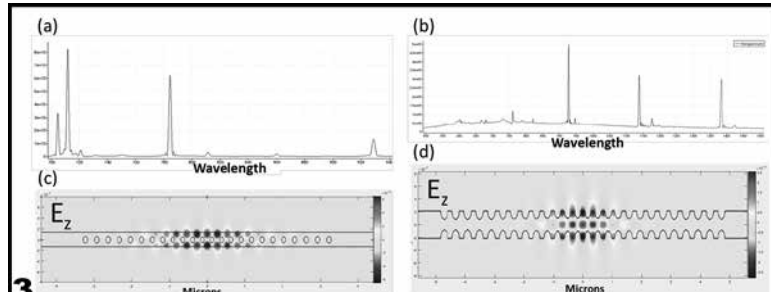


Figure 3, top: (a), (c) Nanobeam spectrum and  $E_z$  field profile. (b), (d) Fishbone spectrum and  $E_z$  field profile. Figure 4, bottom: (a), (c) 1550 nm mode spectrum and electric field profile. (b), (d) 775 nm mode spectrum and electric field profile.

modes have the same effective index, giving the modes significant overlap which allows the creation of higher frequency photons. The waveguide was separated by a gap of 100 nm from a 10  $\mu\text{m}$  radius ring with a coupling section length of 3  $\mu\text{m}$ .

## Results and Conclusions:

In summary, three optical resonators were designed to be integrated with 2D material heterostructures.

As evident from the  $E_z$  fields of the nanobeam and fishbone designs in Figure 3, both resonators support a TM mode that will interact with the interlayer excitons in  $\text{WSe}_2\text{-MoSe}_2$  heterostructures. The ring resonator’s electric field profile exhibits coupling for both modes (see Figure 4).

## Future Work:

Once these optical resonators are fabricated they will be integrated with 2D material heterostructures. Then these devices will be characterized in a confocal microscopy setup to be used in future experimentation.

## Acknowledgments:

I am grateful to my mentors Taylor Fryett and Alan Zhan, and my Principal Investigator, Dr. Arka Majumdar, for providing a supportive and enjoyable experience. I also thank the National Nanotechnology Infrastructure Network Research Experience for Undergraduates (NNIN REU) Program and site coordinator Paul Neubert for coordinating this internship with the University of Washington. This research was supported by the National Science Foundation under Grant No. ECCS-0335765.

## References:

- [1] S. Wu, et al. *Nature* 520, 7545 (2015).
- [2] AK Geim and IV Grigorieva, *Nature* 499, 419-425 (2013).
- [3] P. Rivera, et al. *Nature Communications* 6, 6242 (2015).
- [4] Y. Zhang, M. W. McCutcheon, I. B. Burgess, and M. Lončar, *Opt. Lett.* 34, 2694 (2009).
- [5] Tsan-Wen Lu and Po-Tsung Lee, *Opt. Lett.* 38, 3129 (2013).

# Fabrication of Bio-Inspired Photonic Structures for Antireflectivity in Cadmium Telluride for Infrared Detectors

Scott Blankenbaker

Engineering Physics, Rose-Hulman Institute of Technology

NNIN REU Site: UCSB Nanofabrication Facility, University of California, Santa Barbara, CA

NNIN REU Principal Investigator: Prof. Michael J. Gordon, Chemical Engineering, University of California, Santa Barbara

NNIN REU Mentor: Dr. Federico Lora Gonzalez, Chemical Engineering, University of California, Santa Barbara

Contact: scott.blankenbaker@rose-hulman.edu, mjgordon@engr.ucsb.edu, fedlora@gmail.com

## Abstract:

Moth-eye structures are emerging as an anti-reflection surface capable of enhancing broadband transmission and functioning at off-normal incidence, providing an alternative to interference based thin-film coatings. A procedure has been developed by the Gordon group to produce moth-eye structures on cadmium telluride (CdTe) for infrared detection applications. Photoresist was spun onto a CdTe wafer, which was then coated with colloidal silica nanoparticles to form a mask. A  $\text{CF}_4/\text{O}_2$  inductively coupled plasma etch was used to reduce the size of the nanoparticles, after which the photoresist was etched by  $\text{O}_2$ . This allows for a  $\text{CH}_4/\text{H}_2/\text{Ar}$  etch of the CdTe, followed by an additional  $\text{O}_2$  clean and an acetone rinse to strip the mask. The result was a set of CdTe columns retaining the order of the colloidal mask. This has been shown to increase transmission through the interface between the air and CdTe by 10% over a range of wavelengths from 3 to 8  $\mu\text{m}$ .

## Introduction:

There is a constant need for improvement in infrared detectors for military, medical, or astronomic applications. Mercury-cadmium-telluride devices with interference based thin-film coatings form the current state of the art for infrared sensing devices in the range of 1-25  $\mu\text{m}$ . These antireflective coatings function only for normal incidence, and require deposition of many materials to perform across a broad wavelength range. Moth eyes have a structure of nanoscale protrusions, causing a gradient index of refraction that decreases reflection. Biomimetic moth-eye structures provide antireflective properties superior to those of interference based thin films on silicon and germanium, functioning over broad wavelength ranges and at off-normal incidence, and can be fabricated using a one mask, one etch process [1]. By adapting this process to CdTe, a superior antireflective coating (Figure 1) for infrared detectors can be fabricated. Additionally, this geometric pattern decreases the area of the surface, which will reduce dark current. The combination of higher transmission and lower dark current will allow for more sensitive devices. This work adjusted the process for etching a moth-eye pattern into silicon by the addition of both a protective photoresist layer and an additional etch to reduce the mask size. This resulted in successful pattern transfer into CdTe and improvement in transmission in the near infrared.

## Experimental Procedure:

The two-step process used in silicon was found to be ineffective for CdTe, as the etch angle was too shallow. A mask reduction step was added to allow plasma to reach the surface, then a protective photoresist layer was needed to prevent surface damage to the CdTe during the mask

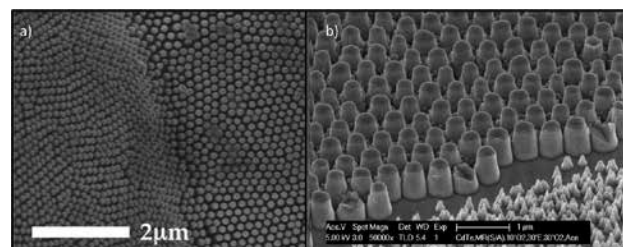


Figure 1: (a) SEM of a moth's eye [2]. (b) SEM of fabricated moth-eye nanostructure on CdTe.

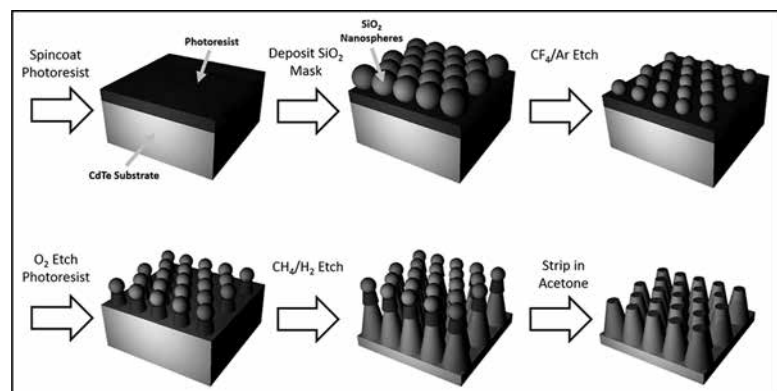


Figure 2: Moth-eye structure process flow and etch parameters.

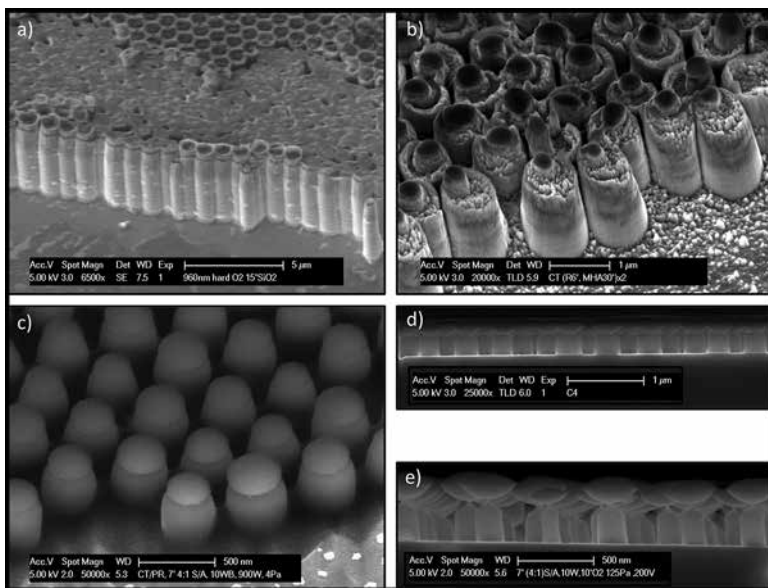


Figure 3: (a) Lack of pillar separation; (b) Micromasking; (c) Successful mask reduction; (d) Vertical photoresist etch; and (e) Isotropic photoresist etch.

reduction (Figure 2). The initial attempt without a mask reduction technique consisted of Langmuir-Blodgett deposition of 310, 540, and 960 nm colloidal silica nanospheres onto the 8  $\mu\text{m}$  CdTe layer grown epitaxially on <211> silicon by collaborators at the U.S. Army Research Laboratory. Next, a reactive ion etch ( $\text{CH}_4/\text{H}_2/\text{Ar}$ ) was performed with clean steps ( $\text{O}_2$ ). The mask was stripped with an inductively coupled plasma silica etch ( $\text{CHF}_3/\text{O}_2$ ). The resulting structure did not result in distinct pillars (Figure 3a), so a mask reduction step was introduced.

First attempts at mask reduction involved adding a silica etch ( $\text{CHF}_3/\text{O}_2$ ) before the CdTe etch. Crystal growth was observed, and energy-dispersive x-ray spectroscopy indicated fluorine on the sample's surface, suggesting a  $\text{CdF}_2$  precipitate. The presence of this growth led to micromasking (Figure 3b). A layer of protective photoresist was spun before the deposition of the silica mask. The previous silica etch had too high an etch rate in photoresist, so additional etches were developed. First, a  $\text{SF}_6/\text{Ar}$  etch was used (Figure 3c), then  $\text{CF}_4/\text{Ar}$  was found to have higher selectivity to silica over photoresist. A vertical oxygen etch was performed after the mask reduction step to expose the CdTe (Figure 3d), and an isotropic oxygen etch was used to strip the photoresist, lifting off the silica

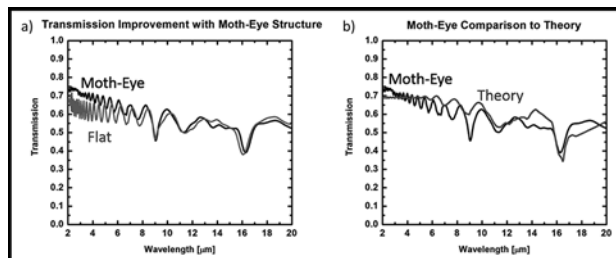


Figure 4: (a) CdTe moth-eye transmission improvement; (b) CdTe moth-eye transmission comparison to theory.

mask (Figure 3e). The optical properties of the sample were analyzed using a custom Fourier-transform infrared spectrometer with integrating sphere.

### Results and Conclusions:

A 10% increase in transmission was observed though the sample in the near IR, bringing the absolute transmission to the theoretical maximum of  $\sim 70\%$  for wavelengths below 4  $\mu\text{m}$  (Figure 4). This increase did not continue into the mid IR, likely due to shallow etch depths. At no wavelength of interest did transmission fall below the initial sample.

The final procedure developed consisted of spinning photoresist on the wafer, depositing the colloidal silica mask, reducing the size of the silica nanospheres, etching through the photoresist, etching the CdTe, and stripping the photoresist.

This process successfully etched a moth-eye structure into CdTe. Nanosphere size controls pillar spacing, and mask reduction controls pillar width. The mask pattern was reliably transferred onto the surface, and the expected increase in transmission was observed in the near infrared.

### Future Work:

Mask and etch procedures will be adjusted for better control over pillar geometry, with a focus on controlling the shape of the pillar edges and increasing the aspect ratio. Theory suggests this will increase transmission in the mid IR. Additionally, this process will be applied to HgCdTe devices so that changes in dark current can be measured.

### Acknowledgements:

I thank Prof. Michael Gordon and Federico Lora Gonzalez for their guidance and trust, along with Lesley Chan, for acting as both a partner and a second mentor. I would like to recognize the contributions of Alex Berry, for mask preparation, and collaborators at the ARL, particularly Eric deCuir, for the MBE growth of CdTe samples. This work was supported by the NNIN REU Program, the National Science Foundation under Grant No. ECCS-0335765, and the Institute for Collaborative Biotechnology.

### References:

- [1] Federico Lora Gonzalez, et al. JVST B. 32(5), 051213.1-051213.2(2014).
- [2] Federico Lora Gonzalez, Michael J. Gordon, Opt. Express 22, 12808-12816 (2014).

# Simulation and Nanofabrication for Tip-Enhanced Raman Spectroscopy

**Bryan W. Brasile**

**Chemical and Biomolecular Engineering, The Ohio State University**

**NNIN REU Site: Microelectronics Research Center, The University of Texas, Austin, TX**

NNIN REU Principal Investigator: Edward T. Yu, Electrical and Computer Engineering, The University of Texas at Austin

NNIN REU Mentor: Zhongjian Zhang, Electrical and Computer Engineering, The University of Texas At Austin

Contact: brasile.2@osu.edu, ety@ece.utexas.edu, zjzhang@utexas.edu

## Abstract and Introduction:

Tip-enhanced Raman spectroscopy (TERS) is a fast-growing branch of spectroscopy using inelastic light scattering to characterize and analyze materials with nanoscale spatial resolution. By placing a metal coated tip or probe in close proximity to a sample, incident laser radiation creates a surface plasmon on the surface of the probe, which generates a high intensity localized electric field that produces greater signal strength when compared to conventional Raman spectroscopy as well as achieving resolutions below the diffraction limit.

The goals of this project are to; (1) realistically model and simulate the TERS set-up for gold-coated AFM tips, and (2) explore the use of nanosphere lithography (NSL) to fabricate periodic plasmonic gold nanotriangles (AuNTs). Much effort was placed into creating realistic tip models and simulations that are lacking in the literature. This was achieved using RSoft's DiffractMod software package and agreed with both theoretical intuition and experimental results. NSL techniques were then used to create AuNTs that can be used for TERS experiments in the future.

## Experimental Procedure:

Rsoft and DiffractMod were used to build and perform computational electrodynamics simulations for TERS experiments. Due to RSoft's limited drawing capabilities it was decided that as a first approach in realistic TERS simulations to model the gold-coated AFM tip as a cone with a rounded tip. Though AFM tips are generally much more complicated and angular the additions made to the typical simple-sphere model are suspected to be a valid first approximation.

Three simulations were performed including; (1) no-tip, (2) a simple-sphere tip, and (3) a realistic tip. Using parameters previously optimized by Dr. Edward Yu's group, the simulations were set up using incident light polarized perpendicular to the samples (Ge-Si<sub>0.5</sub>Ge<sub>0.5</sub> core-shell nanowires, CSNWs) at a wavelength of 633 nm and an incidence angle of 30°. All simulations were performed for a CSNW with a core radius of 40 nm and a shell thickness of 5 nm. The realistic tip was modeled as a cone 125 nm in height with a rounded tip of radius 50 nm.

The simple-sphere was also 50 nm in radius and both tip models were modeled as pure gold with the tip at a distance of 3 nm from the sample surface. As with previous work, the quantity of interest is the Electric Field Density, U, which was calculated for each of the three set-ups [1,2].

The nanofabrication portion of this project focused on the creation of AuNTs using nanosphere lithography (NSL), which is a quickly emerging technique due to its low cost, quick production time and the quality of the structures formed. This method offers a more flexible in-house alternative to commercially produced AuNTs.

The first step in the NSL process is to deposit a monolayer of polystyrene (PS) nanospheres onto a glass substrate. This was achieved by pipetting a 1:1 nanosphere:ethanol solution into a shallow water bath. After adding the nanospheres, the substrate was used to scoop up the nanospheres. After drying, the substrate was then coated with 300Å gold on a 50Å adhesion layer of titanium using electron beam physical vapor deposition (EBPVD). After depositing the gold, the nanospheres were lifted off by sonicating the substrate in a toluene bath.

## Results:

The electric field density (EFD) for each of the three simulations is shown in Figures 1-3. Immediately obviously is the drastic difference in the EFD produced by adding a tip — roughly a 500% increase in intensity. This serves to show that the modeling software correctly predicts intensity changes found in TERS experiments. The more interesting difference is that between Figures 3 and 4. Here it is noted that though the simple-sphere model has a greater maximum intensity the realistic tip model has a greater overall sample penetration with slightly more localization near the tip. This suggests that the simple-sphere model is not appropriate for TERS simulations and that more realistic tip modeling is necessary to ensure accurate results.

An AFM image of the AuNTs created through NSL is presented in Figure 4. Though there appears to be a somewhat periodic array of AuNTs, there are very clearly

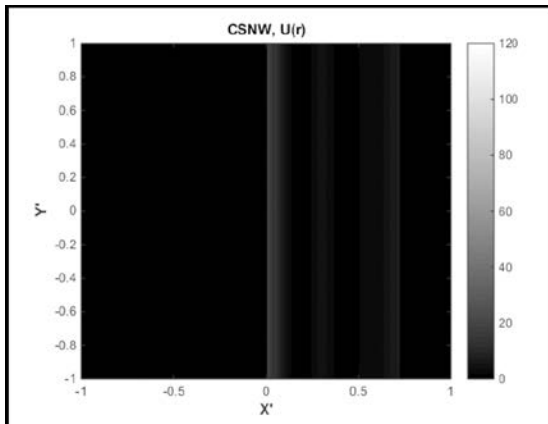


Figure 1: EFD for a CSNW sample without tip.

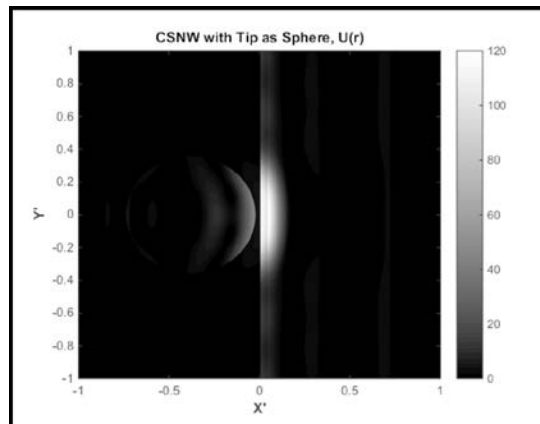


Figure 2: EFD for a CSNW with a simple-sphere tip.

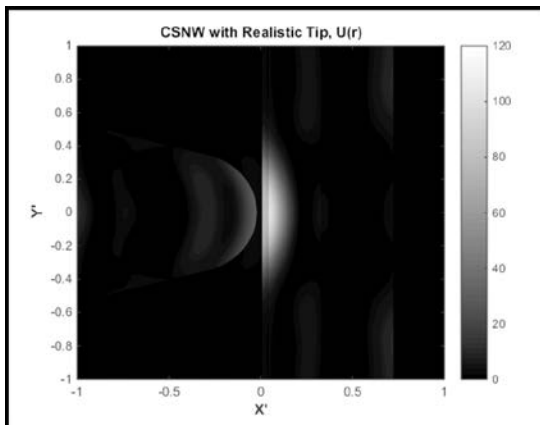


Figure 3: EFD for a CSNW with a realistic tip.

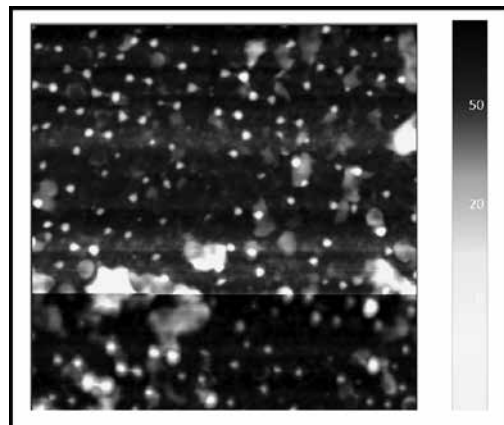


Figure 4: AFM of AuNTs deposited onto glass substrate.

defects and imperfections. There also appears to be debris or other substances on the substrate. Though AuNTs were created using them in tip- and surface-enhanced Raman spectroscopy (SERS) experiments is required to verify the viability of this procedure.

### Future Work:

In future simulations it may prove fruitful to model a more angular tip. Electric fields concentrate around edges and thus more accurate results may be obtained from an angular tip model [3]. Similarly in the simulations for this project, the tips were modelled as solid gold even though the tips were actually gold-coated Si tips. Future simulations should incorporate this material layering (though it is believed that with a  $\sim 120$  nm Au coating the effects of this addition would be minor).

In future AuNT fabrication using NSL, it will be necessary to perfect the NS monolayer deposition as this is the step that determines the quality of the structures. One way this can be achieved is through evaporating the water from the bath allowing the monolayer of NS to deposit uniformly

instead of using the scoop technique. Also other substrates should be explored to determine the best fit for the process.

### Acknowledgements:

Thanks are given to Zhongjian Zhang, Gabriel Cossio, and Dr. Edward Yu for assisting with and preparing this project. Thanks are also given to the Microelectronics Research Center at The University of Texas at Austin, NNIN REU Program, and the NSF, which provided funding for this project under Grant No. ECCS-0335765.

### References:

- [1] Z. Zhang, D. Dillen, E. Tutuc, E. Yu, Strain and Hole Gas Induced Raman Shifts in  $\text{Ge}-\text{Si}_x\text{Ge}_{1-x}$  CoreShell Nanowires Using TERS, *Nano Lett.* 2015, 15, 4303-4310.
- [2] Griffiths, David J. *Introduction to Electrodynamics*. Upper Saddle River, N.J: Prentice Hall, 1999. Print.
- [3] Novotny, L., Hecht, B. *Principles of Nano-Optics*. Cambridge University Press, Cambridge. 2012.

# Image Reconstruction through Scattering Media Using a Single-Pixel Camera

**Nathan Brooks**

**Physics, University of Arizona**

**NNIN REU Site: Colorado Nanofabrication Laboratory, University of Colorado, Boulder, CO**

NNIN REU Principal Investigator: Dr. Rafael Piestun, Electrical and Computer Engineering, University of Colorado Boulder

NNIN REU Mentor: Antonio Miguel Caravaca Aguirre, Electrical and Computer Engineering, University of Colorado Boulder

Contact: [nbrooks3@email.arizona.edu](mailto:nbrooks3@email.arizona.edu), [rafael.piestun@colorado.edu](mailto:rafael.piestun@colorado.edu), [caravaca86@gmail.com](mailto:caravaca86@gmail.com)

## Abstract:

Improved techniques to efficiently image (at optical wavelengths) objects embedded in or obscured by highly scattering media are desirable due to the large number of potential applications, most notably in the arena of biomedical imaging. In this experiment, we tested the performance of an image reconstruction technique utilizing Hadamard analysis and single-pixel photodetection of both forward and backscattered light. Resolution targets were fabricated and obscured by scattering media, and subsequently illuminated with structured light patterns projected by a digital micromirror device. Outgoing scattered light was collected and focused onto a photodiode, and the resulting signal analyzed in order to reconstruct an image. We tested imaging of reflective targets illuminated with incoherent white light, and are currently doing the same with fluorescent targets illuminated by a supercontinuum laser source tuned to the proper excitation frequency.

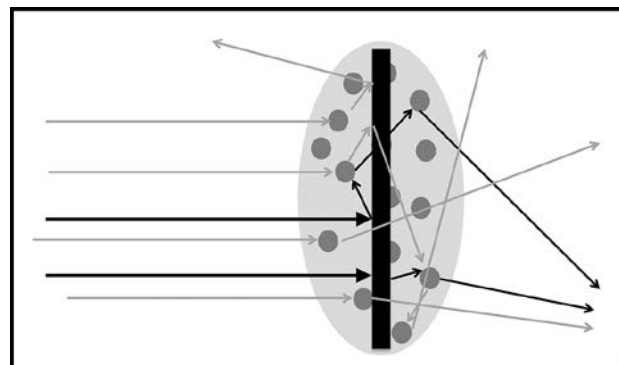


Figure 1: Incident light is scattered due to impurities in a medium. The bold rays represent the few “ballistic photons” that make it to an obscured target without scattering.

## Introduction:

Certain types of materials scatter light in complex and unpredictable fashions due to the presence of irregularities/impurities, or “scattering centers,” suspended throughout the otherwise regular medium. One example of this type of material is biological tissue, and so a viable technique to image objects obscured by or embedded in highly scattering media is highly sought after for its potential applications in biomedical fields.

If an object is embedded inside a highly scattering medium and subsequently illuminated by light, the light that propagates through and exits the system can be divided into two classes. Assuming the object is embedded at a depth greater than the transport mean free path of light, the majority of photons will be scattered away from their initial trajectory before reaching the object. These are

the **multiply scattered photons**, and it is very difficult to retrieve any useful information about the embedded object. However, some photons will travel in effectively a straight line towards the object, either through forward scattering or avoiding scattering altogether. These **ballistic photons** will subsequently interact with the object, and their subsequent behavior will depend on the object’s optical properties along the photon’s initial trajectory. The technique we test for imaging through scattering media depends on the collection of these ballistic photons.

To accomplish this, we “scan” our medium/object ensemble by projecting light in a sequence of patterns, each illuminating some particular fraction of the ensemble. Formally, these **Hadamard patterns** are an orthonormal basis of 2D Walsh functions, and thus completely sample the ensemble. We collect the emergent light signal with a photodiode (a “single-pixel camera”). This signal consists of a noisy “blur” from the multiply scattered photons, as well as important fluctuations resulting from the ballistic photons, the intensity of which are related to the object’s optical properties in the areas illuminated by a given Hadamard pattern. Collecting this signal for a complete set of patterns allows us to reconstruct an image of the embedded object.

## Experimental Procedure:

We fabricated high-contrast imaging targets using standard deposition and lithography techniques, in general using silver or aluminum resolution patterns on glass. We used a variety of scattering materials throughout our experiments, including commercial diffusers, polyester resin with  $TiO_2$ ,

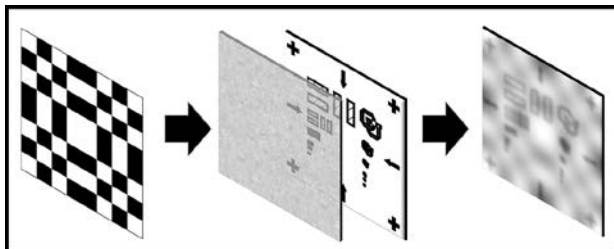


Figure 2: Projecting a light pattern on an obscured sample. The emerging light consists of diffuse noise plus “ghost” fluctuations related to the projected pattern and the properties of the target.

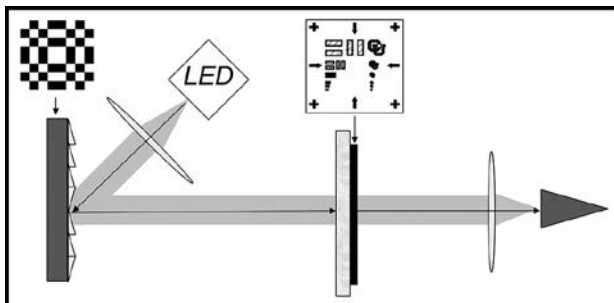


Figure 3: Simplified optical setup for transmission mode. Detector is located behind the scattering layer/target.

impurities, and gelatin. In each experiment, the target was obscured by the scattering layer and placed into our optical setup. The Hadamard patterns were projected in rapid succession using a Texas Instruments Digital Micromirror Device, an FPGA-controlled array of two-orientation mirrors.

The single-pixel imaging technique was tested in transmissive, reflective, and fluorescence experimental configurations, using several types of objectives with magnifications between 10 $\times$  and 50 $\times$ . In our transmissive setup, we used a high-powered white LED source. The photodetector was placed on the far side of the scattering layer and target, so as to collect the light transmitted through the ensemble. The second, “reflection mode” configuration involved using a standard beam splitter to capture the light scattered backwards from the ensemble instead. Finally, we used imaging targets with fluorophore-heavy photoresist rather than reflective metal. For this setup, we replaced our LED source with a supercontinuum laser tuned to the excitation frequency, and the beam splitter with an appropriate dichroic mirror.

In each experiment, the spatially resolved cross-correlation measurement between projection and response was summed over for the full set of patterns and normalized to a grayscale intensity value (0-255) in order to reconstruct an image.

## Results and Future Work:

For our transmission mode experiment, we were able to achieve submillimeter resolution through several types of scattering media, each with thicknesses of several millimeters. An example set of images from this setup is shown in Figure 4. We subsequently demonstrated limitations with this imaging technique in more complicated optical setups. In reflection mode, the high level of backscattered light coming from the very front layer of our scattering media results in a high level of noise that makes extracting a useful signal much more difficult than in transmission. Our fluorescence experiment is an attempt to address this problem, as we use a dichroic mirror to filter out laser light coming off the front of the medium. More advanced detection systems are necessary for fluorescence imaging due to the very low amount of light making it to the detector; thus, future work involves combining a detection system such as a photomultiplier tube with sophisticated computer algorithms to compensate for noise levels.

## Acknowledgments:

Prof. Rafael Piestun, Antonio Miguel Caravaca Aguirre, Alex Denton, and Dakota Smith, Molly Ennenbach, CNL, National Nanotechnology Infrastructure Network Research Experience for Undergraduates (NNIN REU) Program, CU Boulder, NSF Grant No. ECCS-0335765.

## References:

- [1] Tajahuerce, E., et al.; “Image transmission through dynamic scattering media by single-pixel photodetection”; Opt. Express 22, 16945-16955 (2014).
- [2] Durán, V., et al.; “Imaging at depth in tissue with a single-pixel camera.”; arXiv:1411.2731 [physics.optics] (2014).

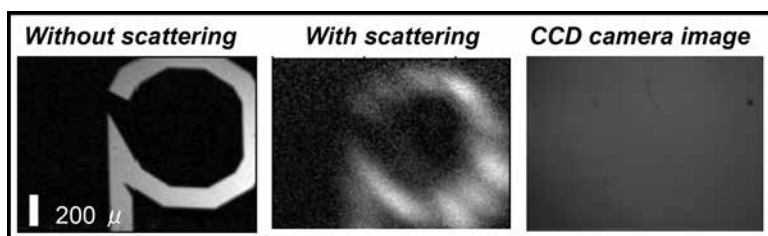


Figure 4: Sample image set from transmission experiment.

# Fabrication of Test Samples for Calibration and Testing in 3D Super Resolution Microscopy

**Molly Enenbach**

**Biology, New Mexico Highlands University**

**NNIN REU Site: Colorado Nanofabrication Laboratory, University of Colorado, Boulder, CO**

NNIN REU Principal Investigator: Prof. Rafael Piestun, Computational Optical Sensing and Imaging, University of Colorado, Boulder

NNIN REU Mentor: Dr. Anthony Barsic, Computational Optical Sensing and Imaging, University of Colorado, Boulder

Contact: menenbach9@gmail.com, rafael.piestun@colorado.edu, anthony.barsic@colorado.edu

## Abstract:

In order to verify the performance of three-dimensional super-resolution microscopy systems, we used nanofabrication techniques in non-traditional ways in order to generate sub-wavelength test samples. Such samples allowed unprecedented control of the arrangement of fluorescent probes, and the resulting images provided valuable metrics regarding super-resolution results.

## Introduction:

Three-dimensional (3D) super resolution microscopy allows researchers to circumvent Abbe's Diffraction Limit while capturing images of biological specimens with immense detail (one order of magnitude better than the diffraction limit). Due to the increasing resolution and ability to examine nanoscopic features, knowledge of our measurement accuracy and precision is essential. The focus of this project was to create test samples with known dimensions that emulated biological samples in order to calibrate and test 3D super resolution microscopy systems.

We made two types of samples: apertures in chrome for use in transmission mode, and sub-wavelength arrangements of fluorescent particles. For the transmissive samples, a focused ion beam (FIB) was used to transfer nanoscopic patterns into thin layers of opaque chrome deposited on a glass substrate. These test samples allowed us to evaluate the precision of a given instrument, as well as investigate the extent of optical aberrations across the field of view. Secondly, a new method of nanoscopic fabrication was used to generate a nano-scale patterned sample with a controlled arrangement of fluorescent probes. With such a sample, we were able to demonstrate the proof of concept of this fabrication technique and additionally, test the resolution limit of point sources in close proximity due to the ambiguity caused by overlapping Point Spread Functions.

## Experimental Procedure:

**Sub-Wavelength Apertures in Chrome.** We used AutoCAD (Autodesk, USA) to design sub-wavelength apertures and fabricated the design with a FIB. Before fabrication, 50 nm of chrome was sputtered onto the cover slide (18 × 18 × 0.16 mm) with a reactive DC sputter deposition System. The samples were examined with an Olympus IX83 super-resolution system, which consisted of a 1.45 NA 100x objective, an Andor iXon electron multiplying CCD camera, and white light illumination with a halogen lamp. A double helix-point spread function phase mask was placed in the Fourier plane to collect 3D information from the sample.

**Nano-Scale Patterning of Fluorescent Probes.** We used AutoCAD (Autodesk, USA) to design nanoscopic features and fabricated the design with the FIB. After gold deposition of 4 nm to reduce charging, the FIB milled 50 nm into the silicon dioxide cover slide (18 × 18 × 0.16 mm). F8789 fluorophores (ThermoFisher Scientific) were sonicated for 15 minutes. A  $10^3$  dilution of F8789 fluorophores and HPLC Water was made and sonicated for five minutes. The glass cover slide was placed in the March Jupiter III reactive ion etcher for five minutes (standard procedure) to remove the 4 nm of gold. Next, 5  $\mu$ l of  $10^3$  F8789 fluorophore, water solution was pipetted over the milled area. After 30 minutes, the solution evaporated and the sample rinsed with HPLC Water, 3 × 500  $\mu$ l. The remaining liquid was allowed to evaporate at room temperature in a dark covered container that blocked light. After evaporation was complete, the sample was examined with a Nikon stochastic optical reconstruction microscopy (STORM) system, with a similar objective and camera as above. The illumination involved a 647 nm 500 nW laser, and a dichroic mirror to separate the excitation and emission (fluorescence) light.

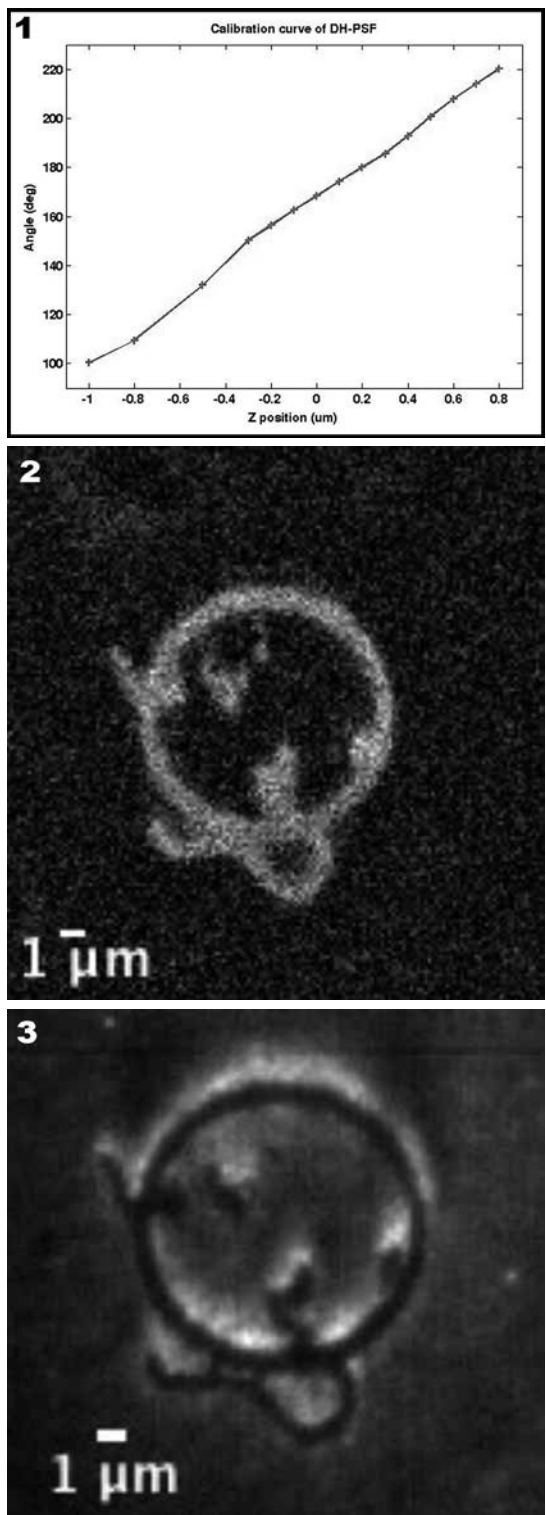


**Figure 1, top:** Calibration Curve: Calibration curve of the rotation of the Double Helix point spread function through a Z stack, analyzing Angle vs. Z position.

**Figure 2, middle:** Fluorescent Probes patterned in the shape of a Cell: A fluorescent image of mock bacterial cell designed in CAD.

**Figure 3, bottom:** Fluorescent Cell post STORM: A fluorescent image of a designed bacterial cell after photobleaching.

## Results and Conclusions:

The sub-wavelength apertures in chrome provided an aberration sample. We successfully tested the aberration sample and found that 50 nm of chrome was too transmissive and allowed for light transmission not localized in the apertures. With the data collected, a calibration curve for the double helix-point spread function phase mask was created as seen in Figure 1. The nano-scale fluorescent probe sample was excited with a 647 nm laser, showing fluorophore localization in the patterned areas (Figure 2). Due to the diffraction limit, the feature size increased, but this demonstrated resolution limit of point sources in close proximity.

During photobleaching, images were taken of a mock bacterial cell. With photobleaching, fluorophores not localized within the patterned area fluoresced as seen in Figure 3. From the images collected, we were able to prove the nano-scale patterning of fluorescent probes concept.

## Future Work:

The aberration slides for three-dimensional super resolution microscopy systems are being further developed. To improve the results and quality of the apertures in chrome experiment, the same design will be replicated on a cover slip with 100 nm of chrome, with holes varying in sizes of 50, 100, 150, and 200 nm. From this new sample, the aberrations from the center of the field of view will be compared to the aberrations at the edges of the field of view. Next, new methods will be designed and tested for nano-scale patterning of fluorescent probes to create a standard calibration slide for a variety of three-dimensional resolution microscopy systems.

## Acknowledgements:

I would like to thank the National Nanotechnology Infrastructure Network Research Experience for Undergraduates (NNIN REU) Program for this opportunity, and everyone at CU Boulder, especially Dr. Rafael Piestun for allowing me to work in his lab group, and Dr. Anthony Barsic for all of his help and guidance. I would also like to thank Dr. Tomoko Borsa, Alex Denton, Dakota Smith, the other NNIN REU students at CU Boulder, and the National Science Foundation, Grant No. ECCS-0335765.

# Nanoscale Light Emitting Diodes with Tunable Emission Colors

**Yaset Evo**

**Electrical Engineer, New Jersey Institute of Technology**

**NNIN REU Site: Lurie Nanofabrication Facility, University of Michigan, Ann Arbor, MI**

NNIN REU Principal Investigator: Pei-Cheng Ku, Electrical Engineering and Computer Science Department, University of Michigan, Ann Arbor, MI

NNIN REU Mentor: Chu-Hsiang Teng, Electrical Engineering and Computer Science Department, University of Michigan, Ann Arbor, MI

Contact: ye26@njit.edu, peicheng@umich.edu, chteng@umich.edu

## Abstract:

Indium gallium nitride/gallium nitride (InGaN/GaN) nanopillar arrays of different diameters were formed in a green multiple quantum well (MQW) light emitting diode (LED), Figure 1. Using a top-down approach, the fabricated nanoLED was able to achieve multiple color emissions using strain engineering from the same InGaN active region. During the etchback of the spin-on-glass (SOG), using  $SF_6/C_4F_8/Ar$  gas, the tip of the nanopillar, made of p-type GaN, was exposed using inductively coupled plasma. Consequentially, the electrical properties of the p-GaN deteriorated, e.g. the turn-on voltage and contact resistance increased. In order to optimize the nanoLED, a recovery treatment is necessary to restore the damage induced. We report on damage recovery by means of wet chemical treatments and rapid thermal annealing (RTA) on planar p-GaN test samples. We measured the contact resistance using rectangular and circular transmission line methods (TLM) to determine which treatment can be used to optimize the fabrication of the nanoLED. The results demonstrated that for our sample boiling potassium hydroxide (KOH) yields the most improvement in resistance. However, KOH does not fully restore the sample. We concluded that the combination of chemical treatment and annealing is necessary or a different dry etching scheme has to be developed to minimize the plasma damage.

## Introduction:

InGaN/GaN nanopillars have been studied and used in the fabrication of multiple color pixels LEDs in a single chip [1]. This nanoLED is suitable for micro display applications, lighting and sensors. The InGaN nanopillar structure is used over planar structure because of its advantages: improved internal quantum efficiency and light extraction efficiency of photonic devices, enhancement in emission intensity and improvement in decay rate. To form p-GaN/metal contact on nanopillars, one common method is to planarize the sample surface by spin-on-glass or polymer materials, such as polyimide. After planarization, dry etching is required to expose the p-GaN, however, it induces damage on the GaN surface. Using hydrogen chloride (HCl), KOH, and molten KOH, the wet chemical treatment can etch the damaged layer formed by the dry-etch process. RTA provides thermal

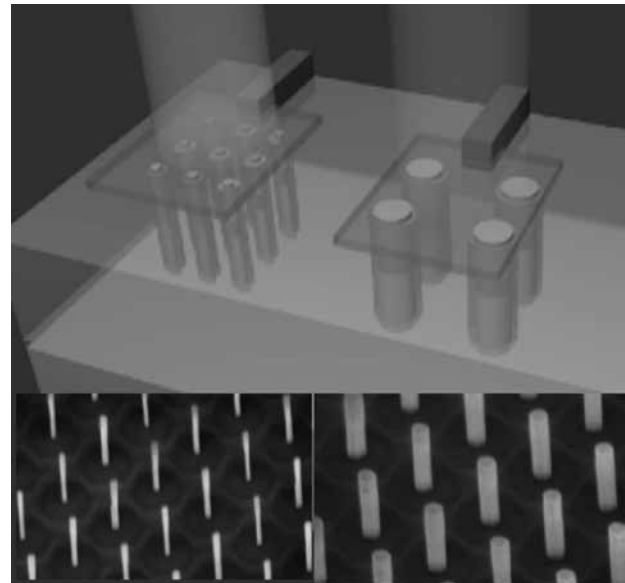


Figure 1: Top, nanoLED and bottom, SEM images of different nanopillar sizes.

energy that results in dopant reactivation and repairs surface damage from ion bombardment. The TLM is a technique used to calculate the contact resistance used to compare the restoring methods [3]. For this experiment, we calculated the specific contact resistance instead because the contact resistance depends on the size of the contact, which provides a bad comparison.

The technique involved making a metal test structure deposited in the planar p-GaN sample. The pattern deposited was separated by various distances, Figure 2. A voltage was applied between the metal contacts and the total resistance of each separation was calculated.

As a result, one can plot a linear graph of total resistance vs. spacing, which then can be used to calculate the specific contact resistance, Figure 2. The purpose of having two

patterns was that the current from the rectangular contact was not uniform [3].

### TLM Pattern Fabrication/Experiment Procedure:

The nanoLED detailed top-down fabrication is clearly described elsewhere [1]. The TLM pattern fabrication procedure is as follows; first, the planar p-GaN samples were intentionally damaged, followed by the restoring method. Then the samples were patterned via photolithography and a Ni/Au layer was deposited, 8 nm each. Then the sample was oxidized Ni/Au layer. The final thickness was 10/200 nm respectively.

For the first experiment, the samples were tested for the wet chemical treatment method. The samples were individually soaked; at room temperature HCl:H<sub>2</sub>O (1:1), boiling HCl:H<sub>2</sub>O (1:1), and boiling KOH:H<sub>2</sub>O (1:1) solutions for ten min. From the current-voltage (IV) curve, KOH showed an improvement.

For the second experiment, a higher concentration of KOH was investigated, i.e., molten KOH. A sample was also tested for the RTA method at 600°C in nitrogen ambient.

Finally, the specific contact resistance was measured using Keithley 4200, a semiconductor characterization system.

### Results and Conclusion:

Molten KOH, boiling KOH and annealing treatments on planar structure p-type GaN samples improved the specific contact resistance, Figure 3.

The calculated value of the circular and rectangular pattern of the intact sample were 0.042 and 0.788  $\Omega\text{-cm}^2$ , respectively. The calculated value of the boiling KOH circular and rectangular pattern were 0.640 and 7.53  $\Omega\text{-cm}^2$ , respectively. The difference between the rectangular and circular patterns' corresponded to the current not flowing uniformly. The calculated value of the damaged sample, although inaccurate, was 130,000  $\Omega\text{-cm}^2$  and demonstrated that when the sample was damaged it was almost not conducting.

In other experiments, HCl has been used to effectively etch surface oxide, such as gallium oxide (Ga<sub>2</sub>O<sub>3</sub>) on a GaN layer formed by a dry etch process [4]. HCl showed no improvement, a possible reason being that the oxide layer was not formed with the plasma species used in these experiments.

Prior to these experiments, the nanoLED was annealed and it showed an improvement, Figure 4. Our results showed that none of these processes fully restored the sample. In future work, boiling KOH and annealing can be combined as a restoring method. Another alternative is to substitute SOG by polyimide. This polymer can be dry-etched using an oxygen gas species. The restoration from an oxygen based plasma can be easier than fluorine based plasma.

### Acknowledgments:

I want to thank my mentor, Chu-Hsiang Teng, principal investigator, Pei-Cheng Ku, and the LNF staff. This research was

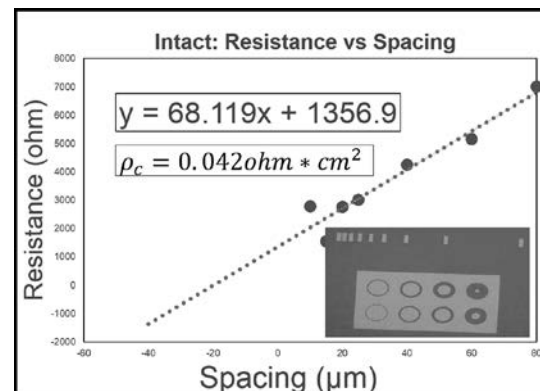


Figure 2: Total Resistance vs Spacing. TLM pattern.

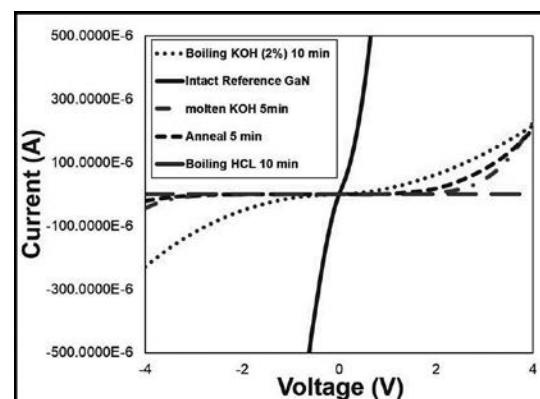


Figure 3: Recovering method.

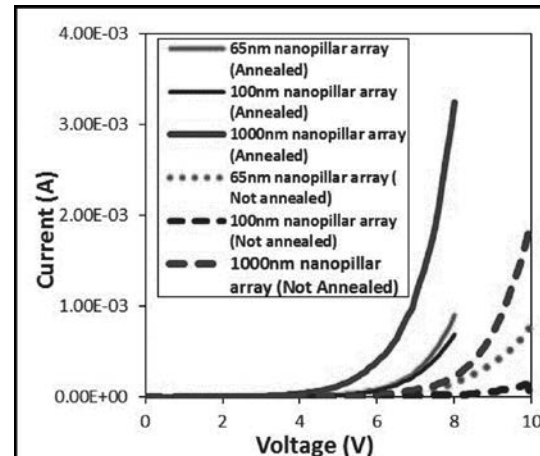


Figure 4: Annealed recovering method on nanoLED.

supported by the NNIN REU Program and NSF, Grant No. ECCS-0335765.

### References:

- [1] Teng, Chu-Hsiang, et al. In CLEO:Science and Innovations, pp. SF2G-4. Optical Soc. of America, 2015.
- [2] Zhang, Lei, et al. Applied Physics Letters. 104, 5, 051116-1-051116-5, 2014.
- [3] Klootwijk, et al. Proceedings of the 2004 International Conference on Microelectronic Test Structures, 2004.
- [4] I. Shalish, et al. Appl. Phys., 89, 390, 2001.

# Fabrication of Diamond Ultraviolet Light Emitting Diodes

**Janay Frazier**

**Optical Engineering, Norfolk State University**

**NNIN REU Site: Howard Nanoscale Science and Engineering Facility, Howard University, Washington, DC**

**NNIN REU Principal Investigator: Dr. Gary Harris, Howard Nanoscale Science and Engineering Facility, Howard University, Washington DC**

**NNIN REU Mentor: James Griffin, Howard Nanoscale Science and Engineering Facility, Howard University**

**Contact: j.a.frazier@spartans.nsu.edu, gharris1124@gmail.com, jagriffin@howard.edu**

## **Abstract:**

Ultraviolet light emitting diodes (UV LEDs) have been used in a variety of applications and as a result are becoming cheaper to fabricate. LED products have reached 12 watts at 914 amperes. Initial UV LEDs were fabricated with GaN films grown on sapphire substrates. The main disadvantage of this fabrication technology is the difficulty in growing high quality GaN films on sapphire because of the large lattice mismatch. Diamond has a wide energy band gap of 5.47 eV, which makes it attractive for opto-electrical applications. Its high thermal conductivity makes it an excellent material for UV LED fabrication. In this work, diamond UV LEDs were fabricated by growing high-quality diamond films on silicon and silicon carbide (SiC) substrates by hot filament chemical vapor deposition (HFCVD). Methane was used as the carbon source gas with solid source boron used as the p-type dopant and N used as the n-type dopant. Hall measurements confirmed a hole concentration of approximately  $3 \times 10^{19} \text{ cm}^{-3}$ , a carrier mobility of  $73 \text{ cm}^2/\text{V}\cdot\text{sec}$ , and a resistivity of  $5 \times 10^{-3} \Omega\cdot\text{cm}$ .

## **Introduction:**

Light emitting diodes are semiconductor light sources that are fabricated from a p-n junction that emits light when activated. When a suitable voltage is applied to the contacts, free electrons recombine with holes within the device. Once recombination happens, photons are emitted as a function of the bandgap energy of the semiconductor material.

The objectives of this work were to grow high quality diamond films on silicon and silicon carbide substrates, dope the diamond films with boron (p-type) and nitrogen (n-type) dopants, and characterize the diamond epitaxial films by Raman spectroscopy, scanning electron microscopy, Hall effect measurements, and current-voltage (I-V) measurements. The final objective was to fabricate ultraviolet light emitting diodes by photolithography.

The semiconductor material used for the fabrication of the ultraviolet light emitting diodes was diamond. Diamond behaves as an insulating material as a result of its covalent carbon bonds but can be rendered electrically conductive by doping.

## **Methodology:**

To grow diamond heteroepitaxially, wafers must be seeded with nanodiamond slurry or "Opalseed" mixture. This process was done by placing the wafers in a 1:1 ratio mixture of nanodiamond slurry and methanol, and sonicated for

10 minutes for nanodiamond adhesion. After rinsing with methanol, the wafers were blow-dried with nitrogen gas. The samples were then loaded into the HFCVD reactor for growth. Growth conditions were as follows: hydrogen and methane flow rates of 80 sccm and 1 sccm respectively, growth pressure of 20 torr and a substrate temperature of 750°C. These conditions yielded a growth rate of about 0.16  $\mu\text{m}/\text{hr}$ . P-type doping of diamond was accomplished by placing a piece of 99.7% boron in the center of the substrate holder and very close to the hot filaments (1-2 mm) during growth. N-type doping was performed by introducing nitrogen-15 gas into the chamber during growth at an elevated substrate temperature ( $>>750^\circ\text{C}$ ).

## **Results:**

Current-voltage measurements on unannealed titanium-gold contacts on diamond revealed ohmic behavior indicating degenerate boron doping, see Figure 1. Hall measurements on boron doped diamond yielded a mobility, resistivity and carrier concentration of  $73 \text{ cm}^2/\text{V}\cdot\text{s}$ ,  $5 \times 10^{-3} \Omega\cdot\text{cm}$ , and  $3 \times 10^{19} \text{ cm}^{-3}$  respectively. Raman spectroscopy measurements of undoped diamond indicated a sharp intense peak at  $1333 \text{ cm}^{-1}$  while the boron doped diamond indicated a less intense  $1333 \text{ cm}^{-1}$  peak and a broad intense peak at  $1219 \text{ cm}^{-1}$ , shown in Figure 2, characteristic of heavy boron doping [1].

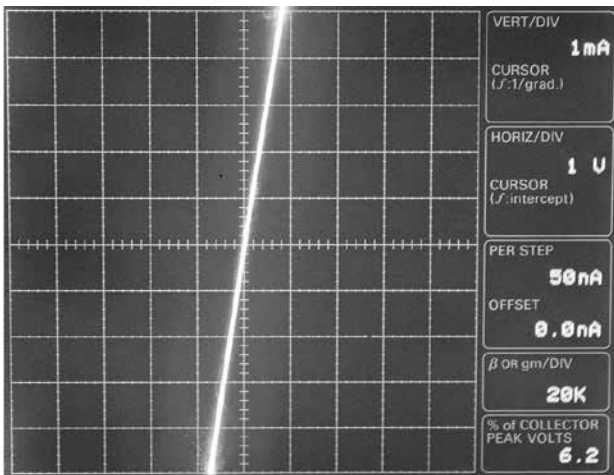


Figure 1: Current-voltage curve of unannealed titanium-gold contacts to boron doped diamond.

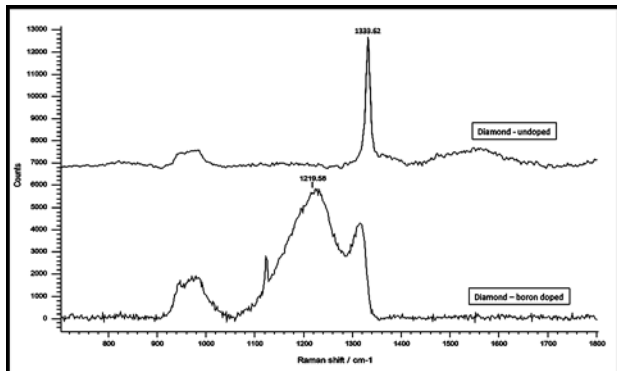


Figure 2: Raman spectrum of doped and undoped diamond.

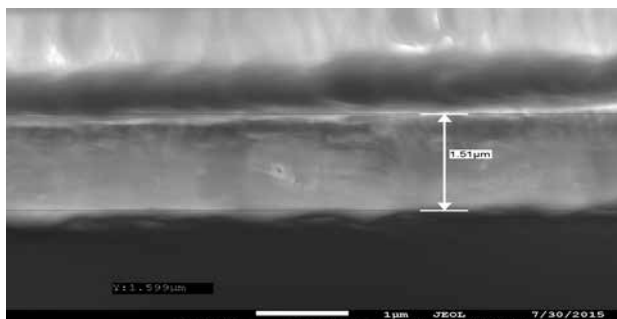


Figure 3: Cross sectional scanning electron micrograph of the interface between the boron doped diamond (top layer) and the nitrogen doped layer, 1.51  $\mu\text{m}$  thick.

Nitrogen doping to produce n-type diamond was not successful. Previous work [2] had indicated that nitrogen doping in diamond produces defects that trap free carriers and produces insulating diamond. The incorporation of nitrogen-15 and growth at an elevated substrate temperature did not change the outcome. Therefore no p-n junction was created within the final device structure due to a lack of n-type carriers.

### Conclusions:

High quality diamond films were grown by HFCVD and doped with boron. Hall effect measurements and Raman spectroscopy verified the presence of boron doping at very high concentrations (greater than  $3 \times 10^{19} \text{ cm}^{-3}$ ). While nitrogen doping to produce n-type carriers in diamond proved unsuccessful, there are a number of elements in groups V and VI of the periodic table that may prove effective as an n-type dopant in HFCVD, with phosphorus as the leading candidate. Once the n-type doping problem is solved, fabrication of ultraviolet light emitting diodes should be straightforward. Growth of polycrystalline diamond on silicon and silicon carbide may prove detrimental to device performance. Therefore growth of diamond on diamond substrates is preferable, even with their small size and large cost.

### Acknowledgments:

I would like to thank my mentor Mr. James Griffin and my Principal Investigator Dr. Gary Harris. I also give my utmost gratitude to the National Nanotechnology Infrastructure Network Research Experience for Undergraduates (NNIN REU) Program. This research was supported by the National Science Foundation under Grant No. ECCS-0335765.

### References:

- [1] Ferreira, N. G.; "Brazilian Journal of Physics - Electrochemical Characterization on Semiconductors P-type CVD Diamond Electrodes." Scielo; 8 Feb. 1999. Web. 28 Aug. 2015.
- [2] Dobrinets, I. A; "HPHT-Treated Diamonds — Diamonds Forever"; Springer Series in Mat.Science, page 7; 2013. Web. 07 Aug. 2015.

# Optical Characterization of AlInAsSb Digital Alloy Films

**Harold Fu**

**Chemical Engineering, Cornell University**

**NNIN REU Site: Microelectronics Research Center, The University of Texas, Austin, TX**

NNIN REU Principal Investigator: Seth R. Bank, Electrical and Computer Engineering, The University of Texas at Austin

NNIN REU Mentor: Scott D. Sifferman, Electrical and Computer Engineering, The University of Texas at Austin

Contact: [hjf42@cornell.edu](mailto:hjf42@cornell.edu), [sbank@ece.utexas.edu](mailto:sbank@ece.utexas.edu), [scott.d.sifferman@utexas.edu](mailto:scott.d.sifferman@utexas.edu)

## Abstract:

Aluminum indium arsenide antimonide (AlInAsSb) is a promising material because its band gap can be widely tuned while maintaining lattice matching to a substrate by varying the constituent element compositions. These characteristics allow for applications as photodetectors in the near- to mid-infrared region. These materials were grown on a gallium antimonide (GaSb) substrate via molecular beam epitaxy using a digital alloying technique. This report focuses on the optical characteristics of these digital alloys. Emission spectra were measured using photoluminescence spectroscopy at both 77K and 300K to determine bandgaps. Transmittance and reflectance data were measured using Fourier transform infrared spectroscopy. Due to the absorbance of the GaSb substrate, absorption features of wide-bandgap AlInAsSb alloys are obscured. To mitigate this, the spectra were also taken after thinning the substrate to  $\sim$ 150  $\mu$ m. Absorption characteristics were extracted from the measurements using transfer matrix methods and numerical fitting. From these data, optical parameters of the films such as absorption coefficients and refractive indices were obtained.

## Introduction:

AlInAsSb shows promising application as a photodetector material throughout the near- to mid-infrared. The band gap of AlInAsSb can be widely tuned by adjusting the constituent element concentrations, while maintaining lattice matching to the substrate. Unfortunately, the fabrication of arbitrary alloys of AlInAsSb is hampered by a large miscibility gap. Using molecular beam epitaxy and a growth technique called digital alloying, AlInAsSb can be grown by alternating layers of III-V binary alloys of the constituent elements. The grown films would thus reproduce the macroscopic optical properties of the bulk alloy.

AlInAsSb films, 300 nm thick, were lattice matched to 500  $\mu$ m GaSb substrates. Since GaSb has a smaller bandgap than many of the wider bandgap films with higher Al percentages, the absorption within the thick substrate would be much greater than that of the thin film. GaSb would thus obscure the absorption features of these digital alloys. Therefore, substrate thinning was needed to reduce the GaSb absorption.

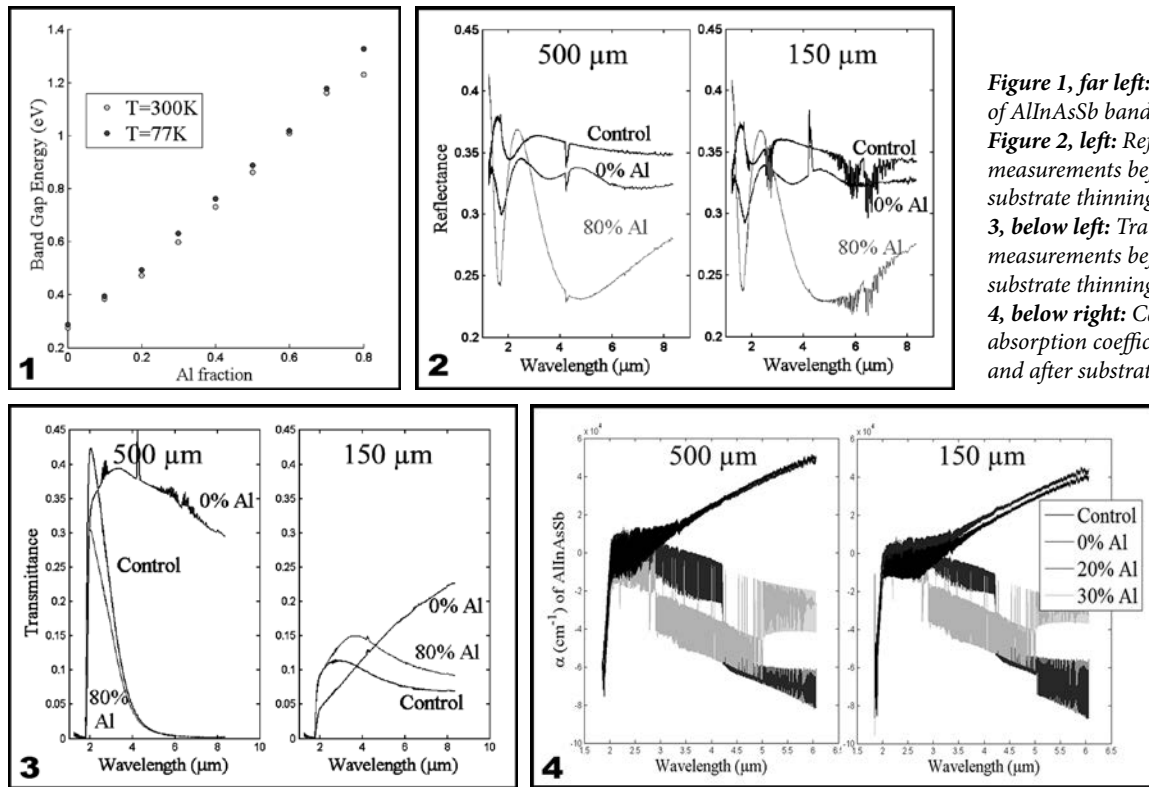
Here, we report on the emission and absorption characteristics of these digital alloys. Using various spectroscopic techniques and numerical modeling, we obtained AlInAsSb band gap energies, absorption coefficients, and indices of refraction.

## Experimental Procedure:

Photoluminescence spectroscopy was conducted on a GaSb control and 0-80% Al containing digital alloy samples at 300K and 77K. A 532 nm laser was used to excite the samples, and an InSb detector gathered emission data [1]. Substrate thinning was performed on each sample to thin GaSb substrates from 500  $\mu$ m to 150  $\mu$ m. Using a KBr beamsplitter and SiC globar source, Fourier transform infrared spectroscopy (FTIR) was used to gather reflectance and transmittance data before and after thinning. The transmittance data was used in a numerical model to calculate absorption spectra [2]. Using obtained absorption coefficients, the refractive index was calculated from Kramers-Kronig relations.

## Results and Conclusions:

Emission spectra from photoluminescence measurements at 300K and 77K indicate a monotonic increase of band gap energy with increasing Al fractions, as illustrated in Figure 1. At 77K, the emission spectra were narrowed and more intense than 300K due to reduced thermal broadening [1]. In FTIR reflectance measurements shown in Figure 2, there was decreased reflectance with increasing Al fraction. After substrate thinning, there was little change in the spectra, making it unsuitable for differential calculations of absorption spectra. The transmittance spectra in Figure 3 indicated lowered transmittance in the 2-3  $\mu$ m region, which was attributed to surface scattering effects of light



on the roughened GaSb after thinning. Diminished transmittance for various samples like the control and 80% Al at higher wavelengths were attributed to higher doping levels in the GaSb substrate, which contribute to increased free carrier absorption.

Using a transfer matrix model, we first solved for the absorption spectra of GaSb, in which the physical characteristics obtained served as a proof of concept for the model [3]. The transmission coefficient of polished and roughened GaSb surfaces were then found to account for surface scattering. Differential calculations using transmittance data before and after thinning were used to find substrate absorption within the digital alloy samples, which can be used to find the absorption spectra of AlInAsSb.

As shown in Figure 4, nonphysical absorption coefficients of AlInAsSb were obtained because the GaSb substrate were strongly absorbing despite thinning. Furthermore, samples with stronger free carrier absorption further masked the optical characteristics of AlInAsSb. Extreme oscillations in the spectra were attributed to the etalon effect. The band gap for the 0% Al sample was observed at 0.294 eV (4.22 μm), which closely matches the respective band gap at 0.287 eV found in photoluminescence spectroscopy at 77K. Due to nonphysical nature of the absorption spectra, the calculated indices of refraction also do not provide realistic results.

While photoluminescence measurements do provide promising results towards the ability to tune the band

gap of AlInAsSb, the nonphysical absorption coefficients illustrate the difficulty of separating AlInAsSb absorption from that of the substrate.

### Future Work:

The numerical model may be refined to account for individual binary layers in the digital alloy. Experimentally, AlInAsSb may regrow with an etch stop layer used for membrane liftoff onto a substrate transparent in the IR region. This would allow direct measurement of AlInAsSb without obscuration from absorption in GaSb.

### Acknowledgements:

I want to thank Scott Sifferman, Dr. Seth Bank, and the rest of the LASE group for their incredible guidance. I also want to thank the National Nanotechnology Infrastructure Network Research Experience for Undergraduates (NNIN REU) Program and the National Science Foundation for their support under Grant No. ECCS-0335765.

### References:

- [1] Gfroerer, T.H.; Encyclopedia of Analytical Chemistry, R.A. Meyers, 9209-9231 (2000).
- [2] Katsidis, C.C., Siapkas D.I.; Applied Optics, 41 (19), 3978-3987(2002).
- [3] Adachi, S.; Journal of Applied Physics, 66, 6030 (1989).

# Optical Resonant Frequency Detection System for Mass-Sensing MEMS Resonators

**Kasia Gibson**

**Bioengineering, Northeastern University**

**NNIN REU Site: Washington Nanofabrication Facility and Molecular Analysis Facility, University of Washington, Seattle, WA**

NNIN REU Principal Investigator: Lih Y. Lin, Electrical Engineering, University of Washington-Seattle

NNIN REU Mentors: Ethan Keeler, Peifeng Jing, Conner Ballew, and Jingda Wu; Electrical Engineering, University of Washington-Seattle

Contact: gibson.kasia@gmail.com, lylin@uw.edu, e.keeler@live.com, peifengjing@gmail.com, ckballew@uw.edu, albuswu@gmail.com

## Introduction:

A newly proposed biomedical application for the combination of optical tweezers and micro-electro-mechanical systems (MEMS) resonators has promise for long-term mass monitoring of single cells. In cell trapping, a laser beam is focused through a microscope onto a cell to trap and position it on the resonator; a separate laser beam is incident onto the vibrating resonator and produces an optical deflection signal for frequency detection. The problem with using traditional optical trapping in this scheme is a decoupling between the cell trap and the resonating substrate, mitigating the cell's influence on the resonant frequency.

This can be remedied with the integration of photonic crystals. The MEMS resonator measures the cell mass by detecting the resonant frequency change of a resonant beam [1], and the photonic crystal optical tweezers are applied to improve the mass sensing capability of the MEMS resonator by fixing the cell position with low light intensity [2]. With the usage of photonic crystals on a MEMS resonator, the position of a cell can be finely controlled to enhance the ability of the resonator to monitor changes in cell mass over time by inducing shifts in the device's resonant frequency [1]. A detection circuit was necessary to measure these shifts. Being able to trap and measure the resonant frequency enables the

manipulation and identification of living cells, parallel manipulation of DNA strands and nanoparticles, and identifying a cell's biophysical characteristics.

## Experimental Procedure:

**Detection Circuit.** The original detection circuit included two transimpedance amplifiers and a difference amplifier, serving the purpose of amplifying the signal produced by the optical deflection signal provided by a split photodiode. Figure 1 displays a general overview of the circuit. The circuit design software, Multisim, was used to establish an effective circuit schematic that would predict the behavior of the circuit to ensure a sinusoidal waveform as the output of the difference amplifier. In Multisim, the split photodiode was replaced with an AC current source at an initial frequency of 1 kHz. Through simulations, appropriate revisions to the circuit were conducted to provide an accurate layout to ensure the success of the circuit.

Originally the voltage ranges were from -2.5V to +2.5V, which was an issue considering an Arduino microcontroller would be programmed and combined with the circuit to calculate the resonant frequency. This

was solved by inserting voltage dividers that would offset the voltage to an appropriate range of 0V to 5V. To counteract noise, a low pass filter was added (a  $3.6\text{ k}\Omega$  resistor and a  $0.1\text{ nF}$  capacitor) with a cutoff frequency of approximately 420 KHz. A major issue was maintaining five volts throughout the circuit. To counter that, a voltage buffer was added, a unified power supply for the transimpedance amplifiers was established and the resistor values for the difference amplifier were modified.

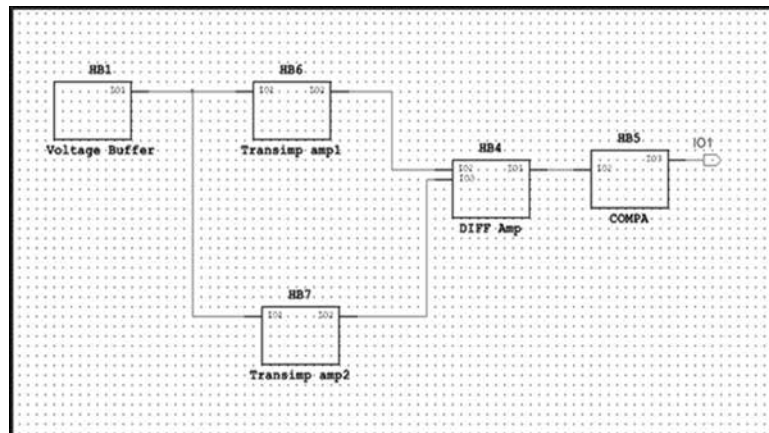


Figure 1: Circuit design overview.

A comparator was added to change the sinusoidal waveform into a square wave to make detection with the Arduino easier. One of the final steps using Multisim was increasing the frequency of the AC current source from 1 kHz to 300 kHz (split photodiode) to accurately reflect the frequency of the laser beam that will hit the split photodiode. That, however, changed the sinusoidal waveform from the difference amplifier to a triangular wave due to slew rate limits. This was remedied by lowering the gain (changing the resistor values from 100 k $\Omega$  to 10 k $\Omega$ ) of the transimpedance amplifiers. During the assembly of the circuit, the comparator V<sub>cc+</sub> was changed from 5V to 10V, so that the oscilloscope can display the comparator signal.

**Arduino Programming.** With the usage of an Arduino microcontroller and programming software, the frequency of the vibrating resonator could then be measured by inputting the output of the comparator directly into the Arduino. The Arduino code was programmed to monitor overflow, count rising edges, enable the timer, temporarily store data and calculate the frequency after one hundred cycles.

## Results and Conclusions:

With the laser beam collimated onto the split photodiode, the detection circuit was able to output an expected sinusoidal waveform (resonant frequency) from the difference amplifier and a square wave from the comparator, while maintaining a viable output voltage

between the 0 to 5 volt range that allowed the Arduino microcontroller to calculate the resonant frequency. Figure 2 shows the output of the difference amplifier. Arduino code was tested using a signal from the function generator. With the proper adjustments to the code, the Arduino was able to calculate the frequency provided by the function generator. However, with a minuscule shift in the positioning of the laser beam onto the split photodiode, the expected frequency was compromised. While there are minor setbacks with the Arduino code and cell viability in terms of optical trapping of cells, there is great evidence that photonic crystal optical tweezers will not only be able to distinguish different types of cells, but also enable long-term biological mass studies.

## Future Work:

The next step in this process is to modify the Arduino code that will allow the accurate measuring of the resonant frequency regardless of the positioning of the collimated laser beam as it hits the split photodiode. With the modification of the detection circuit on the optical setup, the durability and efficiency of the circuit can be enhanced. The last major step would be to mount the detection circuit on the bio-sensing resonator, and calculate resonant frequency shifts using the optical deflection signal produced by living cells.

## Acknowledgments:

I would like to thank my mentors Peifeng Jing, Ethan Keeler, Conner Ballew and Jingda Wu for greatly assisting me, as well as my Principal Investigator, Professor Lih Y. Lin, for giving me this opportunity to assist in this research project. This research was supported by the National Science Foundation under Grant No. ECCS-0335765 and Grant No. DBI-1353718, and by the National Nanotechnology Infrastructure Network Research Experience for Undergraduates (NNIN REU) Program.

## References:

- [1] E. G. Keeler, J. Wu, P. Jing, and L. Y. Lin, "MEMS Resonator and Photonic crystal integration for enhanced cellular mass sensing," in OSA Optics in the Life Sciences, 2015, paper BWiA.6.
- [2] Peifeng Jing, Jingda Wu, and Lih Y. Lin, "Patterned Optical Trapping with Two-Dimensional Photonic Crystals", ACS Photonics, 1(5), 398-402, 2014.

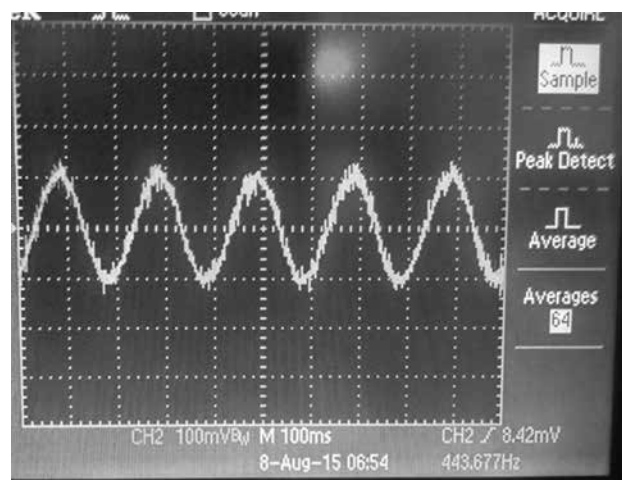


Figure 2: Signal output of difference amplifier. Output with a time base of 100 ms and a scale of 100 millivolts per division.

# Parylene/GaAs Nanowire Composites for Optoelectronics

**Cristina Guillen**

**Chemical Engineering, North Carolina State University**

**NNIN REU Site: Lurie Nanofabrication Facility, University of Michigan, Ann Arbor, MI**

NNIN REU Principal Investigator: Prof. Jamie Phillips, Electrical Engineering and Computer Science, University of Michigan

NNIN REU Mentor: Alan Teran, Electrical Engineering and Computer Science, University of Michigan (2008 NNIN REU at Stanford)

Contact: cristimguillen@gmail.com, jphilli@umich.edu, asteran@umich.edu

## Abstract and Introduction:

Complementary metal oxide semiconductor (CMOS) technology is continually decreasing in size. Right now, the smallest device is the Micro-Mote, which is less than a half a centimeter. This small device can be implanted in people with diseases such as glaucoma, and it can monitor the intraocular pressure. Its power source is a solar cell on the very top layer. A smaller design has been proposed that will reduce the weight and increase the reliability. Instead of having a 3D cube with layers of chips stacked on top of each other with wire bonding between each layer [1], the device can be placed all on one layer. The problem is directly integrating LEDs and solar cells onto the processor. This can potentially be done with thin-film gallium arsenide (GaAs) nanowires, which have been shown to make high efficiency light emitters and photovoltaic cells, and have the potential for integration on arbitrary substrates [2]. However, nanowires have dangling bonds that can decrease the efficiency of light emitters and photovoltaic cells. To improve the efficiency of GaAs nanowires, deposition of parylene on GaAs nanowire arrays are studied in this work to provide both structural support and surface passivation. Before testing could be done on the device, two questions about the deposition of parylene on the nanowires had to be answered: does the parylene seep in between the nanowires, if so does it reach the bottom?

## Design:

The proposed design of the solar cells consists of indium tin oxide (ITO) sitting on top of the processor. GaAs nanowires are grown on top of the ITO, which are then embedded in parylene. Finally, ITO is deposited on top of the nanowires as the transparent conductor.

## Methods:

Parylene is deposited on top of the nanowires using the Special Coating System Parylene Deposition System (PDS). The amount of parylene to deposit was determined by the length of the nanowires. The deposited parylene should have, approximately, the same height as the nanowires. After the parylene was deposited the sample is taken to the LAM dry etching tool to etch the parylene off until nanowires are visible. Once the etching has finished the samples are taken to the Hitachi scanning electron microscope (SEM) to see if nanowires are visible. If they are not, then etching continues until the nanowires are seen.

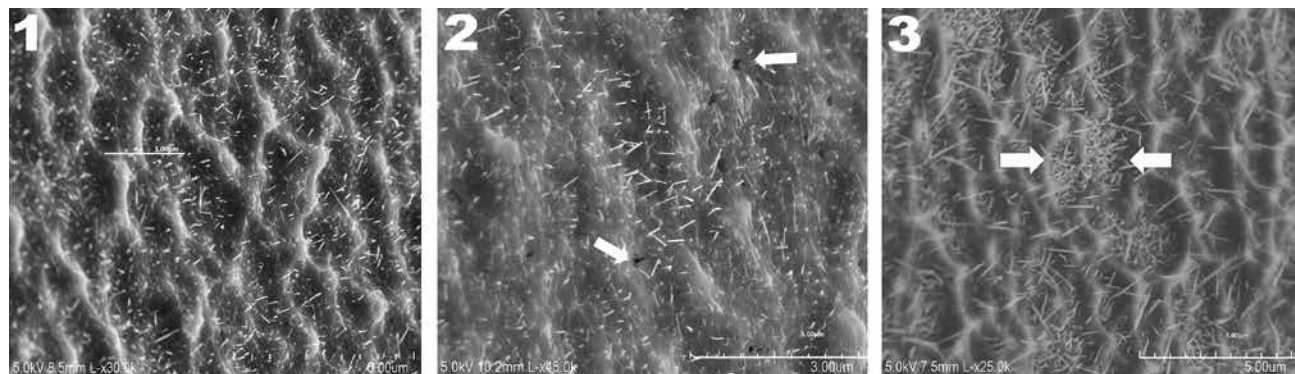


**Figure 1, left:** SEM picture of the nanowires sticking out of the parylene. **Figure 2, middle:** Holes of parylene, which can mean that there is no more parylene in that area. **Figure 3, right:** Parylene does not embed in thick clusters of the nanowires.

## Results and Discussion:

The process was repeated on samples with nanowires of different heights and it was determined that the parylene does seep in between the nanowires. After several microns of parylene were etched the nanowires always started poking out as shown in Figure 1. However, although the amount of parylene deposited was the same length of the nanowires, a significant amount of parylene had to be etched before the nanowires were visible. This shows that the parylene is not reaching the bottom of the nanowires. To confirm this, etching was continued for several samples. For some samples, small holes started appearing throughout the parylene that can be seen in Figure 2. This means that the parylene is not distributed evenly, or there is no more parylene in that area. In other samples where it was etched more, small clusters of nanowires started appearing as shown in Figure 3. This demonstrates that the parylene is not seeping through those areas.

Throughout the experiment, the sample sizes that were being used were  $1\text{ cm} \times 1\text{ cm}$ . In the etch tool these samples had a different etch rate than the standard four inch wafer. It was determined that the smaller samples were etched at half the rate. This helped us determine the amount of parylene that was actually being etched. This new information helped make a device with three different etch times to see if the current was going through the nanowires with parylene passivating them. The graph in Figure 4 demonstrates that current is going through the nanowires.

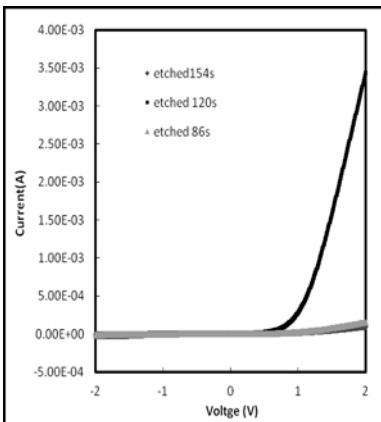


Figure 4: This graph shows that current does go through the nanowires with parylene.

## Conclusion and Future Work:

Parylene does seep in between the GaAs nanowires providing some structural support and passivation, but since the parylene is not reaching the bottom of the nanowires, the nanowires are not as efficient as they can potentially be. To solve this problem a new way of depositing parylene on top of the nanowires can be experimented with. Instead of having the parylene deposited all at once, there can be several smaller cycles of parylene deposition on the samples.

## Acknowledgments:

I would like to thank my mentor Alan Teran, my Principal Investigator Prof. Jamie Phillips, Matt Dejarld and Prof. Millunchick for providing us with the nanowires, all the individuals on this project, and all of the LNF staff. Funding for this project was provided by NNIN REU Program and NSF, Grant No. ECCS-0335765.

## References:

- [1] Fojtik, M., Kim, D., Chen, G., Lin, Y., Fick, D., Park, J., and Sylvester, D. (2013). A Millimeter-Scale Energy-Autonomous Sensor System With Stacked Battery and Solar Cells. *IEEE J. Solid-State Circuits IEEE Journal of Solid-State Circuits*, 48(3), 801-813. doi:10.1109/JSSC.2012.2233352
- [2] Teran, A., Wong, J., Lim, W., Kim, G., Lee, Y., Blaauw, D., and Phillips, J. (n.d.). AlGaAs Photovoltaics for Indoor Energy Harvesting in mm-Scale Wireless Sensor Nodes. *IEEE Trans. Electron Devices IEEE Transactions on Electron Devices*, 20(10), 2170-2175.

# Graphene/III-V Electro-Optic Hybrid Devices

**Yusuke Hayashi**

**Department of Electrical and Electronic Engineering, Tokyo Institute of Technology**

**NNIN iREG Site: Colorado Nanofabrication Laboratory, University of Colorado, Boulder, CO**

NNIN iREG Principal Investigator: Prof. Thomas Schibli, Department of Physics, University of Colorado Boulder

NNIN iREG Mentor: Chien-Chung Lee, Department of Physics, University of Colorado Boulder

Contact: [hayashi.yao@m.titech.ac.jp](mailto:hayashi.yao@m.titech.ac.jp),  
[trs@colorado.edu](mailto:trs@colorado.edu), [chienchung.lee@colorado.edu](mailto:chienchung.lee@colorado.edu)

## Abstract and Introduction:

Intracavity loss modulation is a promising method for broadband noise suppression in a modelocked laser. However, pure loss modulation with bandwidth beyond megahertz is rarely achieved with traditional electro-optic materials due to intrinsic resonances, amplitude and phase coupling or signal propagation delays. Graphene, arising as an unconventional two-dimensional material, exhibits an interband absorption of 2.3% from visible to infrared wavelengths, which is controllable by an external electric field [1]. This exciting property has been utilized recently and has led to unprecedented noise levels in compact fiber-based modelocked lasers [2,3]. In this work, we integrate a graphene modulator on a semiconductor-based saturable absorber mirror (SESAM), which serves as a device for initialization and stabilization of modelocking. This hybrid device exhibits modulation bandwidth beyond 5 MHz, which is sufficient for most noise-suppression applications. The realization of this hybrid device is based on the design and improvement of the top silicon-doped GaAs layer of the saturable absorber mirror, functioning as a transparent electrode. Various annealing conditions of the top layer and the resulting sheet resistance, carrier lifetime, and optical absorption changes are presented and discussed, along with the modulation performance of the graphene modulator.

## Experimental:

A SESAM wafer consists of a 24-pair GaAs/AlAs distributed Bragg reflector (DBR), a low-temperature grown Er-doped InGaAs quantum well (LT-Er:InGaAs QW), a LT n-GaAs cap layer (Si:  $5 \times 10^{17} \text{ cm}^3$ ). The LT-Er:InGaAs QW was used as a saturable absorber, which enables ps-order carrier relaxation times. In order to reduce the carrier relaxation time, the InGaAs QW and the following n-GaAs layer were epitaxially grown at low temperature, which led to a large number of crystal defects. Before the device fabrication the SESAM wafer was annealed at 500°C for 30 s by rapid thermal annealing (RTA) in order to lower the sheet resistance of the wafer; 20 nm Ni and 80 nm AuGe were then thermally evaporated onto the SESAM as a bottom electrode. The device was then annealed again at 350°C for 120 s by RTA to form ohmic contacts. A 50 nm  $\text{Ta}_2\text{O}_5$  was then deposited using reactive DC sputtering; 10 nm Ti and 90 nm Au were thermally evaporated as a top electrode onto

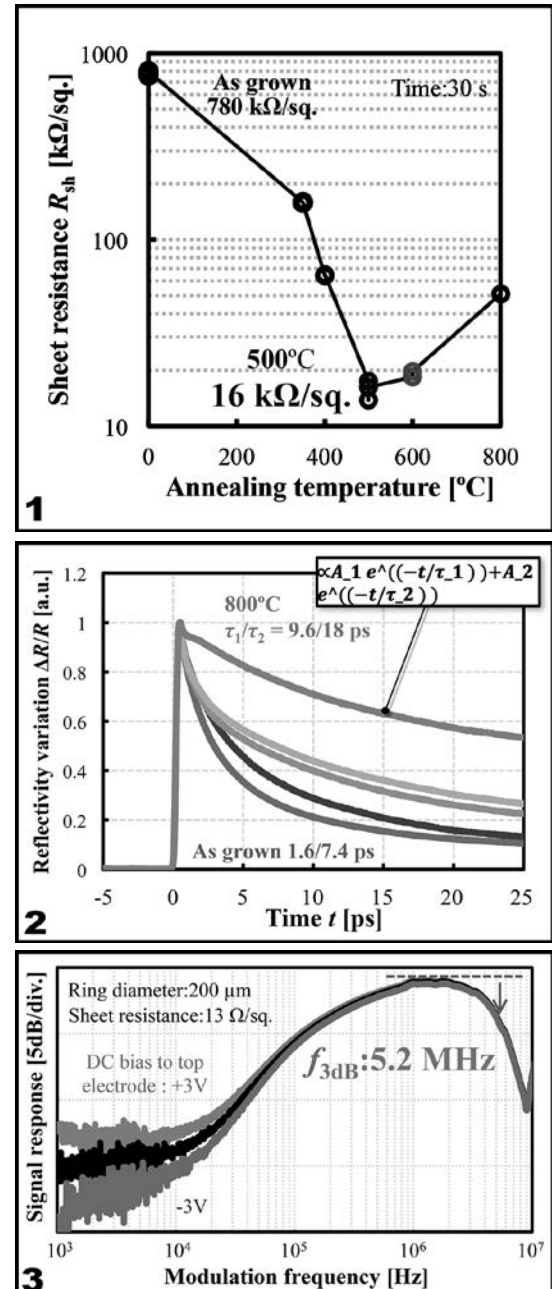


**Figure 1, top:** The sheet resistance of the annealed SESAM, measured by four-point probe method directly without metallic pads. **Figure 2, middle:** The carrier relaxation time properties of SESAMs after the annealing process. The curves represent from the bottom as grown, 400°C, 500°C, 600°C, and 800°C, respectively. **Figure 3, bottom:** The frequency response properties of the modulator.

which CVD-grown graphene was transferred. Unused graphene was removed by oxygen plasma etching to reduce the device capacitance. After finishing the fabrication, the frequency response and the modulation depth mapping of the modulators were measured by a network analyzer and a lock-in amplifier.

## Results and Discussion:

Figure 1 shows the effects of the annealing process on sheet resistance of SESAMs were examined by 4-probe method directly on SESAM, without metal contacts. At 800°C annealing temperature, silicon oxide was deposited on SESAM before annealing to prevent evaporation of As from the surface. The un-annealed sample exhibited a poor conductivity of 780 kΩ/sq., which likely resulted from crystal defects induced by the low growth temperature and charge traps from surface states of n-GaAs. When SESAM was annealed at 500°C for 30 s, the sheet resistance was improved nearly 50-fold to 16 kΩ/sq. We attribute this to the reduction of crystal defects or charge traps, while at annealing temperatures of more than 500°C dopants diffused out from the conducting layer or Ga diffused into the SiO<sub>2</sub> layer and formed vacancies acting as trapping sites [4].

The saturable absorption of the LT-Er:InGaAs QW after the annealing process was also investigated as shown in Figure 2. It can be seen that annealing increased the slow component of the carrier relaxation; however, for annealing temperatures below 600°C, the resulting longer relaxation time should still be tolerable for sub-picosecond pulse generation.

Figure 3 shows the frequency response of this hybrid graphene/III-V modulator with the SESAM annealed at 500°C for a device with an aperture diameter of 200 μm, and a post-anneal sheet resistance of 13 kΩ/sq, measured by the circular transmission line method (c-TLM). The modulator was operated by an AC voltage of 2 V<sub>rms</sub>, and illuminated by a 1550 nm continuous-wave laser diode.

The device exhibits a modulation bandwidth beyond 5 MHz thanks to the improvement of the sheet resistance. This value is sufficient for most solid-state laser applications. We assume that the DC bias dependence at low frequencies is likely explained by an equivalent circuit model considering the series capacitance that results from the Ta<sub>2</sub>O<sub>5</sub> insulating layer and the depletion region formed at the surface of the n-GaAs layer. The modulation depth mapping in Figure 4 shows uniform modulation area within the active aperture.

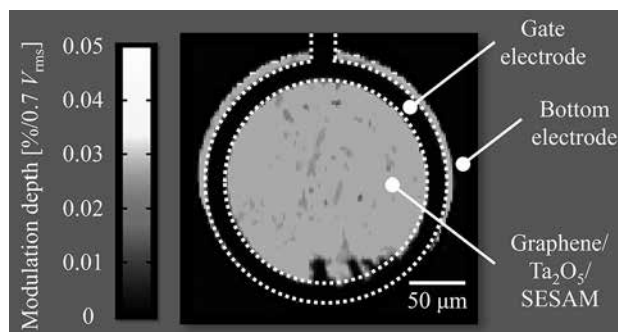


Figure 4: Modulation depth mapping of the modulator. The ring diameter is 200 μm.

## Conclusions and Future Work:

We demonstrated an electro-optic graphene/III-V hybrid modulator achieving an operation bandwidth beyond 5 MHz. A post-growth annealing processes successfully reduced sheet resistance of the SESAM from 780 kΩ/sq. to 16 kΩ/sq., which largely improved the cut-off frequency of the modulator. In the future, we are going to combine the modulator with modelocked lasers for noise suppression applications.

## Acknowledgements:

This research was supported by the National Science Foundation under Grant No. ECCS-0335765. I would like to acknowledge NIMS and the National Nanotechnology Infrastructure Network International Research Experience for Graduates (NNIN iREG) Program. Special thanks goes to Prof. Thomas Schibli, Mr. Chien-Chung Lee, Prof. Bart Van Zeghbroeck, and Dr. Tomoko Borsa for their invaluable assistance. I would like to thank Dr. Kevin Silverman (NIST) and Dr. Richard Mirin (NIST) for the SESAM fabrication.

## References:

- [1] M. Liu, et al.; Nature 474, 64 (2011).
- [2] C.-C. Lee, et al.; Optics Express, 20, 5264 (2012).
- [3] C.-C. Lee, et al.; Optics letter, 37, 3084 (2012).
- [4] B.S. Ooi, et al.; IEEE J. of Quantum Electronics, 33, 1784 (1997).

# Optimizing Hard Mask Etching for Quartz NanoDevices

**Rachel Miller**

**NanoEngineering, University of California, San Diego**

**NNIN REU Site: Center for Nanoscale Systems, Harvard University, Cambridge, MA**

NNIN REU Principal Investigator: Professor Marko Lončar, John A. Paulson School of Engineering and Applied Science, Harvard

NNIN REU Mentor: YoungIk Sohn, John A. Paulson School of Engineering and Applied Science, Harvard University

Contact: ram006@ucsd.edu, loncar@seas.harvard.edu, sohn@seas.harvard.edu

## Abstract:

Quartz is well recognized for its superior mechanical properties in piezoelectric devices and has recently shown potential for use in tunable optical filters. However, due to the lack of thin film technology for quartz, its use has been limited to microscale devices. An angled etching fabrication technique has been adopted to realize nanoscale quartz devices. To employ this technique, an evaporated or sputtered aluminum or titanium mask must be used. In order to achieve high quality for nanomechanical or optical devices, surface smoothness is of utmost importance. To achieve this, we optimized hard mask dry etching to transfer a smooth sidewall to the final device. We tested various etch recipes, tracking the effect of temperature, gas flow, and DC bias on anisotropy and selectivity. Our most successful recipes with both aluminum and titanium etching resulted from increasing temperature and optimizing DC bias. Aluminum yielded an acceptable quality etch product. Titanium had issues with selectivity and stress.

## Introduction:

The Lončar group has published work on angle-etching diamond for use in “A variety of nanoscale photonic, mechanical, electronic, and optoelectronic devices” [1]. We desired to apply this technique to quartz, a well studied and commonly used material in electrical and computer engineering. To do so, we required a reliable quartz etch procedure that preserved high selectivity and high aspect ratio [2]. In previous experimentation, photoresist and oxides had not been sufficient and instead aluminum and titanium were the most promising candidate mask materials.

Once these methods are employed, as depicted in Figure 1, the group can create and test quartz nanodevices for advanced scanning microscopy or optoelectromechanical devices such as optical tuners.

## Experimental Procedure:

One centimeter by one centimeter samples were cut from a standard thickness quartz wafer. When ready to be used,

4-6 samples were then put into a 1:3 ratio  $\text{H}_2\text{SO}_4:\text{H}_2\text{O}_2$  solution followed by sonication in acetone, then methanol, then isopropyl alcohol to remove impurities.

**Hard Mask Fabrication, Patterning, and Etching.** One micrometer of aluminum or titanium was electron beam vapor deposited. Pressure would rise as the deposition rate increased as a result of increased chamber temperature and increased particle count. Samples were then spincoated with photoresist and electron beam patterned. We then etched individual samples in the Plasma Therm Unaxis Shutline reactive ion inductively coupled plasma etcher. As we observed changes in etch quality, we changed pressure, gas flow, and heat exchanger temperature.

**Aluminum.** In aluminum (Al), the variables commonly changed were pressure and temperature. Al was etched with various recipes, the most successful, as displayed in Figure 2B was with twelve standard cubic centimeters per minute (sccm) of  $\text{BCl}_3$ , 25 sccm of  $\text{Cl}_2$ , and 6 sccm of  $\text{CH}_4$  flowing at a pressure of 8 milliTorr, which yielded a DC bias of 380.7 volts.

**Titanium.** With titanium, the etch recipe variables most commonly changed were time interval and temperature. We experimented with using multiple shorter time intervals (one to two minutes) to achieve more control over etch progression and avoid over or under etching.

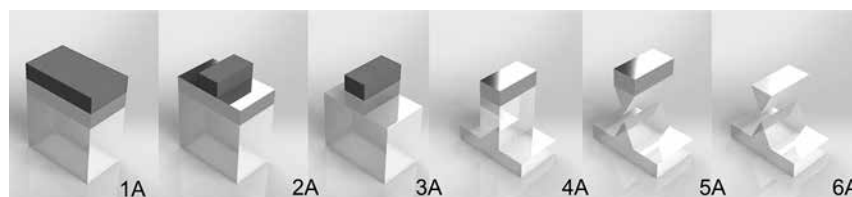
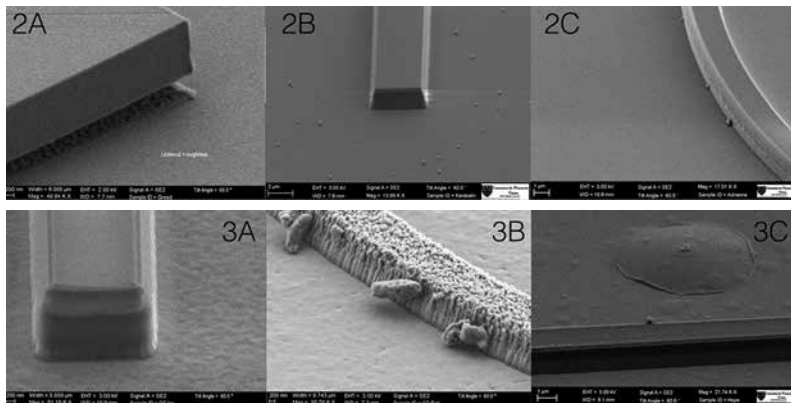


Figure 1: Top layer represents resist. Middle layer represents aluminum or titanium thin film. Bottom transparent layer represents quartz.



**Figure 2, top left:** (2A) 300 nm aluminum film undercut and rough due to film being too thin and lack of polymer sidewall coating. (2B) One micron, more anisotropic, but residue remained. (2C) Almost all residue gone, anisotropic, clean sidewalls.

**Figure 3, bottom left:** Titanium film under etching, over etching, and film breakage.

**Imaging and Evaluation.** These samples were imaged with the Zeiss Supra scanning electron microscope at a sixty degree tilt to observe changes in etch quality between recipes.

## Results and Conclusions:

**Aluminum Hard Mask Etch.** Etch quality of aluminum was improved to be applied in full device fabrication. Figures 2A and 2B are from the first and last etch recipes, respectively. They demonstrate how introducing methane gas and increasing temperature yielded a more anisotropic etch with cleaner sidewalls. They also show that a thicker thin film of aluminum was needed to combat over etching and improve selectivity.

Methane was introduced to create polymers that would form protective layers on sidewalls, preventing undercutting and roughness during etching. However, once these polymers are introduced they can settle along with aluminum chloride, leading to over etching and/or disruption of structures. To reduce residue, we increased heat exchanger temperature to increase chamber volatility and easily reacting combined polymers or aluminum chloride out of the solid phase.

As seen in Figure 2B, we were successful in creating an anisotropic and clean etched product suitable for fabricating an angle-etched quartz nanodevice.

**Titanium Hard Mask Etch.** Titanium was not as successful because of its tendency to under etch (Figure 3A), over etch (Figure 3B), or structurally fail due to stress (Figure 3C).

## Future Work:

**Aluminum Mask Improvements.** We were able to create a more anisotropic and clean etch with aluminum. Depositing aluminum at a lower pressure should eliminate minor film inconsistencies. Full cleaning of the etching tool should eliminate significant substrate residue.

**Titanium Mask Improvements.** In addition to over and under etching, film stress occurred in titanium. We hypothesized based on literature [2] that sputtering at a high temperature will alleviate stress. To simulate this change in the process we sputtered titanium onto a full wafer and measured bowing stress versus temperature. These preliminary tests supported that sputtering and increasing temperature could relieve stress, as seen in Figure 4.

## Acknowledgments:

A special thanks to my Principal Investigator Professor Marko Lončar, my mentor YoungIk Sohn, and the whole Lončar group, in addition to Harvard University's Center for Nanoscale Systems, and the NNIN REU Program and NSF under Grant No. ECCS-0335765.

## References:

- [1] Burek, M.; et al., Free Standing Mechanical and Photonic Nanostructures in Single Crystal Diamond. *Nano Letters* 2012, 12, 6084-6089.
- [2] Plummer, J.; Deal, M.; Griffin, P. *Silicon VLSI Technology*; Prentice Hall: Upper Saddle River, NJ, 2000.
- [3] Chang, R.; et al., Residual Stresses of Sputtering Titanium Thin Films at Various Substrate Temperatures. *Journal of Nanoscience and Nanotechnology* 2010, 10, 4562-4567.
- [4] Kovacs, G. *Micromachined Transducers Sourcebook*.

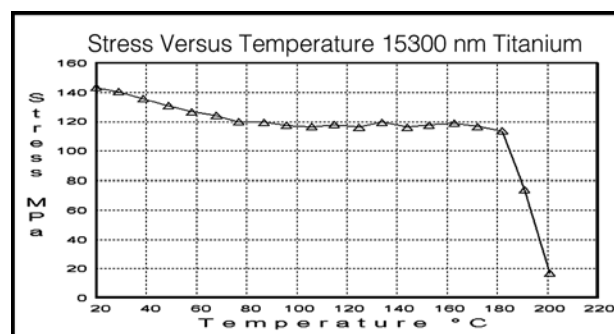


**Figure 4:** Stress vs. Temperature 15300 nm titanium.

# Minimizing Losses in $\text{TiO}_2$ Thin-Film Waveguides for Nanophotonic Applications

Anoosha Murella

Materials Science and Engineering, Arizona State University

**NNIN REU Site: Cornell NanoScale Science and Technology Facility, Cornell University, Ithaca, NY**

NNIN REU Principal Investigator: Professor Jin Suntivich, Materials Science and Engineering, Cornell University

NNIN REU Mentors: Chengyu Liu, Applied and Engineering Physics, Cornell University;

Dr. Christopher Evans, Laboratory of Atomic and Solid State Physics, Cornell University

Contact: [anoosha.murella@asu.edu](mailto:anoosha.murella@asu.edu), [jsuntivich@cornell.edu](mailto:jsuntivich@cornell.edu), [cl986@cornell.edu](mailto:cl986@cornell.edu), [cce34@cornell.edu](mailto:cce34@cornell.edu)

## Introduction:

Nanophotonics is a growing field within optics that studies the applications and behavior of light and matter on the nanoscale. Developments here have been especially important to integrated optics, an area devoted to combining various optical functions onto a single chip [1]. As light-based devices are becoming more commonplace, improving the efficiency of base chip devices (especially by minimizing loss) is growing in importance.

The Suntivich group at Cornell has been studying such light-matter interactions using titanium dioxide ( $\text{TiO}_2$ ) for integrated optical devices due to its high refractive index ( $> 2.2$ ), transparency in the visible and infrared (IR) regions of the electromagnetic spectrum, and low-cost [2]. A particular area of focus is on the construction of optical waveguides, which are the basic component for integrated optical applications. These waveguides are composed of a high refractive-index core material surrounded by a lower-index cladding material and light is transmitted through the core via total internal reflection [1]. As the light wave propagates through the material, however, photons are lost due to scattering from defects, impurities, grain boundaries, and interface roughness.

Rayleigh scattering from interfacial roughness (e.g., surface roughness in films and sidewall roughness in structured channel waveguides) is a major source of loss at visible wavelengths. Rayleigh scattering is often significant even within unstructured thin-film planar waveguides and limits the achievable losses in nanophotonic waveguides. Therefore, the goal of this work was to develop planar waveguides from amorphous  $\text{TiO}_2$  that exhibit a high refractive index and low planar waveguiding losses. To achieve this goal, we deposited films using radio-frequency (RF) sputtering of  $\text{TiO}_2$  and observed how the deposition temperature, pressure, and power affected optical propagation loss, surface roughness, index of refraction, and sputtering efficiency.

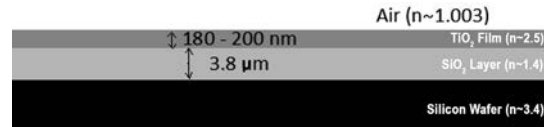


Figure 1: Schematic of a planar  $\text{TiO}_2$  waveguide.

## Experimental Procedure:

**Sample Preparation.** Silicon wafers with a previously grown layer of thermal oxide ( $3.8 \mu\text{m}$ ) were sonicated and rinsed with acetone, isopropanol, and deionized water. The substrates were then dried with pressurized air and heated on a hot plate to ensure no solvent was remaining. Samples were finally subjected to plasma ashing for 120 seconds to purge any persistent organics from the surface.

**Deposition Process.** The Kurt J. Lesker PVD75 (sputtering) was used for 6000 s depositions with a  $\text{TiO}_2$  target and an argon flow of 25 sccm (limit of 50 sccm)/oxygen flow of 0.8 sccm. Figure 1 shows the resulting planar waveguide.

- *Temperature* range tested (at 120 W, 3.5 mTorr):  $25^\circ\text{C}$ - $225^\circ\text{C}$  in 25 degree intervals.
- *Power* range tested (at  $75^\circ\text{C}$ , 3.5 mTorr): 120-135 W, every 5 watts.
- *Pressure* range tested (at  $75^\circ\text{C}$ , 120 W): 3.3-3.7 mTorr, every 0.2 mTorr.

**Characterization.** The refractive index and thickness of the  $\text{TiO}_2$  layers were first estimated from the Filmetrics F50 (a thickness mapping system and spectrometer) to help obtain more accurate values using the Woollam variable angle spectroscopic ellipsometer. Surface roughness/morphology was imaged and quantified using atomic force microscopy. Loss was measured using a prism coupler setup with a red laser ( $\lambda = 638 \text{ nm}$ ) and transverse electric/magnetic (TE/TM) polarizers.

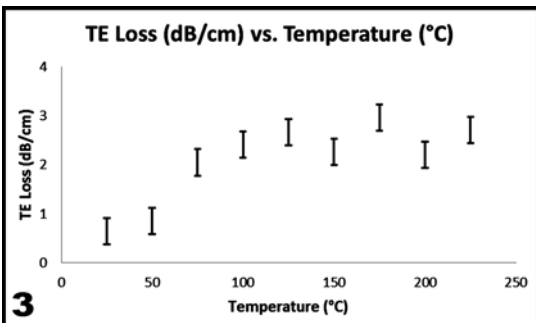
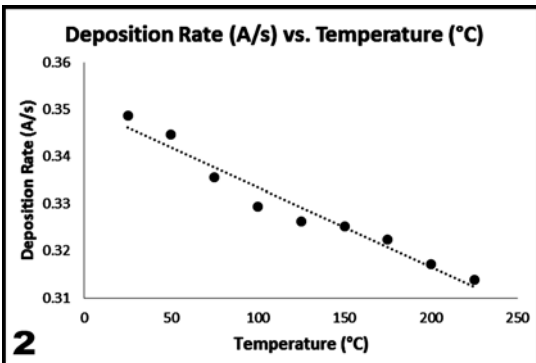


**Figure 2, top:** Deposition Rate (A/s) vs. Temperature (°C) graph. Deposition rate was obtained by dividing the thickness of the film by the run time of 6000 s. Higher temperatures lead to thinner films. **Figure 3, bottom:** TE Loss (dB/cm) vs Temperature (°C) graph. The two data points for each temperature value provide the range of the loss measured. Higher temperature samples have increased loss. The TM Loss graph looks similar.

## Results and Conclusions:

**Thickness/Deposition Rate.** As the temperature of the deposition increased, the thickness of the film dropped linearly. This relationship can also be understood as higher temperatures leading to a lower rate of deposition (see Figure 2). Increased film density is the most likely cause, as higher temperature  $\text{TiO}_2$  molecules have a greater range of motion to find a local energy minimum on the substrate. As the power increased, the deposition rate likewise increased, as a larger amount of plasma hitting the target leads to more molecules being deposited.

**Refractive Index.** Increasing temperature increases the refractive index linearly. This trend is consistent with the temperature-thickness relationship if we assume that the reduced deposition rate at higher temperature produced higher density films, which exhibit higher refractive indices.

**Surface Roughness.** The film roughness was minimized between 75°C and 100°C (RMS roughness was  $\sim 1.1$  nm).

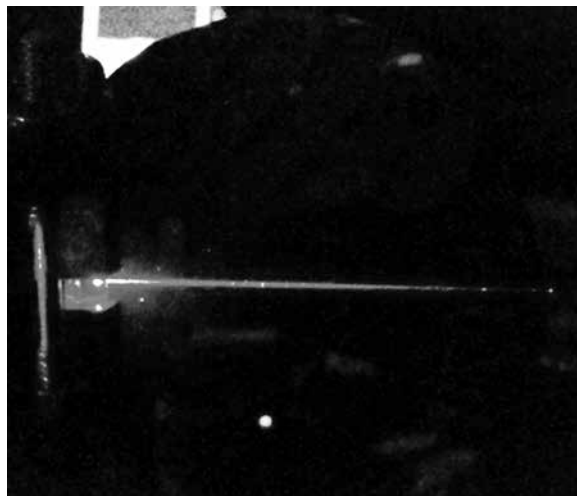


**Figure 4:** Image of the lowest loss film at 25°C ( $0.7 \pm 0.2$  dB/cm). The “red light” can still be observed at the end of the wafer, which does not occur at higher deposition temperatures.

**Losses.** For both TE and TM polarizations of light, losses increased with increasing temperature (Figure 3). At higher temperatures,  $\text{TiO}_2$  gradually begins to transition from amorphous to crystalline form. This leads to larger grains that scatter more as they approach in size the wavelength of light used.

Taking into account all of these results, it appears that the ideal deposition parameters (where loss is minimized while still maintaining a high rate of deposition) are at 25°C, 130 W, and 3.5 mTorr (as there was no conclusive relationship between pressure and the film qualities observed above, the pressure of most runs, 3.5 mTorr, can continue to be used). Figure 4 shows the lowest loss film deposited.

## Acknowledgements:

I would like to thank Chris Evans, Chengyu Liu, and Dr. Suntivich for their patience and mentorship this summer, the program coordinators and staff at CNF for all of their help, NNIN REU Program for the opportunity, and NSF for the funding under Grant No. ECCS-0335765.

## References:

- [1] Tien, P.K. “Light Waves in Thin Films and Integrated Optics.” *Applied Optics*, 10(11). 2395-2413 (1971).
- [2] Evans, C.C., Liu, C., Suntivich, J., Low loss titanium dioxide waveguides and resonators using a dielectric lift-off fabrication process, *Opt. Express*. 23 9 (2015), pp. 11160-11169.

# Bandwidth Expansion for Lippmann-Bragg Holographic Photopolymers

**Michael Valerino**

**Chemical Engineering, University of Maryland, Baltimore County**

**NNIN REU Site: Colorado Nanofabrication Laboratory, University of Colorado, Boulder, CO**

NNIN REU Principal Investigator: Robert McLeod, Department of Electrical, Computer, and Energy Engineering, University of Colorado Boulder

NNIN REU Mentor: Marvin Alim, Department of Electrical, Computer, and Energy Engineering, University of Colorado Boulder

Contact: [mvaler1@umbc.edu](mailto:mvaler1@umbc.edu), [robert.mcleod@colorado.edu](mailto:robert.mcleod@colorado.edu), [marvin.alim@colorado.edu](mailto:marvin.alim@colorado.edu)

## Abstract:

A reflection hologram that has a high reflectance over a broad range of wavelengths is desirable for many applications. Thicker holograms, which have a higher reflectance, also have a very narrow bandwidth, thus obtaining a higher bandwidth typically requires layering. A post-processing method called “chirping” is used to expand the bandwidth of these reflection holograms. By diffusing mobile monomer into a recorded hologram, we are able to swell the material and create a distribution of fringe spacing that increases the bandwidth.

Starting with a bandwidth of 2.5 nm with a maximum reflectance of 2.25% occurring at 457.0 nm, after one hour of chirping the bandwidth expanded to 9.7 nm while the maximum reflectance dropped to 0.60% and shifted to 466.6 nm. This trend was observed until five hours of chirping at which point the bandwidth narrowed and the maximum reflectance went back up. The change in mass of the hologram was 8.05% that matches closely with the 8.35% swelling observed from the shift in maximum reflectance from 457.0 nm to 495.2 nm.

## Introduction:

Reflection holograms are formed from interference from opposing beams of monochromatic and coherent light. To create a hologram, diode laser beams are focused on a urethane material containing photo-initiators and mobile monomer. When light hits the photo initiators, radicals are formed and free radical polymerization reaction is started forming polymer chains from the free monomer. Reflection holograms have many applications including use in Heads Up Displays (HUDs) and Holographic Optical Elements (HOEs). There is a design tradeoff with these holograms: the thicker the hologram the higher the reflectance, but this reflectance occurs over a smaller range of wavelength. This range is called the bandwidth and to obtain both a high reflectance and a high bandwidth, typically layering is required.

Another method to achieve a higher bandwidth is called “chirping.” Chirping refers to the linear variation of pitch spacing in the gratings of the holograms, much like the frequency of a chirping bird. This process requires diffusing monomer into the sample [1]. The wavelengths reflected are a function of the pitch spacing, so as added monomer swells the gratings, the bandwidth is increased and can be tuned based on the distribution of monomer [2].

## Procedure:

Spacers of known thickness were used to make the material a desired size. Two strips of 25  $\mu\text{m}$  thick spacer were put on either end of the glass slide on which the material would be contained. After degassing the 5% monomer material in a vacuum, the liquid material was then pipetted onto one of the glass slides. Another glass slide coated in Rain-X® was then carefully placed on top of the glass slide. Binder clips were used to compress the glass slides together ensuring a uniform material thickness. After allowing the material to set, holograms could now be recorded into the sample.

Using 405 nm laser, the beams were split and focused on the material in the optical setup. Using various exposure times, holograms were recorded in the material. The glass slide with Rain-X was now removed and what remained was a glass slide with an even coating of material in which a hologram was recorded.

Next the chirping process began. A 100  $\mu\text{m}$  sponge containing a 20% monomer within the urethane matrix was pressed against the recorded hologram sample with a vise to ensure contact.

To then read the holograms, a UV-Vis spectrophotometer was used. Black shim paper with a hole-punch in it was used to isolate the hologram. The black paper was also put behind the material for a better reading.

## Results and Conclusions:

A simple model was created for the process using one dimension Fickian diffusion assumptions and an estimated diffusivity value [3]. The results of this model are shown in Figure 1. Initial chirping results show a predictable increase in bandwidth as seen in Figure 2. This linear increase is an indication that the diffusion process was not near steady state even after seven hours. A new material was used for the remainder of the study so that the hologram and sponge contained the same writing monomer, speeding the process. The results of this test as can be seen in Figure 3 closely match the model. The bandwidth had a large initial increase of around 250% and then decreased after around five hours as monomer concentration within the hologram became uniform, as well as the swelling of the diffraction gratings.

The percent increase of the wavelength shift of peak reflection matches with the percent increase in mass of the sample. This process allowed us to tune a hologram to reflect a range of wavelengths that we intended.

## Future Work:

The initial reflectance of the holograms needs to be improved. Finding the time at which the hologram achieves its maximum bandwidth is another important topic that needs to be investigated. To shift the reflectance peak to a lower wavelength, monomer can be diffused out of the sample, allowing control of which wavelengths are reflected. Finally, we need to “lock in” the monomer. If allowed to sit, the free monomer in a chirped hologram will continue to diffuse throughout the sample, reaching steady state that will decrease the new bandwidth.

## Acknowledgements:

I would like to thank my PI Dr. Robert McLeod, mentor Marvin Alim, colleague Philip Zurek, graduate students Josh Noble, Ben Kowalski, and David Glugla, and the National Nanotechnology Infrastructure Network Research Experience for Undergraduates (NNIN REU) Program for coordination of this project. All funding was provided by the Minority Access to Research Careers (MARC) Scholarship Program.

## References:

- [1] Jannson, T., et al. “Lippmann-Bragg broadband holographic mirrors.” *JOSA A* 8.1 (1991): 201-211.
- [2] Gambogi Jr, W.J., A.M. Weber, and T. J. Trout. “Advances and applications of DuPont holographic photopolymers.” *Optics Quebec. International Society for Optics and Photonics*, 1994.
- [3] Kowalski, B.A., et al. “Quantitative modeling of the reaction/diffusion kinetics of two-chemistry diffusive photopolymers.” *Optical Materials Express* 4.8 (2014): 1668-1682.

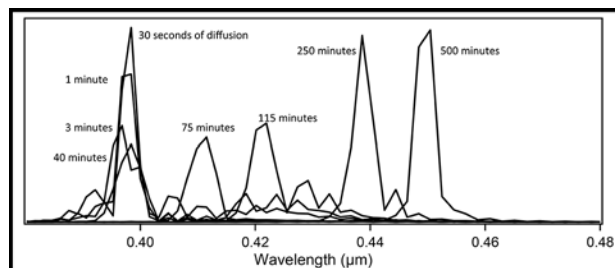


Figure 1: Model results of the chirping process.

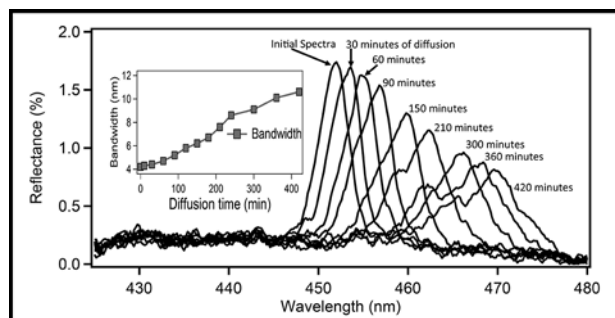


Figure 2: A linear increase in bandwidth was initially observed.

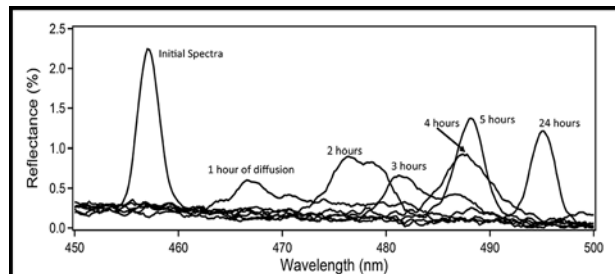


Figure 3: The initial bandwidth increase followed by a decrease matches the model.

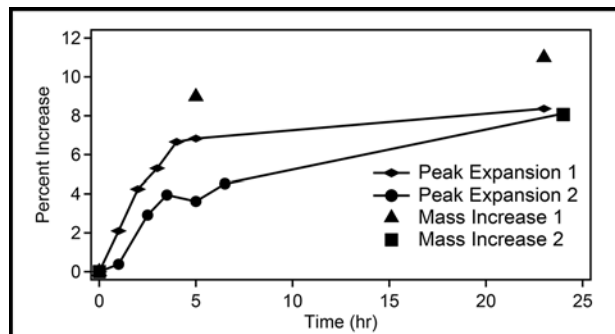


Figure 4: Wavelength shift and mass increase match closely as expected.

# High-Efficiency Broadband Lippmann-Bragg Reflection Holograms

Philip Zurek

Electrical Engineering, New Jersey Institute of Technology

NNIN REU Site: Colorado Nanofabrication Laboratory, University of Colorado, Boulder, CO

NNIN REU Principal Investigator: Dr. Robert McLeod, Electrical, Computer, and Energy Engineering, University of Colorado at Boulder

NNIN REU Mentor: Marvin Alim, Department of Electrical, Computer, and Energy Engineering, University of Colorado at Boulder

Contact: pjz2@njit.edu, robert.mcleod@colorado.edu, marvin.alim@colorado.edu

## Abstract:

Reflection holograms are written into a light-sensitive media using a source of coherent monochromatic light. The interference pattern between two interfering light waves causes polymerization of certain regions of the recording medium. Unreacted monomer diffuses into the regions that polymerized, creating a nonuniform refractive index across the media. This uniform fringe pattern that occurs, a reflection hologram, reflects light. Typically, reflection holograms are very wavelength selective. In order to broaden the region over which the reflection holograms are reflective, the fringe patterns must be non-uniformly stretched. By introducing a monomer sponge next to the holographic media, monomer diffuses into the fringes and stretches the ones closest to the interface first, causing nonuniform swelling. We have found that reflection holograms, once chirping has begun, take one hour in order to reach their maximum FWHM bandwidth state. During the entire chirping process, the peak wavelength location is steadily increasing. Concluding after 79 hours, the bandwidth decreased and reflectivity increased to near their original values as monomer equally diffused. At maximum FWHM bandwidth, reflectivity decreased by 230% and bandwidth increased by 200%. After 79 hours, holograms experienced a volumetric expansion of 11% coupled with a peak wavelength shift wavelength shift of 12%.

## Introduction:

When two sources of coherent monochromatic light interact, they interfere with one another forming an interference pattern. Once exposed to a recording medium, a fringe grating of uniform thickness called a reflection hologram appears. Only wavelengths of light that match the pattern are reflected. Therefore, these holograms tend to have a narrow bandwidth and high reflectivity.

Bright regions in the media cause polymerization of the monomer. Unreacted monomer from the dark regions diffuses into these, causing a change in the refractive index across the media. This index change is the desired fringe pattern.

Reflection holograms find uses in applications such as the heads-up-display of fighter pilots. The bandwidth of these reflection holograms, however, is insufficient for common light sources such as LEDs. This can be increased with a thinner recording media, however, diffraction efficiency is sacrificed. We chose a thicker media for a higher diffraction efficiency and expanded the bandwidth by diffusion of new monomer into the holographic media.

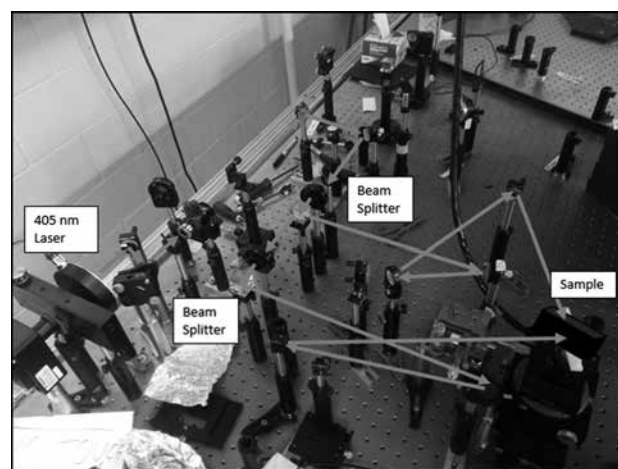
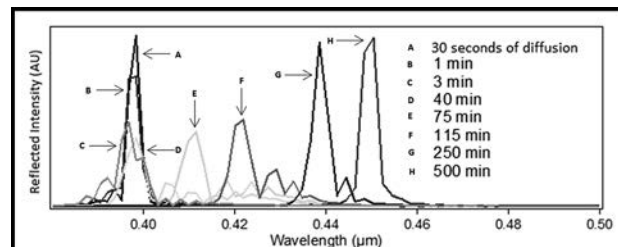


Figure 1, top: Model reflectivity vs. wavelength at different diffusion times. Figure 2, bottom: Optical setup.

## Experimental Procedure:

A model was developed to simulate reflectivity after bandwidth expansion. Ideal Fickian diffusion was assumed, therefore an analytic solution exists for the 1D diffusion equation. The diffusion rate was estimated from previous measurements that used other similar materials. The output plot, which includes curves for varying amounts of diffusion, is included in Figure 1.

A light-sensitive polyurethane matrix solution of 5% monomer was created and placed on one glass plate. This matrix was a scaffold for the monomer; once exposed to light the monomer would be held in place to record the fringe pattern. Two spacers of 25  $\mu\text{m}$  were placed on either side of the glass plate, another plate was placed on top, and the setup was squeezed. This was left to cure, typically overnight.

Once cured, the sample was placed in an optical setup, seen in Figure 2. Using a 405 nm laser, light was redirected and split with beam splitters, so that two of the same light sources would come from opposite sides of the sample and interfere within the recording media.

Exposure times varied from 0.2s to 60s, however, we found that 20s gave the largest reflectivity. Shorter times would not polymerize enough monomer and longer times would diffract light more from within the sample, degrading its quality.

The top glass plate was removed and the hologram was tested in a UV-VIS spectrophotometer. After, a sponge of 20% monomer (the same polyurethane matrix as before, but not light-sensitive) was pressed on the holographic media. At specified time intervals, the reflectivity was retested.

The application of the sponge caused diffusion of new monomer into the holographic media. This pulled the fringes closest to the interface first, creating a nonuniform fringe spacing. There are locations for various wavelengths of light to reflect from, increasing the bandwidth.

## Results and Conclusions:

After one hour of diffusion, maximum full-width-half-max bandwidth was achieved, an expansion of 200%. Reflectivity decreased at the same time by 230%. This data is shown in Figure 3, along with the curves for other diffusion times.

Initially, FWHM bandwidth increased rapidly due to a large diffusion gradient across the hologram and sponge. Over time as monomer more evenly distributed, the fringe spaces became uniform once again. This explains why with time, bandwidth decreased and reflectivity increased about a higher peak-wavelength-location.

As diffusion occurred, the weight of the holographic material increased 11%. This increase closely matched the peak-wavelength-location increase of the sample, 12%, as seen in Figure 4.

The computer model was quite accurate, given that the timescales were off by about a factor of two. Once appropriate values for the material used are found, the model accuracy can be improved.

## Future Work:

Future work could focus on creating new polymer solutions to increase hologram reflectivity. These holograms can be seen quite well before diffusion but not at maximum bandwidth. A method to keep reflectivity high, even after bandwidth expansion, could also be researched.

## Acknowledgments:

I would like to thank the NNIN REU Program for affording me the chance to carry out this research, Dr. Robert McLeod, Marvin Alim, and the rest of the McLeod Lab group for being wonderful mentors, Dr. Tomoko Borsa, the site coordinator, as well as the rest of the CNL/NCF staff, and Michael Valerino, with whom I researched this topic. The National Science Foundation provided funding, Grant No. ECCS-0335765.

## References:

- [1] William J. Gambogi, et al, "Advances and Applications of DuPont Holographic Photopolymers", SPIE, vol. 2043, 9, 1993.
- [2] T. Jansson, et al, "Lippmann-Bragg broadband holographic mirrors", J. Opt. Soc. Am., vol. 8, 201-211, 1991.
- [3] Benjamin A. Kowalski, et al, "Quantitative modeling of the reaction/diffusion kinetics of two-chemistry diffusive photopolymers", OSA, vol. 4, 1-15, 2014.

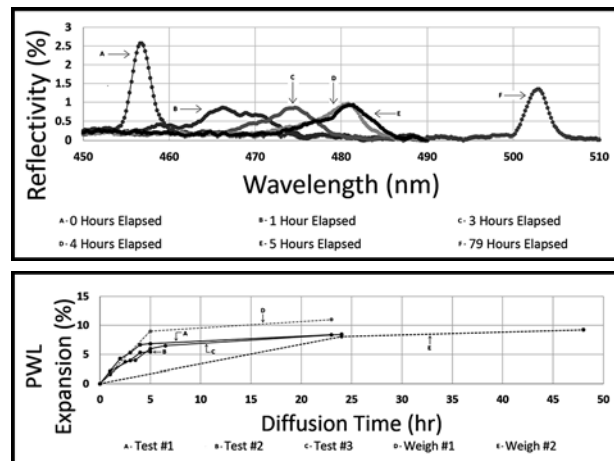


Figure 3, top: Experimental reflectivity vs. wavelength at different diffusion times. Figure 4, bottom: Peak-wavelength-location expansion and weight vs. diffusion time.

# Temperature Dependence of Carbon Nanotube Growths

**Joshua Alden**

**Biomedical Engineering, Georgia Institute of Technology**

**NNIN REU Site: Cornell NanoScale Science and Technology Facility, Cornell University, Ithaca, NY**

NNIN REU Principal Investigator: Paul McEuen, Department of Physics, Laboratory of Atomic and Solid State Physics and Kavli Institute for Nanoscale Science, Cornell University

NNIN REU Mentor: Alejandro Cortese, Department of Physics, Cornell University

Contact: [joshualden@gmail.com](mailto:joshualden@gmail.com), [pmceuen@gmail.com](mailto:pmceuen@gmail.com), [ajc383@cornell.edu](mailto:ajc383@cornell.edu)

## Introduction:

Carbon nanotubes (CNTs) have unique electrical and physical properties that make them candidates for many different applications ranging from high-speed field-effect transistors to biosensors. For reliability and efficiency in such applications, it is important to run many devices in parallel, which requires nanotubes to be grown in consistent arrays at appropriate densities. In this project we explored how nanotube growth temperature is correlated with carbon nanotube density, nanotube diameter, and catalyst size. We also investigated the accuracy with which an atomic force microscope (AFM) measures nanotube diameter. Being nature's smallest wire, nanotubes have the potential to act as biosensors capable of sensing small molecules such as individual nucleotides in DNA. The sensitivity of these biosensors would then be dependent on the nanotube diameter, thus making it an important point of study.

## Experimental Procedure:

Carbon nanotubes are grown from iron catalyst nanoparticles on quartz wafers in a high temperature chemical vapor deposition process, as illustrated in Figure 1. The quartz wafers used are ST cut, which means that they have atomic-scale terraces running in parallel across the wafer. Nanotubes can grow along these, leading to arrays of aligned nanotubes. Wafers were fabricated and nanotubes grown using standard procedures [1,2].

Following growth, AFM imaging was used to collect the heights and thus the diameters of the iron catalyst particles after growth and the diameters of the nanotubes while SEM imaging was used to measure the density of nanotubes after each growth. To calibrate the AFM nanotube diameter measurements, AFM-measured nanotubes from a quartz substrate were transferred onto TEM grids. The nanotubes were then imaged again using transmission electron microscopy (TEM) and their diameters were measured.

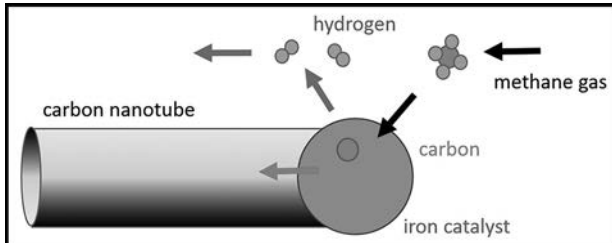


Figure 1: Chemical vapor deposition. Methane gas flows near an iron catalyst which absorbs the carbon into itself, and after saturation, the carbon moves to the outside of the catalyst and begins to form a nanotube.

## Results and Discussion:

In the temperature range from 855°C to 915°C, we observed that average catalyst diameter increases with increasing temperature as shown in Figure 2a. However, the width of the distribution of catalyst sizes within each growth was larger than the observed increase. Ostwald ripening is the phenomenon suspected to be causing this trend. As temperature goes up, the iron atoms gain the energy necessary to migrate from smaller catalyst particles to larger ones, since this minimizes the number of atoms exposed at the surface. As a result, larger catalysts form during higher temperature growths.

We also observed a strong temperature-dependence to number of nanotubes per micron that grew from a given catalyst line, as shown in Figure 3. We noticed that CNTs grown at 855°C have low number density as can be seen in Figure 3a. Between 870°C and 885°C, the nanotubes grow at high densities, as in Figure 3b. Above 885°C, the density tapers off to 0, as seen in the

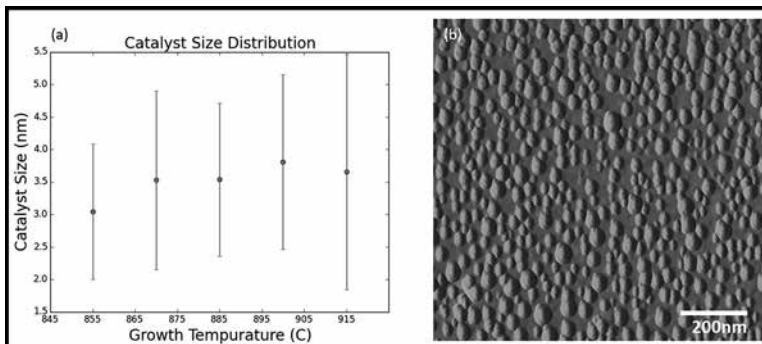


Figure 2: a) Catalyst size increased with increasing temperature. The dots and lines show respectively, the mean and standard deviation of observed catalyst sizes by AFM. b) AFM image of catalysts after an 870°C growth.

image in Figure 3c. Because nanotubes grow from the surface of catalyst particles, catalyst size and nanotube density are linked together. Once the catalysts reach an optimal size, many nanotubes will grow thus creating a high density of CNTs at that temperature. But at higher temperature growths, many of the catalysts are too large to initiate growth as resulting in a lower density as observed in Figure 3d.

Figure 4a shows AFM measurements of the average nanotube diameter as a function of temperature. The average nanotube diameter increases with increasing temperature. To calibrate these measurements, which can have systematic error due to tip-substrate interactions, one of the samples was AFM'd, then TEM'd. The resulting histogram of observed diameters is shown in Figure 4b. The more-accurate TEM measurements measured larger nanotube diameters than the AFM (Figure 4b).

In summary, we found that catalyst size, and nanotube diameter increase with increasing temperature and that nanotube density is tightly linked with the catalyst size. Knowing the temperature-dependence of carbon nanotubes on temperature allows us to reliably grow nanotubes of a pre-selected density and diameter, bringing wafer-scale production of nanotube biosensor arrays one step closer to viability.

### Future Work:

Having developed an understanding and methodology for nanotube growth in a 5-inch furnace, we can now begin testing 4-inch wafer growths. If our methods successfully scale, this work will be used in the McEuen group's work on developing arrays of DNA sequencing devices. Other interesting expansions of this project include varying parameters such as the anneal time, and hydrogen and methane flow times and rates to create more uniform catalyst sizes with a narrower distribution. This may allow for more precise control over nanotube diameter and possibly a more exact density-temperature relationship.

### Acknowledgments:

I would like to thank my mentor Alejandro Cortese and fellow lab members Jonathan Alden and Bryce Kobrin for their help and support on this project. I would also like to thank the McEuen lab and CNF for a positive and productive work environment. This research was supported

by the National Nanotechnology Infrastructure Network Research Experience for Undergraduates (NNIN REU) Program and National Science Foundation under Grant No. ECCS-0335765.

### References:

- [1] Ding, L.; Yuan, D.; Liu, J. "Growth of High-Density Parallel Arrays of Long Single-Walled Carbon Nanotubes on Quartz Substrates." *J. Am. Chem. Soc.* 130, 5428-5429, 2008.
- [2] Kocabas, C.; Hur, S.-H.; Gaur, A.; Meitl, M. A.; Shim, M.; Rogers, J. A. "Guided Growth of Large-Scale, Horizontally Aligned Arrays of Single-Walled Carbon Nanotubes and Their Use in Thin Film Transistors." *Small* 1, 1110-1116, 2005.

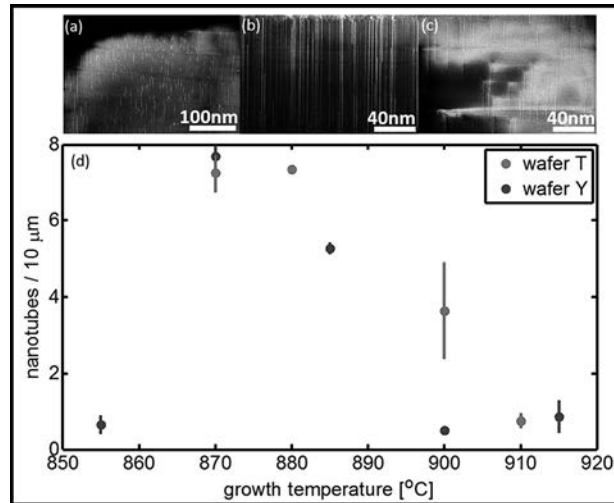


Figure 3: a) SEM image of nanotubes after an 855°C growth. b) SEM image of nanotubes after an 885°C growth. c) SEM image of nanotubes after a 915°C growth. d) Nanotube Density vs. Temperature. The dots and lines show respectively, the mean and standard deviation of the measured nanotube densities. The two different wafers are from two different fabrication batches and growths.

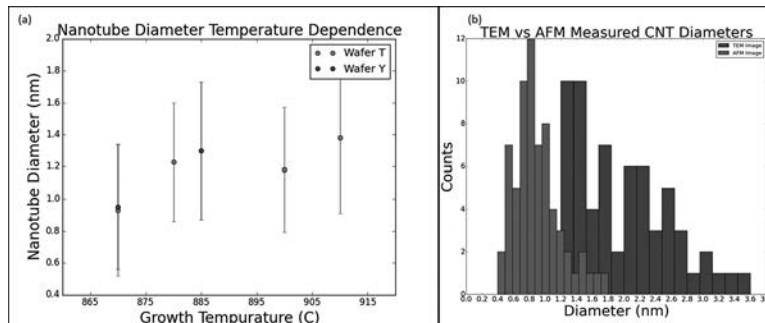


Figure 4: a) Shows the mean and standard deviation of AFM measured nanotubes from two separately fabricated wafers. b) Shows a histogram of the nanotube diameters measured by the AFM and TEM.

# Determining the Spin Hall Angle of Gadolinium

Robyn Collette

Physics and Mathematics, Shippensburg University

NNIN REU Site: Cornell NanoScale Science and Technology Facility, Cornell University, Ithaca, NY

NNIN REU Principal Investigator: Dan Ralph, Physics Department, Cornell University

NNIN REU Mentor: Jonathan Gibbons, Physics Department, Cornell University

Contact: rcollette12@gmail.com, dcr14@cornell.edu, jg833@cornell.edu

## Abstract:

The spin Hall effect is observed when electrons from a charge current are deflected based on their spin orientation, causing an accumulation of spins on the boundaries of a material. The spins can then exert a torque on an adjacent ferromagnetic material, potentially manipulating the orientation of the magnetization. It has been found that manipulating nanomagnets through spin transfer torques is much more practical than using a magnetic field. Therefore, spin transfer torques present advantages in non-volatile magnetic memory applications [1]. Spin-torque ferromagnetic resonance (STFMR) measurements were performed on various gadolinium-ferromagnetic multilayers, and the spin Hall angle was extracted. The anisotropic magnetoresistance (AMR) of Py and CoFeB was measured. The saturation magnetization, the conductivity of Gd, and the x-factor were also measured for use in analysis. It was found that the spin Hall angle of Gd is 2%.

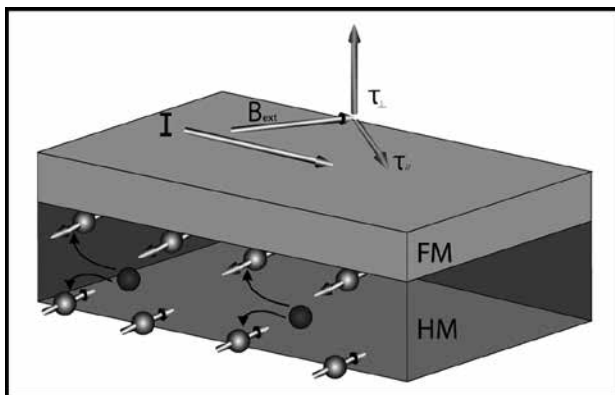


Figure 1: Stack device of a heavy metal (HM) and a ferromagnetic material (FM). Electrons deflected based on their spin orientation. Torque exerted on adjacent layer magnetization can be observed.

electrons from a charge current are deflected based on their spin orientation, causing an accumulation of spins on the boundaries of a material. The spins can then exert a torque on an adjacent ferromagnetic material, potentially manipulating the orientation of the magnetization as seen in Figure 1. The effectiveness of the spin Hall effect in a given material is described by the spin Hall angle, a ratio of the generated spin current to the applied charge current.

## Experimental Procedure:

Material stacks of 10 nm of gadolinium (Gd) and 5 to 10 nm of a ferromagnetic material were deposited on a sapphire wafer through sputter deposition. Permalloy (a NiFe alloy) or cobalt iron boron (CoFeB) were used as the ferromagnetic layer. Hall bars were then patterned through

## Introduction:

Technology is rapidly evolving, presenting a need for a universal memory that is nonvolatile, has a high storage density, and has a fast access time. One solution for this is magnetoresistive random access memory (MRAM). In MRAM, information is stored in the magnetization state of a nanomagnet; this information is read and written electronically. Research has successfully developed a way to easily read the state, but manipulating the state effectively still poses a problem. One method of manipulating the magnetization state being explored in current research is spin transfer torques. Spin transfer torques are caused by the spin Hall effect. The spin Hall effect is observed when

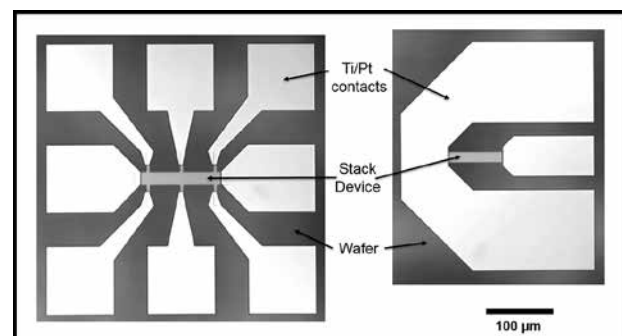


Figure 2: (Left) Device geometry used for STFMR measurements. (Right) Device geometry used for resistance measurements. The Hall bars shown are 80  $\mu\text{m}$  by 24  $\mu\text{m}$ .

optical photolithography and ion milling procedures. Platinum contacts were deposited through sputter deposition. Various device geometries were fabricated to accommodate electrical measurement set ups, as seen in Figure 2.

Devices were characterized using spin-torque ferromagnetic resonance (STFMR) measurements. An RF ground-signal-ground probe was connected to the device. A fixed microwave frequency was applied to the sample while sweeping an in-plane magnetic field from -0.25 T to 0.25 T. The magnetization of the ferromagnet precessed due to the oscillating current induced torque, which yielded an oscillating anisotropic magnetoresistance (AMR). The AMR and applied ac current were used to calculate the mixing voltage. This mixing voltage was recorded against the magnetic fields over a range of applied frequencies [2].

AMR is observed when the resistance of a material has a dependence on the angle between the current direction and the magnetization direction. Since this angle changes during STFMR measurements, the AMR of each sample was characterized in order to properly analyze the spin Hall angle.

The saturation magnetization, conductivity of gadolinium and x-factor (a ratio of stack resistance to the resistance of gadolinium) were measured for use in the analysis.

## Results and Conclusions:

This analysis was run on four different sample stacks. The results of the analysis are compiled in Figure 3. It was determined that the spin Hall angle of gadolinium is about 2%. There is a sign ambiguity that would require further analysis to determine whether the spin Hall angle is positive or negative. Based on the resistance measurements of the sample stacks, there likely is a problem with Py grown on Gd. However, a 2 nm Hf spacer seems to alleviate this in the Gd/Py samples; this problem is not seen in the Gd/CoFeB samples.

## Future Work:

More analysis will be done on other devices to ensure the accuracy of the spin Hall angle. The sign of the spin Hall angle will also be further explored. The difficulty of growing Py on Gd will also be examined to determine why the problem occurs.

## Acknowledgments:

I would like to thank my principal investigator, Dan Ralph, as well as my mentor, Jonathan Gibbons. I would like to thank Neal Reynolds and the rest of the Ralph group members. I would like to thank the CNF REU Program Coordinators, Melanie-Claire Mallison, Lynn Rathbun, and Michael Skvarla as well as the CNF staff. I would also like to thank the National Science Foundation, the National Nanotechnology Infrastructure Network, and the Cornell NanoScale Science & Technology Facility for funding (under Grant No. ECCS-0335765) and facility use.

## References:

- [1] Liu, L., Moriyama, T., Ralph, D. C., and Buhrman, R. A. Spin-Torque Ferromagnetic Resonance Induced by the Spin Hall Effect. *Phys. Rev. Lett.* 106, 036601 (2011).
- [2] Mellnik, A. R. (2015). Measurements of spin torques generated by topological insulators and heavy metals. (Doctoral Dissertation). Cornell University, Ithaca, NY.

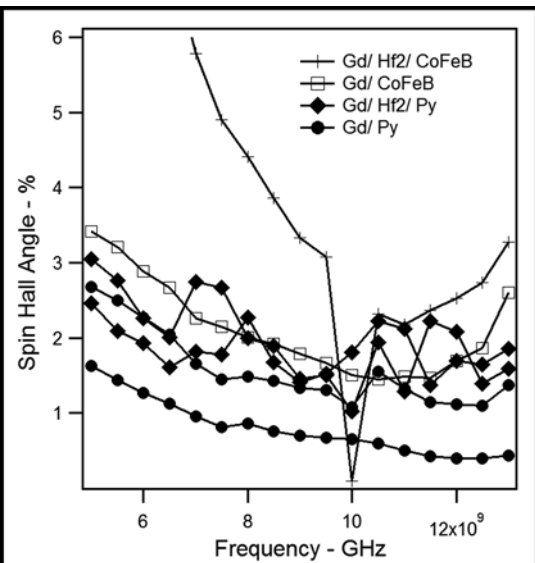


Figure 3: Compiled results of spin Hall angle analysis for six different devices. Spin Hall angle axis is cut off at 5% in order to better see what is recorded around 2%.

# Design and Fabrication of Plasmonic Device for MIR Absorption Spectroscopy

**Jacob Heppner**

**Applied Physics and Computer Science, Bethel University**

**NNIN REU Site: Minnesota Nano Center, University of Minnesota-Twin Cities, Minneapolis, MN**

NNIN REU Principal Investigator: Prof. Sang-Hyun Oh, Electrical and Computer Engineering, University of Minnesota

NNIN REU Mentors: Daniel Mohr, Daniel Klemme\*, and Daehan Yoo; Electrical and Computer Engineering, University of Minnesota

(\* 2012 NNIN REU Intern at University of Colorado)

Contact: [jah73854@bethel.edu](mailto:jah73854@bethel.edu), [sang@umn.edu](mailto:sang@umn.edu), [mohrx117@umn.edu](mailto:mohrx117@umn.edu), [klemm023@umn.edu](mailto:klemm023@umn.edu), [yooxx094@umn.edu](mailto:yooxx094@umn.edu)

## Abstract:

Plasmonic structures, such as slits, grooves, or apertures in metal films can be used to guide optical energy beyond the conventional diffraction limit of light, allowing for optical measurements that would not be possible with standard techniques. Annular nanoapertures have been utilized for applications in plasmonic sensing and spectroscopy. We have developed a fabrication technique to utilize strongly enhanced plasmonic fields in such structures. These techniques allow small changes in the absorption or reflection spectra of the device to detect compounds within close proximity to the structures. It is expected that device sensitivity will be increased through the reduction of critical dimensions.

## Introduction:

Surface plasmon polaritons (SPPs) are hybrid electromagnetic waves across a metallic interface that are commonly excited by coupling light to conduction electron plasma. The electromagnetic field from SPPs can be confined to a smaller volume with much greater intensity than is possible using conventional diffractive optics. These properties make plasmonically-active patterned metal films ideal candidates for a variety of optical sensing applications. In particular, plasmonic biosensors have been used for observing association and dissociation in binding kinetics, lowering the limit of detection of analyte in solution, and detection of known particles in solution using spectroscopy. These biosensors are metallic nanostructures that have been engineered to increase confinement of plasmons and create regions of high field enhancement.

In this work, we present the design and fabrication of annular nanogaps tuned to operate plasmonically in the mid-infrared (MIR) region of the electromagnetic spectrum. An annular nanogap is a coaxial structure where an annular gap is formed in a conducting material that is attached to the substrate. These annular nanogaps were created using a lift-off process.

## Experimental Procedure:

The first step of the process was spin coating flowable oxide-16 photoresist (FOx-16), a negative tone resist, on a calcium fluoride substrate. A 5 nm thick layer of gold was then sputtered on the insulating substrate to prevent unwanted charging during the exposure. The FOx-16 was

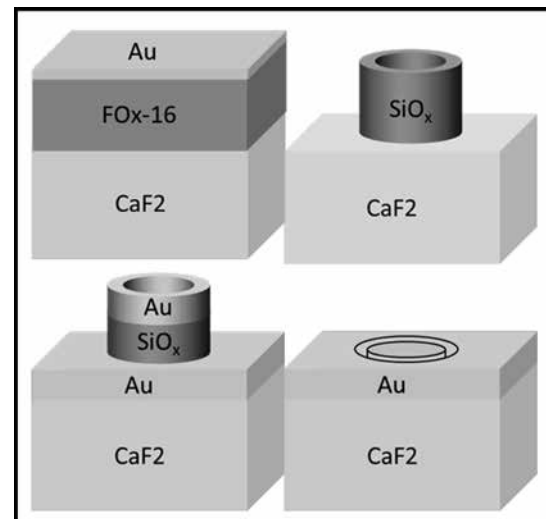


Figure 1: Process diagram for annular nanogap fabrication.

then exposed using electron-beam (e-beam) lithography, after which the sample was developed in a 1% NaOH 4% NaCl solution. Gold, 100 nm thick, was then evaporated onto the sample by electron-beam evaporation. The sample was then sonicated in buffered oxide etch to dissolve the photoresist in the annular gaps, lifting the gold above this region. This process is shown in Figure 1. FOx-16 was chosen because it is a negative tone resist that can be spun on at large thicknesses and it would not react with the potassium iodide that we used to etch the gold discharge layer before developing.

We would like to use these annular nanogaps for MIR absorption spectroscopy to identify molecular species. These annular nanogaps will focus light into regions of high field enhancement, which will provide high sensitivity to identifying particular molecular species. One of the advantages of using an annular nanogap structure above using a thin film of gold is the ability to tune the structure to the MIR region of the electromagnetic spectrum, which is important for vibrational absorption spectroscopy of molecules. The critical dimensions on device performance are the gap width, inner radius of the annular gap, and the thickness of the metal film. The thickness was chosen to be 100 nm to balance plasmonic enhancement of the sensor and the transmission through the sensor, maximizing the signal to noise of the device. Both 300 nm and 700 nm inner radius annular gaps were fabricated, each having the same 200 nm gap width to test to different regions within the MIR.

Full fabrication of the annular nanogaps was accomplished on a silicon substrate (Figures 2 and 3). These samples were characterized using Fourier transform infrared spectroscopy, and simulations of the structures using the finite-difference time-domain technique were also performed (Figure 4).

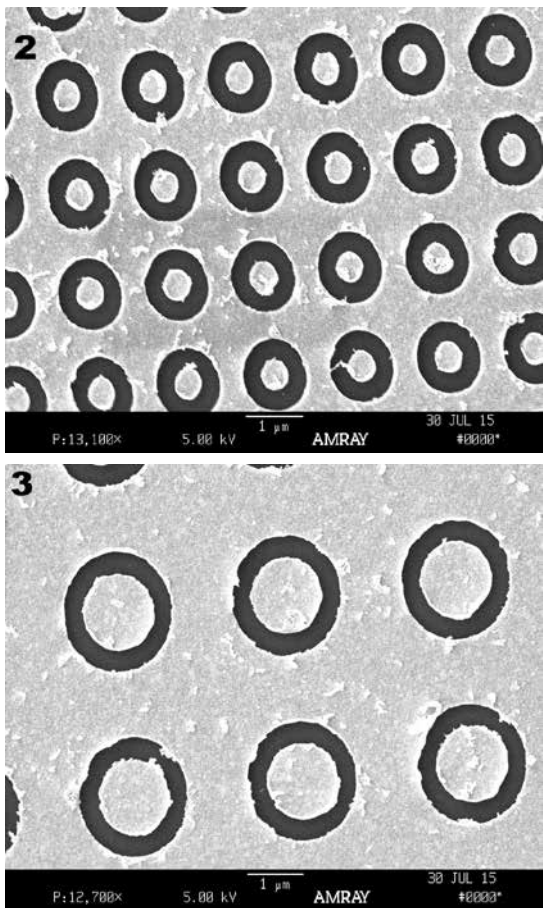


Figure 2, top: 300 nm inner radius annular nanogaps.  
Figure 3, bottom: 700 nm inner radius annular nanogaps.

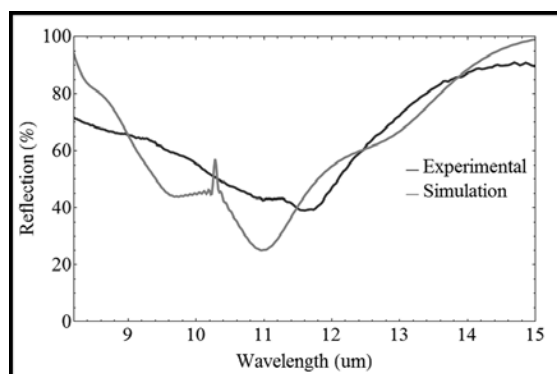


Figure 4: Reflection spectra for 700 nm inner radius sensors.

### Results and Conclusions:

We saw some agreement between simulated models and the experimental data, though we did find that there were significant sources of error that contributed to lowering the agreement. One of the sources that we think played the largest part in lowering agreement is erosion of the critical features. This erosion we think came from the wet etching process that was used during the lift off process. The erosion would have occurred unevenly and would have an effect on the resonances. We also noticed that the gold that eroded away often re-deposited on the surface, which may have affected the resonances of the structure. The erosion most likely occurred from the lift-off bath etching the native oxide on the silicon substrate, undercutting the edges of the critical features. The lift-off method used will not etch calcium fluoride to the same degree, so it is unlikely that undercutting will be an issue in the future.

To conclude, annular nanogaps were fabricated for potential applications in plasmonic sensing and spectroscopy. In the future, fabrication of the annular nanogaps on calcium fluoride substrates will be completed. We will then take measurements with the sensors and compare the experimental data with simulated data to determine viability of the sensors as biosensors in real-world applications.

### Acknowledgments:

I would like to acknowledge Professor Sang-Hyun Oh and his research group, specifically my mentors Daniel Mohr, Daniel Klemme, and Daehan Yoo, for their assistance in this research. I would like to thank James Marti for his assistance and oversight. I would like to thank the Minnesota Nano Center for use of their facilities. I would also like to thank the National Nanotechnology Infrastructure Network Research Experience for Undergraduates Program for giving me this opportunity to research. This research was supported by the National Science Foundation under Grant No. ECCS-0335765.

# Quantum Dot Superlattice Hybrid Structures for Solar Cell Applications

Rachel Lucas

Physics/Aerospace Engineering, Purdue University

**NNIN iREU Site: National Institute for Materials Science (NIMS), Tsukuba, Ibaraki, Japan**

NNIN iREU Principal Investigators: Dr. Takeshi Noda, High Efficiency Solar Cell Group, NIMS, Tsukuba, Ibaraki, Japan;

Professor Hiroyuki Sakaki, Toyota Technological Institute, Nagoya, Aichi, Japan

NNIN iREU Mentor: Dr. Martin Elborg, High Efficiency Solar Cell Group, NIMS, Tsukuba, Ibaraki, Japan

Contact: [lcas27@purdue.edu](mailto:lcas27@purdue.edu), [noda.takeshi@nims.go.jp](mailto:noda.takeshi@nims.go.jp), [elborg.martin@nims.go.jp](mailto:elborg.martin@nims.go.jp)

## Introduction:

Using quantum structures (QSS) in the absorption layer of a solar cell has been of great interest in potentially overcoming the Shockley-Queisser conversion efficiency limit of solar cells. QSSs produce an intermediate band (IB) that allows absorption of sub-bandgap photons and thus increases photocurrent generation [1]. This process occurs in two steps wherein one photon excites a carrier from the valence band (VB) to the IB and a second photon excites this carrier from the IB to the conduction band (CB). This process is called two-step photocurrent generation (Figure 1) and it increases the number of carriers reaching the CB thus increasing the current created.

A hybrid quantum dot (QD) quantum well (QW) structure was proposed as a method to create intermediate energy states. This hybrid structure is expected to provide advantages of both QWs and QDs, surpassing the issues of using only one type of quantum structure. QDs afford a discrete density of states, but large absorption of light requires many layers of QDs, which is difficult to realize. QWs allow a relatively large absorption of photons however two-step photocurrent generation is less efficient when light is incident perpendicular to this structure. Using both structures is expected produce a combination of all desired traits.

A GaAs/AlGaAs superlattice (SL) structure and InAs QDs were grown and intermediate band solar cells (IBSC) were fabricated from them. In this work carrier transfer between the SL and QD structures was studied in addition to two-step photocurrent generation.

## Fabrication Procedure:

A superlattice structure of ten 4 nm thick GaAs wells separated by 3 nm thick AlGaAs barriers was grown beneath an InAs QD layer. The QDs were grown using the Stranski-Krastanov growth mode. In this growth mode, the initial growth proceeds layer-by-layer until a critical thickness is reached. A further deposition of the material causes the growth mode to change from two-dimensional to three-dimensional creating dots. This hybrid structure was grown between layers of AlGaAs on a p-type GaAs  $<100>$  substrate. All samples were grown using molecular beam epitaxy (MBE). Solar cells were fabricated using photolithography, sputtering, and chemical etching. The devices were then packaged and bonded for testing.

## Results:

Atomic force microscopy (AFM) was used to characterize the QDs. Approximate QD density was found to be  $6.6 \times 10^{10} \text{ cm}^{-2}$ , while approximate dot size was found to be 20 nm in diameter and 2 nm in height. Photoluminescence (PL) measurements performed at 10 K revealed that SL emission energy was 1.6 eV while QDs had a broad curve of emission energies peaking at 1.4 eV (Figure 2).

Through a comparison of the sample containing only the SL structure and the sample containing both SL and QD structures it is seen that the intensity of the SL peak decreases with the addition of QDs to the sample structure. This indicates that carriers are being transferred out of the SL and into the QDs in the hybrid structure.

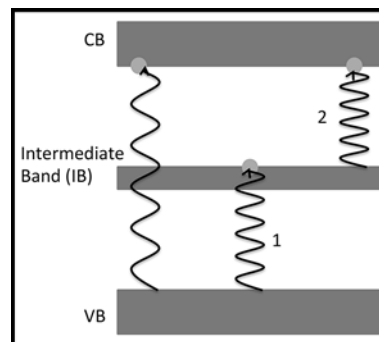


Figure 1: Band diagram of two-step photocurrent generation where 1 marks the transition from VB to IB due to one photon and 2 marks the transition from IB to CB due to a second photon.

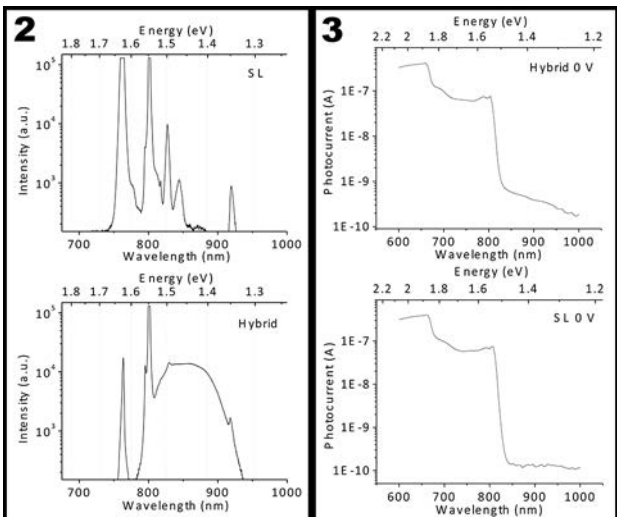


Figure 2, left: Photoluminescence data for superlattice and hybrid samples. Figure 3, right: Photocurrent data for superlattice and hybrid solar cell samples.

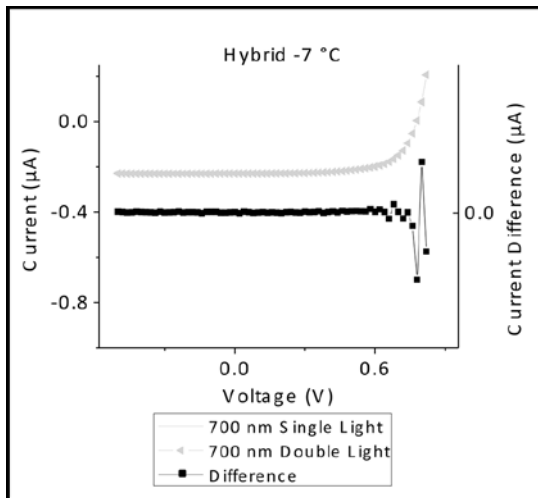


Figure 4: Room temperature two-step photocurrent generation for hybrid sample. Squares correspond to the right-hand y-axis while triangles correspond the left-hand axis.

Photocurrent measurements performed on the solar cell samples at room temperature (RT) reveal a step-like structure for each of the samples (Figure 3). These steps appear because of the sample's dependence of carrier generation on incident light energy. Light having energies greater than 1.9 eV can create carrier pairs throughout the entire solar cell sample. Therefore light with these energies produces the largest photocurrent. Between 1.9 eV and 1.5 eV light no longer has enough energy to create carrier pairs in AlGaAs causing a drop in photocurrent. A second, larger drop in photocurrent occurs at energies below 1.5 eV because carrier pairs can no longer be created in the SL structure. It is seen beyond this second drop in photocurrent that the addition of QDs to the structure causes a small increase in photocurrent by absorbing longer wavelengths.

A 1.55  $\mu$ m laser was used along with a 700 nm (1.77eV) monochromatic light source to investigate two-step photocurrent generation. The 700 nm light creates the carrier pairs while the laser is expected to excite these carriers from trapping in QSS to generate additional photocurrent. However, when the samples were lit with the laser there was no visible current difference than when only lit with the 700 nm light (Figure 4). In addition, saturated photocurrent flows until the voltage is close to the open circuit voltage. This indicates that the carriers escape trapping due, presumably, to thermal escape processes without the need for the laser. Therefore no two-step photocurrent generation is seen at RT.

## Conclusions and Future Work:

Growth of solar cell structures was successful as indicated by photocurrent spectra and current generation in current-voltage (IV) curves. Carrier transfer was confirmed from the SL to QD structures in PL data. In measurements at RT, however, two-step photocurrent generation was not observed in samples. This is explained by no or negligible carrier trapping at RT due to thermal escape processes. Low temperature measurements or adjusting the SL and QD hybrid structure are future works in order to prove the possibilities of our proposed structure.

## Acknowledgements:

Thanks to Dr. Takeshi Noda, Dr. Hiroyuki Sakaki, and Dr. Martin Elborg as well as the High Efficiency Solar Cell/Quantum Nanostructures Group. Thank you to the National Nanotechnology Infrastructure Network International Research Experience for Undergraduates and the NSF, Grant No. ECCS-0335765, for funding and thanks to NIMS.

## References:

- [1] Jo, M., Y. Ding, T. Noda, T. Mano, Y. Sakuma, K. Sakoda, L. Han, and H. Sakaki. "Impacts of Ambipolar Carrier Escape on Current-Voltage Characteristics in a Type-I Quantum Well Solar Cell." *Applied Physics Letters* 103, 061118 (2013).

# Multidimensional Metal-Dielectric Plasmonic Array

Quang Nguyen

Engineering Physics, Case Western Reserve University

NNIN REU Site: Lurie Nanofabrication Facility, University of Michigan, Ann Arbor, MI

NNIN REU Principal Investigators: Dr. Somin E. Lee, Biomedical Engineering, University of Michigan;

Dr. Young Geun Park, Chemical Engineering, University of Michigan

NNIN REU Mentor: Dr. Young Geun Park, Chemical Engineering, University of Michigan

Contact: [nguyenq12@gmail.com](mailto:nguyenq12@gmail.com), [sleee@umich.edu](mailto:sleee@umich.edu), [ygspark@umich.edu](mailto:ygspark@umich.edu)

## Abstract:

We present a new multi-dimensional plasmonic array consisting of a metal-dielectric-metal interface. This array enhances plasmonic interactions between layers and exhibits tunneling effects dependent on dielectric thicknesses. Plasmon-driven growth is used to controllably fabricate the multi-layer nanogap structure. This multi-dimensional structure, which cannot be easily produced through conventional lithographic methods, takes advantage of plasmonic coupling effects and provides increased tunability of the optical resonance as well as greater enhancement of the near-field. In addition, we report high electric field focusing in the multidimensional plasmonic nanogap array, which confirms the enhancing nature of the structure and shows a potential for high sensitivity in detection applications. We demonstrate the uniformity and stability of the plasmonic structures through characterization of nanoparticle size and absorption spectra. Such a substrate can find uses in many areas, including optofluidic platforms for the detection of biological molecules such as proteins.

## Introduction:

In recent years there has been extended exploration of plasmonic substrates due to their uniquely enhanced optical properties that are a result of localized surface plasmon resonances (LSPRs). Such substrates have largely consisted of either isolated or ordered two-dimensional metallic nanostructures in various shapes and sizes. Some examples of shapes that have been prepared include spheres, pyramids, cubes, bowties, rods, stars, and other varied shapes [1].

Much effort has been placed into optimizing geometric properties because the optical characteristics of a plasmonic structure depend critically on features like shape, size, particle spacing, etc. [2]. However, as a result of the focus on shape alteration, relatively little work has been done on increasing the dimensionality of plasmonic structures, which can lead to new interactions and emergent phenomena.

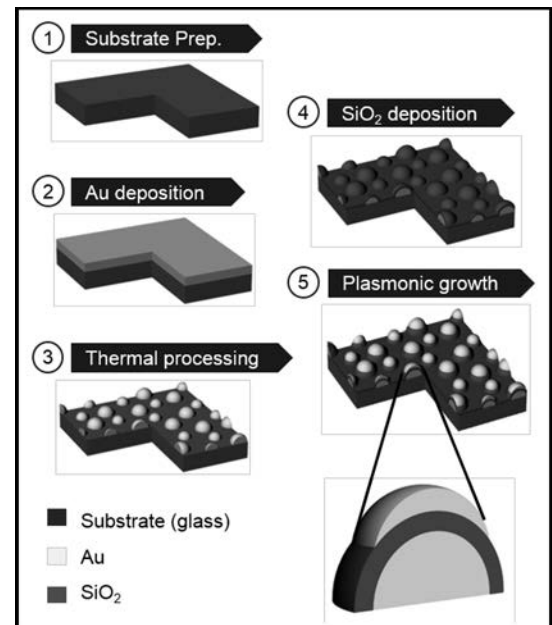


Figure 1: Schematic illustration of fabrication process for the multidimensional array.

Here we introduce a multi-dimensional plasmonic array that consists of two metal nanostructure arrays separated by an insulating dielectric layer. The increased dimensionality introduces new coupling effects that must be considered, and the solid dielectric layer (as compared to the empty space of air) means that the substrate will exhibit different field decay behavior and see a potential for tunneling and backscattering effects.

## Experimental Procedure:

After thoroughly cleaning bare glass slides, gold (Au) films were deposited onto the glass through electron-beam evaporation. The samples were thermally processed by heating in a furnace to produce islands of Au, which comprised the nanogap array of the first layer of nanoparticles (NPs). Then, using  $\text{SiO}_2$  as the insulator, the dielectric layer was deposited over the Au NP array through e-beam evaporation.

The second layer of Au NPs was grown on top of the  $\text{SiO}_2$  layer through a seed-mediated, plasmon-induced method. We first immersed the samples in an Au seed solution and ensured seed adsorption by taking advantage of the electric field produced by LSPR excitations, which attracted the seeds to adhere to the surface of the previously produced NPs. Then, we grew the second layer of Au NPs on the seeds by chemical reduction of an Au precursor, attracting the Au ions in the same manner using LSPR excitations. In this way, we could direct the growth sites of the secondary Au layer.

## Results and Conclusions:

We proceeded to analyze the morphological and optical properties of our plasmonic array to produce a rigorous characterization. To confirm the structure of the substrate we used scanning electron microscopy (SEM) in combination with an image analysis program, ImageJ, to visually as well as quantitatively describe the geometry of the NPs.

From Figure 2, it is evident through simple visual inspection that the number of Au NPs grown in the second metal layer, shown by the white spheres, increased from the controlled growth case to the plasmon-induced growth case. By further analysis in ImageJ, we obtained size distribution data for the particles as shown in Figure 3. The effect of introducing our plasmon-induced method to the growth process was that the size of the NPs grown

with the method was increased at all  $\text{SiO}_2$  thicknesses over the control growth.

We demonstrate that the overall size of the NPs, as well as the size difference between the control and experimental cases, decreases with increasing  $\text{SiO}_2$  thickness. This result is expected as with a larger insulating layer, the strength of the electric field is reduced and the size of the particles grown should be smaller. With a 20 nm  $\text{SiO}_2$  thickness, the difference between the plasmon-induced growth method and the control is almost entirely eliminated. We also see that the dielectric layer cannot be eliminated entirely, as that then results in the smallest size of NPs.

Next we characterized our substrate optically through ultraviolet-visible (UV-VIS) spectroscopy. The absorption spectra, shown in Figure 4, demonstrate a redshift of the resonance peaks with increasing silica thickness. The effect of growing the secondary Au layer, in comparison, is a blueshift of the peaks. In the dark or control growth, which produced smaller NPs than the plasmon-induced method, the blueshift is smaller than in the plasmon-induced growth, which produces larger NPs and exhibits a larger blueshift as a result.

## Future Work:

Given the complete characterization of our array and its favorable properties as a plasmonic substrate, we will look to integrate it into practical devices that require the sensitivity and robustness of our substrate. Creation of an optofluidic device to allow detection of biological proteins is an application that has many practical uses, and is one in which our bioplasmonics group at the University of Michigan has experience.

## Acknowledgments:

This work was performed in part at the Lurie Nanofabrication Facility at the University of Michigan. We would like to acknowledge support from the NNIN REU Program and the NSF under Grant No. ECCS-0335765.

## References:

- [1] Sharma, Bhavya, et. al. High-performance SERS substrates: Advances and challenges. *MRS Bulletin*, 2013, 38, 615-624.
- [2] Willets, Katharine A., and Van Duyne, Richard P. Localized Surface Plasmon Spectroscopy and Sensing. *Annual Review of Physical Chemistry*, 2007, 108, 267-297.

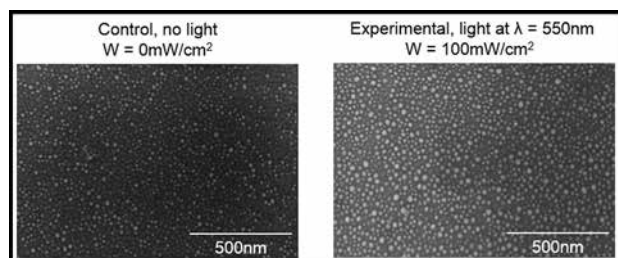


Figure 2: Growth of secondary Au layer without an excitation source (left) and with an excitation source (right).

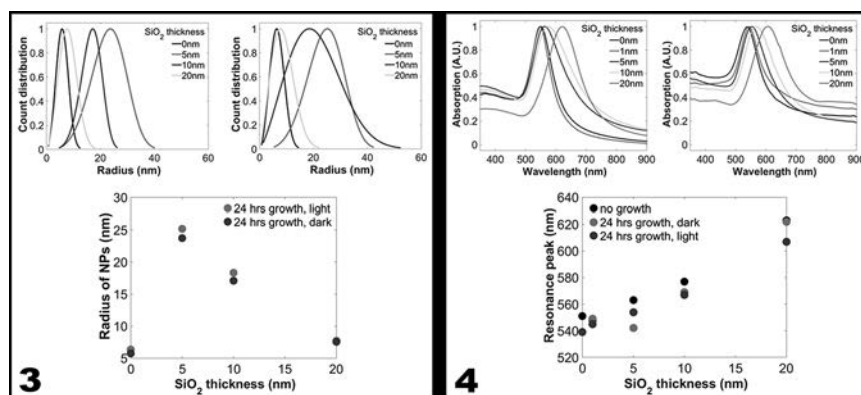


Figure 3, left: Radii of NPs grown without an excitation source (top left), with an excitation source (top right), and comparison of peak location (bottom). Figure 4, right: Absorption spectrum before growth (top left), after 24 hours growth with excitation source (top right), and comparison of peak location (bottom).

# Magnetic Fano Interferences in Plasmonic Metal Oligomers

Claire West

Physics, University of California, Santa Barbara

NNIN REU Site: Washington Nanofabrication Facility and Molecular Analysis Facility, University of Washington, Seattle, WA

NNIN REU Principal Investigator: Professor David Masiello, Chemistry, University of Washington

NNIN REU Mentors: Dr. Charles Cherqui and Steven Quillin, Chemistry, University of Washington

Contact: clairewest@umail.ucsb.edu, masiello@chem.washington.edu, cherqui@uw.edu quills@uw.edu

## Abstract:

Plasmonic metal nanoparticles possess exotic optical properties impacting a variety of fields from basic science to energy, defense, and medicine. One such property of broad importance is a Fano interference. This interference can be modeled by two coupled charged oscillators, in which the driven bright mode transfers its energy to the dark mode and stops. Thus, the system is still absorbing energy, but does not scatter. The resulting localization of energy is dependent on the coupling strength and mass ratio of the oscillators. These parameters, when properly tuned, alter the Lorentzian nature of the scattering spectrum, leading to an asymmetric Fano lineshape. The conditions that produce a Fano lineshape in the oscillator model were used to predict parameters in electric and magnetic plasmonic nanoparticle systems. This research focused on showing magnetic-magnetic Fano interferences for the first time. In particular, a magnetic plasmon was created from a cyclic assembly of metal nanospheres each with an electric dipole oriented head-to-tail around the ring, mimicking an electrical current loop. A second plasmonic ring was coupled to the first and driven by an electron beam, and their resulting interference was studied through numerical simulations of Maxwell's equations.

## Introduction:

Plasmonic nanoparticle assemblies offer a variety of tunable properties that are highly dependent on the separation of the particles. If the particles are close enough such that the plasmons interfere with each other through near-field interactions, they may experience a Fano interference. This interference is observed by analyzing the light scattered and absorbed from the system, and pinpointing the energy that corresponds to a dip in the scattering spectrum where there is non-zero absorption. This effect has been observed between electric-electric plasmon interferences [1], and electric-magnetic plasmon interferences [2]. But for the first time, this project focused on understanding the Fano interferences between magnetic-magnetic plasmons on a different configurations of nanospheres.

## Methods:

The interferences between plasmons were modeled using a damped oscillator system, because the time-dependent dipole moment of a nanosphere in an oscillating electric field is proportional to the Green's function of the damped harmonic oscillator. Figure 1 shows a schematic of this model. The Hamiltonian of this system can be diagonalized to solve for the new hybridized eigenmodes, which represent the electric dipole orientations. The parameters of this model were tuned until the Fano lineshape was most clearly seen in the spectra, which occurred when the masses of the oscillators were different and when the coupling was small. For the first time, this understanding of which parameters produced Fano interferences was used in an attempt to induce a Fano interference between two magnetic modes.

A nanosphere configuration motivated by previous research [3] was adapted to excite a magnetic plasmon Fano interference. Cherqui, et al., excited a ferromagnetic and antiferromagnetic mode on a hexamer oligomer configuration as shown in Figure 2a. An electron-beam was placed next to one sphere to excite the electric dipole on that sphere to point in a given direction and polarize the other dipoles.

The two eigenmodes under consideration were the modes that corresponded to the dipoles orienting head-to-tail because they produced a ferromagnetic and an

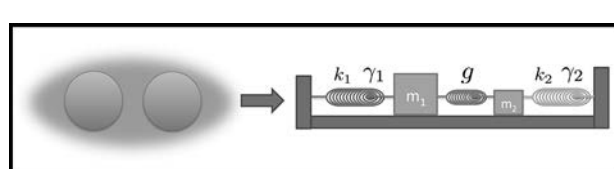


Figure 1: Oscillator system to model plasmonic interferences where  $k_1$ ,  $k_2$ , and  $g$  represent spring constants, and  $\gamma_1$  and  $\gamma_2$  represent damping coefficients.

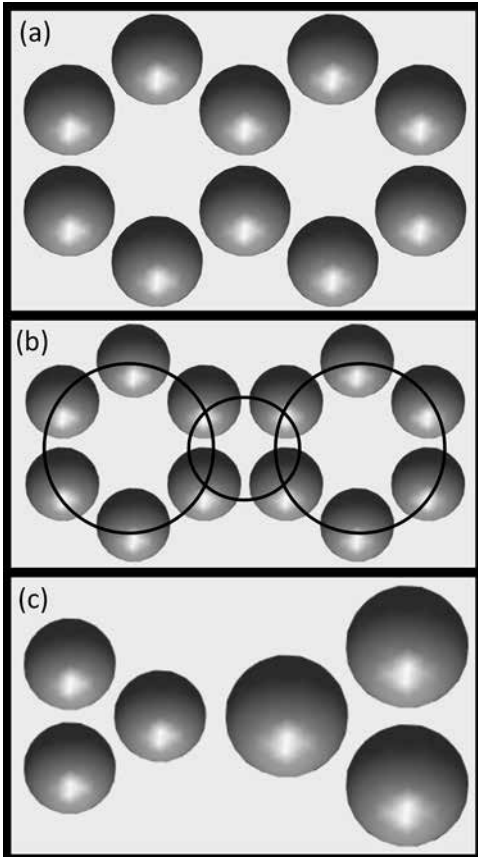


Figure 2: (a) Fused ring system motivated by Cherqui, et al. (b) Separated hexamer system with three magnetic moments circled. (c) New triangular configuration to eliminate third magnetic moment.

antiferromagnetic mode. As learned from optimizing the parameters in the oscillator model, the coupling between the modes had to be small, and therefore the hexamer oligomer configuration was modified by separating the hexamers.

### Results and Conclusions:

Ferromagnetic and antiferromagnetic modes created from plasmonic nanoparticle systems were attempted to be excited through numerical simulations on two different nanosphere arrangements. The separation of the rings and the placement of the electron beam were independently varied to excite the two different modes.

In the two hexamer system, the ferromagnetic mode could not be excited due to interferences generated from a magnetic moment that formed from a third electric dipole loop, shown in Figure 2b. Therefore, a new configuration was considered with two separated triangular nanosphere assemblies as shown in Figure 2c. Through various placements of the electron beam and separation distances of the triangular rings, it was realized that although this configuration corrected the previous problem, the

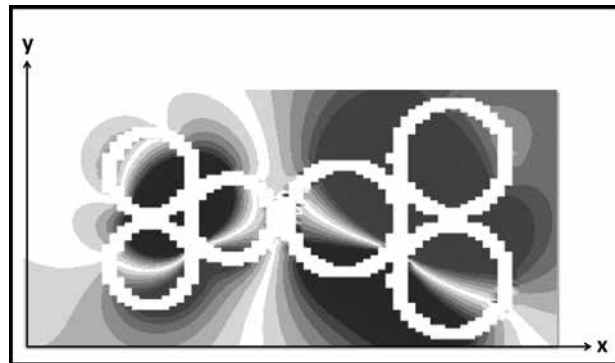


Figure 3: Magnetic fields in triangular system did not form localized moments.

magnetic modes did not completely close in and become localized, as shown in Figure 3.

In conclusion, by changing the ring separation and electron beam placement in two different configurations, a ferromagnetic mode was never excited.

### Future Work:

For the future work on this project, a new configuration must be considered in order to excite these two localized magnetic modes. One possible system would be to amend the triangular arrangement and add a fourth nanosphere to each triangle in order to form the magnetic modes.

Once this system achieves the desired ferromagnetic and antiferromagnetic modes, the scattering spectra can be analyzed to find the Fano interference. The ring distance and nanosphere separation can be varied and optimized to analyze which conditions produce the Fano effect.

### Acknowledgments:

This work was supported by the National Science Foundation's NNIN Research Experience for Undergraduates Program via grant number ECCS-0335765. I would like to thank Professor David Masiello for supervising me, and Charles Cherqui, Steven Quillin, Nick Montoni, and Niket Thakket for advising me during this project. I would also like to thank Melanie-Claire Mallison for organizing this program.

### References:

- [1] Lovera, A.; Gallinet, B.; Norlander, P.; Martin, O. Mechanisms of Fano Resonances in Coupled Plasmonic Systems. *ACS Nano* 2013, 7, 4527-4536.
- [2] Sheikholeslami, S. N.; Garca-Etxarri, A.; Dionne, J. A. Controlling the Interplay of Electric and Magnetic Modes via Fano-like Plasmon Resonances. *Nano Letters* 2011, 11, 3927-3934.
- [3] Cherqui, C.; Bigelow, N.; Vaschillo, A.; Goldwyn, H.; Masiello, D. Combined Tight-Binding and Numerical Electrodynamics Understanding of STEM/EELS Magneto-optical Responses of Aromatic Plasmon-Supporting Metal Oligomers. *ACS Photonics* 2014, 1, 1013-1024.

# High Aspect Ratio Dry Etching of Gallium Nitride

**Joshua Bostwick**

**Physics, University of Massachusetts Amherst**

**NNIN REU Site: UCSB Nanofabrication Facility, University of California, Santa Barbara, CA**

**NNIN REU Principal Investigator: Mark D'Evelyn, Vice President of Bulk Technology, Soraa**

**NNIN REU Peer Mentors: Jonathan Cook, Chemical Process Engineer, Soraa; Dr. Kevin Jiang, Senior Materials Physicist, Soraa**

**Contact: jbostwic@umass.edu, mdevelyn@soraa.com, jcook@soraa.com, kjiang@soraa.com**

## Abstract:

Light emitting diodes (LEDs) are made by depositing doped layers of material through epitaxial growth on a substrate. However, substrates are usually foreign materials and have different crystal structures than their epilayer; because of this, epitaxy becomes nonideal and overall LED performance suffers. The focus of this project was to construct dry etched gallium nitride (GaN) pillars that can be generated on top of foreign substrates to improve epitaxial growth and maximize LED power by enabling a three-dimensional (3D) LED architecture. By using an inductively coupled plasma (ICP) system and changing etch plasma parameters, GaN pillars were constructed. These pillars were then analyzed by measuring their radius of curvature, characterizing their profile, and evaluating the quality of the fabricated pillars. As the GaN pillars developed, the magnitude of the radius of curvature increased. This relaxed the wafers and increased the potential for higher quality epitaxial growth. However, due to a decrease in pillar diameter and inconsistent pillar and surface roughness created by this process, more research needs to be done fabricating these types of pillars on foreign substrates for LED and electronic device use.

## Introduction:

LEDs are a common electronic device in the world due to their high efficiency and long lifetime. One common material found in LEDs is GaN due to its good semiconductor properties and its applications to high temperature devices in the blue ultraviolet spectrum [1].

The first step in making an LED is growing a buffer layer of GaN on top of a foreign substrate, like sapphire, to limit the mismatch between the different crystal structures. From this, a negatively doped GaN layer, an indium gallium nitride (InGaN) active region, and a positively doped GaN layer are grown on the buffer layer with epitaxial growth (Figure 1); this allows the active region to emit light with a blue wavelength and shine through the substrate when a voltage is applied across the grown epitaxial structure [2]. However, even a buffer layer cannot overcome all issues caused by the different crystal structures of GaN and sapphire. Because of this, epitaxial growth is not optimized — creating features like uneven morphology and dislocations in the epitaxial structure, which diminish LED performance.

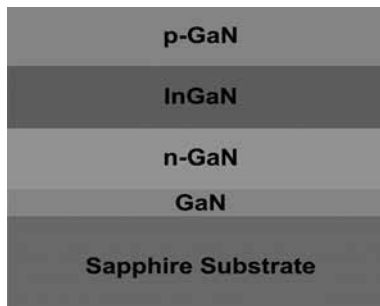


Figure 1: Standard GaN LED structure.

To improve this process, the initial GaN buffer layer must be transformed to produce higher quality epitaxial growth and maximize LEDs with the eventual goal of growing 3D epitaxial structures for LED construction [3]. This project focused on constructing dry etched GaN pillars with the hope that they can be generated on top of foreign substrates to improve epitaxial growth and enable a 3D architecture.

## Experimental Procedure:

Eight micron ( $\mu\text{m}$ ) thick GaN template wafers were employed and placed into a plasma enhanced chemical vapor deposition system, where  $2\ \mu\text{m}$  of silicon dioxide ( $\text{SiO}_2$ ) were deposited. The wafers were then taken to a photolithography phase where a coating of positive photoresist was spun onto the wafers and then exposed to a masking pattern with  $100\ \mu\text{m}$  circles with  $150\ \mu\text{m}$  separation. Once exposed to ultraviolet light and developed, the photoresist served as a protective coating for the  $\text{SiO}_2$ .

After photolithography, the wafers underwent a  $\text{SiO}_2$  etch with hydrofluoric acid to remove all the exposed  $\text{SiO}_2$  and create a protective layer for the GaN layer. Following a quick liftoff process where the remaining photoresist was removed, the wafers were then taken to an ICP system for dry etching. Here, etch plasma removed the exposed GaN by physically knocking it off the surface and chemically changing the composition of the material to remove it (Figure 2). By changing pressure, chemical composition, and radio frequency power in the etch plasma, GaN pillars were fabricated. This was followed by a final  $\text{SiO}_2$  etch removing the last of the  $\text{SiO}_2$  and allowing the GaN pillars to be analyzed quantitatively.

### Results and Conclusion:

A Tencor Flexus system, which shines a laser onto a wafer surface and gives a map of its radius of curvature, showed that as the amount of GaN dry etched from the wafer increased, so did the magnitude of the radius of curvature in each of the wafers tested (Figure 3). Because of this, the wafer became more relaxed allowing for better crystallographic alignment of the GaN buffer layer and the potential for higher quality epitaxial growth. Microscopic analysis also showed minimal defects were found between the pillars and 4-17% of pillars had defects on top of them (Figure 4). However, this process created pillars with a decrease in diameter between 25-30% of the original mask pattern on each of the wafers. Further analysis with atomic force microscopy showed that the pillar and surface roughness were very inconsistent with one another. While half of the recipes created surfaces with little to no change in roughness, the other half created varying roughnesses between the surface, including a recipe with a worse

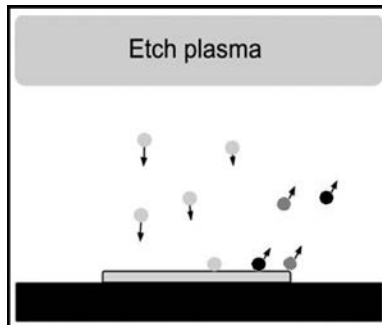


Figure 2: ICP etch schematic.

roughness difference of over 100%. Because of this, even though dry etched GaN pillars become relaxed relative to continuous GaN layers, more research can be done to improve the decrease in pillar size with inconsistent surface roughnesses.

### Future Work:

The next steps of this project will be to refine the lithography process and use a dry etch for  $\text{SiO}_2$  removal,

both of which are to minimize undercutting the  $\text{SiO}_2$  etch mask so the pillar diameter does not decrease. In addition, more analysis will be done creating pillars of different thicknesses and geometries to see how pillar height and spacing affects the radius of curvature change.

### Acknowledgements:

I would like to thank my mentors Jonathan Cook and Kevin Jiang as well as my principal investigator Mark D'Evelyn and the Soraa staff for their help on this project. I would also like to thank the University of California, Santa Barbara, the National Nanotechnology Infrastructure Network Research Experience for Undergraduates (NNIN REU) Program and the National Science Foundation under Grant No. ECCS-0335765 for funding this project.

### References:

- [1] Cheung, R., et al. J. of Vacuum Sci. & Tech., 17, 2759-2764 (1999).
- [2] Schubert, E. Light-emitting Diodes, 2, 1-23 (2003).
- [3] Rishinaramangalam, A.K., et al. J. Elec.Mats, 44, 1255-1262 (2014).

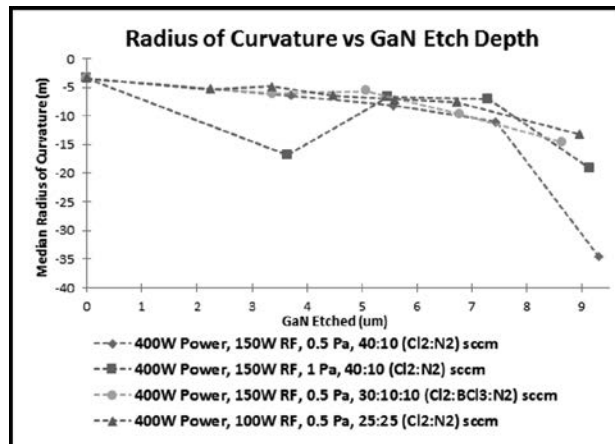


Figure 3: Comparison of radius of curvature vs. GaN etch depth with different etch recipes.

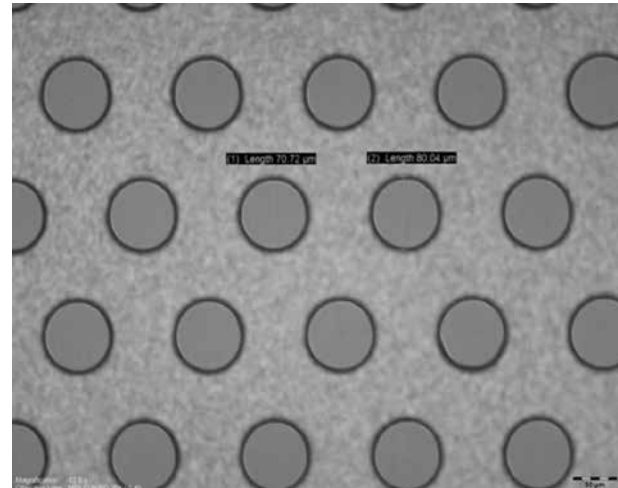


Figure 4: Microscope image of dry etched pillars created through a mask with 100  $\mu\text{m}$  circles and a 150  $\mu\text{m}$  separation between them.

# Engineering the Fixed Charge of Aluminum Oxide for Field-Assisted Passivation in Heterojunction Solar Cells

Scott Chow

Computer Science, Harvey Mudd College

NNIN REU Site: Stanford Nanofabrication Facility, Stanford University, Stanford, CA

NNIN REU Principal Investigator: Professor Krishna C. Saraswat, Department of Electrical Engineering, Stanford University

NNIN REU Mentor: Raisul Islam, Department of Electrical Engineering, Stanford University

Contact: schow@hmc.edu, raisul@stanford.edu, saraswat@stanford.edu

## Abstract:

Surface recombination is a detrimental phenomenon in heterojunction solar cells when electrons recombine with holes at defects in the interface between oxide and silicon. The effects of surface recombination can be reduced through chemical and field-assisted passivation. Chemical techniques improve the actual interface by rendering defects ineffective and are typically achieved through annealing. Field-assisted passivation involves placing a layer of high fixed charge material adjacent to silicon. This charge creates an electric field that attracts opposite charge carriers and repels same charge carriers, reducing carrier interaction with surface defects. In this work, the viability of field-assisted passivation using aluminum oxide ( $\text{Al}_2\text{O}_3$ ) is explored by engineering a process that maximizes fixed charge. Different thicknesses of  $\text{Al}_2\text{O}_3$  are deposited on n- and p-type silicon using plasma-assisted atomic layer deposition and metallized with tungsten or aluminum and titanium nitride. The capacitance-voltage (C-V) characteristics of the resulting structures are measured before and after annealing in forming gas. From the C-V curves, the flat band voltage is derived, and the fixed charge of  $\text{Al}_2\text{O}_3$  is calculated. From these measurements,  $\text{Al}_2\text{O}_3$  is found to have a high negative fixed charge, on the order of  $10^{12}$ , indicating that  $\text{Al}_2\text{O}_3$  has great potential to be used for field-assisted passivation.

## Introduction:

Traditionally, solar cells are based on homojunctions formed by n- and p-type silicon. However, there are disadvantages to using this p-n junction. Dark current caused by the potential difference between the two ends of the p-n junction flows counter to the photocurrent and heavy doping in silicon requires high temperatures, increasing production cost.

The newly-proposed heterojunction solar cell involves replacing the p-n junction with hole-selective and electron-selective contacts,  $\text{NiO}$  and  $\text{TiO}_2$  respectively [1]. These selective contacts suppress dark current, by increasing the potential barriers, and require a lower thermal budget, reducing the cost significantly. However, the interface between the passivating oxides and silicon becomes a problem. Interface traps facilitate recombination of electron-hole pairs in a process known as surface recombination, greatly reducing efficiency [1].

Field-assisted passivation is one way to reduce surface recombination. A high fixed charge material is inserted between the carrier selective contact and silicon. This charge creates an electric field that attracts carriers of one type and repels carriers of the other type, reducing carrier interaction with surface defects (Figure 1). In this work, we explore the possibility of using  $\text{Al}_2\text{O}_3$  as a negative fixed

charge material for field-assisted passivation of the hole-selective contacts by quantifying the fixed charge of  $\text{Al}_2\text{O}_3$ .

## Experimental Process:

In the experiment, we fabricated a metal-oxide-semiconductor capacitor (MOSCAP) (Figure 2). N-type silicon wafers with a resistivity of 5-10 ohm-centimeters ( $\Omega\text{-cm}$ )

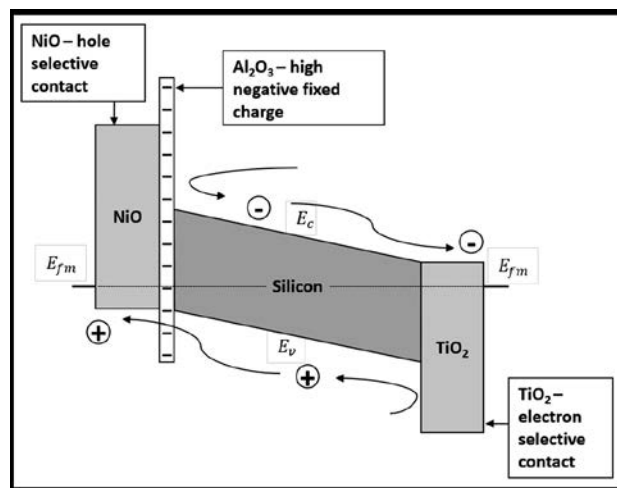


Figure 1: Field-assisted passivation of heterojunction solar cells using  $\text{Al}_2\text{O}_3$ .

and p-type wafers with resistivity of 10-20  $\Omega\cdot\text{cm}$  were cleaned using standard pre-diffusion RCA clean (SC1-HF-SC2).  $\text{Al}_2\text{O}_3$  was deposited onto the wafers using plasma-assisted atomic layer deposition (ALD); 250  $\mu\text{m}$  diameter circular metal contacts were sputtered using a shadow mask on the front. Blanket metal was sputtered on the back. Then capacitance-voltage (C-V) measurements were performed from 1 kHz to 1 MHz at a standard Cascade probe station on the sample before and after rapid thermal annealing at 400°C in forming gas (95%  $\text{N}_2$  + 5%  $\text{H}_2$ ) for 30 minutes.

## Results and Discussion:

Three main problems were encountered when measuring C-V: noise caused by current leakage, series resistance caused by bad contacts, and frequency dispersion caused by interface traps. Current leakage was minimized by increasing the thickness of the  $\text{Al}_2\text{O}_3$  layer as well as using non-reactive tungsten as the metal contact. Annealing reduced the amount of series resistance and decreased the number of interface traps, resulting in less frequency dispersion. The C-V curves from our final structures on n- and p-type silicon can be seen in Figures 3 and 4. The fixed charge of  $\text{Al}_2\text{O}_3$  is calculated by obtaining the oxide capacitance and flat-band voltage shift from the curves. Calculation of fixed charge at the highest and lowest frequencies provides a range for the fixed charge density in  $\text{Al}_2\text{O}_3$ . At 1 kHz, the measured fixed charge for n-type was  $2.1 \times 10^{13} \text{ cm}^{-2}$  and for p-type, the fixed charge was  $4.8 \times 10^{12} \text{ cm}^{-2}$ . At 1 MHz, the measured fixed charge for n-type was  $6.8 \times 10^{12} \text{ cm}^{-2}$  and for p-type, the measured fixed charge was  $2.5 \times 10^{12} \text{ cm}^{-2}$ . In general, the negative fixed charge was on the order of  $10^{12} \text{ cm}^{-2}$ , which is comparable with other measurements of high fixed charge oxides used for field-assisted passivation [2]. Uncertainty in the measurements was caused by frequency dispersion.

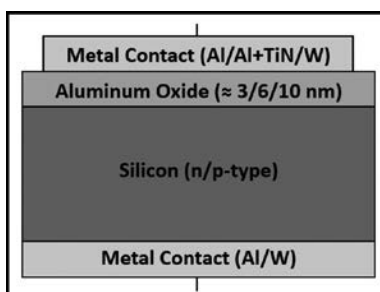


Figure 2: Final fabricated MOSCAP.

We observed that plasma-assisted ALD deposited  $\text{Al}_2\text{O}_3$  contains high negative fixed charge, making it suitable for field-assisted passivation.

## Summary and Conclusions:

In this work, we investigated plasma-assisted ALD  $\text{Al}_2\text{O}_3$  as a source of negative fixed charge for field-assisted passivation. We found ways to reduce noise, frequency dispersion, and series resistance in C-V measurements of the MOSCAP by increasing the thickness of the  $\text{Al}_2\text{O}_3$ , using tungsten contacts, and annealing the samples.

From the C-V curves,  $\text{Al}_2\text{O}_3$  was found to have negative fixed charge upwards of  $10^{12} \text{ cm}^{-2}$ , which is suitable for providing field-assisted passivation. The  $\text{Al}_2\text{O}_3$  ALD recipe will be further optimized to control the amount of fixed charge. Further work will be done to incorporate high fixed charge  $\text{Al}_2\text{O}_3$  in heterojunction solar cells.

## Acknowledgements:

I would like to thank Raisul Islam and Pranav Ramesh for mentoring me. Also, thanks to Professor Krishna Saraswat for allowing me to work with his lab and for his guidance. Many thanks to Dr. Michael Deal, for coordinating this REU, and NSF funding (Grant No. ECCS-0335765), NNIN REU Program, and CIS for supporting and funding this experience.

## References:

- [1] Islam, Raisul, and Krishna C. Saraswat. "Metal/insulator/semiconductor Carrier Selective Contacts for Photovoltaic Cells." 2014 IEEE 40<sup>th</sup> Photovoltaic Specialist Conference (PVSC): 285-89.
- [2] Werner, Florian, et al. "Very low surface recombination velocities on p-and n-type c-Si by ultrafast spatial atomic layer deposition of aluminum oxide." Applied Physics Letters 97.16 (2010): 162103.

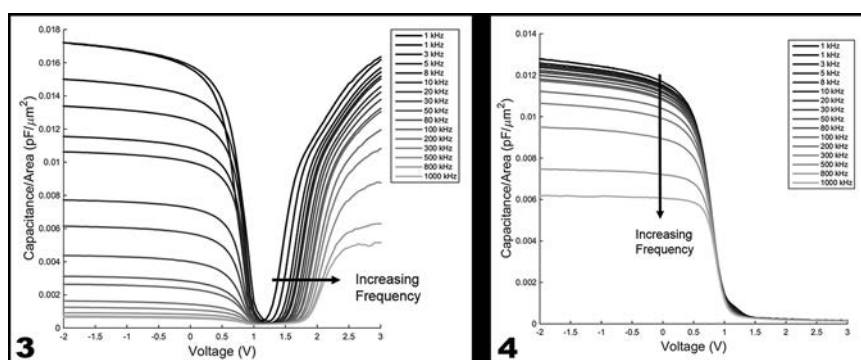


Figure 3, left: C-V plot of final structure on n-type silicon after annealing.

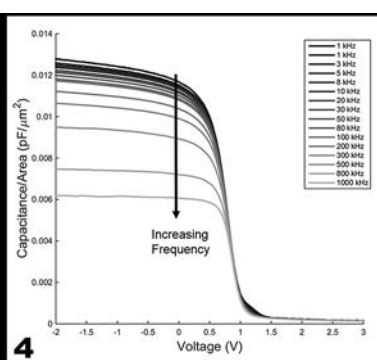


Figure 4, right: C-V plot of final structure on p-type silicon after annealing.

# SERS Study of BNNS on Au as a Catalyst for Oxygen Reduction Reaction

Emiliana Cofell

Physics, Scripps College

NNIN iREU Site: National Institute for Materials Science (NIMS), Tsukuba, Ibaraki, Japan

NNIN iREU Principal Investigator: Prof. Kohei Uosaki, Director of Global Research Center for Environment and Energy based on Nanomaterials Science (GREEN), NIMS

NNIN iREU Mentor: Kentaro Tomita, Global Research Center for Environment and Energy based on Nanomaterials Science (GREEN), NIMS

Contact: ercofell@gmail.com, uosaki.kohei@nims.go.jp, tomita.kentaro@nims.go.jp

## Abstract:

Non-precious-metal catalysts for the oxygen reduction reaction (ORR) in fuel cells are in high demand to decrease fuel cell cost and increase cathode stability. One candidate for an ORR catalyst in fuel cells that use an acidic electrolyte is boron nitride nanosheets (BNNS). In order to better understand the potential of BNNS as a catalyst, identification of the intermediates during the ORR of BNNS on a gold (Au) substrate was performed by *in situ* measurements using surface enhanced Raman scattering (SERS) spectroscopy.

## Introduction:

Boron nitride nanosheets (BNNS) are a promising material for use in catalysts for the oxygen reduction reaction (ORR) in fuel cells that use an acidic electrolyte. Uosaki, et al., reported that BNNS on gold showed high electrocatalytic activity for ORR. Ordinarily an insulator, BNNS has semiconducting properties when deposited on a conducting substrate. In order to better understand the reaction catalyzed by this material, this project focused on the use of Raman spectroscopy to view surface intermediates formed during the reaction of BNNS on Au. However, since intensity during the reaction was low and peaks were initially difficult to identify, a technique known as surface enhanced Raman scattering (SERS), was implemented to increase intensity and allow for better characterization of the reaction.

## Experimental Procedure:

BNNS was prepared from the suspension of hexagonal BN in 2-propanol by ultrasonic irradiation for 96 h [1]. A sputter deposited layer of 150 nm thick Au on a n-Si<111> wafer was used as a substrate. A 0.1 mg/mL solution of BNNS was drop casted onto substrates, then heated for two hours at 200°C. To increase Raman intensity by plasmon resonance effect [2], BNNS was modified with gold nanoparticles, which were prepared by chemical reduction of HAuCl<sub>4</sub> with NaBH<sub>4</sub>. The substrate was chemically roughened in 0.1 M KCl by repeated oxidation-reduction cycles (ORCs) for 3-7 minutes. The ORCs were performed from -0.28 V to +1.22 V (vs. NaCl saturated Ag/AgCl) with the sweep rate of 500 mV/s. Samples were also analyzed using SEM imaging and EDS.

In order to measure *in situ* Raman spectra during the reaction, a three-electrode electrochemical cell with a

fused quartz window was used. The electrolyte for the reaction was a 0.5 M H<sub>2</sub>SO<sub>4</sub> aqueous solution, the reference electrode was Ag/AgCl, and the counter electrode was Pt wire. The electrochemical cell was mounted on the stage of a confocal Raman microscope (RAMANtouch, Nanophoton Co.) with a CCD detector and a CW laser (785 nm, 9 mW at focal point). The scattered signal was exposed to the CCD for seven seconds, with four accumulations per spectra. A scan rate of 2 mV/s was used during SERS measurements.

## Results and Discussion:

SEM images of samples showed differences in surface morphology between the original (Figure 1A) and roughened samples (Figure 1B, C). The BNNS with gold nanoparticles on the gold substrate roughened for 7 min (Au/BNNS on Au) is shown in Figure 1D as 200~300 nm sheets (BNNS) and < 30 nm particles (Au) in diameter, respectively. Figure 2 shows the linear sweep voltammograms of bare Au and Au/BNNS on Au. In the case of Au/BNNS on Au, a reduction current less than 4  $\mu$ A/cm<sup>2</sup> was observed at the potential from +0.6 V to +0.2 V, in addition to a larger reduction current (< 80  $\mu$ A/cm<sup>2</sup>) at the negative potential than +0.2 V. The reduction current at +0.2 V was also measured on the bare Au electrode. This result suggests that a part of ORR on Au/BNNS contained the four electron reduction process of O<sub>2</sub> catalyzed by BNNS.

The SERS spectra measured during potential sweeping are shown in Figure 3. On the bare gold, broad peaks at 1150 cm<sup>-1</sup> and 1500 cm<sup>-1</sup> were observed at +0.13 V (Figure 3A). They correspond with O-O stretching bonds of HO<sub>2</sub> radical and molecular O<sub>2</sub>, respectively. The SERS spectra

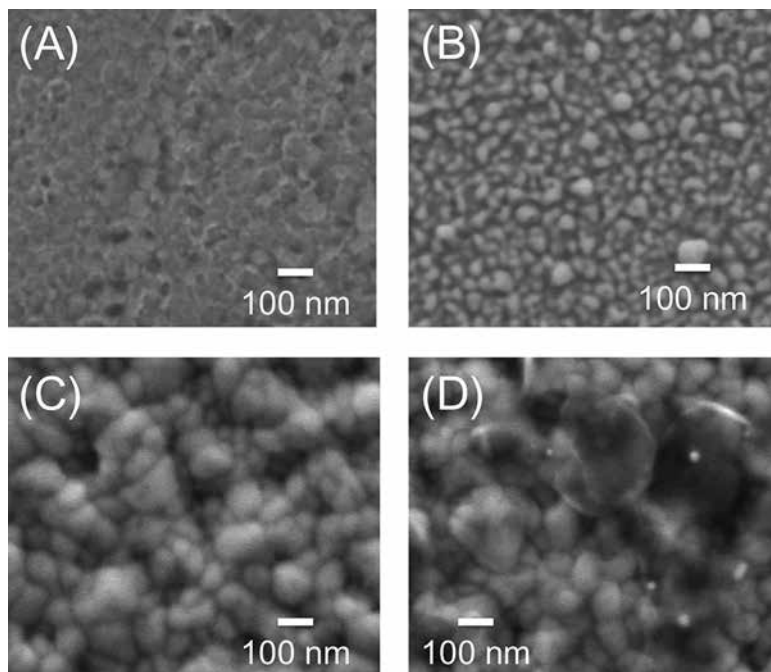


Figure 1: SEM images of (A) sputtered Au, (B) three and (C) seven minutes roughened Au, and (D) Au/BNNS on seven minutes roughened Au. Figure 2, top right: Linear sweep voltammograms of bare Au (black curve) and AuNPs/BNNS on Au (grey curve) measured in O<sub>2</sub> saturated 0.5 M H<sub>2</sub>SO<sub>4</sub> solution. Figure 3, bottom right: SERS spectra of (A) bare Au and (B) AuNPs/BNNS on Au during potential sweep. The corresponding voltammograms are shown in Figure 2.

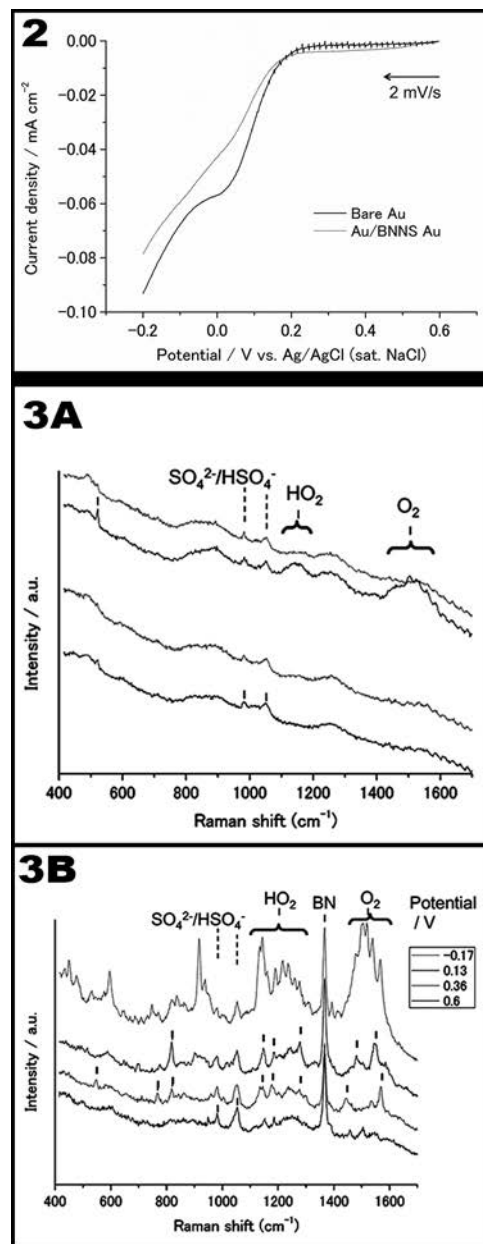
of Au/BNNS contained a sharp peak at 1366 cm<sup>-1</sup>, which corresponds with the E<sub>2g</sub> phonon mode of bulk hexagonal BN. Similarly, the frequency of BNNS suggested the formation of aggregations of BNNS [3]. In Figure 3B, the spectra measured at 0.38V and +0.13 V contained additional peaks at 545 cm<sup>-1</sup>, 775 cm<sup>-1</sup> and 818 cm<sup>-1</sup>, 1100~1300 cm<sup>-1</sup>, and 1400~1600 cm<sup>-1</sup>. By comparison with Raman spectrum of boric acid [4], these frequencies correspond to O-B-O bending, B-O stretching ( $\nu_1$ ), B-O-H bending, and B-O stretching ( $\nu_6$ ), respectively.

### Future Work:

Although repetition of the measurements is required in order to confirm peak position of these intermediates, the formation of B-O bonding seemed to be the key process of the catalytic activity of BN. Further study of the intermediates formed during the reaction will help to construct BNNS based catalyst for use in the cathode of fuel cells.

### Acknowledgements:

I would like to thank Professor Uosaki for the opportunity to work in his lab, and his entire lab group for their support and guidance, especially my mentor Kentaro Tomita. I would also like to thank NIMS for this opportunity, as well as National Nanotechnology Infrastructure Network



International Research Experience for Undergraduates (NNIN iREU) Program and NSF for funding this project (under Grant No. ECCS-0335765).

### References:

- Uosaki, Kohei, Ganeshan Elumalai, Hidenori Noguchi, Takuwa Masuda, Andrey Lyalin, Akira Nakayama, and Tetsuya Taketsugu. J. Am. Chem. Soc. 2014, 136.18, 6542-545.
- Ikeda, K.; Fujimoto, N.; Uosaki, K. J. Phys. Chem. C 2014, 118, 21550-21557.
- Gorbachev, Roman V., Ibtisam Riaz, Rahul R. Nair, Rashid Jalil, Liam Britnell, Branson D. Belle, Ernie W. Hill, Kostya S. Novoselov, Kenji Watanabe, Takashi Taniguchi, Andre K. Geim, and Peter Blake. Small. 2011, 7.4, 465-68.
- Servoss, R. R.; Clark, H. M. J. Chem. Phys. 1957, 26, 1175-1178.

# Smart-Cut Processing for Transfer of High-Temperature Ceramic Materials to Silicon

**Mikayla Essigmann**

**Chemical Engineering, University of Massachusetts Lowell**

**NNIN REU Site: Stanford Nanofabrication Facility, Stanford University, Stanford, CA**

NNIN REU Principal Investigator: Debbie G. Senesky, Aeronautics and Astronautics, Stanford University

NNIN REU Mentor: Ashwin Shankar, Electrical Engineering, Stanford University

Contact: [mikayla\\_essigmann@student.uml.edu](mailto:mikayla_essigmann@student.uml.edu), [dsegesky@stanford.edu](mailto:dsegesky@stanford.edu), [ashanka@stanford.edu](mailto:ashanka@stanford.edu)

## Abstract:

Micromechanical resonator devices that naturally oscillate at certain frequencies are currently used in communication, signal processing, and sensor applications. Piezoelectric-based resonators, which utilize nonconductive ceramic materials such as quartz, are commonly used for such applications and are historically constructed with a quartz material platform. However, applications with harsh surroundings, such as space environments, combustion engines, and down-hole drilling, can cause failure of quartz resonators at temperatures above 573°C due to phase change of the material and upon radiation exposure. Langatate, a high-temperature crystalline piezoelectric material, is well suited for resonator applications in these environments because of its inherent temperature stability and ability to remain piezoelectric at temperatures above 1400°C.

Here, we are developing a microfabrication technique to place thin langatate films (approximately 1  $\mu\text{m}$ ) on a silicon substrate using the “Smart-Cut” process, which involves the exfoliation of a large portion of an ion-implanted langatate piece when heated to high temperatures. Results of spin-on glass bonding, measurements of the hydrophilicity of the langatate surface, and the analysis of the exfoliation of ion-implanted langatate will be presented. Thin-film single-crystal langatate on a silicon substrate can ultimately serve as a platform for the realization of micromechanical resonators for harsh environment applications.

## Introduction:

“Smart-Cut” processing has been a major development in the fabrication of silicon-on-insulator (SOI) technologies [1]. This process can also be used to transfer thin-films of other monocrystalline materials, such as langatate, allowing for a uniform high quality crystalline thin-film and has been shown to be successful with silicon carbide, a similar high-temperature material [2]. The langatate thin-film structure will be composed of a silicon wafer, a layer of  $\text{SiO}_2$  that improves temperature stability and bonding strength, a coating of spin-on glass acting as an adhesive bond able to withstand high temperatures and forgiving to rough surfaces, and a thin-film of previously hydrogen ion-implanted langatate. The thin-film structure can be suspended by isotropically etching the underlying silicon with  $\text{XeF}_2$  gas to obtain a suspended resonator, shown in Figure 1, which has a good quality factor to help keep stable timing [3].

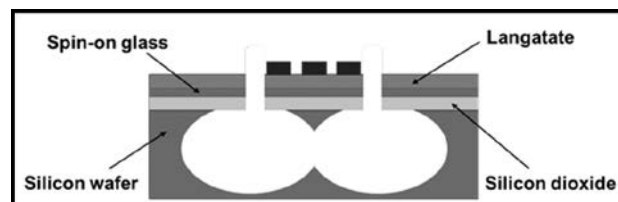


Figure 1: Suspended resonator structure.

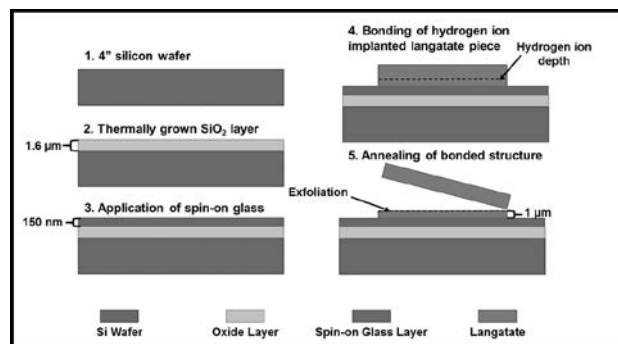


Figure 2: “Smart-Cut” process.

## Procedure:

The “Smart-Cut” process is shown in Figure 2. First, a 4-inch silicon wafer topped with a 1.6  $\mu\text{m}$  layer of thermally grown  $\text{SiO}_2$  was coated with a 150 nm layer of spin-on glass (hydrogen silsesquioxane). Hydrogen ion-implanted

and diced langatate pieces were cleaned with a chemical solution to create a hydrophilic surface. Three pieces were placed on the spin-on glass coated silicon substrate

equidistant from one another. A pressure of approximately 1 MPa was applied and the structure was heated to 25°C, 80°C, and 150°C each for one minute and 250°C for four hours. The bonded structure was annealed at temperatures above 600°C to form blisters. These blisters cause the slicing of a large portion of the langataate and leave behind a 1  $\mu\text{m}$  thin-film.

### Results and Conclusions:

To ensure that the hydrogen atoms were at a depth of 1  $\mu\text{m}$ , Stopping and Range of Ions in Matter (SRIM) software was employed to find the energy level of the ion beam needed to achieve a large distribution of hydrogen ions at that depth below the surface directly bonded to the substrate. Energies of 170 and 190 keV and a constant fluence of  $5 \cdot 10^{16} \text{ cm}^{-2}$  were chosen for this project.

Exfoliation blisters, which are the precursors to the large portion of material slicing off, appeared when implanted hydrogen atoms were heated and hydrogen gas formed. Atomic force microscopy (AFM) was used to measure the surface roughness of exfoliation blisters, shown in Figure 3, formed after an ion-implanted (170 keV) langataate piece was heated to 950°C for three hours. The depth of the blisters analyzed was approximately 0.6  $\mu\text{m}$ , which was close to our target depth.

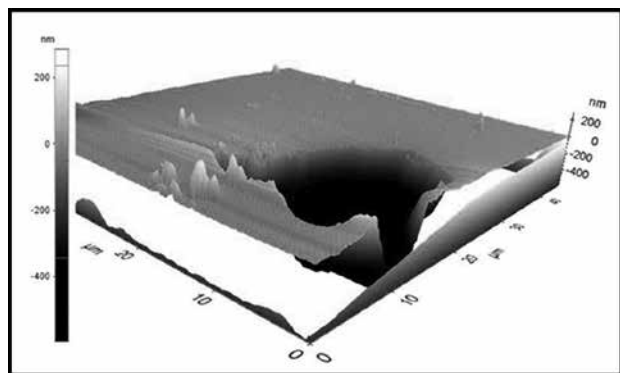


Figure 3: AFM of an exfoliation blister.



Figure 4: Contact angle of a water droplet on the langataate surface.

Different cleaning methods were implemented on langataate and the hydrophilicity of the surface was examined. After cleaning, the contact angle of a water droplet placed on the surface was measured using a goniometer, shown in Figure 4. A cleaning procedure using HF created a hydrophobic surface. However, changing the chemical clean to a solution of  $\text{H}_2\text{SO}_4$  and higher percentages of  $\text{H}_2\text{O}_2$ , or piranha clean, led to a hydrophilic surface. Yet, as the time the langataate was left outside of deionized water increased the hydrophilicity of the surface decreased. Therefore, a piranha clean with higher concentrations of  $\text{H}_2\text{O}_2$  and minimized time outside of deionized water gave optimal results for a hydrophilic surface.

The final step of the “Smart-Cut” process was the annealing of the bonded structure to temperatures over 600°C. However, the spin-on glass bond did not survive when heated up to 950°C. This de-bonding may have been due to a mismatch in the coefficients of thermal expansion (CTEs). Stress calculations were performed and found that langataate and silicon place 48.45 MPa and 55.29 MPa of stress on the spin-on glass bond respectively at temperatures of 950°C. This significant amount of stress being placed on the bond may be the cause of failure.

### Future Work:

Future work for this research includes finding new methods of bonding langataate to a silicon substrate, attempting a “Smart-Cut” of langataate on a different substrate with a similar CTE, and ultimately fabricating a suspended resonator from the thin-film structure.

### Acknowledgements:

I would like to thank my PI Professor Debbie G. Senesky, mentor Ashwin Shankar, and coordinator Dr. Mike Deal for their guidance, the Stanford Nanofabrication Facility staff, the other Stanford REUs, and Stanford’s Center for Integrated Systems. This research was funded by the National Nanotechnology Infrastructure Network Research Experience for Undergraduates (NNIN REU) Program and the National Science Foundation under Grant No. ECCS-0335765.

### References:

- [1] Bruel, M., et al. ““Smart cut”: a promising new SOI material technology.” SOI Conference, 1995. Proceedings., 1995 IEEE International. IEEE, 1995.
- [2] Lee, Jae-Hyung, et al. “Smart-cut layer transfer of single-crystal SiC using spin-on-glass.” Journal of Vacuum Science and Technology B 30.4 (2012): 042001.
- [3] Lin, Chih.Ming, et al. “AlN/3C-SiC Composite Plate Enabling High-Frequency and High-Q Micromechanical Resonators.” Advanced Materials 24.20 (2012): 2722-2727.

# Fabrication of All-Aluminum p-Type Silicon Solar Cells

**Raul Flores**

**Chemical Engineering, the University of Kansas**

**NNIN REU Site: ASU NanoFab, Arizona State University, Tempe, AZ**

NNIN REU Principal Investigator: Professor Meng Tao, Electrical Engineering, Arizona State University

NNIN REU Mentors: Laidong Wang and Wen-cheng Sun, Electrical Engineering, Arizona State University

Contact: raulf2012@gmail.com, meng.tao@asu.edu, lwang186@asu.edu, wen-cheng.sun@asu.edu

## Abstract and Introduction:

Two substantial impediments to the large scale adoption of photovoltaic solar cell technologies are the high-cost and scarcity of the materials used to produce them. Of the numerous potential solar cell structures—substrates, passivation layers, and anti-reflection coatings being some of the most common—the silver front finger electrode is perhaps one of the most widely-used in solar cell design. The high-cost and relative scarcity of silver, then, would bottleneck the implementation of photovoltaic devices, which use silver as the front finger electrode material. Therefore, there is an imperative to replace silver with a cheaper and more abundant metal.

The use of aluminum as a replacement for silver as the front finger electrode material was investigated. The aluminum was deposited via electroplating to construct a simple p-type silicon solar cell. The cell's various operational parameters were measured, then compared to a control device.

## Experimental Procedure:

The p-type silicon substrate was partially processed when received. Specifically, both surfaces were textured, and the n-type silicon layer was formed via the diffusion of phosphorus. A silicon nitride ( $\text{SiN}_x$ ) layer was then applied via plasma-enhanced chemical vapor deposition (PECVD), followed by a screen-printed aluminum backside contact, which was subsequently fired. The front surface then went through the following treatments to form the front-contact finger pattern: photoresist application, patterned UV-exposure, alkaline development/selective photoresist removal, hydrogen fluoride (HF) bath for  $\text{SiN}_x$  and silicon dioxide ( $\text{SiO}_2$ ) removal. Then, nickel was sputtered into the etched pattern. Finally, aluminum was electroplated onto the nickel. See Figure 1 for the fabrication process. See Figure 2 for the schematic of the finished cell.

## Results:

The finished solar cell was characterized using a Sun 2000 Solar Simulator from ABET Technologies (see Table 1). The following parameters can be directly obtained by fitting the I-V data to a simple, idealized solar cell model: efficiency, fill factor, short-circuit current ( $I_{SC}$ ), open-circuit voltage ( $V_{OC}$ ), series resistance ( $R_{Series}$ ), and shunt resistance ( $R_{Shunt}$ ).



Figure 1: Process flow for the fabrication of this study's p-type solar cell. The silicon wafer was received with the first two steps already completed.

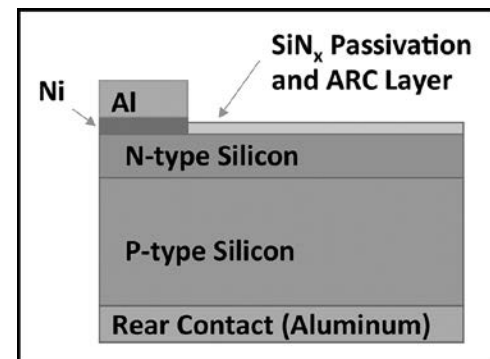


Figure 2: Illustration of the finished device's structure. The relative thicknesses are not to scale. Note that the back surface field (BSF) is not shown.

Our group's device was compared to another group's solar cell. The reference cell's structure is almost identical to this study's cell; the difference being that the reference cell uses a silver front contact, and has no intermediary seed layer between the front contact material and the silicon substrate, as opposed to the nickel layer in this study's device (see Figure 2).

Arguably, the most important parameter in the analysis of solar cells is efficiency. The efficiency of the reference cell is significantly higher than our group's solar cell (a discrepancy of 4.4 percentage points absolute). The poor performance of our cell is likely due to a combination of factors. Fabrication errors in conjunction with non-optimized cell parameters—parameters being any cell quantity whose value can be controlled during fabrication, including: layer thickness, diffusion temperature/time, front finger dimensions, etc.—are partially culpable for our device's poor performance. For instance, it is hypothesized that the silicon-nickel and/or the aluminum-nickel interfaces have high contact resistances, which could be alleviated by optimizing the electroplating procedure.

The fact that our group's device efficiency was due to fabrication errors and/or poorly optimized cell specifications, was corroborated by our cell's substandard  $R_{\text{Shunt}}$  and  $R_{\text{Series}}$  (see Table 1). A poor  $R_{\text{Shunt}}$  is often associated with manufacturing defects, which implies that fabrication errors—such as contamination and sample damage—occurred during the assembly of the cell. The potentially high contact resistances between the front contact layers may contribute to the cell's high series resistance. The detrimentally high  $R_{\text{Series}}$  is a probable contributor to the marginally decreased  $J_{\text{SC}}$  and  $J_{\text{MP}}$  values of our cell, relative to the reference (see Table 1).

	Our Lab's Cell	Reference Cell	Percent Difference
Efficiency [%]	12.4	16.8	35
$J_{\text{SC}}$ [mA/cm <sup>2</sup> ]	31.8	35.5	12
$V_{\text{oc}}$ [V]	0.60	0.61	2
$R_{\text{Shunt}}$ [ $\Omega \cdot \text{cm}^2$ ]	183	808	342
$R_{\text{Series}}$ [ $\text{m}\Omega \cdot \text{cm}^2$ ]	1030	393	62

Table 1: Table of various solar cell parameters (Efficiency,  $J_{\text{SC}}$ ,  $V_{\text{oc}}$ ,  $R_{\text{Shunt}}$ , and  $R_{\text{Series}}$ ) for this study's device and a reference device. Also shown: the percent difference between the two solar cell devices.

It should be noted that our group's solar cell has values for  $J_{\text{SC}}$  and  $V_{\text{oc}}$  that are reasonably similar to the reference's values. It is therefore believed that if the problems of the poor  $R_{\text{Shunt}}$  and  $R_{\text{Series}}$  are addressed, the solar cell designed by our group will be able to perform at a level comparable to, or better than, the reference device.

## Conclusions and Future Works:

A cell employing an aluminum front contact was fabricated and characterized. The device has a poor efficiency relative to the reference, which is likely due to substandard  $R_{\text{Series}}$  and  $R_{\text{Shunt}}$  values. The poor values of  $R_{\text{Series}}$  and  $R_{\text{Shunt}}$  are due to fabrication errors and non-optimized cell parameters. These flaws will have to be addressed to increase the efficiency of the device, and thus demonstrate the efficacy of aluminum as an alternative front contact material.

## Acknowledgments:

I would like to express my gratitude towards my PI, Professor Meng Tao, and to my mentors, Laidong Wang and Wen-cheng Sun, for their guidance and support. I would also like to thank the National Nanotechnology Infrastructure Network Research Experience for Undergraduates (NNIN REU) Program, the National Science Foundation (NSF), Arizona State University, and the Center for Solid State Electronics Research for the support, funding and opportunity provided. This research was supported by the National Science Foundation under Grant No. ECCS-0335765.

## References:

- [1] Tao, C.; Jiang, J.; Tao, M., Natural Resource Limitations to Terawatt-scale Solar Cells. *Solar Energy Materials and Solar Cells* 2011, 95 (12), 3176-3180.
- [2] Sun, W.C.; Han, X.F.; Tao, M., Electroplating of Al on Silicon in an Ionic Liquid. *Ecs Electrochem Lett* 2015, 4 (4), D5-D7.
- [3] Sun, W.C.; Zhang, H.; Tracy, C. J.; Tao, M., Electroplated Al as the Front Electrode in Crystalline-Si Solar Cells. *IEEE 42<sup>nd</sup> PVSC Conference*.

# Construction of a Substrate for Characterizing the Real-Time Electrical Conductivity of Thin Films as Deposited

Andrew S. King

Materials Science and Engineering, New York State College of Ceramics, Alfred University

NNIN REU Site: Cornell NanoScale Science and Technology Facility, Cornell University, Ithaca, NY

NNIN REU Principal Investigator: James R. Engstrom, School of Chemical and Biomolecular Engineering, Cornell University

NNIN REU Mentor: Jiun-Ruey Chen, School of Chemical and Biomolecular Engineering, Cornell University

Contact: ask7@alfred.edu, jre7@cornell.edu, jc2642@cornell.edu

## Abstract:

Atomic layer deposition (ALD) is presently employed in important semiconductor manufacturing processes, which include the deposition of ultrathin layers for gate dielectrics and diffusion barriers for interconnects. As many of the exciting applications of ALD involve forming ultrathin, atomically thin films, depositing a conformal and continuous ALD film with a controlled thickness is critical to performance. Moreover, the ability to assess the film properties *in situ* is essential to avoid the complications that arise when samples are exposed to laboratory air. In this work, we designed and fabricated a substrate with patterned electrodes, which allowed *in situ*, real time electrical measurement of ALD films being deposited in a custom-built microreactor. Fabrication of the substrate consisted of two patterned layers on thermal oxide: electron beam evaporated gold (with a chromium adhesion layer) followed by plasma-enhanced chemical vapor deposition (PECVD) of silicon dioxide (silica) as an insulating, protecting layer. Feature size and film morphology were confirmed by profilometry and scanning electron microscopy (SEM), respectively.

## Introduction:

A typical atomic layer deposition (ALD) process starts with exposing a surface to a gaseous organometallic precursor, followed by an inert gas purge. This process reacts with the surface and thus leaves a surface layer of reacted molecules. This layer of atoms is then exposed to a co-reactant such as water or oxygen, followed by a second purge cycle. This process repeats until the desired thickness is produced. The ALD process does not necessarily produce a continuous monolayer every cycle. Having a continuous film is important when making electrical contacts or diffusion barriers. Our project aimed to detect the number of cycles of ALD needed to produce a continuous film using non-linear four-point probe electrical conductivity measurements as outlined in Figure 1.

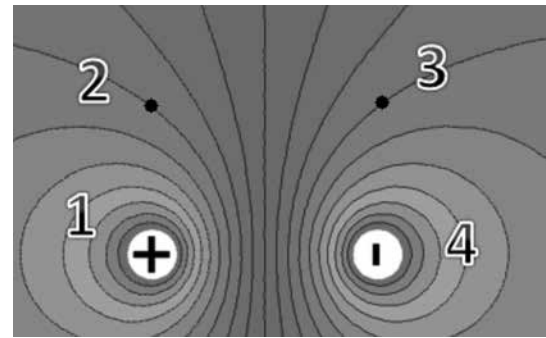


Figure 1: Non-linear four-point probe setup for substrate showing equipotential lines and points of measure. Image Courtesy zureks@gmail.com.

## Experimental Procedures:

The custom-designed microreactor in the Engstrom research group allows real time electrical measurement during vapor-phase deposition/reaction, including chemical vapor deposition (CVD) and ALD. The 4-point probes are in a rectangular geometry of 3.8 cm by 2.2 cm. We therefore designed a patterned electrode on a 4-inch wafer based on the probe geometry shown in Figure 2.

Four gold pads (1 cm x 1 cm) were contacts to the probes, and each pad had a lead wire (50  $\mu$ m wide) heading to central reaction zone (0.1 cm x 0.1 cm). The reaction zone provided a flat substrate surface for a continuous ALD film to be deposited on without possible effects due to the topology, which could then be

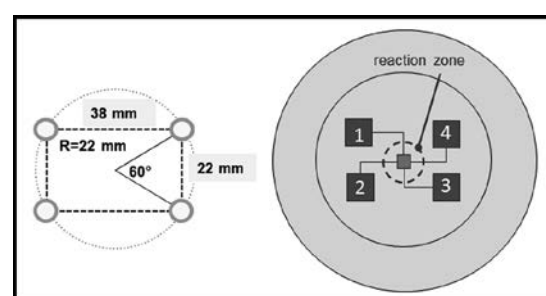


Figure 2: Substrate layout for four-point probe with contact pads and wires connecting to electrodes in the reaction zone.

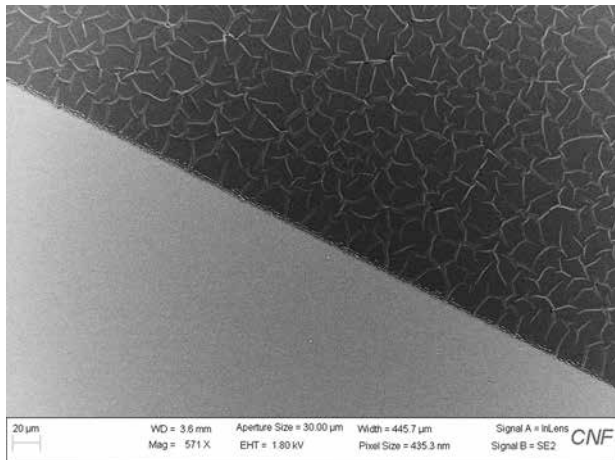


Figure 3: Silica deposited via electron beam evaporation on gold with no adhesion layer.

used to accurately observe the point where an ALD film was continuous on a two-dimensional surface.

Substrates were produced with 100 mm silicon wafers with a surface layer of 500 nm of thermal oxide. The wafers were then coated with a lift-off resist and baked at 180°C for 300 s, followed by coating with photoresist and baking at 115°C for 180 s. The substrates were then UV exposed on an ABM contact aligner to produce a pattern for the substrate electrodes and developed for 90 s with MIF-726. Substrates then were coated with 10 nm Cr|100 nm Au|10 nm Cr via electron beam evaporation, and soaked in 1165 stripper for not less than six hours to lift off the metal.

Similar processes were employed for the deposition of a 500 nm layer of plasma-enhanced chemical vapor deposited (PECVD) silica, after which the substrates were submerged in chrome etch solution to remove the exposed chromium adhesion layer.

## Results and Discussions:

Profilometry of the samples revealed that thicknesses of the samples after evaporating chrome and gold layers varied within 11% of the target thickness, which suggested good reproducibility of the process. Optical microscopy of the metal films revealed small features on the surface of the film, indicating metal spitting occurred during evaporation. SEM images of the gold electrodes reaffirmed that spitting was occurring during evaporation of the gold. By fine tuning the process parameters, the quality of the e-beam evaporated metal layer was greatly improved: Instead of using a single deposition rate throughout the evaporation process, we found that a smooth surface could be generated by slowing down the deposition rate from 1.0 Å/s to 0.3 Å/s for the last 20 nm.

Evaporated silica was initially chosen for depositing dielectric layer on top of the electrodes, and scanning

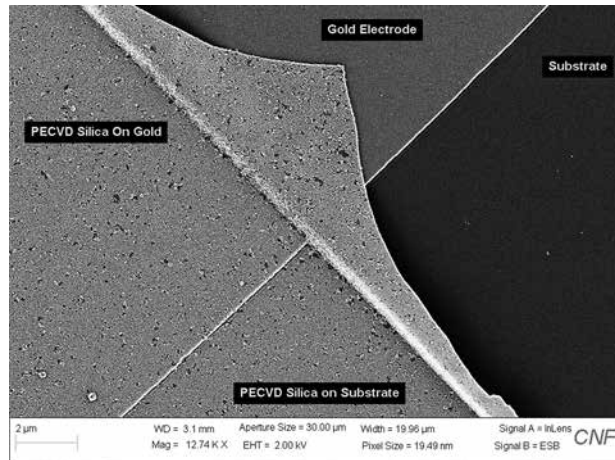


Figure 4: PECVD silica on gold with 10 nm chromium adhesion layer, after lift-off and prior chromium etching.

electron microscopy (SEM) images displayed in Figure 3 revealed crazing of the oxide on gold after deposition. We demonstrated that the craze can be alleviated by an additional chromium adhesion layer on top (i.e.,  $\text{SiO}_2|\text{Cr}|\text{Au}|\text{Cr}|\text{SiO}_2$ ).

Furthermore, PECVD deposition of silica gave a denser film that adhered better despite being more difficult to lift-off and required damaging the film manually with tweezers. Floating silica left behind after lift-off was observed by electron microscopy shown in Figure 4, which again demonstrated the process difficulty resulting from the density of PECVD silica layer. The dimension of the floating silica is three orders of magnitude smaller than that of the reaction zone, thus was of no concern to the performance of the substrate.

## Conclusions and Future Work:

With the above characterization, we show that substrates with patterned electrodes for real time electrical measurement of ALD film were made as designed. Deposition of thin films should be performed *ex situ* using the IV-probe station in the clean room and *in situ* electrical measurements in the Engstrom lab to complete the objective of this work.

## Acknowledgements:

I would like to thank and acknowledge the following persons, and organizations for their contributions of funding, facilities, and time: Aaron Windsor, Beth Rhodes, Tom Pennell, Vince Genova, Melanie-Claire Mallison, Michael Skvarla, Lynn Rathbun, the National Science Foundation grant Number ECCS-0335765, the NNIN Research Experience for Undergraduates Program, the Cornell NanoScale Facility, and NYSTAR.

# Magneto-Optic Characterization of Ferromagnetic Thin Films for Use in Nano-Scale Computer Applications

Elizabeth Lee

Engineering, Harvey Mudd College

NNIN REU Site: UCSB Nanofabrication Facility, University of California, Santa Barbara, CA

NNIN REU Principal Investigator: Prof. Chris Palmstrøm, Electrical and Computer Engineering, and Materials, UCSB

NNIN REU Mentor: Tobias Brown-Heft, Materials, University of California, Santa Barbara

Contact: elee@g.hmc.edu, palmstrom@ece.ucsb.edu, tobias@umail.ucsb.edu

## Abstract:

Magnetic tunnel junctions (MTJs) utilizing materials with perpendicular magnetic anisotropy (PMA) are an attractive area of research due to applications in nanoscale computing. In particular, PMA facilitates spin-transfer-torque switching (STT) and high thermal stability in magnetic random access memory. While previous studies have shown that  $L1_0$  ordered iron platinum (FePt) films exhibit strong PMA, we illustrate that epitaxial Fe/Pt bilayers on  $MgO<001>$  can exhibit PMA if annealed after the initial deposit. All films were grown in the MBE system in the Palmstrøm Lab at UCSB. *In situ* magneto-optic Kerr effect (MOKE) measurements were taken in the in-plane and out-of-plane directions to determine the magnetic anisotropy of each sample. In order to investigate the effects of annealing on interdiffusion and chemical reactions, we performed x-ray photoemission spectroscopy (XPS) measurements on samples before and after annealing at different temperatures. Component fitting shows a decrease in Pt peak area and increase in Fe peak area with increasing annealing temperature, suggesting Fe outdiffusion into the Pt cap or Pt indiffusion into the Fe. Therefore, we suspect the formation of an ordered Fe-Pt phase between the Fe base layer and the Pt cap. We believe that performing x-ray diffraction (XRD) and transmission electron microscopy (TEM) studies on future samples will give valuable insight into how annealing changes the crystal structure and affects compound formation.

## Background:

Energy efficient data storage systems are required by battery-powered portable devices and large-scale internet server farms. Magnetic random access memory (MRAM), which uses magnetic tunnel junction (MTJ) arrays to represent computer bits, is a very promising solution. MRAM is desirable because its data storage method requires little energy to write, no energy to store, is nonvolatile and remains stable for years [1]. In a magnetic crystal, we can consider the crystal anisotropy as the energy required to magnetize a material in a given direction. It is advantageous for the magnetic films used in MTJs to exhibit perpendicular magnetic anisotropy (PMA), in which it is energetically favorable for the

magnetic moments in the material to lie out of plane. PMA is advantageous for two main reasons:

- Decrease of spin transfer torque critical current, aiding device writing efficiency [2]
- High thermal stability, facilitating device scalability and long-term storage [3]

$L1_0$  ordered Fe/Pt films have been shown to exhibit PMA, but Fe/Pt bilayers on  $MgO$  have not been previously investigated. Studying the Fe/Pt interface may give insight into the mechanism that causes PMA, helping to advance the nanoscale computing industry.

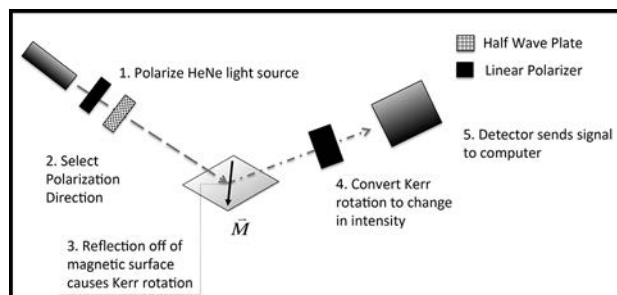
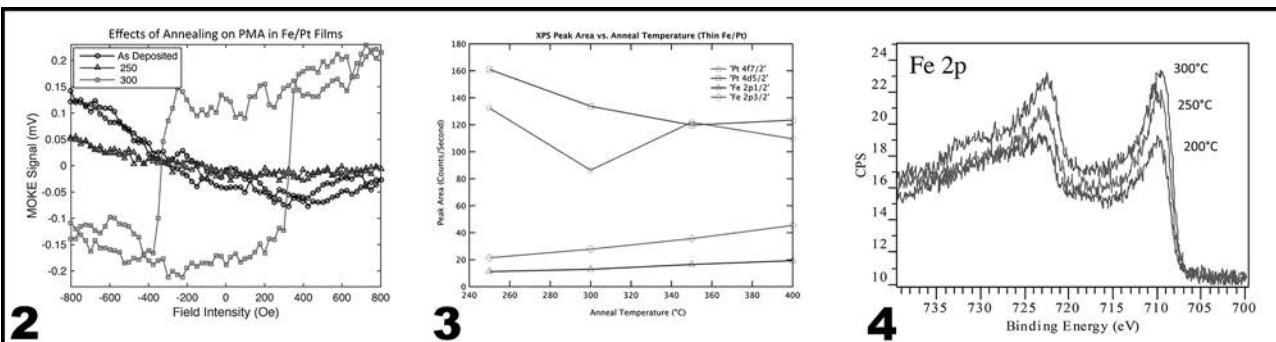


Figure 1: Magneto-optic Kerr effect (MOKE) schematic.

## Experimental Procedure:

All samples were grown on  $MgO<001>$  crystal substrates in the Palmstrøm Lab at University of California, Santa Barbara. All growth and characterization was performed under continuous ultra high vacuum (UHV). After growth, samples were analyzed *in situ* using the magneto-optic Kerr effect (MOKE), which takes advantage of the fact that light changes polarization and intensity when reflected off of a magnetic surface (see Figure 1 for schematic).



**Figure 2, left:** MOKE hysteresis loops indicate transition to ferromagnetic behavior at 300°C. **Figure 3, middle:** XPS peak area as a function of annealing temperature. **Figure 4, right:** Sample XPS results for Fe 2p orbital.

This phenomenon can be used to measure magnetic hysteresis loops that show changes in sample magnetization as an external field is applied. For our samples, we used an electromagnet to generate a maximum external field of  $\pm 3500$  Oersteds (Oe). Due to the small size of the magnetic samples, one Oersted of applied field intensity approximately corresponds to one Gauss of magnetic flux. Samples were measured *in situ* using MOKE and x-ray photoemission spectroscopy (XPS) both before and after annealing at temperatures ranging from 200°C to 400°C.

XPS is a useful technique because it can be used to examine changes in atomic composition and bonding near the sample surface. Samples that exhibited PMA were re-measured by *ex situ* superconducting quantum interference device (SQUID) magnetometry to verify magnetic behavior and saturation magnetization.

## Results and Conclusion:

Hysteresis loops collected via MOKE reveal that while Fe/Pt does not exhibit PMA as deposited, annealing to 300°C significantly changes the magnetic behavior (see Figure 2). After annealing to this temperature, MOKE hysteresis loops transitioned from a hard-axis to an easy-axis in the out-of-plane direction. That is, after annealing, the sample magnetized almost completely in the perpendicular applied field direction and created an approximately square hysteresis loop. This loop shape is indicative of strong PMA in the sample. XPS measurements in Figures 3 and 4 indicate an increase in Fe peak area and a decrease in Pt peak area as annealing temperature increases.

XPS is only sensitive to the top few nanometers of a given film, so an increase of Fe peak area indicates that Fe atoms may be migrating into the Pt cap or vice versa. The correlation between the PMA transition detected by MOKE and the peak area trends in XPS suggest that

annealing produces a very thin L1<sub>0</sub> ordered FePt phase, which has been previously shown to exhibit strong PMA in bulk samples [4]. Another possibility is that annealing produces a highly ordered interface between the Fe and Pt layers, facilitating novel interfacial spin-orbit interactions between the magnetic Fe and high atomic number Pt atoms. Future studies will focus on using x-ray diffraction and transmission electron microscopy to verify the behavior of the Fe-Pt interface and the origin of PMA in Fe/Pt heterostructures.

## Acknowledgements:

I would like to thank the members of Palmstrøm group and the UCSB Nanofab for their experience and assistance in the lab. I would also like to extend a special thanks to the National Nanotechnology Infrastructure Network Research Experience for Undergraduates (NNIN REU) Program and the National Science Foundation for the opportunity to conduct research at the University of California, Santa Barbara (under Grant No. ECCS-0335765).

## References:

- [1] Gallagher, W. J. and Parkin, S. S. P. Development of the magnetic tunnel junction MRAM at IBM: From first junctions to a 16-Mb MRAM demonstrator chip. *IBM J. Res. Dev.* 50, 5-23 (2006).
- [2] Thomas, L., Jan, G., Zhu, J. and Liu, H. Perpendicular spin transfer torque magnetic random access memories with high spin torque efficiency and thermal stability for embedded applications. *J. Appl. Phys.* 115, 172615 (2014).
- [3] Gajek, M., et al. Spin torque switching of 20 nm magnetic tunnel junctions with perpendicular anisotropy. *Appl. Phys. Lett.* 100, 1-4 (2012).
- [4] Lairson, B. M., Visokay, M. R., Sinclair, R. and Clemens, B. M. Epitaxial PtFe<001> thin films on MgO<001> with perpendicular magnetic anisotropy. *Appl. Phys. Lett.* 62, 639-641 (1993).

# Conformation of Organic Electronics to the Hemispherical Shape Using Elastomeric Transfer Elements

Anna Smith

Chemical Engineering, University at Buffalo SUNY

NNIN REU Site: Stanford Nanofabrication Facility, Stanford University, Stanford, CA

NNIN REU Principal Investigator: Dr. Zhenan Bao, Chemical Engineering, Stanford University

NNIN REU Mentor: Yeongjin Kim, Electrical Engineering, Stanford University

Contact: acsmith7@buffalo.edu, zbao@stanford.edu, kimyj@stanford.edu

## Abstract:

A camera inspired by the human eye offers attractive design features for imaging devices. The hemispherical detector geometry enables a simpler and superior optical imaging system facilitating wide field of view with few-component imaging optics. We have demonstrated a simple fabrication process with reduced cost that takes advantage of the flexible nature of organic electronics by constructing an image sensor using organic field-effect transistors. The transfer process demonstrated in this work can transform organic electronics on polyimide substrates into unconventional three-dimensional shapes that can be applied not only to the artificial eye camera but also to many bio-inspired applications to come.

## Introduction:

The conventional camera, due to the planar nature of its imaging sensor, requires elaborate optical components to obtain good quality images. In comparison to the planar geometry, the human eye is an optical system with an attractive hemispherical surface enabling an outstanding imaging system with simple lens design, wider field of view, and low aberrations [1]. Biomimetic-inspired research and product design are transferring optimum designs from nature to technical applications and creating a demand for flexible electronics that will conform to three-dimensional shapes such as the electronic eye camera [2].

Ko, et. al., has created a single-crystalline silicon based hemispherical electronic eye camera using planar semiconductor device fabrication technologies [3]. Islands of silicon diodes and connecting compressible bridges made of metal and polyimide capping layers were used to make an imaging array. The planar layout of the image sensor was released using a hydrofluoric acid etch and mechanical lift-off and transformed using elastomeric transfer elements made of polydimethylsiloxane (PDMS) into a hemispherical geometry.

Organic field-effect transistors (OFET) have many benefits over silicon-diode-based electronics such as low cost; flexible nature; lightweight and potentially easier conformation to the hemispherical sensor. However, organic semiconductors are sensitive to aggressive wet chemical etching. The objective of this project was to design a release and transfer method to conform OFETs to the hemispherical surface using relatively gentle anodic

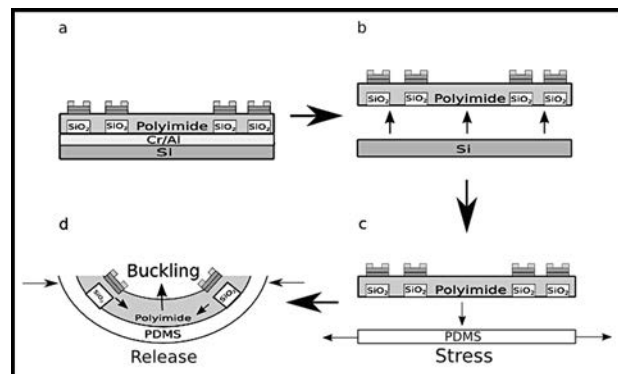


Figure 1: Release and transfer process of OFET based image sensor. A) Device fabrication. B) Anodic dissolution lift-off. C,D) Transformation to hemispherical surface.

dissolution as a release mechanism. Moreover, we aimed to optimize processing steps such as the bridge and island method. We would then fabricate device structures using the proposed process, and assess the conformity.

## Release and Transfer Process:

Figure 1 shows a detailed visualization of the release and transfer process method. The fabrication was carried out on a Si carrier wafer with a Cr/Al sacrificial layer, SiO<sub>2</sub> islands (1 μm thick) and polyimide (1.2 μm thick). The OFETs were stacked on the polyimide supportive layer

directly above the  $\text{SiO}_2$  islands. Following fabrication, the substrate was released from the carrier wafer by anodic dissolution. Using electrolysis, the Cr/Al sacrificial layer was the anode and platinum was the cathode in a NaCl catalyzed solution. Anions were absorbed on the surface of the passive aluminum-oxide layer and caused the breakdown of the passive oxide film, which was then followed by the pitting corrosion of the Cr/Al layer and its release from the carrier wafer [4].

Once the substrate was removed from the carrier wafer it was ready to be transferred onto a transfer element made using Teflon® coated balls placed in a beaker of PDMS that was cured for six hours at room temperature. Both the image sensor and the transfer element underwent  $\sim 10$  seconds of  $\text{O}_2$  plasma treatment. The transfer element was then stretched from its hemispherical surface to form a planar surface for  $\text{O}_2$  plasma bonding to the  $\text{SiO}_2$  islands. The transfer element was then released and the image sensor conformed to the hemispherical surface. Finally,

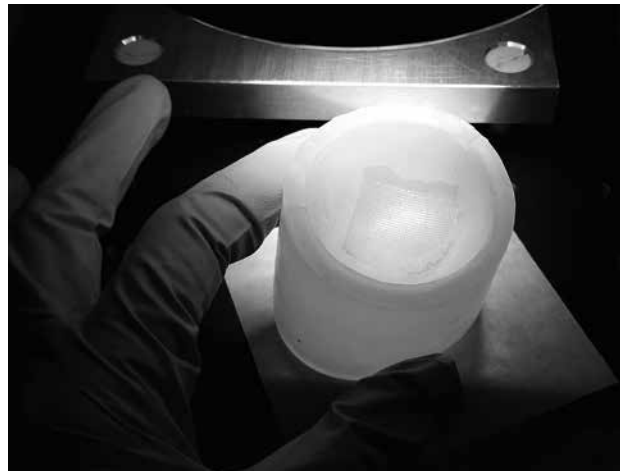


Figure 2: Substrate conformation to hemispherical surface.

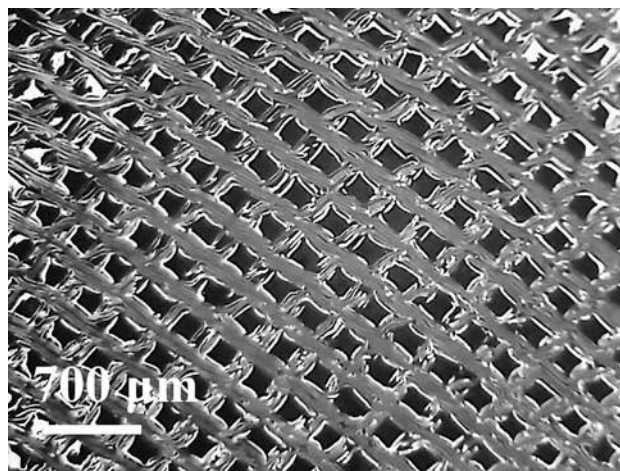


Figure 3: Polyimide and  $\text{SiO}_2$  conformation to substrate.

the polyimide support was compressed around the  $\text{SiO}_2$  islands causing uniform buckling on the hemispherical surface.

### Release and Transfer Process Results:

We were able to reach our project objectives by observing a damage free release of the substrate from the carrier wafer using anodic dissolution, and the successful conformation of the substrate to the transfer element, as seen in Figure 2. By using selective adhesion of the  $\text{SiO}_2$  islands to the PDMS transfer elements, we were able to control the contractive buckling of the polyimide in between the bonded regions. According to the images taken with the optical microscope in Figure 3, uniform buckling is observed.

### Summary:

We designed an effective release and transfer method for the OFET based image sensor by demonstrating an effective release method for polyimide films sub  $2 \mu\text{m}$  thick, and reducing the production length and cost by eliminating the island and bridge method. For future work we would like to demonstrate the release and transfer method with the full device fabrication and test the electrical and optical performance once the release and transfer process are complete.

### Acknowledgements:

I want to thank Professor Zhenan Bao for the opportunity to be a part of her group, my mentor Yeongin Kim for his guidance, the Bao group for all of their support, the site coordinator Dr. Michael Deal for his dedication to the program, The Stanford's Center for Integrated Systems (CIS), The National Science Foundation (NSF) and The National Nanotechnology Infrastructure Network Research Experience for Undergraduates (NNIN REU) Program (under Grant No. ECCS-0335765).

### References:

- [1] J.E. Ford, et al., "Fiber-coupled monocentric lens imaging," *Imaging and Applied Optics Conference*, 2013.
- [2] K. Yu, et al., "Biomimetic optical materials: Integration of nature's design for manipulation of light," *Progress in Materials Science*, Vol. 58 pp.825-873, 2013.
- [3] H.C. Ko, et al., "A Hemispherical electronic eye camera based on compressible silicon optoelectronics," *Nature*, Vol. 454 pp.748-753, 2008.
- [4] K. Mansouri, et al., "Anodic Dissolution of Pure Aluminum during Electrocoagulation Process: Influence of Supporting Electrolyte, Initial pH, and Current Density," *Industrial and Engineering Chemistry Research* 2011; 50(23): 13362-72.

# Measurement and Management of Thin Film Stresses

**Taylor Soucy**

**Chemistry, The Pennsylvania State University**

**NNIN REU Site: UCSB Nanofabrication Facility, University of California, Santa Barbara, CA**

**NNIN REU Principal Investigator: Mark D'Evelyn, Vice President of Bulk Technology, Soraa**

**NNIN REU Peer Mentors: Jonathan Cook, Chemical Process Engineer, Soraa; Dr. Kevin Jiang, Senior Materials Physicist, Soraa**

**Contact: tzs5319@psu.edu, mdevelyn@soraa.com, kjiang@soraa.com, jcook@soraa.com**

## Abstract:

Metallization is a crucial step in microelectronic device fabrication. Stress in metal thin films causes yield and reliability problems. In severe cases, improperly controlled stress results in delamination of the metal film. This project systematically studied the intrinsic stresses in titanium tungsten (TiW) and gold (Au) films as a function of deposition conditions. The metal films were deposited on 2-inch  $<001>$  silicon wafers. Measuring the change in radius of curvature of the Si wafer after metal deposition derived stresses and the thickness of the metal film deposited. This information is important towards controlling the stresses in the metal film to minimize the shear force at the metal/semiconductor interface, improving device reliability.

## Introduction:

Light emitting diodes (LEDs) and other microelectronic devices use is widespread. The creation of this nanotechnology involves depositing very thin layers of different materials. When depositing these layers, in-plane stresses are often generated, which can have a significant effect on the devices' performance and reliability [1]. There are two sources of stress: thermal and intrinsic. Thermal stress is generated by the difference in coefficient of thermal expansion (CTE) between different materials [2]. In single crystalline thin films, intrinsic stress is generated when the films and substrate have different lattice parameters. In amorphous or nanocrystalline films in which the film/film and film/substrate interfaces aren't coherent, the packing density of thin films determines intrinsic stress. The effect of interface bonding between films and substrates is negligible. Once the shear force resulting from the film stress exceeds the bonding strength between films or substrates, delamination occurs [3]. In order to have reliable devices, film stress must be managed.

Sputter deposition of Au at 5 mT can create a 0.30.5  $\mu\text{m}$  layer over 10 minutes, while the more efficient electroplating process can add up to 2  $\mu\text{m}$  of film in 20 minutes. Electroplating—which takes place in an isolated bath—only coats the conductive wafer, while sputtering coats the entire chamber. Because electroplating is done at 55°C, thermal considerations are important—which are calculated by the following equation

$$\sigma_f = (\alpha_{Tf} - \alpha_{Ts})(T_s - T_0)(Y')$$

where  $\alpha$  is the coefficient of thermal expansion of the substrate and film, respectively,  $T$  is the temperature before and after processing, and  $Y'$  is the biaxial elastic modulus.

$$\sigma = \frac{E * t_s^2}{(1-\nu) * t_f} * \left( \frac{1}{R} - \frac{1}{R_o} \right)$$

Figure 1: Stoney equation, used to calculate stress.

## Experimental Procedure:

In this work, we systematically studied the thin film stresses in sputtered TiW and Au as a function of sputtering pressure, and electroplated Au as a function of electroplating current. The Stoney equation (Figure 1) is used to calculate the stress, where  $E$  is Young's Modulus,  $\nu$  is Poisson's ratio [4], and  $t_s$  and  $t_f$  are the thicknesses of the substrate and thin film, respectively.  $R_o$  and  $R$  are the radius of curvatures (RoC) of the substrate before and after deposition, respectively. Since both sputtered and electroplated film are amorphous or nanocrystalline, the intrinsic stresses aren't dependent on the underlying substrate.

We used double-side polished  $<001>$  silicon substrates for this study since its material properties are well understood. The results are applicable to other substrates, such as gallium nitride.

The radius of curvature of the wafer was measured using a Tencor Flexus laser scanning instrument. The sputter deposition was performed using a custom built AJA ATC 2200-V DC magnetron sputtering system. The Au electroplating was performed using a Technic SEMCON 1000 plating system. Film thickness was measured by lithographically patterning the blanket-deposited film

and etching trenches through the film to the substrate. A step profilometer was used to measure the step height of the trench, obtaining film thickness.

### Results and Discussion:

For TiW deposition, sputter pressures ranged from 2 mT Ar to 5 mT Ar. The depositions at each pressure were performed at 300W DC power for 10 mins. Stresses in the TiW film as a function of sputtering, calculated using the Stoney equation, are shown in Figure 2. The stress changed from compressive to tensile as the pressure increased. At higher pressures, there were more gas phase collisions before the deposition, reducing the kinetic energy of the atoms colliding with the substrate.

While TiW has good adhesion to many substrates, it's not stable and oxidizes easily. TiW/Au systems are often used in industry where the Au serves as a passivation layer. The Au sputter pressure is fixed at 5 mT. Figure 3 shows the overall stress in the TiW/Au calculated from the difference in RoC between a fresh Si wafer and a Si wafer with TiW/Au.

Electroplating was also investigated due to its industrial applications. Figure 4 shows stress of electroplating on a wafer as a function of current density, both with and without adjustments due to CTE. Because the stress is so low, it's determined that it's due only to the thermal expansion between electroplating and measurement times.

### Conclusions:

Electroplating stress is due to CTE mismatch and is lower than the stress due to sputtering. Though the stress due to electroplating is low, shear force is high due to the thickness of the film. Sputter deposition conditions had a large effect on the stress. While this information is vital to minimize the stress at metal/semiconductor interfaces and increase reliability, future research should investigate more sputter deposition pressures and temperatures.

### Acknowledgments:

My utmost gratitude goes to Ms. Wendy Ibsen, Kevin Jiang, Jonathan Cook, and Dr. Mark D'Evelyn, and the UCSB nanofabrication staff. I also acknowledge this extraordinary opportunity, courtesy of Soraa, UC Santa Barbara, and the NNIN REU Program. This research was funded by NSF Grant No. ECCS-0335765, and Grant No. ECCS-1125017.

### References:

- [1] Schubert, E. (2006). Light-emitting diodes (2nd ed.). Cambridge, UK: Cambridge University Press.
- [2] Smith, D. (1995). Thin-film deposition: Principles and practice. New York: McGraw-Hill.
- [3] Thornton, J., et al. Thin Solid Films, 171, 5-31 (1989).
- [4] Guilbaud-Massereau, et al. Thin Solid Films, 258, 185-193. (1998).

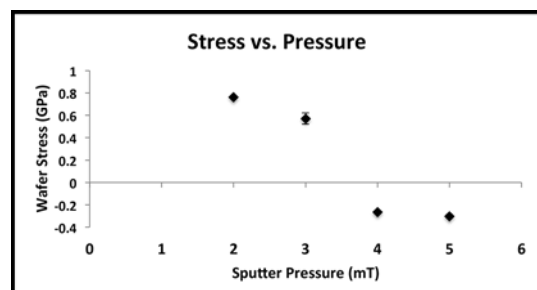


Figure 2: TiW stress due to pressure changes.

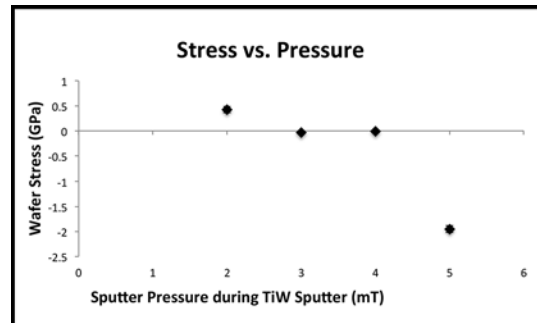


Figure 3: Stress change of sputtered Au as a function of different TiW pressures.

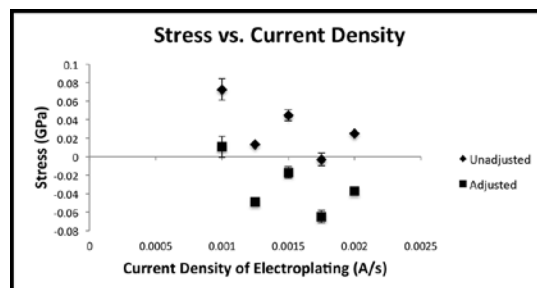


Figure 4: Stress vs. electroplating current density without adjustment for CTE and with adjustment for CTE.

# Nanofabrication and Characterization of Quasicrystal Metasurfaces Using Shadow-Sphere Lithography

Caroline Zellhofer

Mechanical Engineering, University of Maryland Baltimore County

**NNIN REU Site: Center for Nanoscale Systems, Harvard University, Cambridge, MA**

NNIN REU Principal Investigator: Professor George Whitesides, Dept. of Chemistry and Chemical Biology, Harvard University

NNIN REU Mentor: Dr. Alex Nemiroski, Nanotechnology Department, Illumina, Inc.

(Previously at Dept. of Chemistry and Chemical Biology, Harvard University)

Contact: caroz1@umbc.edu, gwhitesides@gmwgroup.harvard.edu, alex.nemiroski@gmail.com

## Abstract:

Quasi-crystals may have useful optical characteristics with applications in biosensing, however they have previously been difficult to fabricate, characterize, and simulate, as well as involving processes that are costly and time-consuming. This project focused on optimization of the quasicrystal fabrication and characterization process using template self-assembly and shadow-sphere lithography (SSL), a process of depositing metal, particularly gold, at different angles, onto a pattern of silica microspheres. The angle of deposition creates "shadows" behind the spheres, places where gold has not been deposited. Once the spheres are removed, these complex shadow patterns are left behind, with features as small as 20 nm visible. The quasi-crystals are fabricated in an array of 78 different quasi-crystals to be created on a single 50 mm × 100 mm surface. Being able to produce many quasi-crystals rapidly allows for the crystals to be characterized faster than they can be simulated. The self-assembly and SSL process have drastically decreased the time required to fabricate quasicrystals, reducing the time from days to make one quasicrystal to hours to make hundreds. Characterization of these quasicrystals has revealed sharp peaks in reflectance, which is useful in biosensing.

## Introduction:

Optical quasicrystal metasurfaces – patterned arrays of plasmonic nanoantennas that enable the precise manipulation of light – are emerging as critical components in many nanophotonic materials [1]. The development of these materials has been slowed by the difficulty of efficiently fabricating patterns with the required combinations of intricate nanoscale structure, high areal density, and/or heterogeneous composition. The only fabrication strategies that permit broad control over appropriate arrays use conventional photo-, electron-beam, and/or ion-beam lithography. These fabrication processes, however, are expensive, time-consuming, and often lack scalability. In addition, due to the small area of the quasicrystals fabricated, specialized equipment must be used to characterize the surfaces. Lastly, current technology is not robust enough to simulate the properties of the quasicrystals due to the complexity of the patterns.

To improve methods of processing quasicrystals, a previous method for processing, nanosphere lithography, was examined. Nanosphere lithography involved depositing gold directly onto spheres that were self-assembled in a hexagonal pattern. By depositing from directly above, the spheres create perfectly spherical shadows that block the gold and leave a pattern underneath. While simple, this method is limited in its complexity and customization, as it can only form honeycomb shadow patterns. The idea of

using nanosphere lithography to leave shadow patterns was combined with a more robust self-assembly process and angular deposition in order to create more complex, smaller features that retain definition.

## Experimental Procedure:

**Templated Self-Assembly.** Seen in Figure 1, the templated self-assembly reduces the time of fabrication from weeks to a few hours per sample, compared to more traditional methods [1]. The silicon template was created by first direct-writing a pattern into a mask using a micro pattern generator. The image on the mask was an array of 78 different quasicrystals, with various sizes and orientations. Being able to produce hundreds of quasicrystals in parallel allowed for these crystals to be fabricated and characterized within hours—much faster than they could be simulated.

The image on the mask was then projected five times smaller, using an i-line stepper, onto a 76.2 cm photoresist-covered silicon wafer. The pattern, each a single 3.5 × 7 mm rectangle, was repeated to cover the wafer. The wafer was then etched using a dry anisotropic etch, effectively etching the silicon where the photoresist was exposed. The spheres were assembled into the holes of the wafer, which measured slightly shallower than the diameter of the spheres, and then transferred to a glass slide using PDMS.

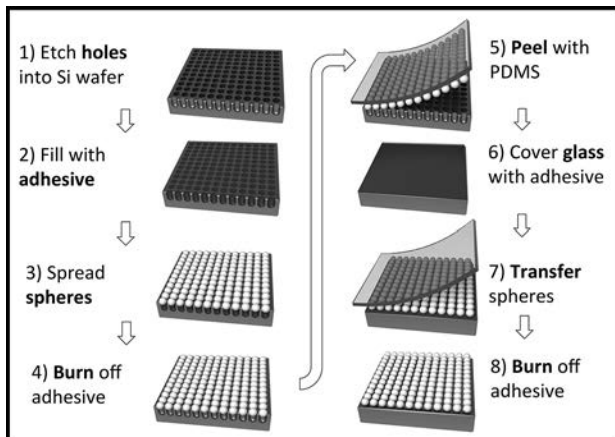


Figure 1: Diagram of the templated self-assembly process.

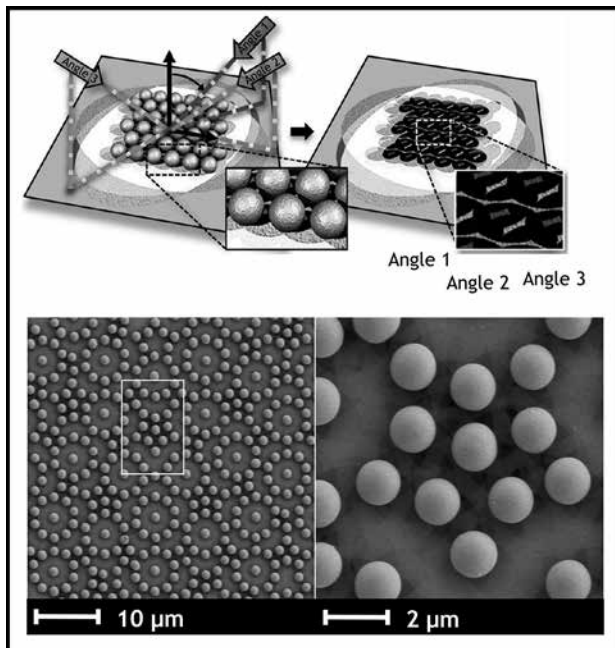


Figure 2: Top; Diagram of SSL process. Bottom; SEM of gold-coated microspheres, with shadow patterns visible underneath.

**Shadow-Sphere Lithography (SSL).** Shadow-sphere lithography was created by the Whitesides lab as a method to efficiently, cheaply, and quickly fabricate metasurfaces [1]. To fabricate, the glass substrate with the patterned microspheres on top was placed on a custom-made stage at anywhere between a  $45^{\circ}$ - $70^{\circ}$  angle to the horizontal inside an electron-beam evaporator. Using electron beam physical vapor deposition (EBPVD), a thin film of titanium was deposited onto the spheres. The titanium was deposited as an adhering layer between the gold and the glass. The sample was then rotated a set number of degrees and titanium was again deposited. The sample was rotated until all angles had been covered with titanium, and then gold was deposited at the same angles. The spheres were then removed using a simple piece of tape, leaving the shadow patterns — the places where the spheres blocked — behind, which can be seen in Figure 2.

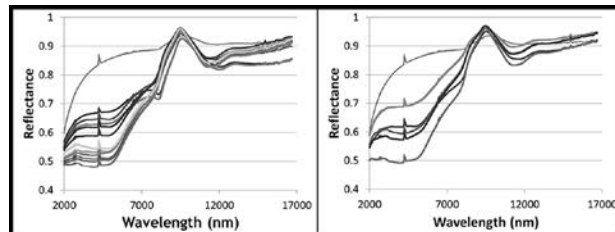


Figure 3: Left; Graph of reflectance from an FTIR scan from 2-17  $\mu$ m of one column. The topmost line is the background reflectance of the substrate. As the other lines approach the background, the orientation of the quasicrystal is rotated. Right; Graph of reflectance from an FTIR scan from 2-17  $\mu$ m of one row. The topmost line is the background reflectance of the substrate. The size of the spacing between the spheres is changed, creating more densely packed patterns and finer features. The lowest line belongs to the most densely packed pattern.

## Results:

The combination of template self-assembly and SSL resulted in repeatable, defined features as small as 20 nm, covering a space as large as 50 mm by 100 mm. A Fourier transform infrared spectroscopy (FTIR) scan revealed nothing of significance for transmission. Changing the rotational orientation and the spacing of the spheres in the template both revealed differences in the reflectance spectrums. The difference in spacing led to a sharper peak for the patterns with more densely packed spheres, where the shadow patterns are finer. These trends can be seen in Figure 3. The difference in rotational orientation led to an even spacing between the resulting lines on the graph, but seemingly had little effect on the sharpness of the peak.

## Conclusions:

In conclusion, templated self-assembly is possible and allows for a rapid, low-cost method of patterning spheres for the fabrication of quasicrystals. Shadow-sphere lithography creates fine features with replicable accuracy, and allows for quasicrystals to be created in parallel, which would be useful for high-throughput testing of sensors. Although more experiments are necessary to fully explore the properties of quasicrystalline metasurfaces, trends can be seen in changing the spacing of the spheres and the rotational orientation in an array of quasicrystals.

## Acknowledgements:

Special thanks to Dr. Baris Unal, and to the staff of Harvard University's Center for Nanoscale Systems. Funding was provided by the National Nanotechnology Infrastructure Network Research Experience for Undergraduates (NNIN REU) Program via the National Science Foundation, Grant No. ECCS-0335765.

## References:

[1] Nemirovski A, Gonidec M, Fox JM, Jean-Remy P, Turnage E, Whitesides GM. 2014. Engineering shadows to fabricate optical metasurfaces. *ACS Nano*. 8(11), pp 11061-11070.



# Index of Reports, by Site

## NNIN REU Sites:

**ASU NanoFab, Arizona State University, Tempe, AZ** ... 28, 30, 72, 174

**Cornell NanoScale Science and Technology Facility, Cornell University, Ithaca, NY** ... 14, 42, 120, 148, 154, 156, 176

**Institute for Electronics and Nanotechnology, Georgia Institute of Technology, Atlanta, GA** ... 36, 38, 54, 58, 108, 116

**Center for Nanoscale Systems, Harvard University, Cambridge, MA** ... 40, 98, 122, 146, 184

**Howard Nanoscale Science and Engineering Facility, Howard University, Washington, DC** ... 12, 74, 86, 102, 136

**Penn State Nanofabrication Laboratory, The Pennsylvania State University, University Park, PA** ... 62, 64, 76, 90, 100

**Stanford Nanofabrication Facility, Stanford University, Stanford, CA** ... 80, 82, 168, 172, 180

**UCSB Nanofabrication Facility, University of California, Santa Barbara, CA** ... 78, 112, 126, 166, 178, 182

**Colorado Nanofabrication Laboratory, University of Colorado, Boulder, CO** ... 70, 104, 130, 132, 150, 152

**Lurie Nanofabrication Facility, University of Michigan, Ann Arbor, MI** ... 34, 84, 114, 134, 142, 162

**Minnesota Nano Center, University of Minnesota-Twin Cities, Minneapolis, MN** ... 2, 20, 60, 158

**Microelectronics Research Center, The University of Texas, Austin, TX** ... 6, 66, 118, 128, 138

**Washington Nanofabrication Facility and Molecular Analysis Facility, University of Washington, Seattle, WA** ... 24, 56, 106, 124, 140, 164

**Nano Research Facility, Washington University in St. Louis, St. Louis, MO** ... 16, 18, 44, 46, 50

## NNIN iREG Sites:

**Institute for Electronics and Nanotechnology, Georgia Institute of Technology, Atlanta, GA** ... 52, 96

**Colorado Nanofabrication Laboratory, University of Colorado, Boulder, CO** ... 144

**Microelectronics Research Center, The University of Texas, Austin, TX** ... 110

## NNIN iREU Sites:

**Centre Microélectronique de Provence, École Nationale Supérieure des Mines de Saint-Étienne, France** ... 4, 10, 26

**National Institute for Materials Science (NIMS), Tsukuba, Ibaraki, Japan** ... 8, 22, 32, 48, 68, 88, 92, 94, 160, 170

# Index of 2015 NNIN Interns (in Bold), Mentors, and Principal Investigators

## A

<b>Acero, Victor Pablo</b> .....	2
<b>Alden, Joshua</b> .....	154
Alim, Marvin .....	150, 152
<b>Alsobrooks, Mary E.</b> .....	58
Andrich, Kathrin .....	16
Appel, Jennie .....	28
<b>Arias, Mariella</b> .....	4

## B

Ballew, Conner .....	140
Bank, Seth R. .....	138
Bao, Zhenan .....	180
<b>Barakat, Raymond</b> .....	6
Barsic, Anthony .....	132
Basu, Anindita .....	40
Beatty, Brian .....	96
<b>Bemis, Brian</b> .....	124
<b>Benson, Emilie</b> .....	60
<b>Benton, Tanaka</b> .....	74
Bersch, Brian .....	62
Bertoni, Mariana .....	72
Bhandari, Sagar .....	122
Bieschke, Jan .....	16
Bihar, Eloïse .....	10
Biswas, Pratim .....	18
Blain Christen, Jennifer .....	30
<b>Blankenbaker, Scott</b> .....	126
Boehm, Sarah .....	76
<b>Bostwick, Joshua</b> .....	166
<b>Bosworth, Allison</b> .....	8
Brasile, Bryan W. .....	128
Brljak, Nermina .....	76
<b>Brooks, Nathan</b> .....	130
Brower-Thomas, Tina .....	12
Brown-Heft, Tobias .....	178

## C

<b>Campbell, Jyoti</b> .....	46
Campbell, Philip .....	108
Caravaca Aguirre, Antonio Miguel .....	130
<b>Carberry, Benjamin</b> .....	78
Carothers, James M. .....	24
Castner, David G. .....	24
Chado, Garrett .....	104
Chae, Junseok .....	28
Chakravarty, Swapnajit .....	6
<b>Chase, Danielle</b> .....	114
Chavis, Michelle .....	86
Chen, Boxue .....	66
Chen, Guoping .....	32
Chen, Jiun-Ruey .....	176
Chen, Ray .....	6
Cherqui, Charles .....	164
<b>Chow, Scott</b> .....	168
<b>Cofell, Emiliana</b> .....	170
<b>Collette, Robyn</b> .....	156
Cook, Jonathan .....	166, 182
Cortese, Alejandro .....	154
Cui, Tianhong .....	2

## D

D'Evelyn, Mark .....	166, 182
Dauskardt, Reinhold H. .....	80, 82
<b>Davidson, Christopher</b> .....	10
Davidson, Patricia .....	42
<b>Demos, Catherine</b> .....	12
DenBaars, Steven .....	78
Devlin, Matthew .....	14
<b>DiGennaro, Isaac</b> .....	80
Ding, Laura .....	72
Du, Renzhong .....	64

**E**

Elborg, Martin .....	160
Enenbach, Molly .....	132
Engelmann, Shaun .....	16
Engstrom, James R. ....	176
Essigmann, Mikayla .....	172
Evans, Christopher .....	148
Evo, Yaset .....	134

**F**

Fedorchak, Gregory .....	42
<b>Flores, Raul</b> .....	174
Forest, Craig .....	36
Fortner, John .....	50
<b>Fostvedt, Jade</b> .....	82
Fragoza, Robert .....	14
<b>Franke, Christina</b> .....	18
<b>Frazier, Janay</b> .....	136
<b>Freas, Dylan J.</b> .....	48
Fryett, Taylor .....	124
<b>Fu, Harold</b> .....	138
<b>Fuhrman, Isaac</b> .....	50
Fujita, Daisuke .....	88
<b>Fukuzawa, Masashi</b> .....	52
Furbert-Harris, Paulette .....	12
<b>Furniturewalla, Abbas</b> .....	116

**G**

<b>Galarneau, Michelle</b> .....	20
Gawalt, David .....	118
<b>George, Tom</b> .....	84
Gibbons, Jonathan .....	156
<b>Gibson, Kasia</b> .....	140
Gonidec, Mathieu .....	98
Gonzalez, Federico Lora .....	126
<b>González López, Lorelis</b> .....	86
<b>Goodwill, Justin</b> .....	62
Gordon, Michael J. ....	126
Griffin, James .....	102, 136
<b>Guillen, Cristina</b> .....	142
<b>Gunawansa, Taliya</b> .....	88
Gund, Ved .....	120
Guo, L. Jay .....	84

**H**

Hainey, Jr., Mel .....	90
Hall, Neal A. ....	118
Hanagata, Nobutaka .....	22
Harris, Gary L. ....	74, 86, 102, 136
<b>Hayashi, Yusuke</b> .....	144
<b>Heppner, Jacob</b> .....	158
Hesketh, Peter .....	116
<b>Hill, Staci</b> .....	22
<b>Hittinger, Joseph P.</b> .....	24
Holmberg, Vincent .....	106
<b>Hu, Lucy</b> .....	26
<b>Hu, Sophia</b> .....	90
Huang, Rixiang .....	54
<b>Huber, Nathan</b> .....	64
<b>Hultz, Margot</b> .....	54

**I**

Imura, Masataka .....	68
<b>Innocent-Dolor, Jon-L</b> .....	92
Isaacson, Scott G. ....	82
Islam, Raisul .....	168
Ismailova, Esma .....	4

**J**

Jalan, Bharat .....	60
Jiang, Kevin .....	166, 182
Jiang, Taizhi .....	110
Jiang, Yi .....	50
Jing, Peifeng .....	140
Jun, Young-Shin .....	46

**L**

Lal, Amit .....	120
Lammerding, Jan .....	42
Lee, Chien-Chung .....	144
<b>Lee, Elizabeth</b> .....	<b>178</b>
Lee, Jason .....	56
Lee, Lap Man .....	114
Lee, Somin E. ....	162
Lee, Soohyung .....	106
Li, Qi .....	64
Li, Xianglan .....	22
Lin, Lih Y. ....	140
Liu, Allen .....	114
Liu, Chengyu .....	148
Liu, Ruxiu .....	38
Liu, Yongjian .....	44
Lončar, Marko .....	146
Lonjaret, Thomas .....	4
Lu, Xinran (Daniel) .....	20
<b>Lucas, Rachel</b> .....	<b>160</b>
Luscombe, Christine K. ....	56

**M**

<b>MacDonald, Emily</b> .....	<b>98</b>
<b>Magee, Abigail</b> .....	<b>30</b>
Mahdavifar, Alireza .....	116
Majumdar, Arka .....	124
Malliaras, George .....	4, 10
Marlar, Saw .....	8
Maruyama, Satofumi .....	92
Masiello, David .....	164
<b>Mathew, Marilyn</b> .....	<b>118</b>
McEuen, Paul .....	154
McLeod, Robert .....	150, 152
Miao, Ludi .....	64
<b>Miksi Kalayjian, Alin</b> .....	<b>56</b>
<b>Miller, Rachel</b> .....	<b>146</b>
Mohr, Daniel .....	158
Mori, Takao .....	92
Mu, Li .....	94
Mughal, Asad .....	78
<b>Mulero, Adriana</b> .....	<b>32</b>
<b>Murella, Anoosha</b> .....	<b>148</b>

**N**

Nakanishi, Jun .....	8
Nemirovski, Alex .....	98, 184
Newton, Michael A. ....	24
<b>Nguyen, Quang</b> .....	<b>162</b>
Nidetz, Robert .....	34
<b>Nietzold, Tara</b> .....	<b>68</b>
Noda, Takeshi .....	160

**O**

<b>O’Neil, Travis</b> .....	<b>100</b>
Obahiagbon, Uwa .....	30
Oh, Sang-Hyun .....	158
Ou, Tzu-Min .....	70
Owens, Roisin .....	26

**P**

Palmstrøm, Chris .....	112, 178
Pandres, Elena .....	106
Pappa, Anna-Maria .....	26
Park, Young Geun .....	162
<b>Pastor, Stephanie</b> .....	<b>102</b>
<b>Pauls, Tayler</b> .....	<b>34</b>
Pendharkar, Mihir .....	112
Perini, Christopher .....	96
<b>Phenicie, Christopher</b> .....	<b>104</b>
Phillips, Jamie .....	142
Piestun, Rafael .....	130, 132
<b>Pizzella, Elyse</b> .....	<b>106</b>

**Q**

Quillin, Steven .....	164
-----------------------	-----

**R**

Raliya, Ramesh .....	18
Ralph, Dan .....	156
<b>Randolph, Andrea</b> .....	<b>70</b>
Redwing, Joan .....	90
Robinson, Joshua .....	62
Rolston, Nick .....	80
<b>Rosner, Alexander</b> .....	<b>72</b>
<b>Rousseau, Erin</b> .....	<b>36</b>
Ruyack, Alexander .....	120
<b>Ryu, Brian</b> .....	<b>38</b>

**S**

Sagisaka, Keisuke .....	88
Sakaki, Hiroyuki .....	160
<b>Sanchez, Alejandro</b> .....	<b>40</b>
Sando, Shota .....	2
Saraswat, Krishna C. ....	168
Sarioglu, A. Fatih .....	38
<b>Schaffer, Zachary</b> .....	<b>120</b>
Schibli, Thomas .....	144
Schwartz, Jared M. ....	52, 58
Senesky, Debbie G. ....	172
Shankar, Ashwin .....	172
Sifferman, Scott D. ....	138
<b>Smith, Anna</b> .....	<b>180</b>
Sohn, YoungIk .....	146
<b>Soucy, Taylor</b> .....	<b>182</b>
<b>Statt, Michael</b> .....	<b>108</b>
Stoy, William .....	36
Stoykovich, Mark P. ....	104
Sun, Wen-cheng .....	174
Suntivich, Jin .....	148
<b>Swei, Anisa</b> .....	<b>42</b>

The NNIN REU Research Accomplishments are also available online:  
<http://nnin.org/reu/past-years/2015-nnin-reu-program>

**T**

Takai, Atsuro .....	48
Takeuchi, Masayuki .....	48
Tang, Yuanzhi .....	54
Tao, Meng .....	174
Tarasov, Alexey .....	108
Taylor, Crawford .....	74
Teng, Chu-Hsiang .....	134
Teran, Alan .....	142
<b>Thompson, Cyrus</b> .....	<b>44</b>
Tomita, Kentaro .....	170
Trolier-McKinstry, Susan .....	100
<b>Tsujiura, Yuichi</b> .....	<b>110</b>

**U**

Uosaki, Kohei .....	170
---------------------	-----

**V**

<b>Valerino, Michael</b> .....	<b>150</b>
Van Zeghbroeck, Bart .....	70
Vogel, Eric M. .....	96, 108

**W**

Wang, Laidong .....	174
Wang, Xinlong .....	32
Wang, Zheng .....	66
Weitz, David .....	40
<b>Werner, Veronika</b> .....	<b>112</b>
<b>West, Claire</b> .....	<b>164</b>
Westervelt, Robert .....	122
Whitesides, George M. ....	98, 184
Wood, David .....	20
Wu, Jingda .....	140

**X**

Xu, Andrew .....	60
------------------	----

**Y**

<b>Yang, Bilan</b> .....	<b>122</b>
Ye, Jinhua .....	94
Yee, Shannon .....	116
Yeo, Hong Goo .....	100
Yoo, Daehan .....	158
Yu, Edward T. .....	128
Yu, Haiyuan .....	14

**Z**

Zellhofer, Caroline .....	184
Zhan, Alan .....	124
Zhang, Cheng .....	84
Zhang, Zhongjian .....	128
Zhao, Yongfeng .....	44
Zou, Zongsen .....	46
<b>Zurek, Philip</b> .....	<b>152</b>



**It was a grand summer — thank you!**  
**Melanie-Claire**



<http://www.nnn.org/>